

ELECTRON AND ION BEAM SCIENCE AND TECHNOLOGY

SIXTH INTERNATIONAL CONFERENCE

Edited by

Robert Bakish
Bakish Materials Corporation
Englewood, New Jersey

With the editorial assistance of

Anthony J. Gonzales
Motorola Incorporated
Phoenix, Arizona

Alex N. Broers
IBM Thomas J. Watson
Research Center
Yorktown Heights, New York

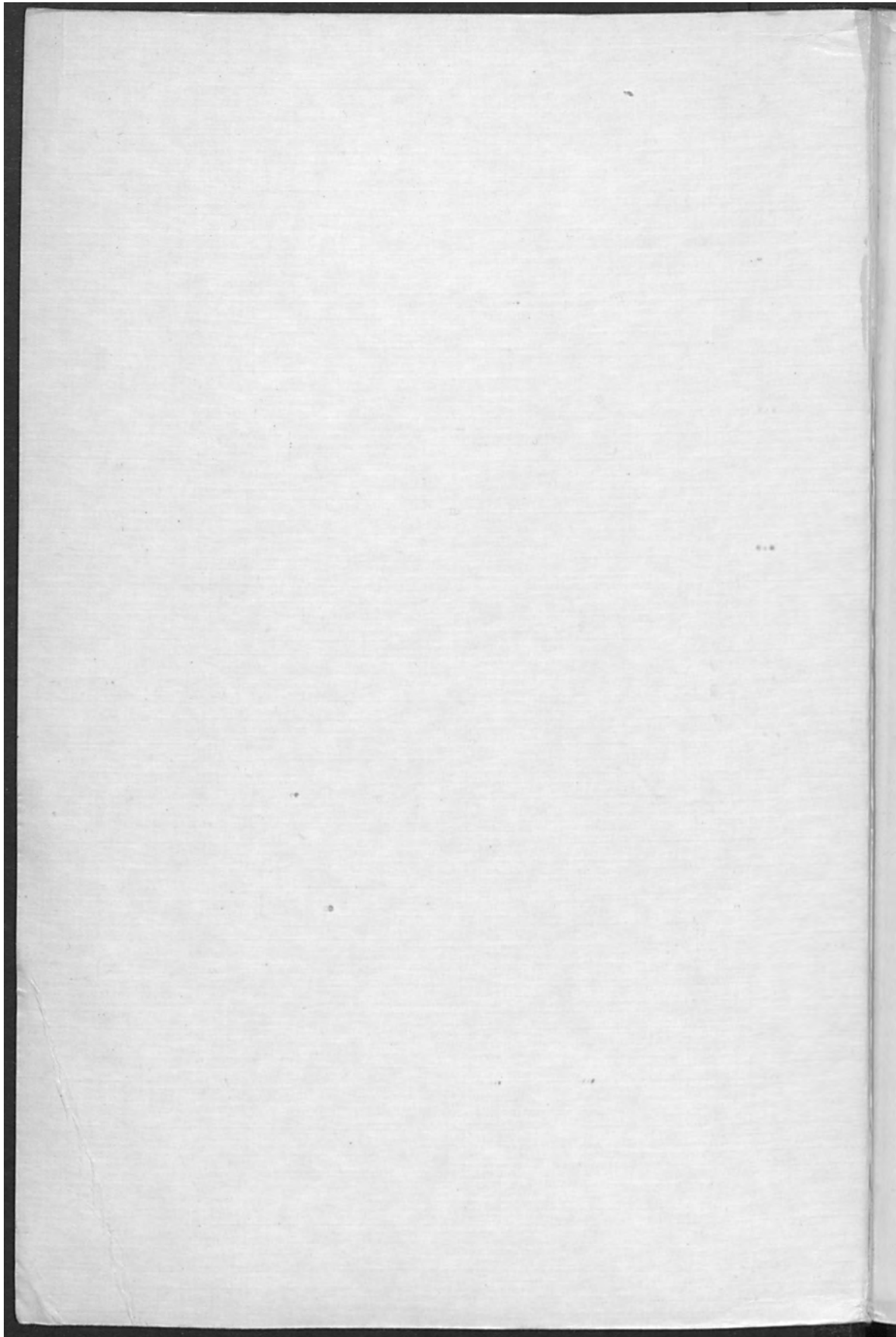
Kurt Amboss
Hughes Research Laboratories
Malibu, California

Henry I. Smith
Lincoln Laboratories
Massachusetts Institute of Technology
Lexington, Massachusetts



ELECTROTHERMICS AND METALLURGY AND ELECTRONICS DIVISIONS

THE ELECTROCHEMICAL SOCIETY, INC., Post Office Box 2071,
Princeton, New Jersey 08540



ELECTRON AND ION BEAM SCIENCE AND TECHNOLOGY

SIXTH INTERNATIONAL CONFERENCE

Edited by

Robert Bakish
Bakish Materials Corporation
Englewood, New Jersey

With the editorial assistance of

Anthony J. Gonzales
Motorola Incorporated
Phoenix, Arizona

Kurt Amboss
Hughes Research Laboratories
Malibu, California

Alex N. Broers
IBM Thomas J. Watson
Research Center
Yorktown Heights, New York

Henry I. Smith
Lincoln Laboratories
Massachusetts Institute of Technology
Lexington, Massachusetts



ELECTROTHERMICS AND METALLURGY AND ELECTRONICS DIVISIONS

THE ELECTROCHEMICAL SOCIETY, INC., Post Office Box 2071,
Princeton, New Jersey 08540

SYMPOSIUM ON ELECTROCHEMISTRY
IN ELECTRON AND ION BEAM
SCIENCE AND TECHNOLOGY
AND INTERNATIONAL CONFERENCE

Copyright 1974

by

The Electrochemical Society, Incorporated

*Papers contained herein may not be
reprinted and may not be digested by pub-
lications other than those of The Electrochemical
Society in excess of 1/6 of the material presented.*

Library of Congress Catalog Card Number: 71-120300

Printed in the United States of America

TABLE OF CONTENTS

Preface	vii
Introductory Remarks	ix
Conference Committee and Session Chairmen and Vice-Chairmen	xi
Progress in X-Ray Lithography	
J. H. McCoy and P. A. Sullivan.....	3
X-Ray Lithographic Fabrication of Blazed Diffraction Gratings	
A. R. Neureuther and P. I. Hagouel.....	23
X-Ray Lithography Applied to Silicon Device Fabrication	
S. E. Bernacki and H. I. Smith.....	34
Electron-Resist Exposure Contours for Various Patterns	
R. E. Jewett, T. Van Duzer, and J. S. Greeneich.....	49
Properties of Metal Acrylate Compositions as X-Ray Resists	
R. G. Brault.....	63
High Speed Electron Resists	
T. L. Brewer.....	71
Effect of Olefin Structure on the Electron Beam Vaporization of Poly(Olefin Sulfones)	
M. J. Bowden and L. F. Thompson.....	81
Experimental Utilization of Monte Carlo Models for Electron Beam Lithography	
R. J. Hawryluk, A. Soares, H. I. Smith, and A. M. Hawryluk.....	87
High Speed Electron Beam Pattern Generation	
G. L. Varnell, D. F. Spicer, A. C. Rodger, and R. D. Holland.....	97
A Modular System for Electron Beam Microfabrication	
N. C. Yew.....	111
Electron Image Projector	
J. P. Scott.....	123
Elemental Analysis with Auger Electron Spectroscopy and Secondary Ion Mass Spectrometry	
J. M. Morabito.....	139

Contactless Short/Open Test Method Using Two Electron Beams	
H. Engelke.....	153
A Versatile In-Depth Analyzer	
K. Wittmaack, J. Maul, and F. Schulz.....	164
Junction Depth Measurements in a Scanning Electron Microscope	
J. D. Schick.....	177
A Simple Method for Studying Deflection Aberrations in the Scanning Electron Microscope	
W. J. DeVore.....	188
Measurement of the Grueneisen Parameter of Two Dimensional Carbon Phenolic (2DCP)	
R. D. Evans.....	196
Monte Carlo Simulation of Electron Beam Scattering and Energy Loss in Thin Films on Thick Substrates	
D. F. Kyser and K. Murata.....	205
Photoluminescence and Channeling Study on Annealing Behavior of Te Ion-Implanted GaAs	
M-S. Lin, K. Gamo, K. Masuda, and S. Namba.....	226
Micro Ion Milling of Electronic Devices with 1μ Periodicity	
D. F. Bazzarre and R. W. Barr.....	241
Magnetically Enhanced High-Rate Sputtering	
R. L. Cormia, P. S. McLeod, and N. K. Tsujimoto.....	248
Ion Plating - Review and Update	
D. M. Mattox.....	254
High Volume Production of Automotive Components by Electron Beam Welding	
H. A. James.....	264
Considerations of Nonvacuum Electron Beam Welding Capabilities and Applications	
J. M. Wells.....	287
Application of Electron Beam Welding to the Heavy Constructions	
R. Roudier.....	307

Electron Beam Welding of MM Waveguide Flanges B. T. Barcelo and E. J. Canning.....	319
Some Investigations in Non-Vacuum EB-Welding V. Bödecker, W. Jüptner, and H.-D. Steffens.....	337
Effect of Welding Parameters on the Penetration in Electron Beam Welding P. Dumonte and G. Sayegh.....	346
Influence of the Spatial Intensity Distribution on Deep Welding Geometry W. Jüptner, V. Bödecker, and G. Sepold.....	366
Shape Decision of High Energy Density Beam Y. Arata, M. Tomie, K. Terai, H. Nagai, and T. Hattori.....	377
Quantitative Analysis of Spiking Behavior A. M. Joglekar, S. J. Deutsch, and R. A. Moll.....	399
The Physical Fundamentals of Thin Film Machining S. Schiller, S. Panzer, and U. Heisig.....	412
Electron Beam Machining - The Process and Its Applications D. v. Dobeneck and A. Parrella.....	431
On the Electron-Metal Vapour Interaction in High-Power Evaporators S. Schiller and G. Jäsch.....	447
Limitation of Ring Type Electron Gun Efficiency as a Result of Magnetron Effect K. P. Friedel.....	457
The Neptune-C Pulsed Electron Beam R. S. Wenstrup.....	469
Charged Particle Acceleration with Intense Relativistic Electron Beams D. C. Straw and R. B. Miller.....	482
The Design of Large Area Electron Beam Guns K. Amboss.....	497
Low Perveance Ion Beam Extraction from an Electron Bombardment Discharge R. L. Seliger and J. W. Ward.....	518

Mask Alignment by X-Ray Method in an Electron Projection System	
B. Fay.....	527
A Large Field Deflection System for Scanning Electron Beam Technology	
G. Owen and W. C. Nixon.....	534
Fundamental Aspects of Electron Beam Exposure of Polymeric Resist System	
M. Hatzakis, C. H. Ting, and N. Viswanathan.....	542
Electron Beam Lithography for Complex High Density Devices	
T. H. P. Chang, A. D. Wilson, A. J. Speth, and A. Kern.....	580
Subject Index.....	589

PREFACE

This volume contains most of the papers presented at the Sixth International Conference on Electron and Ion Beam Science and Technology held during the San Francisco, California, Meeting of The Electrochemical Society, May 12-17, 1974. With the exception of one paper which was submitted for publication to J. Electrochem. Soc., the missing papers failed to reach the Editor in time to meet the twice extended deadline for submission of manuscripts. While it is important to have a complete record of a conference, it is perhaps even more important to be able to disseminate its substance to the public at large, to those who were unable to attend the San Francisco Meeting, while the material is still timely. In all this volume contains 42 papers divided into three parts as follows:

Part I consists of five sections. The first section presents the x-ray lithography papers which were presented in the first session of the meeting. This is an exciting new approach with interesting potential in the microelectronics field. The second section contains the papers dealing with electron photoresists; these papers constituted the second session of the meeting. The third section contains the papers dealing with electron projection systems, while the fourth section's papers deal with various analytical aspects of this technology. The last and fifth section here is comprised of the papers on ion implantation and related subject matter. One can look at all of the papers in Part I and say that in one way or another their substance is related to microfabrication of solid-state devices, an area in which both electron and ion beams have gained increased importance.

Part II of this volume consists of papers dealing with high power beams, and here the papers are divided into two sections, the first containing the papers on electron beam welding, machining, and evaporation. The greatest number of papers here are those dealing with various aspects of electron beam welding which has become an important industrial joining technique. The second section contains papers dealing with relativistic electron beams, an area where considerable future applied potential is envisaged by some.

Part III contains the papers which arrived within a couple of weeks of the submission of the manuscript of this volume to the printer. They were received several months past all deadlines, and as a consequence, they are not indexed, yet it was felt that their inclusion here was important despite this fact.

In closing I wish to thank those of The Electrochemical Society staff whose task will be the conversion of this manuscript into a Society symposium volume. Sincere thanks are due to Anthony J. Gonzales and to Henry I. Smith, as well as to my good old friends Kurt Amboss and Alec Broers for reviewing some papers.

R. Bakish
Englewood, New Jersey
November 1974

MEMORANDUM

This volume contains the report of the papers presented at the International Conference on Electrostatics and Dielectric Phenomena held during the 28th Annual Meeting of the Electrostatic Society, May 12-17, 1966. The program was arranged for publication by the Electrostatic Society. The papers were arranged in two parts: Part I, containing papers on the theory of electrostatics, and Part II, containing papers on the applications of electrostatics. The papers were arranged in order of presentation at the conference. This volume contains 43 papers divided into three parts as follows:

Part I consists of 15 papers. The first section presents the theory of electrostatics. The second section contains papers on the applications of electrostatics. The third section contains papers on the theory of electrostatics. The fourth section contains papers on the applications of electrostatics. The fifth section contains papers on the theory of electrostatics. The sixth section contains papers on the applications of electrostatics. The seventh section contains papers on the theory of electrostatics. The eighth section contains papers on the applications of electrostatics. The ninth section contains papers on the theory of electrostatics. The tenth section contains papers on the applications of electrostatics. The eleventh section contains papers on the theory of electrostatics. The twelfth section contains papers on the applications of electrostatics. The thirteenth section contains papers on the theory of electrostatics. The fourteenth section contains papers on the applications of electrostatics. The fifteenth section contains papers on the theory of electrostatics.

Part II of this volume consists of 28 papers dealing with high power beams, and here the papers are divided into two sections: the first section contains papers on electron beam welding, machining, and coating. The second section contains papers on electron beam welding with various applications. The third section contains papers on electron beam welding with various applications. The fourth section contains papers on electron beam welding with various applications. The fifth section contains papers on electron beam welding with various applications. The sixth section contains papers on electron beam welding with various applications. The seventh section contains papers on electron beam welding with various applications. The eighth section contains papers on electron beam welding with various applications. The ninth section contains papers on electron beam welding with various applications. The tenth section contains papers on electron beam welding with various applications. The eleventh section contains papers on electron beam welding with various applications. The twelfth section contains papers on electron beam welding with various applications. The thirteenth section contains papers on electron beam welding with various applications. The fourteenth section contains papers on electron beam welding with various applications. The fifteenth section contains papers on electron beam welding with various applications. The sixteenth section contains papers on electron beam welding with various applications. The seventeenth section contains papers on electron beam welding with various applications. The eighteenth section contains papers on electron beam welding with various applications. The nineteenth section contains papers on electron beam welding with various applications. The twentieth section contains papers on electron beam welding with various applications. The twenty-first section contains papers on electron beam welding with various applications. The twenty-second section contains papers on electron beam welding with various applications. The twenty-third section contains papers on electron beam welding with various applications. The twenty-fourth section contains papers on electron beam welding with various applications. The twenty-fifth section contains papers on electron beam welding with various applications. The twenty-sixth section contains papers on electron beam welding with various applications. The twenty-seventh section contains papers on electron beam welding with various applications. The twenty-eighth section contains papers on electron beam welding with various applications.

Part III contains the papers which arrived within a month of the submission of the manuscript of this volume to the publisher. They were received several months past all deadlines, and as a consequence, they are not indexed, yet it was felt that their inclusion was an important feature of this book.

In closing I wish to thank those of the Electrostatic Society staff whose help will be the conversion of this manuscript into a book. Special thanks are due to Anthony J. Conner and to Henry L. Smith, as well as to my good old friends Jack Johnson and Alan Bowers for reviewing these papers.

L. Smith
Englewood, New Jersey
November 1966

INTRODUCTORY REMARKS

In the Programming Session early this year, with a number of scheduling problems, no time was set aside for Introductory Remarks. As a Conference Co-Chairman and a Proceedings Editor I am taking a couple of pages here to rectify this omission.

The Sixth International Conference on Electron and Ion Beam Science and Technology, held during the San Francisco, California, Meeting of The Electrochemical Society, May 12-17, 1974, was a worthwhile get together. The Conference was part of a biannual series and had a crowded schedule both in terms of the number of presentations (54) and in terms of attendance at the sessions, with attendees exceeding 180 in many instances. This is the longest duration series of conferences sponsored by The Electrochemical Society and after 12 years it appears to show continued vigor and spirit. Scientific effort in the area is much in evidence and is producing developments with potential for, in the process of transition to and in technology, providing financial returns to managements supporting this scientific effort.

At the inaugural conference held in Toronto in 1962, high power beams in melting and refining had completed the cycle and things were just about beginning to move in welding. Today we are talking of a multimode welding process with important penetration in virtually all industrial domains. The impact of low power electron and ion beams in the analytical area has been even broader, and problems solved with devices using these beams have made a major contribution to corporate profits in a broad spectrum of industrial domains. The day is most rapidly approaching when no solid-state device could be produced without a major reliance on electron and/or ion beams in some aspects of its manufacturing process, production control process, and/or failure analysis.

It is perhaps the productivity of the technology that has provided management with sufficient incentive to continue the support of its research and development as reported here. I am confident that this trend will continue in the future as it has in the past, and lead to new scientific breakthroughs followed by developments and profitable products. It is this peculiarity of electron and ion beam science and technology, coupled with its most extensive diversity in applications, which has provided the "fuel" for our conferences over the years.

The long time span of activities in connection with this series of conferences has developed personal relationships and many friendships among individuals working in the field the world over. To many these relationships are as important as the technical substance of the conferences, and it is here, and through personal contacts in the ultimate, that we scientists and engineers can contribute to the resolution of the problems between East and West. In this series of conferences we have certainly endeavored through the years to maintain, improve, and expand these contacts.

At this time I wish to take the opportunity to thank Anthony J. Gonzales of Motorola Inc. who co-chaired the event and who helped in the development of the program. Thanks are due to all conference committee members, the ones who over the years past and again in connection with this conference have lent generously of their time to help gather from their respective lands the contributions which render strength and dynamism to the conference. Thanks are due to the Electrothermics and Metallurgy and the Electronics Divisions of The Electrochemical Society for co-sponsoring this event. Thanks are also due to The Electrochemical Society for its continued support of this worthwhile endeavor, and in particular to its Headquarter's staff for its readiness to provide needed assistance. Last but perhaps the most sincere thanks are offered to those who contributed papers to and discussion during the conference. In the final analysis it is they who made the event what it was. We again met our conference objectives: to monitor and record progress in electron and ion beam science and technology, to monitor their impact on our society, to disseminate this information, and to expand individual contacts and further cooperation among engineers and scientists working in the field.

May I kindly remind all of you that the completion of activities of one conference, which the publication of its proceedings is, signals the beginning of activities for the next one. Yes, we are indeed beginning to plan our seventh conference which will coincide with the 200th anniversary of our nation. Coincidentally, it will take place in Washington, D.C. I hope all of you will plan to be present and yours truly will be on hand to welcome you.

R. Bakish
Englewood, New Jersey
November 1974

CONFERENCE COMMITTEE AND SESSION CHAIRMEN AND VICE-CHAIRMEN

- M. Allais, C.I.T.-Alcatel, Centre P. Hereng, 91 Bruyere le Chatel,
France
- K. Amboss, Hughes Research Laboratories, Malibu, California
- R. Bakish, Bakish Materials Corporation, Englewood, New Jersey and
Farleigh Dickinson University, Teaneck, New Jersey
- W. Barwicz, Unitra O.B.R.E.P., Ul. Długa 44/50, Warsaw, Poland
- E. Bas, Swiss Federal Polytechnic Institute, Zurich, Switzerland
- F. Benesowski, Metalwork Plansee, Reutte/Tyrol, Austria
- M. Boston, Torvac Limited, Histon, Cambridge, England
- A. N. Broers, IBM Thomas J. Watson Research Center, Yorktown Heights,
New York
- D. L. Crosthwait, Semiconductor Research and Development Laboratories,
Dallas, Texas
- L. Derose, Ebtac Corporation, Agawam, Massachusetts
- A. J. Gonzales, Motorola Incorporated, Phoenix, Arizona
- L. Habraken, CNRM, Liege, Belgium
- M. Hatzakis, IBM Thomas J. Watson Research Center, Yorktown Heights,
New York
- C. Hayashi, Ulvac Corporation, 2500 Hagusano, Chigasaki City,
Kanagawa, Japan
- A. E. Jenkins, University of New South Wales, N.S.W., Australia
- J. G. Kelly, Sandia Corporation, Albuquerque, New Mexico
- H. Koch, Schweistechische Lehr und Versuchsanstalt, Mannheim, West
Germany
- N. C. MacDonald, Physical Electronics Industries Corporation, Edina,
Minnesota
- J. H. McCoy, Hughes Research Laboratories, Malibu, California

CONFERENCE COMMITTEE AND SESSION CHAIRMEN AND VICE-CHARIMEN CONTINUED

- G. Molenstedt, University Tubingen, Tubingen, West Germany
- S. Namba, The Institute of Physical and Chemical Research, Tokyo, Japan
- W. C. Nixon, Cambridge University, Cambridge, England
- N. A. Olshanski, Moscow Power Institute, Moscow, U.S.S.R.
- B. Paton, Institute for Electro-Welding, Kiev, U.S.S.R.
- P. Rose, Extrion, Peabody, Massachusetts
- J. G. Siekman, Philips Research Laboratories, Eindhoven, Holland
- G. Slodzian, University of Paris, Centre d'orsay-91, Orsay, France
- W. W. Smeltzer, McMaster University, Hamilton, Ontario, Canada
- H. I. Smith, Lincoln Laboratories, Massachusetts Institute of Technology, Lexington, Massachusetts
- F. J. Streiter, Texas Instruments Incorporated, Dallas, Texas
- M. von Ardenne, am Weisen Hirsch, Dresden, East Germany
- R. W. Wilson, Motorola Incorporated, Phoenix, Arizona
- O. Winkler, Balzers AG, Balzers, Lichtenstein

PROGRESS IN X-RAY LITHOGRAPHY

J. H. McCoy and P. A. Sullivan
Hughes Research Laboratories
Malibu, California 90265

ABSTRACT

Exposure requirements for off-contact printing with x-rays show that geometrical distortions are a limitation on the resolution over large areas. Tradeoffs in the design of a soft x-ray source are discussed and it is shown that if it is desired to maintain 0.5 μ m resolution over a 2.5 cm diameter area and the mask-to-substrate gap is 5 μ m, then a 3 kW aluminum K α x-ray source is required to achieve one-minute exposure times on a sensitive resist (5 mJ/cm²) with a 50% transmissive silicon mask, unless some other form of illumination can be implemented. Modified processes for making the established gold-on-silicon mask are given. The exposure sensitivities of polydimethyl methacrylate and Kodak Micro Resist 931 were determined to be 500 and 72 mJ/cm², respectively. A stress analysis of a silicon mask shows the maximum stress during an x-ray dose above 80 μ W/cm² is 100 MPa. A procedure differential thermal analysis was used to determine the thermal expansion of a 5 μ m aluminum vacuum window. The design and fabrication of a mask alignment system with a goal of 0.5 μ m accuracy are discussed.

PART I

Section 1

X-Ray Lithography

INTRODUCTION

The use of soft x-rays rather than ultraviolet light for the exposure of resists in the lithography of submicron patterns for optical and electron devices shows promise for the practical production of such devices. The original results of Speare and Smith¹ and Smith, Speare, and Bernicki² have been verified, and we report here our contributions to this new technology.

Specifically, we discuss some background for this research: exposure requirements, tradeoffs in the design of an x-ray source, our processing sequence for the fabrication of gold-on-silicon masks, exposure results, a thermal model for this mask structure, a soft x-ray vacuum window, and a mask alignment system.

MEMORANDUM FOR THE RECORD

DATE: 10/15/54

TO: SAC, NEW YORK

FROM: SA [Name], NEW YORK

SUBJECT: [Subject]

RE: [Subject]

[Text]

[Text]

[Text]

[Text]

[Text]

[Text]

[Text]

[Text]

[Text]

[Text]

[Text]

[Text]

[Text]

[Text]

[Text]

[Text]

[Text]

[Text]

[Text]

[Text]

[Text]

[Text]

[Text]

PROGRESS IN X-RAY LITHOGRAPHY

J. H. McCoy and P. A. Sullivan
Hughes Research Laboratories
Malibu, California 90265

ABSTRACT

Exposure requirements for off-contact printing with x rays show that geometrical distortion is a limitation on the resolution over large areas. Tradeoffs in the design of a soft x-ray source are discussed and it is shown that if it is desired to maintain 0.2 μm resolution over a 2.5 cm diameter area and the mask-to-substrate gap is 5.0 μm , then a 9 kW aluminum anode x-ray source is required to achieve two-minute exposure times on a sensitive resist (5 mJ/cm^2) with a 50% transmissive silicon mask, unless some other form of collimation can be implemented. Modified processes for making the established gold-on-silicon mask are given. The exposure sensitivities of polymethyl methacrylate and Kodak Micro Resist 747 were confirmed to be 500 and 72 mJ/cm^2 , respectively. A thermal and stress analysis of a silicon mask shows the need for cooling for an x-ray flux above 80 $\mu\text{W}/\text{cm}^2$. Two-atmosphere pressure differential was achieved with a 2-in. diameter, 8.5 μm aluminum vacuum window on a 2.3 mm hexagonal grid. The design and fabrication of a mask alignment system with a goal of 0.1 μm accuracy are discussed.

INTRODUCTION

The use of soft x rays rather than ultraviolet light for the exposure of resists in the lithography of submicron patterns for optical and electron devices shows promise for the practical production of such devices. The original results of Spears and Smith^{1,2} and Smith, Spears, and Bernacki³ have been verified, and we report here our contributions to this new technology.

Specifically, we discuss some background for this research, exposure requirements, tradeoffs in the design of an x-ray source, our processing sequence for the fabrication of gold-on-silicon x-ray masks, exposure results, a thermal model for this mask structure, a soft x-ray vacuum window, and a mask alignment system.

Additional exposure results using the gold-on-silicon x-ray masks are reported by Brault⁴ in a paper describing a new x-ray sensitive resist.

BACKGROUND

At Hughes Research Laboratories, an extensive capability for fabrication of devices with submicron dimensions using a computer-controlled scanning electron beam system has been developed by Ozdemir, Wolf, and Buckley.⁵ Acoustic surface wave devices⁶ and integrated optic structures⁷ have been fabricated, and FET processes⁸ are being developed which require the submicron resolution and registration capability of this pattern delineation system. Other laboratories have used electron lithography for the fabrication of IGFET circuitry.^{9,10} A technique for replicating such electron beam generated patterns has been sought for two purposes: to reduce the time and costliness of generating patterns serially on every device, and to reproduce accurately a specific pattern many times with perfect fidelity. The latter requirement relates to the fabrication of identical acoustic surface wave signal processing devices.

We studied several approaches and concluded that x-ray lithography offers the greatest promise for fulfilling our requirements for a replication system. Contact and projection photolithography ultimately suffer from the diffraction of light from submicron line patterns. In addition, there is reflection of light from interfaces and scattering of light in the resist polymer. Even though Smith¹¹ has demonstrated that conformable glass photolithography can produce well-defined 0.4 μm wide structures in positive resist, and we also have reproduced acoustic surface wave transducers containing 635, 0.6 μm wide aluminum lines by liftoff of such patterns,¹² this technique does require high pressure contact and is applicable only to substrates with exceptional flatness. It would not be suitable for processing semiconductor wafers.

Electron projection lithography, using 1:1 projection from a masked photocathode, has been pursued as a replication technology at several laboratories.¹³⁻¹⁶ Koops¹⁷ has discussed projection of a demagnified electron image. Systems using electrons for exposure suffer from several drawbacks: (1) electron images are subject to aberrations and distortion by imperfect lenses and stray fields, (2) electron exposed resists are subject to line broadening by back-scattered electrons from the substrate, especially when submicron width lines are produced at a pitch less than 2.0 μm , and (3) the substrate must be placed in vacuum.

X-ray lithography does not suffer these rather fundamental problems, and we believe it will ultimately prove to be the superior system for replication of device patterns with submicron dimensions.

Some advantages of this approach are

- Large area parallel exposure
- Mask fabricated by scanning electron lithography
- 0.1 μm resolution
- Off contact exposure (10 μm)
- Insensitive to dust and low atomic number contamination
- Use of positive or negative resists
- Uniform exposure with depth
- No requirement to place the mask or substrate in vacuum.

In this paper we examine some of the limitations of x-ray lithography and present our progress. Our immediate goal is the fabrication of an acoustic surface wave device and a FET with sub-micron dimensions using the device patterns and processing technology being developed by Wolf, et al.,⁶ and Ozdemir.⁸

EXPOSURE REQUIREMENTS

The exposure of sensitive resists through a contact mask by soft x rays is the basis of x-ray lithography. The x rays may be produced by electron bombardment of a suitable target such as aluminum which produces characteristic x rays at 8.34 \AA . A typical exposure geometry is shown in Fig. 1. The important features are the x-ray source of diameter A, the mask with absorbing and transmitting areas, and the resist coated wafer of diameter D which is separated from the mask by a gap s. Although very small, this gap must inevitably exist to a measurable degree over some part of the mask-to-substrate interface. In fact, it has been proposed that a significant advantage of x-ray lithography is that the gap can be made relatively large in order to avoid contact damage and to allow movement for mask registration. No loss in resolution results from diffraction across the gap. Two other effects, however, degrade the results. Referring to Fig. 1(a), a point x-ray source produces a geometric distortion Δ at the edge of the wafer. With a practical source of diameter A, penumbral shadowing δ occurs, as shown in Fig. 1(b), at the center of the wafer. One should consider the worst case of both penumbral shadowing and geometric distortion which occurs at the edge of a wafer, with a finite source size, as shown in Fig. 1(c). This combined error is denoted by p. To make p a small fraction of s, the source distance d must be large compared with the diameter D.

The resolution parameter p may be expressed as

$$p = \frac{s}{d} \left(\frac{A}{2} + \frac{D}{2} \right) . \quad (1)$$

In order to optimize the x-ray source size and distance, it is necessary to consider the exposure flux at the wafer and the maximum power dissipation permissible in the anode. A reasonable thermal model for the soft x-ray source is that all the electron beam energy is dissipated in a circle of diameter A on a semi-infinite solid of thermal conductivity K. The temperature rise ΔT at the center of the circle is then¹⁸

$$\Delta T = \frac{W}{2AK} \text{ or } W_{\text{max}} = \Delta T 2AK, \quad (2)$$

where W is the input power in watts, A in cm, and K in $W/^\circ\text{C-cm}$.

Maximum power can be obtained by increasing T above the melting point of the material. A molten aluminum anode has been used in an x-ray lithography system by Smith, et al.³ A simple 45° heat-spreading model can be used to account for a liquid zone at the target

$$W_{\text{max}} = F_{\text{th}} A \quad (3)$$

for a thermal factor,

$$F_{\text{th}} = (T_A - 660) 2K_l + (660 - T_w) 2K_s \quad (4)$$

where T_A is the maximum temperature of the liquid surface, T_w is the cooling water temperature, 660°C is the melting point of aluminum, and K_l and K_s are the thermal conductivities of the liquid and the solid, respectively. Numerical values of $K_s = 2.37$, $K_l = 1.21$, and $T_w = 30^\circ\text{C}$ results in

$$F_{\text{th}} = 2.4 (T_s - 660) + 2980 \quad (5)$$

From Langmuir's relationship,¹⁹ the rate of evaporation for aluminum on a shield 10 cm away is only $0.1 \mu\text{m/h}$ at 975°C . Using this value for T_A results in $F_{\text{th}} = 3700 \text{ W/cm}$. Thus,

$$W_{\text{max}} = 3700 A \quad (6)$$

It should also be possible to fabricate a composite anode target since the aluminum layer needs to be only $2 \mu\text{m}$ thick to stop all the electrons. If the base material is copper, a K_s value of 4 may be inserted into either eq. (2) or (4). Operation just at the melting point of aluminum results in a value of $F_{\text{th}} = 5000$. A significant feature of these formulas is that the maximum power is proportional to the diameter and not the area of the source.

The exposure requirement must take into account the inverse square law dependence of the x-ray flux as a function of distance from the source. The flux Φ can be calculated from

$$\Phi = I\epsilon hv/d^2 = \frac{W\epsilon hv}{Vd^2} \quad (7)$$

where I is the electron current, V is the accelerating potential, ϵ is the electron-to-photon quantum conversion efficiency of the anode (measured in photons/electron-steradian), and hv is the photon energy in electron volts. The distance from the source to mask was previously defined as d .

It is desirable to maximize Φ for a given value of image error p , so combining eqs. (1) and (3) with eq. (7) results in

$$\Phi = \frac{F_{th} \epsilon h 4p^2 A}{V s^2 (A + D)^2} \quad (8)$$

Only the last factor is a variable depending upon the relative values of A and D . To maximize Φ , we set the partial derivative with respect to A equal to zero,

$$\frac{\partial \Phi}{\partial A} = 0 = 1 - \frac{2A}{A + D} \quad (9)$$

This results in $A = D$; the anode can be as large as the wafer. This result is important because it shows that the x-ray anode can be made large enough to dissipate considerable power for fast exposure. For example, a 5.5 cm diameter molten aluminum anode can be used for a 5.5 cm wafer and has a power capability of 20 kW. This is approaching a practical limit for laboratory or production equipment. Larger wafers would be exposed with an anode smaller than optimum but at corresponding greater values of d to minimize p as in eq. (1).

The exposure time can be calculated from a knowledge of the minimum energy per unit area J_{min} required to expose a given resist, including loss factors in the mask and heat shield. Because the absorption of most x-ray resists is about 1000 cm^{-1} the exposure is independent of thickness. Thus,

$$t_{min} = \frac{J_{min}}{\Phi} = \frac{1}{F_{th}} \frac{V}{\epsilon hv} \frac{s^2}{p^2} D J_{min} \quad (10)$$

for $D = A$.

In eqs. (3) and (10) the source power and the exposure time are seen to increase linearly with D . If an upper limit is placed on W and the value of A is used from eq. (3), the exposure time then increases with $(A + D)^2$ as follows:

$$t_{\min} = \frac{V}{\epsilon h\nu} \frac{1}{W_{\max}} \frac{s^2}{4p^2} (A + D)^2 J_{\min} \quad (11)$$

for

$$D > A = \frac{W_{\max}}{F_{\text{th}}}$$

It is also possible to show that in either case, represented by eqs. (10) or (11), a step-and-repeat exposure of subwafer areas offers no exposure time advantage over moving the source away far enough for a single exposure.

It is useful to plot the ratio of the exposure time to the exposure factor as a function of the wafer diameter D . The exposure factor is simply the resist exposure requirement J_{\min} divided by the transmission factor of the mask substrate, which shall be taken as 50% for these examples. Figure 2 shows this plot as well as the maximum anode dissipation as a function of D according to eq. (6). The solid straight line indicates both the power and the exposure according to eqs. (6) and (10). Also shown are the cases in which the maximum power is limited to 5 kW and to 20 kW. The exposure time then follows eq. (11) and the power remains constant above the appropriate values of D . The other numerical values used for Fig. 2 are $V = 10^4$ V, $\epsilon = 2.3 \times 10^{-4}$ photons/electron-steradian, $h\nu = 1500$ eV, $F_{\text{th}} = 3700$, and $s/p = 10$. Note the distance from mask to source d is simply $10D$ for all the cases, including the power limited ones.

Another plot of eq. (10) is useful because it indicates the actual exposure times as a function of resolution parameter p and resist sensitivity J_{\min} . In Fig. 3 this plot is shown for a wafer 2.5 cm in diameter (D), a maximum anode dissipation of 9200 W, a gap s of 5 μm , and other parameters as for Fig. 2 including 50% mask absorption. To prevent contact points the gap s must be determined in practice. Exposure factors of 2 to 1000 mJ/cm^2 are shown and these represent the range of resists under investigation. Representative resists are shown as polymethyl methacrylate,¹ Kodak Micro Resist 747 (Ref. 3), metal acrylate resist,⁴ and polyglycidyl methacrylate-co-ethyl acrylate.²¹ The inverse square law cost for resolution is obvious from the figure. The conclusion is that high resolution (0.2 μm) off-contact lithography over a large (2.5 cm)

wafer with exposures less than 2 min will require sensitive resists (5 mJ/cm^2) and high power sources (9 kW).

Commercial electron beam evaporators are available that could be modified to provide a 2.5 cm anode at 9 kW in order to achieve the results of Fig. 3. Larger sources could be developed. Recent papers^{22,23} on laser pumped dense plasmas indicate highly efficient conversion of electrical energy to soft x rays in short pulses. However, pulse exposure is limited by the instantaneous temperature rise in the gold absorber on the mask as shown below.

Our current experimental work with x-ray exposure has been accomplished with a 3 kW Balzers EVR-3 electron beam evaporator of the cylindrical geometry type. The only modification is the use of a solid flat-topped aluminum anode in place of the crucible holder. Typical operation is with a focused spot at 8 kV, 20 mA. The mask is thermally shielded from the source by an $8 \mu\text{m}$ aluminum foil and is typically at a distance of 7.6 cm. The calculated flux at the mask is $33 \mu\text{W/cm}^2$. Increased source power for exposing large areas and a combined vacuum window and heat shield are subjects of a continuing investigation.

X-RAY MASK

As discussed by Spears and Smith¹ the soft x-ray wavelength must be 5 to 15 \AA because of limitations in mask fabrication. Because a large x-ray flux is required, the anode material of the x-ray source must be capable of high heat dissipation. Consequently, aluminum was chosen for the source. Aluminum K-alpha characteristic x rays (8.34 \AA) allow the widest choice of materials for both the transmissive mask substrate and the thin absorber pattern. The material tradeoffs are discussed below. We will illustrate the process sequence used to fabricate gold-on-silicon x-ray masks. Finally, a thermal analysis of this mask structure is presented and limitations on dimensional stability are discussed.

Absorber Selection — The mask absorber material must exhibit a very high absorption coefficient for soft x rays because it is not possible to fabricate high resolution structures in thick films. We believe that x-ray lithography will be useful for replicating line structures as narrow as $0.2 \mu\text{m}$. Present fabrication technology would limit these lines to a thickness of about $0.5 \mu\text{m}$.

By utilizing scanning electron lithography, it is possible to create a developed pattern in polymethyl methacrylate (PMMA) with a height-to-width aspect ratio greater than 2:1. If this pattern is used to lift off an evaporated absorber film, the resulting absorber could have an aspect ratio of 2:1 (Ref. 24). If the resist pattern is

used as an ion sputter mask the resulting thin film will have an aspect ratio of less than 2:1 since the sputter removal rate of polymethyl methacrylate is higher than most metals that might be used for the absorber thin film.²⁵ Aspect ratios up to 3.5:1 may be obtained by combining both approaches. The PMMA resist could be used to create an aluminum negative replacement mask by lift off which could then be used as a sputter mask. Aluminum has a sputter removal rate of 0.3 times that of gold.²⁵

A high contrast resist material for x-ray exposure is PMMA which exhibits a differential dissolution rate that is proportional to the cube of the exposure.¹ Thus, it is possible to utilize a mask absorber material which will absorb only 90% of the x rays, i. e., an absorption coefficient greater than $4.6 \times 10^4 \text{ cm}^{-1}$ for a $0.5 \mu\text{m}$ thick material. Those elements that have an absorption coefficient greater than $4 \times 10^4 \text{ cm}^{-1}$ at 8.34 \AA are listed in Table I.

Of the possible absorber materials listed in Table I, gold or copper would seem the likely choices because high resolution structures have been defined in these materials and the processing is well understood.

Substrate Selection — The thinnest feasible substrate for supporting the high resolution absorber pattern is about $3 \mu\text{m}$. Several materials are readily available as foils. An efficient substrate should transmit at least 50% of the soft x-ray flux and thus must have an absorption coefficient less than $2.3 \times 10^3 \text{ cm}^{-1}$. Possible substrate materials are listed in Table I.

As suggested by Spears and Smith,¹ silicon is a near ideal substrate material at 8.34 \AA and its processing technology is well developed. Another important advantage of silicon is its high thermal conductivity and match of thermal expansion coefficient to the silicon wafers used for device fabrication.

MASK FABRICATION

X-ray masks have been fabricated by placing gold patterns on thin silicon substrates as described by Smith, et al.³ The process sequence currently used in our laboratory is illustrated in Fig. 4.

1. Wafer Preparation

Wafers of $1 \Omega\text{-cm}$ phosphorus-doped $\langle 100 \rangle$ silicon, polished one side, 5 cm diameter, 0.36 mm thick are sawed to 3.17 cm square and cleaned by a standard procedure.

2. Boron Diffusion

Combined deposition and drive-in occurs in an open tube furnace in a flowing atmosphere of diborane, N_2 and O_2 . At a temperature of $1150^\circ C$, a diffusion time of 75 min leads to a boron distribution so that after etching a membrane thickness of $5\ \mu m$ is obtained. Low temperature oxidation is used to aid removal of the boron glass. The boron-doped layer is removed from the back side of the wafer by waxing the front surface to a ceramic disk and thinning, in a $HF-HNO_3$ type etch in a rotating beaker.

3. Oxidation

A $5000\ \text{\AA}$ thick film of Si_3O_4 is then pyrolytically deposited on the back side of the wafer at $350^\circ C$. A $500\ \text{\AA}$ film of SiO_2 is deposited on the front side to protect the silicon and provide a good surface for the gold pattern. A thermal oxide was previously used in this step, but the etched membranes that resulted were bowed, possibly as a result of boron out-diffusion.

4. Gold Patterns

Both ion beam sputter etching and liftoff have been used to produce the gold pattern on the front surface of the wafer. In the first case, a $5000\ \text{\AA}$ film of gold is evaporated onto the wafer and it is then coated with a positive resist. A pattern is exposed with a computer controlled scanning electron microscope⁵ or by optically exposing through a contact mask. After development, the pattern is machined into the gold with a $0.5\ kV$ beam of argon ions. Alternatively, a liftoff pattern can be obtained by evaporating the gold over the developed resist pattern. Removing the resist in a stripper selectively removes the gold, leaving behind the delineated pattern.

5. Membrane Etching

Positive photoresist is applied to both sides of the wafer by dipping. Windows are formed in the SiO_2 on the back side of the wafer using standard photolithography and buffered HF etching. The wafers are then immersed directly in a beaker containing ethylene diamine-pyrocatechol etch at $115^\circ C$ (Ref. 26). This etches the $0.36\ mm$ thick $\langle 100 \rangle$ silicon through to the boron doped layer in about 4 hours. We have observed no etching of the gold pattern or of the smooth boron-doped side of the silicon wafer, which is afforded additional protection by $500\ \text{\AA}$ of oxide. The wafers are placed in methanol immediately after being withdrawn from the etching solution as suggested by Bernacki.²⁷ This prevents the formation of small crystallites on the silicon surface. The wafers are then rinsed in acetone and blown dry.

Figure 5 is a photograph of an x-ray mask prepared by this procedure. Examples of exposure through these masks are illustrated by Brault⁴ in metal acrylate resist. These patterns also have been replicated in polymethyl methacrylate and Kodak Micro Resist 747 with optimized exposure time of 420 and 60 min, respectively. As described above, our x-ray source produces a flux of $33 \mu\text{W}/\text{cm}^2$ at the mask (60% of the incident energy is absorbed in the $8.5 \mu\text{m}$ aluminum foil thermal shield). With 40% absorption in the mask the exposure flux is $20 \mu\text{W}/\text{cm}^2$ from which we deduce a required exposure of $500 \text{ mJ}/\text{cm}^2$ for polymethyl methacrylate and $72 \text{ mJ}/\text{cm}^2$ for Kodak micronegative resist.

THERMAL ANALYSIS OF A MASK

As a model, consider the silicon x-ray mask depicted in Fig. 6. This mask is suitable for exposing a 2-in. diameter wafer; it has 0.5 mm wide ribs on 6.5 mm centers fabricated as described above. We assume that one third of the membrane areas are covered with a gold pattern. Approximately half the x-ray flux is absorbed in the silicon membranes. The gold and the ribs absorb nearly all of the x-ray flux incident upon them. The generated heat is conducted along the ribs to a heat sink at the edge of the mask. We will calculate the heat capacity of the mask and the steady-state temperature profile of the rib structure and a typical membrane.

The flux incident upon the mask is dependent upon the exposure time requirement and the sensitivity of the resist polymer. A sensitive negative x-ray resist is polyglycidyl methacrylate-co-ethylacrylate which requires an exposure of $5 \text{ J}/\text{cm}^2$ at 8.34 \AA (Ref. 21). Because the absorption coefficient is about 1000 cm^{-1} , an incident flux of $5.0 \text{ mJ}/\text{cm}^2$ is required. Because a $4.0 \mu\text{m}$ thick silicon mask absorbs 40% of the 8.34 \AA x rays, the incident flux on the mask must be $8.4 \text{ mJ}/\text{cm}^2$. Of the remaining $5.0 \text{ mJ}/\text{cm}^2$ incident on the gold, a $0.5 \mu\text{m}$ thickness absorbs $4.5 \text{ mJ}/\text{cm}^2$. The relevant parameters for the mask shown in Fig. 6 are listed in Table II.

If the exposure were to occur in a very short pulse (10^{-6} sec) there would be no thermal conduction and the instantaneous temperature rise would be given by

$$\Delta T = \frac{Q}{c\rho V} \quad (12)$$

where Q = absorbed energy, calories, c = specific heat, calories/g- $^{\circ}\text{C}$, ρ = density, g/cm³, and V = volume, cm³. The computed values are listed in Table II.

For a high throughput system, an exposure time of 10 sec would be desirable. This would require an incident flux on the mask of

0.84 mW/cm². The time for the mask to come to within 90% of its steady-state temperature is given by¹⁸

$$\frac{Kt}{\rho c l^2} = 1 \quad (13)$$

where K = thermal conductivity, calories/cm-sec-°C, t = time, seconds, and l = length, cm. For the rib structure take l = 2.54 cm, then t = 0.7 sec. For the silicon membrane take l = 0.3 cm, then t = 0.01 sec. Thus, a steady-state temperature distribution is quickly established.

The steady-state temperature distribution across a thin square plate with its edges x = ± a, y = ± a kept at zero temperature, and with internal heat production at a constant rate A_o, is given by

$$T(x, y) = \frac{A_o(a^2 - x^2)}{2KD} - \frac{16 A_o a^2}{KD\pi^3} \sum_{n=0}^{\infty} \frac{(-1)^n \cos(Nx) \cosh(Ny)}{(2n+1)^3 \cosh(Na)} \quad (14)$$

where N = (2n + 1) π/2a, a = half cell width = 0.3 cm, K = thermal conductivity = 0.8 W/cm-°C, D = membrane thickness = 4 × 10⁻⁴ cm, and A_o = heat generation rate = 4.67 mW/cm². The profile T(x) versus x is plotted in Fig. 7 for y = 0, 0.1, 0.2, and 0.25 cm.

The thermal stress introduced in the membrane is compressive in nature and tends to relieve the tensile stress existing as a result of doping the silicon membrane with boron. Boron is a substitutional impurity with a lattice misfit ratio, Γ of 0.746 (Ref. 28). This introduces a strain given by

$$\epsilon = [1 + f(\Gamma^3 - 1)]^{1/3} - 1 \quad (15)$$

where f is the atom fraction. The boron doping must be greater than 7 × 10¹⁹ cm⁻³ to stop the selective etch described above.²⁶ However, if the boron doping is much in excess of this value, the stresses can lead to fracture of the membranes. The solubility limit of boron at 1150°C is 5 × 10²⁰ which gives f = 1 × 10⁻². The tensile stress in the membrane is then

$$\sigma = E_{100} \epsilon = -2.6 \times 10^9 \text{ dynes/cm}^2 \quad (16)$$

where E₁₀₀ = Young's modulus = 1.31 × 10¹² dynes/cm² (Ref. 29) and ε = Strain (from eq. (15)) = -1.95 × 10⁻³.

Below 600°C, silicon undergoes purely elastic deformation before fracture. Sylwestrowicz estimated the theoretical yield strength to be

2.3×10^{10} dynes/cm² and observed fracture stress of about 2×10^9 to 8×10^9 dynes/cm², depending upon the surface perfection.³⁰ A value of 6×10^9 dynes/cm² was observed by Patel and Chaudhuri³¹ in dislocation free silicon with lesser values for crystals with high dislocation densities.

The temperature profile across the center of the membrane in Fig. 7 ($y = 0$) produces an average stress across the center of the constrained membrane ($2a = 0.6$ cm) of

$$\sigma = E_{100} \frac{\alpha}{2a} \int_{-a}^a \Delta T(x) dx = 5.6 \times 10^5 \text{ dynes/cm}^2 \quad (17)$$

where α is the thermal expansion coefficient. Thus, the thermal stress would not be sufficient to cancel the built-in tensile stress, much less cause any deformation of the membrane, even if the membrane temperature were to increase substantially. A thermal expansion analysis of the rib structure is more significant, however.

The steady-state temperature of the rib structure was calculated at the nodal points identified in Fig. 6 for a flux of 0.84 mW/cm^2 . The heat into each node was taken from the power absorbed in the surrounding gold-patterned silicon membrane, i. e., 0.23 mW for center node. The thermal conductivities between each node were represented in a matrix, e. g., $K = 0.173 \text{ mW/}^\circ\text{C}$ for ribs not at the border. With the mask attached to a heat sink at its periphery, the temperature rise above ambient at each node was calculated and is indicated in Fig. 6.

Assuming that the thermal expansion of the rib is accommodated by an increase in the linear dimensions of the mask, the radial shift of a point at the edge of a mask relative to a fixed center would be $0.68 \mu\text{m}$. Alternatively, if the edge of the mask were clamped, the deformation would be accommodated by circular bowing causing a center deflection of $160 \mu\text{m}$.

For high resolution replication it will be necessary to keep the temperature rise of the mask structure below 1°C . This can be accomplished by increasing the cross-sectional area of the ribs or decreasing the exposure flux with correspondingly longer exposure times.

Another solution is more efficient cooling of the mask. This can be accomplished by placing the x-ray mask outside the vacuum environment of the soft x-ray source and cooling the mask with a flowing gas.

SOFT X-RAY VACUUM WINDOW

In x-ray lithography it is necessary to use a thin aluminum foil between the source and the mask to act as a radiant heat shield and a filter to pass the aluminum K-alpha x rays but block the higher energy continuum. This same foil may be used as an atmospheric window if properly supported. A 2.3 mm center-to-center hexagonal grid structure has been used to support an 8.5 μm thick aluminum foil over a 2-in. diameter opening. This structure successfully supported a pressure of 2.0 atm. With a broad area source as described above, the only effect from the grid is a loss of intensity.

GAS COOLING

Helium is a very efficient gas for convective cooling because it has a heat capacity of 1.24 cal/g- $^{\circ}\text{C}$ (Ref. 32). It is suitable for use in an x-ray lithography system because it has a very low absorption coefficient for soft x rays ($3.0 \times 10^{-3} \text{ cm}^{-1}$ at STP) and will not adversely affect sensitive resist materials. The 10.7 mW dissipated in the mask in the above example (10 sec exposure of polyglycidal methacrylate-co-ethylacrylate) could be removed with a temperature rise of 1 $^{\circ}\text{C}$ by helium flowing at 11 cm^3/sec .

MASK ALIGNMENT

To fabricate microwave transistors and high density integrated circuits, it is necessary to register masks on a working wafer with enough precision to utilize any increased resolution. Therefore, an alignment accuracy of 0.1 μm has been chosen as a goal for an x-ray lithography system. This system has been completely designed and most of the subsystems have been fabricated. Position error signals will be derived from the transmission of x rays through complementary registration marks on the mask and wafer as proposed by Smith, et al.³ Because their technique requires thin areas in the working wafer beneath the marks which is an undesirable feature, our system will also be used to evaluate alternate alignment detection schemes.

Custom thin window gas proportional counter tubes have been tested. These will be used with the electronic system shown in Fig. 8. The stage consists of an electronic micromovement stage mounted on a microscope stage to provide both fine and coarse mask positioning. Four piezoceramic cylinder transducers provide the independent x, y, and θ micromovements. An important feature is the electronic dither on the x and y directions at separate frequencies. Digital synchronous phase detectors then provide signs and magnitudes of the three error signals x, y, and θ . The digital processing is essential to make the best use of the small x-ray

signals. These error signals are matrixed with the dither signals and provide the drive to the four transducer amplifiers. The system can eliminate vibration and drift misalignment through continuous small amplitude operation.

The 0.1 μm accuracy is a reasonable goal because (1) the mechanism contains no sliding bearings in order to allow motion approaching this precision. (2) the dynamic range of the electronic feedback system should be about 1000:1 corresponding to an uncertainty of 0.01 μm , and (3) consideration of typical registration marks and counting statistics with a 100 Hz bandwidth for the system indicates that a 0.1 μm precision can be attained with an x-ray flux greater than 30 $\mu\text{W}/\text{cm}^2$ at the mask. The detection signal will be limited by background noise because of photons transmitted through the gold, but it should be possible to handle a background of 5×10^5 counts/sec within the linear range of the detector.

CONCLUSIONS

The work on x-ray lithography reported in this paper represents progress toward the application of this technology to the fabrication of electron devices. The original work of Spears, Smith, and Bernacki with respect to the use of soft x-rays (aluminum K-alpha) and the gold-on-silicon mask has been confirmed. A careful consideration of resolution degradation effects for an off-contact mask shows that a point x-ray source offers no advantage and, therefore, the source can be made large enough and powerful enough to allow reasonably short exposure time. The importance of sensitive x-ray resists was also shown, however. Our analysis of the thermal and mechanical properties of the silicon mask show the importance of proper cooling and mounting of the mask in order to maintain high resolution. This cooling and convenient operation of the exposure system is shown feasible by the experimental results on an x-ray vacuum window. The mask alignment system described will make available an x-ray lithography system for application to microelectronics.

ACKNOWLEDGMENTS

The authors wish to acknowledge the collaboration and encouragement of Hank Smith and Steve Bernacki of Lincoln Laboratories. We are indebted to Bob Brault, Hugh Garvin, Faik Ozdemir, and Ed Wolf for many helpful discussions and for reviewing this manuscript. We thank Frank Hause and Gene Stevens of our laboratory who deserve much credit for accomplishing the work.

REFERENCES

1. D. L. Spears and H. I. Smith, "High-Resolution Pattern Replication Using Soft X-Rays," *Electronics Letters* 8, 102 (1972).
2. D. L. Spears and H. I. Smith, "X-Ray Lithography - A New High Resolution Replication Process," *Solid State Technology* 15, 21, July 1972.
3. H. I. Smith, D. L. Spears, and S. E. Bernacki, "X-Ray Lithography: Complementary Technique to Electron Beam Lithography," *J. Vac. Sci. Technol.* 10, 913 (1973).
4. R. G. Brault, "Properties of Metal Acrylate Compositions as X-Ray Resists," This conference, paper No. 199.
5. F. S. Ozdemir, E. D. Wolf, and C. R. Buckley, "Computer-Controlled Scanning Electron Microscope System for High Resolution Microelectronic Pattern Fabrication," *IEEE Trans. Electron Devices* ED-19, 629 (1972).
6. E. D. Wolf, F. S. Ozdemir, and R. D. Weglein, "Precision Electron Beam Microfabrication of Acoustic Surface Wave Devices," *Proc. IEEE Ultrasonics Symposium*, Monterey, California, Nov. 1973, p. 510.
7. E. D. Wolf, "Electron Beam and Ion Beam Microfabrication of Integrated Optic Elements," Chapter 7 in *Introduction to Integrated Optics*, M. K. Barnoski, ed., Plenum, New York, in press.
8. F. S. Ozdemir, Hughes Research Laboratories, unpublished results.
9. F. Fang, M. Hatzakis, and C. H. Ting, "Electron-Beam Fabrication of Ion-Implanted High-Performance FET Circuits," *J. Vac. Sci. Technol.* 10, 1082 (1973).
10. R. F. W. Pease, R. C. Henderson, and J. V. Dalton, "IGFET Inverter Circuits made with Electron Lithography," *J. Vac. Sci. Technol.* 10, 1078 (1973).
11. H. I. Smith, N. Efremow and P. L. Kelley, "Photolithographic Contact Printing of 4000 Å Linewidth Patterns," to be published in *J. Electrochem. Soc.* (1974).
12. F. L. Hause and P. A. Sullivan, Hughes Research Laboratories, unpublished results. (We are indebted to E. D. Wolf and W. E. Perkins for fabrication of chrome masks on thin glass by scanning electron beam delineation.)
13. P. R. Malmberg, T. W. O'Keeffe, M. M. Sopira, and M. W. Levi, "LSI Pattern Generation and Replication by Electron Beams," *J. Vac. Sci. Technol.* 10, 1025 (1973).
14. W. R. Livesay, "Integrated Circuit Production with Electron Beams," *J. Vac. Sci. Technol.* 10, 1028 (1973).
15. J. E. Picquendar, "Nanoelectronic Project and Astec Logic," *J. Vac. Sci. Technol.* 10, 1132 (1973).
16. J. P. Scott, "Electron Image Projector," This conference, paper No. 219.

17. H. Koops, "On Electron Projection Systems," *J. Vac. Sci. Technol.* 10, 909 (1973).
18. H.S. Carslaw and J.C. Jaeger, Conduction of Heat in Solids, 2nd Ed. (Oxford, London, 1959).
19. K. Chopra, Thin Film Phenomena (McGraw-Hill, New York, 1969), p. 11.
20. C.E. Dick, A.C. Lucas, J.M. Motz, R.C. Placious, and J.H. Sparrow, "Large Angle K X-Ray Production by Electrons," *J. Appl. Phys.* 44, 815 (1973).
21. P.V. Lenzo and E.G. Spencer, "High-Speed Low-Power X-Ray Lithography," *Appl. Phys. Lett.* 24, 289 (1974).
22. D.J. Johnson, "Study of the X-Ray Production Mechanism of a Dense Plasma Focus," *J. Appl. Phys.* 45, 1147 (1974).
23. P.J. Mallozzi, et al., "Laser Generated Plasmas as a Source of X-Rays for Medical Applications," *J. Appl. Phys.* 45, 1891 (1974).
24. M. Hatzakis and A.N. Broers, "Electron Beam Techniques for Fabricating Fine Metal Lines," Record of 11th Symp. on Electron, Ion, and Laser Beam Technology, Boulder, Colorado, May 12-14, 1971, R.F.M. Thornley, ed., (San Francisco Press, San Francisco, 1971).
25. H.L. Garvin, "High Resolution Fabrication by Ion Beam Sputtering," *Solid State Technology* 16, 31, Nov. 1973.
26. A. Bohg, "Ethylene Diamine-Pyrocatechol-Water Mixture Shows Etching Anomaly in Boron-Doped Silicon," *J. Electrochem. Soc.* 118, 401 (1971).
27. S.E. Bernacki, Lincoln Laboratories, Lexington, Mass., private communication (1973).
28. J.R. Carruthers, R.B. Hoffman, and J.D. Ashner, "X-Ray Investigation of the Perfection of Silicon," *J. Appl. Phys.* 34, 3389 (1963).
29. W.R. Runyan, Silicon Semiconductor Technology (McGraw-Hill, N.Y., 1965).
30. W.D. Sylwestrowicz, "Mechanical Properties of Single Crystals of Silicon," *Phil. Mag.* 7, 1825 (1962).
31. J.R. Patel and A.R. Chaudhuri, "Macroscopic Plastic Properties of Dislocation-Free Germanium and Other Semiconductor Crystals. I. Yield Behaviour," *J. Appl. Phys.* 34, 2788 (1963).
32. R.C. Weast, ed., Handbook of Chemistry and Physics, 53rd Ed. (Chemical Rubber Co., Cleveland, 1972).
33. B.L. Hënke and E.S. Ebsu, "Low Energy X-Ray and Electron Absorption within Solids," to be published in *Advan. X-Ray Analysis* 17, (1974).

Table I. Absorption Coefficient of Several Solid Materials at 8.34 \AA Wavelength (Mass Absorption Coefficient³³ Times Density³²)

Absorber		Transmissive	
Material	Absorption Coefficient ($\times 10^3 \text{ cm}^{-1}$)	Material	Absorption Coefficient ($\times 10^3 \text{ cm}^{-1}$)
Copper	40.7	Lithium	0.03
Samarium	44.5	Beryllium	0.33
Terbium	44.8	Boron	0.96
Dysprosium	48.5	Carbon	1.62
Holmium	50.5	Aluminum	1.09
Erbium	57.6	Silicon	1.30
Osmium	43.5	Phosphorus	1.49
Iridium	46.1	Sulphur	1.71
Platinum	46.6	Potassium	1.27
Gold	44.5	Calcium	2.72
Protoactinium	57.8	Rubidium	1.91
Uranium	72.0	Mylar	0.98
		SiO ₂	2.93

Table II. Some Relevant Thermal Parameters for a Gold-On-Silicon X-Ray Mask

	Silicon Ribs	Silicon Membrane	Gold Pattern	Total Mask
Area (cm ²)	2.35	17.90	5.97	20.25
Power absorbed (mJ)	19.7	60.9	26.6	107.3
Thermal conductivity (W/cm-°C)	1.5 (Ref. 29)	0.8 (Ref. 29)	3.1 (Ref. 32)	
Specific heat (cal/g-°C)	0.17	0.17	0.03	
Density (g/cm ³) (Ref. 32)	2.33	2.33	19.3	
Temperature rise for instantaneous exposure (°C) from eq. (12)	0.33	5.1	36	
Coefficient of thermal expansion ($\times 10^6 / ^\circ\text{C}$) (Ref. 32)	3.0	3.0	14	

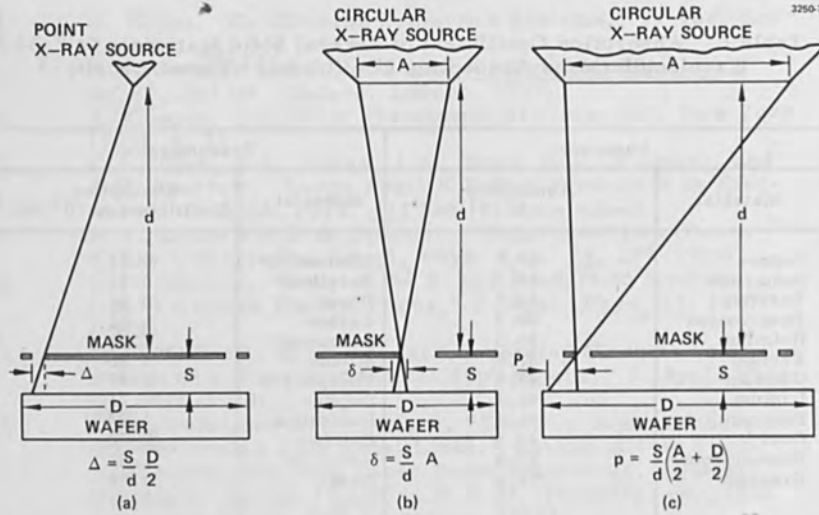


Fig. 1. X-ray exposure configurations. (a) Geometric distortion. (b) Penumbral shadowing. (c) Combination.

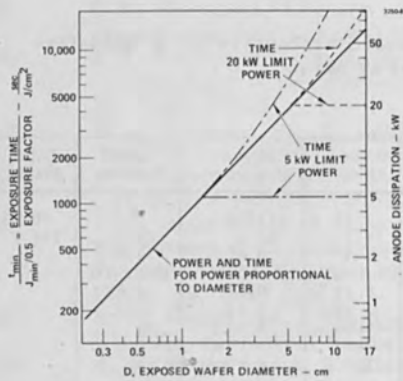


Fig. 2. Normalized exposure time and anode power as a function of wafer diameter and source distance.

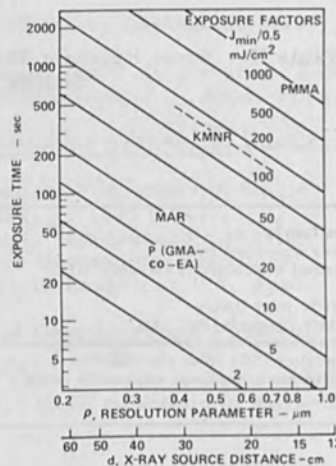


Fig. 3. Exposure time as a function of the resolution parameter p for various exposure factors.

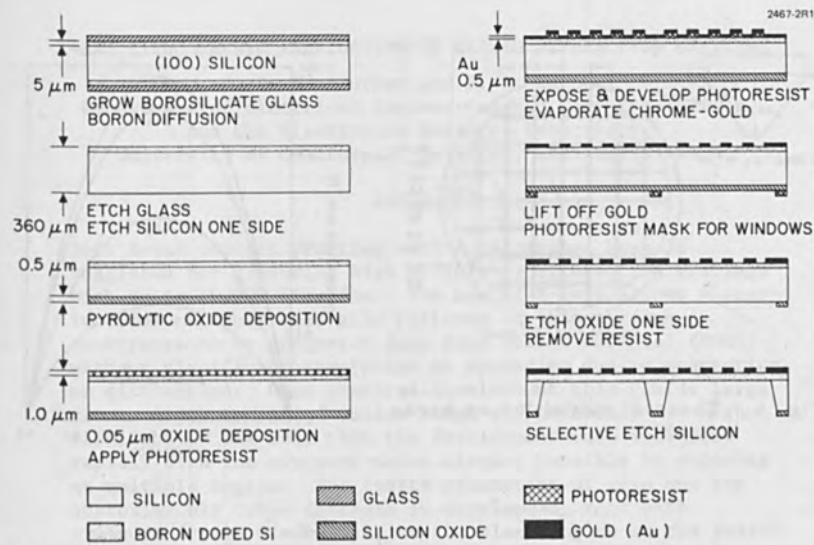


Fig. 4. Processing sequence for fabricating x-ray masks.

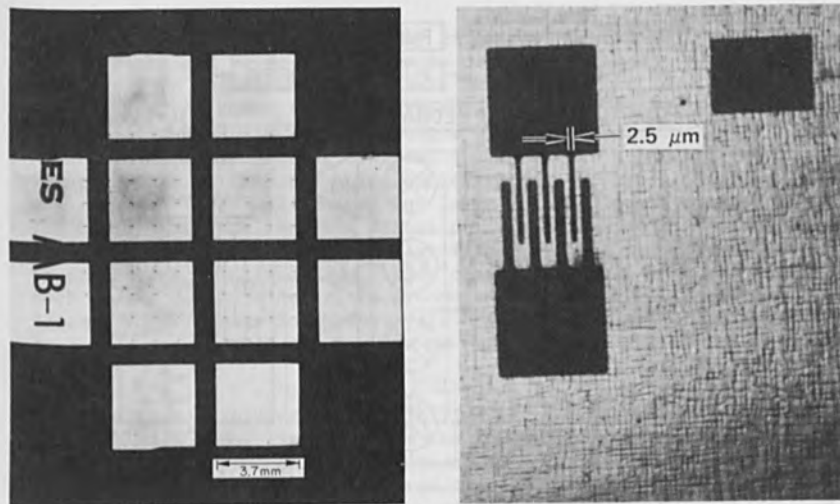


Fig. 5. An x-ray mask viewed with transmitted light.

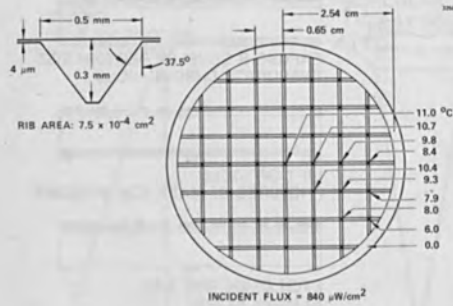


Fig. 6. Thermal model for an x-ray mask.

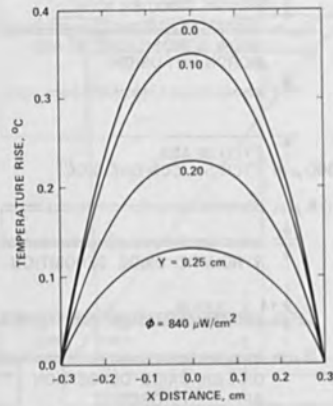


Fig. 7. Temperature versus distance across one membrane.

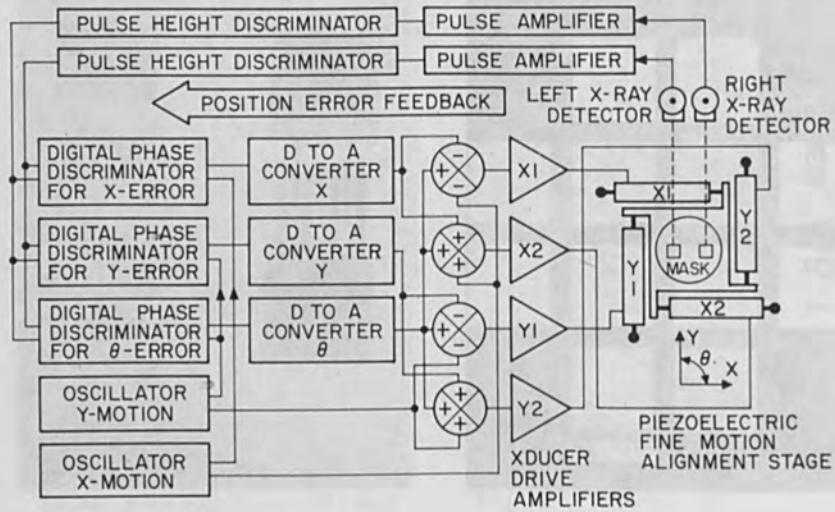


Fig. 8. Electronic mask alignment system.

X-RAY LITHOGRAPHIC FABRICATION OF BLAZED DIFFRACTION GRATINGS

A. R. Neureuther and P. I. Hagouel
Department of Electrical Engineering and Computer Science
and the Electronics Research Laboratory
University of California, Berkeley, California 94720

ABSTRACT

Soft X-ray contact printing with a columnated beam is suggested for producing high efficiency diffraction gratings with up to 10,000 lines/mm. The use of X-rays allows planar interferometrically made gold patterns on thin silicon substrates to be projected deep into resist material (PMMA) without significant absorption or spreading due to scattering or diffraction. Upon chemical development this yields large groove depth to period ratios which are necessary for high efficiency. The fact that the development rate increases rapidly with the exposure makes blazing possible by exposing at multiple angles. The finite absorption of gold and the approximately cubic increase in development rate with exposure impose limitations on the blaze angles as the period and hence mask thickness is decreased. An evaluation of the trade offs between shape and period as well as an experimental study in progress are described.

I. INTRODUCTION

A process similar to the X-ray lithography technique described by D. L. Spears and H. I. Smith¹ can be used to fabricate diffraction gratings. In particular, it appears that blazed gratings can be produced by the multiple angle exposure technique sketched in Figure 1. This process has potential advantages over both mechanically ruled and direct holographic grating fabrication techniques. Since the contact printing mask is itself a holographic grating the two advantages of small period (10,000 lines/mm) and large area uniformity are preserved. The use of X-rays allows the planar pattern to be projected deep into resist material (PMMA) without significant absorption or spreading due to scattering or diffraction. Upon chemical development this yields both deeper and more desirable groove shapes than those producible interferometrically in photoresists. An additional process advantage is that a single mask can be used to replicate gratings with a variety of blaze angles.

This paper explores the feasibility of producing blazed diffraction gratings with X-ray lithography. The X-ray exposure system design and fabrication processing techniques which are currently being experimentally tested are presented initially. The major new feature is a rotating angular mount with a differential pressure mask contact mechanism. In evaluating the process a major conceptual complication arises due to the fact that the development rate of the PMMA is not a

sharp threshold function of exposure. Theoretically an isotropic etching model is used to show that it is still feasible to obtain planar facets as long as the etch rate increases reasonably rapid with exposure. Curves for designing blazed gratings with specified blaze and groove angles in the presence of nonthreshold development are then presented. Finally the fundamental limit on groove shape imposed by the fact that smaller period gratings require thinner masks having lower exposure contrast is explored.

II. BASIC FABRICATION PROCESS

The blazed grating fabrication process is a combination of the X-ray lithographic technique¹ and interferometrical production of gratings via photoresist.² The process consists of two distinct steps, constructing an almost planar mask and replicating it with X-rays. The mask step begins with doping one surface of a (100) silicon wafer with a fairly high concentration of boron.³ Then the surface is coated successively with chromium for adhesion, gold for masking and finally with Shipley AZ 1350 photoresist for optical pattern generation. The resist is then exposed interferometrically using a laser. The groove spacing a for a holographically recorded diffraction

grating is given by $a = \frac{\lambda}{2n \sin \alpha}$ where α is the angle of incidence of the laser beam, λ is the wavelength of the beam and n is the index of refraction if a liquid immersion is used. The recorded pattern is developed to uncover the gold for removal by chemical etching. On the reverse surface of the wafer after coating with photoresist, a window is exposed and developed. The silicon is etched with a (100) plane preferential etch, and the process abruptly stops at a boron concentration of about $2 \times 10^{19}/\text{cm}^3$.⁴ The result is a thin window of Si (.5 to 2 μm) supporting the gold mask as shown in Figure 2. The smallest grating period which can be produced with ruling techniques is about 2780 \AA ; however, by using optical techniques with refractive index liquids as explained by C. V. Shank and R. V. Schmidt², periods of the order of 1800 \AA and 1000 \AA can be achieved with the Argon and Helium-Cadmium lasers respectively.

Replication consists of contact printing the mask on a PMMA coated (.1 μ to 1 μ) substrate with a columnated beam of soft X-rays. Good contact between the mask and substrate can be obtained by using a flexible glass mask (.2mm).⁵ The incorporation of this idea for the grating fabrication system is shown in Figure 3. In this case the flexible glass is used as a substrate and the vacuum contact scheme is replaced by an automatic substrate pressure technique. Air trapped between the thick microscope slide and the flexible glass substrate automatically provides a distributed substrate-mask contact force when the vacuum system is pumped down. The aluminum block serving as the substrate-mask holder is designed to rotate about a center parallel to the mask lines for making multiple angle exposures.

The X-ray exposure system is described in Figure 4. It has been constructed from existing laboratory equipment and designed as one of several systems sharing the same vacuum chamber as shown in Figure 5. An electron beam from a straight electron gun strikes a water cooled aluminum coated flat side of a steel pipe. The penetration depth is on the order of 1μ and the aluminum produces strong characteristic radiation at 8.3\AA . At the mask the X-rays appear to be well collimated as the source spot size (10mm^2) is much smaller than the distance to the mask (10cm). The thin gold masks attenuate the soft X-rays yet the supporting silicon window has high transmission.¹ The pattern of the mask is projected in an almost parallel ray manner because there is no apparent diffraction and little attenuation in the PMMA. The exposure time for this system at an electron beam current of 200ma and voltage of 7kev is anticipated to be about 25 min. The overlapping of partial exposures at two angles should yield blazed grating according to the scheme of Figure 1.

This grating fabrication technique has many of the usual X-ray lithography and flexible glass problems as well as additional difficulties. Common problems are that X-ray exposure times are quite long and that the flexible glass is subject to distortion. This distortion might be particularly important in incorporating a PMMA grating into a standard optical or integrated optics device. More important unique problems are introduced by the finite transmission of the thin gold laser and the fact that the development rate does not show a sharp threshold behavior with respect to exposure energy. The mask transmission and multiple angle exposures lead to low exposure contrast ratios (2:1). The non-threshold development behavior implies that the development effects in the shadowed or partially shadowed regions may lead to significant groove shape changes. These non-threshold development effects eventually impose fundamental limitations on the blazed grating shapes which can be produced. However, it appears that these effects can be modeled by the technique presented in the next section and that the net development effect is an increase in the effective groove angle which can be compensated in the initial exposure.

III. BLAZING WITH NON-THRESHOLD DEVELOPMENT

Although the development of PMMA is not a sharp energy threshold phenomena it appears possible to produce and in fact specifically design blazed gratings with a wide range of blaze angles and periods. The plausibility of this idea is based on the key assumption that during development PMMA can be modeled by a surface etching process in which the local surface etch rate is determined by the local exposure at that point. That is the developer action is confined to the active surface and the developer solution has a strength which is independent of the relative amount of previously dissolved material. Such a surface etching model has been shown to be applicable and useful in photoresist processing.⁶ Recent PMMA development measurements by J. Greeneich⁷ tend to show a surface etching rate for electron beam

exposure which depends only on the local fragmented molecular weight. Quantitative measurements for X-ray exposure¹ indicate that the development rate is roughly a cubic function of the X-ray dose. Most of the quantitative assessments which will be made will be based on the assumption of an isotropic surface etching process in which the rate is a cubic function of exposure.

The exposure process can be modeled with varying degrees of accuracy. The simplest and most generally applicable approach was to calculate a finite gold transmission factor based on the thickness and angle of incidence. The attenuation in the PMMA ($e^{-\alpha d}$; $\alpha \sim 10^3 \text{cm}^{-1}$) was neglected and absolute exposure levels and the silicon attenuation were not considered as the development process effects depend only on relative exposure ratios. Generally the gold thickness was scaled to be 10 to 30% of the period. For certain studies a modification of the effective opening to allow for an approximately 45° gold mask slant angle anticipated in chemical etching was added.

Conceptually the above model predicts a planar front etching phenomena which preserves the possibility of producing blazed facets in the presence of non-threshold development effects. A sketch of how the planar etching front occurs is given in Figure 6. In this case a single exposure results in distinct regions having exposed and background etch rates R_E and R_B respectively. When developer is applied to the top surface the locus of the active surface for the development process can be found by using a technique analogous to Huygens principle for electromagnetic theory. At any time t each point on the active surface can be thought of as an etching center about which a sphere (or cylinder in two dimensions) of radius $R\Delta t$ is produced. The envelope of these intersecting spheres where R is the etch rate at the center of each sphere forms the active surface at $t+\Delta t$. Due to the fact that R depends on position the appropriate limits on Δt discontinuities of R at shadow boundaries must be considered.

For the exposure profile shown in Figure 6, the development process can be solved analytically. The planar surface of the exposed and background regions translate vertically at rates R_B and R_E respectively. For an exposure at an angle θ_i , the horizontal planar front in the R_E region intercept a point on the shadow boundary of the mask which moves at a velocity $R_{ES} = R_E / \cos \theta_i$. This moving interception point generates a continuous sequence of etching centers whose spheres move into the background region at a rate R_B . The largest of these spheres is centered at the exposed to background transition point on the top surface and has a radius $R_B t$. At time t the envelope of the sequence of interception point generated spheres is a new planar front tangent to the largest sphere and passing through the transition point a distance $R_{ES} t$ down the mask shadow boundary. This new planar front forms an angle $\alpha = \text{arc sin} \left(\frac{R_B t}{R_{ES} t} \right)$ with respect to the

innerface. The net planar front angle is thus $\theta_F = \theta_i + \arcsin\left(\frac{R_B}{R_E \cos \theta_i}\right)$.

This planar front phenomena makes blazng of gratings possible even when development can occur in partially or totally shadowed regions. Two exposure techniques for blazng gratings are shown in Figure 7. The single source approach uses planar fronts on both sides and the exposed shaft is removed at a rate R_E . A groove angle

$\theta_G = 2 \arcsin\left(\frac{R_B}{R_E}\right)$ is produced. This is the smallest possible groove angle and can be used to estimate the ultimate capabilities of X-ray lithography. Assuming that the development rate is a cubic function of exposure and that the gold has an attenuation constant 2.3025 per micron the minimum groove angle has been calculated for various gold thickness to period ratios. The results are shown in Figure 8.

As the period is decreased and hence the gold thickness is also decreased, the mask transmission increase which in turn increases the ratio of R_B/R_E and consequently increases the minimum groove angle. The curves for various gold thickness to period ratios emphasize the importance of mask thickness. The angle of incidence changes the apparent mask thickness but this is only a relative minor effect. Typical gratings used in the optical region have groove angles of 100° . With chemical mask etching requiring low thickness to period ratios (.1) for good edge definition, the traditional optical grating shapes down to 3500 lines/mm can be obtained. Sharper edge definition which may be possible with other techniques such as ion beam etching⁸ would make blazng possible beyond 10,000 lines/mm.

The more flexible two source exposure technique shown in Figure 7 which also takes advantage of the planar etching front phenomena can be treated analytically as well. In this case the exposure at θ_1 and θ_2 create regions having etch rates R_B , R_1 , R_2 and R_{12} corresponding to direct exposure by neither, source 1, source 2 and both source 1 and 2 respectively. Planar etching fronts along the shadow boundaries which intersect at an angle θ_G deep in the resist form the grating facets. It is necessary to stop the development process when the direct vertical etching of region exposed to both source 1 and 2 reaches the intersection $t_d = R_{12}/h$. The parameters must be chosen such that the planar etching fronts at angles α and β intersect each other. The actual grating height will necessarily be less than h . The blaze angle is $\theta_B = 90^\circ - \theta_R - \beta$.

A variety of formulas have been developed for calculation purposes. The effective mask opening is defined as d_e . Typically it is $(p/2)+t$ where p is the grating period and t is the thickness of the mask which allows for undercutting in chemical etching. For the shadow boundaries to intersect at depth h , θ_R is given by

$$\theta_R = \arcsin \left(\frac{d_e}{h} - \tan \theta_i \right)$$

For a cubic dependence of etch rate on exposure the groove and blaze angles are then given by

$$\theta_G = \theta_i + \theta_R + \alpha + \beta$$

$$\theta_B = 90^\circ - \theta_R - \beta$$

where

$$\alpha = \arcsin \left[\frac{\left(\frac{-t/\cos \theta_i}{8} \right)^3}{\cos \theta_i} \right]$$

and

$$\beta = \arcsin \left[\frac{\left(\frac{-\alpha t/\cos \theta_R}{8} \right)^3}{\cos \theta_R} \right]$$

The determining parameters are d_e/h and t .

A technique for designing blazed gratings in the presence of non-threshold development effects has been developed from these formulas. Figure 9 shows that for a given d_e/h and t the groove angle θ_G is a relatively insensitive function of θ_i . The thickness of the mask is chosen to be a small percentage of the grating period and the appropriate d_e/h value is read from the curves. The blaze angle dependence on θ_i is shown in Figure 10. Given the desired θ_B the required θ_i is read from the particular t and d_e/h curve selected previously. For example to construct a typical optical grating with $p = .5\mu$, $\theta_B = 37^\circ$ and $\theta_G = 100^\circ$, first select a gold thickness $.2\mu$. Figure 9 indicates that $d_e/h = .76$. According to Figure 10, θ_i should be 16° . This gives $\theta_R = 25^\circ$, $\alpha = 31^\circ$, $\beta = 20^\circ$ and the resulting profile shown in Figure 11. A final important consideration is the selection of the duty cycle or percentage of photoresist opened at the gold surface. It is chosen such that the two facets forming the peak of the groove profile intersect at the intersection of the shadow boundaries for the two exposures. For this particular grating $d_e = .67p$ satisfies this requirement. For ideal mask edge definition the duty cycle is 67%, but with chemical etching producing about $.1\mu$ undercutting on each side, the duty cycle is only 27%. The gold thickness must also be checked to be sure that the etching in the completely shadowed region $R_B t_d$ does not reach the groove peak at the shadow boundary intersection.

IV. CONCLUSION

Soft X-ray contact printing with a columnated beam appears quite promising for producing efficient blazed gratings up to 10,000 lines/mm. It is clear that X-rays can produce deeper and hence more efficient gratings than holographic techniques due to negligible diffraction and absorption. The fabrication of blazed gratings is complicated by the fact that the development rate for X-ray resists such as PMMA does not have a sharp threshold with respect to exposure energy. However, using a local rate dependent isotropic etching model for PMMA for which there is increasing evidence, it has been shown that planar etching front facets can be produced. Specific design techniques compensating for non-threshold development effects have been developed. The basic planar etching front phenomena and theoretical design approach should be valid for other sources of resist materials and etching processes.

ACKNOWLEDGEMENT

Research sponsored by the Joint Services Electronics Program, Contract F44620-71-C-0087.

REFERENCES

1. D. L. Spears and Henry I. Smith, *Solid State Technology* 15, 21 (1972)
2. C. V. Shank and R. V. Schmidt, *Appl. Phys. Lett.* 23, 154 (1973).
3. S. Maekawa and T. Oshida, *J. Phys. Soc. Japan*, 19, 253 (1964).
4. R. A. Cohen, R. W. Mountain, H. I. Smith, M. A. Lemma, D. L. Spears and S. E. Bernacki, MIT Lincoln Laboratory Technical Note 1973-38.
5. H. I. Smith, N. E. Fremow and P. L. Kelley, Preprint of article submitted to the *Journal of the Electrochemical Society*.
6. F. H. Dill and A. R. Neureuther, Polytechnic Institute of New York - MRI Symposia Series Vol. XXIII (1974).
7. J. S. Greeneich, Preprint.
8. H. L. Garvin, Kodack Microelectronics Seminar, San Diego, Dec. 11-12, 1972.

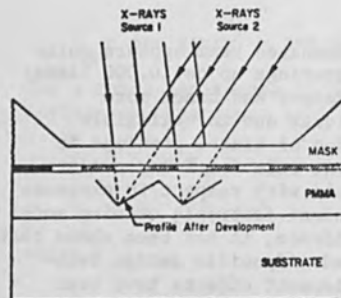


Fig. 1. Multiple angle soft x-ray contact printing of blazed gratings.

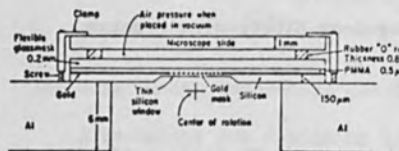


Fig. 3. Mask-substrate holder having pneumatic pressure contact and angular rotation center.

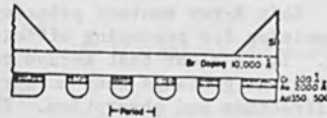


Fig. 2. Planar gold mask on the silicon substrate produced by interferometric exposure of AZ1350 and chemical etching.

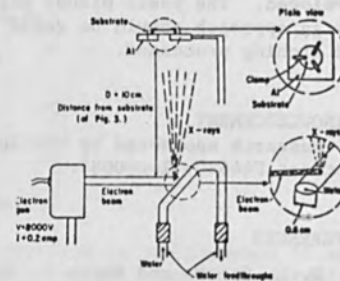


Fig. 4. Soft x-ray exposure source geometry.

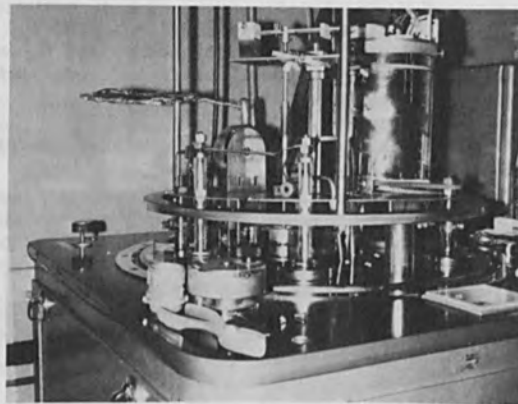


Fig. 5. Photograph of the x-ray exposure system sharing vacuum chamber with other systems.

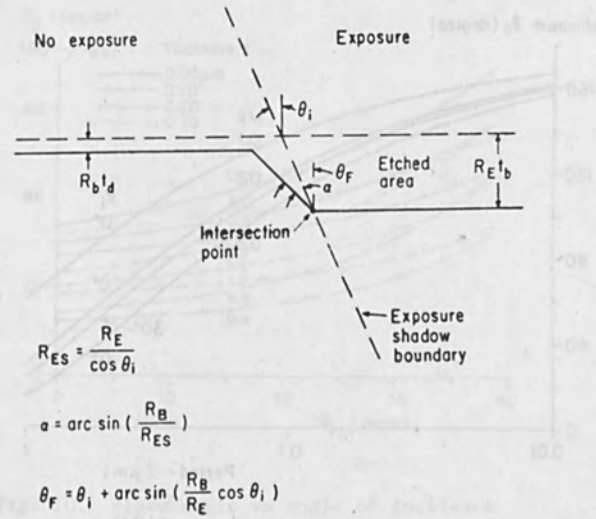


Fig. 6. Isotropic etching model showing planar etching front phenomena.

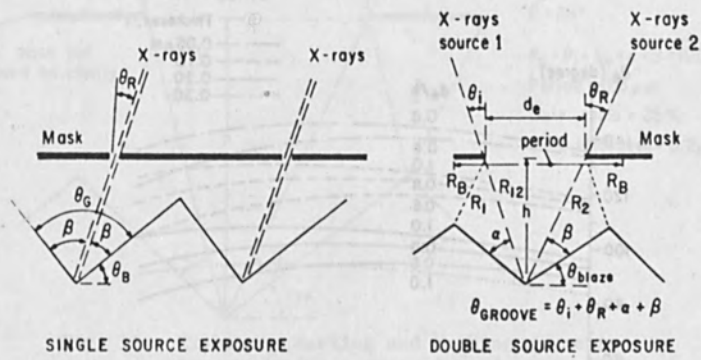


Fig. 7. Single source and multiple source exposure techniques for producing blazed gratings.

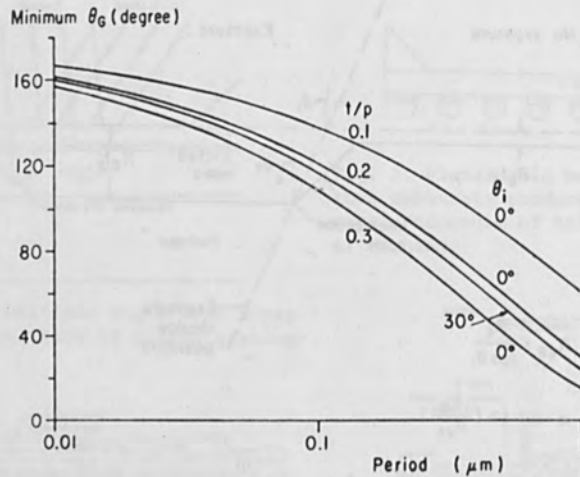


Fig. 8. Minimum groove angle for single source exposure as a function of grating period for various gold thickness to period ratios. (θ_i = angle of incidence which is zero unless otherwise indicated.)

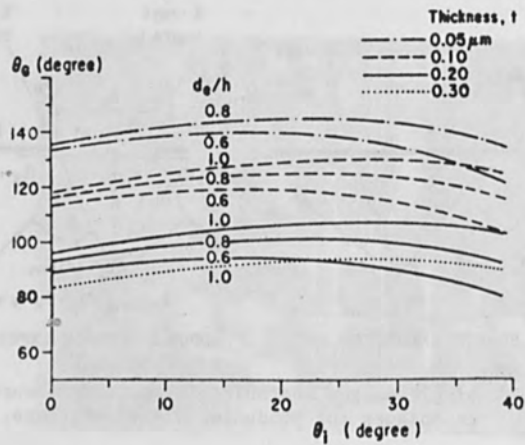


Fig. 9. Groove angle vs angle of incidence for various thickness and d_e/h ratios.

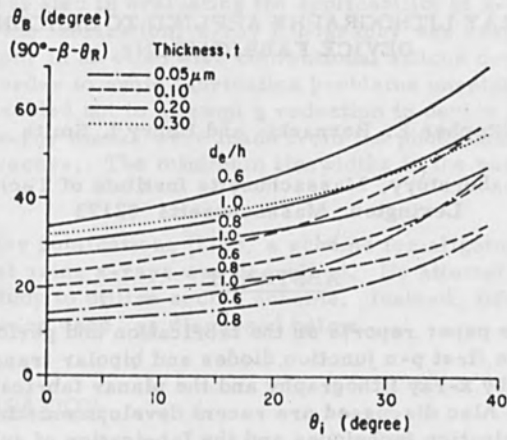


Fig. 10. Blaze angle vs angle of incidence for various thickness and d_e/h ratios.

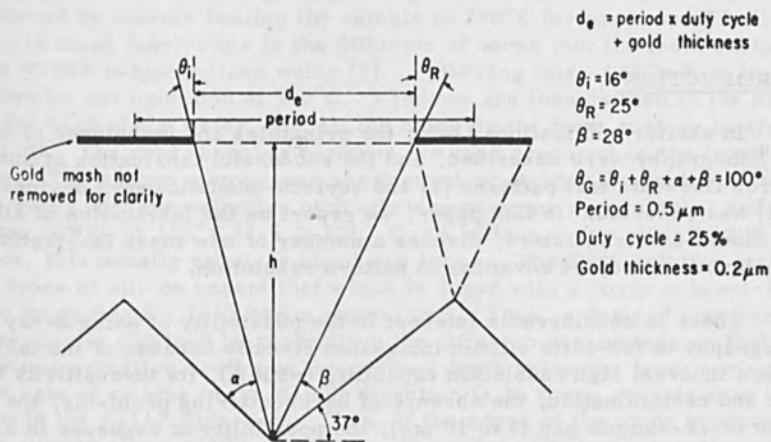


Fig. 11. Exposure, masking and etching geometry for producing a typical optical grating with $\theta_G = 110^\circ$, $\theta_B = 37^\circ$ and period of $.5\mu$.

X-RAY LITHOGRAPHY APPLIED TO SILICON
DEVICE FABRICATION*

Stephen E. Bernacki⁺ and Henry I. Smith

Lincoln Laboratory, Massachusetts Institute of Technology
Lexington, Massachusetts 02173

ABSTRACT

This paper reports on the fabrication and performance of the first p-n junction diodes and bipolar transistors produced by x-ray lithography and the planar fabrication process. Also discussed are recent developments in x-ray mask fabrication techniques and the fabrication of submicron linewidth relief structures in thick PMMA.

INTRODUCTION

In earlier publications [1-5], the principles and techniques of x-ray lithography were described, and the successful fabrication of submicron linewidth test patterns [1] and surface-acoustic-wave devices [2-4] was reported. In this paper, we report on the fabrication of silicon diodes and transistors, discuss a number of new mask fabrication techniques and report advances in pattern resolution.

There is considerable interest in the possibility of using x-ray lithography to fabricate silicon integrated circuits because of the technique's inherent high resolution capability ($\sim 500 \text{ \AA}$), its insensitivity to dust and contamination, the absence of backscattering problems, the finite mask-sample gap (3 to 10 μm), the possibility of exposure in a non-vacuum environment, and the fact that the x-ray mask is made of silicon and thus matches the thermal expansion of silicon substrates.

*This work was sponsored by the Department of the Air Force and the Department of the Army.

⁺Also at the Division of Engineering and Applied Physics, Harvard University, Cambridge, Massachusetts 02138.

As a first step in evaluating the applicability of x-ray lithography to silicon device fabrication, x-ray lithography was used in place of photolithography in an otherwise conventional silicon device fabrication process. In order to avoid fabrication problems unrelated to lithography, it was decided not to attempt a reduction in device geometries. Instead, the x-ray masks were made from the photomasks ordinarily used in the process. The minimum linewidths in the patterns were $2.5 \mu\text{m}$.

In earlier publications [2, 4], a scheme for aligning the several masks of a set using x-rays was described. No attempt was made in the present study to utilize such a scheme. Instead, infrared and optical methods were used, as discussed below.

MASK FABRICATION

The basic structure of the x-ray lithography mask used in the present work is illustrated schematically in Figure 1. This differs from earlier configurations [4] in that there is no chromium film under the gold. It was found that excellent gold-to-silicon adhesion could be achieved by merely heating the sample to 350°C for one hour. The first step in mask fabrication is the diffusion of boron into the front surface of a $\langle 100 \rangle$ n-type silicon wafer [5]. Following this, a SiO_2 film is grown by wet oxidation at 950°C . Windows are then defined in the oxide on the back of the wafer, and all the oxide on the front surface is stripped off. The gold absorber patterns are then produced on the front surface. The silicon membranes are formed by etching the back side of the wafer with the selective etch ethylene-diamine pyrocatechol and water (EPW) at 105°C [2-5, 7-10]. For a silicon wafer initially $200 \mu\text{m}$ thick, this usually requires about two hours. The EPW solution etches all types of silicon except that which is doped with a boron concentration exceeding 2×10^{19} boron atoms/ cm^3 . Thus, a desired membrane thickness is obtained by controlling the diffusion parameters so that this concentration occurs at the desired depth below the front surface. The rate of etching in the $\langle 100 \rangle$ direction is 16 times greater than the rate in the $\langle 111 \rangle$ direction. Thus, if the edges of the oxide windows are aligned along $\langle 110 \rangle$ directions, the silicon window sidewalls are $\langle 111 \rangle$ planes, as indicated in Figure 1.

Experiments indicate that EPW etches thermal SiO_2 at a rate of about 400 \AA per hour. Thus, the thermal oxide should be at least 800 \AA thick in order to mask throughout a 2 hour etch. Typically, 2000 \AA of thermal oxide is grown. If the oxide is made very much thicker than this, or grown at a high temperature, there is a risk that the silicon

membrane will be dimpled. This occurred with samples whose masking oxides were grown at 1100°C to a thickness of 4400 Å or greater, presumably because of stress in the membrane caused by boron out-diffusion into the oxide [6]. If a 2000 Å thick wet oxide is grown at 950°C, no dimpling of the membranes is observed.

During EPW etching, the front surface of the silicon must be protected because it is slowly attacked by the EPW etch. This attack undermines the gold absorber pattern, and gives the silicon a frosted appearance. A variety of different films to protect the front surface were tried, but with no success. In the current process, the sample is held in a teflon fixture in such a way that only the back surface of the silicon mask is exposed to the EPW etch.

The mask-making procedure has been developed to the point where it is now routine. From the point of view of membrane integrity, the yield is essentially 100 percent. A photograph of a large area mask is shown in Figure 2. An x-ray mask with the same absorber pattern but with no supporting rib structure was also made. The membrane was 3 cm in diameter, 5 μm thick, and was supported by the rim of a 4 cm diameter, 200 μm thick silicon wafer. A 3.5 μm thick silicon membrane, 2.5 mm square is very rugged, is easily handled and cleaned and will support a pressure differential of at least one atmosphere. Such strength and ruggedness is very impressive and is due to the fact that the membranes are single crystal silicon of low defect density. From the points of view of strength and low distortion they are quite suitable as masks.

EXPOSURE RESULTS

The requirements for an efficient soft x-ray source have been discussed elsewhere [1-3]. For laboratory experimentation, a commercial electron beam evaporation gun [11] such as illustrated in Figure 3 is adequate. At an accelerating potential of 10 kV, it can provide 50 mA of current in a 1 millimeter diameter spot. The vast majority of experiments have been done with an aluminum target ($\lambda_{AlK} = 8.34 \text{ \AA}$). However, copper is also a desirable source ($\lambda_{CuL} = 13.3 \text{ \AA}$) particularly in combination with low contrast high sensitivity polymers [12].

With an aluminum target operated at 10 kV, one can assume that the radiation incident on the polymer film is entirely the Aluminum K at 8.34 Å. The reasons for this can be understood as follows: The

electrons bombard the target at near normal incidence, and only those x-rays which are emitted in the backward normal direction expose the sample. The intensity of the Bremsstrahlung x-rays produced by the deceleration of electrons is a minimum in this backward direction [13]. Characteristic x-rays, on the other hand, are radiated isotropically by the target atoms, but due to target reabsorption have a maximum intensity in the back direction. The aluminum foil filter shown in Figure 3 is designed to reduce substrate heating by reflecting the visible and infrared radiation given off by the x-ray source. However, it also acts as a strong filter for any residual Bremsstrahlung x-rays with wavelengths below the aluminum absorption edge at 7.9 \AA . The silicon membrane, with a K-absorption edge at 6.7 \AA , performs the same role. On the long wavelength side of 8.34 \AA , the absorption coefficients of both aluminum and silicon increase as λ^3 , and any long wavelength tail of the Bremsstrahlung spectrum is quickly attenuated.

The x-ray energy flux ϕ at the substrate surface is given by:

$$\phi = \frac{I \epsilon \eta h \nu \alpha}{q r^2} \quad (1)$$

where I is the electron beam current, ϵ is the number of x-ray quanta produced per electron per steradian, η is the target reabsorption factor, α the filter absorption factor, q the electronic charge and r the target-to-sample distance. The published value for ϵ is 2.7×10^{-4} photons per steradian-electron [14]. η is 0.93 [15]. For a 2.5 \mu m thick Al filter α is 0.768. Thus, for $r = 3.0$ centimeters and a target current $I = 30 \text{ mA}$, the flux of 8.34 \AA x-radiation at the substrate surface is 1.1 mW/cm^2 . From this one can calculate the energy dissipation per unit volume in the substrate polymer film.

Figure 4 is a plot of the development rate of 950,000 molecular weight PMMA as a function of radiation dosage for the Al_K x-ray (8.34 \AA). It shows that the development rate varies as the 3.4 power of the radiation dose. Earlier measurements made with the 2.3 \AA chromium x-ray showed a cubic dependence [2,3]. Measurements by Hawryluk [19] of the development rate of the same PMMA showed that over the range of development rate from 100 \AA/min to $10,000 \text{ \AA/min}$ the dependence was to the 2.75 power.

The abscissa in Figure 4 is in arbitrary units. However, if the above calculation of the energy flux (1.1 mW/cm^2) is used together with a value of 1000 cm^{-1} for the absorption coefficient of PMMA at 8.34 \AA , then the number 1 on the abscissa corresponds to 100 Joules/cm^3

absorbed in the PMMA. If Figure 4 with this absolute abscissa scale is compared with the data obtained by Hawryluk [19], the two plots are within 20% of one another at a point corresponding to a development rate of 1000 Å/min. This agreement in the absolute sensitivity of PMMA to electron and x-ray exposure is within the uncertainties in the parameters in the Equation (1) and the value of the absorption coefficient for PMMA. This agreement is significant and implies that the development rate of PMMA is essentially independent of the nature of the ionizing radiation, and depends only on the energy dissipated per unit volume; a conclusion consistent with the work of Mikitishin [17].

It should be noted that the PMMA used in the present work was obtained commercially [18] and was specified to have a narrow molecular weight distribution around 950,000. This material was further refined to remove any low molecular weight fragments and unreacted monomer. A small quantity of the polymer (1% by weight) was stirred overnight in a mixture of 40% methyl isobutyl ketone (MIK) and 60% isopropyl alcohol (IPA). The material which would not dissolve was then filtered out, dried, dissolved in toluene in a 5% by weight solution, and spun onto substrates. The substrates were baked at 170°C for one hour prior to exposure. The developer solution used with this PMMA was also 40% MIK and 60% IPA, and thus the unexposed polymer film was insoluble in the developing solution.

Figure 5 shows the kind of profile obtained when a thick film of PMMA is exposed by x-ray lithography. Note that the pattern consists of submicrometer linewidth stripes standing alone in a completely exposed field. Such a structure would be very difficult to obtain with electron lithography because of electron backscattering problems [16, 19]. Thus, the figure illustrates the absence of a backscattering problem in x-ray lithography, and that exposure takes place only at points in a direct line-of-sight to the source. The non-vertical slope of the sidewalls is attributed to the finite extent of the x-ray source.

DIODE FABRICATION

A large area array of silicon p-n junction diodes having minimum linewidths of 2.5 μm was fabricated using x-ray lithography in place of conventional photolithography. The starting wafers were 4 cm diameter, 0.1 Ω-cm, n-type silicon, oxidized with 4400 Å of SiO₂. They were coated with KMNR [20] and exposed using the x-ray mask of Figure 2 and a target-sample distance of 49 mm. After development of the KMNR, the oxide cuts were chemically etched and the p-dopant, boron, diffused in until a junction depth of 0.5 μm was achieved. After doping,

the sample was coated with a 3000 Å thick film of evaporated aluminum. The sample was then coated with 1000 Å of PMMA and a pattern of contact pads exposed by x-ray lithography. The aluminum was then chemically etched. The contact pad mask was aligned relative to the oxide cuts by means of an infrared microscope. Both the silicon sample and the x-ray mask are transparent to infrared, and the alignment is relatively straightforward. This method lacks resolution, however, and in the fabrication of transistors described in the next section visible light in conjunction with alignment marks on SiO₂ windows was used instead.

Figure 6 is a photograph of a typical diode, showing the rectangular oxide cut and three contact fingers. The physical alignment of the mask was done manually and as a result, is displaced vertically by about 5 microns and rotationally by about one degree. Figure 7 is an I-V curve of one of the diodes. This is believed to be the first time that x-ray lithography was used to fabricate silicon p-n junction devices.

TRANSISTOR FABRICATION

Figure 8 is a cross-sectional schematic of the transistors that have been fabricated using x-ray lithography. In summary, the fabrication steps were as follows:

- 1) Oxide grown on n-type silicon.
- 2) Patterns for oxide base cuts defined by x-ray lithography in 3000 Å of PMMA.
- 3) Oxide chemically etched and boron base diffusion driven in.
- 4) 3500 Å oxide regrown on sample.
- 5) Patterns for emitter oxide cuts defined by x-ray lithography in 3000 Å of KMNR.
- 6) Oxide chemically etched and emitter phosphorous diffusion driven in.
- 7) Sample recoated with 3000 Å of KMNR and base contact windows defined by x-ray lithography.
- 8) Sample metallized with 4000 Å of 96% aluminum - 4% silicon.
- 9) Pattern of contact pads exposed by x-ray lithography in 4000 Å thick PMMA and the metallization chemically etched.

In steps 5, 7 and 9, the x-ray masks had to be aligned relative to the oxide cuts formed in steps 2 and 3. This alignment utilized gold

patterns supported on 10,000 Å thick SiO₂ windows distributed around the periphery of the x-ray mask. The oxide film was deposited by rf sputtering techniques after the boron had been diffused into the silicon. After formation of the silicon membrane, the boron doped silicon behind the oxide windows was etched by means of an isotropic silicon etch consisting of nitric, hydrofluoric and acetic acids. The resulting x-ray mask is shown in schematic cross-section in Figure 9.

Figure 10 is a view looking into a 125 μm × 125 μm alignment window. The gold alignment marks are clearly visible and can be aligned optically with a split field microscope. The oxide windows tend to wrinkle, but the lateral displacement of the patterns is very small and could be neglected in the present work.

The alignment of the masks was done by hand, which severely limited its accuracy and repeatability. However, in principle, the alignment could be as good as is provided by current optical mask alignment systems. With x-ray alignment [2,4] an accuracy of 1/10 μm appears feasible.

Figure 11 is a photograph of a typical transistor and Figure 12 is a family of characteristic curves. Results so far indicate that there is very little x-ray induced charge formation in the oxide, and that which does occur is annealed out during the 5 min, 455°C sintering of the metallization.

HIGH RESOLUTION GRATINGS

X-ray masks consisting of silicon membranes supporting gold lines 3000 Å thick and approximately 1800 Å wide on 3600 Å centers were produced by laser holographic techniques and ion beam etching [21]. These in turn were replicated in PMMA films by x-ray lithography as verified by optical diffraction and scanning electron microscopy. This result clearly demonstrates the extreme high resolution capability of x-ray lithography.

CONCLUSIONS

The technique of making large area silicon masks for x-ray lithography has been reduced to a routine procedure. Both infrared and visible optical methods have been used to superimpose patterns from several masks on a substrate. Junction diodes and bipolar transistors made by x-ray lithography have exhibited expected performance

and have shown no adverse effects due to x-ray exposure. Sharp relief structures of sub-micrometer linewidth were obtained in 11,000 Å of PMMA by x-ray lithography, and gratings of 1800 Å linewidth were replicated in 3000 Å thick PMMA, thereby demonstrating the high resolution capability of the technique.

ACKNOWLEDGEMENTS

The authors are grateful to D.L. Spears for many helpful discussions and suggestions, to B. Kenney for his valuable semiconductor processing advice and for carrying out the oxide growth and thermal diffusion, to S. Chinn for holographic exposure of the grating, to J. Raffel and E. Stern for encouragement and support, and to N. Efremow, M. Lemma, G. Foley and R. Reinhard for technical assistance.

References

1. D.L. Spears and Henry I. Smith, *Electron, Lett.* 8, 102 (1972).
2. D.L. Spears and Henry I. Smith, *Solid State Technol.* 15, 21 (1972).
3. D.L. Spears, Henry I. Smith, and E. Stern, in Proceedings of the Fifth International Conference Electron and Ion Beam Science and Technology, edited by R. Bakish (The Electrochemical Society, Princeton, 1972), p. 80.
4. Henry I. Smith, D.L. Spears, and S.E. Bernacki, *J. Vac. Sci. Technol.* 10, 913 (1973).
5. R.A. Cohen, R.W. Mountain, D.L. Spears, H.I. Smith, M.A. Lemma, and S.E. Bernacki, "Fabrication procedure for silicon membrane x-ray lithography masks," Technical Note 1973-38, 20 September 1973, Massachusetts Institute of Technology, Lincoln Laboratory, Lexington, Massachusetts 02173.
6. Taketoshi Kato and Yoshio Nishi, Japan, *J. Appl. Phys.* 3, 377 (1964).
7. R.M. Finne and D.L. Klein, *J. Electrochem. Soc.* 114, 965 (1967).

8. J. C. Greenwood, *J. Electrochem. Soc.* 116, 1325 (1969).
9. A. Bohg, *J. Electrochem. Soc.* 118, 401 (1971).
10. F. Hayashi, Y. Tarui, et al. *Denshi Gijutsu Sogo Kenkyujo Iho* 36, 27 (1972).
11. Vacuum Generators Limited, model EG-1, East Grinstead, Sussex, England.
12. H. I. Smith, Fabrication Techniques for Surface Acoustic Wave and Thin Film Optical Devices, to be published in Proceedings IEEE, Fall 1974.
13. Burton L. Henke, X-ray Microscopy and Microradiography, V. E. Cosslett, Arne Engstrom and H. H. Pattee, Eds. (Academic Press, New York, 1957), p. 72.
14. M. Green, X-ray Optics and X-ray Microanalysis, H. H. Pattee, V. E. Cosslett and A. Engstrom, Eds. (Academic Press, New York, 1963), p. 185.
15. M. Green, X-ray Optics and X-ray Microanalysis, H. H. Pattee, V. E. Cosslett and A. Engstrom, Eds. (Academic Press, New York, 1963), p. 361.
16. R. J. Hawryluk, A. M. Hawryluk, and H. I. Smith, Energy Dissipation in a Thin Polymer Film by Electron Beam Scattering, to be published in *J. Appl. Phys.* June 1974.
17. S. I. Mikitishin, A. N. Tinne, and Z. A. Bazilevich, "Strength of Irradiated Polymethylmethacrylate," *Fiz.-Khim Mekh. Mater.*, 1968, 4, pp. 459-462.
18. Esschem Corporation, Essington, Pennsylvania, mol. wt. 950,000.
19. R. J. Hawryluk, Energy Dissipation by Electron Beam Scattering in Thin Polymer Films, Ph. D. Thesis, MIT, June 1974.
20. Kodak Micronegative Resist, Eastman Kodak Company, Rochester, New York.
21. S. E. Bernacki, S. R. Chinn, and H. I. Smith, 3600 Å Periodicity Gratings Produced by X-ray Lithography, to be published.

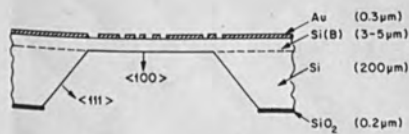


Fig. 1. X-ray lithography mask consisting of a 3000 Å thick gold absorber pattern on a 3 to 5 μm thick single crystal silicon membrane.

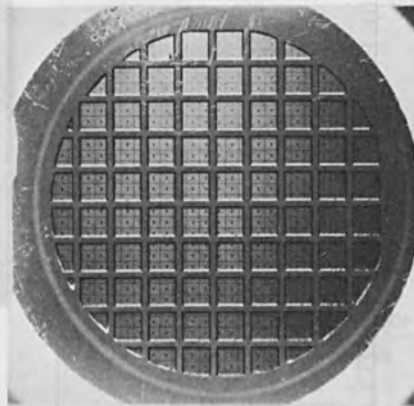


Fig. 2. Large area x-ray lithography mask fabricated from a 4 cm diameter silicon wafer. The windows are 2.5 mm square and are separated by 0.5 mm wide supporting ribs. The photograph was taken from the etched side of the wafer at normal incidence. Light transmitted through the silicon membranes reveals the gold absorber patterns. Light from the etched side reflects off the $\langle 111 \rangle$ faces of the windows thus highlighting the supporting rib structure.

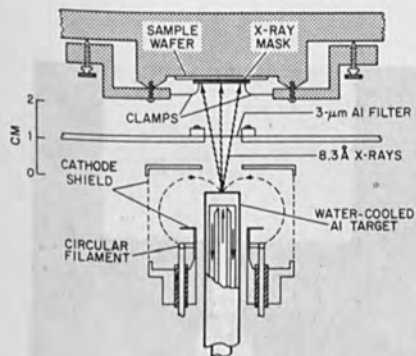


Fig. 3. Cross sectional drawing of the x-ray exposure system. The source is cylindrically symmetric. For exposure of 4 cm diameter samples, the source to sample distance is increased from the 30 mm shown to 49 mm.

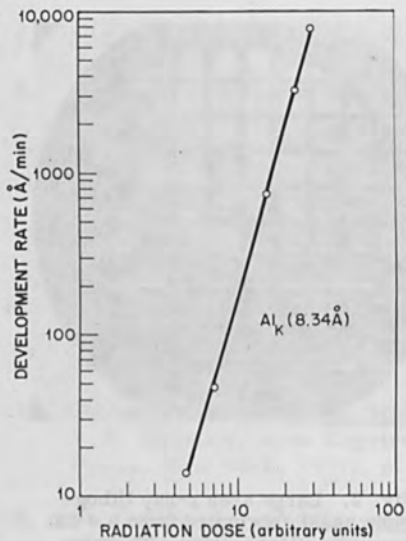


Fig. 4. Graph of development rate of PMMA versus radiation dose of 8.34 Å aluminum K x-rays. The PMMA molecular weight was 950,000. Development was by immersion in a room temperature solution of 40 percent MIK and 60 percent IPA. Calculations indicate that the number one on the abscissa scale corresponds to 100 Joules per cm³ absorbed in the PMMA.

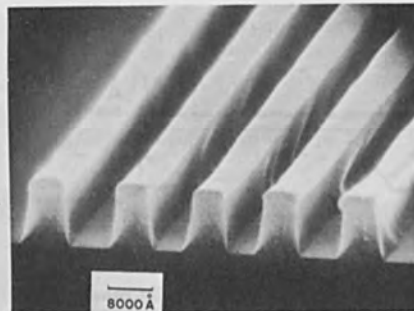
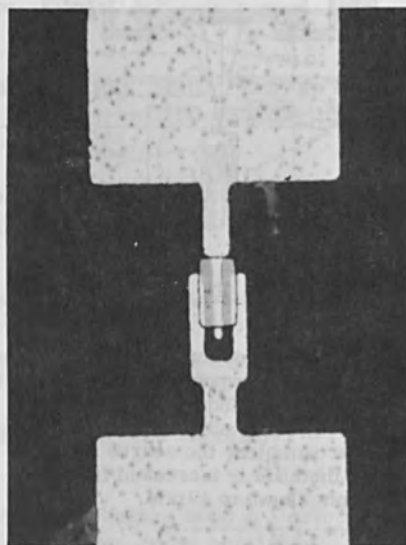


Fig. 5. Scanning electron micrograph of relief structures exposed in 11,800 Å thick PMMA by x-ray lithography. There are five stripes of PMMA in an otherwise completely exposed field. Micrograph by R. Eager.

Fig. 6. Optical micrograph of a diode fabricated using x-ray lithography. The minimum linewidth is 2.5 microns.



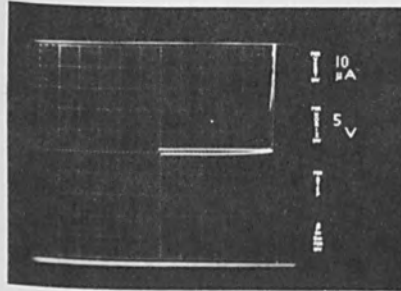


Fig. 7. Reverse I-V curve of a diode of the type shown in Figure 6. Reverse breakdown occurs at -27 volts.

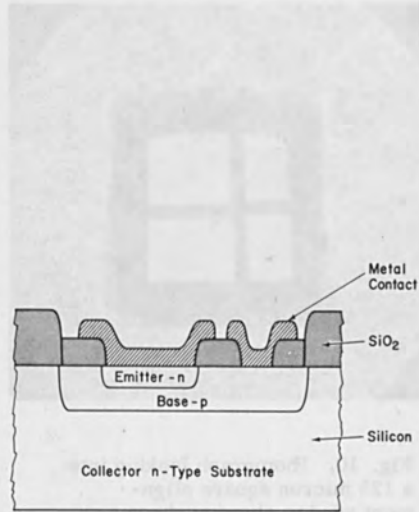


Fig. 8. Schematic cross section of a transistor fabricated using x-ray lithography. The emitter oxide cut also serves as the contact cut. Four lithographic steps were required, in three of which the mask pattern had to be registered with respect to previous patterns.



Fig. 9. Schematic cross section of an x-ray lithography mask used in transistor fabrication. The thick SiO_2 supports benchmarks for optical alignment and also acts as a spacer between the mask and the sample.

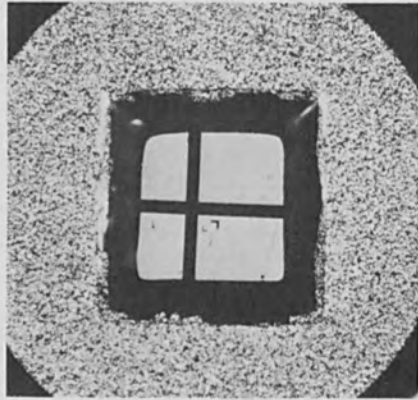


Fig. 10. Photograph looking into a 125 micron square alignment window showing chrome-gold alignment marks supported by clear silicon dioxide.

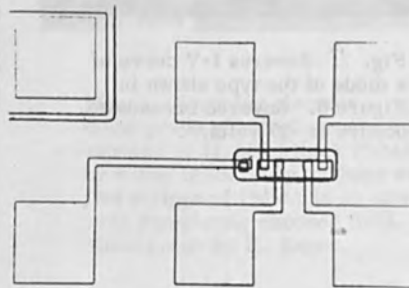


Fig. 11. Typical transistor fabricated using x-ray lithography. The emitter has four metallized contacts for resistivity measurements, the base has one contact, and the collector contact is made at the back of the wafer. Minimum linewidth here is $10 \mu\text{m}$.

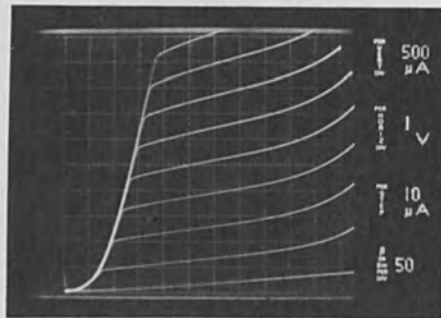


Fig. 12. Grounded emitter family of curves for transistor of Figure 11. The collector-emitter leakage was unchanged by annealing and is attributed to cleaning procedures and the large base area-to-width ratio.

ELECTRON-RESIST EXPOSURE COEFFICIENT FOR VARIOUS PATTERNS

A. K. JONES and T. VAN DER

Department of Electrical Engineering and Computer Science
and the Microelectronic Research Laboratory
University of California, Berkeley, California 94720

General Motors Research

General Motors Research Laboratory

Warren, Michigan 48090

ABSTRACT

Using our previously developed model for the electrostatic exposure coefficient, we have calculated the exposure coefficient for patterns of equal density of energy absorption for several important situations. These include: (1) isolated lines of various widths on substrates of 0.25 μ m, 0.5 μ m and infinity; (2) thick films; (3) thin films; (4) by using a thin substrate and a thick resist layer, it is possible to achieve a resist layer thickness of 1.2 μ m which is about 10% of the substrate thickness. We have also calculated the exposure coefficient for patterns of the same density of energy absorption for thick films and thin films.

PART I

Section 2

Electron and X-Ray Resists

It is shown that there is an simple value of exposure which gives good undercutting for all values of the charge in the resist. Calculations for films have been done for several regions also that for a 20 kV beam, a 0.5 μ m resist layer, and a 0.25 μ m substrate, the critical ray is about 0.1 μ m. In all cases the model was used as having an effective resist under and density typical of resists.

1. INTRODUCTION

The fabrication of especially of microelectronic circuits is done at present with photolithographic processes which have dimensional accuracies of the order of a few microns. There is a continuing pressure to further reduce the size of electronic circuits and this has led to the search for improved photolithographic and the development of 1- μ m and submicron lithography. This paper is concerned with the development of techniques for electron-beam exposure of

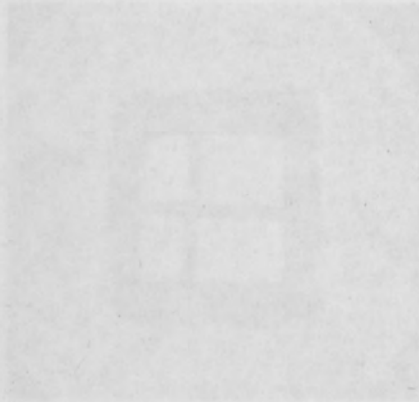


Fig. 10. Transistor structure showing a 100-ohm emitter region and a 100-ohm base region. The collector region is 100-ohm.



Fig. 11



Fig. 12. Transistor structure showing a 100-ohm emitter region and a 100-ohm base region. The collector region is 100-ohm.

Fig. 11

Fig. 11. Typical transistor fabricated using x-ray lithography. The emitter has four metallized contacts for resistivity measurement, the base has one contact, and the collector contact is made at the back of the wafer. Minimum dimensions were 10, μ .

ELECTRON-RESIST EXPOSURE CONTOURS FOR VARIOUS PATTERNS

R. E. Jewett and T. Van Duzer
Department of Electrical Engineering and Computer Science
and the Electronics Research Laboratory
University of California, Berkeley, California 94720

J. S. Greeneich
General Motors Research Laboratory
Warren, Michigan 48090

ABSTRACT

Using our previously developed model for the electron-beam exposure of resist films on substrates, we have examined the contours of equal density of energy absorption for several important situations. These include single, isolated lines and sets of parallel lines on substrates of 0.05 μm , 0.4 μm and infinite thickness. It is found that, by using a thin substrate and resist layer, it should be possible to fabricate thin-film parallel lines of 0.1 μm thickness with about 0.075 μm center-to-center spacing. We have studied the energy-absorption contours at the edges of large exposed regions for thick substrates. This includes straight edges and inside and outside right-angle corners. It is found that there is no single value of exposure which gives good undercutting for all cases unless the charge is programmed. Calculations for linear gaps between large exposed regions show that for a 20 kV beam, a 0.4 μm resist layer, and a thick substrate, the minimum gap is about 0.2 μm . In all cases PMMA was used as having an average atomic number and density typical of resists.

I. INTRODUCTION

The fabrication of essentially all commercial electronic microcircuits is done at present with photolithographic processes which have dimensional accuracies of the order of a few microns. There is a continuing pressure to further reduce the size of electronic circuits and this has led to the search for improved photoresist techniques and the development of X-ray and electron-beam lithography. This paper is directed toward providing guidelines for electron-beam exposure of

patterns in a resist layer. These guidelines are of greatest importance where the ultimate in small sizes is being sought. To date the narrowest thin-film single lines that have appeared in the literature are about $0.06 \mu\text{m}$ wide; we investigate here the details of the exposure of a resist for such small lines. The use of thin substrates to obtain ultrafine parallel lines has been demonstrated by Sedgwick, *et al.* [1] where lines of $0.06 \mu\text{m}$ width with a periodicity of about $0.33 \mu\text{m}$ were fabricated using a 25 kV beam on $0.15 \mu\text{m}$ windows of Si_3N_4 on Si frames. We study here the pattern of energy absorption in the resist effected by using thin substrates and show that even more closely spaced lines of smaller width should be achievable.

We have developed a model [2] to describe the patterns of energy absorption in a resist film which is similar to one presented by Hawryluk and Smith [3] who have later compared both models with Monte Carlo calculations and found reasonably good agreement [4]. The usefulness of the calculated distribution of the density of energy absorption lies in the concept that the large molecules of the polymer resist are broken in proportion to the amount of energy absorbed. Thus, contours of equal energy absorption density are also contours of equal average molecular size. It is then assumed that a developer will dissolve all molecules smaller than a certain size, which depends on the composition of the developer.* With this assumption, contours of equal energy absorption density ultimately form the boundaries of the developed resist. It should be pointed out here that proper modeling of the developer action remains to be done and that the accuracy of the predictions of calculations such as are presented in this paper will be improved thereby. However, we believe the assumption that a developer simply removes all molecules smaller than some given size is sufficient to give results of first-order accuracy for positive resists.

With our model we find the fraction of the incident electrons passing through each point in the resist in the neighborhood of the point of incidence of the beam and also determine the rate of energy loss of the electrons at each point. Thus we can determine, for an electron incident with a certain energy on a resist film coating some possibly complex substrate, the probability distribution of the energy lost by the electron. We subsequently apply this to find the distribution of energy absorption in the resist for a beam with a Gaussian density distribution. Patterns of exposure can be made in a variety of ways in practice. One is to form its shape with an array of discrete point positions of the beam; in this case the exposure can be calculated as the superposition of an array of dot exposures. This is the procedure we follow but the basic model can also be adapted to a continuously scanned beam or any other scheme of beam control. Line exposures can be formed as a series of discrete dots; if their separation is comparable with the $1/e$ diameter of the Gaussian

* There has been some recent evidence that this is not a good assumption for negative resists.

distribution within the beam, this will be a good approximation to a continuous line. The results presented in this paper all employ such closely spaced dots.

The language used and conclusions reached herein are related mainly to the lift-off technique devised by Hatzakis [5]. That involves development along a boundary which leaves the resist undercut so a film thinner than the resist, deposited on the developed resist and exposed substrate, will have the two parts unconnected. Then removal of the remaining resist will lift off the undesired parts of the film. Thus we emphasize obtaining undercut exposure patterns; other applications, such as masks for ion implantation, may have different requirements.

We first present results for single lines of exposure formed as a row of closely spaced dots for both thin and thick substrates. Some numerical data are given to permit programming to calculate other patterns. We then present the results of calculations on parallel lines of exposure to show what must be done to obtain distinct lines. Area exposures are obtained as the limit of closely spaced lines with nearly uniform resulting energy absorption. Consideration is then given to some situations at edges of large exposed regions to see how the exposure must be designed to achieve good edge definition at all points in a single circuit. Finally, we analyze a linear gap between two large exposed regions to find the smallest strip of resist that could be left undeveloped.

II. SINGLE-LINE EXPOSURES

We have calculated the line responses of the resist to the electron beam for conditions including a variety of beam voltages (10, 20, and 30 kV) and substrate thicknesses (0.05, 0.4 μm and infinite). In these calculations, the resist thickness was 0.4 μm in all cases; the results for thinner resists can be deduced from these in a simple way for some situations, as discussed below. The beam is taken to have a cylindrical Gaussian distribution of current density with a $1/e$ radius of 125 \AA . It is assumed to be positioned in a series of dots as discussed in the Introduction with the dot spacing here taken to be 300 \AA . With such close spacing, the series of dots is nearly equivalent to a continuously distributed line of incident charge. However, the exposure along a line perpendicular to the row of dots will be somewhat different depending on whether or not the line passes through a dot; this difference becomes more pronounced for increased dot spacing.

We show in Fig. 1 the exposure of a 0.4 μm -thick resist by a 30 kV beam for two different substrate thicknesses. The exposure is measured in electron volts/cm³ for one coulomb per centimeter ($\text{eV/C}\cdot\text{cm}^2$), and is plotted as a function of the distance perpendicular to the row of dots with the line of calculation passing through a dot. The solid lines show the results for the infinitely thick substrate and the

patterns in a resist layer. These guidelines are of greatest importance where the ultimate in small sizes is being sought. To date the narrowest thin-film single lines that have appeared in the literature are about $0.06 \mu\text{m}$ wide; we investigate here the details of the exposure of a resist for such small lines. The use of thin substrates to obtain ultrafine parallel lines has been demonstrated by Sedgwick, *et al.* [1] where lines of $0.06 \mu\text{m}$ width with a periodicity of about $0.33 \mu\text{m}$ were fabricated using a 25 kV beam on $0.15 \mu\text{m}$ windows of Si_3N_4 on Si frames. We study here the pattern of energy absorption in the resist effected by using thin substrates and show that even more closely spaced lines of smaller width should be achievable.

We have developed a model [2] to describe the patterns of energy absorption in a resist film which is similar to one presented by Hawryluk and Smith [3] who have later compared both models with Monte Carlo calculations and found reasonably good agreement [4]. The usefulness of the calculated distribution of the density of energy absorption lies in the concept that the large molecules of the polymer resist are broken in proportion to the amount of energy absorbed. Thus, contours of equal energy absorption density are also contours of equal average molecular size. It is then assumed that a developer will dissolve all molecules smaller than a certain size, which depends on the composition of the developer.* With this assumption, contours of equal energy absorption density ultimately form the boundaries of the developed resist. It should be pointed out here that proper modeling of the developer action remains to be done and that the accuracy of the predictions of calculations such as are presented in this paper will be improved thereby. However, we believe the assumption that a developer simply removes all molecules smaller than some given size is sufficient to give results of first-order accuracy for positive resists.

With our model we find the fraction of the incident electrons passing through each point in the resist in the neighborhood of the point of incidence of the beam and also determine the rate of energy loss of the electrons at each point. Thus we can determine, for an electron incident with a certain energy on a resist film coating some possibly complex substrate, the probability distribution of the energy lost by the electron. We subsequently apply this to find the distribution of energy absorption in the resist for a beam with a Gaussian density distribution. Patterns of exposure can be made in a variety of ways in practice. One is to form its shape with an array of discrete point positions of the beam; in this case the exposure can be calculated as the superposition of an array of dot exposures. This is the procedure we follow but the basic model can also be adapted to a continuously scanned beam or any other scheme of beam control. Line exposures can be formed as a series of discrete dots; if their separation is comparable with the $1/e$ diameter of the Gaussian

* There has been some recent evidence that this is not a good assumption for negative resists.

distribution within the beam, this will be a good approximation to a continuous line. The results presented in this paper all employ such closely spaced dots.

The language used and conclusions reached herein are related mainly to the lift-off technique devised by Hatzakis [5]. That involves development along a boundary which leaves the resist undercut so a film thinner than the resist, deposited on the developed resist and exposed substrate, will have the two parts unconnected. Then removal of the remaining resist will lift off the undesired parts of the film. Thus we emphasize obtaining undercut exposure patterns; other applications, such as masks for ion implantation, may have different requirements.

We first present results for single lines of exposure formed as a row of closely spaced dots for both thin and thick substrates. Some numerical data are given to permit programming to calculate other patterns. We then present the results of calculations on parallel lines of exposure to show what must be done to obtain distinct lines. Area exposures are obtained as the limit of closely spaced lines with nearly uniform resulting energy absorption. Consideration is then given to some situations at edges of large exposed regions to see how the exposure must be designed to achieve good edge definition at all points in a single circuit. Finally, we analyze a linear gap between two large exposed regions to find the smallest strip of resist that could be left undeveloped.

II. SINGLE-LINE EXPOSURES

We have calculated the line responses of the resist to the electron beam for conditions including a variety of beam voltages (10, 20, and 30 kV) and substrate thicknesses (0.05, 0.4 μm and infinite). In these calculations, the resist thickness was 0.4 μm in all cases; the results for thinner resists can be deduced from these in a simple way for some situations, as discussed below. The beam is taken to have a cylindrical Gaussian distribution of current density with a $1/e$ radius of 125 \AA . It is assumed to be positioned in a series of dots as discussed in the Introduction with the dot spacing here taken to be 300 \AA . With such close spacing, the series of dots is nearly equivalent to a continuously distributed line of incident charge. However, the exposure along a line perpendicular to the row of dots will be somewhat different depending on whether or not the line passes through a dot; this difference becomes more pronounced for increased dot spacing.

We show in Fig. 1 the exposure of a 0.4 μm -thick resist by a 30 kV beam for two different substrate thicknesses. The exposure is measured in electron volts/cm³ for one coulomb per centimeter ($\text{eV/C}\cdot\text{cm}^2$), and is plotted as a function of the distance perpendicular to the row of dots with the line of calculation passing through a dot. The solid lines show the results for the infinitely thick substrate and the

broken lines show the exposure for the 0.05 μm -thick substrate for which there is essentially no backscattering. It is clear that there is a strong reduction in the range of influence of a line exposure where the backscattering from the substrate is missing.

In Fig. 2 we show four sets of exposure contours for single, isolated lines. Figure 2a contains the contours for 20 kV exposures with the left half illustrating the shapes obtained with a thin substrate and the right side showing those with a thick substrate. Figure 2b shows the same kind of information for 30 kV exposures. The values are in units of 10^{30} eV/coulomb \cdot cm². It is clear that for an isolated line the effect of backscattering is minimal except for the weakest contours. It appears possible to make exposures which will lead to undercut patterns that can be used to make lines of width approximately equal to twice the $1/e$ diameter of the electron beam.

Since we cannot calculate all the possibly important configurations of lines, we have chosen to list data which could be used to make other calculations. Again, there is some limitation on the amount of data that could be listed here so we have chosen what may be the most important for the majority of calculations. In Tables 1 and 2, we list for 20 and 30 kV exposures on thick substrates a sufficient amount of data to determine points on contours at the surface, midway, and at the bottom of a 0.4 μm -thick resist on an Al substrate (chosen because of having an atomic number between Si and SiO₂). Since superposition applies, one could use these data to calculate any exposure (for these combinations of voltages, substrate, and resist thickness) which could be described as a combination of lines.

III. PARALLEL-LINE EXPOSURES

There is a variety of circumstances in which it is desired to have a set of parallel-line exposures. If one attempts to make lines too close together, the exposure from one line exerts an influence on those of the neighboring lines. This will be affected by such factors as beam voltage and resist and substrate thicknesses. Here we present the results of a study of these dependences and see how the most closely spaced lines should be obtained.

In Figures 3 and 4 we show contours for a beam voltage of 20 kV for two different line spacings and for two different substrate thicknesses. The corresponding contours in the case of a 0.4 μm -thick substrate have shapes which lie between those for the 0.05 μm and infinitely thick substrates.

In order to achieve a development of the resist that will expose some area on the substrate (for example, for subsequent deposition of a metal film), it is required that there be some contour which starts from the resist surface and extends to the substrate. That this does not always occur is illustrated by the case of exposure by a 10 kV beam

of a $0.4\ \mu\text{m}$ resist on a deep substrate. We show one example of this in Fig. 5 for lines spaced by $0.2\ \mu\text{m}$. The condition for useful exposures for lift-off procedures is actually a little stronger than stated above. The contour must also be shaped in such a way that the developed region will leave an undercut undeveloped resist such that subsequent thin-film deposition will make the portion reaching the substrate disconnected from that on top of the resist.

When attempting to make parallel lines, excessive, or otherwise poorly designed, exposures can lead to removal of all the resist upon subsequent development. Clearly, even for rather large line spacing (say, up to about $2\ \mu\text{m}$) sufficient amounts of charge will raise the energy absorption at all points in the resist to levels above that required for removal by the developer. Another factor in the production of distinct parallel lines which we have discussed earlier [2], is that the pattern of energy absorption must be such that there is a significant difference between the exposures at the resist-substrate interface at the line and half-way between lines. Otherwise, if the exposure is sufficient at the line for the developer to remove the resist on the substrate, it will also be sufficient to lead to development of the resist between lines. Thus, the ratio of the energy absorbed at line to that half-way between (both on the resist-substrate interface) is an important criterion for the achievability of a desired pattern. For example, if one can assume that he has control of the developer and exposure to no better than 50 percent, he should require the above mentioned ratio to be greater than 1.5. In Fig. 6 we show some energy-absorption contours in a $0.4\ \mu\text{m}$ resist for a 30 kV exposure with a $0.2\ \mu\text{m}$ line spacing on a $0.05\ \mu\text{m}$ substrate. The contour marked c is for the energy at the minimum exposure point on the substrate mid-way between lines. The contour marked a is the one having the maximum exposure which will lead to undercut developed patterns and therefore be useful in the lift-off process. We assume that it is desired to arrange the exposure so that contour a will bound the developed region and errors in the control of the exposure and developer sensitivity must not be sufficient to develop as far over as contour c. We have plotted the ratio of the exposure on a to that on c as a function of line spacing for the thin-substrate case for three beam voltages in Fig. 7. It can be seen that a ratio of 2.0 is obtained for 30 kV exposure with a line spacing as small as $0.15\ \mu\text{m}$. The higher voltages have a clear advantage for achieving closely spaced lines on a thin substrate. (Though not shown here, a somewhat smaller advantage is found for higher beam voltages on thick substrates.) The ratio of the exposure on contour a to that on c is shown for various substrate thicknesses and a 20 kV beam as a function of line spacing in Fig. 8.

We should point out here that whereas the calculations were done for a $0.4\ \mu\text{m}$ resist layer, the results can be used to deduce the expected contours for thinner resists when there is no significant backscattering, as in the case of the thin substrate. Thus, to see the contours for a 30 kV exposure of a thinner resist on a thin

substrate, one need only consider the substrate to lie closer to the top of the resist in Fig. 6. We have found that the maximum-to-minimum exposure ratio discussed above can be as high as 3.0 for a line spacing as small as $0.075 \mu\text{m}$ with a resist thickness of $0.2 \mu\text{m}$. This is a conservative estimate as the actual ratio should be slightly more favorable since the backscattering from $0.2 \mu\text{m}$ of resist is eliminated.

Another useful piece of information which can be deduced from the parallel-line calculations is the expected width as a function of the line spacing for thin-film lines deposited through the mask resulting from these exposures and developments. We present the line-width data for two situations in Figs. 9 and 10: 20 kV on $0.05 \mu\text{m}$ substrate, and 20 kV on a thick substrate, respectively. The line width will be taken to be the spacing between contours at a level $0.1 \mu\text{m}$ below the resist surface. In earlier work [3] we saw that this is the criterion which best represents the experimental data; the possible reasons have been presented there. The minimum line width is the spacing between contours a and a' in Fig. 6 at $0.1 \mu\text{m}$ below the surface and is plotted as a function of line spacing in Figs. 9 and 10. The maximum line width cannot be defined as unambiguously. The absolute (but probably unusable) maximum is set by the contours c and c' that barely reach the substrate at the mid-points between lines. The contours b and b' are for exposures twice those of c and c' and set a more usable limit for the maximum line width. The maximum line width is shown as a band in Figs. 9 and 10.

The limit of the parallel-line exposure in which one obtains area exposures is where the energy absorbed at all points in the resist is greater than that necessary to break down the molecules sufficiently for development.

IV. EXPOSURE CONTOURS AT EDGE OF LARGE EXPOSED REGION

One potential difficulty in making exposures for complex circuits of the smallest sizes is that backscattering makes the contours at the edge of an exposed region depend on the size and shape of the region.* Then if the same charge is used for every point in the entire exposure, it may not be possible to find a level of exposure that will lead to the simultaneous development of all parts of the circuit. Such a result would obtain, for example, where a pattern contains both large exposed regions and single, isolated lines. Therefore, we have determined the exposure profiles for a variety of potentially important configurations to see how the exposure might be programmed in various

*We consider here only thick substrates though it is conceivable that the need to have especially high resolution at some points in an integrated circuit would require the inclusion of thin regions in which there is no important backscattering.

parts of a pattern to achieve uniform development.

We have studied the exposure contours at the edge of large exposed regions for four different situations. In all cases the parameters were: beam voltage = 20 kV; beam 1/e radius = 0.0125 μm ; dot spacing = 0.03 μm ; resist thickness = 0.4 μm ; thick substrate. The first of the four situations is a large region with a straight edge and the contours are calculated along a line perpendicular to the edge. The second is an outside 270° angle on a large region with the line of examination along the bisector of the angle. The third is an inside angle of 90° on a large exposed region and the contours are found along the bisector of the angle. The last is for the straight edge but extra charge was added to the line at the edge to adjust the shape of the exposure contours. The results are shown in Figs. 11-14. The numbers shown on the contours, when multiplied by 10^{18} give the energy absorbed per cm^3 if there were one electron per dot in the exposure. For a given amount of charge per dot and a given developer, the development will take place along some set of contours which have the same labeling in each of these figures.

We see in Fig. 11 that the contour marked 1.0 would be a good choice to obtain an undercut resist mask. In fact, contours between about 0.5 and 1.2 would probably be satisfactory so there is more than a factor of 2 range of allowed exposure and developer sensitivity. However, conditions are less favorable when other situations coexist with the straight edge. Comparison of the outside and inside right-angle edges in Figs. 12 and 13 show that there is no single value of exposure which will give good contours for both situations. The value 0.5 is suitable for the outside corner in Fig. 12 but the 0.5 contour for the inside corner does not reach the substrate for a distance of about 1.0 μm because of the backscattering from the semi-surrounding exposed regions. Single exposed lines require exposures which would be in the range of 0.3 in the units used here, which is incompatible with the proper exposures for the edges of large exposed regions. The resolution of this problem would be to program the charge per dot so that in places where there is less contribution by backscattered electrons, the charge would be increased. The contours in Fig. 14 are for the straight edge but with the charge doubled in the row of dots along the edge. The effect is to push the higher values of energy absorption out into the region where the beam is not incident. The same technique should be applied to the outside corner of Fig. 12 and to any single lines present. We have not pursued this matter in detail but it seems clear that charge patterns could be included in the computer programs that perform the control of the electron beam to make exposures so that the development will give a properly undercut resist mask at all edges of the circuit pattern. We have done this in the fabrication of constricted thin films where two large areas are connected by a single narrow line.⁶

V. LINEAR GAPS IN LARGE EXPOSED REGIONS ON THICK SUBSTRATES

The aim in this section is to determine the minimum size of gap that can be left between straight, parallel edges of two large exposed regions. The beam voltage is 20 kV and it has a $1/e$ radius of $0.0125 \mu\text{m}$. The dot spacing is $0.03 \mu\text{m}$, the resist thickness is $0.4 \mu\text{m}$, and the substrate is thick. It should be clear that this is a situation where the backscattered electrons play a dominant role so the picture would be much different for thin substrates.

Figure 15 defines the gap; its width will be specified in terms of the number of rows missing so its actual width will be approximately the number of rows missing times the $0.03 \mu\text{m}$ spacing of the rows. The widest gap shown here (Fig. 16) has 20 rows missing so the gap size is about $0.6 \mu\text{m}$ and there is no difficulty in finding a suitable exposure (e.g., contour marked 1.5) but there is not a very large allowed range. The minimum gap size for these conditions is about 7 rows ($\approx 0.21 \mu\text{m}$) and this is seen in Fig. 17.⁷ Here the exposure range is only about 10 percent. If the gap is further reduced as where only two rows are missing in Fig. 18, there is no value of exposure that will work. The value chosen must be lower than that midway down the resist in the exposed region so that part will be completely developed; the numerical value here is 2.7. The exposure contour must further reach the substrate in two places so as to leave an undeveloped zone in contact with the substrate since this sheet of resist is to perform, for example, as a mask for subsequent thin-film deposition. It is clear that there is no contour in Fig. 18 that meets these criteria so a gap of that size cannot be left. It is questionable that anything much can be done about these kind of gaps by charge programming as the backscattered electrons which limit the achievable gap come from substantial distances ($\approx 7.0 \mu\text{m}$). As mentioned previously, the use of thin substrates would allow much smaller gaps.

VI. CONCLUSIONS

We have seen that it should be possible, by using a thin substrate, to make single lines and parallel lines having a width very close to twice the $1/e$ diameter of the Gaussian electron beam used for exposure. It should also be possible to make parallel thin-film lines of about $0.1 \mu\text{m}$ thickness with center-to-center spacing of about $0.075 \mu\text{m}$.⁸ Further reduction of line spacing may be possible for lines of lesser thickness since thinner resist layers could be used.

For exposures on thick substrates, we have seen that there is a necessity for programming of the charge supplied to different parts of an exposure in order to get good undercutting at all edges. Again thin substrates would ameliorate this problem because it is a result of backscattering from the substrate. We have seen that there is a lower limit on the width of an undeveloped strip of resist that can be left between two large developed regions. For a $0.4 \mu\text{m}$ resist layer and a thick substrate, this is about $0.2 \mu\text{m}$.

ACKNOWLEDGEMENT

Research sponsored by the Army Research Office - Durham, Grant DA-ARO-D-31-124-74-G165.

REFERENCES

1. T. O. Sedgwick, A. N. Broers, and B. J. Agule, J. Electrochem. Soc. 119, 1769 (1972).
2. J. S. Greeneich and T. Van Duzer, Twelfth Symposium on Electron, Ion, and Laser Beam Technology, Cambridge, Massachusetts, May 21-23, 1973. J. Vac. Sci. Technol. 10, 1056 (1973), see IEEE Trans. on Electron Devices, ED-21, (May 1974).
3. R. J. Hawryluk and H. I. Smith, 5th Inter. Conf. on Electron and Ion Beam Science and Technology, R. Bakish, Ed. (The Electrochemical Society, Princeton, New Jersey) 51 (1972).
4. R. J. Hawryluk, A. M. Hawryluk, and H. I. Smith, to be published.
5. M. Hatzakis, J. Electrochem. Soc., 116, 1033 (1969).
6. J. S. Greeneich, Ph.D. Dissertation, University of California, Berkeley, 1973.
7. It is of interest to note that the minimum gap reported for similar conditions (resist thickness not reported) was 0.2 μm . R. B. Laibowitz, Meeting of the American Physical Society, San Diego 19-20 March 1974.
8. We note that holes of 0.15 μm spacing formed into rows spaced by 1.5 μm have been fabricated in earlier work by means similar to those described here in PMMA films with no substrate underlying the exposed region. See J. J. Kim, H. G. Sampson, and T. E. Everhart, J. Vac. Sci. Technol., 10, 1005 (1973).

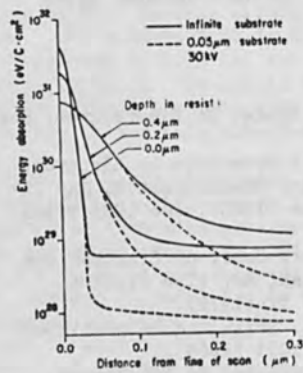


Fig. 1. Energy absorption for line exposure at various levels in a resist for two substrate thicknesses.

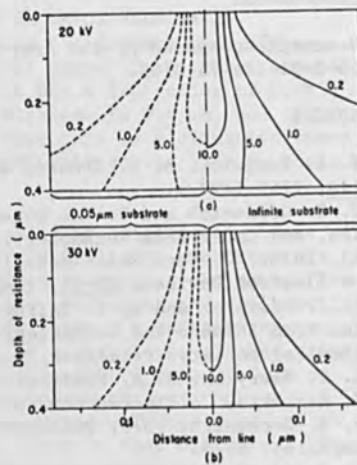


Fig. 2. Line-exposure contours of equal energy absorption for two beam energies and substrate thicknesses.

TABLE 1 20 kV
Energy absorption ($\text{eV}\cdot\text{cm}^{-3}$). Three levels in $0.4\ \mu\text{m}$ resist on thick Al substrate. Line exposure ($1\ \text{C}/\text{cm}$).

DISTANCE FROM ROW CENTER (μm)	DEPTH (μm) Values $\times 10^{30}$		
	0.0	0.2	0.4
0.00	57.876	18.288	6.703
0.01	31.463	15.504	6.562
0.02	6.442	10.491	6.167
0.03	0.515	6.014	5.620
0.04	0.148	3.287	4.983
0.05	0.143	1.878	4.314
0.07	0.140	0.755	3.090
0.09	0.138	0.424	2.151
0.12	0.135	0.267	1.271
0.16	0.132	0.204	0.715
0.25	0.127	0.165	0.354
0.35	0.123	0.149	0.262
0.49	0.117	0.137	0.216
0.75	0.107	0.120	0.179
1.25	0.090	0.095	0.139

TABLE 2 30 kV
Energy absorption ($\text{eV}\cdot\text{cm}^{-3}$). Three levels in $0.4\ \mu\text{m}$ resist on thick Al substrate. Line exposure ($1\ \text{C}/\text{cm}$).

DISTANCE FROM ROW CENTER (μm)	DEPTH (μm) Values $\times 10^{30}$		
	0.0	0.2	0.4
0.00	41.199	18.828	7.175
0.01	22.374	14.071	6.795
0.02	4.547	7.248	5.881
0.03	0.102	2.903	4.736
0.04	0.063	1.196	3.619
0.05	0.060	0.595	2.685
0.07	0.059	0.229	1.441
0.09	0.059	0.139	0.806
0.12	0.058	0.098	0.398
0.16	0.057	0.080	0.216
0.25	0.055	0.069	0.122
0.35	0.054	0.064	0.098
0.49	0.052	0.060	0.085
0.75	0.049	0.055	0.074
1.25	0.043	0.048	0.062

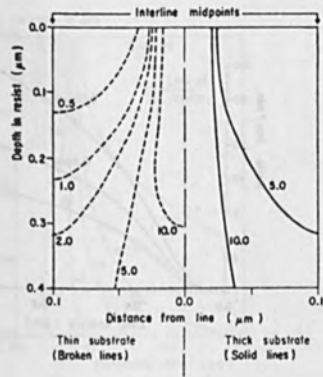


Fig. 3 Exposure contours for periodic lines. 20 kV; 0.2 μm line spacing. Exposure values in units of 10^{30} eV/C-cm².

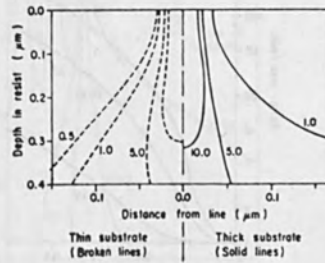


Fig. 4 Exposure contours for periodic lines. 20 kV; 0.8 μm line spacing. Units as in Fig. 3.

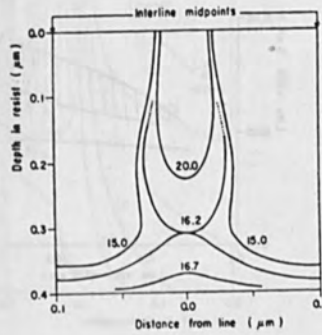


Fig. 5 Exposure contours for periodic lines. 10 kV; 0.2 μm line spacing. Thick substrate. (Unusable exposure.)

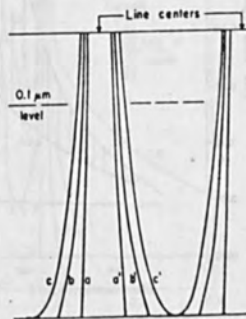


Fig. 6 Exposure contours for periodic lines. Contours defined for graphs in Figs. 7-10. See text.

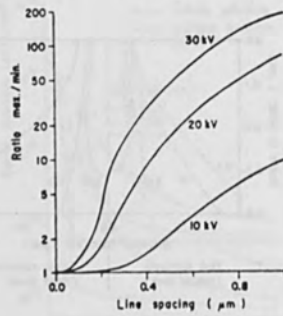


Fig. 7 Ratio of exposure on contour a to that on c in Fig. 6. Thin substrate; 0.4 μm resist. Gives allowed exposure range.

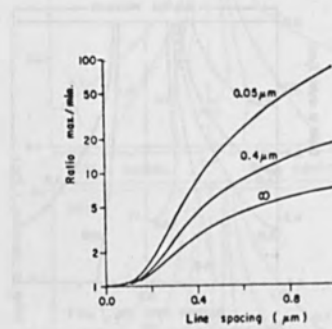


Fig. 8 Ratios as in Fig. 7 except all curves for 20 kV and various substrate thicknesses.

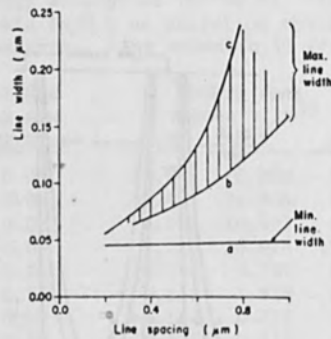


Fig. 9 Line widths for parallel lines on thin substrate. 20 kV; 0.4 μm resist. Width is contour gap at 0.1 μm from top of resist.

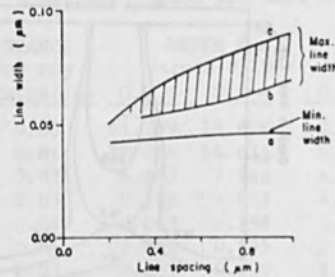


Fig. 10 As in Fig. 9 but for thick substrate.

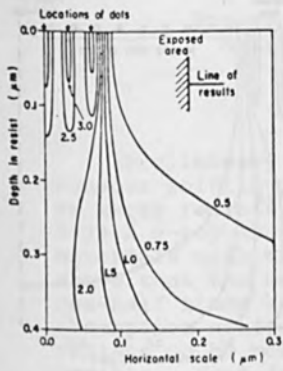


Fig. 11 Contours at edge of large exposed region. Exposure values in units of 10^{18} eV/cm³ per electron per dot.

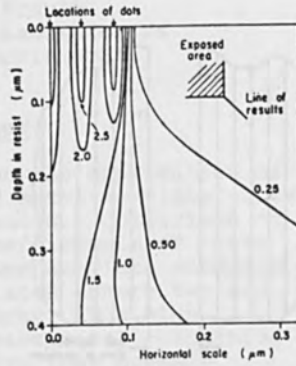


Fig. 12 Exposure contours along bisector of outside corner. Units as in Fig. 11.

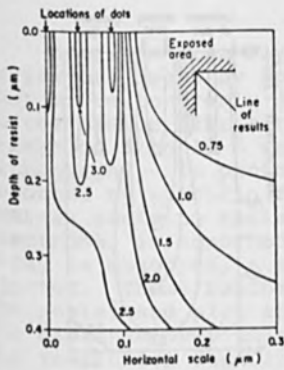


Fig. 13 Exposure contours along bisector of inside corner. Units as in Fig. 11.

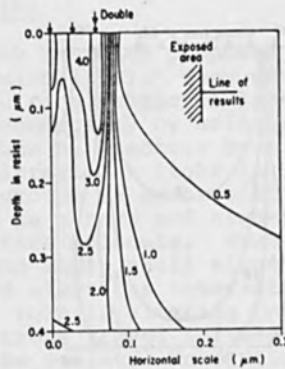


Fig. 14 Exposure contours as in Fig. 11 except with charge doubled in edge row of dots.

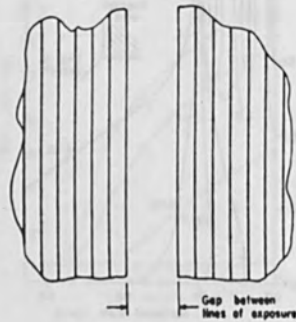


Fig. 15 Configuration of linear gap between two large exposed regions for data in Figs. 16-18.

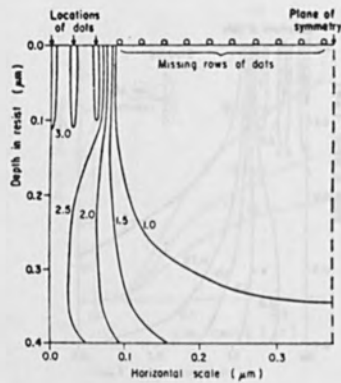


Fig. 16 Exposure contours with linear gap with 20 rows of dots missing. (gap $\approx 0.6 \mu\text{m}$).

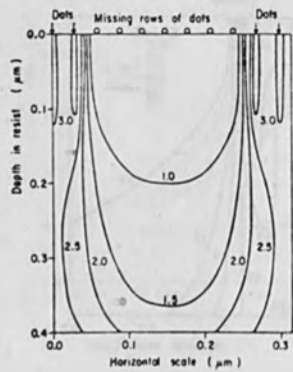


Fig. 17 Exposure contours with linear gap with 7 rows of dots missing (gap $\approx 0.21 \mu\text{m}$).

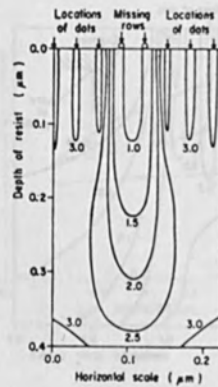


Fig. 18 Exposure contours with linear gap with 2 rows of dots missing (gap $\approx 0.06 \mu\text{m}$).

PROPERTIES OF METAL ACRYLATE COMPOSITIONS AS X-RAY RESISTS

Robert G. Brault
Hughes Research Laboratories
Malibu, California 90265

Abstract

Preliminary results on the application of aqueous solutions of mixed metal acrylate salts as x-ray resists are presented. Comparison of 8.34 Å x-ray absorption coefficients of these materials with that of other acrylate monomers shows that the metal acrylates absorb two and one-half times as much energy. The high absorption coefficient causes metal-containing resists to be more sensitive than organic resists. Good images were obtained when 1.5 to 1.7 µm thick films were exposed with 10 mJ/cm². This is compared with 500 mJ/cm² for PMMA and 72 mJ/cm² for Kodak micro-negative resists. These compositions have been used as a resist for ion-beam etching an image with ~1 µm wide metal lines in a 6000 Å gold film on glass.

Introduction

A system of x-ray lithography has been proposed in a series of papers by Spears and Smith [1,2]. They conclude that microelectronic devices requiring submicron line-widths can be fabricated more economically by using soft x-rays of 5 to 15 Å wavelength than by electron beam lithography. In photoresists, ultraviolet light is absorbed by specific functional groups in an organic film, whereas ionizing radiation, such as x-rays and high-energy electrons, is absorbed by the entire molecule. When an x-ray is absorbed, a tightly bound inner shell electron is ejected. These randomly directed electrons interact with the resist and play the dominant role in altering the film. The distance over which the electrons travel influences the resolution capabilities of the resist. Resolutions better than 0.2 µm are obtainable with characteristic copper, aluminum and molybdenum x-rays. The long range of the 10 to 20 keV electrons used in scanning electron beam lithography has made negative-type resists undesirable [3]. With x-ray lithography, both negative and positive resists are expected to have the same high

resolution capabilities. Several limitations must be overcome before x-ray lithography can be used for production. One of these limitations is the development of adequately sensitive resists [4]. In this paper we shall present preliminary data on resists having good sensitivity based on metal acrylates.

Metal-containing compositions are of interest because of their favorably high absorption coefficients. Figure 1 is a plot of absorption coefficient versus atomic number for 8.34 Å x-rays [5], the wavelength of x-rays characteristic of the aluminum K α line which we are using for lithography. It is observed that the absorption coefficient for carbon, oxygen, nitrogen and sulfur, the elements common to organic monomers and polymers, are between 1200 and 2500 cm⁻¹, while that of many metals, for example zinc, silver, cadmium, barium and some of the lanthanides, are from 16,000 to over 40,000 cm⁻¹. Hence, compositions containing these metals should absorb a greater fraction of the x-rays and therefore be more sensitive than non-metal containing compositions. For example, the comparison of the calculated absorption coefficient at 8.34 Å of barium lead acrylate and a typical organic monomer, methyl methacrylate, shows the metal acrylate film to be two and one-half times as efficient at absorbing x-rays as the organic monomer.

TABLE I

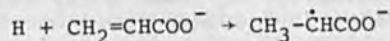
Approximate Absorption Coefficients (cm⁻¹)

X-ray Source (kVp)	1.5
X-ray Wavelength (Å)	8.34
Barium Lead Acrylate Film	2450
Methyl Methacrylate	1000

We became interested in the x-ray polymerization of metal acrylates several years ago when we polymerized both aqueous solutions and dried films of mixed metal acrylates with exposures of 20 to 100 kV x-rays. Mixtures of metal acrylates can be dried to form glassy films [6]. When formulations based on a 4:1 mixture of barium diacrylate and lead diacrylate were exposed to 50 to 100 kV (0.125 to 0.25 Å) x-rays through metal masks and the unexposed

monomer was removed by development with water, a relief image was formed. Figure 2 shows an image and the mask used to produce it. In this case a non-reactive dye was added to the monomer so that the resulting polymer film was easier to observe. It can be seen that the polymer had the same contour as the mask. Because these materials are more sensitive to x-ray polymerization than organic monomers and have been shown to produce tough films, we decided to investigate similar compositions as resists for x-ray lithography.

Radiation polymerization of metal acrylate and methacrylate hydrates has been studied in some detail [7-10]. Most of this work was on crystalline material irradiated with γ -rays at -196°C to generate the initiating species; then the polymerization rate was studied at higher temperatures. This technique was used so that initiation and propagation could be studied separately. Resist films are non-crystalline amorphous glasses, and initiation and polymerization occur simultaneously at ambient temperature. However, some of the observations and conclusions do relate to the current work. Polymerization is initiated by free-radical ions [7], which are formed by the addition of a hydrogen atom to the monomer



and takes place most efficiently at defects [8], under conditions where the monomer has more freedom of motion than in the crystal lattice. Studies on crystalline hydrates of calcium acrylate and barium methacrylate [9,10] have shown that post-irradiation polymerization is affected more by the relative position of monomer units than by the degree of hydration.

Experimental

Resist solutions are prepared by mixing proprietary additives with an aqueous solution of barium diacrylate and neodymium diacrylate. Because they have the desired volatility characteristics for spin-coating, alcohols such as methanol are used to dilute the resist mixtures to the desired concentration.

Resists are spin-coated on oxidized (5000 Å) silicon wafers and baked five minutes at 80°C . Films $1.5\ \mu\text{m}$ to $1.7\ \mu\text{m}$ are obtained when the resist is spin-coated at 3000 rpm for 30 seconds. The films are then exposed to $8.3\ \text{\AA}$ x-rays produced by an 8 kV, 20 mA electron beam

from a Balzer electron beam evaporator impinging on a non-volatilizing aluminum target and filtered from radiation heating and scattered electrons by 1/3-mil aluminum foil. The apparatus is described in more detail by McCoy and Sullivan [4]. After exposure, the wafer is developed in water and the resist thickness is measured on a Sloan Dektak.

Differential scanning calorimetry (DSC) and thermogravimetric analysis (TGA) were performed with a du Pont Model 900 Thermal Analyzer. Samples were weighed in aluminum pans and dried to constant weight at 52% relative humidity and analyzed directly or after baking at 80°C for 20 minutes. Temperature was scanned at 2°C per minute.

Results and Discussion

Drying Characteristics

A resist-coated wafer must be dried before a mask can be put in contact with it. The x-ray exposures are made in a vacuum which also would remove water. The effect of drying on the sensitivity of these x-ray resists was investigated because it had been found during the photopolymerization studies of metal acrylates that aqueous solutions polymerized more rapidly than "dried" films. Figure 3 is a plot of the normalized polymer thickness after exposure on wafers exposed to 15.8 mJ/cm² after being dried at 80°C for various times. There is little decrease in sensitivity until after ten minutes at that temperature. Figure 4 shows two DSC curves of a metal acrylate resist composition that had been dried to constant weight at 52% relative humidity (RH), which was assumed to leave them with about the same moisture content as that of the freshly spun resist. The sample in the top curve was run with no further treatment, and the sample in the bottom curve had been dried at 80°C for 20 minutes. These curves are identical. There was less than 4% weight loss when a sample which had been dried to constant weight at 52% RH was baked at 80°C for 20 minutes, and the sample was water soluble showing that it was still monomeric. Heating this sample to 100°C had little effect. Between 100°C and 120°C is a sharper endotherm due to a more rapid loss of water which was confirmed by TGA. The exotherm between 120°C and 160°C is probably due to initiation of polymerization. Since the sample was no longer water soluble, it was concluded that it was polymeric.

This shows that samples can be dried sufficiently to make them convenient to handle. The DSC curves do not show the sharp endotherm observed by Costaschak, Gilson and St. Pierre on calcium acrylate, which they attribute to the complete loss of water by the hydrated crystal. Instead, thermogravimetric analysis of our compositions shows a steady weight loss, probably because they are non-crystalline. Being amorphous, there is more molecular motion than in crystalline materials, which allows an enhanced polymerization rate.

Sensitivity

Figure 5 is a plot of the normalized film thickness versus exposure of the developed sample. When a wafer with a resist coating of $1.5 \mu\text{m}$ is exposed with 25 mJ/cm^2 through an etched metal mask, a good relief image is produced. Also shown in this figure is data for exposures of 10 mJ/cm^2 . The sensitivity is excellent when compared to over 500 mJ/cm^2 required to expose PMMA with this apparatus and 72 mJ/cm^2 required for Kodak micro-negative resist [4].

The resist film has good adhesion to the substrate and is tough enough to be handled during processing. It has been toughened further by post-baking at 150°C for several hours. Progress has been made in preparing compositions and processing techniques which are resistant to etching conditions.

Etch Resistance

Figure 6a is a picture of a gold-on-silicon mask used to produce the image. The metal acrylate resist was spun on a 6000 \AA film of gold on a glass substrate. After the metal acrylate resist had been exposed (10 mJ/cm^2 at the polymer surface) and developed in water, the resist was hardened by post-baking at 150°C for two hours and then ion beam etched to produce the image in the gold film (Figure 6b). Figure 7 is a magnification of the center of the etched pattern and shows that the lines are still quite clear. The final metal line is $\sim 1 \mu\text{m}$ wide.

Progress is being made toward developing a metal acrylate material which will also resist buffered HF etchant.

In summary, we have developed x-ray resist compositions based on metal acrylates with excellent sensitivity.

These compositions are processed with water. They are resistant to ion-beam etching. Further improvements are anticipated which will make the resulting films even tougher and resistant to other etching techniques.

Acknowledgment

The author wishes to acknowledge and thank Frank Hause for his considerable help with the equipment and supplying the oxidized wafers used on this project. He also appreciates the help of Hugh Garvin and Klauss Robinson for the ion-beam etching and Dektak measurements, Dave Margerum, John McCoy, Leroy Miller and Paul Sullivan for their helpful discussions throughout this project.

References

1. D. L. Spears and H. I. Smith, *Electronics Letters* 8, 102 (1972).
2. D. L. Spears and H. I. Smith, *Solid State Technology* 15, 21 (1972).
3. M. Hatzakis, *J. Electrochem. Soc.* 116, 1033 (1969).
4. J. H. McCoy and P. A. Sullivan, *This Conference*, Paper 198.
5. B. L. Henke and E. S. Ebsu, to be published in *Advances in X-Ray Analysis* 17 (1974).
6. J. B. Rust, U. S. Patent 3,615,627 (1971).
7. J. H. O'Donnell, B. McGarvey and H. Morawetz, *J. Am. Chem. Soc.* 86, 2322 (1968).
8. B. Arnold and G. C. Eastmond, *Trans. Faraday Soc.* 67, 772 (1971).
9. J. R. Lando and H. Morawetz, *J. Polym. Sci. C*, 789 (1964).
10. F. M. Costaschuk, D. F. R. Gilson, L. E. St. Pierre, *Macromolecules* 3, 593 (1970).

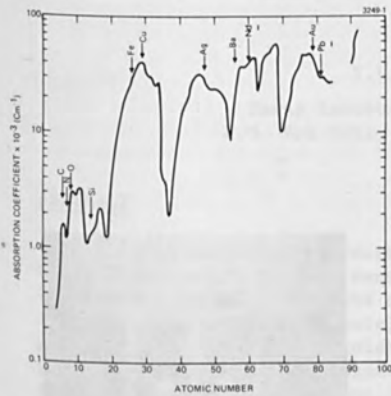


Fig. 1. Absorption coefficient as a function of atomic number for 8.34 Å x-rays.

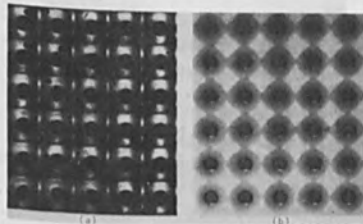


Fig. 2. X-ray polymer image from monomer film containing dye. (a) Photomicrograph of a filter screen. (b) Photomicrograph of image produced by x-rays exposed through the same filter screen in contact with monomer film.

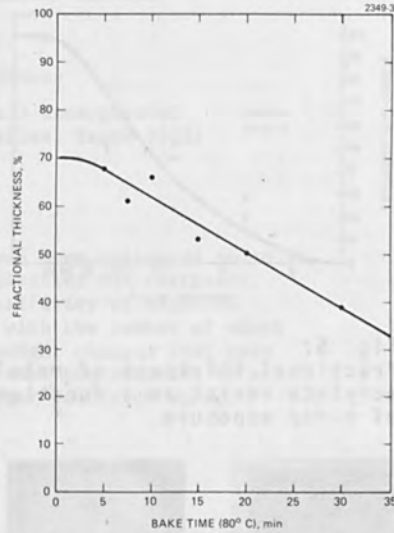


Fig. 3. Effect of drying time on sensitivity. Fractional thickness of developed film after 15.8 mJ/cm² exposure as a function of drying time.

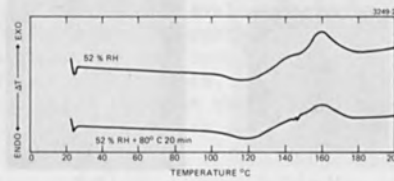


Fig. 4. Differential scanning calorimetry curves of resist at 20°C/minute.

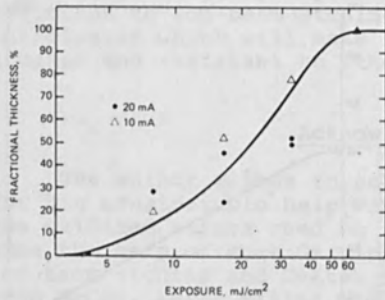


Fig. 5.
Fractional thickness of metal acrylate resist as a function of x-ray exposure.

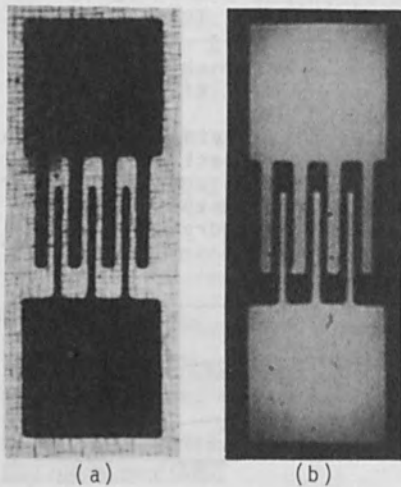


Fig. 6.
Pattern ion-beam etched in 6000 Å gold on glass.
(a) Photomicrograph of gold on silicon mask. (b) Photomicrograph of image produced by etching a barium neodymium acrylate resist with 2 kV argon ions.

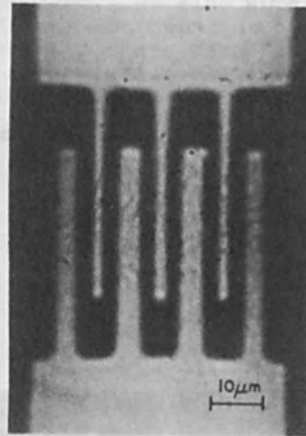


Fig. 7.
Pattern ion-beam etch in 6000 Å gold on glass.

HIGH SPEED ELECTRON RESISTS

T.L. Brewer

Texas Instruments Incorporated
P.O. Box 5012, Dallas, Texas 75222

ABSTRACT

A large number of polymers has been evaluated as to their electron irradiation sensitivities and contrasts. The results indicate that the sensitivity of negative resist increases proportionately with the number of vinyl groups. In addition, molecular weight changes that take place during irradiation suggest that the contrast of a negative resist is better for larger values of G_x/G_s .

INTRODUCTION

In order to develop practical electron beam resists for micro-circuit fabrication, it is paramount that one understands the effects of chemical structure on the functioning of a polymer as an electron resist. The amount of energy absorbed by the polymer and the distribution of the energy in the polymer is essentially independent of the chemical makeup of the polymer. Therefore, the performance of an electron resist depends more upon the secondary chemistry occurring after the initial energy transfer.

To acquire this understanding it is necessary to evaluate a large number of different polymers under a given set of laboratory conditions. As a beginning toward this end, several polymers have been evaluated in terms of their respective sensitivities and contrasts. These parameters were defined and measured in such a way that they can be directly related to the quality of a patterned IC device geometry.

EXPERIMENTAL

The experiments were designed to obtain information on the sensitivity, contrast, and molecular weight changes of various polymers with electron irradiation. The polymers were in the form of thin films coated on various substrates. Solutions of all polymers were spin coated on either silicon or chrome clad glass to obtain the films, which were from 500 and 5000 Å thick.

All exposures were made using a 15 kev electron beam. The exposure

equipment consisted of a computer controlled beam writing machine that has been previously described¹ and a small electron irradiation system. This irradiation system consisted of a variable high voltage gun with a tungsten filament, a magnetic lens, beam deflection system, and sample chamber. The instrument can expose spots from 0.1 to 2.5 inches in diameter with variable intensities for precise times from 10⁻⁵ to 10 seconds. The deflection system can place these spots anywhere over a 4 square inch area.

The technique used in obtaining resist sensitivity has been previously described.² It essentially involved exposing a series of lines in which the dose per line increased 10 per cent until a 1 X 10⁵ total differential in dose was obtained.

The resist contrast was obtained from both the variation of line width and resist thickness with dose. The line width measurements were done on a Reichert microscope with an eyepiece scale. The measurements were done at a magnification of 600X. The resist thicknesses for the experiments were measured on a Taly-Step.

In order to determine molecular weight changes due to electron bombardment, a 2.25 inch diameter area of resist on a chrome clad glass plate was exposed for a given amount of time. The resist was removed from the plate by soaking in chloroform. The polymer solutions were then analyzed with a Waters 501 gel permeation chromatograph (GPC). The weight average and number average molecular weights were calculated from the GPC curves.

RESULTS AND DISCUSSION

Table I list the sensitivities of a large number of polymers with varying chemical structures. Several trends indicated by the data have been perviously discussed.² However, there are two features worth noting. First, polymethacrylic acid is a water soluble resist. It gives very good coatings from water solutions. It's interesting that the sensitivity of the polymer is almost equal to that of PMMA. Yet, in the photolysis of polymethacrylic acid, the decomposition yield is much lower than that of PMMA.³

A second feature of the table that bears discussion is the diene results. The broad range of sensitivities is not only due to molecular weight changes,² but also to structural variations. The butadiene can be polymerized either through the 1,2 positions or the 1, 4 positions. The 1, 2 polymerization results in dangling vinyl groups, whereas the 1, 4 reaction yields unsaturation in the backbone. The vinyl group is much more susceptible to crosslinking than the internal olefin. Table II list the sensitivity results for several diene polymers with varying amounts of vinyl present. There is almost a linear increase in speed of the resist with increasing vinyl concentration. These dangling

olefins are also most likely responsible for the high sensitivities of diallylphtalate and vinyl siloxane polymers.

RESIST CONTRAST

Although high sensitivity of electron irradiation is an important quality for an e-beam resist, it is not the only property required. Just as important is the contrast of the resist, that is, the ability for very narrow lines and spaces to be resolved. The standard method of determining contrast involves taking the ratio of the threshold flux to the lowest usable flux.⁴ However, this method does not give any direct information on line widths. Therefore, another method for determining contrast has been devised. The line width contrast (LWC) of the resist is given by:

$$\frac{\Delta (\log \text{dose})}{\Delta (\text{normalized line width})} = \text{LWC}$$

The LWC curves all show an interesting feature. At approximately the dose needed to fully expose the film, the curve changes slope. The LWC values are therefore determined in the overexposed region. This allows values to be taken over several orders of magnitude of dose.

Table III gives the LWC values for several resists. For comparison, some thickness contrast values are also given. These values are calculated by taking the slope of the normalized film thickness versus log dose curve. There are several interesting facts which this data point out. As has been previously demonstrated, the sensitivity and contrast of PMMA (and presumably all positive resists) are independent of molecular weight.⁵ The table shows that for polystyrene the contrast is independent of the speed and molecular weight. In fact, it appears generally true that the contrast is not related to the speed of the resist. (i.e., fast resists can have high contrast.) Although the table does not represent a large enough sampling, the data indicate that poor contrast is related to the efficiency at which crosslinking and decomposition compete with each other. This was first noted in the epoxy polymers.⁶ In polymers such as polystyrene and vinylsiloxane where it is expected that very little decomposition occurs, the negative resist contrast is high. On the other hand, in polymers such as caprolactone, where it might be expected that decomposition would compete favorably with crosslinking, the resist contrast is much lower. The contrast of polyvinylacetate is also low despite the fact that its decomposition yield is low. However, in this case, the low contrast value is due to a high polydispersity of 7.3 for this particular sample.

There is very little information on the crosslinking and scission yields of solid polymers irradiated with moderate energy (5-25 kev) electrons. A large number of yields have been reported for other types of radiation.^{7,8} Therefore, molecular weight changes with electron irradiation were investigated for three polymers. The ratio of crosslinking to scission yields was then determined using the equations of Saito.⁹ The results are shown in Table IV. Unfortunately, the polydispersity of polyvinylacetate was too large to utilize Saito's equations. The data for this polymer is therefore simply tabulated in Table V. The G_x/G_s ratios are qualitatively in line with what is expected. However, the quantitative value for polystyrene is lower than that reported for other systems. This may be due to the experimental method which tends to favor the lower molecular weights. It should be noted that great care must be taken to ensure that all of the exposed polymer will dissolve in the chloroform.

SUMMARY

In summary, the data presented indicate:

- 1) There is almost a linear increase in sensitivity with increasing vinyl content for negative resists.
- 2) The sensitivity and contrast of positive resists are independent of molecular weight in the range investigated.
- 3) There is no direct relationship between contrast and sensitivity.
- 4) The contrast of a negative resist decreases as G_x/G_s decreased.

ACKNOWLEDGEMENTS

I would like to thank Eldarie Shelton, John Burchard, and Toby Landes for their assistance with this project.

REFERENCES

1. Varnell, G.L., D.F. Spicer, and A.C. Rodgers, "12th Symposium in Electron, Ion, and Laser Beam Technology," Cambridge, Mass., May, 1973.
2. Brewer, Terry L., "Society of Plastics Engineers," Technical Conference on Photopolymers, Oct. 24-26, 1973, p. 138.
3. Jellinek, H.H.G., Pure and Appl. Chem. 4 419 (1962).
4. Broyde, Barrett, J. Electrochem. Soc., 116, 1241 (1969).
5. Harris, R.A., J. Electrochem. Soc., 120 270. (1973).
6. Thompson, L.F., E.D. Feit, and R.D. Heidenreich, "Society of Plastics Engineers," Technical Conference on Photopolymers, Oct. 24-26, 1973, p. 127.
7. Chapiro, A., "Radiation Chemistry of Polymeric Systems," Interscience Publishers, New York, (1962).
8. "The Radiation Chemistry of Macromolecules," ed. by Malcolm Dole, V.I., II., Academic Press, 1973.
9. Saito, O., "The Radiation Chemistry of Macromolecules," ed. by Malcolm Dole, V.I., Academic Press, 1973, p. 223

Table I

ELECTRON SENSITIVITIES

<u>Polymer</u>	<u>Relative Sensitivity</u>	<u>Type</u>
Polymethylmethacrylate	1	P
Negative Photoresists	25	N
Chlorinated Polyethylene	25	N
Diene Polymers	10-100	N
Vinylchloride Copolymers	5	N
Monomeric Epoxide	1	N
Epoxidized Polymers	100+	N
Polydimethylsiloxane	1	N
Polyvinylsiloxanes	100	N
Kel-f	3	N
Polycaprolactone	.3	N
Polyorthodiallylphthalate	10	N
Cellulose Acetate	.2	P
Cellulose Triacetate	.2	P
Cellulose Acetate Phthalate	.2	P
Polyacetal	.5	P
Poly (α -methylstyrene)	.5	P
Polyisobutylene	1	P
Polymethacrylic Acid	.6	P

Table II

BUTADIENE POLYMERS WITH
VARYING VINYL CONTENT

<u>Polymer</u>	<u>M.W.</u>	<u>% Vinyl</u>	<u>Relative Sensitivity</u>
1	250,000	11	1
2	186,000	23	1.5
3	300,000	9.3	2
4	10,000	90	0.5
5	100,000	90	6.5
6	200,000	85	10

Table I

ELECTRON SENSITIVITIES

<u>Polymer</u>	<u>Relative Sensitivity</u>	<u>Type</u>
Polymethylmethacrylate	1	P
Negative Photoresists	25	N
Chlorinated Polyethylene	25	N
Diene Polymers	10-100	N
Vinylchloride Copolymers	5	N
Monomeric Epoxide	1	N
Epoxidized Polymers	100+	N
Polydimethylsiloxane	1	N
Polyvinylsiloxanes	100	N
Kel-f	3	N
Polycaprolactone	.3	N
Polyorthodiallylphthalate	10	N
Cellulose Acetate	.2	P
Cellulose Triacetate	.2	P
Cellulose Acetate Phthalate	.2	P
Polyacetal	.5	P
Poly (α -methylstyrene)	.5	P
Polyisobutylene	1	P
Polymethacrylic Acid	.6	P

Table II

BUTADIENE POLYMERS WITH
VARYING VINYL CONTENT

<u>Polymer</u>	<u>M.W.</u>	<u>% Vinyl</u>	<u>Relative Sensitivity</u>
1	250,000	11	1
2	186,000	23	1.5
3	300,000	9.3	2
4	10,000	90	0.5
5	100,000	90	6.5
6	200,000	85	10

Table III

CONTRAST AND SENSITIVITY OF
SELECTED ELECTRON RESISTS

<u>Polymer</u>	<u>Type</u>	<u>Relative Sensitivity</u>	<u>LW Contrast</u>	<u>Contrast</u>
Vinyl acetate	N	1	0.385	0.42
Vinyl acetate copolymer	N	5	0.59	
Kel f	N	3	0.55	
Polybutadiene	N	50	0.52	
Diallylphtalate	N	10	0.55	0.35
Vinyl Siloxane	N	100	0.8	0.76
Polycaprolactone	N	0.3	0	
Polymethylmethacrylate (med. mol. wt.)	P	1	0.8	
Polymethylmethacrylate (high mol. wt.)	P	1	0.8	
Polymethacrylic acid	P	0.6	0.7	
Polystyrene (mw = 100,000)	N	0.4		2.2
Polystyrene (mw = 20,000)	N	0.10		2.8

Table IV

RELATIVE CROSSLINKING AND SCISSION YIELDS

	<u>Polydispersity</u>	<u>G_x/G_s</u>
Polystyrene	1.06	3.1
Polycaprolactone	2	0.2
Polyvinylacetate	7.3	--

Table V

MOLECULAR WEIGHT CHANGES OF
IRRADIATED POLYVINYLACETATE

<u>Exposure Time</u>	<u>MW_n</u>	<u>MW_w</u>
0	32,202	230,958
1	48,686	270,270
2	56,504	277,562
3	83,300	331,398
4	81,086	335,529 **

EFFECT OF OLEFIN STRUCTURE ON THE ELECTRON BEAM
VAPORIZATION OF POLY(OLEFIN SULFONES)

M. J. Bowden and L. F. Thompson
Bell Laboratories
Murray Hill, New Jersey 07974

ABSTRACT

The rate of vaporization of poly(olefin sulfones) subjected to electron beam irradiation is markedly dependent upon the olefin structure. At room temperature, poly(butene-1 sulfone) and poly(cyclopentene sulfone) vaporize at rates several orders of magnitude lower than, for example, poly(2-methyl pentene-1 sulfone). Differences in vaporization rate for the various sulfones are shown to be related to differing rates of depolymerization which in turn are related to differences in ceiling temperatures for polymer formation.

INTRODUCTION

It has been observed previously^{1,2} that the film thickness of poly(olefin sulfones) decreases with electron irradiation time at rates determined primarily by the temperature and olefin structure. Other parameters such as molecular weight and accelerating voltage were of minor importance.³ This phenomenon has been termed vapor development^{1,2} or print-out.⁴ It is possible to completely vapor develop the resist thereby removing the necessity for solvent development, an attractive feature for certain applications. Solution-developed poly(olefin sulfones) all showed similar sensitivities, viz., $1-2 \times 10^{-6}$ C/cm².^{1,2} This paper is concerned with the reason underlying the differences in rates of vapor development.

EXPERIMENTAL

The polysulfones investigated in this paper were prepared either by UV initiation at 0°C or by initiation with tert-butyl¹ hydroperoxide at -80°C. Details are given elsewhere.¹ Low temperature polymerization was necessary

for some systems, notably 2-methyl pentene-1, because of ceiling temperature considerations. The ceiling temperature, T_c , is that temperature above which it is thermodynamically impossible to form polymer. Values of T_c for the systems studied are listed in Table I.

Films 100-500 nm thick were spin-coated from suitable solvents onto SiO_2/Si substrates and exposed using a Cambridge Mark II Scanning Electron Microscope as described previously. The exposed pads were gilded using standard vacuum evaporation techniques and the depth of film removed measured by polarization interferometry at 590 nm using a Nomarski optical interferometer.³

RESULTS AND DISCUSSION

Normalized plots of film thickness removed after exposure versus dose for several polysulfones irradiated at room temperature are shown in Figure 1. It is seen that poly(butene-1 sulfone) PBS and poly(cyclopentene sulfone) PcyloPS vaporize at rates several orders of magnitude lower than for example poly(2-methyl pentene-1 sulfone) PMPS. The vaporization rates of the other polysulfones were intermediate between these two extremes. It may be noted that the initial rate of vapor development decreases as the T_c for polymer formation increases.

The effect of temperature during exposure on the rate of vaporization of PBS and PMPS is shown in Figures 2 and 3. It is seen that PBS in particular shows a marked increase with temperature. At 140°C, 90% of a PBS film can be removed with a dose of $5 \times 10^{-6} \text{ C/cm}^2$ compared with negligible loss for the same dose at room temperature. As previously observed for PMPS, the rate is independent of initial film thickness (Figure 4) and justifies plotting the curves as normalized values of film thickness removed.

For systems undergoing only random scission, the dose Q required to effect a fracture density p_s (number of main chain bonds broken per monomer unit) is given by the equation

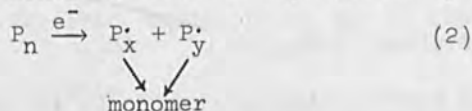
$$Q = \frac{p_s 100 q \rho z N}{E G(s) M_o} \quad (1)$$

where q = electron charge, ρ = density, z = film thickness, N = Avogadro's number, E = energy absorbed in the film

per incident electron, $G(s) = G(\text{scission})$ and $M_0 =$ molecular weight of a monomer unit.

One means of achieving a vapor development process is to attain a fracture density of unity, the monomer fragments being removed by the vacuum system. Such a model would not predict maximum rate of film removal at the commencement of irradiation. Neither would it explain the marked temperature dependence nor the high sensitivity of the process which indicates values of $p_g \ll 1$. Obviously then some process must be acting which enhances the reversion of the fractured chain to monomer.

The results from radiolysis studies⁶ indicated that chain fracture is accompanied by depolymerization of the fractured chain ends to monomer. This is represented by

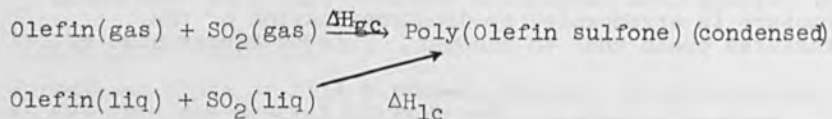


Thermodynamic analysis of a typical exothermic polymerization process predicts that for a given monomer concentration there exists a temperature known as the ceiling temperature, T_c , above which polymerization will not take place.⁷ This may be understood kinetically in terms of the reversibility of the propagation reaction. Conversely at any temperature there will be an equilibrium monomer concentration which is independent of the amount of polymer in the system.⁸ The attainment of this equilibrium requires that there be a continuous supply of polymer radicals. The vapor-development process refers to the reaction



Radicals are being continually formed during electron irradiation and the product gases continually removed by the vacuum system. Hence equilibrium cannot be attained and the reaction moves entirely to the right. We may then see the vapor development process as one of initial chain scission followed by depolymerization from the fractured chain ends. However, side reactions leading to chain termination can interrupt the depolymerization process (termination is taken to include those processes such as abstraction and recombination). It seems probable that the rate of termination is related to the rate of depropagation since the faster a chain unzips the less likely secondary reactions will terminate the depropagating chain.

One way of increasing the depropagation rate would be to increase the temperature as shown in Figures 2 and 3. An increase in rate can also be accomplished by lowering the activation energy for depropagation (E_d). This may be the reason for the observed dependence of the rate of vapor development on olefin structure (Figure 1), viz., that the magnitude of E_d is determined by the olefin structure. There is evidence to suggest that the observed variation of T_c with olefin structure in the liquid-phase copolymerization is due to changes in the heat of polymerization ΔH_{1c} .^{9,10} Application of thermodynamic additivity principles to the cycle



would predict similar changes in the heat of polymerization (ΔH_{gc}) for polymerization in the gas phase. (ΔH_{vap} varies little with olefin structure).

The activation energy for the depropagation reaction is given by $E_d = E_p - \Delta H_{gc}$.¹¹ Therefore assuming the magnitude of E_p is relatively unaffected by changes in olefin structure the variation of ΔH_{1c} (and hence ΔH_{gc}) with olefin structure would be reflected in E_d predicting rates of vapor development in agreement with the order shown in Figure 1.

However, such an argument does not explain the wide difference in vapor-development rates between for example, PBS and PHS whose ceiling temperatures differ by only a few degrees. It might alternatively be argued that the rate determining step in the vapor-development process is the rate of chain termination and that this is determined by olefin structure.

REFERENCES

1. M. J. Bowden and L. F. Thompson, J. Appl. Polym. Sci., 17, 3211 (1973).
2. L. F. Thompson and M. J. Bowden, J. Electrochem. Soc., 120, 1722 (1973).
3. M. J. Bowden and L. F. Thompson, paper presented at the Third Photopolymer Conference, Nevele Country Club, Ellenville, New York, October 24-26 (1973).

4. A. W. Levine, M. Kaplin and J. Fech, *J. Polym. Sci.*, A1, 11, 311 (1973).
5. H. Y. Ku and L. C. Scala, *J. Electrochem. Soc.*, 116, 980 (1969).
6. J. R. Brown and J. H. O'Donnell, *Macromolecules*, 5, 109 (1972).
7. F. S. Dainton and K. J. Ivin, *Proc. Roy. Soc., A*, 212, 96 (1952).
8. K. J. Ivin, *Trans. Faraday Soc.*, 51, 1273 (1955).
9. R. E. Cook, F. S. Dainton and K. J. Ivin, *J. Polym. Sci.*, 29, 549 (1958).
10. K. J. Ivin, W. A. Keith and H. Mackle, *Trans. Faraday Soc.*, 55, 262 (1959).
11. F. S. Dainton and K. J. Ivin, *Quart. Rev.*, 12, 61 (1958).

Table I
Ceiling Temperature for Polymerization of Various
Olefins with Sulfur Dioxide. $[\text{Olefin}][\text{SO}_2] = 27 \text{ mol F t}^{-2}$

Olefin	Polymer Code	T_c (°C)
cyclopentene	PcycloPS	102.5
butene	PBS	64
hexene	PHS	60
cis butene-2	PcB-2S	46
cyclohexene	PcycloHS	24
2-methyl pentene-1	PMPS	-34

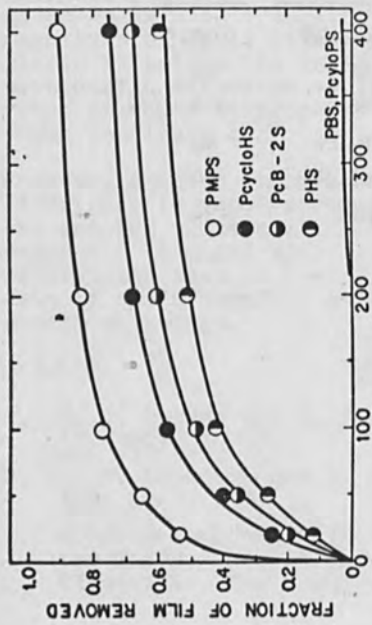


Fig. 1. Effect of olefin structure on the rate of vapor development. $z = 5000\text{\AA}$; $I = 5 \times 10^{-10}$ A.

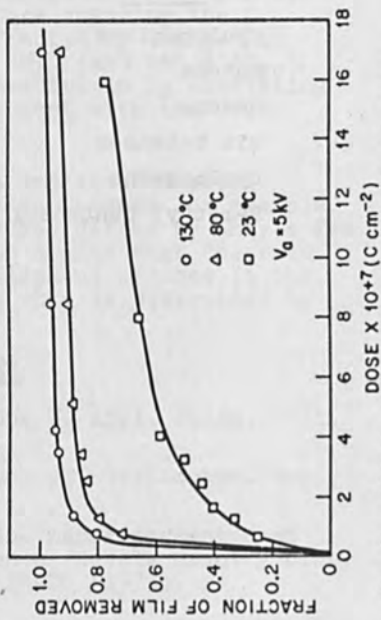


Fig. 3. Effect of temperature on rate of vapor development of PMPS.

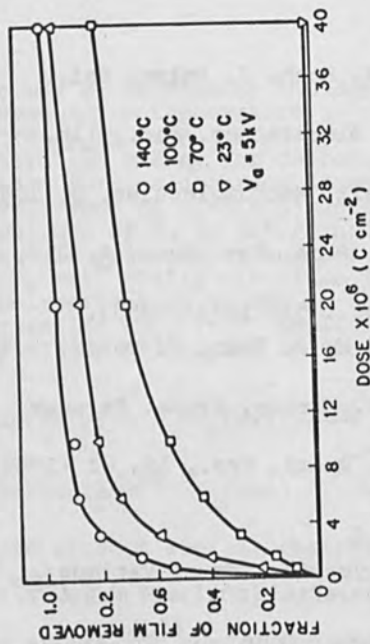


Fig. 2. Effect of temperature on the rate of vapor development of PBS.

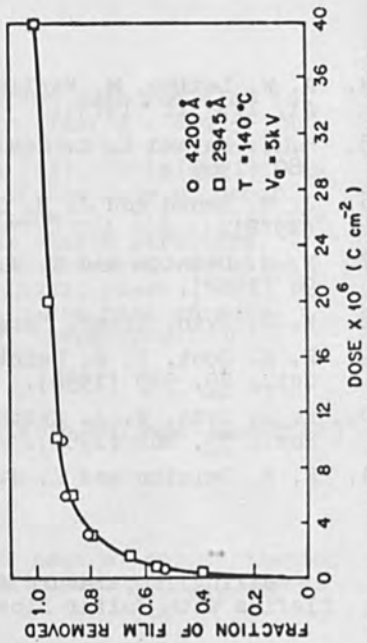


Fig. 4. Effect of initial film thickness on rate of vapor development of PBS.

EXPERIMENTAL UTILIZATION OF MONTE CARLO MODELS
FOR ELECTRON BEAM LITHOGRAPHY*

R. J. Hawryluk,[†] A. Soares, Henry I. Smith
Massachusetts Institute of Technology, Lincoln Laboratory
Lexington, Massachusetts 02173

Andrew M. Hawryluk
Department of Electrical Engineering
Massachusetts Institute of Technology
Cambridge, Massachusetts 02139

ABSTRACT

Recently, analytic and Monte Carlo models have been proposed to calculate the relief structures produced in a polymer film by electron lithography. A detailed comparison of the predictions of these models for the exposure of isolated lines and dots has demonstrated their validity over a wide range of parameters. In this paper, the utility of electron exposure models is demonstrated by using Monte Carlo calculations to predict the success or failure of the metal liftoff technique for an array of closely spaced lines, as a function of the linear charge density and the interline spacing. The predictions are found to be in good agreement with experimental data.

The electron beam exposure required in order to obtain a given relief structure in a polymer film depends on the beam energy, the beam diameter, the film thickness, the atomic number and nature of the polymer film, the atomic number and density of the substrate, and the pattern geometry. In the past, the required dosage has always been determined experimentally. While an empirical approach permits one to write patterns and fabricate devices, it provides neither a basic understanding of the physical mechanism involved in polymer film exposure, nor a means for predicting quantitatively how changing a given parameter will affect the polymer relief structure. Recently, several electron beam exposure models have been proposed which calculate the spatial distribution of energy dissipation in a polymer film resulting from electron scattering in the film and the substrate.¹⁻⁶ Such models

* This work was sponsored by the Department of the Air Force and the Department of the Army.

[†] Also with Massachusetts Institute of Technology, Department of Physics, Cambridge, Massachusetts 02139.

enable one to put in perspective a large body of experimental data. The crucial question is, of course, how well do the models agree with experimental results.

In order to answer this question, a series of experiments were recently conducted using polymethyl methacrylate (PMMA) as the polymer film on silicon, copper and gold substrates. The patterns exposed consisted of widely separated dots and lines. In the case of dots, the charge was varied from 10^{-13} to 10^{-8} coulombs. In the case of lines, the linear charge density, b , was varied over the range $1.0 \times 10^{-9} \leq b \leq 1.0 \times 10^{-5}$ C/cm. On silicon substrates, 10, 15 and 20 keV electron beams were used, and on copper and gold substrates only a 20 keV electron beam was used. The polymer film thickness was varied from 1000 to 10,000 Å. After exposure, the PMMA films were developed and the polymer relief structures measured using scanning electron microscopy. The results were then compared with the predictions of an analytic model and a set of Monte Carlo calculations. The comparison which is reported elsewhere⁶ showed that the Monte Carlo calculations are in very good agreement with the experimental results over the entire range of parameters used. The analytic model also gives good agreement except: (1) at large line half-width, (2) for a 10 keV incident electron beam, (3) for the experiments conducted on copper and gold substrates.

The good agreement between experimental results and Monte Carlo calculations for isolated single lines and dots implies that one ought to be able to calculate the three dimensional polymer relief structure produced for any arbitrary pattern of exposure, and from this to predict if a particular fabrication technique will succeed or fail. In this paper we will illustrate this capability by using Monte Carlo calculations to predict whether the metal liftoff technique will succeed or fail when gratings of adjacent parallel lines are exposed in a PMMA film. The PMMA film thickness was 4000 Å for the calculations and 4400 Å in the experiments. In order to optimize resolution, a 20 keV beam was used. The calculations assume a 250 Å diameter electron beam. Experimentally, the beam diameter was probably closer to 500 Å due to difficulty in focusing it on the polymer coated gold benchmarks. Grating periodicity, and linear charge density are varied over a wide range. The metal liftoff technique is used to test the predictions because it is a sensitive function of the polymer film's cross-sectional profile. PMMA was chosen because the contours developed in it after exposure can be identified as surfaces of equal energy dissipation per unit volume,^{6,7} and thus a direct comparison with theoretical calculations is possible.

Figure 1 illustrates the coordinate system used for a line exposure and the undercut contour typically developed in a PMMA film. The electron exposure models¹⁻⁶ do not calculate this contour directly, but instead calculate energy dissipation per unit volume as a function of position in the polymer. From this, the contour $y(z)$ can be determined from

$$E(y, z) b = D_{\text{CRIT}} \quad (1)$$

where $E(y, z)$ [erg/cm² · C] is the energy dissipation per unit volume for a line exposure of one coulomb per centimeter, b is the linear charge density [C/cm], and D_{CRIT} [ergs/cm³] is the energy dissipation per unit volume required for development of the polymer for a given combination of development parameters.

For an array of lines separated by an interline spacing l the energy dissipation per unit volume $E(y, z)|_{\text{ARRAY}}$ can be calculated from $E(y, z)$

$$E(y, z)|_{\text{ARRAY}} = E(y, z) + \sum_{n=1}^N [E(nl-y, z) + E(nl+y, z)]. \quad (2)$$

In analogy to Equation (1), to develop a particular contour $y(z)$,

$$E(y, z)|_{\text{ARRAY}} b = D_{\text{CRIT}} \quad (3)$$

The first term in Equation (2) is just the contribution from a single line while the second term is the contribution from the adjacent lines. The series is terminated beyond the Bethe electron range, when $nl \pm y > R_B^{\text{PMMA}}$. Figures 2 and 3 present the Monte Carlo calculations using Equation (2) for 10,000 electron trajectories. From such information, one can readily determine the cross-sectional profile developed in a PMMA film.

From the point of view of the metal liftoff technique, the polymer is properly exposed if the sidewalls are vertical or undercut, since distinct metal lines can then be formed on the substrate. Figure 4 illustrates when the polymer is underexposed or overexposed. The polymer is overexposed, if at every point on the substrate thin film interface the energy dissipated per unit volume exceeds D_{CRIT} , since then no polymer will be left on the substrate surface after development. The polymer is underexposed if it is not developed all the way to the substrate surface, or if the sidewalls are not vertical or undercut. In either case, no metal pattern will be formed on the substrate.

In Figure 5, the solid curves are based on the Monte Carlo calculations of Figures 2 and 3 for an infinite array of lines. The dotted curves are for an array of only six lines. The upper set of curves mark the predicted borderline between overexposure and proper exposure. The lower curves mark the predicted borderline between underexposure and proper exposure. D_{CRIT} was determined from a series of experiments described elsewhere⁶ to be 1.8×10^{10} ergs/cm³ for the polymer (PMMA, 950,000 molecular weight) and development process used (40% methyl isobutyl ketone and 60% isopropyl alcohol). The curves predict that the range of b over which an array of lines can be correctly exposed decreases as the lines are brought closer together, and as the number of lines in the array is increased. These effects have been observed experimentally.^{8,9}

The present experiments were conducted on a 4400 \AA thick film of PMMA on a silicon substrate using a 20 keV electron beam. The pattern exposed consisted of four arrays of lines, with interline spacings of 0.25, 0.5, 1.0 and 2.0 \mu m , each array containing six lines. The linear charge density, b , was varied from $\sim 8 \times 10^{-10}$ to $\sim 2.5 \times 10^{-8} \text{ C/cm}$. After exposure, development and subsequent metallization, each array was examined in a scanning electron microscope to determine if it was overexposed, underexposed or correctly exposed. These results are plotted in Figure 4 as open circles, triangles and closed circles respectively.

For the array of lines corresponding to a linear charge density of $1.46 \times 10^{-8} \text{ C/cm}$ and an interline spacing of 1.0 \mu m , the Monte Carlo calculations predict that it is on the verge of overexposure. In fact it was observed after development and before metal deposition that the middle line of the polymer relief structure failed to adhere to the substrate while all other lines did adhere. This indicates that the middle of the pattern which received the greatest amount of cooperative exposure was overexposed while the regions away from the middle, which received less exposure, were correctly exposed.

Figure 5 indicates that experimentally the range of b for correct exposure of the six line arrays is smaller than predicted. This is probably due to the fact that the beam diameter was closer to 500 \AA than the 250 \AA assumed in the calculations. As mentioned above, focussing an electron beam to a 250 \AA diameter on a polymer coated substrate is very difficult. In the present experiments, a thin-film gold benchmark pattern on the silicon substrate was used to focus the electron beam. Notwithstanding the discrepancy in beam diameter, the agreement between theory and experiment is reasonably good.

This discussion has illustrated how Monte Carlo calculations of the spatial distribution of energy dissipation in a polymer; together with an empirical determination of D_{CRIT} , can be used to predict the feasibility of a particular fabrication process for complex geometries of interest to electron beam lithography.

ACKNOWLEDGEMENTS

We are very grateful to E. Stern for his support and encouragement, and to R. Eager, N. Efremow, and M. Lemma for their able technical assistance.

References

1. R. W. Nosker, *J. Appl. Physics*, 40 1872 (1969).
2. R. J. Hawryluk and H. I. Smith, 5th International Conference on Electron and Ion Beam Science and Technology, Ed. Robert Bakish, (The Electrochemical Society, Princeton, New Jersey) 51 (1972).
3. J. S. Greeneich and T. Van Duzer, *J. Vac. Sci. and Tech.*, 10, 1056 (1973); J. S. Greeneich Ph. D. thesis University of California, Berkley, unpublished 1973; J. S. Greeneich and T. Van Duzer, *IEEE Trans. Electron Devices*, ED-21, 286 (1974).
4. Norio Saitou, *Japan J. Appl. Phys.*, 12, 941 (1973).
5. R. J. Hawryluk, Andrew M. Hawryluk and Henry I. Smith, *J. Appl. Phys.* to be published in June 1974.
6. R. J. Hawryluk, Ph. D. thesis (M. I. T. 1974); and R. J. Hawryluk, A. Soares, Henry I. Smith and Andrew M. Hawryluk to be published.
7. R. F. Herzog, J. S. Greeneich, T. E. Everhart and T. Van Duzer, *IEEE Transactions on Electron Devices*, ED-19, 635 (1972).
8. E. D. Wolf, F. S. Ozdemir, W. E. Perkins, and P. J. Coane, Record of the Eleventh Symposium on Electron, Ion and Laser Beam Technology, Boulder Colorado, May 1971, R. F. M. Thornley, Ed. San Francisco Press, Inc. IEEE Catalog No. 71, C23-ED. p. 331.
9. M. Hatzakis and A. N. Broers, *ibid.* p 337.

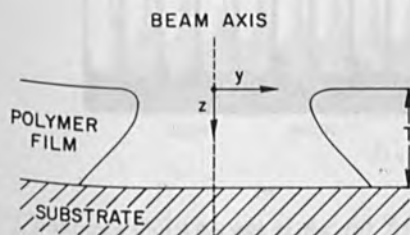


Figure 1. A schematic diagram illustrating the undercut contours typically developed in a PMMA film of thickness T on top of a substrate after exposure by a scanned electron beam.

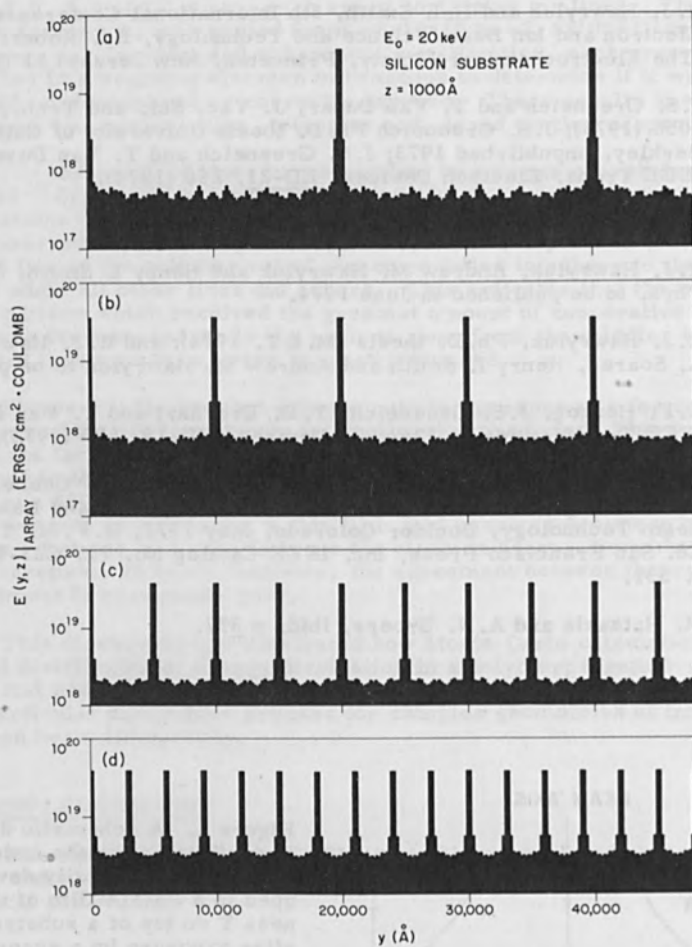


Figure 2. $E(y, z)|_{\text{ARRAY}}$ at $z = 1000 \text{ \AA}$ for an array of lines exposed with 20 keV electrons in a 250 \AA diameter beam. The substrate is silicon, and the PMMA is 4000 \AA thick. The interline spacings are (a) $2 \mu\text{m}$, (b) $1 \mu\text{m}$, (c) $0.5 \mu\text{m}$ and (d) $0.3 \mu\text{m}$.

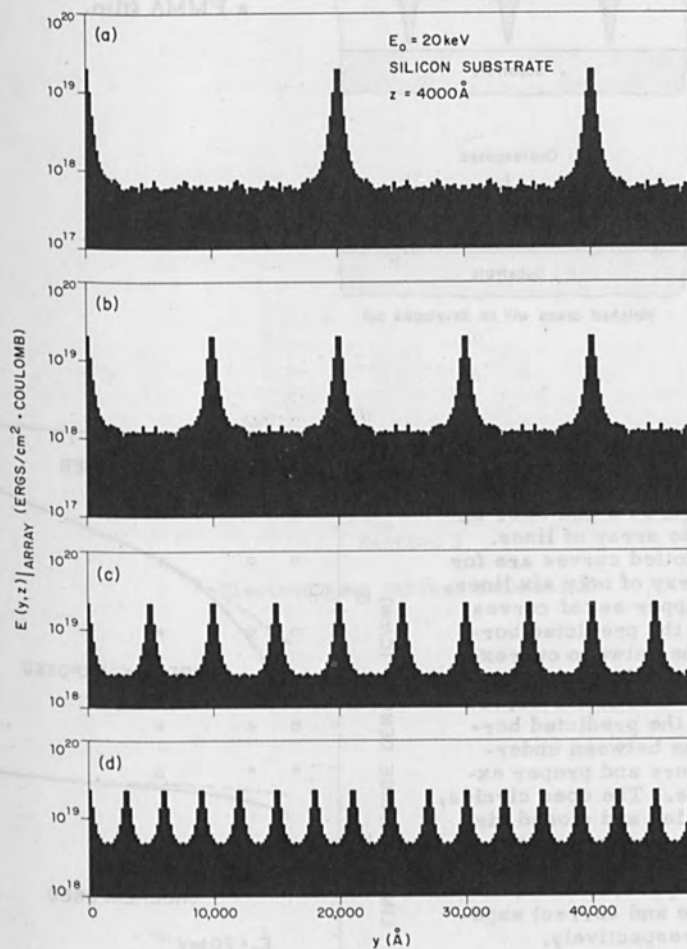


Figure 3. $E(y, z) |_{\text{ARRAY}}$ at $z = 4000 \text{ \AA}$ for an array of lines exposed with 20 keV electrons in a 250 \AA diameter beam. The substrate is silicon, and the PMMA is 4000 \AA thick. The interline spacings are (a) 2 \mu m , (b) 1 \mu m , (c) 0.5 \mu m and (d) 0.3 \mu m .

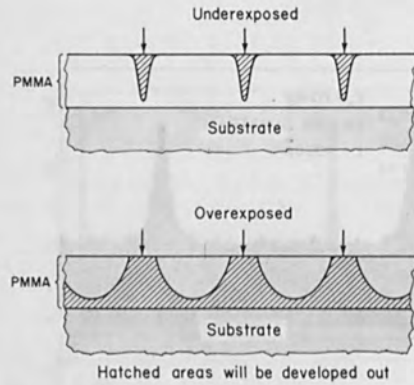
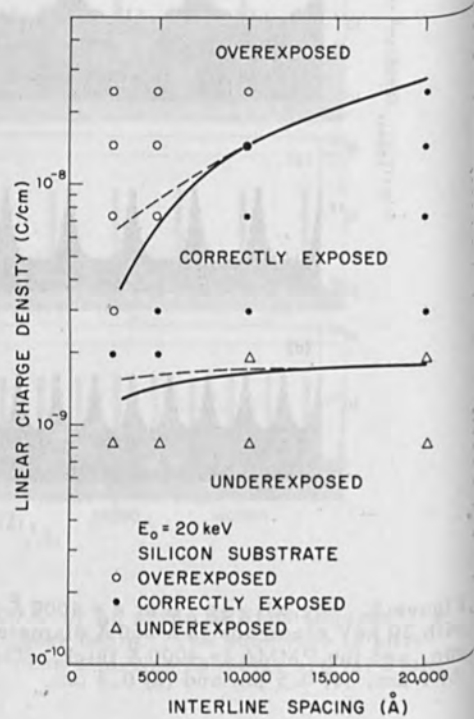


Figure 4. Illustrates under exposure and overexposure of a PMMA film.

Figure 5. The solid curves are based on the Monte Carlo calculations of Figures 2 and 3 for an infinite array of lines. The dotted curves are for an array of only six lines. The upper set of curves mark the predicted borderline between overexposure and proper exposure. The lower curves mark the predicted borderline between underexposure and proper exposure. The open circles, triangles and closed circles are experimental results corresponding to overexposure, underexposure and correct exposure respectively.



der
tre!

NEW HIGH-RESOLUTION ELECTRON BEAM SYSTEMS

C. L. Nagels, D. R. Taylor, and J. H. ...
and R. D. ...

Texas Instruments Incorporated
P. O. Box 5011, Dallas, Texas 75210

ABSTRACT

An electron beam writing instrument has been developed that allows accurate, high speed, large area, microcircuit pattern delineation of photoresist on silicon. This instrument (EMIT) incorporates most of the principles of an earlier e-beam system (EMIT) but has several additional features and possibly improved performance. Dynamic focusing and air-spoke deflection coils design...

PART I

Section 3

Electron Beam Pattern Generation

Electron beam pattern generation system consists of a cathode electron gun and a positive electron resist of 2.5 μm diameter. Beam width pattern generation is standard 10 patterns with 1 or 1.5 μm per line. Typically 10-15 patterns per bit. The combination of a commercial laser interferometer, an automatic pattern registration system, scope shift correction circuitry, and high speed stepping motor provide accuracy and speed without reliance of any individual components. The...

INTRODUCTION

The electron beam writing system using a computer to generate the patterns by controlling the deflection of the electron beam are well suited for rapid device design, mask fabrication and high yield device processing because they permit delineation of microcircuit patterns from computer data. These e-beam systems are also attractive for high frequency and high packing density microcircuit applications because they permit higher resolution and better alignment accuracy than attainable with conventional photolithography.

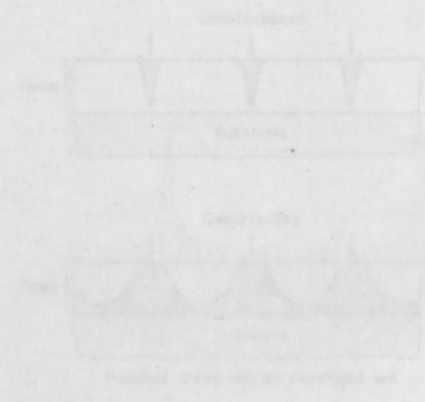
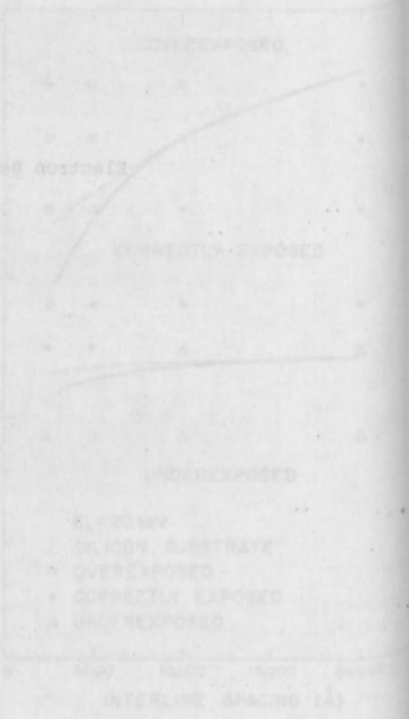


Figure 4. Illustrates both underexposure and overexposure of a PMMA film.

Figure 5. The effect of the polymerization rate on the Monte Carlo simulation. The effect of the polymerization rate on the Monte Carlo simulation is shown in Figure 5. The effect of the polymerization rate on the Monte Carlo simulation is shown in Figure 5. The effect of the polymerization rate on the Monte Carlo simulation is shown in Figure 5.



HIGH SPEED ELECTRON BEAM PATTERN GENERATION

G.L. Varnell, D.F. Spicer, A.C. Rodger,
and R.D. Holland

Texas Instruments Incorporated
P.O. Box 5012, Dallas, Texas 75222

ABSTRACT

An electron beam writing instrument has been developed that allows accurate, high speed, large area microcircuit pattern delineation of photomasks or wafers. This instrument (EBMII) incorporates most of the principles of an earlier e-beam writing system (EBMI) but has several additional features and greatly improved performance. Dynamic focusing and air-core deflection coils designed by computing exact electron trajectories permit delineation of $1.0 \mu\text{m}$ lines in electron resist over a $6.35 \text{ mm} \times 6.35 \text{ mm}$ area. The pattern generating electronics coupled with the electron optical deflection system allows beam writing speeds of up to $5 \mu\text{m}/\mu\text{s}$. This writing system combined with a LaB_6 electron gun and a negative electron resist of $2.5 \mu \text{ couls}/\text{cm}^2$ sensitivity permits generation of standard IC patterns with $5 \text{ mm} \times 5 \text{ mm}$ bar size in typically 10-15 seconds per bar. The combination of a commercial laser interferometer, an automatic pattern registration system, stage shift correction circuitry, and high speed stepping motors permits master mask overlay accuracy of $\pm 0.5 \mu\text{m}$ over a $5.5 \text{ cm} \times 5.5 \text{ cm}$ array without the use of any fiducial markers on the photomask.

INTRODUCTION

Electron beam writing systems using a computer to generate the pattern by controlling the deflection of the electron beam are attractive for rapid device design, mask fabrication, and high yield device processing because they permit delineation of microcircuit patterns from computer data. These e-beam systems are also advantageous for high frequency and high packing density microcircuit fabrication because they permit higher resolution and better alignment accuracy than achievable with conventional photolithographic

techniques. Previously developed e-beam writing systems have been severely limited in cost effectiveness by the restricted throughput of this serial exposure technique. Parallel techniques (x-ray and e-beam projection systems) may provide the required throughput, resolution, and alignment accuracy for high density device fabrication but will still require serial e-beam exposure for generation of the master mask. For these reasons, an electron beam writing instrument has been developed that allows accurate, high speed, large area microcircuit pattern delineation of photomasks or wafers.

This instrument (EBMII) incorporates most of the principles of an earlier e-beam writing system (EBMI)^{1,2} but has several additional features and greatly improved performance. Dynamic focusing and air-core deflection coils designed by computing exact electron trajectories permit delineation of 1.0 μm lines in electron resist over a 6.35 mm X 6.35 mm area. The pattern generating electronics coupled with the electron optical deflection system allows beam writing speeds of up to 5 $\mu\text{m}/\mu\text{s}$. This writing system combined with a LaB₆ electron gun and a negative electron resist of 2.5 $\mu\text{ couls}/\text{cm}^2$ sensitivity permits generation of standard IC patterns with 5 mm X 5 mm bar size in typically 10-15 seconds per bar. The combination of a commercial laser interferometer, an automatic pattern registration system, stage shift correction circuitry, and high speed stepping motors permits master mask overlay accuracy of $\pm 0.5 \mu\text{m}$ over a 5.5 cm X 5.5 cm array without the use of any fiducial markers on the photomask.

ELECTRON BEAM PATTERN GENERATOR (EBMII)

The electron beam pattern generator developed for microcircuit fabrication is shown in Fig. 1 and a block diagram of the instrument is shown in Fig. 2. This instrument (EBMII) incorporates most of the principles of EBMI but has several additional features and greatly improved performance. The electron beam column has been redesigned and incorporates a new ion pumped LaB₆ electron gun and three lens "shaped beam" electron optics to provide well defined beam diameters with non-gaussian current profiles. The ion pumped mechanical stage is laser interferometer controlled and incorporates semi-automatic material handling. The system computer is a TI980A with 32K of memory and extensive peripherals (magnetic disc, magnetic tape, punched card reader and TI Silent 700 data terminal). Improvements have also been made to the electronics and electron optical deflection system for greater reliability and higher speed performance. The major features of EBMII are listed below:

0 Scan Area (Field Size)	Up to 6.35 X 6.35 mm
0 Line Resolution	6,250 Lines @ 3 m RADS Beam Semiconvergence Angle

0 Point Resolution	0.125 μm (6.35 X 6.35 mm Field)
(Least Significant Bit Size)	0.0625 μm (3.2 X 3.2 mm Field)
0 Pattern Non-Linearity	< 0.05% of Field Size
0 Figure Drafting	Steered Beam
0 Beam Diameter	Variable from 0.25 μm to 5.2 μm (Computer Controlled Option of Pre-Set "Large" or "Small" Beam)
0 Accelerating Voltage	15 kV
0 Objective Lens Focal length	7.5 cm
0 Scanning Speed	Programmable from 40 $\mu\text{m/s}$ to 5 $\mu\text{m}/\mu\text{s}$
0 Pattern Writing Time	10-15 Seconds for 5 mm X 5 mm Field (2.5 μ couls/cm ² Resist, 50% Area)
	(1.0 μm Beam Diameter and 0.25 μm Raster Spacing)
0 Mask Overlay Accuracy	\pm 0.5 μm over a 5.5 cm X 5.5 cm Array
0 X-Y Table Stepping Speed	Up to 5 cm/sec over 12.5 cm X 12.5 cm
0 Data Input	
- Complex IC Patterns	Magnetic Tape After Decomposition on IBM 360
- Simple Devices and Test Patterns	Card or Teletype

DEFLECTION COILS AND PATTERN GENERATING ELECTRONICS

The major technical barrier (besides gun brightness and resist sensitivity) which has limited widespread use of e-beam writing is the performance of the deflection system and the pattern generating electronics.

The deflection coils of commercial scanning electron microscopes permit extremely high resolution but at a trade-off of small field coverage. Unacceptable astigmatism, curvature of field, distortion, and non-linearities occur when the beam is scanned over a large area.

A deflection system for microcircuit fabrication should permit 5000 lines resolution (i.e., $1.25 \mu\text{m}$ over a $6.35 \times 6.35 \text{ mm}$ field for standard IC devices and $0.5 \mu\text{m}$ over a $2.5 \text{ mm} \times 2.5 \text{ mm}$ field for special devices) and minimal non-linearity (i.e., $< 0.1\%$).

The distortion and non-linearity requirements of the deflection system for EBMI were met by writing a computer program to combine the fields from the individual coils, computing the trajectory of the electron beam, and optimizing the coil dimensions by calculating partial-differential coefficients.³ The resolution requirements over the large field were met by designing a full dynamic focus correction system which corrects for curvature of field and deflection introduced astigmatism (see Fig. 3). The deflection system is essentially similar to that in EBMI except that the working distance is increased and the number of turns on the deflection coils has been halved to increase the deflection amplifier bandwidth to 3 MHz.

The pattern generating electronics of an e-beam writing system can be the limiting factor on cycle time rather than the resist sensitivity and the gun brightness. The pattern generating system in EBMI is essentially similar to that in EBMI and has been described in detail in a previous article.⁴

Pattern figures are decomposed into basic trapezoid shapes having the two parallel sides parallel to the X or Y axes. The beam is scanned in a raster format parallel to the parallel sides of the trapezoid. The coordinates of the individual end points defining the sloped ends of the trapezoid are calculated in real time by a hard wired raster logic unit which has been loaded by the computer with nine basic parameters defining the trapezoid.

Digital to analog conversion is performed by two 16 bit digital to analog converters for each axis, defining the "LEFT" and "RIGHT" trapezoid endpoints respectively. An analog multiplexer switches between the DAC outputs defining the trapezoid endpoints and a ramp generator moves the beam at a constant (programmed) rate between these endpoints. This multiplexer-ramp generator (MURGE) technique combined with the electron optical deflection system permits writing speeds in EBMI up to $5 \mu\text{m}/\mu\text{sec}$. For a $0.25 \mu\text{m}$ raster spacing this is adequate for exposing 50% of the area of a 5 mm square photomask pattern in less than 10-15 seconds (assuming sufficient resist speed/gun brightness).

Fig. 4 shows an extremely dense metal leads photomask pattern of a 1024 bit PROM. This pattern was exposed and stepped to the next field position in eight (8) seconds. Exposure occurs at a raster spacing of $0.25 \mu\text{m}$ and a beam writing speed of $3.75 \mu\text{m}/\mu\text{s}$. The bar size is $0.095" \times 0.130"$. Fig. 8 shows less dense levels of the same device. The times required for pattern delineation and X-Y table

movement were 5.0 and 3.7 seconds/bar respectively. All patterns were delineated in chrome using a negative electron resist of $2.5 \mu \text{ couls/cm}^2$ sensitivity.

PATTERN REGISTRATION SYSTEM

A closed loop automatic pattern registration system (APR2) utilizing four L-shaped fiducial markers in a rectangular format was previously developed for slice printing.⁵ The system utilized the secondary and backscattered electrons emitted from these markers to determine their X and Y coordinate positions. Corrections were then electronically made in X position, Y position, X gain, Y gain, rotation, and orthogonality and the position of markers was subsequently measured again, to insure the desired accuracy had been achieved. By correcting for X and Y gain, rotation and orthogonality at each field (bar) minor changes in accelerating voltage, lens current, deflection coil current, slice flatness, z banking, and focus were made insignificant.

The only disadvantage with this method for microcircuit fabrication is the delineation of the fiducial markers (several hundred for a 2.0 inch wafer) and maintaining their utility through the process. Photomasks could be fabricated in this manner but the process would be costly and greatly increase the number of defects in the starting material. Laser interferometer systems for e-beam writing instruments have been reported previously⁶ but these systems only make corrections for the X-Y table position. For this reason a new technique has been developed to eliminate any type of fiducial markers on the mask (substrate) but still provide some of the closed loop features of the APR2 system.

The new technique incorporates the use of a commercial laser interferometer and an automatic pattern registration system. The interferometer is utilized to determine the X and Y coordinate positions of the table (mask) and the e-beam APR2 system is used in combination with a special fiducial marker mask (fixed to the table and in the image plane) to determine X and Y gain, rotation and orthogonality. This procedure eliminates the problems with minor changes in accelerating voltage, lens current, deflection coil currents and focus over long periods of time. The X and Y positional measurement is closed loop (measured at each field) but X and Y gain, rotation and orthogonality are only measured at the beginning of the generation of an entire mask.

Figs. 5 and 6 show a schematic and a photograph of the mechanical portion of the pattern registration system (APR3) developed for EBMII. The basic components are a 5525B Hewlett-Packard Laser Interferometer System (a helium-neon laser, 2 remote interferometers, and 2 beam detection units), a beam splitter, a beam bender, and two 6"

chromium carbide reflecting surfaces mounted on the X-Y table.

The light beam emitted from the laser/detector housing is directed toward the remote interferometers by a beam splitter and a beam bender. The beam consists of two slightly different optical frequencies (f_1 and f_2) which are linearly polarized. The relative displacement of the cube corner reflector in the remote interferometer and the chromium carbide reflector is measured by splitting the beam into f_1 and f_2 , directing the beam components to these two reflectors, and returning the resultant signals to a common point in the remote interferometer where the beam components are made to interfere with each other. The combined beams are directed to a photodetector in the laser/detector housing.

The measurement is made between the remote interferometer and the X-Y table mirrors so that no wavelength compensation is necessary since the measurement path is evacuated to $\approx 10^{-6}$ Torr. Cosine error is eliminated by insuring that the laser beam is perpendicular to the X-Y table mirror surfaces. The resolution of the laser interferometer system is 1.038 microinches and stepping speeds up to 3"/sec are permitted.

The principle of operation of the pattern registration system (APR3) is given below:

- 1) The mask (or wafer) is loaded manually into the Y position with a mechanical pusher. The X and Z banking is then performed pneumatically.
- 2) The X and Y stepping motors (under computer control) move the X-Y table to a coordinate position determined by optical sensors. The laser interferometer counters are set to zero at this position.
- 3) The X-Y table is driven to the fiducial marker position and the automatic pattern registration (APR2) system⁷ determines X_0 , Y_0 , X and Y gain, rotation and orthogonality from the four L-shaped silicon etched fiducial markers (permanently attached to the X-Y table).
- 4) The X-Y table is moved within $\pm 1/2$ step of the required array position (stepping increment = 1.25 mils) using X_0 and Y_0 as the reference position.
- 5) The difference between the desired position and the laser interferometer computed position is determined by the stage shift correction electronics and this difference (ΔX , ΔY) is input electrically to the deflection system to delineate the pattern at the desired X,Y position.

Figure 7 shows a schematic of the stage shift correction loop. In the stage control hardware the required stage destination is defined by a 24 bit data word for each axis. The stage position is held in the stage position counters which are continuously updated by the laser interferometer. The difference between the required destination and the actual stage position is computed continuously by a 24 bit full adder for each of the X and Y axes. The 16 most significant bits of the adder output are used by the stage control hardware to determine when a stage move has been completed. The eleven least significant bits are called the stage shift data and represent the error in the required stage position with a range of plus or minus 1.063 mils and a least significant bit of 1.038 microinches. Since the stage moves in steps of 1.25 mils the stage control software must insure that the stage stops within plus or minus half a step of the required destination.

The stage shift data is converted to two analog voltages by two eleven bit digital to analog converters and after scaling to allow for the field size the analog voltages are added to the pattern defining waveforms. Thus, the beam deflection origin is moved by an amount equal to the stage position error and the resulting exposure is correctly positioned on the photomask plate. In principle, the digital to analog conversion could be performed continuously directly from the stage shift data. In practice, the conversion is strobed once immediately before each trapezoid comprising the mask pattern is exposed. This avoids the problem of severe glitches in the output of the eleven bit DAC's which could occur if the stage shift data was incrementing and decrementing around a major transition at mega-hertz rates.

The major factors limiting the positional accuracy of the APR3 system are listed in Table 1. For comparison the limiting factors of the APR2 system (substrate fiducial markers and no laser interferometer system) are also given. The important difference is that the APR3 system (as with conventional mask fabrication) is dependent on substrate flatness, vertical table displacement, and temperature variations of the substrate. The APR3 system is also subject to minor changes in accelerating voltage, lens current, and deflection coil currents during the time required for delineation of the entire mask, instead of one bar, as in the case of the APR2 system. The one advantage of the APR3 system (other than the absence of substrate fiducial markers) is that it corrects for X-Y table position before generation of each trapezoid (\approx every ms); hence, table drift is eliminated. However, under normal conditions almost no table movement occurs during pattern generation of one bar.

By proper temperature and flatness control of the substrate the combination of APR2 accuracy, laser interferometer accuracy, stage shift correction accuracy, and beam placement accuracy limits pattern

stackability of mask sets to $\pm 20 \mu''$ ($\pm 0.5 \mu\text{m}$). This is of the same order as the measuring errors of the overlay comparator used for mask stacking accuracy measurements. Fig. 8 shows two typical levels measured. Overlay measurements were made on random bars over a 5.5 X 5.5 cm array.

SUMMARY

An electron beam pattern generator has been developed which enables fast cycle times and excellent pattern registration accuracy for IC master mask fabrication. It is capable of large field coverage ($1.0 \mu\text{m}$ over 6.35 X 6.35 mm) and can be extended even further by the laser interferometer controlled X-Y table and a mosaic approach of drawing patterns. Development of a higher speed pattern generation system and higher speed electron resists and/or higher brightness electron guns should permit an even greater impact on microcircuit fabrication by e-beam writing systems.

Table 1

POSITIONAL ACCURACY

	<u>APR3</u>	<u>APR2</u>
1) Automatic Alignment and Correction Accuracy		
O Gain, Rotation, and Orthogonality	X	X
2) X, Y Measurement and Correction Accuracy		
O Laser Interferometer and Stage Shift Correction Accuracy	X	-
O Mirror Flatness	X	-
O Stage Tilt, Pitch, and Yaw	-	-
3) Beam Placement Accuracy		
O Eddy Currents	X	X
O Stray Fields	X	X
4) Deviation Between Substrate and Image Plane		
O Mask Flatness	X	-
O Vertical Table Displacement as a Function of X,Y	X	-
5) Table Movement During Exposure		
O Vibration	-	X
O Stepping Motor Movement	-	X
6) Temperature Variations of the Substrate	X	-
7) Minor EHT Variations		
O Greater than 15 Seconds Intervals	X	-
O Greater than Mask Exposure Time	-	-

References

1. G.L. Varnell, D.F. Spicer, and A.C. Rodger, "E-Beam Writing Techniques for Semiconductor Device Fabrication," 12th Symposium on Electron, Ion, and Laser Beam Technology, Cambridge, Mass., May, 1973.
2. D.F. Spicer, A.C. Rodger, and G.L. Varnell, "Computer Controlled Pattern Generating System for Use with Electron Beam Writing Instruments," 12th Symposium on Electron, Ion, and Laser Beam Technology, Cambridge, Mass., May, 1973.
3. Varnell, loc. cit.
4. Spicer, loc. cit.
5. Varnell, loc. cit.
6. O. Cahen, R. Sigelle, J. Trotel, "Automatic Control of An Electron Beam Pattern Generation," The Electrochemical Society Meeting, Houston, Texas, May, 1972.
7. Varnell, loc. cit.

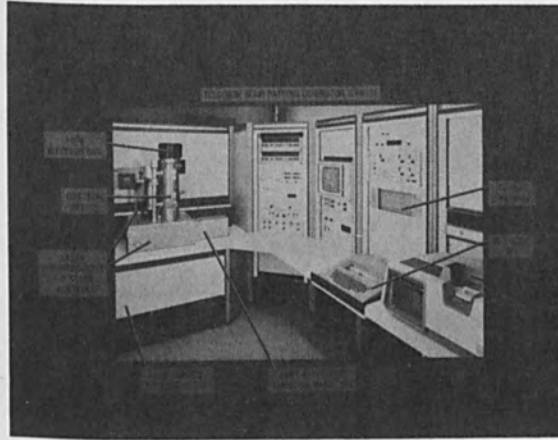


Fig. 1. Electron Beam Pattern Generator (EBMII)

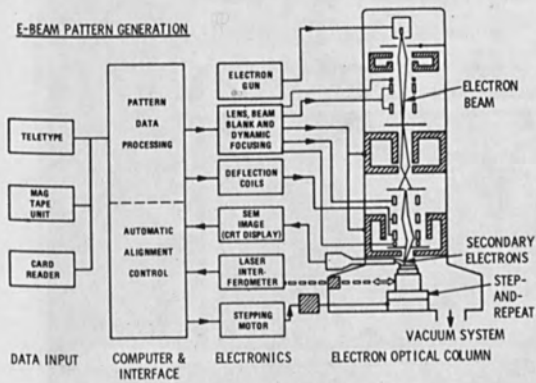


Fig. 2. E-Beam Pattern Generator

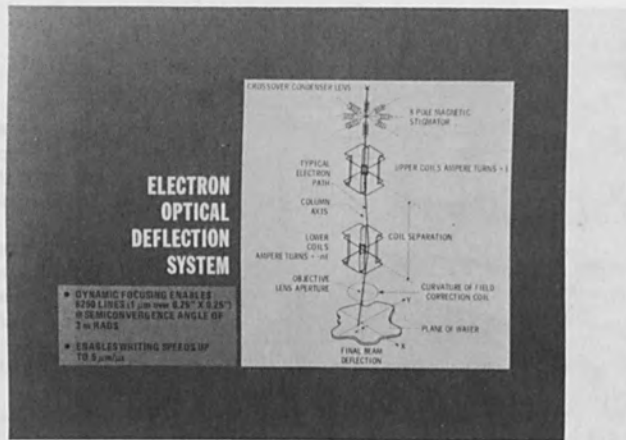


Fig. 3. Electron Optical Deflection System

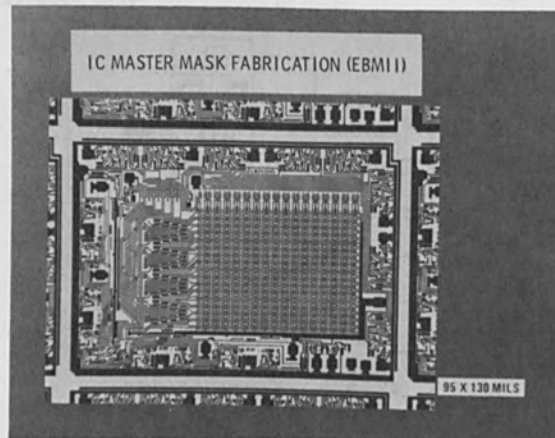


Fig. 4. IC Master Mask Fabrication (EBMII)

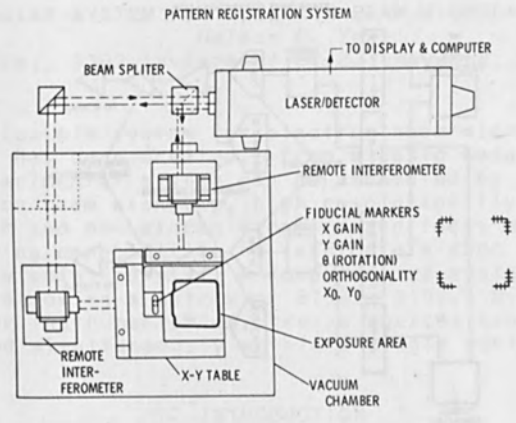


Fig. 5. Pattern Registration System

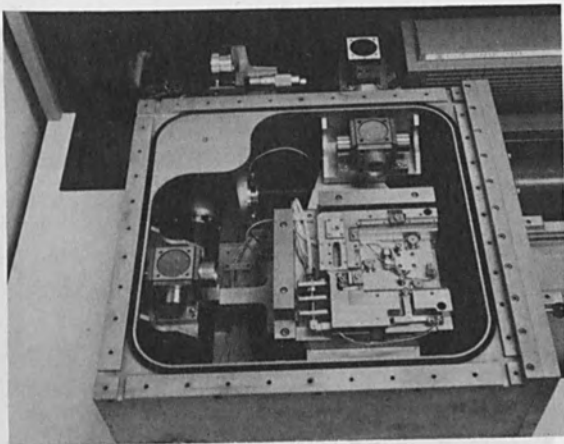


Fig. 6. Laser Interferometer Controlled X-Y Table

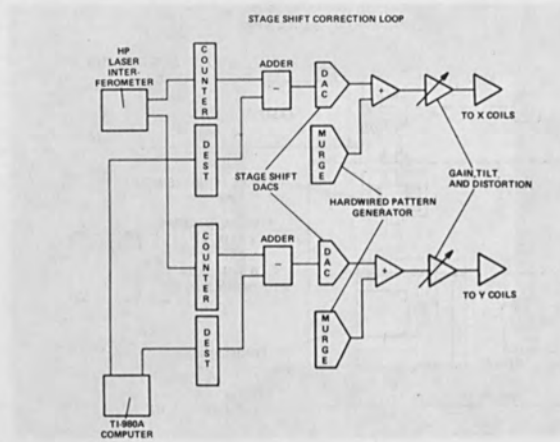


Fig. 7. Stage Shift Correction Loop

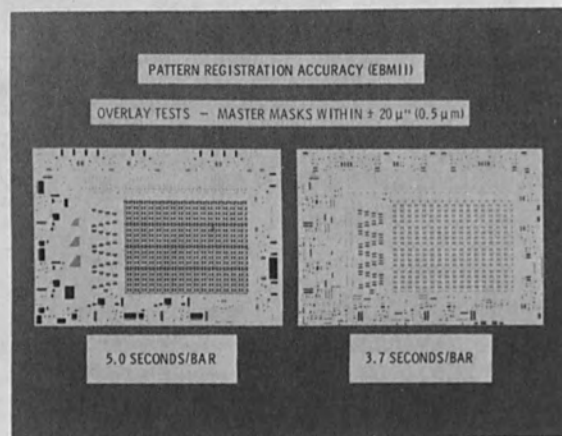


Fig. 8. Pattern Registration Accuracy (EBMII)

A MODULAR SYSTEM FOR ELECTRON BEAM MICROFABRICATION
Nelson C. Yew
Etec Corp., 3392 Investment Blvd., Hayward, Ca. 94545

A flexible system for electron beam microfabrication has been created. From a basic modular SEM, an experimental system can be assembled by adding electron beam blanking, high resolution flying spot scanner and manual registration and focus modules providing capabilities to fabricate a 4000 x 4000 picture point matrix. A computerized system can be added allowing a matrix of 8192 x 8192. By adding further instrumentation, twelve devices can be fabricated simultaneously within a single system.

INTRODUCTION

Electron beam lithography has recently been found to be extremely useful in direct microfabrication of special purpose devices such as acoustic surface wave devices, microwave transistors, charge coupled devices, large capacity MOS memory arrays and high density magnetic bubble memory arrays. It has also proven useful for generating extremely high quality primary masks for subsequent normal contact or projection photolithography.

In direct fabrication, line width down to 0.1 micrometer has been reported by several workers in this field.^{1,2,3,4} These extremely small geometry devices have been proven to operate into higher frequencies than possible before with devices fabricated by conventional photolithography. Although line width, in the case of primary mask generation for photolithography, cannot be substantially reduced because of the subsequent photolithographic process, higher edge acuity on these masks generated by electron lithography, has been proven valuable to improve the resolution achievable in projection photolithography. Since electron lithography is capable of fabricating primary masks by a single step process directly from CAD data input via a magnetic tape reader to the final 1X mask without involving photographic reduction or photorepeater processing, the turnaround time for generating a set of masks can be greatly reduced.

Scientists working in this field have been devoting much time and effort in modifying commercial SEM systems, in developing supporting hardware and software, in order to investigate experimentally the various aspects of electron

lithographic techniques. The hardware systems described in this paper are intended to provide new scientists entering into this field with all the necessary building blocks to assemble an expandable electron beam microfabrication facility so that experimental scientific investigation on device techniques, etc., can be started immediately without prolonged development and engineering delay.

SYSTEM DESCRIPTION

A building block approach has been taken to provide a flexible microfabrication system that can be tailored to individual needs. Starting from a basic SEM, a simple system suitable for initial experimental investigation of electron resist characteristics device processing, device geometry, etc., can be achieved by adding a pattern generation system, electron beam blanking facility, and registration facility. Two methods of pattern generation can be used, a flying spot scanner based system and a computer based pattern generation system.

Flying Spot Scanner Pattern Generation System

This is a system based on a high resolution CRT coupled with an optical lens system and a photomultiplier detector. A minute spot of light is generated on the face of the CRT and used as a resolution element to scan an optical mask in the form of a normal TV raster. The transparent and opaque regions of the mask control the on and off of the electron beam striking the substrate and, hence, forming an exposure pattern on the resist coating on the substrate. Both a 4000 line system with minimum resolution element of 20 microns on the mask and a 2000 line system with minimum resolution of 40 microns are available. Active mask areas up to 8cm square can be used with these flying spot mask readers. A typical application for this type of pattern generator would be, starting from an existing 10X reticle normally used in an optical repeater, to fabricate experimental devices with size as a varying parameter.

Registration and focusing can be achieved by the use of bench marks at the four corners of the reticle. When this registration procedure is used, the electron beam in the column is unblanked only over the appropriate registration bench mark areas while the flying spot scanner is scanning simultaneously over the appropriate bench mark on the mask. A superimposed image is displayed with the four corner bench marks showing simultaneously in a 4-way split screen display on the viewing CRT. Magnifications up to 100X of the

registration bench marks can be used with this system. Manual registration and focusing can then be performed by both the mechanical and electrical shifts as well as objective lens current controls for optimized conditions determined by the operator.

Computer Based Pattern Generation System

When a more flexible computer based pattern generation system is needed, the flying spot scanner can be exchanged by a small computer coupled to a direct access digital scan generator. The most basic computer system used is composed of an Interdata 716 (16-bit minicomputer) with 16K of memory, a high speed paper tape punch and reader and a teletype terminal. The 13-bit accuracy high speed digital-to-analog converters in the direct access digital scan generator are interfaced directly to the computer data-buss when it is switched to remote operating mode. The high speed paper tape reader provides a low cost means for data and program input at reasonable speeds. A 9-track magnetic tape transport can be added when CAD generated data input is required. For the storage of more complicated programs and patterns, a 10 megabyte dual drive disc store can also be added.

Basic pattern generation and control software completes the operating system. Subroutines are written in machine language for efficiency and linked together by an interactive language similar to BASIC. Patterns are built up with rectangle generating subroutines where the user defines X and Y coordinates of a corner and ΔX and ΔY to define the size of the rectangle. A number of rectangles are then formed into a desired pattern. Any group of basic rectangles can be defined as a subfield and the subfield can then be step and repeated throughout the standard 8192 x 8192 address matrix. This step and repeat subroutine greatly reduces the amount of data input necessary to build up an overall pattern with repetitive features such as a typical magnetic bubble memory. Other basic patterns such as chevrons and vectors can also be used to build up the desired pattern. Additional software subroutines to generate such shapes as triangles, polygons, circles, arcs of circle, etc., can also be added when it becomes necessary.

A postlens deflection system can also be added to provide lower deflection aberrations over larger fields and higher deflection speed capability. With this option, a 16-bit digital-to-analog conversion system, together with higher speed and high stability deflection amplifiers, completes a set-up for exposure of large scale integrated

circuits where multiple split-field matching is felt to be undesirable.

Stages

For direct fabrications up to a wafer diameter of 2-1/4", an SEM based stage with direct mounted stepping motor drive on the X and Y axis can be used. The step increment on this stage is 1 micrometer at maximum speeds up to 1mm per second. The stepping motors are controlled either manually or by the computer directly for automated step and repeat operation.

For primary mask generation use, a 4" x 4" travel stage, together with a laser interferometer feedback system in a larger specimen chamber, can also be added. This stage is capable of absolute accuracies down to 0.1 micron level. The output of the laser interferometer system is directly coupled to the on-line computer so that the relative position of the electron beam and the sample can be kept to the desired tolerance level of down to 0.1 micron. With this system, split field matching accuracies better than 0.2 microns is also possible. Automatic registration to bench marks for long term unattended operation can also be added.

High Volume Production Oriented System

One of the major objections to electron lithography is the slow throughput of such a system due to its serial nature. Typically, one hour or more is required to fully expose a 3" diameter wafer or a 3" x 3" primary mask. By utilizing the above mentioned building block approach, as many as 16 electron optical columns can be mounted on a single extended specimen chamber containing an enlarged version of the high precision X-Y stage. With individual electronic shift and deflection control for each electron optical column, operating with a single laser interferometer system on the stage, up to 16 wafers or masks can be simultaneously exposed under the control of a single pattern generating system. By this technique, the overall throughput of the electron beam microfabrication system can be increased by a factor of 16 without substantially multiplying the system hardware cost. Such a system can reduce the exposure time of each 3" diameter wafer from about 1 hour down to 5 minutes of instrument time.

RESULTS

Figure 1 is an overall view of a typical flying spot scanner based electron beam lithography system. Figure 2 is a close-up view of the control panel of the flying spot scanner system showing the various controls for threshold setting and the registration and focus functions. Figures 3 and 4 are SEM micrographs of a portion of a developed resist pattern exposed by the flying spot scanner based system. Figure 5 is an illustration of the split field superimposed registration/focus image. Figure 6 is an overall view of the basic computer based pattern generator together with the electron optical system. Figure 7 shows the direct motor driven SEM stage with a 1-1/2" wafer mounting platform and Faraday cage for measuring the electron beam current during setup. Figures 8 and 9 are SEM micrographs of developed resist on the first test pattern generated by the computer based microfabrication system. Figure 10 is an SEM micrograph of a developed resist pattern similar to those used in magnetic bubble memory. Figures 11 and 12 are SEM micrographs of the same area as shown in Figure 10 after depositing gold and performing the lift-off process. Figure 13 is an overall view of an experimental four-column electron optical system.

CONCLUSION

A modular building block electron beam microfabrication system can greatly reduce the cost and time required by scientists and engineers to enter into the field of electron lithography. Such a system can be tailored to meet individual scientists' needs at a minimum amount of capital investment, and yet provide the flexibility to extended capability when desired, as experimental technology improves. Even a full-fledged production system with parallel multiple wafer processing can be assembled at the end.

REFERENCES

1. A.N. Broers and M. Hatzakis: Microcircuits by Electron Beam, Scientific America, 1973.
2. F.S. Ozdemir, E.D. Wolf and E.R. Buckey: Computer Controlled Scanning Electron Microscope System For High Resolution Microelectronic Patterns Application, IEEE Transactions on Electron Devices, vol. ED-19, No. 5, May 1972.
3. F.S. Ozdemir, W. Perkins, R. Yim and E.D. Wolf: Precision Electron Beam Microfabrication, Vacuum Science Technology, vol. 10, No. 6, November 1973.
4. G.L. Varnell, D.S. Spizer and A.C. Rodger: E.B. Writing Techniques for Semiconductor Device Fabrication, Journal of Vacuum Science Technology, vol. 10, No. 6, November 1973.

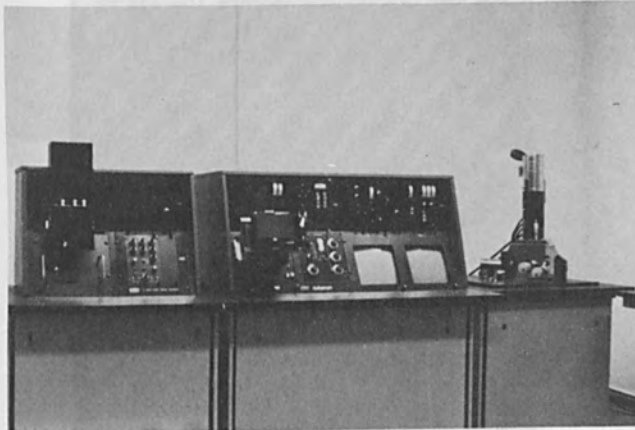


Figure 1

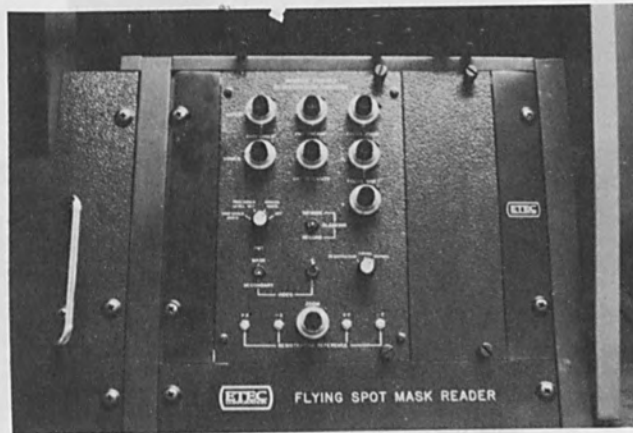


Figure 2

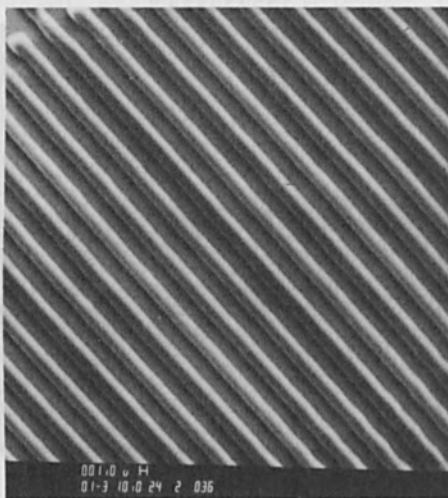


Figure 3

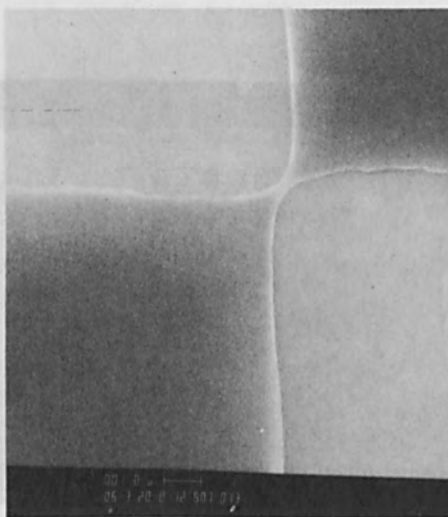


Figure 4

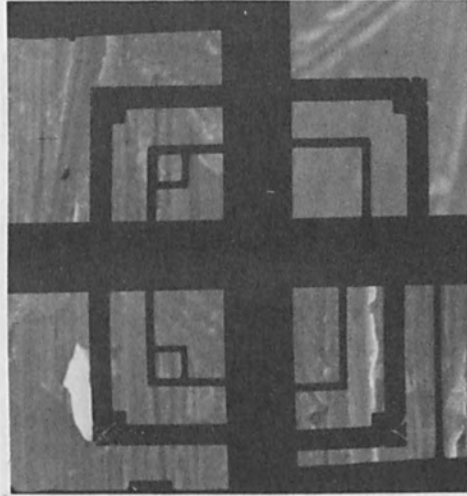


Figure 5



Figure 6

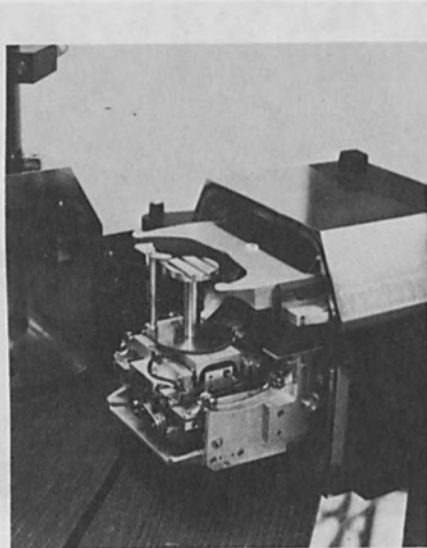


Figure 7

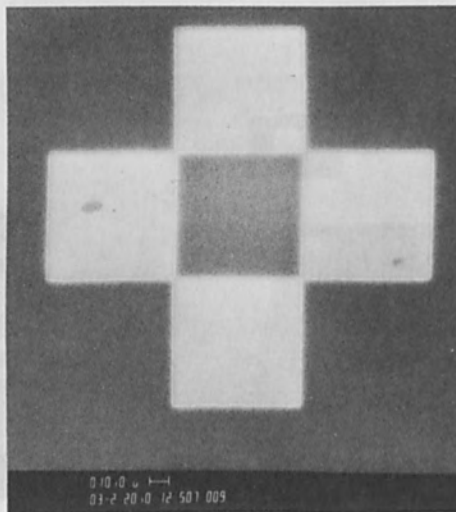


Figure 8

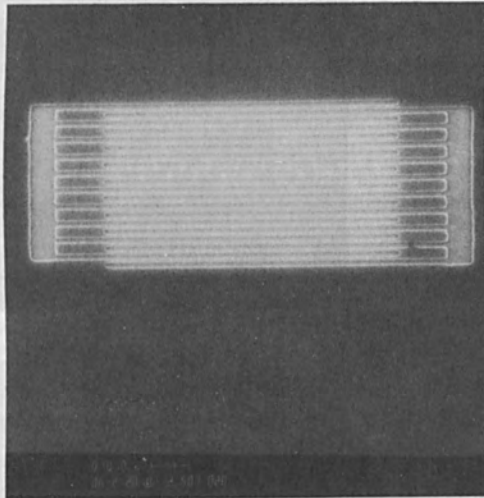


Figure 9

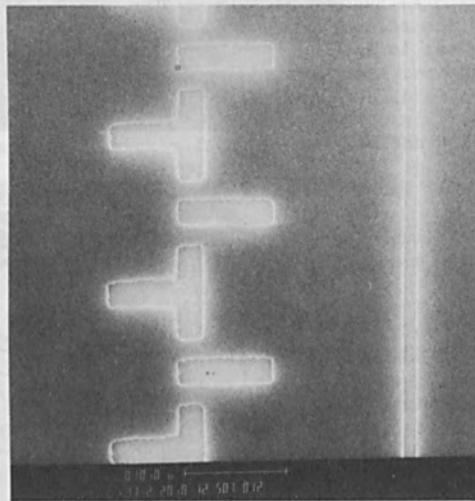


Figure 10

Figure 11

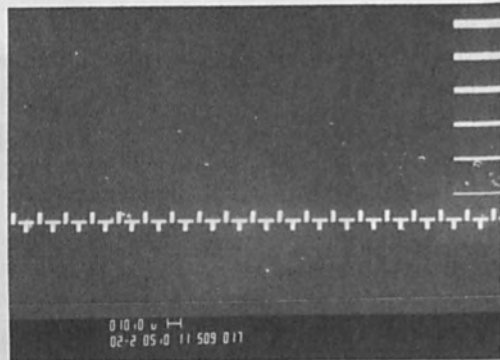


Figure 12

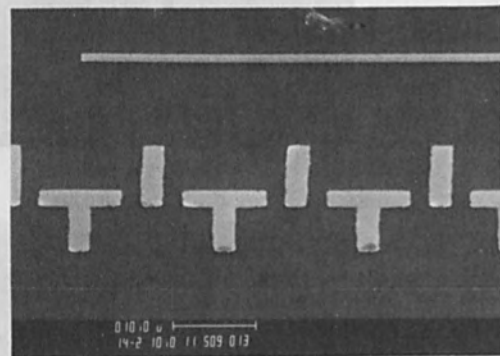
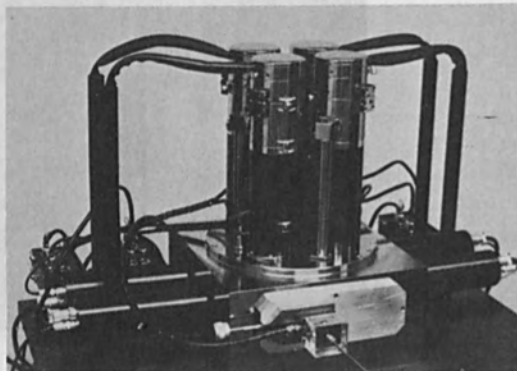


Figure 13



ELECTRON IMAGE PROJECTOR

J.P. Scott

Mullard Research Laboratories,
Redhill, Surrey, England

ABSTRACT

An electron image projector for reproducing high resolution masks onto a 50 mm silicon slice at unity magnification is described. There are three developments which considerably simplify its operation. The high homogeneity magnet gives easy access to the mask and slice. The CsI photocathode allows operation in poor vacuum conditions and reduces the cycle time including pumpdown to three minutes. The X-ray alignment method due to C.S.F. has been improved by the use of semiconductor detectors and phase sensitive signal processing.

INTRODUCTION

The Electron Image Projection method of reproducing high resolution patterns on silicon slices, due to O'Keefe(1) at Westinghouse is the only economical way of fabricating high resolution integrated circuits. In this equipment the mask is coated with a photocathode and illuminated from behind by an intense ultra violet lamp so that electrons are emitted in the areas of the photocathode above the clear areas of the mask, but not above the dark areas. The electrons are accelerated onto the slice by a high electric field and focussed by a parallel magnetic field and thus the pattern is transferred simply and quickly from the mask to the slice. However, in the past it has suffered from difficulties of operation and difficulties of alignment, which have made its use impracticable.

In this paper we outline some recent developments which have so simplified operation of the Image Projector that we are confident that its use will soon be widespread.

There are three developments in particular which will be discussed; firstly the design of the high homogeneity air-cored magnet which makes access to the working area easy; secondly, the caesium iodide photocathode which simplifies operation and reduces cycle time to less than three minutes; thirdly, the X-ray alignment method, due to C.S.F. Thomson-Houston, which has been improved by the use of solid state detectors and a new method of signal extraction.

THE MAGNET

The largest and most expensive single item in an image projector is the focussing magnet, and its design determines the general pattern of the whole machine, as it determines the position of pumping ports and the way that slices and photocathodes can be taken in and out.

The main constraint on the magnet itself is that the field over the central region must be extremely uniform (a few parts in 10^5 over the whole slice) in order to reduce image distortion to less than $1/10 \mu\text{m}$, and the traditional solutions to this problem impose very severe restrictions on the access to the central region. The present image projector uses a magnet which has been specially designed to give good access from each end, and has a gap in the central region to take the pumping port. It is of an air-cored construction, and it uses a principle that is well established for long solenoids but previously not developed for split magnets, namely taking notches out of the windings in order to improve the uniformity.

The method of calculating where to put the notches in the case of a solenoid is straightforward (though very longwinded) and is as follows. The expression for the magnetic field close to the centre of the magnet may be written as a power series expansion about that point:

$$H_z(r, \theta) = H_0 \left\{ 1 + E_2 \left[\frac{r}{a} \right]^2 P_2(\cos\theta) + E_4 \left[\frac{r}{a} \right]^4 P_4(\cos\theta) + \dots \right\}$$

$$H_r(r, \theta) = H_0 \left\{ E_2 \left[\frac{r}{a} \right]^2 P_2'(\cos\theta) + E_4 \left[\frac{r}{a} \right]^4 P_4'(\cos\theta) + \dots \right\}$$

where r, θ are polar coordinates, a is the inner radius of the magnet, P_2 and P_4 are Legendre polynomials and P_2' and P_4' their derivatives. The coefficients E_2 and E_4 are dependent on the geometry and the notch is chosen which reduces them to zero simultaneously. The first term in the expansion then varies as the sixth power of distance from the origin and is very small near the centre. The problem of solving the simultaneous equations for E_2 and E_4 involves very complex algebra, and generally requires the use of a computer.

In the case of a split magnet the calculation is more difficult because there is an extra variable, the spacing in between the two halves, and there are now three variables and only two equations to specify them. As it turns out, the gap between the two halves can never be greater than about 0.3 times the inner diameter of the magnet. If the gap exceeds this value then it is not possible to cancel out the error coefficients merely by taking notches out and it is necessary to introduce extra turns with the current flowing in the opposite direction. Normally a gap of 0.3 times the inner

diameter is slightly smaller than the ideal, so the third equation is provided by setting the gap to the maximum allowable.

Design curves have been obtained along these general lines, and a 1 kG magnet built with a homogeneity of three parts in 10^5 over a 2" disc. It can be seen from Figure 1, a schematic of the image projector, what enormous advantages this magnet confers in the way of access to the central region. With the pumping port taken vertically through the gap, the photocathode and slice can be mounted on the same level and placed at a convenient height for hand insertion, and all parts of it are readily available for inspection. By eliminating complex inserting tools the volume of the vacuum chamber is reduced with corresponding reduction in the pumping time. For an experimental model it is also very convenient to be able to look at the central portion when things go wrong!

THE PHOTOCATHODE

A part of the image projector system which has given problems is the palladium photocathode. Experiments we have carried out have confirmed results of other workers(2) in its susceptibility to water vapour and the erratic nature of the photocurrent. For this reason we have adopted caesium iodide as the photocathode, with the 1845Å illumination from a low pressure mercury discharge lamp. This has advantages over palladium in almost every respect and considerably simplifies the overall operation of the image projector. The main properties of caesium iodide as a photocathode are compared to palladium in table 1. There are only two disadvantages in using CsI. Firstly, it is an insulator so it is necessary to have a conducting layer underneath which is transparent to 1849Å radiation. Secondly, 1849Å radiation dissociates oxygen, leading to the formation of ozone, so the ultra violet has to be contained in an atmosphere of nitrogen. This is also a disadvantage inside the vacuum when the atomic oxygen attacks any residual organic matter and great care has to be taken over cleanliness.

These disadvantages are outweighed by the many advantages, of which perhaps the most important is the operation in a poor vacuum, for this means that it is feasible to let up to air and pump down the chamber for each slice exposure. In the present machine the complete exposure cycle including loading and pumping takes less than three minutes. The photocathode may be renewed in situ in less than six minutes.

TABLE 1

Table Comparing Palladium and Caesium Iodide Photocathodes

Material	Pd	CsI
Ease of fabrication	Evaporated palladium is very sensitive to traces of W.	Very easy to evaporate (650°C), though tends to spit.
Ease of removal	Requires concentrated acids, thus limiting the choice of material.	Rinses off in water.
Emitted electron energy	1 to 2 eV	0.3 to 0.5 eV
Current stability	Very poor. Can vary up to 50% during exposure.	Good. Variations of less than 3% during exposure.
Number of exposures	Adequate - up to 50 exposures if great care is taken.	Good. Several hundred exposures if care is taken.
Maximum current density	Very high $\sim 20 \mu\text{A}/\text{cm}$.	Adequate $\sim 5 \mu\text{A}/\text{cm}$.
Vacuum conditions required.	10^{-7} torr	10^{-4} torr

DEPTH OF FOCUS AND RESOLUTION

As mentioned in Table 1, the photoemission from CsI is relatively stable and insensitive to vacuum and deposition conditions. For this reason the characteristics of the energy spectrum of the photoemitted electrons have been extensively measured(3) and these results may be taken as valid in the situation of an image projector, enabling reliable computer based calculations of the resolution and depth of focus to be made.

In Figure 2 the current density on the slice due to a point source on the cathode is plotted as a function of distance from the centre. The double peak seen in this diagram is due to the fact that the point of least confusion is slightly away from the theoretical point of focus. It will be seen that there is a large penumbral region, but that 90% of the current falls in a circle with a radius

one fifth the maximum radius. This accounts for the high resolution that has been obtained with palladium photocathodes even though the emitted electron energy is of the order of a volt. Caesium iodide, with a much smaller emitted electron energy has an ultimate resolution of $0.01 \mu\text{m}$ when working at 1 kG as shown in Figure 3, where the blurring of a line (20% to 80% full exposure) is plotted against distance out of focus. From this curve it can be seen that if a blurring of $0.1 \mu\text{m}$ is acceptable, then the depth of focus is $100 \mu\text{m}$. These results have been confirmed by experiment. Figure 4 shows a test pattern in two different exposures; the top one is at the point of best definition and the lower one is $80 \mu\text{m}$ out of focus. Figures 5 and 6 show aluminium lines over an oxide step. There appears to be no disadvantage in using thick resists provided the thickness is less than the smallest detail required. In these specimens a resist thickness of $1.5 \mu\text{m}$ was used so that the aluminium $1 \mu\text{m}$ thick could be defined by lift-off.

X-RAY ALIGNMENT

One of the outstanding problems of the image projector is the problem of alignment. It is not possible to use an optical method unless the electrons can be made visible by, for example, a phosphor, and even then there are severe mechanical constraints. It is also not possible to use secondary electrons as they are trapped by the high electric field at the surface of the slice. Two methods which have been favoured recently are the method of boring a hole in the silicon slice and measuring the electrons that pass through, and the X-ray alignment method which uses Bremsstrahlung X-rays. Both of these methods suffer from the disadvantage that a marker must be defined before processing can start. The X-ray method has an advantage over the hole method in that it is easier to define high resolution metal patterns than it is to define holes with great accuracy. Moreover, the metal patterns can be varied with ease and patterns chosen which suit a particular method of alignment.

There are two innovations to the X-ray alignment method that we have introduced, firstly the use of semiconductor detectors which speeds up the alignment so much that it can be carried out to $0.1 \mu\text{m}$ in a fraction of the exposure time, and the phase sensitive detection method which considerably simplifies the alignment electronics.

SEMICONDUCTOR DETECTORS

It can be shown that the traditional method of detecting X-rays by means of an avalanche ionisation tube is inferior to the use of semiconductor detectors for an image projector, as it means that the alignment will take unnecessarily long. The basic reason for this is the shot noise due to the random arrival of the quanta of X-rays.

In order to reduce the noise to signal ratio it is necessary either to increase the count rate or to increase the time constant of the smoothing circuit. As the count rate of avalanche tubes is limited to about 10^4 counts per second because of the lifetime of ions, this means that the only option available is to extend the time constant, which results in minimum alignment times of the order of a minute.

Using semiconductor X-ray detectors (these are really just photodiodes with large depletion depths) which, in contrast to the gas filled detector, only give good signals at count rates above about 10^4 per second, the signal to noise ratio is so improved that it is possible to do away with separate illumination for the markers and align the pattern while the whole mask is being exposed. Although the pattern is being exposed during the alignment the time taken is a small fraction of the exposure time so that it has a negligible effect on the resultant image.

That this method can indeed be used is demonstrated in Figure 8, which was obtained by the phase sensitive detection method described in the next section. The current density from the photocathode was only $1 \mu\text{A}/\text{cm}^2$ and the time constant for averaging the X-ray signal was 0.1 sec., and it can be seen that the noise level is less than the equivalent of $0.1 \mu\text{m}$. If a resist is used which has a sensitivity of $100 \mu\text{C}/\text{cm}^2$, the total exposure time is 100 secs and the allowable time for alignment is 5 secs., i.e. 50 times the time constant.

PHASE SENSITIVE DETECTION

The phase sensitive detection method was introduced primarily to eliminate the effect of the leakage current in the solid state detectors, but it has been found that since the resultant signal is proportional to the misalignment the electronics for alignment is considerably simplified. In addition, both fine and coarse alignment can be carried out using the same marker area. This marker consists of grid patterns with both fine and coarse bars. (See Figure 7). There are two of these marker areas, one on each side of the slice so that X,Y and rotation errors can be corrected with accuracy. The pitch of the fine grid on the markers is in the region of $10 \mu\text{m}$ and the pitch of the coarse markers has to be greater than the maximum misalignment that is expected on inserting the slice into its holder. This is likely to be of the order of $200\text{-}300 \mu\text{m}$.

In understanding the method of alignment it is simplest to start at the point of the fine alignment, during which a small a.c. current is put into the deflection coils so that the electron pattern oscillates backwards and forwards. This produces a modulation of the X-ray signal, and if the marker is misaligned to the right then the modulation is in phase with the modulating current, and if it is

misaligned to the left then the modulation is in antiphase with the modulating current. If the two markers are aligned perfectly, then there is a large component of the X-rays at exactly twice the modulating frequency, but a zero component at the fundamental. This signal can be extracted with a phase sensitive detector, where the output is proportional to the in-phase component of the input signal. In this way an output signal is obtained which is directly proportional to the degree of misalignment. When the two patterns are perfectly aligned the output signal is zero, and so effects due to fluctuations of photocathode current, gain etc. are considerably reduced.

There are two more advantages in the phase sensitive detection method; firstly, that different frequencies can be used to modulate the X and Y deflection coils, so that when the combined X-ray signal is processed through two separate phase sensitive detectors, one will give only the X signal and one only the Y signal; secondly, coarse and fine patterns may be used on the same alignment marker. They are distinguished by using a square wave for the a.c. modulating current and arranging that the distance over which the square wave moves the electron pattern is exactly equal to one pitch of the fine grid. The fine grid is then stepped backwards and forwards between two identical positions and contributes no a.c. component to the output. Thus, the only output is due to the coarse alignment marks. Figure 8 shows a trace which has been obtained by this method. On the top line is the signal due to the fine pattern where the pitch is $10\ \mu\text{m}$ and on the lower line the signal due to the coarse pattern where the pitch is $200\ \mu\text{m}$. In this trace the pitch of the modulation is not correctly set and there is a small amount of ripple appearing on the coarse signal due to the fine pattern.

It can be seen that this method provides a signal which is proportional to the misalignment, and readily separates out the contributions in X and Y. This means that it is possible to use analogue electronics and conventional servo techniques. Any other way would almost certainly necessitate the expense and complication of a digital computer.

CONCLUSIONS

The image projector described has several innovations which make it a viable machine for the production of integrated circuits.

1. The magnet has a very high homogeneity and hence introduces very little distortion, while allowing great freedom of access. It is short in length, so that both the slice and the mask can be easily reached, and by taking the pumping port through the side the mask and slice can both be mounted in readily accessible positions.

2. The caesium iodide photocathode is very simple to prepare and remove and allows more flexibility in choice of mask materials. It has a life of up to 200 exposures and the stability of the emitted current makes the alignment problem simpler. As it works well in poor vacuum conditions the whole cycle time including loading and pumpdown is reduced to less than three minutes.

3. The X-ray alignment method due to C.S.F. Thomson-Houston has been improved by the use of solid state detectors. This enables alignment to be carried out during the exposure of the slice and eliminates the need for separate illumination for the markers. The phase sensitive detection allows fine and coarse registration to be carried out with the same marker and allows analogue circuitry to be used for the alignment in place of a computer with corresponding reduction of cost and simplicity of operation.

REFERENCES

- (1) T.W. O'KEEFE, J. VINE and R.M. HANDY, Solid State Electronics, 12, 841, (1969).
- (2) W.B. LIVESAY and R.B. FRITZ, IEEE Trans.Electron.Dev., 19, 647, (1972).
- (3) H.R. PHILLIPP and E.A. TAFT, J.Phys.Chem.Sol., 1, 159, (1956).

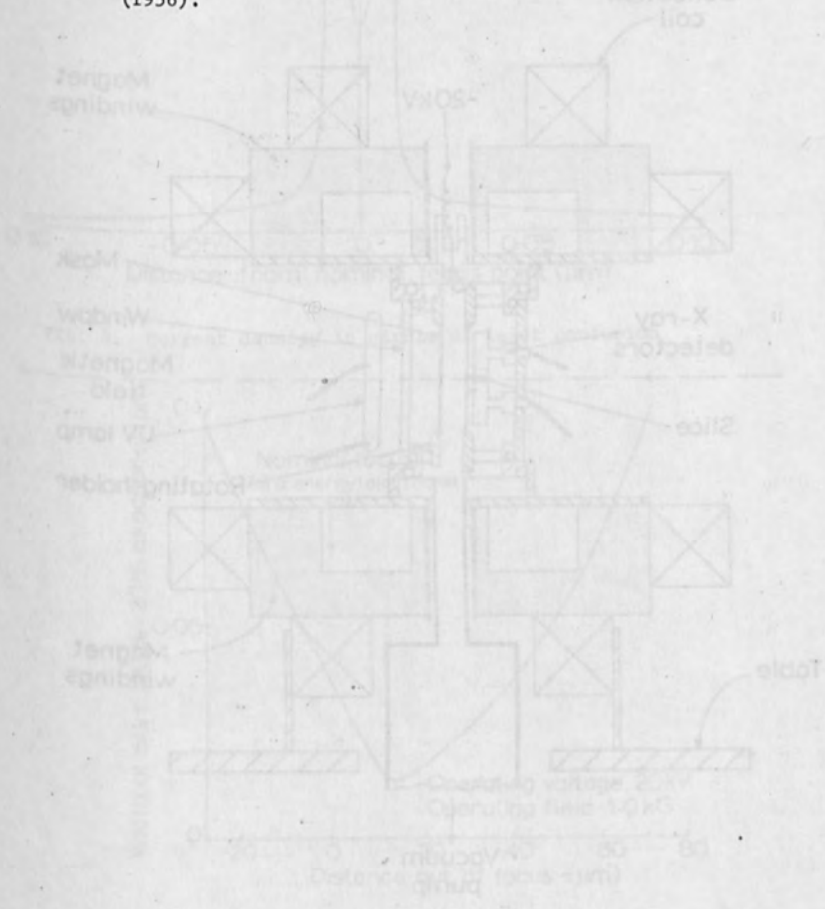


Fig. 1. Schematic of protection studies
vacuum furnace system.

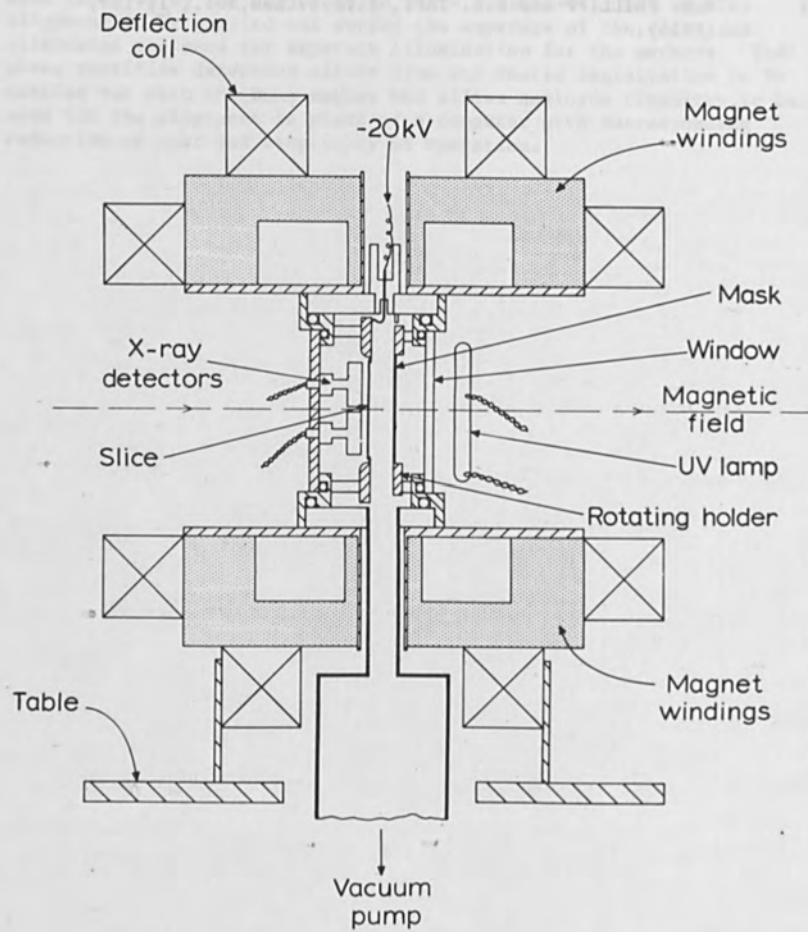


Fig. 1. Schematic of projection machine

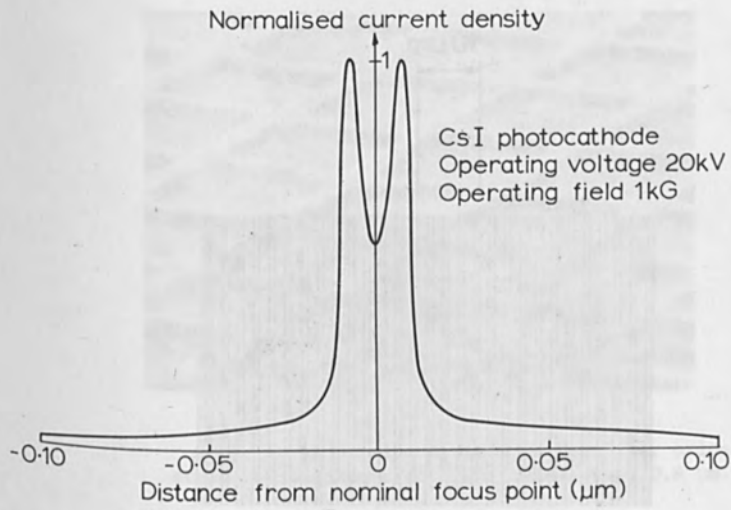


Fig. 2. Current density in circle of least confusion

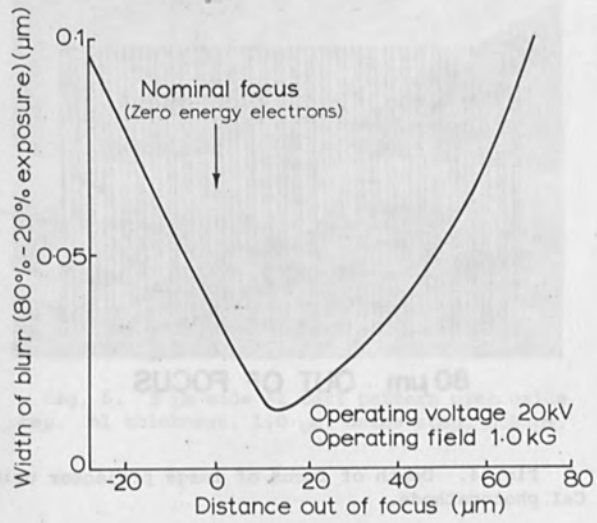
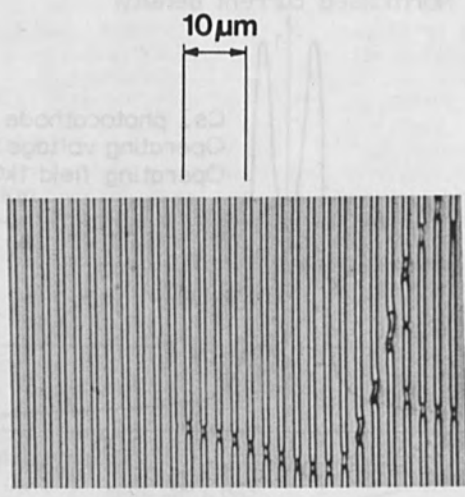


Fig. 3. Blurring and depth of focus



IN FOCUS

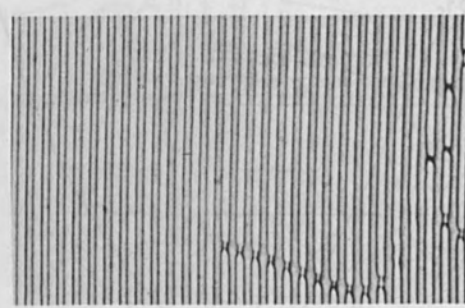


Fig. 4. Depth of focus of image projector using CsI photocathode.

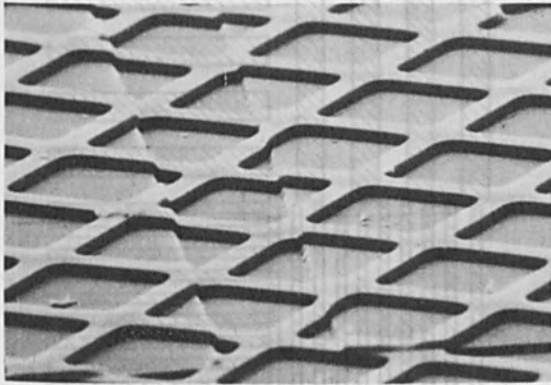


Fig. 5. 3 μm wide Al test pattern over oxide step. Al thickness, 1.0 μm ; oxide step, 0.8 μm .

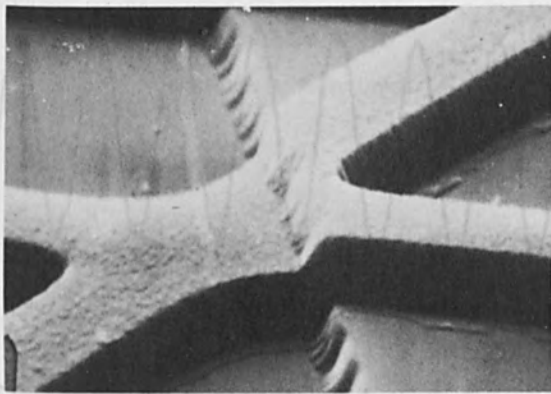


Fig. 6. 3 μm wide Al test pattern over oxide step. Al thickness, 1.0 μm ; oxide step, 0.8 μm .

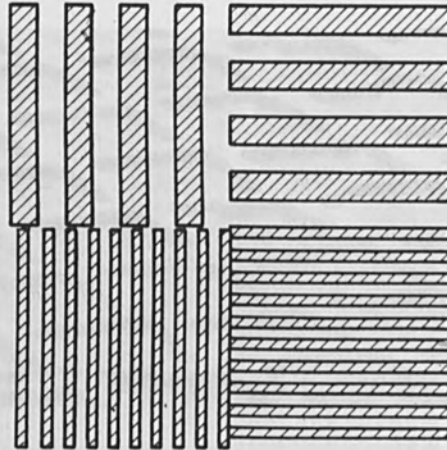


Fig. 7. X-ray marker pattern

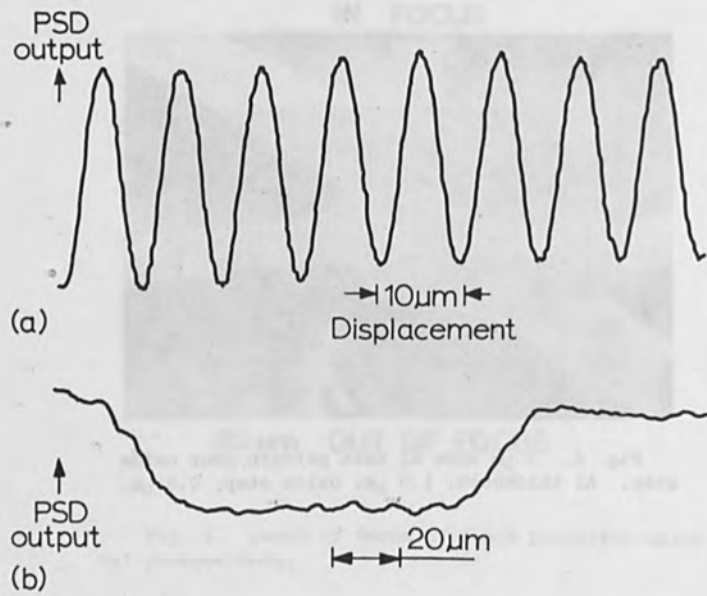


Fig. 8. Signal from x-ray marker after phase sensitive detection

ELEMENTAL ANALYSIS WITH AUGER ELECTRON
SPECTROSCOPY AND SECONDARY ION MASS SPECTROMETRY

J. H. Norberto

Bell Telephone Laboratories, Incorporated
Allentown, Pennsylvania 18103

This paper will compare, by way of specific examples, the capabilities and limitations of Auger electron spectroscopy (AES) and secondary ion mass spectroscopy (SIMS) for surface analysis, depth profile analysis, and quantitative analysis. The analytical capabilities and limitations of both AES and SIMS are such that they are complementary techniques. The combined use of both on the same material system can often provide increased insight in the interpretation of both SIMS and AES data. There is, unfortunately, very little published data on the use of both AES and SIMS techniques on the same type of samples. This is due in part to the fact that both are relatively new techniques and very few laboratories have both available. The author was therefore limited in the number of examples which demonstrate the complementary nature of the two techniques.

PART I

SAMPLE SELECTION

Section 4 (B. S. for Silicon)

Analytical Techniques

Tantalum thin films, both tantalum and silicon materials for integrated circuits, tantalum nitride (TaN) and tantalum pentoxide (Ta_2O_5) are precision resistor materials and can be conveniently trimmed to a desired resistor value by progressive modification or by laser trimming. Tantalum thin films are also used to fabricate tantalum oxide capacitors.

The importance of silicon in the fabrication of active electronic devices based on semiconductor properties has been well established. The amount and distribution of dopants such as boron, phosphorus, arsenic, etc., introduced into silicon play a major role in controlling the characteristics of active devices. These dopants can be conveniently introduced into silicon from a chemical source or by ion implantation, but the concentration of these dopants are typically below detection by conventional techniques such as the electron microprobe. Electrical methods of measuring the distribution of the dopants reveal only that presence of dopant which is electrically active. Electrical profiling methods are also extremely tedious.



Fig. 2. X-ray marker pattern

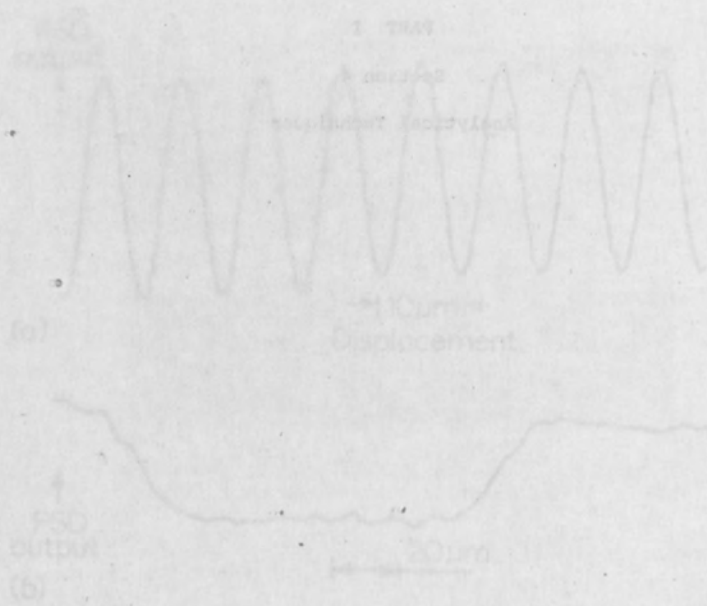


Fig. 3. Signal from x-ray marker after phase sensitive detection

ELEMENTAL ANALYSIS WITH AUGER ELECTRON
SPECTROSCOPY AND SECONDARY ION MASS SPECTROMETRY

J. M. Morabito
Bell Telephone Laboratories, Incorporated
Allentown, Pennsylvania 18103

This paper will compare, by way of specific examples, the capabilities and limitations of Auger electron spectroscopy (AES) and secondary ion mass spectrometry (SIMS) for surface analysis, depth profile analysis, and quantitative analysis. The analytical capabilities and limitations of both AES and SIMS are such that they are complementary techniques. The combined use of both on the same material system can often provide increased insight in the interpretation of both SIMS and AES data. There is, unfortunately, very little published data on the use of both AES and SIMS techniques on the same type of samples. This is due in part to the fact that both are relatively new techniques and very few laboratories have both available. The author was therefore limited in the number of examples which demonstrate the complementary nature of the two techniques.

SAMPLE SELECTION

Tantalum Thin Films and Doped (B, P, As) Silicon

There is considerable interest in both tantalum and silicon materials for use in microelectronics. Tantalum nitride (Ta_xN_y) and tantalum oxynitride (TaO_xN_y) are precision resistor materials¹ and can be conveniently trimmed to a desired resistor value by progressive anodization² or by laser trimming.³ Tantalum thin films are also used to fabricate tantalum oxide capacitors.⁴

The importance of silicon in the fabrication of active electronic devices⁵ based on semiconductor properties has been well established. The amount and distribution of dopants such as boron, phosphorus, arsenic, etc., introduced into silicon play a major role in controlling the characteristics of active devices. These dopants can be conveniently introduced into silicon from a chemical source⁶ or by ion implantation,⁷ but the concentration of these dopants are typically below detection by conventional techniques such as the electron microprobe. Electrical methods^{8,9} of obtaining the distribution of the dopants reveal only that fraction of dopant which is electrically active. Electrical profiling methods are also extremely tedious.

SELECTION OF INERT OR REACTIVE PRIMARY ION BOMBARDMENT IN AES AND SIMS PROFILING

Inert argon or xenon are used in AES profiling. Xenon has the advantage of providing higher sputtering rates; and must be used when the distribution of argon in a sample is of interest. Primary ion energies in the range of 1 to 2 KeV are typically used with maximum current densities of 250 $\mu\text{A}/\text{cm}^2$. Sputtering rates in AES profiling are usually in the range of 50-100 $\text{\AA}/\text{min}$. depending on film thickness.

The primary ions must frequently used in SIMS are oxygen, argon, and nitrogen. Oxygen ions are used most often since they produce the highest secondary ion yield for the majority of elements which results in the highest detection sensitivity. Both $^{16}\text{O}^+$ and $^{16}\text{O}^-$ ions can be extracted from the ion source. The advantage of using $^{16}\text{O}^+$ primary ions is that higher sputtering rates are possible, while the use of $^{16}\text{O}^-$ reduces charge buildup when analyzing insulators. The use of reactive ion bombardment has the disadvantage of producing more interfering molecular ion species from the matrix. Argon, on the other hand, does not produce the M_xO_y species but does produce more intense polyatomic M_x species. The principal use for argon bombardment is in analysis for oxygen.

SPUTTERING RATE MEASUREMENTS AND DEPTH RESOLUTION IN AES AND SIMS PROFILING

Since sputtering is used for both AES and SIMS depth profiling, accurate sputtering rate measurements are necessary to relate sputtering time to the depth sputtered. This rate is usually determined by measuring the crater depth and total time elapsed during sputtering. The depth measurement can be made on well polished large single crystal specimens, and most evaporated or sputtered thin films on smooth substrates. Light interferometers¹⁰ or a mechanical stylus device such as a Talystep¹¹ are typically used for this measurement. The accuracy of the depth measurement with a Leitz microscope equipped with a Michelson interferometer is about one-fifth of a fringe ($\lambda/2 = 2700\text{\AA}$) corresponding to $\pm 300\text{\AA}$. The accuracy of multiple beam interferometry is $< 50\text{\AA}$. The accuracy of the Talystep is in the range of 100\AA . When polycrystalline specimens are being analyzed, the crater bottom can often be uneven when sputtering to depths over several thousand angstroms making the light interference method less suitable. The Talystep method is used on these samples, but the error with the Talystep is higher than the light interference methods.

When it is not possible to measure the depth of a crater, it is necessary to have an accurate measurement of the beam current density and knowledge of the sputter yield of the matrix sputtered to obtain the sputtering rate. Data on sputtering yields are available in the literature. However, a large fraction of the bombarded area will be at a lower and varying beam current density than the selected area analyzed; consequently, it is difficult to derive a precise beam current density measurement from primary current measurements. When this problem is encountered, an excellent technique for determining beam current density is to sputter into a reference material. A transparent amorphous material with a high light refractive index such as Ta₂O₅ which develops interference colors in white light is an excellent reference material. The integral light optics available on the Auger¹² or SIMS instruments¹³ can be used to observe the specimen while sputtering. The time when a specific color fringe develops and changes to another color fringe can then be recorded. The uniformity of the beam density over a given area can also be established with these color fringes. This technique compares favorably with the technique described by Guthrie¹⁴ and has the added advantage of providing depth information. The depth scales indicated on the figures of this paper have been obtained by either light interference or the Talystep methods.

Accurate depth profile measurements in both AES and SIMS depend on obtaining a flat bottomed crater and restricting the secondary ions or Auger electrons detected to this flat region which avoids crater wall effects. Under proper operating conditions, the depth resolution possible with AES or SIMS on amorphous samples such as Ta₂O₅ using sputtering has been shown to be 5-10% of the thickness removed.¹⁵ Any variation in sputtering rate, preferential sputtering effects, crystal orientation effects, etc., can lead to non-uniform crater bottoms and hence degradation in depth resolution. The depth resolution possible on polycrystalline samples, where there is a possibility of different sputtering rates at the grain boundaries, has not been established but is believed to be < 20% of the thickness removed.¹⁶

QUANTITATIVE ANALYSIS OF SPUTTERED TANTALUM FILMS INTENTIONALLY DOPED WITH NITROGEN, CARBON AND OXYGEN BY AES AND SIMS

Prior to the development of simultaneous ion sputtering-Auger analysis, quantitative AES by calibration methods had been restricted to submonolayer, uniformly distributed surface deposits prepared and analyzed under ideal vacuum conditions as first described by Weber and Johnson¹⁷ and more recently by Meyer and Vrakking.¹⁸ The in-situ ion sputter-

ing removes contamination such as surface carbon and surface oxides which can attenuate the intensity of low energy (< 500 eV) Auger electrons and prevents the recontamination of the surface by contaminants present in the vacuum chamber such as water vapor and hydrocarbons. There is, however, a surface compositional change due to in-situ ion sputtering. The magnitude of this compositional change (neglecting diffusion effects) for a binary system (AB) will be a function of the bulk concentration (C) ratio and the sputtering yield (S) ratio of the two components.

Therefore, for the Ta-N system

$$\frac{C_S^N}{C_{Ta}^N} = K \frac{I_{Ta}^N}{I_S^N} \quad (3)$$

or the magnitude of the Auger peak height ratio ($\frac{I_{Ta}^N}{I_S^N}$) measured while sputtering is a relative measure of the actual bulk composition of the film which for a homogeneous sample can be accurately measured by techniques such as the electron microprobe,¹⁹ high energy ion backscattering²⁰ or nuclear reactions.²¹ K is a constant related to the sputtering yields and Auger yields of the two components.

The actual steady state surface concentration ratio ($\frac{C_S^N}{C_{Ta}^N}$) could be calculated if the Auger and sputtering yields of both tantalum and nitrogen were accurately known. Calibration of Auger data for quantitative analysis is therefore possible for homogeneous samples of known composition by maintaining the same in-situ ion sputtering conditions on samples with increasing amounts of a given dopant.

The intentional doping was accomplished by adding a varying, but well-controlled, partial pressure of a single reactant or reactant mixture (N₂, O₂, CH₄) to an inert gas such as argon during sputtering from a pure metal cathode. All the films were deposited on glass substrates. The films were optically smooth and flat, which minimized surface roughness effects on the Auger signal intensity and made accurate sputtering rate measurements possible. The depth profiles obtained by both AES and SIMS confirmed that the N, C, and O dopants were homogeneously distributed throughout the films, and it was possible to accurately ($\pm 10\%$) measure the amount of these dopants in the films by

the electron microprobe. This analysis was then used to calibrate the AES measurements for quantitative analysis. Details on sample preparation, instrument settings (accelerating voltage) etc., necessary for the quantitative analysis of light elements such as nitrogen, carbon, and oxygen in tantalum by the electron microprobe have been discussed in the literature.²²

The data²² generated for nitrogen, carbon, and oxygen are shown in Fig. 1 where the log of concentration as determined by electron microprobe measurements is plotted versus the log of the normalized Auger peak heights, N/Ta, O/Ta, C/Ta. The fact that the relationship is not linear is most probably due to changes in the escape depth (d_e)²³ and backscattering correction (r)²⁴ with increasing dopant concentration.

The nitrogen and oxygen data could be expressed by the following equation

$$C_{N,O} = 48.6 \times X^{.65} \text{ and the carbon data by}$$
$$C_C = 43.1 \times X^{.65}$$

where the concentration C is in at % and X is the normalized Auger peak height (e.g., N/Ta). The above equations do not represent the data below 5 at %.¹¹ Normalizing the data to the matrix (Ta) eliminated the effects of inadvertent changes in beam current, electron multiplier gain, etc.

Although Auger peak heights measured while sputtering provide only a relative measure of the actual bulk concentration, SIMS provides a more direct measure of the bulk concentration since the fraction of ionized particles ejected from the sample while sputtering are detected. Anderson and Hinthorne²⁵ have described a quantitative model based on a thermal equilibrium model of the ion emission process and on an internal standard (e.g., composition of matrix), but the general applicability of this model has not been demonstrated. The limitations of any generalized model due to the presence of chemical and orientational effects on secondary ion emission have been discussed by Castaing.²⁶ Calibration of SIMS data by the use of homogeneous samples of known and accurate composition is at present the most reliable method for quantitative SIMS analysis provided such standards are available or easily prepared.^{28,29,30}

The calibration of SIMS for N, C, and O quantitative analysis³¹ in tantalum is complicated by the change in crystallographic structure of the tantalum films due to the

incorporation of these elements into the tantalum which occurs at concentrations above 5 at %. These reactive gases are accommodated into the sputtered tantalum lattice to form interstitial (random or ordered) solid solutions. The coordination (i.e., number of nearest neighbors) of these elements will be different in the β (tetragonal structure) and b.c.c. structure which could affect the secondary ion yield of those elements. This matrix or coordination effect is shown for carbon in Fig. 2. The abrupt change in slope observed for the normalized secondary ion current of $^{12}\text{C}^+$ is believed to be due to a change in the secondary ion yield of carbon due to the crystallographic transitions ($\beta\text{-Ta} + \beta\text{-Ta} + \text{b.c.c.-Ta} \rightarrow \text{b.c.c.-Ta}$) observed by X-ray analysis. This abrupt change is also suggestive of a change in the mechanism of the secondary ion emission of $^{12}\text{C}^+$ from tantalum with an increase in the amount of carbon in the film. The possibility of chemical and matrix effects on ion yields make the calibration of SIMS data more restrictive than that of the AES calibration. The carbon calibration curve shown in Fig. 2 can only be used for tantalum-carbon films which are known to contain only small amounts of oxygen, since the presence of oxygen could change the secondary ion yield of the carbon and the tantalum. The presence of oxygen in the film is easily detected by the use of $^{40}\text{Ar}^+$ or $^{14}\text{N}_2^+$ primary ion bombardment prior to analysis for carbon. Calibration curves were also obtained³¹ for nitrogen and oxygen (not shown in Fig. 2).

QUANTITATIVE ANALYSIS OF DOPED SILICON BY SIMS AND AES

SIMS and AES measurements on phosphorus doped silicon by the technique of ion implantation have shown that ion implantation is a useful means of calibrating AES and SIMS for quantitative analysis.³²

The phosphorus in-depth profile using AES in combination with in-situ ion sputtering is shown in Fig. 3. The Auger data is in good agreement with the LSS³³ prediction of the location and distribution of the implanted phosphorus ions. These measurements indicated that the detectability limit for an in-depth profile analysis of phosphorus in silicon is 5×10^{19} atoms/cm³ by AES. The in-depth AES detectability limit is determined by the analysis time (time constant on lock-in-amplifier) and sputtering rate used for optimum depth resolution.

The bulk AES detectability for phosphorus and boron was determined by measurements obtained on bulk grown samples. The in-depth profile is constant in these samples and a longer analysis time can be used since depth resolution is

not a consideration. The results³⁴ obtained for phosphorus and boron are shown in Fig. 4. The phosphorus data can be represented by

$$C_{\text{Phos}} = 1.9 \times 10^{21} \left(\frac{\text{P}}{\text{Si}}\right)^{1.16} \text{ and the boron data by}$$

$$C_{\text{B}} = 2.7 \times 10^{20} \left(\frac{\text{B}}{\text{Si}}\right)^{1.14}$$

where P/Si is the phosphorus 120 eV Auger peak normalized to the silicon high energy 1619 eV transition and B/Si the boron 180 eV Auger peak normalized to the Si 1619 eV transition.

The SIMS profile obtained by monitoring $^{31}\text{P}^+$ was in poor agreement with both the AES profile and LSS theory due to a mass interference from $^{31}\text{P}^-$ or $^{47}(\text{PO}^-)$.

SIMS measurements on samples implanted to a total phosphorus dose of 3.2×10^{14} atoms/cm² indicated that the in-depth detectability limit for typical operating conditions and background is in the 10^{18} atoms/cm³ range. At the expense of depth resolution, the bulk detectability limit could be improved to $\sim 10^{17}$ atoms/cm³ which is \sim two orders of magnitude better than AES.

The integral of the SIMS in-depth profiles from silicon samples ion implanted with arsenic doses of 1×10^{14} atoms/cm², 1×10^{15} atoms/cm², and 1×10^{16} atoms/cm² at 50 KeV, were found to be nearly proportional to the ion doses.³⁶ The peak concentration at 360Å was in good agreement with the theoretical projected range (324Å). The profiles (not shown) were obtained with primary oxygen ions ($^{16}\text{O}_2^+$) at 14.5 KeV. The AsO⁻ species provided the highest detection sensitivity for arsenic which was found to be in the 2×10^{18} - 3×10^{18} atoms/cm³ range for the operating conditions used. AES in-depth detection sensitivity for As has been estimated to be in the 10^{+20} range.

The bulk detectability limit for arsenic by SIMS has also been determined³⁷ by use of bulk doped silicon. By defining the detectability limit as the point at which the arsenic signal becomes $\approx 2/1$ of the background signal, the detectability limit for a given background can be estimated. Typically, the background count is in the range of 30 c/s to 300 c/s due perhaps to a mass interference from the $^{91}(\text{Si}_2\text{O}_2\text{H}^-)$ complex. For example, for the background count of 184 c/s the arsenic concentration detectability is 1.0×10^{18} ions/cm³. The arsenic concentration detectability at a background count of 30 c/s is $\sim 4.2 \times 10^{17}$ ions/cm³.

Gittins et al³⁸, Crose²⁹ and Hofker et al⁴⁰ have profiled boron in silicon by SIMS. Profile tails have also been observed on boron implanted samples. The reason for the observed profile tails in boron appears to be associated with a "knock on" phenomenon.⁴¹ The SIMS bulk detectability limit for boron in silicon is in the 10^{14} atoms/cm³ range, whereas AES detectability limits are in the 10^{19} atoms/cm³ range.

It is also possible to profile boron and arsenic when both are present³⁷ as is the case when fabricating a high frequency, high gain transistor.⁴² The comparison, achieved by normalizing the profiles to be integrated implanted dose between the calculated boron and arsenic profiles and those of the measured boron and arsenic profiles, is shown in Fig. 4. Fitting the profiles in this manner causes the peak concentration of the arsenic profile to occur at a concentration of $\sim 10^{21}$ ions/cm³, with the distribution falling off into the background at a concentration of $\sim 2 \times 10^{17}$ ions/cm³.

The exponential tail (see Fig. 4) which is observed at a depth of ~ 0.43 μm , however, indicates the measured arsenic concentration to be greater than the boron concentration for all x . This, in fact, cannot be so since a junction (X_{je}) is known to occur at a silicon depth of ~ 0.41 μm . In addition, there appears to be a substantial redistribution of boron in the vicinity of the emitter-base junction (X_{je}), which is illustrated in Fig. 4. The redistribution is substantial and amounts to as much as 40% at the second boron peak. Measurements⁴³ by the nuclear reaction method on silicon doped with boron and arsenic from a chemical source have also indicated a depletion of boron extending over a range of 2000Å to 4000Å in the region of the boron-arsenic junction.

Blanchard⁴⁴ et al and more recently Dobrott et al⁴⁵ have also observed a similar redistribution for boron and arsenic doped silicon by SIMS profiling. This redistribution of boron could be due to both the arsenic implantation and subsequent anneal, and is not believed to be an artifact of the SIMS technique.

CONCLUSIONS

Both AES and SIMS have unique analytical capabilities. The comparison of data obtained by both on the same sample clearly showed that the individual analytical capabilities of each are such that they are extremely complementary. The combined use of both has, in fact, had a synergistic effect on the final characterization achieved compared to

that possible by AES or SIMS analysis alone. In-depth concentration profiles, can be obtained with good depth resolution, i.e., 5-10% of the depth sputtered, in the absence of preferential sputtering effects from grain boundaries, knock-on, redeposition and crater effects. When possible, comparisons of AES and SIMS profiles with profiles obtained by techniques which do not require the use of sputtering, i.e. high energy ion scattering, should be made.

AES at present appears to be the less ambiguous analysis technique for quantitative analysis. However, its detection sensitivity is 1 to .1 at. %, whereas SIMS can detect concentrations two to five orders of magnitude lower depending on secondary ion yield. Consequently, only SIMS can determine concentration distributions at most dopant levels of interest in semiconductor device technology provided the area available for analysis is sufficient.

Reliable quantitative analysis in both SIMS and AES requires the use of calibration standards. Equations relating the various parameters needed to compare standards against an unknown have been established for both AES and SIMS. However, securing suitable standards in SIMS can often be very difficult in complex materials because neighboring impurities and crystal orientation can alter ion yields unpredictably. It has been possible to produce uniform reactively doped tantalum for use as thin film standards. The concentrations of impurities in these films were calibrated using the electron microprobe. Accurate standards can be prepared for semiconductors by using ion implantation techniques.

It is expected that once escape depths, back scattering correction factors, and Auger currents can be conveniently and accurately measured that the quantitative capabilities of AES will approach that possible with the electron microprobe. It will be more difficult to make the SIMS technique as quantitative as the electron microprobe due to the presence of chemical and orientational effects on secondary ion yield and the possibility of mass interference effects. However, high mass resolution SIMS is possible and the use of low energy secondary ion discrimination does minimize molecular and polyatomic interferences. In addition, a controlled oxygen jet on the sample during primary reactive or inert ion bombardment will reduce secondary ion yield variations due to chemical and orientational effects in many, but unfortunately not all cases.

ACKNOWLEDGMENTS

The author acknowledges with pleasure the cooperation

of a number of colleagues, in particular, D. Gerstenberg, J. C. C. Tsai, R. J. Scavuzzo, M. J. Rand, and J. H. Thomas.

REFERENCES

1. R. W. Berry, P. M. Hall, and M. T. Harris, *Thin Film Technology*, Van Nostrand-Reinhold, Princeton, N. Y. (1968) Chapter 7.
2. W. H. Jackson, R. J. Moore, *Proc. Electron Components Conf.*, Washington, D. C., 45 (1965)
3. L. Braun, D. E. Lood, *Proc. IEEE* 54, 1521 (1966)
4. R. W. Berry and D. J. Sloan, *Proc. IRE*, 47, 1070 (1959)
5. A. S. Grove, *Physics and Technology of Semiconductor Devices*, (John Wiley & Sons, Inc., New York, 1976) Chapter 3
6. C. J. Frosch and L. Derick, *J. Electrochem. Soc.* 104, 547 (1957)
7. J. W. Mayer, L. Eriksson, and J. A. Davies, *Ion Implantation in Semiconductors*, Academic Press, New York, 1970
8. R. A. Moline, *J. Appl. Phys.* 42, 3553 (1971)
9. T. Tokuyama, T. Ikeda, and T. Tsuchimoto, *Fourth Microelectronics Congress.*, Munich (Oldenbourg Verlag, Munich, 1970) p. 36
10. O. S. Heavens, G. Hass, and R. E. Thun (eds.), *Physics of Thin Films*, Academic Press, Inc., New York, 1964) Vol. 2, p. 193
11. N. Schwartz and R. Brown, *Trans. 8th AVS Symp. and 2nd International Congr. Vacuum Sci. Technol.*, p. 836 (1961) Pergamon Press, New York
12. Physical Electronics Industries, Inc., Edina Minnesota
13. Applied Research Labs., Sunland, Calif., Cameca Instruments, Elmsford, New York
14. J. W. Guthrie and R. S. Blewer, *Rev. Sci. Instrum.*, 4, 654 (1972)

15. P. W. Palmberg, *J. Vac. Sci. Technol.*, 10, 274 (1973)
16. J. M. Morabito and M. J. Rand, *Thin Sol. Silms* (in press)
17. R. E. Weber and A. L. Johnson, *J. Appl. Phys.* 40, 314 (1969)
18. F. Meyer and J. J. Vrakking, *Sur. Sci.* 33, 271, (1972)
19. J. Philibert, *Modern Analytical Techniques for Metal and Alloys*, Vol. III, Part 2, edited by R. F. Bunshah, Interscience Publishers, New York (1970) pp. 419-531
20. M. A. Nicolet, J. W. Mayer, and I. V. Mitchell, *Science* 177, 841 (1972)
21. G. Amsel and D. Samuel, *Anal. Chem.* 39 1689 (1967)
22. J. M. Morabito, *Thin Sol. Films*, 19, 21 (1973)
23. P. W. Palmberg and T. N. Rhodin, *J. Appl. Phys.* 39, 2425 (1968)
24. T. E. Gallon, *J. Physics D*. Vol. 822 (1972)
25. C. A. Andersen and J. R. Hinthorne, *Anal. Chem.* 45, 1421 (1973)
26. R. Castaing, *Proceed. of 8th Nat'l Conf. on Electron Probe Analysis*, New Orleans, 1A (1973)
27. J. M. Morabito and R. K. Lewis, *Anal. Chem.* 45, 869 (1973)
28. H. W. Werner, *Develop. Appl. Spectroscopy* 7A, 239 (1969)
29. H. W. Werner and H. A. M. DeFrefte, *Sur. Sci.* 35, 458 (1973)
30. A. Benninghoven, *Sur. Sci.* 35, 427 (1973)
31. J. M. Morabito, *Anal. Chem.* 46, 189 (1974)
32. J. M. Morabito and J. C. C. Tsai, *Sur. Sci.* 33, 422 (1972)
33. J. Lindhard, M. Scharff, and H. Schiott, *Mat. Fys. Medd. Dan Vid. Selsk*, 33, 1 (1973)

34. J. H. Thomas and J. M. Morabito, *Sur. Sci.* 41, 629 (1974)
35. G. Dearnaley, M. A. Wilkins, and P. D. Goode, *Second Intern. Conf. on Ion Implantation in Semiconductors*, Eds. I. Ruge and J. Graul, Germany (1971), 439
36. J. C. C. Tsai, J. M. Morabito, and R. K. Lewis, *3rd Intern'l Conf. on Ion Implantation in Semiconductors*, Pergamon Press, New York, (1973) 89-98
37. R. J. Scavuzzo, R. S. Payne, and J. M. Morabito, unpublished Bell Telephone Laboratories data, 1971
38. R. P. Gittins, D. V. Morgan, and G. Dearnaley, *J. Phys. d: Appl. Phys.* 5, 1954 (1972)
39. M. Croset, *Revue Technique Thompson-CSF* 3, 1, 19 (March, 1971)
40. W. K. Hofker, H. W. Werner, and D. P. Oosthoek, and H. A. M. de Grefte, *Rad. Effects*, 17, 83 (1973)
41. F. Schulz, K. Wittmaack, J. Maul, *Rad. Effects*, 18, 211 (1973)
42. B. Fair and G. R. Weber, *J. Appl. Phys.* 44, 273 (1973)
43. J. F. Ziegler, G. W. Cole, J. E. E. Baglin, *Appl. Phys. Lett.* 21, 177 (1972)
44. M. Bonis, B. Blanchard, M. DeBrebisson, N. Hilleret, and J. Monnier, *Electrochem Soc. Meeting*, Miami, Florida
45. R. D. Dobrott, F. N. Schwettmann, and J. L. Prince, *Proceed of 8th Nat'l Electron Probe Analysis*, New Orleans, 10A (1973)

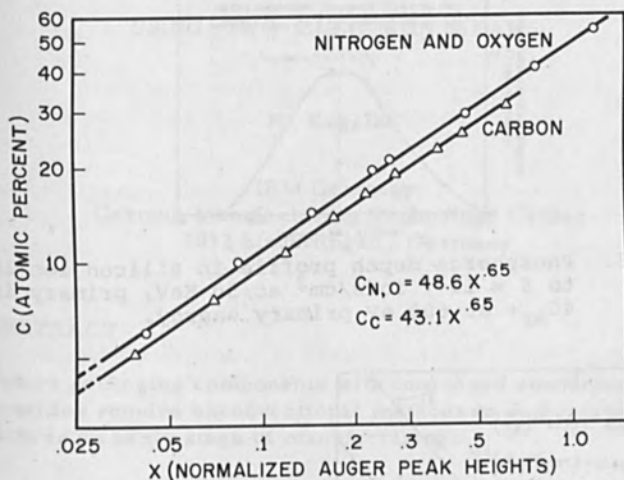


Figure 1. Log C (at %) determined by the electron microprobe vs. log of normalized N, O, C Auger peak height (X) in reactively sputtered tantalum thin films.

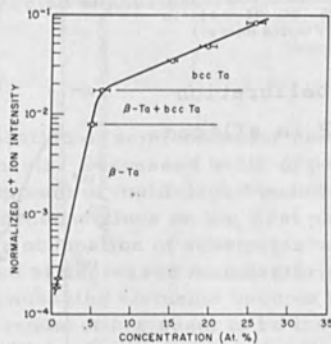


Figure 2. Normalized C^+ ion intensity vs concentration of carbon (at %) in tantalum thin films ($\sim 1000 \text{ \AA}$) reactively sputtered in $(Ar + CH_4)$ mixtures $^{16}O_2^+$ primary ions at 4.5 KeV.

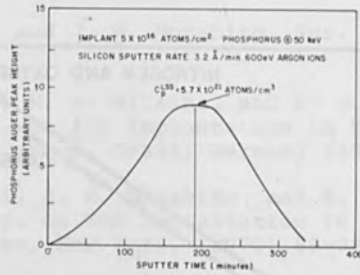


Figure 3. Phosphorus depth profile in silicon ion implanted to 5×10^{16} ions/cm² at 50 KeV, primary ions - 40Ar^+ at 600 eV primary energy.

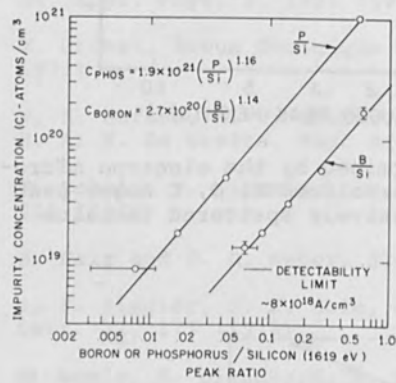


Figure 4. Auger calibration curves for B and P in silicon.

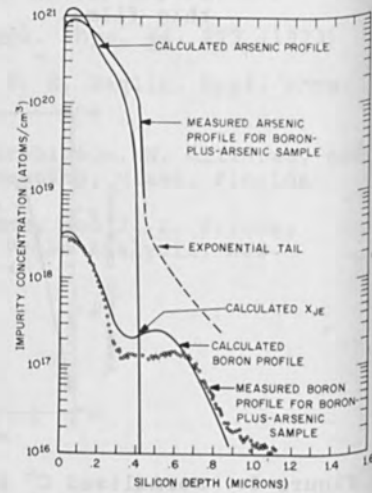


Figure 5. SIMS profiles of arsenic and boron in silicon ion implanted with both boron and arsenic in silicon. Primary ions - $^{16}\text{O}_2^+$ at 14.5 KeV.

CONTACTLESS SHORT/OPEN TEST METHOD
USING TWO ELECTRON BEAMS

H. Engelke

IBM Germany
German Manufacturing Technology Center
7032 Sindelfingen, Germany

ABSTRACT

Future packaging components with increased conductor line densities require unconventional methods to detect line defects in an early stage of manufacturing.

A short/open test method has been developed which employs two low-energy electron beams of between 400 and 1000 eV and an arrangement of collectors on top of the object to be tested. A DC bias field applied between two selected collectors controls the secondary electron flow and the conductor current induced by the two electron beams. The measured collector signal indicates the short/open condition of the tested conductor.

1. INTRODUCTION

The trend to miniaturization of semiconductor components also affected the packaging elements. Decreased width of precisely located conductors and the development of multi-layer techniques permit an increased number of interconnections on the first packaging level and, consequently, a denser occupation of substrates with IC's. Increased signal processing speed at decreased manufacturing cost are the profits of this trend. As packaging elements become more complex functional tests of the interconnections seem to be inevitable. Though very refined mechanical multi-probes have been developed contactless methods are of great interest as the sizes of conductor ends go down below 100 μm .

The application of electron beams for this task has been proposed by

different authors (1). Common to all these methods is that the electron beam is used to charge the conductor to be tested from one end and that continuity is determined by sensing the discharge at the other end. Since conductor capacitances C are in the order of pF, continuity checks must be performed in very short measuring times, otherwise high discrimination resistances R_0 for opens of the order $R_0 \approx t/C$ must be accepted.

Starting with this consideration a test method has been developed which is based on a different test principle and will be reported now.

2. THEORY OF THE TEST METHOD

The fundamental idea of the test process is to apply without physical contact a voltage between the ends of the interconnection to be tested and to measure indirectly the current induced in the conductor. From this measurement the conductor resistance may be roughly determined.

2.1 Controlled Secondary Electron Emission

Contactless application of a voltage to a conductor end may be accomplished by means of controlled secondary emission. This physical effect is well-known in the literature (2) for its applications in electron image storage tubes and is illustrated by Fig. 1. A collector electrode on fixed potential V_c is placed in the neighbourhood of a conductor end which is on floating potential V . A primary electron beam is presumed to have an acceleration voltage that leads to secondary electron emission ratios δ larger than one on the target material. If this electron beam is directed to the conductor end the conductor charges up to a stable equilibrium potential V_{eq} . Towards the end of this charging up an electrostatic field is built up between conductor end and collector which forces "true" secondaries to return to the conductor end and thus equalizes the resulting secondary emission ratio $\delta^{(c)}$ to one. Fig. 1a shows the variation of $\delta^{(c)}$ with the conductor potential V . Trajectories of the secondary electrons are shown in Fig. 1b for the potential differences $V < V_c$, $V \gg V_c$, and $V = V_{eq}$.

The equilibrium potential V_{eq} of the target exceeds the collector potential V_c by a few volts or less. Taking a metallic mask positioned in front of the target surface and assuming a Maxwellian velocity distribution for the "true" secondaries with an average secondary-electron energy, eV, a quantitative calculation for the $\delta^{(c)}$ curve and

and V_{eq} may be carried out (3).

The following relations are obtained :

$$\delta^{(c)} = \begin{cases} \delta \cdot \exp[-(V - V_c) / \bar{V}] & \text{for } V > V_c \\ \delta & \text{for } V \leq V_c \end{cases} \quad (1)$$

$$V_{eq} = V_c + \bar{V} \ln \delta \quad (2)$$

Since the mean energy $e\bar{V}$ of secondaries is almost independent of the energy of primaries and V_{eq} depends only logarithmically on the secondary emission yield, we conclude from equ. (2) that the equilibrium potential V_{eq} of a floating target is rather insensible to variations of target surface conditions and slight variations of the primary energy.

2.2 Principle of Short/Open Test

Fig. 2a shows a typical arrangement for the short/open test of a buried interconnection on floating potential. To that end voltages V_{c1} and V_{c2} are applied to the collector electrodes which are formed in Fig. 2a as metal layers with openings at locations corresponding to the ends of the conductor. By bombarding the conductor ends through the openings these will charge up to the potentials V_1 and V_2 which are close to the respective voltages V_{c1} and V_{c2} . Therefore a stationary current I_{eq} will flow through the conductor. This current may be measured indirectly by making use of the current balance at the conductor ends and sensing one of the collector currents.

The steady state current I_{eq} may be determined by the following set of equations (see Fig. 2a)

$$I_{si} = \delta_i^{(c)} I_{pri} \quad , i = 1, 2 \quad (3)$$

$$I_{pri} - I_{si} + I_i = 0 \quad , i = 1, 2 \quad (4)$$

$$V_1 - V_2 = R I_{eq} \quad (5)$$

$$I_1 + I_2 = 0 \quad (6)$$

$$I_{eq} = I_1 \quad (7)$$

I_{pr1} , I_{si} , I_i being the primary, secondary and emitted electron currents, respectively, and R being the conductor resistance.

A solution of this set of equations may be obtained graphically. Fig. 2b illustrates the special case of equal electron beam currents ($I_{pr1} = I_{pr2} = I_{pr}$). In a first step the currents $I_i = I_{pr} (\delta_i^{(c)} - 1)$ are plotted versus the conductor end potentials V_{ci} . Then a straight line of slope $1/2R$ is drawn which intersects the curves $I_1(V_1)$, $I_2(V_2)$ in points P_1 and P_2 . If the straight line is displaced such that the ordinate segments of P_1 and P_2 are equal, then P_1 and P_2 together represent the solution of the set of equations (3) - (6), i.e.: the steady state currents and voltages at both conductor ends.

2.3 Resistance Discrimination

The sensitivity of the method with respect to the resistance value R of the interconnection may be calculated in analytical form if only low voltages are applied between the collectors, i.e.: if

$$|V_{c1} - V_{c2}| \ll \bar{V}. \quad (8)$$

Under this condition the secondary electron yields $\delta_i^{(c)}$ of equ. (1) may be approximated by the following linearized form:

$$\delta_i^{(c)} = 1 + \ln \delta - \frac{1}{\bar{V}} (V_i - V_{ci}).$$

Using this expression in equations (3) - (7) we obtain for the conductor current:

$$I_{eq} = \frac{V_{c1} - V_{c2}}{R_o + R} \quad (9)$$

$$\text{with } R_o \equiv \bar{V} (1/I_{pr1} + 1/I_{pr2}). \quad (10)$$

R_o can be considered a differentiating or distinguishing limit between continuity and open in the sense that I_{eq} takes half of its maximum value if the conductor resistance R is equal to R_o .

Assuming a value of 5 eV for the mean kinetic energy of slow electrons, $e\bar{V}$, and 100 μ A for both primary currents, from equation (10) one gets a discrimination resistance value R_o of 100 k Ω .

2.4 Electron Beam Conversion

Due to the high complexity of modern packaging components electron beam probes should have good electron-optical properties. Deflection field resolutions of 10^6 to 10^8 points seem to be necessary in many cases. Therefore it is desirable to use acceleration voltages as high as 20 kV. Generation of secondary emission yields δ larger than one, however, require primary electrons of only 200 eV - 2000 eV. To comply with both requirements a beam converter may be integrated into the collector assembly. The beam converter produces an unfocused beam of secondaries that are accelerated to suitable energies (about 500 eV).

Fig. 16 shows three examples. Fig. 16a consists of an additional insulated metallic layer on top of the collector layer. It contains obliquely drilled holes of conductor pad size which prevent primaries from penetration.

To eliminate the need of an alignment of the test mask to the packaging component a mask approach using fine meshes and obliquely incident electron beams has been considered as well (see Fig. 16b).

For beam conversion also thin metal foils seem to be applicable (Fig. 16c). The primary beam is directed to the surface of a thin foil. The secondary electrons released from the rear side are accelerated by an appropriate field between foil and collector. Foil thickness should be of the order of the penetration depth of the primary electrons (about $2 \mu\text{m}$ for Al at 20 keV primary energy).

3. EXPERIMENTS

To investigate the feasibility of the short/open test method a simple set up consisting of two electron sources on high voltage potential with tungsten hairpin cathodes, two electrostatic lenses for focussing and a pair of copper target - collector assemblies were used (see Fig. 4). Two electron beams with beam currents I_{pr} of about $20 \mu\text{A}$ and spot sizes of about 1 mm were generated at acceleration voltages $U_B = -900 \text{ V}$. The ring-shaped collectors were 5.0 mm in diameter and thickness. A further ring-shaped or mesh electrode on top held on negative potential (-100 V) was used to prevent slow secondaries from escaping.

Fig. 5 and 6 show some experimental results together with the corres-

ponding electrical circuits. In Fig. 5 the current I_{eq} induced by the electron beams in a floating conductor is directly measured as a function of the collector voltage difference for various conductor resistance values R . For low voltages a linear characteristic shows up which corresponds with equ. (9) and an estimated value for R_o of $1 M\Omega$. Equ. (10) provides a value R_o of $500 k\Omega$ for $\bar{V} = 5 eV$ and $I_{pr1} = I_{pr2} = 20 \mu A$ this means that experiments and theoretical predictions give the same order of magnitude.

Fig. 6 shows the current-voltage characteristic of a single target-collector assembly. The target was fixed to ground and the screening mesh was biased to $-100 V$.

With respect to short/open testing the most important property of the assembly is the fact that the currents I and I_c are complementary as is seen from the sum curve $I + I_c$. This permits to pick up the short/open information without the need of contact by measuring the collector current I_c .

The curves of Fig. 6 may be interpreted in the following way. The number of electrons absorbed by the assembly is independent of the collector voltage V_c . V_c only controls the partitioning of the currents of "true" secondaries between target and collector. The steps in the current characteristics must therefore be closely related to the energy distribution of "true" secondaries. The regions $I, I_c > 0$ correspond to secondary emission yields $\delta^{(c)} > 1$. Since primary electrons do not strike the collector electrode reflected primaries impinging on the collector must be the reason for a positive collector current.

A beam converting mask of the type shown in Fig. 3a with hole diameters of $500 \mu m$ was tested using a $20 kV$ - electron beam. Applying an acceleration voltage U_B of $900 V$ between the copper layers the current of the secondaries was reduced by a factor of five with respect to the primary current.

An excellent tool to study and optimize the properties of beam converters is a scanning electron microscope. Specimen current pictures of the layers in the deflection mode give a clear and quantitative impression of the flow of free electrons.

The principle of the short/open test method may be easily simulated by the aid of two radio tubes. Here the flow of electrons from cathode to anode replaces an electron beam. Considering the anodes as conductor ends and the control grids as collector electrodes character-

istics very similar to those of Fig. 5 and 6 may be measured under appropriate conditions.

4. CONCLUSION

A short/open test method using two high-energy electron beams and a target mask consisting of beam converter and collector assembly has been presented. The method seems to be superior to other electron beam methods with respect to the following properties: The resistance discrimination capability is about two orders of magnitude lower at comparable primary beams. Also, the method is independent of the electrical properties of the conductor to be tested since a stationary current is induced instead of charging it from one end.

5. REFERENCES

- 1) See for example J.M. Sebeson, J. Vac. Sci. Techn., Vol.10, No. 6, Nov./Dec. 1973
- 2) B. Kazan and M. Knoll, "Electron Image Storage", Academic Press, New York and London, 1968
- 3) M.E. Haine, The intensification of the electron microscope image. J. Phot. Sci. 7, 126-127 (1959)



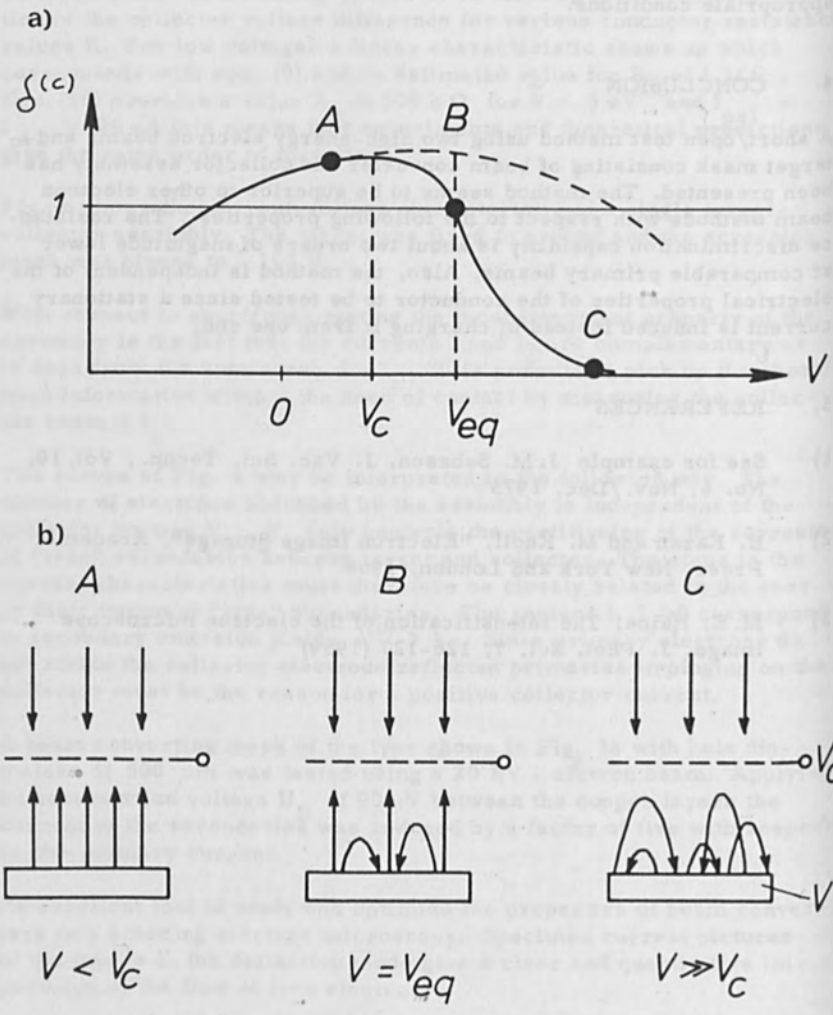


Fig. 1 Collector action on secondary electrons

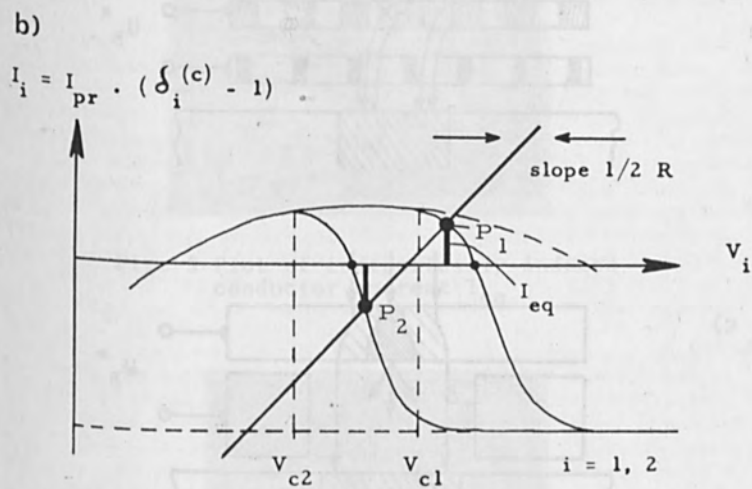
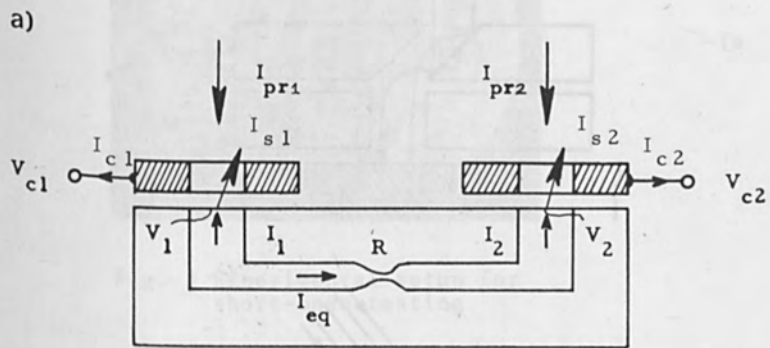


Fig. 2 Test of land - land interconnection

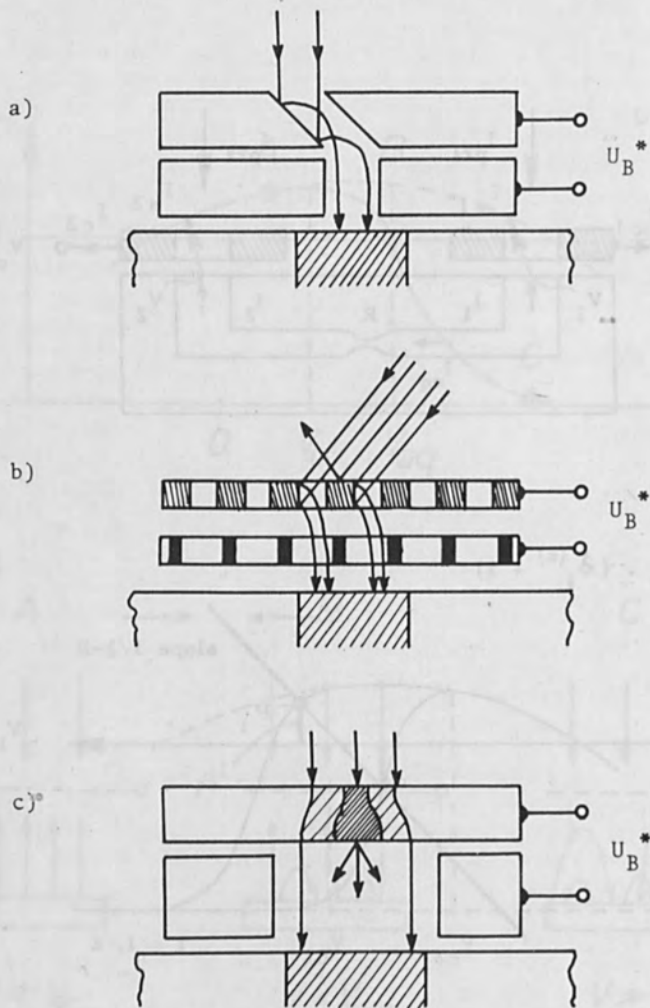


Fig. 3: Electron beam conversion
 a) Hole-mask with oblique holes
 b) Two meshes and obliquely incident beams
 c) Thin metal foil (schematic)

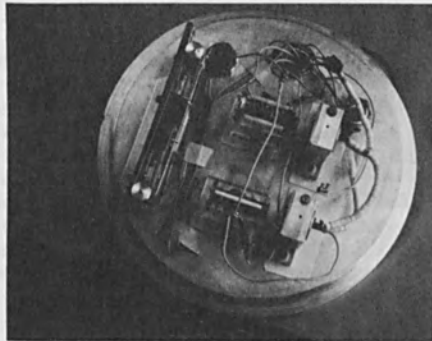


Fig. 4 Experimental setup for short-open testing

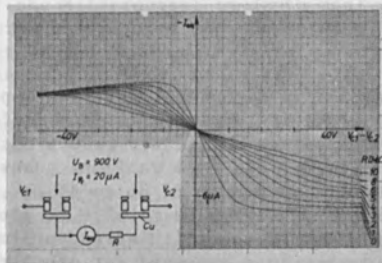


Fig. 5 Plot of contactlessly induced conductor current I_{eq}

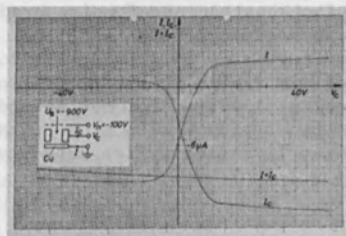


Fig. 6 Current-voltage characteristic of collector-target assembly

A VERSATILE IN-DEPTH ANALYZER

K. Wittmaack, J. Maul and F. Schulz

Gesellschaft für Strahlen- u. Umweltforschung mbH
Physikalisch-Technische Abteilung **
D-8042 Neuherberg
Germany

ABSTRACT

The characteristics of a high sensitivity in-depth analyzer are presented. The system is built in a differentially pumped ultrahigh vacuum version to reduce possible interference with impurities from residual gases. The primary ion beam with an energy of up to 15 keV is supplied by a triode ion gun which is capable to produce beams with constant current density across a 5 mm spot. Either argon or oxygen ions are used for sputtering. Charge neutralization in case of insulating specimens is achieved by means of a low energy electron gun. Small area analysis can be accomplished by use of an additional single lens.

The mass spectrometer consists of an aperture bounded plate capacitor for suppression of noise producing secondaries followed by a quadrupole mass filter. Improved detection sensitivity by up to a factor of 100 in comparison with a previous design is achieved using the energy filter as an acceldecel system for the secondary ions (acceleration voltage ~ 100 V). Optimum operation of the quadrupole analyzer in secondary ion mass spectrometry is discussed.

1. INTRODUCTION

Considerable progress in the technique of in-depth profiling has been achieved during the last years by combining a sputtering secondary ion source with a quadrupole analyzer /1-3/. In addition to the simplicity of their design such in-depth analyzers may provide an improved depth resolution /4/ in comparison with ion microprobes /5/. This is due to the fact that the analyzed area may be larger than 0.1 cm^2 in the former /4/ whereas it is usually between 10^{-4} and 10^{-6} cm^2 in the latter /5/. Improvements, however, still seem to be obtainable, both with respect to the versatility and the sensitivity of quadrupole equipped secondary ion mass spectrometers. In this paper we describe the improved design of such a differential in-depth analyzer (DIDA /6/) and discuss some performance characteristics.

2. EXPERIMENTAL

The lay-out of the differential in-depth analyzer is shown in Fig. 1. The main features of the apparatus concerning the vacuum system and the arrangement of the quadrupole filter with respect to the primary ion gun are the same as reported in ref. /3/.

To increase the current density at the target position, the diameter, D , of extraction electrode (2) and acceleration tube (3) has been enlarged (now $D = 100 \text{ mm}$). Accordingly the ion optical distance of the target from the midplane between the electrodes decreased from $z/D = 17$ to 8. Nevertheless the capability to produce trapezoidal beam profiles /7,8/ is preserved. Slight misalignment ($\sim 1^\circ$) between the axis of the ion gun and the beam transport line usually cannot be avoided in connecting ion gun and analyzer. To keep the beam displacement as small as possible the beam centering plates (7) are mounted close to the immersion lens (2-3) instead of close to the target as in ref./3/. The axis of the target manipulator is now parallel with respect to the beam direction. In comparison with the 45° -arrangement /3/ this facilitates handling of specimens of variable size. Moreover it allows new equipment to be introduced more easily (see below). A suitable hole in the mounting plate of the target holder allows the beam current to be measured correctly with a Faraday cup (13). Different from the previous design /1,3/ the energy filter is insulated from the quadrupole housing (19) so that secondary ions leaving the target can be accelerated before entering the plate capacitor. This improvement was believed /1/ to increase the number of secondaries passing through the entrance opening of the energy filter. Likewise one would expect a gain in the number of secondaries entering the mass filter after deceleration.

Equipment so far not introduced comprises a single lens (10) with deflection plates (11), a low energy electron gun (14), a 75° -target holder (16) and a residual gas analyzer (17). The single lens (10) serves to focus the usually space-charge broadened primary beam /8/.

Using adequate apertures in front of the lens, microprobe beams should be obtainable. Two pairs of deflection plates (11) allow scanning of the beam. The low energy electron gun (14) is used to prevent charge built-up in case of insulating specimens. The geometry of a two-cylinder cathode lens /9/ was chosen for simplicity. An additional 75°-position (16) for a rotatable target holder is introduced for the application of a recently developed method to suppress the growth of sputtering craters in certain target materials /10/. The residual gas analyzer (17) serves to control the pressure of reactant gases in the target chamber.

3. PERFORMANCE CHARACTERISTICS

3.1 Typical vacuum conditions

The DIDA apparatus is pumped differentially to guarantee both a low ultimate residual gas pressure and a low working pressure in the target chamber. Moreover short pump-down times were thought to be a necessary demand because of the need for repeated loading of the target chamber. Combining a 70 l/s turbomolecular pump (Pfeiffer TVS 253) and a 200 l/s (argon: 50 l/s) sputter ion pump (ULTEK D-I) the following vacuum characteristics were obtained in the target chamber for a pressure step with a 3 mm diam aperture (gate valve open):

Residual gas pressure without baking	10^{-9} torr range
Pump-down time to reach the 10^{-7} torr range	< 15 min
Increase in argon partial pressure	
- due to source operation (argon pressure in the source 5×10^{-4} torr /11/)	2×10^{-8} torr
- due to steady state target bombardment with argon ions	3×10^{-9} torr/ μ A

For ions other than those of rare gases the pressure increase is even less pronounced. Therefore one can work routinely at residual gas pressure around and below 10^{-8} torr, the background pressure being mainly determined by the gas load due to sputtering of previously implanted primary ions.

3.2 Maximum current density

It was shown recently /8/ that for ion guns of the type used in this study the current density of a focused beam, drifting distances of more than about 400 mm, is mainly determined by space charge expansion. Accordingly only a certain maximum beam current for each energy can pass through the 3 mm diam aperture in the pressure step. Results obtained for argon ions are shown in Fig. 2. As expected /8/ the maximum beam current increases with increasing acceleration voltage U as $U^{3/2}$. Deviations from the $U^{3/2}$ -law observed below about 2 kV are likely to result from an increasing influence of the energy distribution of the

ions /11/. The probe energy in the DIDA set-up is limited to 15 keV, thus accounting for the fact that profile distortions can be produced in in-depth analysis at energies above about 20 keV /4/.

After having passed through the aperture the beam expands further, achieving a diameter of about 5 mm at the target position. Accordingly the maximum current density at the target is

$$j_{\max}^{\text{Ar}^+} [\mu\text{A}/\text{cm}^2] \approx 1.5 (U [\text{kV}])^{3/2} \quad (1)$$

The sputtering rate obtained at 15 keV for a target of typical atomic density ($5 \times 10^{22} \text{cm}^{-3}$) and a sputtering yield S is thus $S [\text{\AA}/\text{s}]$, i.e. 1 $\text{\AA}/\text{s}$ for $S = 1$. This is a reasonable sputtering rate in most of the in-depth profiling applications. For concentration distributions extending several μm into the bulk, however, increased sputtering rates will be necessary to keep the measuring times within acceptable limits.

In the present set-up current densities in excess of those given by eq. (1) can only be achieved by additional focusing. The three aperture single lens (10) shown in Fig. 1 was designed on the basis of calculated focal properties /12/. The lens has been found to meet present demands very well. The beam size at target position could be reduced by more than a factor of 10. Accordingly the current density increased by at least a factor of 100. To reduce the influence of lens defects on the focused beam profile an additional aperture is introduced in front of the single lens which limits the beam diameter to 1 mm. 100 μm spots were thus obtained on the target. Experiments are under way to determine the minimum spot width achievable with the present set-up.

3.3 Optimum operation of the energy filter

It has already been found in a previous study /1/ that postacceleration of the secondary ions by varying the target potential increases the peak intensity in the mass spectrum. Due to the fact, however, that the transmission of a quadrupole mass filter decreases rapidly for ion energies above about 10 eV /13/ the maximum gain amounted only a factor of three for an aluminium specimen at an optimum target potential $V_t = 20 \text{ V}$.

A much better way to achieve postacceleration without simultaneous reduction in quadrupole transmission is to vary the potential of an electrically insulated energy filter whereas the target is kept at or close to the ground potential. Consequently the secondary ions will propagate at elevated energy only inside the energy filter. When entering the mass filter they are decelerated again to their original energy. The optimum entrance energy may be achieved by adjusting the target potential. From typical energy distributions of secondary ions /14/ one expects V_t^{opt} to be some volts at the most whereas the optimum acceleration potential, V_a , may be expected to be as large as several 100 V.

Either boron doped silicon (p-type, $0.004 \Omega \text{cm}$) or copper were used as target material. Due to the high yield the secondary ion intensities were recorded by direct current measurement using the amplifier electrometer (see Fig. 1). To allow the total transmission of the analyzer section to be calculated (Sect. 4) the ion intensities are converted into counting rates by means of an experimentally determined conversion factor. Finally we mention that all results presented in this paper were obtained for $V_t = 0$. Variation of V_t so as to slightly reduce or increase the ion energy has only little effect ($\sim 10\%$) on the recorded intensity. This means that accurate adjustment of the ion energy to achieve optimum transmission /2/ is not necessary in this case. Obviously ion optical effects are more important.

Results obtained for mass-independent quadrupole transmission (see Sect. 3.5) are presented in Fig. 3. One can see that a very pronounced gain in secondary ion intensity can be obtained with the accel-decel-system. For ions emitted from silicon the maximum yield is achieved at acceleration voltages as low as 100 V, whereas for Cu^+ several hundred volts will be necessary. The gain in intensity is different for the different silicon ion species. The ratio N_d^{max}/N_d^0 is 75, 50 and 20 for Si^+ , Si^{2+} and Si_2^+ , respectively (N_d = number of detected ions, $N_d^0 = N_d(V_a = 0)$). We further see that, at maximum intensity, i.e. at $V_a = 100 \text{ V}$, the relative yields of Si^{2+} and Si_2^+ are 40% and 7%, respectively. Although the quadrupole filter was operated at mass-independent transmission, these data can only be taken as a rough estimate for the ratio of the total ion yields. It should be noted, however, that by use of a magnetic mass analyzer operated at $V_a = 3 \text{ kV}$ /15/ Jurela found exactly the same ratios for sputtering of silicon /16/ with 40 keV argon ions.

Fig. 4 shows the capacitor voltages to be applied for optimum yield at a certain acceleration voltage. Again maximum transmission through the energy filter is obtained by applying the capacitor voltage V_c symmetrically to the capacitor plates, i.e. $|\varphi^-| = \varphi^+$, where $V_c = |\varphi^-| + \varphi^+ / 1$. For an ideal plate capacitor one would expect

$$V_c = (V_i + V_a) 4 yd/l^2, \quad (2)$$

where eV_i is the initial energy of the secondary ions and d , l and y are plate separation, plate length, and position of the entrance opening with respect to the capacitor axis, respectively. From the dimensions of the capacitor one finds $4yd/l^2 = 2.4$, whereas the slope of the straight line through the experimental points in Fig. 4 is 2.6. This indicates that the effective length l_{eff} is slightly smaller than the geometrical length l .

The energy filter may be used to record the energy distribution of the ions transmitted through the mass filter. Using Fig. 4 for energy calibration this can be done by varying the capacitor voltage at a fixed acceleration voltage. In Fig. 5 results are presented for $V_a =$

100 V. A pronounced peak at about 4 eV is obtained. The width (FWHM) of the distribution (8 eV), is significantly smaller than the energy band pass (28 eV), calculated from width and position of the entrance opening of the energy filter. This may be attributed to the strong peaking of the quadrupole transmission below 10 eV. The small hump observed at about 10 eV is likely to be related to the peak in the energy spectrum of the emitted secondary ions. Between 30 and 90 eV the Si^+ -intensity decreases with energy as E^{-3} . This pronounced drop does by no means resemble the energy spectrum $N(E)$ which shows a $1/E$ tail for energies between 10 and 100 eV /16/. Comparing with the observed intensity decrease one can estimate the transmission of the quadrupole to decrease with ion energy as E^{-2} between 30 and 90 eV. However, ion optical effects in the deceleration region may contribute to the measured E^{-3} dependence so that the above estimate should be handled with care.

3.4 Proper adjustment of the low energy electron gun

Charge built-up in case of sputtering insulating specimens with positive ions can be avoided by compensating with a beam of low energy electrons. This may lead to problems if one aims at bombarding the area to be sputtered with accurately equal current densities. We have avoided these difficulties by using a spray type electron gun. The basic idea of such a design is to direct a broad low energy electron beam at the target with a current in excess of that of the ion beam. In such a case possible differences in current density at the ion bombarded area will be compensated immediately since even small electric fields are sufficient to produce the necessary amount of electron deflection.

Proper adjustment of the electron gun can easily be obtained in the present set-up by checking that the optimum acceleration voltage does not vary at constant capacitor voltage when changing from a conductive to an insulating target. An example is shown in Fig. 6. The mass analyzer was first optimized for a silicon target, the acceleration voltage V_a being set at 100 V. The Si^+ -intensity recorded at the chosen quadrupole transmission and beam current was as indicated in Fig. 6. Turning then to a glass target the Si^+ -intensity decreases by more than a factor of 100. The optimum acceleration of 10 V found in that case indicates strong charge built-up.

The Si^+ -intensity recovers very quickly when switching on the electron gun. Spraying with an electron current such that total current detected on the target holder drops to zero, yields near maximum Si^+ -yield. The optimum acceleration voltage V_a^{opt} is still only one third of that for a conductive target. Upon a further increase of the electron current the Si^+ -intensity passes through a pronounced maximum and then decreases gradually. The final value of V_a^{opt} is obtained at quite large electron currents.

The details of Fig. 6 are not easy to interpret. Obviously the space charge of the electron beam has an influence. Nevertheless a very stable secondary ion yield from insulating targets can be obtained by operating a low energy electron spray gun at currents slightly in excess of that of the ion beam.

3.5 Quadrupole transmission and mass resolution

The transmission and the resolution mode of a quadrupole mass analyzer can be varied by simply varying the dc voltage applied to the quadrupole rods. Optimum setting of the dc voltage cannot be deduced from theoretical estimates because ideal entrance conditions as usually assumed in the calculations are by no means achieved in secondary ion mass spectrometry. Therefore one has to determine transmission and resolution experimentally.

The dc voltage, V_{dc} , may be varied with respect to the peak amplitude of the rf voltage, V_{rf} , as follows

$$V_{dc} = \gamma V_{rf} + \delta. \quad (3)$$

Setting $\delta = 0$, the quadrupole used in the DIDA set-up (EN 324-9, Extra Nuclear) is found to operate at or close to constant Δm . As shown in Fig. 7 the transmission is strongly mass-dependent in that case. Beyond a certain limit of Δm the peak intensity does no longer increase. The experimental points are normalized to that value of resolution-independent maximum peak intensity of the mass line. According to Fig. 7 low mass ions such as boron can be detected at both high transmission and reasonable line width ($\Delta m < 0.2$).

The constant Δm mode of operation is suitable in a variety of applications, in particular when mass spectra are recorded. In some cases, however, mass-independent transmission is needed to allow comparison of the yield of different ions. This can be achieved by adjusting δ in Eq. (3). The results shown in Fig. 8 were obtained for $\delta = 6V$. One can see that the decrease in intensity with increasing mass resolution $m/\Delta m$ is the same for the different silicon ion species. Since the normalized intensity is assumed to be closely related to the quadrupole transmission, Fig. 8 indicates that constant transmission can be obtained while operating in the constant $m/\Delta m$ mode.

4. DISCUSSION

The results of Sect. 3.3 are of particular importance since they may be used to estimate possible further improvements with respect to detection sensitivity of the analyzer. A lot of information can be obtained from Fig. 3. The difference in the shape of the curves for Si^+ and Cu^+ is very much likely to result from differences in the

energy distribution of the ions. The distribution for Cu^+ shows a very slowly decreasing tail extending to several hundred eV /14/. For sputtering with 8 keV argon ions the mean energy of the secondary ions emitted from copper at an angle of 45° is 210 eV whereas it is only 75 eV in case of silicon /14/. At 10 keV slightly larger energies have to be expected /14/. Comparison with Fig. 3 shows that an optimum yield can be obtained in the present set-up by applying an acceleration voltage slightly (Si : ~20%) larger than the mean ion energy.

Differences in the yield ratio N_d^{max}/N_d^0 observed for Si^+ , Si^{2+} and Si_2^+ must be attributed to differences in the width and the peak position of the energy spectrum of the ions. For molecular ions of the type M_n^+ the width of the distribution is known to decrease with increasing n, i.e. with increasing number of atoms in the ion /17,18/. In agreement with the experimental result the gain is expected to be less pronounced for Si_2^+ than for Si^+ .

Some information about the energy of the secondary ions can also be obtained from Fig. 4. Extrapolation of the straight line in Fig. 4 to zero capacitor voltage is likely to yield V_i . One finds $V_i = 5\text{V}$ for Si^+ and $V_i = 3\text{V}$ for Cu^+ . This again demonstrates the high transmission of the quadrupole at low ion energies. From the differences in magnitude of the capacitor voltage at zero acceleration voltage we conclude that the energy distribution of Si^+ differs markedly from that of Cu^+ .

For reason of comparison with other in-depth analyzers we calculate the overall transmission T of the system, i.e. the number of ions, N_d , detected after mass analysis, divided by the number of ions of the same mass, N_e , emitted from the target within the same time interval

$$T = N_d/N_e. \quad (4)$$

The ion emission rate \dot{N}_e is simply given by

$$\dot{N}_e = (I/e)K. \quad (5)$$

where I is the primary beam current, e the elementary charge and K the secondary ion yield. Using the experimental data of Fig. 3 and $K(\text{Si}^+) = 10^{-3}/19$ one finds $\dot{N}_e = 4 \times 10^{10}$ ions/s. On the other hand we have from Fig. 3 for Si^+ : $N_d^{\text{max}} = 8 \times 10^5$ ions/s. Therefore

$$T = 2 \times 10^{-5}. \quad (6)$$

At first sight this seems to be a low transmission. It is, however, not much smaller than data reported for ion microprobes with magnetic mass separation of secondary ions accelerated to about 5 keV. Using the CAMECA ion microprobe /5/ Croset /20/ found that only one Si^+ -atom is counted when 10^7 atoms are sputtered. Since the sputtering yield is about 1.5 /21/ we find $T = 10^{-4}$ instead of 1 as deduced by Croset assuming a degree of ionization of only 10^{-7} .

The difference in transmission between the microprobe and the quadrupole equipped analyzer used in this study had been expected to amount much more than a factor of 10 because of the gain to be achieved in analysis at large acceleration energy. Moreover ions emitted from small areas such as in microprobes can be handled much easier ion optically. Obviously a pronounced loss of ions occurs in the analyzer section of ion imaging microprobes.

Further improvements in the transmission of quadrupole equipped secondary ion mass analyzers can be expected because of the fact that the accel-decel system described in this paper represents only a very rigorous design. None of the geometrical dimensions has been optimized so far. Therefore one might expect a gain in transmission by a factor of 10 to be achievable. An upper limit will of course be given by the fact that the quadrupole transmission is strongly peaked at low energies.

5. SUMMARY AND CONCLUSION

The properties of the differential in-depth analyzer (DIDA) are summarized in Table 1. Data so far not discussed in this paper concern detection sensitivity and dynamic range of detector. Due to the increase in transmission (Sect. 3.3) the dynamic range (signal-to-noise ratio) of the analyzer is now in excess of 10^8 not only in favorable cases such as aluminum. The detection sensitivity for boron in silicon has been deduced from range profile measurements /4/ whereas homogeneously doped specimens have been used in case of tin in gallium arsenide. From our measurements it seems to be likely that - provided the transmission of the analyzer can be increased further - quantitative analysis of impurities in the range of 1 ppba and below can only be achieved by use of a mass-analyzed primary ion beam.

REFERENCES

- /1/ K. Wittmaack, J. Maul and F. Schulz, *Int. J. Mass Spectrom. Ion Phys.*, 11 (1973) 23.
- /2/ R. Schubert and J.C. Tracy, *Rev.Sci.Instr.*, 44 (1973) 487.
- /3/ J. Maul, F. Schulz and K. Wittmaack, *Adv.Mass Spectrometry*, VI (1974) 493.
- /4/ F. Schulz, K. Wittmaack and J. Maul, *Rad.Effects*, 18 (1973) 211.
- /5/ A.J. Socha, *Surface Sci.*, 25 (1971) 147.
- /6/ Commercially available from ATOMIKA, Munich, Germany.
- /7/ K. Wittmaack and F. Schulz, *Proc.Fifth Int.Conf.Electron and Ion Beam Science and Technology*, ed. by R. Bakish (The Electrochemical Soc., Princeton 1972), 181.
- /8/ K. Wittmaack, *Nucl.Instr.Meth.*, 119 (1974).
- /9/ V.K. Zworykin, G.A. Morton, E.G. Ramberg, J. Hillier and A.W. Vance, *Electron optics and the electron microscope* (J. Wiley & Sons, New York 1948).

- /10/ H. Yasuda and K. Nagai, Jap.J.Appl.Phys., 11 (1972) 1713.
- /11/ K. Wittmaack and F. Schulz, J.Vac.Sci.Technol., 10 (1973) 1118.
- /12/ F.H. Read, J. Physics E:Sci.Instr., 2 (1969) 679.
- /13/ W. Paul, H.P. Reinhard and U.von Zahn, Z.Physik, 152 (1958) 143.
- /14/ J.F. Hennequin, J. Physique 29 (1968) 655.
- /15/ Z. Jurela and B. Perovic, Canad.J.Phys., 46 (1968) 773.
- /16/ Z. Jurela, Proc.Fourth Yugoslav Symp., Physics fo Ionized Gases, Hereq Novi (1968) 14.
- /17/ G. Staudenmaier, Rad. Effects, 13 (1972) 87.
- /18/ R.F.K. Herzog, W.P.Poschenrieder and F.G.Satkiewicz, Rad.Effects, 18 (1973) 199.
- /19/ J.F. Hennequin, J. Physique, 29 (1968) 957.
- /20/ M. Croset, J. Radioanalyt. Chem., 12 (1972) 69.
- /21/ P. Sigmund, Phys. Rev., 184 (1969) 383.

Table 1. Characteristics of the differential in-depth-analyzer (DIDA)

PRIMARY ION ENERGY	1 - 15 keV
PRIMARY ION CURRENT DENSITY	
homogeneous current density across 5 mm diam	$10^{-10} - 10^{-4} \text{ A/cm}^2$
focused by additional single lens (100 μm spot)	$10^{-10} - 10^{-2} \text{ A/cm}^2$
MASS RANGE	1 - 350
MASS RESOLUTION $M/\Delta M$ (10% quadrupole transmission)	200
IN-DEPTH RESOLUTION (optimum)	< 20 \AA
LATERAL RESOLUTION	
homogeneous current density profile	5 mm
focused beam	< 100 μm
SAMPLE CONSUMED PER COMPLETE SPECTRUM (monolayers)	< 10^{-2}
SPUTTERING RATE	
homogeneous current density profile	$10^{-5} - 10^3 \text{ \AA/s}$
focused beam	$10 - 10^3 \text{ \AA/s}$
DETECTION SENSITIVITY	
B in Si, Sn in GaAs	10 ppba
DYNAMIC RANGE OF DETECTOR	> 10^8
TOTAL TRANSMISSION IN SECONDARY ION ANALYSIS	2×10^{-5}

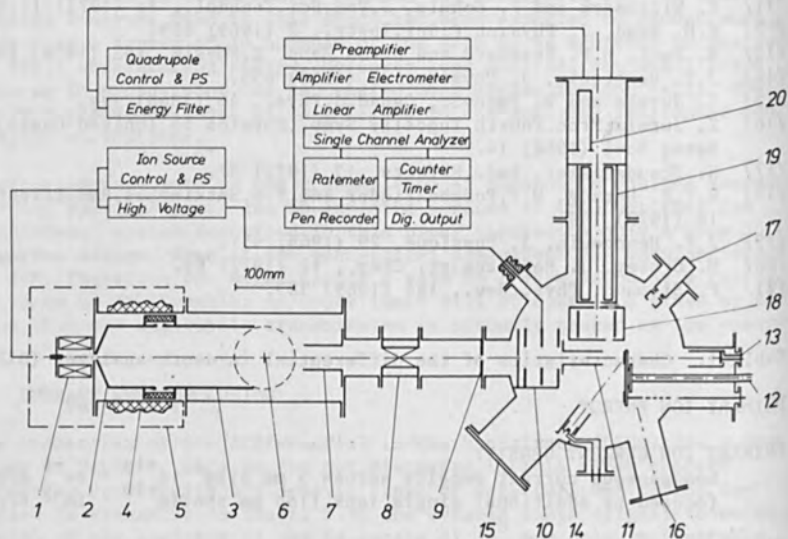


Fig. 1. Construction of the UHV in-depth analyzer

1. Ion source
2. Extraction electrode
3. Acceleration electrode
4. Ceramic insulator
5. Protective cover
6. Turbomolecular pump
7. Beam centering plates
8. Gate valve
9. Pressure step
10. Single lens
11. Deflection plates
12. Target manipulator
13. Faraday cup
14. Electron gun
15. View port
16. 75°-target holder
17. Residual gas analyzer
18. Energy filter
19. Quadrupole mass filter
20. Multiplier

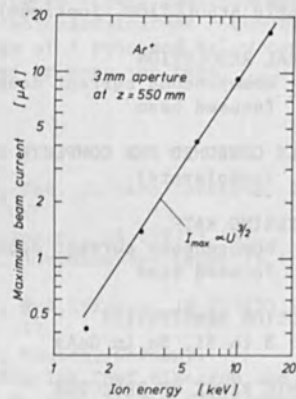


Fig. 2. Maximum beam current versus ion energy for a beam passing through the 3 mm diam pressure step.

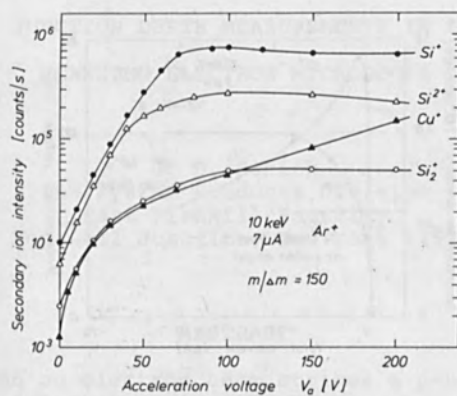


Fig. 3. Detected secondary ion intensity versus acceleration voltage. Mass-independent transmission of the quadrupole analyzer.

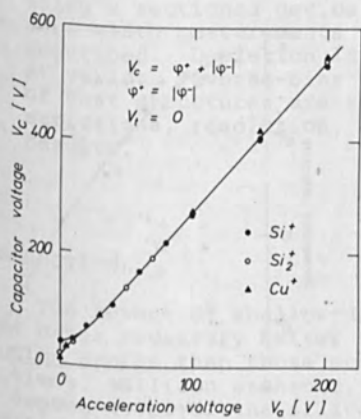


Fig. 4. Capacitor voltage yielding maximum transmission through energy filter at a given acceleration voltage,

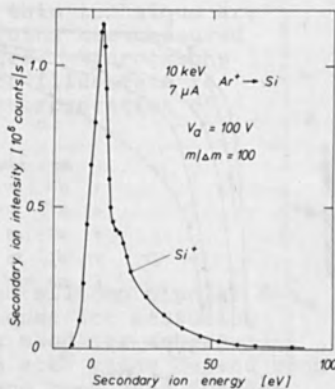


Fig. 5. Energy distribution of mass analyzed Si⁺ ions, the energy filter being operated at V_a = 100 V.

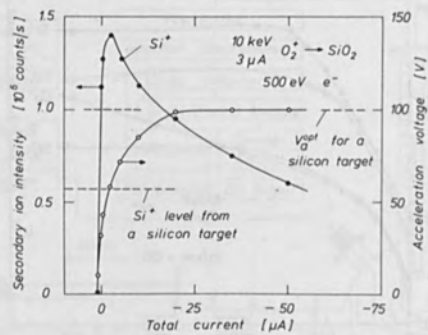


Fig. 6. Si^+ -yield obtained from SiO_2 and optimum acceleration voltage V_a as a function of the total current to the target holder. The data for a silicon target are shown for comparison.

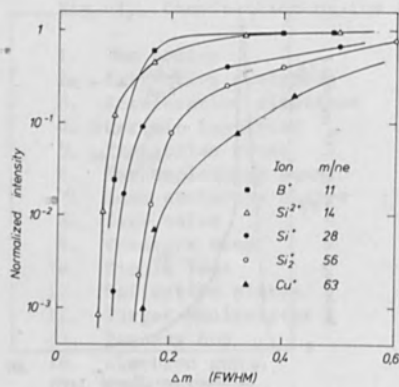


Fig. 7. Normalized ion intensity versus line width Δm .

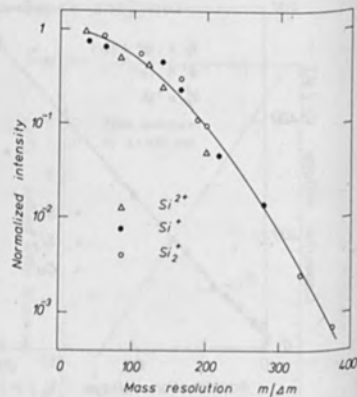


Fig. 8. Normalized ion intensity versus mass resolution $m/\Delta m$.

JUNCTION DEPTH MEASUREMENTS IN A
SCANNING ELECTRON MICROSCOPE

J. D. Schick
IBM System Products Division
East Fishkill Facility
Hopewell Junction, New York 12533

ABSTRACT

When an electron beam strikes a p-n junction, the hole-electron pairs which are generated are swept out by the existing junction potential giving rise to a reverse current. This electron-beam-induced current (EBIC) may be amplified to modulate a CRT in a scanning electron microscope to obtain a micrograph of the junctions in a silicon device either from the surface or in depth using a sectioned device. Junction depth and base width measurements using this technique are described. Depletion layer widths are measured at various reverse-bias voltages. Micrographs of test structures are shown to illustrate restrictions, resolution, and interpretation of results.

INTRODUCTION

The advent of shallow-diffused silicon bipolar devices makes necessary better techniques for measuring junction depths than those commonly used for deeper junctions. Silicon etchants, whose etch rates depend upon the doping level of the silicon, have been used for delineation of metallurgical junctions in silicon devices. Other electrochemical and photochemical methods also provide means of locating areas of different doping levels in silicon.¹ The junction demarcation for all these methods is often not abrupt, and where shallow junctions exist, high-magnification optical microscopy, even for small-angle beveled samples, may not allow accurate measurements.

A method of delineating p-n junctions in silicon devices utilizes beam-induced currents in the scanning electron microscope.² In this technique, the electron beam excites hole-electron pairs in the semiconductor. When this excitation takes place within the depletion region of a junction, the carriers are swept out by the existing junction potential, giving rise to a reverse current.^{3,4} When both sides of a junction are connected to a current amplifier (see Fig. 1), this electron-beam-induced current (EBIC) signal may be used to modulate a CRT whose trace is synchronized with the scanning electron beam. The result is a micrograph of the junctions of the device.

EBIC MEASUREMENTS

Consider an n-p-n transistor sectioned at 90°. The device is mounted on a transistor header and the leads to the emitter, base, and collector of the transistor are wire-bonded to the pins of the header. The header is then inserted into a specially designed stage in the SEM and positioned such that the electron beam is normal to the section face. External electrical connections are then made so that the emitter-base junction is connected across the input of the current amplifier (200 Ω input impedance), and the collector is shorted to the emitter. The resulting micrograph is seen in Fig. 2. Higher magnifications are possible and dimensions may be measured in any direction. A measurement can better be performed if the CRT is operated in the Y-deflection mode rather than brightness modulated, and a line scan is made from top to bottom across the junctions of the device. Two maxima appear at the two junctions, and the distance between the two maxima is easily measured and is the base width of the transistor. It should be kept in mind that the maximum EBIC signal is obtained when the high-resolution beam strikes the true electrical junction, that is, where p=n and where the junction potential is a maximum. The electrical junction may not be at the identical location of the metallurgical junction delineated by chemical means, but the difference will depend on the etchant used and the doping levels in the device. The location of the electrical junction by these EBIC techniques apparently is more relevant to the properties of the transistor.

To measure junction depths of very shallow devices, it is necessary to use low-voltage electron beams. This is because of the penetration of the electron beam into

the silicon and the resulting excitation volume in which the energy of the beam is dissipated. For a 20 kV electron beam, the penetration depth may be as much as 3.5 μm , and the horizontal diameter of the excitation volume would also be of this magnitude. If the diameter of the excitation is 3 μm , the best resolution of EBIC measurements by use of the Y-deflection techniques described would be slightly less than 3 μm at best. However, if a 2 kV electron beam is used, resolutions as small as 500 \AA can be achieved. Thus, base widths of 2000 \AA can be measured to within a few hundred angstroms in the EBIC Y-deflection mode with 90° sectioned devices.

In some cases it is desirable to bevel-section the transistor at some small angle, say 7°. This section can be studied by using EBIC but some restrictions should be noted. Figure 3 shows a diagram of how an electron beam reacts with a beveled device. For a high-voltage electron beam, the penetration depth and the excitation volume are such that the maximum EBIC signal for a junction will occur when the beam is nearer the top of the device than the intersection of the junction with the section. This makes necessary the use of a low-voltage electron beam to minimize this error of measurement. Since the error in locating the junction would be about the same for the emitter-base junction and the base-collector junction, a base-width measurement can be performed on a beveled device.

An EBIC micrograph of a transistor sectioned at 7° is shown in Fig. 4. This micrograph was obtained with the emitter and collector of the transistor across the input of the collector and with a 3 kV electron beam. The emitter-base junction appears dark; the base-collector junction, bright. This is due to the opposing currents induced at the two junctions. The collector-isolation junction appears bright also, and the dark junction on the external side of the isolation is seen but with reduced intensity.

In order to make a base-width measurement as described earlier, a line scan is made across the emitter-base and base-collector junctions from top to bottom of the transistor. This EBIC trace appears in Fig. 5. The distance between these junctions, which is 2600 \AA , can be used as the electrical base width within the restraints mentioned earlier.

ION IMPLANTED GATED DIODE

To demonstrate the application of this technique to measuring shallow junctions, an ion implanted, silicon-gated diode was studied. The interest was to determine the junction depth of the implanted junction and to note differences in the edge of the junction under gate bias conditions.

The device was sectioned at 90° , preserving the contacts to the diffusion, the substrate, and the gate. The device was positioned in the SEM and connected across the input of the current amplifier. A bias supply was also connected to the gate of the device. Figure 6 shows the structure of the device and the Figure 7 shows the resulting EBIC micrographs. They are double exposures to show the relation of the junction to the surface structure, which was obtained in the emission mode at 5 kV.

When a line scan is made across the junction a maximum is seen in the Y-deflection mode of the EBIC CRT. Figure 8 shows this trace for a 3 kV electron beam. For these low-beam voltages, the maximum EBIC has been associated with an electrical p-n junction. The junction depth can be obtained by measuring the distance from zero EBIC signal to the maximum signal. This measurement has been found valid for junction depths of the order of 3000Å. For deeper junctions, a slight etch of the oxide at the section face is necessary to locate the silicon surface in the EBIC trace. For this device, the measurement from zero EBIC signal to the maximum gave a junction depth of 2900Å. This compares favorably with the approximate 2000Å calculated from ion dosage and heat treatment data.

Various voltages were applied to the gate to observe changes in the appearance of the inversion layer. At gate voltages more negative than -0.85V, no inversion channel could be detected. As the gate voltage was decreased to -0.8V, the inversion began to extend from the termination of the junction. At even less negative values, it extended farther, until it reached the isolation at about -0.4V. Any further decrease in the gate voltage brought about a larger signal and an inversion deeper into the silicon.

DEPLETION WIDTH MEASUREMENTS

Another application of the EBIC technique has to do with measurements on Schottky barrier diodes. In these devices, aluminum is contacting lightly n-doped silicon.⁴ This produces a Schottky barrier diode, in which the aluminum side is the anode, and the silicon side is the cathode. (See Fig. 9). The depletion width of this junction depends on the doping level of the silicon.⁵ The depletion width W for a two-sided abrupt junction can be expressed as:

$$W = \sqrt{\frac{2 \epsilon_s}{q} \left(\frac{N_a + N_d}{N_a N_d} \right) \phi}$$

where ϵ_s is the product of the dielectric constant and the permittivity of free space, q is the electronic charge, and ϕ is the built-in voltage of the junction. If the concentration of acceptor states N_a is much greater than the concentration of donor states N_d , this expression becomes:

$$W = \sqrt{\frac{2 \epsilon_s}{q N_d} \phi}$$

This latter expression applies in the case of a step junction, a case similar to the Schottky barrier diodes discussed here. If a reverse bias V_r is applied to this junction, ϕ will be increased by V_r and the depletion width will increase according to:

$$W = \sqrt{\frac{2 \epsilon_s}{q N_d} (\phi + V_r)}$$

In the present work, capacitance measurements were made on a Schottky barrier diode. This resulted in an experimentally determined depletion width W . The diode was then sectioned at 90° , mounted on a header, and positioned in the SEM with the beam normal to the section face. The diode was then connected across the input of the EBIC current amplifier and a power supply was also connected to the diode. The electron beam was scanned across the diode from anode (top) to cathode (bottom) and the EBIC signal was differentiated, producing a maximum and a minimum as seen in Fig. 10. These traces were obtained using a 2 kV electron beam. The distance between these two inflection points was easily measured

and it corresponded to the W obtained earlier. Micrographs were then taken at various reverse bias voltages (Fig. 9) and the distances are shown as a function of reverse bias in Fig. 11 for two different diodes.

If this distance is a measure of the depletion width of the diode, the intercepts give the depletion widths for the two devices shown at zero volts reverse bias. The straight-line plots indicate uniform doping in the two devices, and the two different slopes indicate different doping levels in the two devices. To determine the depletion width in this manner does not require a large-area device for accuracy, which the capacitance measurement does.

SUMMARY

It has been shown that the scanning electron microscope when used in the electron-beam-induced current mode offers a useful technique for measuring junction depth, base width, and depletion layer width. To locate the junction, this measurement utilizes the electrical properties of the silicon, rather than metallurgical properties or chemical and electrochemical reactions. The low beam voltage techniques described allow accurate junction location and information on doping levels for both small and shallow devices.

ACKNOWLEDGEMENT

The author wishes to acknowledge the assistance of Francis G. Trudeau, who operated the scanning electron microscope.

REFERENCES

1. E. A. Efimov and I. G. Erusalimchik, Electrochemistry of Germanium and Silicon, Sigma Press, Washington, D.C. 1963.
2. P. R. Thornton, Scanning Electron Microscopy, Chapman and Hill, Ltd., London, 1968, Chap. 5.

3. A. J. Gonzales, "Electron Beam Induced Current Analysis of Semiconductor Devices", Scanning Electron Microscopy/1974, IIT Res. Inst., Chicago, Illinois, 1974, p. 941.
4. J. D. Schick, "Failure Analysis of Integrated Circuits with SEM Beam Induced Currents", Scanning Electron Microscopy/1974, IIT Res. Inst., Chicago, Ill. 1974 p. 949.
5. A. S. Grove, Physics and Technology of Semiconductor Devices, John Wiley and Sons, Inc., New York, 1967, p. 270.

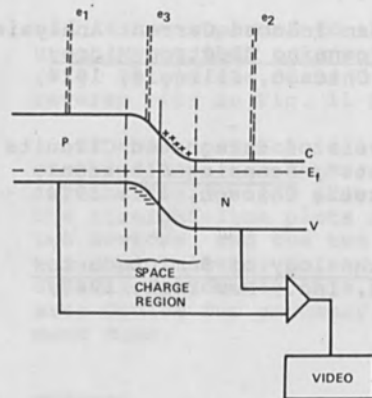


Figure 1. A p-n junction connected for electron-beam-induced current measurements.

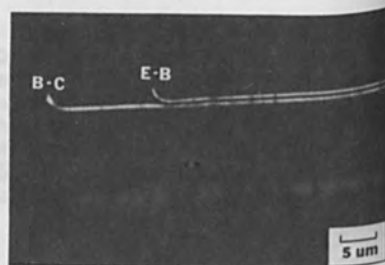


Figure 2. EBIC micrograph showing emitter-base, base-collector, and collector-substrate junctions.

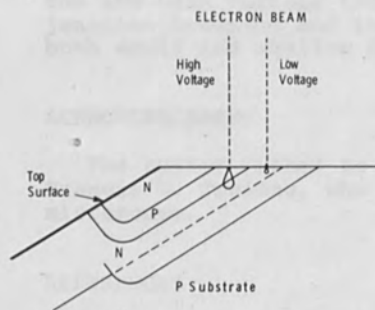


Figure 3. Electron beam impinging on beveled device.

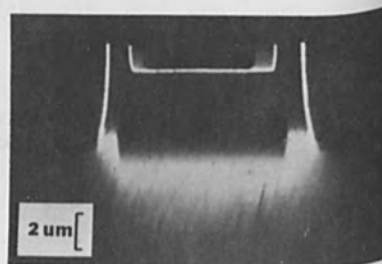


Figure 4. EBIC micrograph of 7° sectioned transistor.

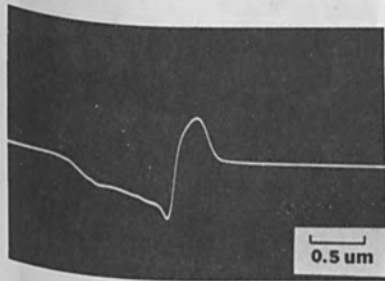


Figure 5. EBIC line scan across junctions of 7° sectioned transistor.

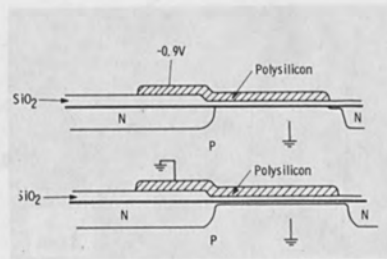
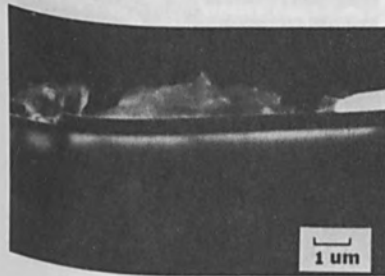


Figure 6. Structure of gated diode.



(a)



(b)

Figure 7. EBIC of gated diode with gate grounded (a) and with -0.9V applied to the gate (b).

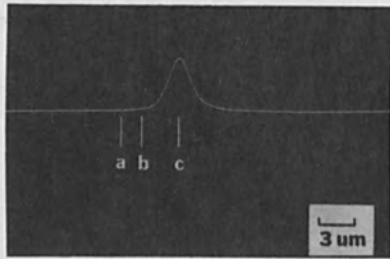


Figure 8. EBIC line scan across ion-implanted junction. The SiO_2 surface is (a), the interface is (b), and the junction is (c).

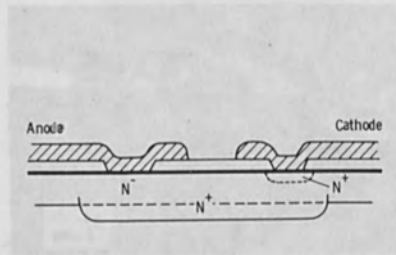


Figure 9. Structure of Schottky-barrier diode.

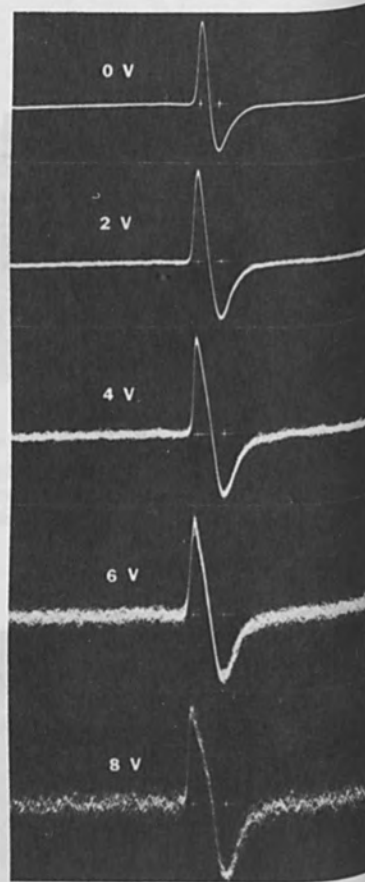


Figure 10. Differentiated EBIC line scan across Schottky-barrier diode at various V_r .

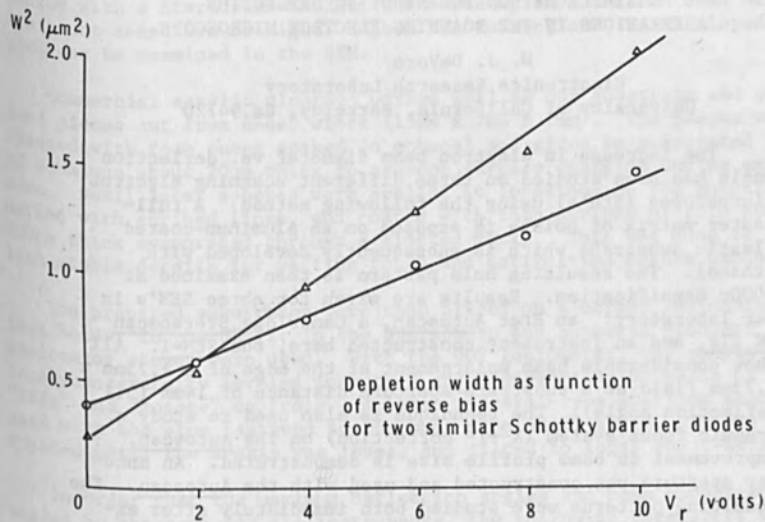


Figure 11. Measured depletion width as a function of applied reverse bias for two Schottky-barrier diodes.

A SIMPLE METHOD FOR STUDYING DEFLECTION
ABERRATIONS IN THE SCANNING ELECTRON MICROSCOPE

W. J. DeVore
Electronics Research Laboratory
University of California, Berkeley, Ca.94720

The increase in electron beam diameter vs. deflection angle has been studied on three different scanning electron microscopes (SEM's) using the following method. A full-raster matrix of points is exposed on an aluminum-coated plastic substrate which is subsequently developed with ethanol. The resulting hole pattern is then examined at 5000x magnification. Results are given for three SEM's in our laboratory: an Etec Autoscan, a Cambridge Stereoscan MK IIa, and an instrument constructed here, the SEM-I. All show considerable beam enlargement at the edge of a 1.75mm x 1.75mm field at a substrate-aperture distance of 14mm (5.1° deflection angle). The technique is also used to study a dynamic focus system (X^2+Y^2 correction) on the Autoscan. Improvement in beam profile size is demonstrated. An annular aperture was constructed and used with the Autoscan. The resulting patterns were studied both immediately after exposure in a light microscope employing Nomarski optics, and after development and coating with gold in the SEM.

Introduction

The scanning electron microscope is being used increasingly for electron-beam fabrication of micro-electronic devices. In order to reduce the number of separate exposures needed to cover an entire wafer, the scan-field should be large. However, mostly due to aberrations of the final lens and the double-deflection system the beam size generally increases as the deflection angle increases, setting a limit on the scan-field area if a given resolution is to be maintained.

This paper describes an experimental study of these aberrations in three SEM's: an Etec Autoscan, a Cambridge Stereoscan Mark 2A, and an instrument built in our laboratory, the SEM-I. The latter has a double-deflection system made up of high quality commercial CRT-type scan coils.¹

Method

Briefly, a matrix of evenly spaced dots is exposed over the scan field on an electron beam sensitive plastic, polymethylmethacrylate (PMM). The PMM is reduced in molecular weight where struck by the beam, and these places can then be dissolved out with a suitable solvent to leave a "profile" of the beam.² The method is a modification of that of K. Amboss and E. D. Wolf³, who used Kodak HRP emulsion as recording

medium with a Stereoscan MK.2A. The advantages of the PMM used here are: not sensitive to light, higher resolution, and the developed samples can be examined in the SEM.

Commercial acrylic plastic⁴ worked well as our substrate and we used pieces cut from sheet stock (15mm x 7mm x 1mm). The pieces were cleaned with foam cubes soaked in ethanol and given an evaporated coat of aluminum about 20nm thick to prevent surface charging during exposure. Small latex spheres were applied at locations on the substrate marked with scribed lines, and coated with thin stripes of gold about 200nm thick evaporated through a slotted mask. This was done to establish stable details for setting focus and astigmatism before exposure.

The prepared substrates were then placed on a normal incidence specimen holder in the SEM-I; in the Stereoscan and Autoscan standard 90° goniometer stages were used. With the 90° goniometer, the sample surface was carefully leveled in both X and Y directions by means of the "tilt" and "rotate" controls. A large pedestal-type specimen stub was used with the stem fastened to the base at a small angle. It was then rotated until the X-axis was level, and tilted to level the Y-axis.

In order that the maximum deflection angles and beam convergence angles be the same for all instruments, the following parameters were used: aperture diameter 200 μm, specimen-aperture distance 14.0mm, (13.8mm in SEM-I) and pattern size 1.75mm x 1.75mm (varied slightly). Simple calculations showed that the specimen-aperture distance gives a better estimate of the beam convergence angle than the "working distance", as is sometimes used. This distance was determined by adding the known aperture-pole piece distance to the pole piece-specimen working distance. "Working distance" meters on the SEM's were found to be in considerable error and had to be recalibrated from the specimen stage micrometers.

An IBM 1800 computer which has been interfaced² to all three SEM's in our laboratory directed the exposure of the dot matrix. A matrix of 33 x 33 dots was used in most of the work. Beam voltage was 20 kV and charge per dot used was 60 pC. Beam currents used in this work ranged from 60 to 240 pA.

After exposure the metal coatings were stripped in a weak solution of NaOH. The substrates were then developed in 95% ethanol for 2-1/2 minutes. After receiving a gold coating of about 50nm thickness, the developed samples were examined in the SEM. The holes were very distinct and appeared stable under observation at $V_{\text{beam}} = 2.5 \text{ kV}$.

Results

Results for the three SEM's are given in Figures 1, 2, and 3 as montages of SEM micrographs from 25 evenly spaced positions over the field.

Both the SEM-I and Stereoscan show signs of beam drift. This apparently caused the pointed tails on the center holes of the SEM-I and the more rounded extra areas on the Stereoscan holes. This could be caused by either a "charging" problem in the column or a drift in the deflection or final lens circuitry. The former seems more likely from other considerations, but an overhaul of the Stereoscan's column brought little change to the patterns. The Autoscan had a similar problem on some exposures; it was cured by changing the column liner tube and final aperture.

The curious difference in the Stereoscan's beam orientation on the X-axis at the two edges of the field and the fact that the beam is considerably larger at the top of the field than the bottom were repeated in 6 different patterns. Neither of these phenomena were observed by Amboss and Wolf³ in their Stereoscan.

The SEM-I certainly has the most regular pattern, the hole orientation changing smoothly around the field. This is an important advantage as any of these instruments would probably need dynamic focus and astigmatism corrections to micro-fabricate circuits over the largest possible field.

The hole sizes indicate that at a substrate-aperture distance of 14mm, (1.75mm x 1.75mm) is an unreasonably large field size for micro-fabrication. Can we do better at larger distances? The increased spherical aberration of the final lens will cause an increase in beam size for the same probe current, with the optimum aperture, but this can be a worthwhile price for a smaller deflection angle and thus smaller deflection aberrations.

To test this notion an exposure was made in the Autoscan at an aperture-substrate distance of 31mm. Final aperture size was 200 μm $Q_D=60$ pC, and field size 1.75mm square, all as before. The results show a tiny increase in the size of the central spot while the outer dots are reduced to about 1/3 the size of those shown in Figure 3. However the dots are slightly bigger than those at the same deflection angle at the shorter aperture-substrate distance.

Discussion

The hole size observed is larger than the beam spot size due to electron scattering in the plastic, a small amount of scattering in the metal film overlaying the plastic, and the finite size of the organic molecules of the plastic. For example, the beam diameter at the center of the field ranged from a few hundred angstroms for the Stereoscan and the Autoscan at the currents used to perhaps 1000 \AA for the SEM-I, yet the developed holes are approximately one micron in diameter. Patterns in thin resist layers on silicon substrates have been fabricated using both the Autoscan and Stereoscan showing better resolution than this.⁶ Hence the patterns shown here should not be used as an estimate of

ultimate resolution in microfabrication, but as an estimate of relative deflection aberrations only.

Determining quantitatively the causes of the observed spots is in general very difficult and will not be attempted in this paper. Several causes of the beam broadening can be listed. One is simple geometrical defocussing due to the increased distance traveled as the beam is deflected. Using the parameters given for the three exposures, it would add 0.8 micron to the central field beam diameter at the corners of the field. The more important effects are off-axis aberrations of the final lens and also aberrations of the double deflection system itself. Analyses on two different double deflection systems^{3,5} came to the conclusion that the latter were the most important in the systems studied, although the former were appreciable. Deflection coma and astigmatism can be caused by non-uniformities in the deflecting fields, deflection by the fringe fields, and in fact astigmatism is inherent in deflecting converging beams by even uniform magnetic fields.

Dynamic Focus

The Etec has a dynamic focus coil on the final lens which can be fed a signal proportional to Y to keep a tilted substrate in focus over the field. Experiments were done to see if this coil could be used to refocus a deflected beam on a level substrate. A signal of the form $k(X^2 + Y^2)$, where X and Y are the beam's displacements from center field, was fed into the dynamic focus coil. A series of exposures was made with differing values of k , evaluated, and then a second series was made with a smaller range of k . An annular aperture (discussed later) was used in the first series so that results could be quickly evaluated in the light microscope. As k was increased, the elliptical spots shrunk and rounded up, then became ellipses again rotated 90° from the original orientations. The result of an exposure with near optimum value of correction (most round spots) is shown in Figure 4, which can be compared to figure 3. Figure 4 shows the central dot, the four corners, and the four mid-edge positions. Since no dynamic astigmatism was applied the spots can only be rounded up, not restored to original center field size. The best value of k varied slightly over the field, for an unknown reason.

Annular Aperture

One technique for the analysis of deflection aberrations is the use of an annular-shaped final aperture and observation of the resulting deformed-ring beam over the scan field³. To investigate the capabilities of the PMM recording medium with this method, an annular aperture was constructed for the Autoscan. It was made by centering a $890 \mu\text{m}$ diameter disk of 1 mil Pt in a $1000 \mu\text{m}$ diameter conventional aperture, and fastening it there with a short piece of 5-mil W wire cemented with silver paint. This produced a $55 \mu\text{m} \pm 10 \mu\text{m}$ annular

slit, broken in two places by the 125 μm support wire.

Exposures were examined both before development in a light microscope using Nomarski optics, and then after development and gold coating in the SEM. The undeveloped pattern was visible on the aluminum surface because the evolution of gas by the exposed PMM causes the metal to bend up. Both methods of observation were useful. The SEM permitted observation at high resolution, but outer rings, which had not enough exposure to develop out completely, could be seen clearly under Nomarski. Figure 5 shows a montage of Nomarski pictures of the outer rings surrounding two SEM micrographs the central spot and one about halfway to the top right corner of the field. Some of the rings double back on themselves, showing the combined effect of astigmatism and coma. One interesting feature of some of the rings is a variation in focus (width) around the ring. A second exposure was made with the ring rotated from the first position. The focussed and unfocussed regions did not rotate, indicating that they are not an artifact introduced by the aperture. This effect could be caused by a coma-type aberration acting on the electrons passing through the slit at slightly different radii.

Conclusions

This paper gives a simple method of studying deflection aberrations in the SEM. Results are given for the three different SEM's in our laboratory under similar operating conditions. The results for the two commercial SEM's are not necessarily typical of that brand; they represent the two instruments we happen to possess.

The method is used to set up and evaluate a dynamic focus scheme on the Autoscan, and also to see the effects of a longer working distance. Solid PMM is also used to study the patterns from an annular aperture, both before and after development to unique advantages.

Acknowledgments

The author wishes to thank Professor T. E. Everhart for suggesting this topic and for advice during the course of this work.

This work was supported by NIH Grant GM17523-04.

References

1. Celco type FY727.
2. R. F. Herzog, J. S. Greeneich, T. E. Everhart, T. Van Duzer, "Computer-Controlled Resist Exposure in the SEM", IEEE Trans. E.D.-19, pp 635-641, May 1972.
3. K. Amboss and E. D. Wolf, "Double-Deflection Aberrations in a SEM," 11th Symp. on Electron, Ion, Laser Beam Tech., pp 195-204, 1971.
4. American Cyanamid Company, Acrylite acrylic sheet.
5. G. Owen and W. C. Nixon, "Aberration Correction for Increased Lines per Field in Scanning Electron Beam Technology," 12th Symp. on Electron, Ion, Laser Beam Tech., in J. Vac. Sci. Technol. 10, pp 983-986, Nov/Dec 1973.
6. N. C. Yew, private communication; E. D. Wolf, private communication.

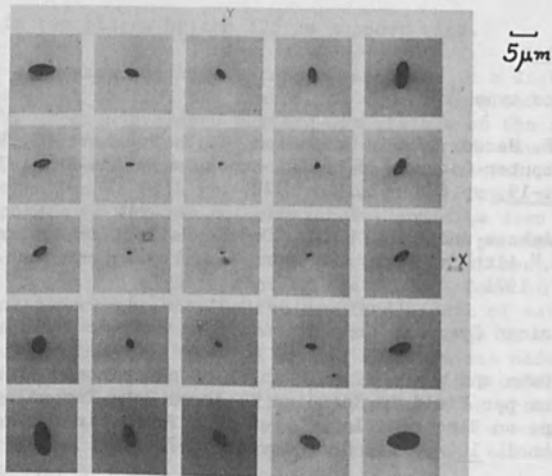


Fig. 1. Pattern from SEM-I. Beam voltage (V_b) = 19.3 kV, Field size (F.S.) = 1.77mm(h) x 1.76mm(v). Substrate-aperture distance ($Z_{s.a.}$) = 13.8mm. Final aperture (d_a) = 200 μ m.

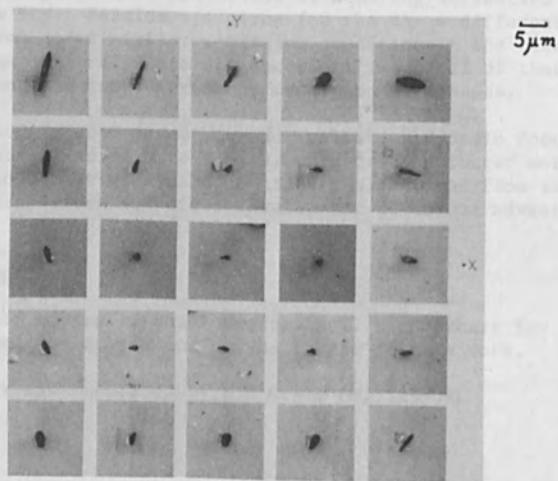


Fig. 2. Pattern from Stereoscan MK2A. V_b = 20.7 kV, F.S. = 1.70mm x 1.74mm, $Z_{s.a.}$ = 14.0mm, d_a = 200 μ m.

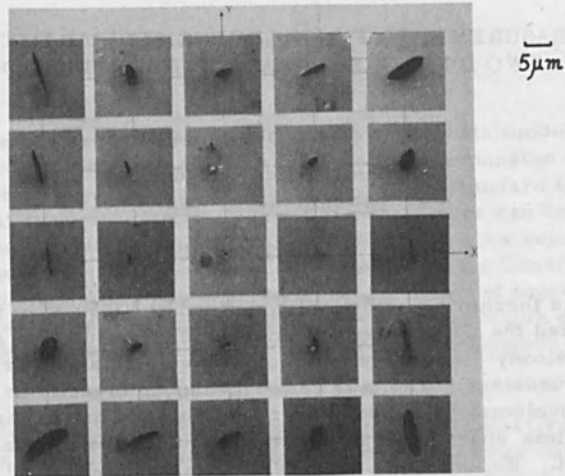


Fig. 3. Pattern from Autoscan. $V_b = 20$ kV, F.S. = 1.76mm x 1.76mm, $Z_{s.a.} = 14.0$ mm, $d_a = 200$ μ m.

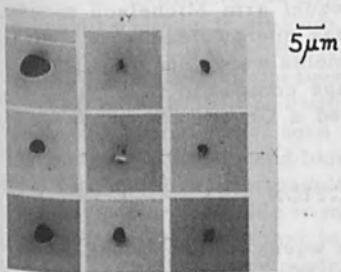


Fig. 4. Autoscan pattern with dynamic focus correction. $V_b = 20$ kV, F.S. = 1.75mm x 1.75mm, $Z_{s.a.} = 14.0$ mm, $d_a = 200$ μ m.

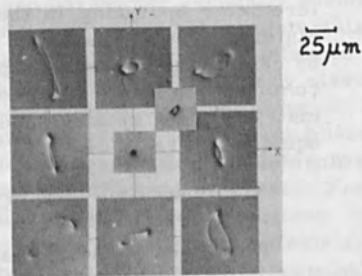


Fig. 5. Autoscan pattern with 1000 μ m O.D. annular aperture. $V_b = 20$ kV, F.S. = 1.75mm x 1.75mm, $Z_{s.a.} = 14.0$ mm.

MEASUREMENT OF THE GRUENEISEN PARAMETER OF
TWO DIMENSIONAL CARBON PHENOLIC (2DCP)*

Robert D. Evans

Ion Physics Corporation
Burlington, Massachusetts 01803

ABSTRACT

The thermodynamic quantity defined by $V(\partial P/\partial E)_V$ is designated the Grueneisen parameter. For solids it is generally a slowly varying function of both volume and energy. The Grueneisen parameter can be measured directly in a quasi-isovolumetric experiment in which material is heated over a time short compared to that required for mechanical relief. Experiments utilized a high energy pulsed electron beam accelerator to produce rapid heating throughout the target volume. Power pulsewidth was about 30 nanoseconds FWHM. Amplitude of the pressure wave resulting from energy deposition in the test material and beam stop was recorded by observing particle velocity with a laser interferometer operating in the unequal arm Michelson mode. Materials were heated to a peak energy density of about 55 calories per gram. Experiments were conducted with a compression molded carbon tape composite in a phenolic matrix. Data obtained indicated a Grueneisen parameter equal to 0.41 ± 0.04 .

INTRODUCTION

Amplitude of thermal shock waves developed under suddenly applied volume heating depends upon the energy dependent equation of state. For solids whose thermodynamic behavior can be described by an equation of state of the Mie-Grueneisen form, thermal pressure is given by the product of energy density and the local slope of the pressure-energy curve in a plane of constant volume. The latter quantity is related to the Grueneisen parameter through the expression

* This work was sponsored by the Defense Nuclear Agency and carried out under contract to the Air Force Weapons Laboratory, U. S. Air Force, Air Force Systems Command, Kirtland Air Force Base, New Mexico 87117.

$$G = \frac{1}{\rho} \left(\frac{\partial P}{\partial E} \right)_V \quad (1)$$

This can be reduced to an equation in the bulk modulus, specific heat at constant volume, density, and bulk expansion coefficient, all of which may be readily determined from standard thermal and mechanical measurements. When these properties can be expressed in a functional form, it is possible to construct a relationship which gives the pressure and energy dependence of the Grueneisen parameter; this approach has been taken by a number of investigators. An excellent review of these efforts has been given by Walsh et al,⁽¹⁾ who applied them to the calculation of Grueneisen parameters for 27 metals.

Sirderhmukh and Rao⁽²⁾ have recently computed Grueneisen constants for a number of Group-V and Group-VI elements using a modification of Slater's method as it was described by Walsh. Barker⁽³⁾ has discussed an extension of earlier methods of calculating the Grueneisen number for polymeric solids and has developed a phenomenological theory based upon a "bundle of tubes" theory.

Calculations of the Grueneisen parameter generally assume a homogeneous isotropic medium, while in practice actual materials of construction do not meet this requirement. In a fiber reinforced polymer both mechanical and thermal properties are distinctly directional, making it difficult to estimate a proper bulk value of the Grueneisen. Furthermore, on a short time scale the separate phases will not be in equilibrium and local acoustic relaxation and interphase energy flow may effect the magnitude of bulk thermal stresses. For these reasons it is desirable to measure the effective Grueneisen parameter directly rather than to compute it for complex materials. Such a measurement can be made using a pulsed electron beam accelerator to provide quasi-isovolumetric heating over a period long enough to allow recording of the inertially clamped thermal stress.

EXPERIMENT DESIGN

Rapid heating at constant volume will produce a thermal stress equal to

$$P = \frac{\rho GE}{2} \quad (2)$$

where P is pressure, ρ is initial density, G the Grueneisen parameter, and E the local energy density. If the heated volume is large compared to the distance which can be traversed by relief waves during the time over which heating takes place, then conditions will be effectively isovolumetric for a brief period. Stresses read during this interval will be characteristic of constant volume heating.

A pulsed electron beam accelerator producing mean electron energies of several megavolts can be used to generate nearly uniform heating over a volume which is an order of magnitude greater than the characteristic relief depth.

Heating pulsewidths are typically 40 nanoseconds for these machines. For fiber reinforced polymers the acoustic velocity is generally near $0.4 \text{ cm}/\mu\text{sec}$. Therefore the depth to which an acoustic wave originating at a free surface can penetrate during the pulse duration is approximately $c\tau = 0.016 \text{ cm}$. For isovolumetric conditions to pertain, it is necessary that target thickness be much greater than this depth, or $x \gg c\tau$. For the experiments reported here, it was demanded that thickness be greater than ten relief depths.

Figure 1 shows a normalized depth-dose profile for an electron beam of 2.6 MeV mean energy heating graphite. The maximum in this curve is a fairly broad one which allows for near uniform heating over a substantial volume. Dose in a target placed between the depths 0.1 and 0.4 gm/cm^2 varies by only ± 7 percent from the average value. This range of depths corresponds to about 15 relief depths for the material tested in the present experiments. Because the target must be thinner than the electron range to guarantee uniform heating, a beam stop is employed to absorb electrons which pass through the target, thus protecting the stress measuring device from beam induced perturbations. The stop material must be able to absorb energy without producing significant thermal stresses itself, otherwise information emanating from the target could be obscured. The stop must also be elastic in the stress range of interest to minimize distortion during transit of the shock from target to stress recording site. Fused silica meets both requirements, having a Grueneisen constant of about 0.04 and a hugoniot yield point in the vicinity of 100 kilobars.^(4, 5)

To read stresses propagated across the beam stop, a displacement interferometer operating in the unequal arm Michelson mode was employed. Interferometry was selected because small stresses are readily resolved and because optical signals are not

modulated by the RF fields accompanying discharge of a high current electron beam, thus noise levels are low. A specularly reflecting surface was provided at the rear of the beam stop by bonding a mirrored fused silica optical flat to it. The flat was made acoustically thick compared to the expected shock pulsewidth to prevent spallation of the mirror prior to completion of the record.

A sketch of the overall target assembly including the target itself, beam stop, and mirrored optical flat is shown in Figure 2.

EXPERIMENTAL SETUP

The Ion Physics FX-35 pulser was employed as the heating source for this work. FX-35 is a 45 ohm coaxial gas capacitor charged by a Van de Graaff generator. The machine stores 2.5 kJ and can produce current pulses whose amplitude is greater than 60 kA in a pulse 40 nsec in width. The accelerator was operated at its maximum rated charging voltage of 4.5 MeV to produce an electron spectrum having a mean energy of about 2.5 MeV. The accelerator is shown in a dimensioned cross sectional view in Figure 3.

Interferometer optics are indicated in Figure 4, which also shows the physical relationship of the elements to the machine. Fringes were projected from the splitter S_2 , where the target and reference beams beat together, to a partially shielded enclosure near the head of the accelerator. This was found to be necessary to limit the transient response of the photodetectors to Bremsstrahlung photons created by electron deceleration. The photo-spike was not eliminated entirely as it provided a convenient fiducial mark for beam arrival at the target.

The interferometer was driven by a Spectra Physics Model 132 He-Ne laser having a CW output of 1 milliwatt. Laser light was passed through the optics indicated in Figure 4 into a dual pulsed photomultiplier assembly manufactured by Systems, Science, and Software Inc. Because the photomultiplier package requires about 5 μ sec to stabilize, triggering of the system was initiated by an external pulse generator as indicated in Figure 5. This trigger pulse was delayed 5 μ sec before commanding machine fire. Sweeps of two Tektronix Type 555 dual beam oscilloscopes were initiated simultaneously with the delivery of the fire signal to the accelerator. Amplification of the 10 V fire signal to the voltage needed to trigger main gap breakdown requires about 0.5 μ sec, therefore the data recording

scopes were swept about 0.5 μ sec ahead of beam emergence with this sequencing arrangement.

Diode voltage and current were recorded for each pulse on a pair of Tektronix 519 traveling wave oscilloscopes triggered internally. Total beam energy was recorded with a graphite calorimeter and depth-dose profiles were measured directly using a stack of 20 10-mil thick graphite foils, each instrumented with a chromel-alumel thermocouple. Spatial uniformity of the beam at the target plane was determined over a series of pulses with graphite calorimeters increasing in diameter from 0.4 inch to 0.75 inch, and it was shown that fluence was constant within 5 percent over this range.

The target material was a graphite cloth reinforced phenolic resin manufactured by Haveg Corporation. The reinforcing material was H. I. Thompson carbon type CCA-1 fabricated per Air Force Specification WS-1119, and the resin was U. S. Polymeric Number 95. Parts were compression molded at 1000 psi under a proprietary curing cycle to give a final product containing 35.6 percent resin by weight and having a specific gravity of 1.50. Specimens were cut for testing in a manner which caused the parallel cloth plies to intercept the surface at an angle of 20 degrees (70 degrees measured from the normal).

RESULTS

Experiments were conducted at a fluence level of 40 cal/cm², corresponding to a peak dose of 54 cal/gm. Interference fringes resulting from mirror motion are shown in the typical oscilloscope photograph of Figure 6. To interpret such records in terms of stress, it is first necessary to deduce mirror velocity. This can be done by differentiation to give

$$u(t) = \frac{\lambda}{2} \dot{F}(t) , \quad (3)$$

where $u(t)$ is the time dependent particle velocity in fused silica at the mirror location, λ the lasing wavelength (632.8 nm for He-Ne), and $\dot{F}(t)$ is the local fringe rate. Stress in the beam stop can then be computed from the linearized hugoniot relation $P = \rho_0 c u$, where ρ_0 is the density of fused silica and c the acoustic velocity. This can be related to stress in the target by accounting for the mismatch in acoustic impedance across the target-to-beam stop interface using linearized transmission theory. When this is done, the

following relationship between target stress and fringe rate is obtained:

$$P_t = \left(\frac{z_{bs} + z_t}{4} \right) \lambda \dot{F} \quad (4)$$

Here z is the acoustic impedance, the product of density and acoustic velocity, and the subscripts t and bs refer to the target and beam stop respectively. Finally, the Grueneisen parameter of the target material can be found by combining (2) and (4) to give

$$G = \left(\frac{z_{bs} + z_t}{2} \right) \left(\frac{\lambda \dot{F}}{\rho_t E} \right) \quad (5)$$

Using $z_{bs} = 1.32 \times 10^6$ gm/cm-sec⁽⁴⁾ and $z_t = 0.57$ gm/cm-sec, (6) this reduces to

$$G = 9.45 \times 10^{-7} \left(\frac{\dot{F}}{E} \right), \quad (6)$$

where E is measured in cal/gm.

Table 1 lists maximum fringing rates which were recorded, gives mirror velocities and reports Grueneisen constants calculated from (5). Cumulative uncertainty in the Grueneisen due to statistical variation in the dose and to limits on the accuracy with which fringe rate can be read is about ± 10 percent. Data obtained at 54 cal/gm indicate a Grueneisen of 0.41.

TABLE 1

Shot Number	Fluence cal/cm ²	Peak Dose cal/gm	Maximum Velocity cm/sec	Maximum Fringing Rate (sec ⁻¹)	2DCP Grueneisen
2020	40	54	788	2.5×10^7	0.43
2041	40	54	725	2.3×10^7	0.40
2076	40	54	725	2.3×10^7	0.40

While the analysis presented above is approximate, it should not be far in error for the small stresses involved. To check this point, the stress history measured on Shot 2021 has been compared with a detailed finite differences computation using the one dimensional elastic-plastic program "PUFF." As can be seen from Figure 7, calculated and measured shock wave profiles are in good agreement for a Grueneisen of 0.4.

CONCLUSION

A pulsed electron beam accelerator has been used to create a condition of quasi-isovolumetric heating in a graphite reinforced polymer matrix. Interferometric recording of the particle motion induced under these conditions has led to the inference of an effective Grueneisen parameter equal to 0.41.

REFERENCES

- (1) Walsh, Rice, McQueen, and Yarger, Phys. Rev. 108, No. 2, Oct. 1957, 196-216.
- (2) Sirdermuckh and Rao, J. Appl. Phys. 44, No. 2, Feb. 1973, 894.
- (3) Barker, J. Appl. Phys. 38, No. 11, Oct. 1967, 4234-4242.
- (4) Wackerle, J. Appl. Phys. 33, No. 3, March 1962, 922-937.
- (5) Barker and Hollenback, J. Appl. Phys. 41, No. 10, Sept. 1970, 4208-4226.
- (6) Micheals et al, AFWL-TR-71-153, Feb. 1973.

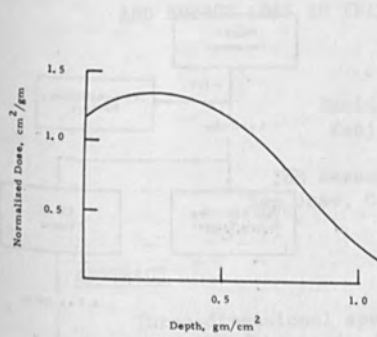


Fig. 1. Measured depth-dose profile for 2.5 MeV mean energy electron beam in graphite.

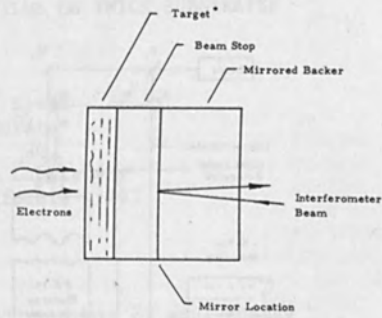


Fig. 2. Sketch of target assembly

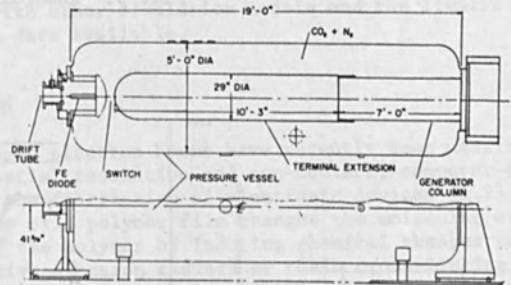


Fig. 3. 4 Megavolt, 2 kilojoule field emission system.

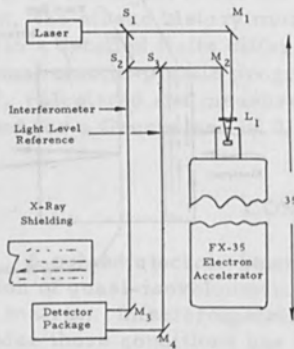


Fig. 4. Optical setup of interferometer. S = Beam splitter; M = first surface mirror; L = focusing lens.

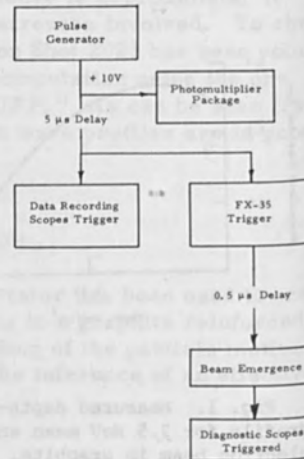


Fig. 5. Recording system timing

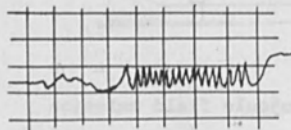


Fig. 6. Oscilloscope trace for typical data shot. Sweep: 200 nsec/cm.

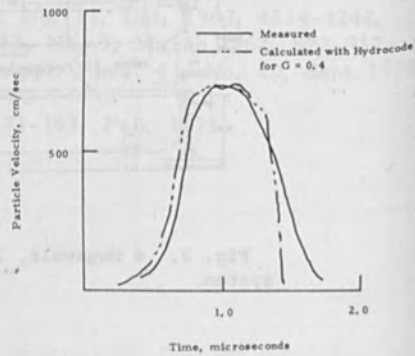


Fig. 7. Comparison of measured and calculated stress histories.

MONTE CARLO SIMULATION OF ELECTRON BEAM SCATTERING
AND ENERGY LOSS IN THIN FILMS ON THICK SUBSTRATES

David F. Kyser
Kenji Murata*

IBM Research Laboratory
San Jose, California 95193

ABSTRACT

Three-dimensional spatial contours of equi-energy density (eV/cm^3) deposited by an electron beam in a thin film-thick substrate configuration have been calculated with Monte Carlo computer methods. These contours are thought to control the geometry of electron beam resist patterns. Point, line and plane source electron beams are simulated. Lateral scattering and energy loss, within the film, of electrons backscattered from the substrate is included. Comparison of this Monte Carlo calculation is made with other simulation models and the limited experimental data available.

I. INTRODUCTION

Highly focused electron beams have recently been utilized to achieve high spatial resolution and non-contact, computer-controlled lithography in the fabrication of electronic devices [1,2]. Electron beam irradiation of a polymer film changes the molecular weight distribution of the polymer by inducing chemical changes such as chain scission (positive electron resist) or chain cross-linking (negative electron resist). Selective solvents are then used to etch the polymer film in patterns which correspond to the electron beam irradiation. The polymer resist remaining can then be used as a mask for subsequent processes such as substrate etchants or film deposition. The spatial contours developed in the polymer film after electron irradiation and chemical etching are dependent upon parameters such as electron beam voltage, film thickness, film components, substrate components, electron dose, and developer characteristics. The shape of the contour is an important process to control and optimize, especially in the "lift-off" process [3].

The spatial contours developed in the polymer film are controlled by two separate processes: (1) Electron scattering and energy deposition within the film and (2) Chemical etching and differential solubility of the irradiated film. There have been a variety of models proposed to simulate electron scattering and energy deposition in

polymer targets. In some early and often-neglected work, Kanaya et al. [4] investigated the effects of electron scattering with a diffusion model, and energy loss with the Thomson-Widdington law. Nosker [5] utilized the Boltzmann transport equation in a multiple-scattering approximation to simulate the spatial distribution of electron density, but not energy density, in film targets. Backscattered electrons were accounted for with a model based on the large-angle approximation of Everhart [6]. Shimizu and Everhart [7] applied a single-scattering Monte Carlo calculation for a thick polymer target to predict contours of equi-energy density with a point source electron beam. Hawryluk and Smith [8] extended the work of Nosker to include energy loss with the Bethe equation for a point source. Greeneich and Van Duzer [9] utilized a plural-scattering model with the Bethe equation, and combined it with Everhart's backscattering model to simulate both point source and line source electron beams on film targets. Finally, in a short note, Saitou [10] applied a single-scattering Monte Carlo calculation to predict contours of equi-energy density in a film target for a point source beam.

The results presented in this paper are based on single-scattering Monte Carlo calculations which were utilized previously by Kyser and Murata [11] for quantitative electron probe microanalysis of thin films on substrates with X-ray fluorescence. Point, line, and plane source electron beams are simulated and the effects of electrons backscattered from the substrate into the film are automatically included within the model. The non-linear (with time) effects of a chemical solvent used to develop the contours, as well as various developer characteristics and processes, are not included in the model. The model assumes that an ideal solvent is available which dissolves all the polymer film irradiated above a threshold energy density E_c (for a positive resist), and this threshold defines the "sensitivity" of the resist. All the calculations are made for polymer films of poly-methylmethacrylate (PMMA) with monomer formula $C_5H_8O_2$. This polymer is a positive electron resist.

II. MONTE CARLO SIMULATION

The single-scattering model used in the present calculations has been described in detail previously [11], and so only a brief outline will be presented here. The model separates angular scattering from energy loss. The Rutherford expression for differential cross-section is utilized to calculate elastic scattering of the incident electrons by the atomic nuclei of the target, and the Bethe expression is utilized to calculate energy loss by the electron between elastic scattering events along the total trajectory. The mean free path Λ of the electron is used as the step length between scattering events and is dependent upon parameters such as atomic number Z and volume density N of the scattering atoms, and energy E of the electron being scattered. The conical angle of scattering θ in the Rutherford expression is chosen with a random number such that there is equal probability for the indefinite integral over space of the fractional

cross-section when integrated from $\theta=0$ to θ . The azimuthal angle of scattering ϕ is chosen with another uniformly distributed random number generated by the digital computer. In a target with more than one kind of atom, another random number is generated to determine which atom is scattering the electron. The probability for scattering by a particular atom is weighted by its fractional cross-section.

The sequence of events for one electron is shown in Fig. 1 for an electron with energy E_0 impinged at the origin and at 90° to the surface of a semi-infinite target. The first scattering event is assumed to occur at the origin. The scattering angles θ_0, ϕ_0 , and the step length Λ_0 is calculated with Monte Carlo techniques as described. Then the spatial position 1 of the next scattering event is determined with respect to 0. Within the step length the electron is assumed to have a constant energy E_0 . The electron energy at point 1 is then calculated by decrementing the energy with respect to its value at point 0 via the Bethe equation for energy loss per unit distance:

$$\frac{dE}{dS} = \frac{-2\pi e^4 \rho N_A}{E} \sum_i \frac{C_i Z_i^2}{A_i} \ln \frac{YE}{J_i}$$

where $\gamma=1.166$, ρ =mass density, N_A =Avagadro's number, E =electron energy, C_i =weight fraction of atom specie i , Z_i =atomic number, A_i =atomic weight, and J_i =mean ionization energy. At point 1 the sequence is repeated using E_1 to calculate θ_1 and Λ_1 . Another random number is used to generate ϕ_1 , and hence the spatial position of point 2 is found. The sequence is repeated continuously until the electron energy has decreased to some arbitrary value $E(\text{min})$ near to, but greater than, J/γ . For $E \leq J/\gamma$ the Bethe equation is not defined. In addition, the step length becomes very small as E approaches J , and the number of steps increases as the energy decreases. Hence, the cutoff energy is also determined by the computer memory allocated for storage of the numerous data. The values for J and $E(\text{min})$ used in the present calculations are listed in Table 1. The values for $E(\text{min})$ were determined by the substrate only since we were interested in low Z film elements on higher Z substrates.

Table 1. Constants used in Monte Carlo calculations.

Atom	Z	J/Z (eV)	E(min) (eV)
H	1	18.700	-
C	6	13.000	-
O	8	11.100	-
Al	13	12.540	200
Si	14	11.000	200
Cu	29	10.820	300
Au	79	10.083	750

If the electron escapes the surface as a backscattered electron, its energy and direction is saved in the computer program. In order to represent the averaging effects of a real electron beam which

contains many incident electrons, a large number of electron trajectories must be simulated. There will not be any identical electron trajectories due to the large number of random numbers and step lengths employed. The statistical accuracy of the calculation increases with increasing number of trajectories n as $(1/n)^{1/2}$. However, the computational time t increases linearly with n so that an economical limit is placed on the number of trajectories which can be simulated. The present calculations were performed on an IBM System/360 Model 195 in our laboratory, and 20,000-50,000 trajectories were simulated for a particular combination of beam voltage, film thickness, and substrate. The CPU time was nominally 1 min./1,000 trajectories.

Figure 2 shows the sequence of events when the target is composed of a thin film with mass thickness ρt (gm/cm²) on top of a thick substrate. As the electron traverses the film-substrate boundary, parameters such as Z and J must be changed in the Rutherford and Bethe equations to describe the appropriate scattering and energy loss. When the electron crosses a boundary, the scattering and energy loss parameters appropriate to the initial point are used to calculate θ , Λ , and ϕ . The parameters appropriate to the terminal point are used in the next calculation.

Figure 3 shows 100 simulated electron trajectories for a 10keV and a 20keV beam incident at the origin for a 0.4 μ m PMMA film on a Si substrate. The point beam is incident along the z -axis at $x=y=0$. The trajectory plots have been projected onto the x - z plane, and hence the y -component is not shown. With an infinitely large number of electrons there will be perfect axial symmetry. This figure qualitatively shows the degree of lateral forward scattering within the film, as well as the degree and position of backscattering. Note that backscattered electrons can emerge at large lateral distances from the axis.

For the case of a point source electron beam and co-axial symmetry around the z -axis, the Monte Carlo computer program divides half-space into concentric donut-shaped volumes with inner radius r_i , outer radius $r_i + \Delta r$, and thickness Δz at depth z_i . The geometric energy loss ΔE (keV) of any and all electrons which traverse this volume is calculated and stored as a histogram of ΔE (total) versus r_i and z_i . The energy density (eV/cm³) per electron is then calculated and plotted as a smooth curve through the midpoints of the histogram. The magnitude of Δr is an input to the program ($\Delta r = \Delta z$) and is typically 0.02-0.10 μ m.

For the case of a line source electron beam and bi-axial symmetry around the y - z plane (i.e. along the x -axis), the Monte Carlo computer program divides half-space into parallelepipeds with cross-sectional dimensions Δx , Δz where $\Delta x = \Delta z$. The parallelepipeds extend from $y = -\infty$ to $+\infty$. The geometric energy loss of any and all electrons which traverse these volumes is stored as a histogram of ΔE (total) versus x_i and z_i . Because of bi-axial symmetry the ΔE calculated for

parallelepipeds with the same values of $|x_1|$ and $|z_1|$ can be added together to enhance the statistical accuracy. Because the volume of each parallelepiped is infinite, the energy density must be expressed as an areal density ($\text{eV}/\text{coul}\cdot\text{cm}^2$). The areal units originate from $(\Delta x)(\Delta y)$ and the coulomb units originate from the number of electrons simulated, accounting for symmetry. Since the units of a line source electron beam are expressed as q_ℓ (coul/cm), the volume energy density (eV/cm^3) is easily obtained by multiplying the areal density ($\text{eV}/\text{coul}\cdot\text{cm}^2$) by q_ℓ (coul/cm). However, it is more convenient to plot the energy density with areal density units in order to normalize for various values of q_ℓ .

For the case of a plane source electron beam with uni-axial symmetry, the Monte Carlo computer program divides half-space into infinite slabs of thickness Δz at depth z_1 . The computer program is identical to the point source case except that now all the energy deposited into concentric donuts with the same value of z_1 are summed together. This is equivalent to lateral integration over planes at constant depth z_1 , and is allowed because a plane source is simply a uniform lateral distribution of point sources. Because the volume of each slab is infinite, the energy density must be expressed as a linear density (eV/cm) per electron (or per coulomb). Since the units of a plane source are expressed as Q (coul/cm^2), the volume energy density (eV/cm^3) is obtained by multiplying the linear density (eV/cm) by Q (coul/cm^2). Again it is more convenient to plot the energy density with linear density units to normalize for different values of Q .

In the following results, only ideal point, line, and plane source electron beams have been simulated to investigate the limiting cases on spatial resolution. Laterally distributed or periodically distributed beams can be simulated by superposition, and these will be calculated in the future.

III. MONTE CARLO RESULTS

A. Spatial Profiles of Energy Deposition

Figure 4 shows the Monte Carlo results for a point source 20keV beam on $0.4\mu\text{m}$ PMMA with an Al substrate. For this calculation 20,000 electron trajectories were simulated. The radial distribution of energy density is shown for two specific values of depth below the surface, namely $0.1\mu\text{m}$ and $0.40\mu\text{m}$ (film-substrate interface). Also shown for comparison are curves published in references [8] and [9] for similar conditions. Reference [8] actually calculated for a Gaussian beam diameter of 250 Å and considered only forward scattering in a thick target for these particular curves. The Monte Carlo results are consistently higher than the other models for $r=0$. In practice, the point source case is not very interesting compared to the other cases. However, it does form the basis for the plane source as described previously.

Figure 5 shows the Monte Carlo results for a line source 20keV beam on 0.4 μ m PMMA with a Si substrate. For this calculation 50,000 electron trajectories were simulated. Also shown for comparison are curves published in reference [9] with an Al substrate. Again, the Monte Carlo calculation yields a higher energy density on axis than reference [9], but the curves then cross and agree better at larger distances laterally. The leveling of the curves at large lateral distances is due to electrons backscattered from the substrate.

Figures 6a,b,c show the Monte Carlo results for a plane source beam of 10, 15, and 20keV on 0.8 μ m PMMA with three different substrates, and also for thick PMMA. For these calculations 20,000 electron trajectories were simulated with a point source, and the data was integrated laterally over slabs of thickness Δz at the same depth z_1 as described previously. For the film curves the data has been plotted only to the film-substrate interface, since the profile within the substrate is not of interest. Note the significant quantitative effect on the magnitude of the energy density profile when PMMA films are put on different substrates, as well as the pronounced change in the shape of the profile at lower beam voltages, when compared to thick PMMA. These effects are due to electrons backscattered from the substrate. The non-linear (with depth) profile of energy deposition will result in a non-linear (with depth) profile of molecular weight distribution in the PMMA film, and hence a non-linear (with depth) etch rate of the film for a particular solvent. Non-linear etch rates for PMMA films on oxidized Si have been experimentally observed by Ting [12] at 15 keV and were interpreted with an empirical model for energy deposition profile proposed by Hoff and Everhart [13] for thick targets. However for general application to other substrates, beam voltage, and film thicknesses, the Monte Carlo model is expected to be more accurate since it accounts for electrons backscattered from the substrate. The change in the apparent sensitivity of a negative electron resist film with different substrates has been experimentally observed by Saitou, Munakata, and Honda [14] at 20keV. They found that the backscattered electron contribution could be accounted for by multiplying the incident electron areal density Q (coul/cm²) by $(1+\eta)$ where η =backscatter yield of substrate. This approximation is better at higher beam voltages than at lower voltages, as shown in Fig. 6. This is because the shape does not change at the higher voltages.

Figures 7a,b,c show the Monte Carlo results for a plane source beam of 15, 20 and 25keV on 1.6 μ m PMMA with three different substrates, and also for thick PMMA. Again note the significant quantitative effect on the magnitude and shape of the energy density profile, especially at 15keV, when compared to thick PMMA.

Figure 8 shows the efficiency of energy deposition by an electron beam into PMMA films. Curves such as those shown in Fig. 6 and Fig. 7 have been integrated with depth z to the film thickness, and then this energy normalized with the total beam energy incident on the

target. As expected qualitatively, the efficiency increases with decreasing beam voltage and constant film thickness, and also increases with increasing substrate atomic number and constant beam voltage. Again the latter effect is due to electrons backscattered from the substrate.

B. Equi-Energy Density Contours With Line Sources

Figure 9 shows the Monte Carlo results for equi-energy density contours of $1.1 \times 10^{22} \text{ eV/cm}^3$ in both thick PMMA and a $0.4 \mu\text{m}$ PMMA film on Si generated by a line source beam of 10 keV with $q_0 = 1 \times 10^{-8} \text{ coul/cm}$. These contours are calculated by smoothly connecting together those parallelepiped areas (Δx) (Δy) which contain the same energy deposited. This particular value of energy density was followed in order to match with experimental data to be discussed. The contours labeled 0.3, 0.7, 1, and $2q_0$ show the movement of that equi-energy density contour with different values of line source. Note that in the case of a PMMA film on Si, the contours are significantly broader with large values of q_0 when compared to thick PMMA. The contours can also represent relative values of energy density when q_0 is constant. For example with $q_0 = 1 \times 10^{-8} \text{ coul/cm}$, the contour labeled $0.3q_0$ would represent an energy density of $(1.1/0.3) \times 10^{22} \text{ eV/cm}^3$. Note that the higher energy density contours have less lateral spread, as expected.

Figure 10 shows a comparison of the Monte Carlo results with the experimental data of Wolf et al. [15] for thick PMMA and 10keV. The Monte Carlo calculations were arbitrarily matched to the experimental contour for $q_0 = 0.3 \times 10^{-8} \text{ coul/cm}$ at $x=0$, i.e. on-axis. This was achieved with a contour of $E_c = 1.1 \times 10^{22} \text{ eV/cm}^3$, and this same contour value was then calculated for the remaining values of 0.7, 1, and $2q_0$. The experimental contours are observed with scanning electron microscopy after etching and cleaving the sample in cross-section. The agreement between theory and experiment shown in Fig. 10 is generally good, in spite of the neglect in the theory of "developer effects." The most obvious discrepancy occurs at the surface where the experiment shows a significant width for the contours and the theory predicts a small width. As proposed previously [9], the large width of the experimental contours at the surface may be due to (a) surface tension in the film after irradiation or (b) finite etching rate of the polymer in regions where $E < E_c$.

Figure 11 shows a comparison of the Monte Carlo results with the experimental data of Wolf et al. [15] for $0.4 \mu\text{m}$ PMMA films on oxidized Si. The Monte Carlo calculations were done for a Si substrate, since the oxide thickness was not specified. The theoretical Monte Carlo contours are for $E_c = 1.1 \times 10^{22} \text{ eV/cm}^3$. Reference [9] proposed a value of $E_c = 6.8 \times 10^{21} \text{ eV/cm}^3$ for the "sensitivity" of the polymer film by matching to the same experimental data. These two values are surprisingly close in spite of the major differences in the simulation models and matching procedures. The Monte Carlo and experimental results both show a maximum in the width of the contours with

increasing beam voltage, and then a continuous narrowing of the width at high voltages. However, the large width observed at the film surface is not predicted by the Monte Carlo model, and may be due to the effects discussed previously.

C. Line Width Calculations

Figures 12a,b show Monte Carlo results for a line source 25keV beam, and Figures 12c,d for a 15keV beam, with $0.8\mu\text{m}$ PMMA on substrates of Si or Au. The lateral profiles are shown for various depths z_0 below the film surface. The leveling of the profiles at large lateral distances from the beam axis ($x=0$) is due to electrons backscattered from the substrate. Before these profiles can be used to predict a "line width," some definition for line width must be stated. Reference [9] chose to define line width as the width of the contour with $E_c = 6.8 \times 10^{21}$ eV/cm³ at the depth $z_0 = 0.1\mu\text{m}$ for a $0.4\mu\text{m}$ thick PMMA film. This definition was chosen by observing that the experimental contours of Wolf et al. [15] showed a minimum width at that depth. In the present work we were interested in thicker films and so for illustrative purposes we have chosen the "line width" to be the width of the contour with $E_c = 1 \times 10^{22}$ eV/cm³ at the depth $z_0 = 0.2\mu\text{m}$ for a $0.8\mu\text{m}$ thick PMMA film. The curves in Fig. 12a,b,c,d can then be used to generate the curves shown in Fig. 13. The line width is also defined as edge-to-edge distance, which is twice the distance from the plane of symmetry.

Figure 13 shows that the line width increases with increasing atomic number of the substrate for constant q_ℓ and beam voltage, but decreases with increasing beam voltage for constant q_ℓ and substrate. Figure 13 also shows the effect of changes in sensitivity E_c on line width. The curves shift laterally in a linear relation with E_c since for a given point in the film $\Delta E \propto q_\ell$. The line width is determined primarily by the forward-scattered electrons at small values of q_ℓ , and primarily by the back-scattered electrons at large values of q_ℓ . Figure 13 also shows the minimum values of q_ℓ required to irradiate particular points in the polymer film above the threshold E_c . At the film-substrate interface ($z=0.8\mu\text{m}$) and on-axis ($x=0$), the threshold occurs for $q_\ell = 2.5 \times 10^{-9}$ coul/cm. At the interface but off axis ($x=0.5\mu\text{m}$), the threshold occurs for $q_\ell = 10^{-7}$ coul/cm for a 25keV beam and a Si substrate.

Experimental confirmation of the effect of electrons backscattered from the substrate on line width has been presented by Sedgwick, Broers, and Agule [16]. They demonstrated that the line width could be decreased by a factor of 2 with elimination of the thick Si substrate in electron beam lithography, utilizing a 25keV beam with $q_\ell = 1.2 \times 10^{-10}$ coul/cm and PMMA. A quantitative comparison with the Monte Carlo calculations cannot be made because the film thickness and sensitivity were not specified.

IV. DISCUSSION

The Monte Carlo simulation of electron scattering and energy loss presented here is a very powerful technique for investigation of discontinuous targets such as thin films on thick substrates. The model was previously shown to be accurate for quantitative analysis of thin films with X-ray fluorescence in the electron microprobe [11], and similar accuracy is expected to apply in the present application to electron beam lithography. However, there is a need for more systematic experimental work such as that of Wolf et al. [15] to confirm the accuracy of the Monte Carlo model over wide ranges in parameters such as film thickness, beam voltage, and substrate atomic number.

The Monte Carlo model has several practical disadvantages such as (a) large computer required for the single-scattering model and (b) results originate in histogram form instead of analytical form like other models [8,9]. However, these are overcome by the simplicity of the physical model, as well as the potential accuracy of the model due to the fact that forward scattering and backscattering are contained in the same model.

The use of areal charge density Q (coul/cm^2) is only valid as a parameter to describe electron resist "sensitivity" in the case of a plane source. In general, the more useful parameter to characterize sensitivity is threshold energy density E_c (eV/cm^3), especially for point or line source electron beam irradiation. For highly focused beams it is difficult to determine the incident areal density Q , and once the beam enters the target it will be scattered laterally and the areal density will not be uniform. In addition, the contribution of electrons backscattered from the substrate is not included in Q . The use of E_c as a sensitivity parameter normalizes any dependence on experimental variables such as beam voltage, film thickness, and substrate atomic number.

The significant contribution to total energy deposition by electrons backscattered from the substrate can be qualitatively understood by separation into two effects, (a) backscatter electron yield with atomic number and incidence angle, and (b) energy loss rate with energy. The backscatter electron yield is a strong function of atomic number [17], and is approximately $Z/100$ for $Z < 40$ and 90° incidence. The yield η is not sensitive to beam voltage, but increases with increasing angle of incidence from normal (90°). Electrons which have been scattered laterally within the film will arrive at the substrate at an oblique angle, and the backscatter yield will be enhanced. For Au ($Z=79$) the yield is about 0.5 at 90° incidence. In addition, the energy distribution of the backscattered electrons is important to consider because the Bethe equation shows that the energy loss rate (eV/cm) increases with decreasing energy, for $E \gg J$. This effect is demonstrated in Fig. 6 and 7. The peak intensity in the energy distribution of backscattered electrons is also shifted to higher

energy with increasing atomic number Z [17]. The resultant decrease in energy loss rate predicted by the Bethe equation for the average backscattered electron energy from Au is overcome by the increased numerical yield η for Au, compared to Si. If the average energy of a backscattered electron is fE_0 where E_0 = beam voltage, then the relative energy deposited in the film by the backscattered electrons with respect to the forward scattered electrons is approximately (η/f) , where η is the yield of the substrate. This approximation is valid for large E_0 and thin films. If $f \approx 1/2$, then $(\eta/f) \approx 0.6$ for a Cu substrate. This approximation compares well with the Monte Carlo result shown in Fig. 6.

V. SUMMARY

Monte Carlo simulation of kilovolt electron beam scattering and energy loss in targets composed of thin films on thick substrates has been developed and applied to electron beam lithography. Point, line, and plane source electron beams have been simulated. Energy density profiles and equi-energy density contours have been calculated for specific combinations of beam voltage, film thickness, and substrate atomic number to illustrate the significant contribution of electrons backscattered from the substrate into PMMA films. These profiles and contours are important factors which determine the final lithography pattern. Chemical developer effects have been neglected in the simulation, but fair agreement is still obtained with the limited experimental data available. Line widths expected for a line source beam have also been calculated, and show that the minimum line width is attained when the energy density is dominated by the forward-scattered electrons. It is proposed that the "sensitivity" of an electron resist be characterized by a critical threshold energy density (ev/cm^3) required for dissolution by a solvent, and not areal density of the incident electron beam (coul/cm^2). The use of a threshold energy density removes any dependence on experimental parameters such as beam voltage, film thickness and substrate.

VI. ACKNOWLEDGMENTS

One of us (K.M.) thanks IBM Japan, Ltd. and the IBM World Trade Corporation for support as a Postdoctoral Fellow. Helpful discussions were held with C. H. Ting, N. S. Viswanathan, and E. D. Wolf.

REFERENCES

* On sabbatical leave from Applied Physics Department, Osaka University, Japan.

- [1] G. R. Brewer, *IEEE Spectrum* **8**, 23 (1971).
- [2] A. N. Broers and M. Hatzakis, *Scientific American* **227**, 34 (Nov. 1972).
- [3] M. Hatzakis, *J. Electrochem. Soc.* **116**, 1033 (1969).
- [4] K. Kanaya, H. Yamazaki, and K. Tanaka, *OPTIK* **25**, 471 (1967).
- [5] R. W. Nosker, *J. Appl. Phys.* **40**, 1872 (1969).
- [6] T. E. Everhart, *J. Appl. Phys.* **31**, 1483 (1960).
- [7] R. Shimizu and T. E. Everhart, *OPTIK* **36**, 59 (1972).
- [8] R. J. Hawryluk and H. I. Smith, *Proc. 5th Int. Conf. on Electron and Ion Beam Science and Technology*, ed. by R. Bakish (The Electrochemical Society, Princeton, N. J., 1972), p. 51. Also see *J. Appl. Phys.* (June, 1974), to be published.
- [9] J. S. Greeneich and T. Van Duzer, *J. Vac. Sci. Technol.* **10**, 1056 (1973). Also see *IEEE Trans. Electron Devices* (May, 1974), to be published.
- [10] N. Saitou, *Jap. J. Appl. Phys.* **12**, 941 (1973).
- [11] D. F. Kyser and K. Murata, *IBM J. Res. and Develop.* **18**, 350 (1974).
- [12] C. H. Ting, *Rec. 11th Symp. on Electron, Ion, and Laser Beam Technology*, ed. by R.F.M. Thornley (San Francisco Press, 1971), p. 345.
- [13] P. Hoff and T. E. Everhart, *Rec. 10th Symp. on Electron, Ion, and Laser Beam Technology*, ed. by L. Marton (San Francisco Press, 1969), p. 454.
- [14] N. Saitou, C. Munakata, and Y. Honda, *Jap. J. Appl. Phys.* **11**, 1061 (1972).
- [15] E. D. Wolf, F. S. Ozdemir, W. E. Perkins, and P. J. Coane, *Rec. 11th Symp. on Electron, Ion, and Laser Beam Technology*, ed. by R.F.M. Thornley (San Francisco Press, 1971), p. 331.
- [16] T. O. Sedgwick, A. N. Broers, and B. J. Agule, *J. Electrochem. Soc.* **119**, 1769 (1972).
- [17] H. E. Bishop, *Proc. 4th Int. Congress on X-Ray Optics and Microanalysis*, ed. by R. Castaing, P. Deschamps, and J. Philibert (Herman, Paris, 1966), p. 153.

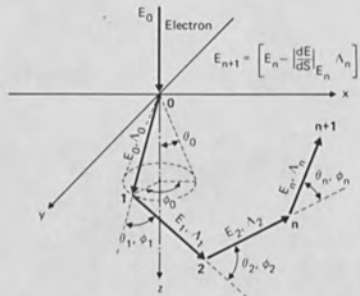


Figure 1. Geometry for Monte Carlo simulation in thick targets.

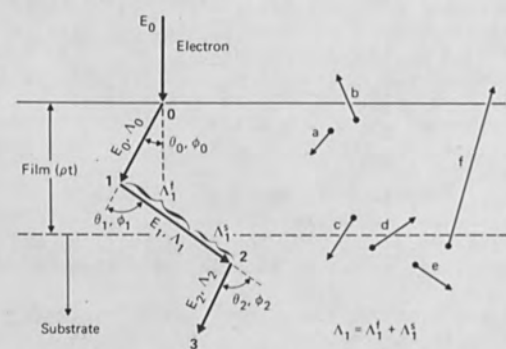


Figure 2. Geometry for Monte Carlo simulation in thin films.

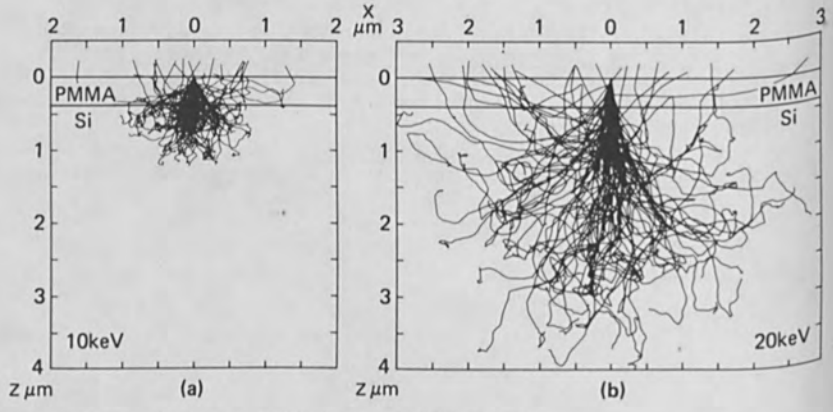


Figure 3. Simulated trajectories of 100 electrons in PMMA film on Si.

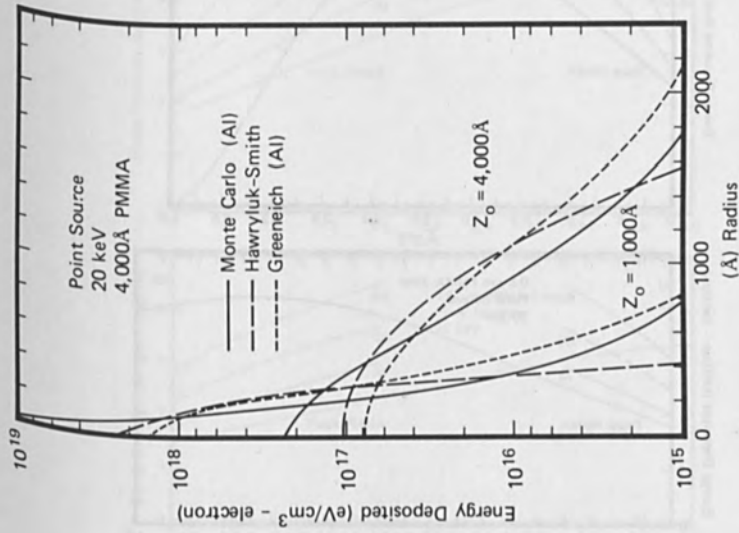


Figure 4. Energy density profiles for point source.

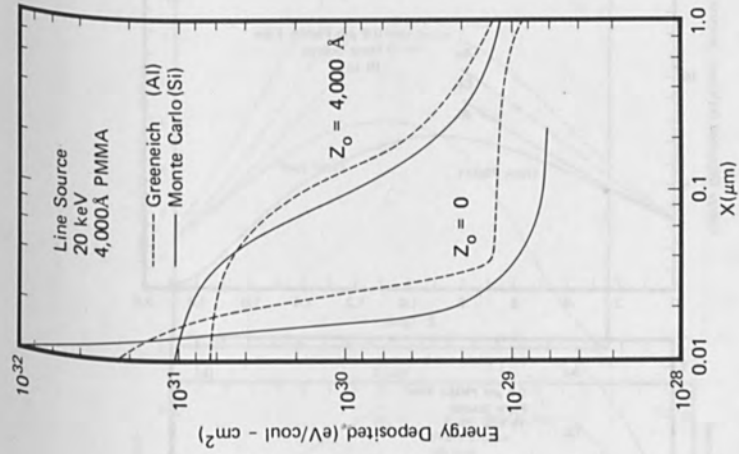


Figure 5. Energy density profiles for line source.

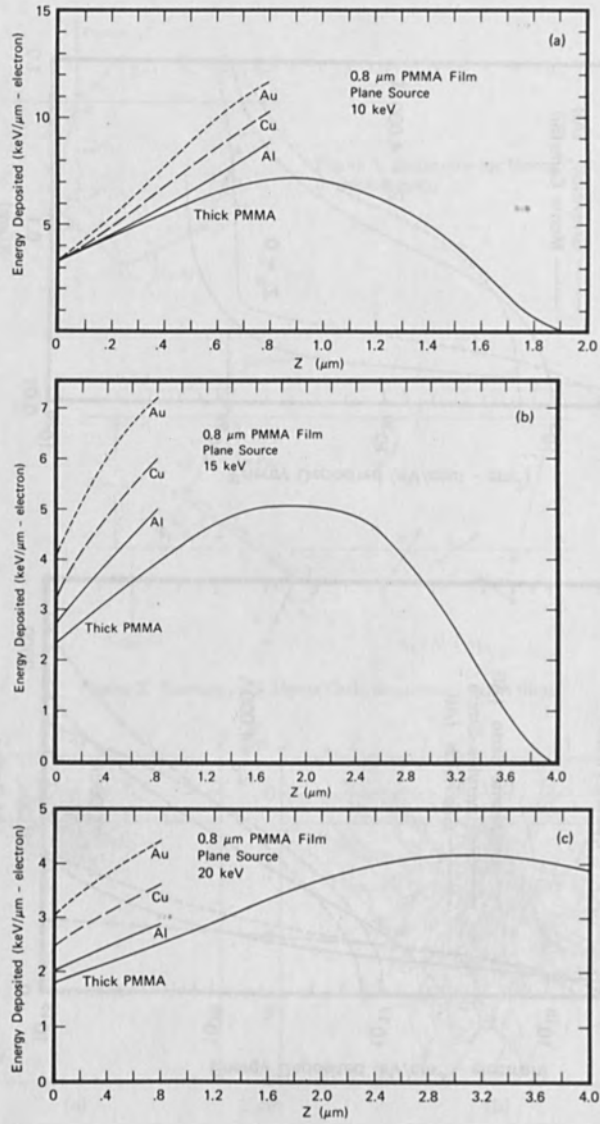


Figure 6. Energy density profiles for plane source.

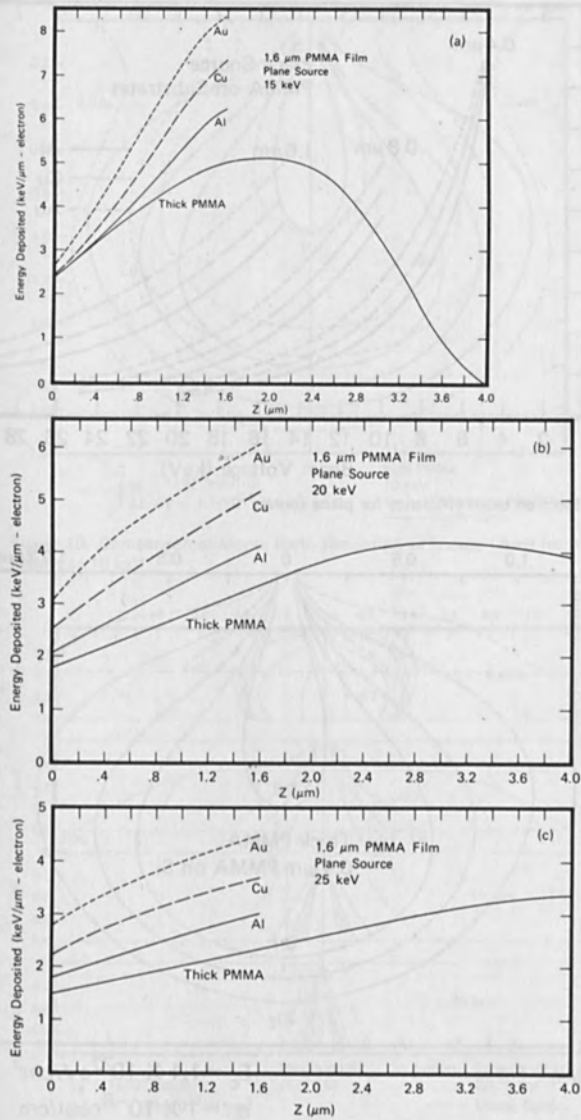


Figure 7. Energy density profiles for plane source.

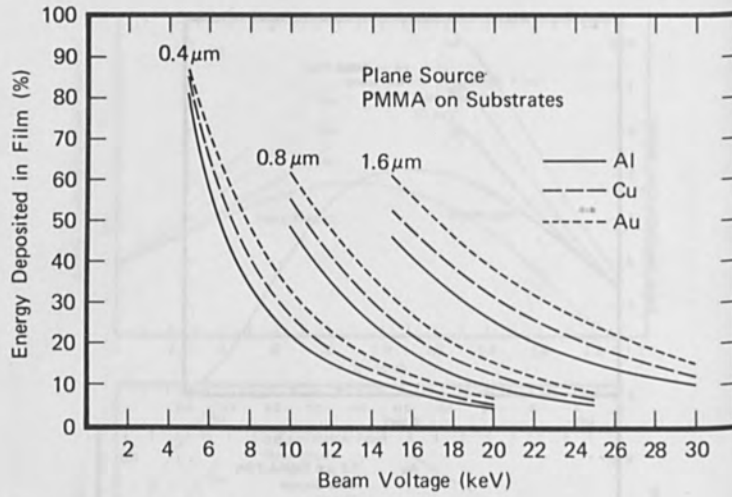


Figure 8. Electron beam efficiency for plane source.

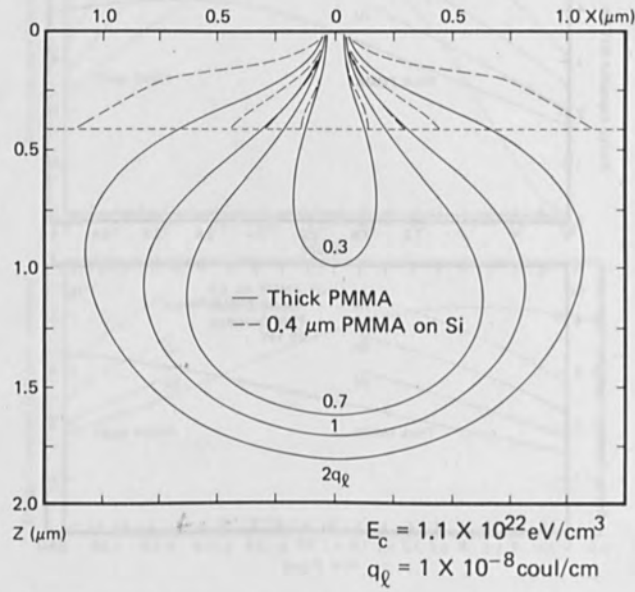


Figure 9. Monte Carlo simulation of energy density contours for line source.

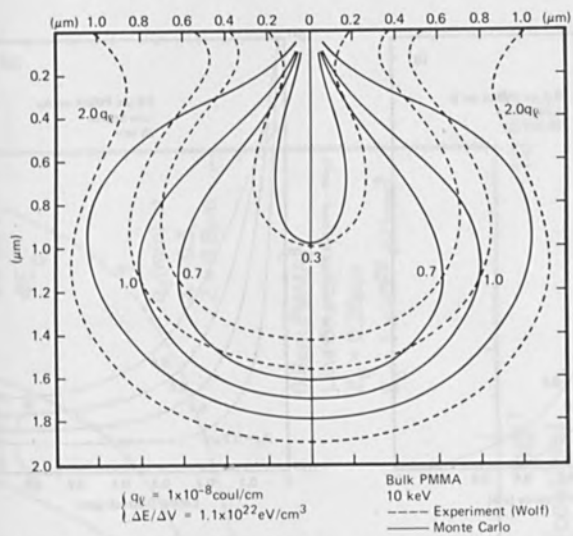


Figure 10. Comparison of Monte Carlo simulation with experiment for thick PMMA at 10 keV.

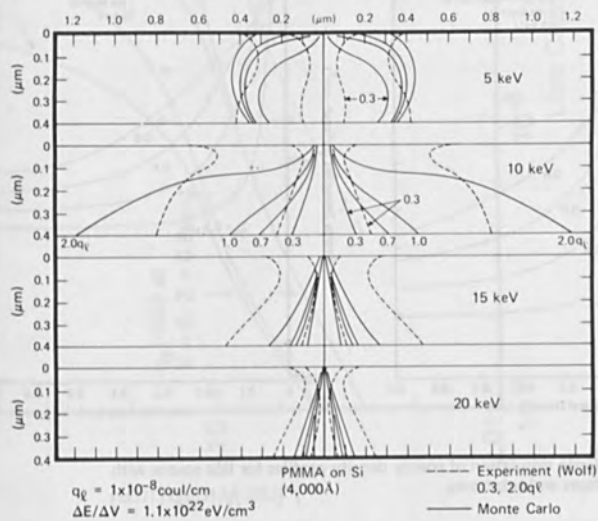


Figure 11. Comparison of Monte Carlo simulation with experiment for thin films of PMMA on Si.

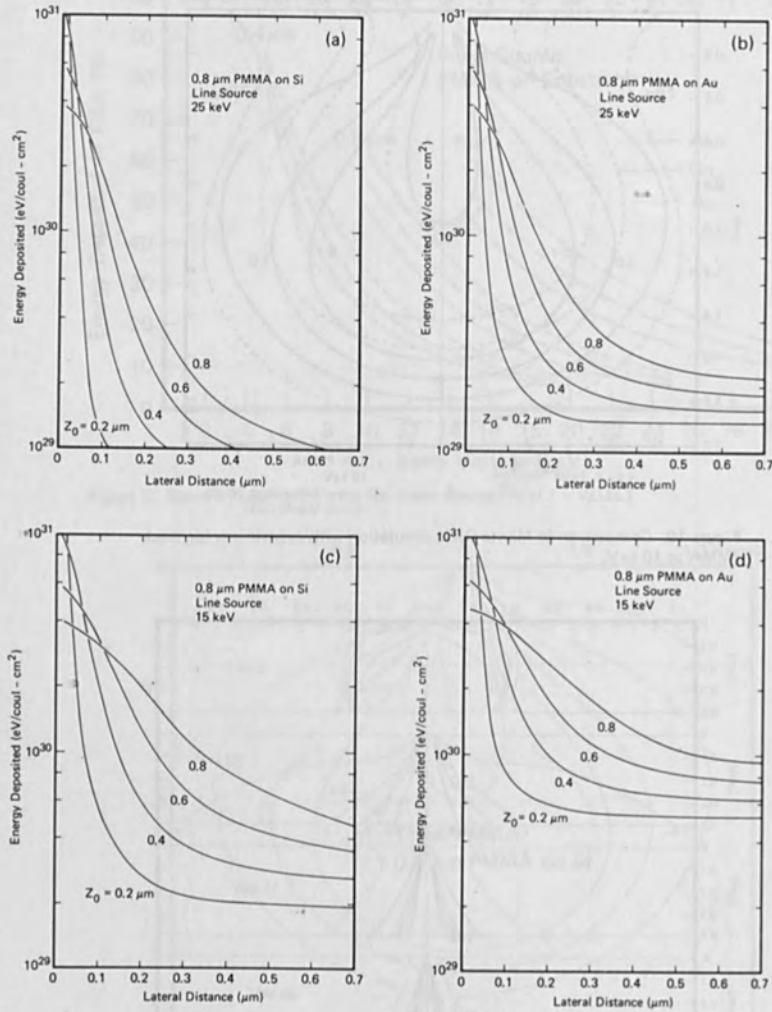


Figure 12. Monte Carlo simulation of energy density profiles for line source with different beam voltages and substrates.

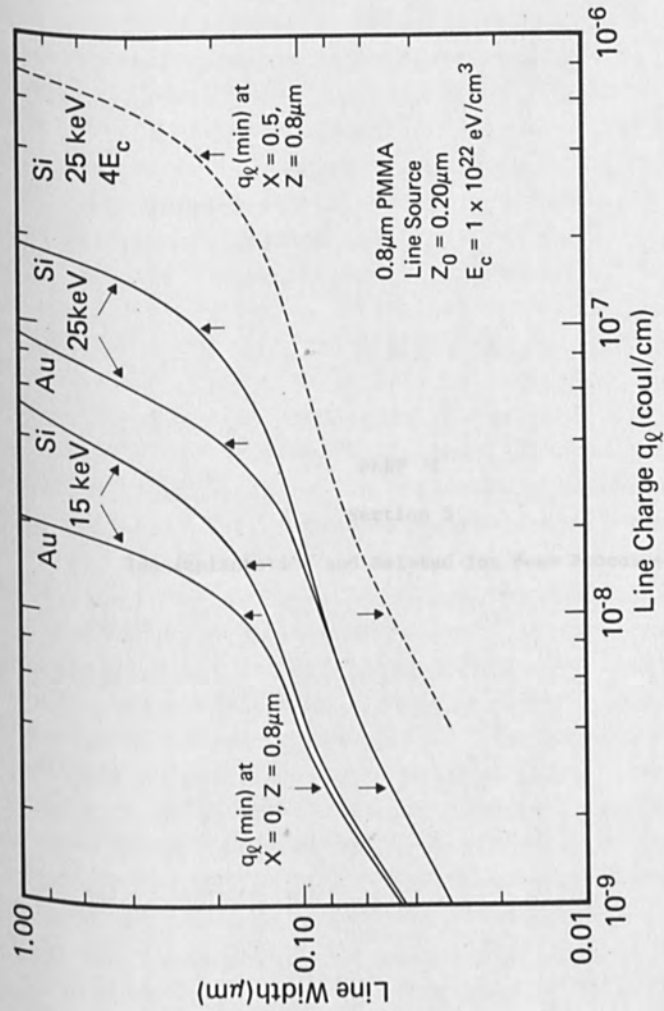


Figure 13. Monte Carlo simulation of line width with different beam voltages and substrates.

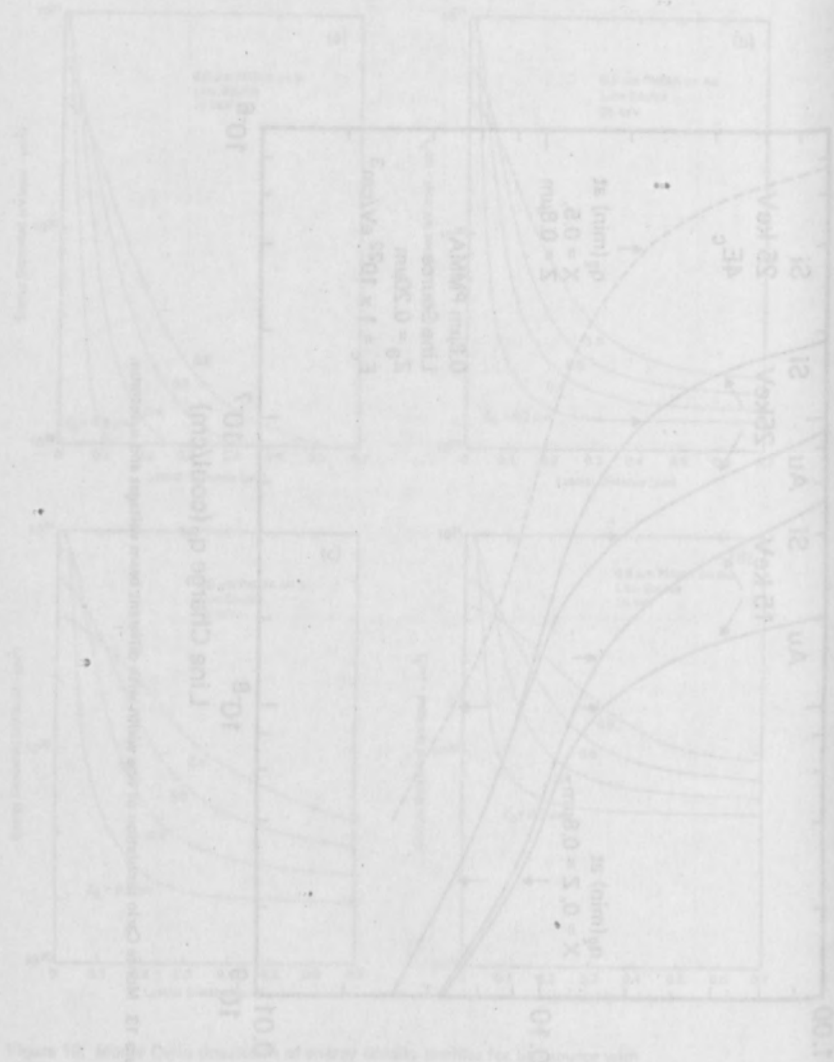


Figure 10. Gas quantity vs. electrode area for different electrode materials.

PHYSICS AND CHEMISTRY OF ION-IMPLANTED SOLIDS
ION-INDUCED PHENOMENA AND CHANNELING STUDY OF
REACTIVE BEHAVIOR OF THE ION-IMPLANTED SOLIDS
FOR BEAM PARTICLES AT HIGH TEMPERATURES

Several studies have been reported on the effect of temperature on the behavior of ion-implanted solids. It is well known that the rate of diffusion of implanted ions increases with increasing temperature. In fact, the rate of diffusion of implanted ions in silicon is reported to be about 10⁻¹⁴ cm²/sec at room temperature and 10⁻¹² cm²/sec at 1000°C. The rate of diffusion of implanted ions in silicon is also reported to be about 10⁻¹⁴ cm²/sec at room temperature and 10⁻¹² cm²/sec at 1000°C. The rate of diffusion of implanted ions in silicon is also reported to be about 10⁻¹⁴ cm²/sec at room temperature and 10⁻¹² cm²/sec at 1000°C.

PART I

Section 5

Ion Implantation and Related Ion Beam Processes

The process of ion implantation is a well-known technique for the introduction of dopants into semiconductors. It involves the bombardment of a solid with ions of a desired element. The ions penetrate the solid and come to rest at a certain depth, depending on their energy and the mass of the ions. The ions then diffuse through the solid, and their distribution is determined by the diffusion coefficient and the time of diffusion. The process of ion implantation is a well-known technique for the introduction of dopants into semiconductors. It involves the bombardment of a solid with ions of a desired element. The ions penetrate the solid and come to rest at a certain depth, depending on their energy and the mass of the ions. The ions then diffuse through the solid, and their distribution is determined by the diffusion coefficient and the time of diffusion.

PHOTOLUMINESCENCE AND CHANNELING STUDY ON
ANNEALING BEHAVIOR OF Te ION-IMPLANTED GaAs

Min-Shyong Lin, Kenji Gamo, Kohzoh Masuda
and
Susumu Namba

Department of Electrical Engineering,
Faculty of Engineering Science, Osaka University
Toyonaka, Osaka, Japan

ABSTRACT

70-keV Te ions were implanted in GaAs single crystals at and above room temperature up to 550°C and annealing behavior of defects and depth distribution was investigated by photoluminescence measurements. Besides the band edge emission, emissions at 9140 and 9900-10200Å were observed after implantation and annealing at 800°C. The emission at 9140Å was observed even after a removal of ~10μ from the surface. This emission is attributed to the As vacancy or the vacancy associated complex from heat treatment study at various temperature. It was found that As vacancies were released during annealing from the damaged region produced by the implantation. The emission at 9900 and 10200Å was observed only near the surface when an amorphous or almost amorphous layer was formed by the implantation. No recovery of the edge emission was observed for amorphized samples after annealing at 800°C. It was concluded that the formation of an amorphous layer should be avoided to obtain an efficient band edge emission.

INTRODUCTION

Ion Implantation in GaAs is a promising method for producing both p-type and n-type layers at relatively lower temperature than those required for diffusion. It is of primary importance to investigate radiation damages and their annealing characteristics in order to produce useful doped layers by ion implantation. Channeling effect measurements gives defect density and defect distribution profiles in a direct way and many investigations have been done by using the channeling techniques¹⁻³⁾. Harris¹⁾ observed that annealing took place at room temperature for defects produced by C and Si implants and Vook et al.²⁾ observed that migration of defects took place during O implants above 275K. The channeling techniques, however, cannot distinguish defects of different structure among each other. Many lattice defects emit photons at their characteristic wavelength and it is possible to assign lattice defects by measuring the emission spectra. Photoluminescence, therefore, is a powerful method to study on lattice defects.

We implanted 70 keV Te ions in GaAs at various temperature and investigated defect properties by measuring photoluminescence. We also measured the distribution of defects by using successive layer removal techniques. Effect of heat treatment on photoluminescence spectra was also investigated to assign the observed emission due to defects.

EXPERIMENTAL PROCEDURE

The GaAs crystals used were undoped, n type, (100) oriented wafers with the carrier density of $1.4 \times 10^{16}/\text{cm}^3$. Samples were polished chemically and mechanically by a bromine-methanol solution. The implantations were made at temperature from room temperature up to 550°C using magnetically mass-separated beams of 70 keV Te ions. Doses ranged from 5×10^{12} to $2 \times 10^{15}/\text{cm}^2$. The GaAs samples were implanted 8° off the $\langle 100 \rangle$ axis in order to reduce channeling effects. After the implantation, the samples were coated at 300°C with about 3000\AA thick SiO_x ($x=2$) layer evaporated in vacuum and were annealed in a flowing hydrogen atmosphere for 20 minutes.

Photoluminescence measurements were carried out by using a grating monochromator and a cooled RCA-7102 photomultiplier. The excitation light from a 1 KW X_e arc lamp was filtered by about 5 cm thick CuSO_4 saturated solution and chopped at 90 HZ. The photoluminescence was detected by using a lock-in amplifier. Measurements were made at 80 K. The stripping of surface layers was accomplished by the successive chemical etching in a solution of 1 mol NaOH and 0.7 mol H_2O_2 at 25°C . The thickness of the removed layers was obtained by the interferometry measurements.

RESULTS AND DISCUSSION

Figure 1 shows photoluminescence spectra of GaAs crystals implanted at various temperature with Te ions to a dose of $2 \times 10^{14}/\text{cm}^2$ and annealed at 800°C for 20 minutes. Several emissions attributed to defect centers were observed

after the implantation. The spectrum (a) observed for the unimplanted and unannealed sample showed the emission peaks at 8250\AA (1.503 eV) and at longer wavelength, while the spectrum (b) observed for the unimplanted, annealed sample showed the emission peak at $\sim 8410\text{\AA}$ (1.474 eV) and the emission at longer wavelength disappeared. The shift of the emission peak after annealing has been observed by Yahata et al.⁴⁾ and Harris et al.⁵⁾ For samples implanted below 100°C , strong, broad emission at longer wavelength (9900\AA for room temperature implant and 10200\AA for 100°C implant) was observed and edge emission was unobservable. For samples implanted above 200°C , the emission at 9900\AA - 10200\AA was disappeared and emissions at $\sim 8410\text{\AA}$ and 9140\AA was observed. Harris et al. also observed the emission at 9140\AA ⁵⁾. They attributed it to the acceptor levels due to As vacancy. The edge emission at $\sim 8410\text{\AA}$ increases with increasing implantation temperature and saturates above 300°C , while the emission at longer wavelength decrease with increasing the implantation temperature. Those emissions observed at 9140 , 9900 and 10200\AA can be considered to be associated with defects produced by the implantation. As shown in Figs. 4 and 5 it is concluded from the results of heat treatment at various temperature that the emission at 9140\AA is due to As vacancy or As vacancy associated defects.

Figure 2 shows photoluminescence intensity (peak height) of the edge emission at $\sim 8410\text{\AA}$ and emissions due to defects as a function of implantation temperature. The samples were annealed at 800°C for 20 minutes. The intensity of the edge emission is normalized to that observed for the non implanted annealed sample and the intensity of defects is normalized to that observed for the room temperature implanted sample. The emissions due to defects decreased sharply

and the edge emission observed at 200°C implantation. For implantations below 100°C recovery of the edge emission was not observed. These results showed a close correlation with our previous channeling effect measurements which are also shown in Fig. 2.⁶⁾ From channeling measurements it was observed that an amorphous layer or heavily damaged layer was formed for implantations below 100°C and that defects reduced sharply at implantation temperature of 100-200°C. Similar behavior has been observed by several authors.^{7,8,9)} These results suggest that the formation of an amorphous layer should be avoided in order to obtain an emission layer of high efficiency.

The depth distribution of the relative emission intensity was measured by using successive layer removal techniques in order to investigate the diffusion of defects. Figure 3 shows the results obtained for room temperature implanted and 800°C annealed samples. The implantations were done to three different doses. In Fig. 3 the intensity (peak height) of edge emission at $\sim 8250\text{\AA}$ is normalized to that of unimplanted, unannealed sample and the others are normalized to the peak height of the edge emission observed for the unimplanted, annealed sample. The edge emission at 8250\AA showed complete recovery, in case of low dose implantation where an amorphous was not formed, after the removal of 0.2-0.3 μ from the surface, but it showed no recovery for samples, in case of high dose implantation where an amorphous layer was formed. The emission at 8360\AA decreased with increasing the ion dose and the maximum intensity observed for $1.25 \times 10^{13}/\text{cm}^2$ implantation was still low compared to that for the unimplanted, annealed sample. The dose dependence of the intensity of this emission was reported elsewhere.¹⁰⁾ The emission intensity for $2 \times 10^{14}/\text{cm}^2$ was almost one hundredth of the unimplanted, annealed sample. The emission at 9140\AA was weak near the surface where heavily damaged layer was produced by the implantation and was attributed to defect centers associated As vacancy as described in the following section.

This emission increased slowly with increasing the dose. This is reasonable because the number of As vacancy produced may increase with increasing the dose. This emission at 9140\AA was observed even after the removal of $\sim 10\mu\text{m}$ from the surface. This indicates that the defects are the rapidly diffusing species. Implanted, unannealed sample did not show any emissions except the band edge emission even after removal of $\sim 0.5\mu\text{m}$ from the surface. Therefore the defects which exhibited an emission at 9140\AA are released from the heavily damaged or an amorphous layer during the annealing and diffused into the bulk. The emission was weak near the surface. The reasons are not known at present but two explanations are possible. One is that the surface may act as quench centers for As vacancy. The other is that the As vacancy change to a divacancy. Ga vacancies are produced during annealing near the SiO_2 -GaAs interface, because Ga diffuse into SiO_2 layer at high temperature¹¹⁾.

Hunsperger et al.¹²⁾ observed that an insulating layer was produced by implantations into GaAs and that the width ranged several tenth of μm to $\sim 100\mu\text{m}$ depending on implantation conditions. He suggested that this was due to As vacancies or As vacancy associated defects. Itoh et al.¹³⁾ observed that the formation of the insulating layer could be avoided by implantations of As.

Besides the emissions at the band edge and 9140\AA , the emission at 9900\AA was observed only when an amorphous layer existed, as shown also in Fig. 3. The defects which exhibited this emission seem to the residuum of the amorphous layer after the annealing at 800°C . This emission was localized near the surface. So it is clear that the defects which exhibited this emission do not diffuse so fast.

Harris et al. observed the emissions at $9140\overset{\circ}{\text{A}}$ for implanted GaAs and attributed these to the acceptor level due to As vacancy. In order to determine whether the emission at $9140\overset{\circ}{\text{A}}$ observed in the present experiment, photoluminescence measurements were done for samples annealed at various temperature with and without the protective coat of SiO_2 on the surface. The spectra observed after heat treatment at 800°C is shown in Fig. 4. All samples were unimplanted. Samples annealed with the SiO_2 film on the surface showed only the edge emission, while those annealed without the SiO_2 film showed the strong emission at $9140\overset{\circ}{\text{A}}$ and the edge emission was weak. The unannealed sample also showed the emission at $9140\overset{\circ}{\text{A}}$ but this was weak and $1/32$ of that for samples annealed without SiO_2 coat.

Figure 5 shows the annealing temperature dependence of the emission intensity at $9140\overset{\circ}{\text{A}}$. The intensity is normalized to the peak height for the unannealed sample. The samples were unimplanted and annealing was done without the SiO_2 film on the surface. At 700°C annealing the intensity was almost the same with that observed before the annealing. From the slope of the $\text{Log}(I/I_0)$ VS $1/T$ plot the activation energy for the growth of the emission at $9140\overset{\circ}{\text{A}}$ was estimated to be -2.0 eV. This value is in good agreement with the activation energy for the formation of As vacancy¹⁴⁾ and the acceptor levels associated with As vacancy.¹⁵⁾ Munoz et al.¹⁵⁾ observed that the n-type GaAs was converted to p-type from the surface to the depth of $7\mu\text{m}$ after annealing at 850°C . We also observed by Hall effect measurement that the samples annealed at 850°C without the SiO_2 films on the surface was converted from n-type to p-type. From these results it is concluded that the emissions at $9140\overset{\circ}{\text{A}}$ observed in the present experiment are associated with As vacancies.

The summary of the present experiment is shown in Table I. The emission at 8250Å may be attributed to the donor levels due to Si substituted for Ga,^{5,16)} because Si is usually the major impurity in undoped GaAs. The assignment of the emission at 9900Å is tentative. This was done because the peak position agreed with that attributed to Ga vacancy-donor complex.¹⁷⁻¹⁹⁾

CONCLUSIONS

70 keV Te ions have been implanted in GaAs at room temperature and elevated temperatures. Photoluminescence spectra have been measured to identify defects. From the results we conclude:

- 1) As vacancies are produced during annealing of implanted damaged layer of GaAs and diffuse deep into the bulk. Defects associated with As vacancy exhibit an emission at 9140Å. The emission at 9900Å is observed only near the surface and is the residuum of an amorphous layer after an annealing at 800°C.
- 2) A sharp increase in edge emission intensity after annealing at 800°C takes place at implantation temperature of 100-200°C. This result is in good agreement with that observed by channeling effect measurement. This means that an annealing of an amorphous layer is difficult.
- 3) The formation of an amorphous layer should be avoided to obtain an efficient edge emission.

ACKNOWLEDGEMENTS

The authors wish to thank Mr. K. Kawasaki for his help in performing the implantation.

REFERENCES

- 1) J.S. Harris: Ion Implantation in Semiconductors ed I. Ruge and J. Graul (Springer-Verlag, 1971) p.157.
- 2) F.L. Vook and S.T. Picraux: *ibid.* p.141.
- 3) G. Carter, W.A. Grant, J.D. Haskell and G.A. Stephens: Radiation Effects 6 277 (1970).
- 4) A. Yahata and M. Ohyama: Solid State Commun. 11 31 (1972).
- 5) J.S. Harris and F.H. Eisen: Radiation Effects 7 123 (1971).
- 6) M. Takai, K. Gamo, K. Masuda and S. Namba: Japan J. Appl. Phys. 12 1926 (1973).
- 7) R. Bicknell, P.L.F. Hemment, E.C. Bell and J.E. Tansey: Phys. Status Solide 12 K9 (1972).
- 8) J.S. Harris, F.H. Eisen, B. Welch, J.D. Haskell, R.D. Pashley and J.W. Mayer: Appl. Phys. Letters 21 601 (1972).
- 9) J.L. Whitton and G.R. Bellavance: Rad. Effects 9 127 (1971).
- 10) M.S. Lin, K. Gamo, K. Masuda and S. Namba: Japan. J. Appl. Phys. 12 1092 (1973).
- 11) J. Gyulai, J.W. Mayer, I.V. Mitchell and V. Rodriguez: Appl. Phys. Letters 17 332 (1970).
- 12) R.G. Hunsperger and O.J. Marsh: Metallurgical Trans. 1 603 (1970).
- 13) T. Itoh and Y. Kushiro: Ion Implantation in Semiconductors ed. I. Ruge and J. Graul (Springer-Verlag, 1971) p.168.
- 14) H.R. Potts and G.L. Pearson: J. Appl. Phys. 37 2098 (1966).
- 15) E. Munoz, W.L. Snyder and J.L. Moll: Appl. Phys. Letters 16 262 (1970).

- 16) E.H. Bogardus and H.B. Beff: Phys. Rev. 176 993 (1968).
- 17) E.W. Williams: Phys. Rev. 168 922 (1968)
- 18) C.J. Hwang: J. Appl. Phys. 40 4584 (1969).
- 19) E.W. Williams and H.B. Bebb: Semiconductors and Semimetals 8 (Academic Press, New York, 1972) Chapt. 5.

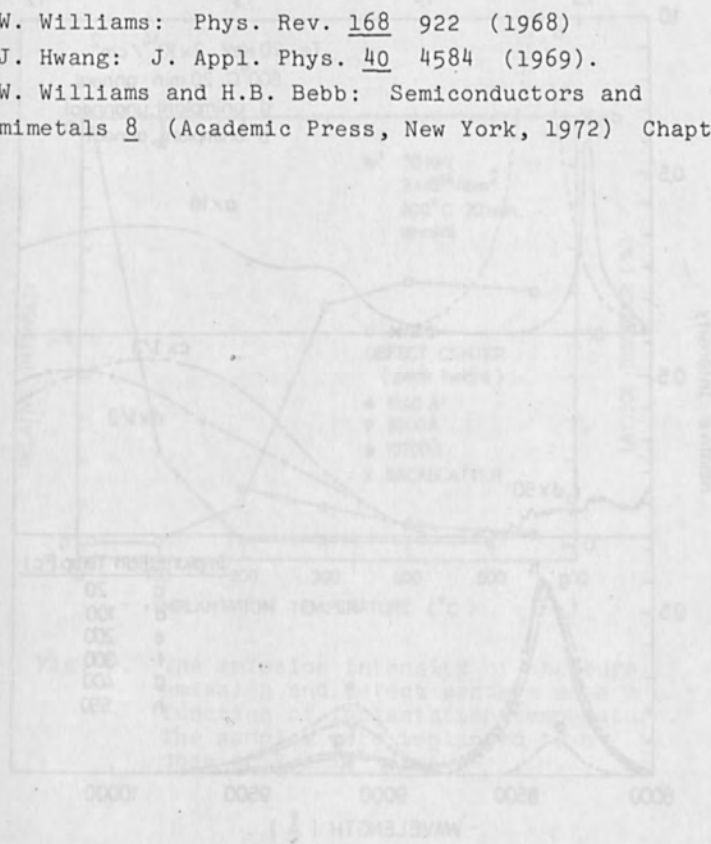


Fig. 1. Photoluminescence spectra as a function of excitation temperature. The spectra were recorded at a dose of 1×10^{-4} cm². All samples (except (ii)) were annealed at 500°C for 30 minutes in a flowing hydrogen atmosphere.

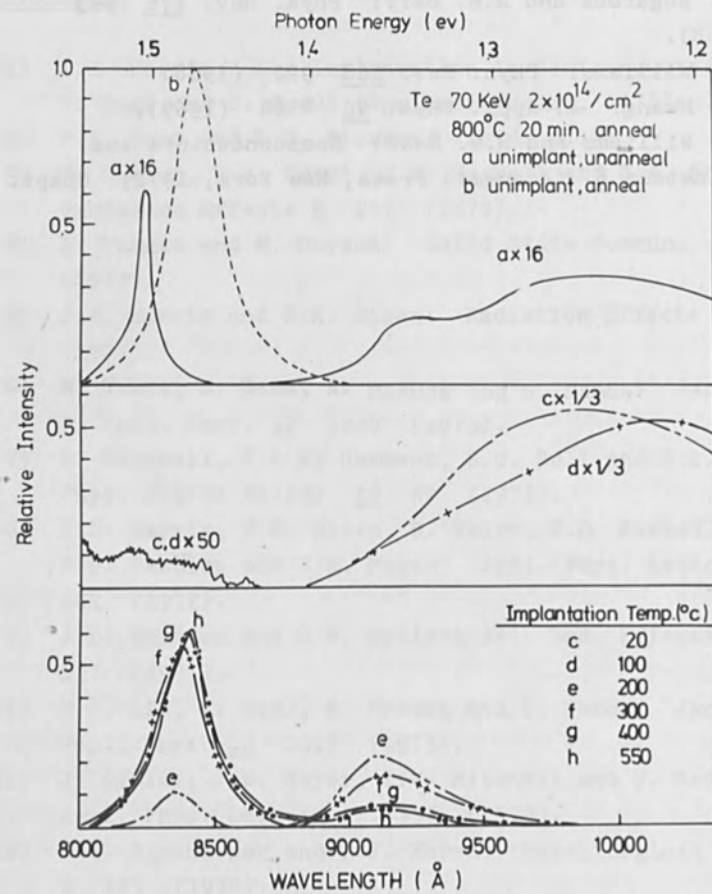


Fig. 1. Photoluminescence spectra as a function of implantation temperature. The samples were implanted to a dose of $2 \times 10^{14}/\text{cm}^2$. All samples (except (a)) were annealed at 800°C for 20 minutes in a flowing hydrogen atmosphere.

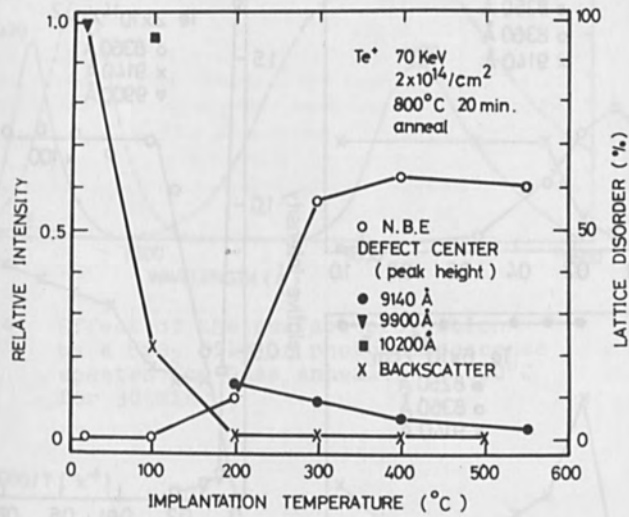


Fig. 2. The emission intensity of the edge emission and defect centers as a function of implantation temperature. The samples were implanted to a dose of $2 \times 10^{14}/\text{cm}^2$.

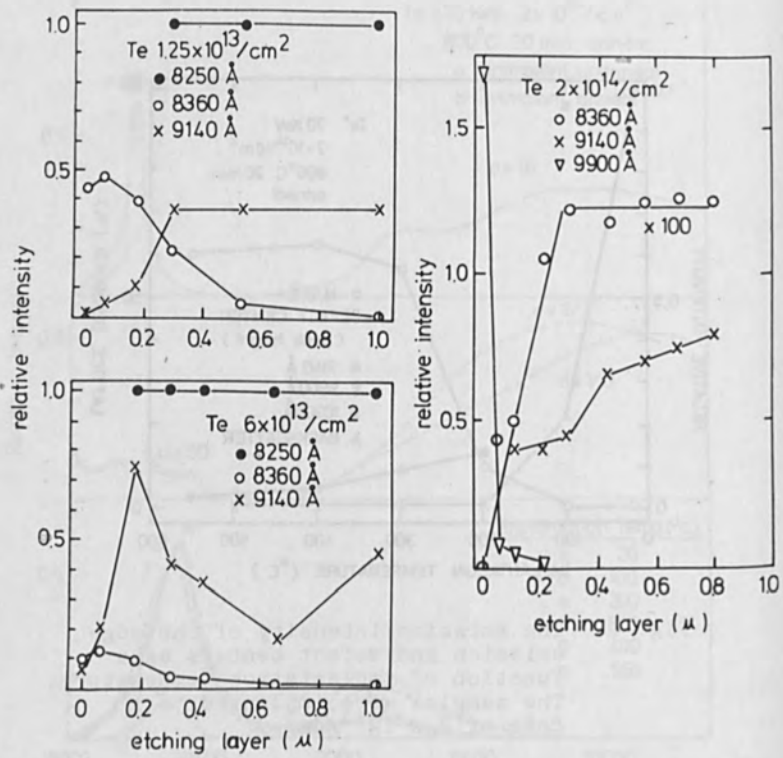


Fig. 3. The depth distribution of the relative emission intensity of luminescent centers observed for room temperature implanted GaAs after annealing at 800°C for 20 min.

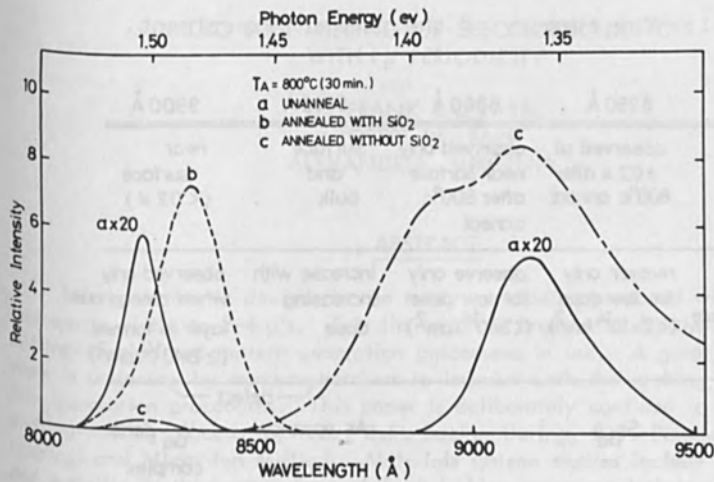


Fig. 4. Effect of the surface protection by a SiO_2 film on photoluminescence spectra for GaAs annealed at 800°C for 30 min.

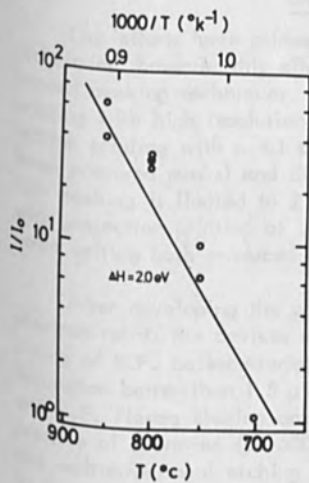


Fig. 5. The emission intensity at 9140Å as a function of the annealing temperature. The annealing time: (●) 10 min. (○) 30 min.

Table. 1. The summary of the present experiment.

wavelength	8250 Å	8360 Å	9140 Å	9900 Å
distribution	observed at $\geq 0.2 \mu$ after 800°C anneal	observed only near surface after 800°C anneal	surface and bulk	near surface ($< 0.2 \mu$)
dose dependence	recover only for low dose ($< 2 \times 10^{14}/\text{cm}^2$)	observe only for low dose ($< 2 \times 10^{14}/\text{cm}^2$)	increase with increasing dose	observed only when amorphous layer is formed ($\geq 2 \times 10^{14}/\text{cm}^2$)
structure	SiGa		As vacancy or complex	defect V_{Ga} -donor complex

MICRO ION MILLING OF ELECTRONIC DEVICES WITH $1\ \mu$ PERIODICITY

D. FRANK BAZZARRE
ROBERT W. BARR
ALEXANDRIA, VIRGINIA

ABSTRACT

Micro electronic devices in use today, are being produced with line and space widths to $2\text{--}4\ \mu$'s. This limitation is brought on by the chemical milling-etching and pattern generation procedures in use. A great deal of work is underway by many researchers to improve both the etching and pattern generation procedures. This paper is deliberately confined to advanced etching-milling procedures, i.e., R.F. backsputtering, R.F. Plasma Etching (Ashing) and Micro Ion Milling. Materials systems studies include dielectric and metallic in thicknesses from $.1\text{--}5\ \mu$'s. Line space resolutions to $1.5\ \mu$'s were obtained by all etching methods on dielectric and metallics with film thickness of $1\ \mu$. Below $1.5\ \mu$ resolution, only Micro Ion Milling produced satisfactory line definitions with no undercut, resolution to $.1\ \mu$'s was obtained and space width to depth aspect ratio of 1 to 10 were obtained.

EXPERIMENTAL APPROACH

Our efforts have primarily been limited to developing etching-milling techniques, however this effort has necessitated some exploration of advanced masking techniques. Masking techniques explored include contact printing with high resolution masks (produced by Micro Ion Milling), projection printing with a 4:1 stepdown ratio, x-ray lithography (from electron beam prepared masks) and direct electron beam writing. In general, contact masking is limited to $2\ \mu$ resolutions, successful results were obtained with projection printing at $.6\ \mu$ resolution; x-ray lithography and electron beam writing both produced desirable patterns to $.1\ \mu$.

After developing the pattern in photograph resists, x-ray resists or electron resists the devices were subjected to etching-milling procedures consisting of R.F. backsputtering, R.F. Plasma Ashing and Micro Ion Milling. Resolution better than $1.5\ \mu$'s could not be produced by R.F. backsputtering and R.F. Plasma Etching on the mean free path of the electrons and ions at pressure of operation (50-500 millitorr) result in omnidirectional collisions and multidirectional etching limiting the depth to undercut ratio to 1:1 and in practice we observed this ratio to be in the order of 1:2. In addition, image defining resists degraded during processing from electron damage and

thermal exposure, also, electron damage was noted in MOS devices.

With the previously mentioned limitations of R.F. backsputtering and R. F. Plasma Etching our attention as well as others including Johnson, Hewitt,³ Schmidt and Spencer, Shank and Tien⁴ of Bell Telephone Laboratories, Garvin of Hughes Aircraft Co. and Smith⁴ of MIT, Lincoln Labs, have extensively explored Micro Ion Milling for the preparation of high resolution devices. Devices under consideration include MOS, CMOS, FET, CCD, Magnetic Domain and integrated optics. Materials have included metallics, semiconductors, dielectrics and organics.

Our program objectives were to 1) improve surface finish, i.e., by utilizing Micro Ion Milling and varying the angle of beam attack on the surface to an angle near grazing (approximately 10°) the projections on the surface mask the recessions and are therefore milled (polished) at a higher rate than the recessions resulting in a polished surface with a RMS finish approaching 0. In addition, normally polished (mechanical) devices have induced defects and dislocations as process artifacts. It has been found that the removal of 5000\AA of material by Micro Ion Milling from the 'used' surface removes these dislocations and results in a surface with no-low residual strain. The 2nd objective as shown in Figure 1 was to define the optical patterns. Methods investigated as previously stated, included contact printing, projection printing, x-ray lithography and electron beam writing. In order to offer practical protection during Micro Ion Milling it is necessary that resist thickness up to $1.5\ \mu\text{'s}$ be readily produced without image degradation. After application of the resist and image the devices are Micro Ion Milled. Figure 2 depicts the procedures employed to ready a device for Micro Ion Milling. Figure 3 illustrates a typical device ready for Micro Ion Milling.

The system utilized for our Micro Ion Milling studies was the MIM/TLA 5.5*. The ion source is illustrated in Figure 4. In general, this source consists of an electron impact source and a magnetic field to produce an electron spin field and 2 ion extractor-accelerators. Ion current is measured with a modified Faraday cup and a flood neutralizer is employed to prevent charging on the device surface. Typical operating conditions for device preparation are shown in Figure 5. The total system is shown in Figure 6 with Figure 7 showing a close up of the controls and Figure 8 showing the ion gun and milling chamber.

RESULTS

Figure 9 shows a Magnetic Bubble Device in which a channel structure has been Micro Ion Milled and 2nd conductor pattern of permalloy was also

*Trademark - Technics Inc. - Alexandria, Virginia

processed. Figure 10 shows the permalloy structure with $1\ \mu$ resolution on both the horizontal and vertical portions of the channel.

Figure 11 shows a 1000 Bit I-Bar shift register with 1 micron line widths. This structure is permalloy₂ and process times for 3000\AA thick films at a current density of $.8\ \text{ma/cm}^2$ is 4 minutes.

Figure 12 is an illustrated grating portion of a thin film laser intergrated optics device with peak to peak resolution of 2000\AA . The material is gallium phosphide. Uniform gratings from $1/2\ \text{mm} \times 1/2\ \text{mm}$ to $5\ \text{cm} \times 5\ \text{cm}$ are readily produced with Micro Ion Milling times of 2-4 minutes/device.

In addition to the preparation of high resolution devices, other applications such as tuning ultra high frequency Quartz Oscilators have become quite practical with Micro Ion Milling and are illustrated in Figure 13. Quartz oscilators have been milled from $86\ \mu$ to $32\ \mu$ with and without supporting rings, with degradation in performance.

Milling applications where wall shape and surface smoothness requirements are stringent such as gas bearings are other applications for Micro Ion Milling. Wall intersecting planes of 90° can be produced while maintaining surface finishes better than $2\ \mu$ inches. Depths to $5\ \mu$'s are practical.

Routinely $1\ \mu$ patterns are being produced utilizing conventional photographic masking and Micro Ion Milling. An effort to further improve the line to space resolution of devices electron beam writing and x-ray lithography are being employed successfully with Micro Ion Milling to produce line to space resolutions better than 1000\AA .

REFERENCES

1. Bell Telephone Laboratories, Murray Hill, N. J.
2. Bell Telephone Laboratories, Holmdel, N. J.
3. Hughes Aircraft Co., Malibu Beach, California
4. MIT - Lincoln Laboratories, Cambridge, Massachusetts



FIGURE 1

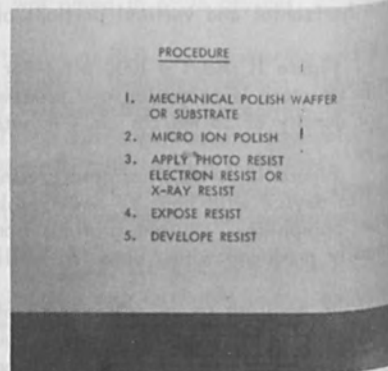


FIGURE 2

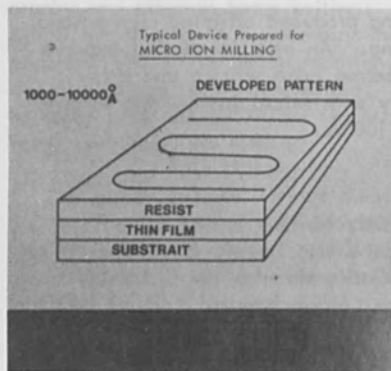


FIGURE 3

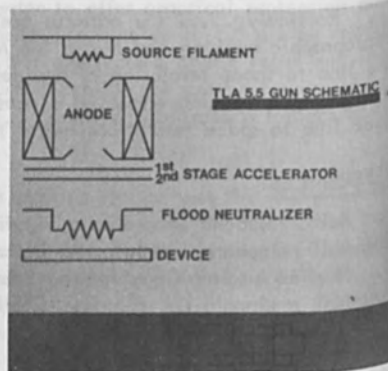


FIGURE 4

MICRO ION MILLING PROCEDURES

1. Place device in milling chamber and evacuate to 1×10^{-5} torr
2. Typical Milling Conditions
 - Source filament - 8v, 2 amps
 - Anode 50v, 100 millamps
 - 1st accelerator 2000v, 10 millamps
 - 2nd accelerator 200v, 1 millamp
 - Neutralizer 8v, 2 amps
 - Pressure 3×10^{-5} torr
 - Angle of Incidence 90°
 - Device Rotation 15 rpm's
 - Ion Current Density .25 millamps/cm²
3. Milling Rate of Typical Material at above conditions approx. 300 Å/minute

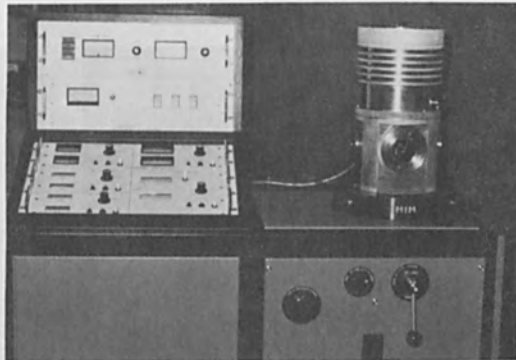


FIGURE 5

FIGURE 6

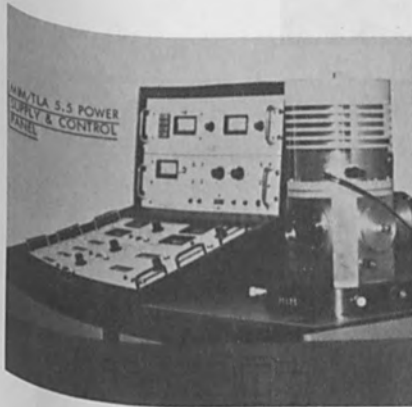


FIGURE 7



FIGURE 8



FIGURE 9

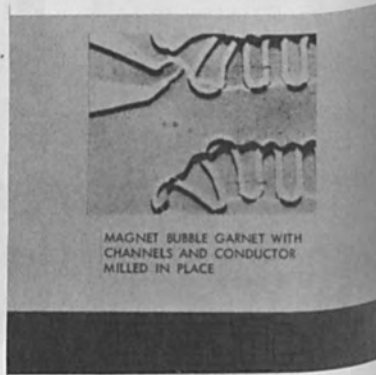


FIGURE 10

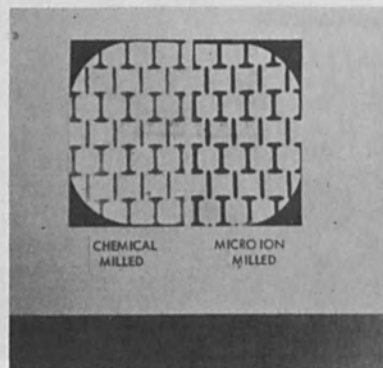


FIGURE 11

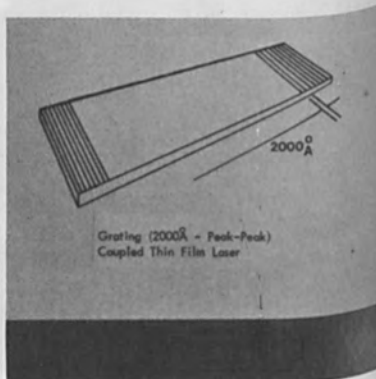


FIGURE 12

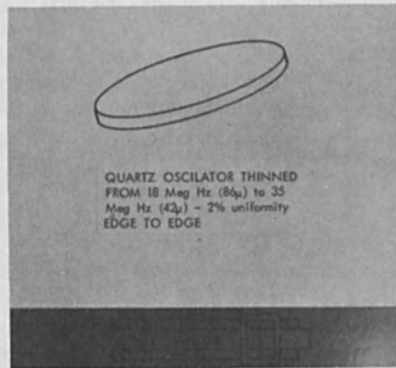


FIGURE 13

MAGNETICALLY ENHANCED HIGH-RATE SPUTTERING

R. L. Cormia, P. S. McLeod, N. K. Tsujimoto
Airco Temescal
2850 Seventh Street, Berkeley, California 94710

ABSTRACT

A new sputtering technique using permanent magnets greatly increases sputtering rates to greater than 1.5 microns per minute in the range of 1 to 5 millitorr. The theory of operation will be discussed with emphasis on trapped electrons and their influence on ion population and resulting sputtering rates. Data on rate and distribution for various sputtering conditions and materials will be presented.

Introduction

Sputtering is disparaged by proponents of electron beam evaporation because rates from diode sputtering targets are often too low to be practical. Attempts have been made to increase sputtering rates by either injecting more electrons into the discharge or by confining the electrons magnetically or physically in the discharge. All of these techniques are successful to some degree in obtaining higher rates than diode sputtering. A new technique recently developed by Airco Temescal utilizes magnetic confinement of the electrons above a planar cathode to achieve sputtering rates much higher than conventional diode sputtering. In addition, this technique offers several advantages not found in other rate enhancing techniques. The new cathode configuration is shown in Figure 1 and is called the HRC-373. The HRC-373 utilizes an anode trap to catch electrons which are scattered out of the confinement region of the plasma. These electrons would otherwise heat the substrates. Therefore, substrate temperature is much lower than attained using most techniques. The shape of the cathode (see Figure 1) allows good deposition uniformity over substrates which are moved across the long axis of the cathode, thus eliminating the constraints placed on a high-rate configuration which must use a planetary fixture to achieve uniformity.

Theory of Operation

The shape of the magnetic field is shown in Figure 2. The constraint that the electron be confined in the area where the magnetic field is perpendicular to the electric field allows the Lorentz force equation to be manipulated to yield:

$$\bar{V}_d = \frac{\bar{E} \times \bar{B}}{|\bar{B}|^2}$$

Where V_d is the particle drift velocity, E the electric intensity and B the magnetic induction. Notice this expression is independent of charge and mass of the particles involved. This implies the drift velocity, V_d , is the same for both electrons and ions. The electrons will tend to drift in the plasma as is shown in Figure 3 providing they do not collide with ions and neutrals in the plasma. Such a drift will retain the electrons in the plasma for relatively long periods of time when compared to diode plasmas.

Method

All sputtering data were taken in an 18-inch-diameter (46 cm) x 10-inch-high (25 cm) chamber. The chamber was pumped by an AIRCO TEMESCAL® Model 814 Turbomolecular Vacuum Pump through a 6-inch (15.2 cm) main valve which partially throttled the pump. The pumping speed in the chamber for air is shown in Figure 4; the pumping speed for argon is found to be about 10% lower. Argon was bled into the chamber through a needle valve without further throttling the turbomolecular pump. When measured on a capacitance manometer, the pressure achieved at a given setting of the valve fluctuated less than 5% daily. Pressure was controlled to less than 0.1 micron change during the runs.

The distribution and rate data were taken by measuring the weight gain of small glass discs placed in an array above the copper sputtering target. The balance used was capable of sensing a weight change of 0.1 mg. Typical weight changes measured were 10 mg or more.

Results

Sputtering rates measured at 4×10^{-3} Torr pressure and at 2-inch (5 cm) source-to-substrate distance are shown in Figure 5. Note palladium sputters at somewhat higher rates than one would expect from previously published⁽¹⁾ yield data. This increase is probably because the palladium plate was 1/8-inch (32 mm) thick instead of the usual 1/4-inch (64 mm), making the magnetic field stronger at the surface.

The distribution of sputtered material from the HRC-373 varies as to be expected⁽²⁾ with source-to-substrate distance. Figure 6 shows the deposition rate above the center of the cathode as a function of the cathode-to-substrate distance. This indicates the highest rates can be obtained at 1-1/2-inches (3.75 cm) with the rates decreasing as the substrates get closer to the cathode.

¹G. K. Wehner et al, Annual Report on Sputtering Yields (General Mills Report #2356, Minneapolis, 15 Nov. 1962)

²L. Holland, Vacuum Deposition of Thin Films (Chapman & Hall Ltd., London 1966), p. 148

The discharge is inhibited as the substrates are brought closer to the cathode; the deposition rates decrease and the operating voltage necessary to maintain a certain power supply current increases indicating an increasing load impedance. Figures 7 and 8 indicate the static distribution of the sputtered material. This is not the way the cathode was designed to operate but the static distribution is instructive in understanding the distribution one would predict when the substrates are moved across the long axis of the cathode. In Figure 9, the predicted integrated distribution is shown for source-to-substrate spacings of 1, 1-1/2, 2 and 2-1/2 inches (2.5, 3.75, 5 and 6.75 cm) at 4×10^{-3} Torr and 2 kW power input to the cathode. The rates for 1-inch (2.5 cm) are higher than at 1-1/2-inches (3.75 cm), but the distribution is considerably worse, the 2-inch (5 cm) spacing being the optimum with $\pm 10\%$ obtainable over 70% of the 8-1/2-inch (21.6 cm) length. The effect of pressure on the distribution is shown in Figure 10. There seems to be little effect on the distribution; however, the higher pressure seems to average out vapor contributions from the ends of the cathode.

The temperature rise of an alumina substrate during deposition from a titanium target was measured and is shown in Figure 11. The temperature of the back side of the substrate was monitored during a five-minute run while approximately 2.5 microns of titanium were deposited on the other side. Admittedly the temperature of the side facing the target was higher; but when the chamber was vented seconds after deposition, the target side of the substrates was not too hot to touch. Independent studies by Auger analysis indicated the diffusion zone between titanium and palladium on alumina substrates is approximately one-half the zone width of conventional electron beam evaporation titanium and palladium.

Conclusions

High sputtering rates can be achieved by confining the electrons close to the sputtering surface when the magnets are arranged to have the magnetic field lines emerge and enter the sputtering surface. The configuration described here provides high sputtering rates and uniform distribution over substrates which are moved across the long axis of the cathode. The addition of an anode minimizes the bombardment of the substrate by electrons so temperature-sensitive materials can be more easily coated.

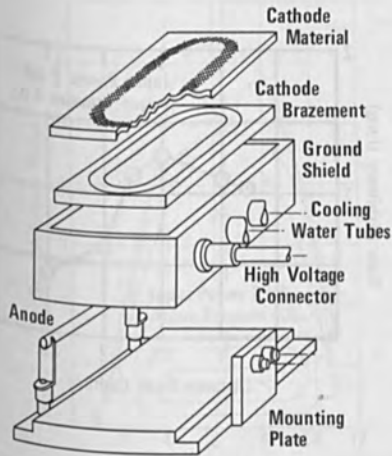


FIGURE 1
Components comprising the standard HRC-373
SPUTTER-RING source.

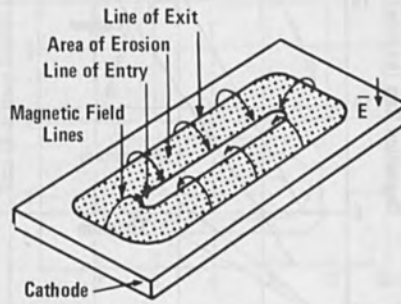


FIGURE 2
Pole pieces behind cathode create magnetic field
in planar device.

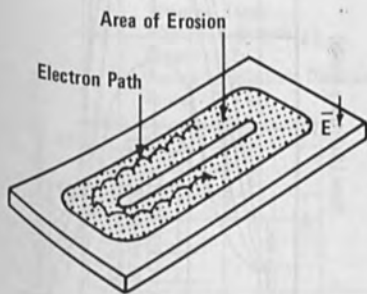


FIGURE 3
Electron path is cycloidal within limits of mag-
netic field.

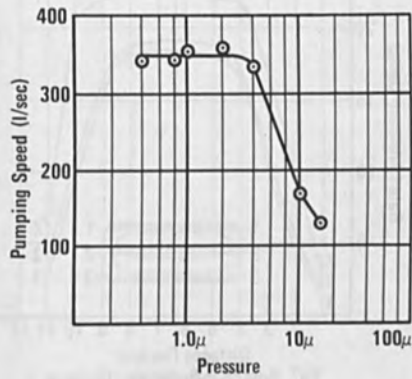


FIGURE 4
Pumping speed as measured in the chamber vs
pressure with Model TMP-814 Turbomolecular
Pumped System.

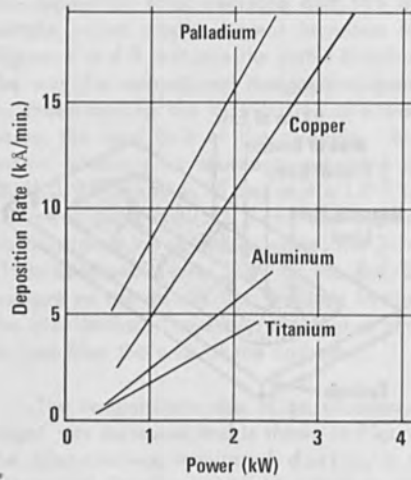


FIGURE 5
Rate vs Power (Typical materials; rates averaged over active area of cathode)

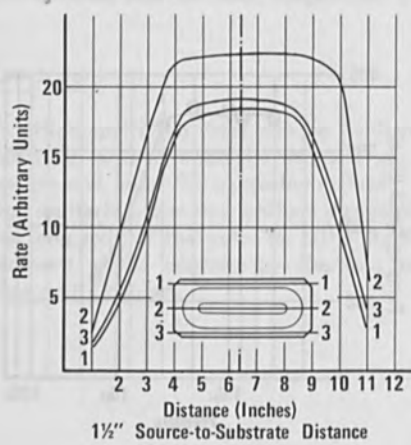


FIGURE 7
Static distribution along the long axis of the cathode.

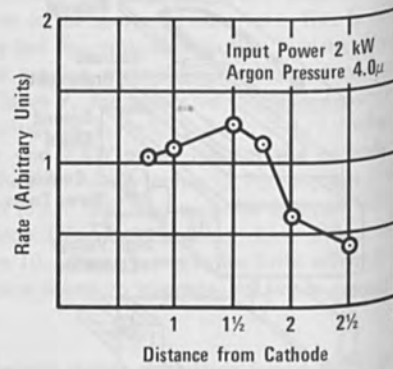


FIGURE 6
Deposition rate above the center of the cathode shown as a function of the cathode-to-substrate distance.

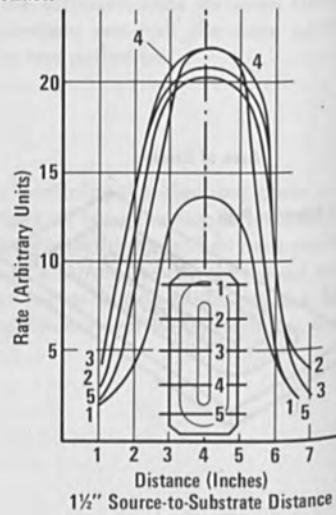


FIGURE 8
Static distribution along the short axis of the cathode.

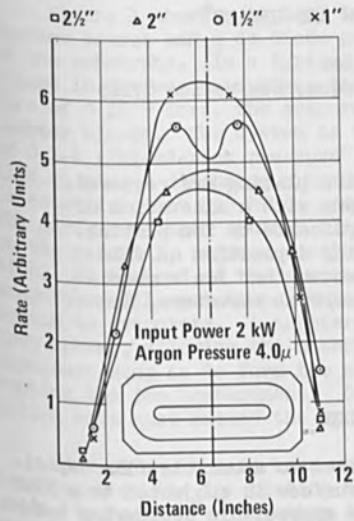


FIGURE 9
Integrated distribution for substrate passing along a line perpendicular to the long axis of the cathode.

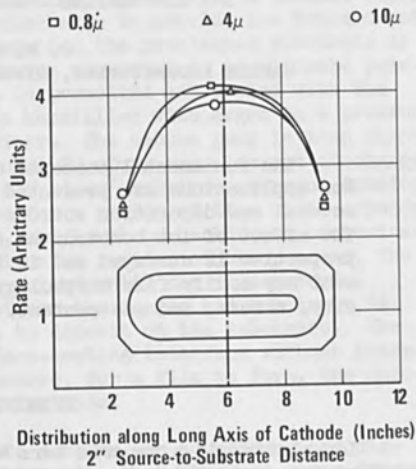


FIGURE 10
Integrated distribution at various argon pressures for substrate passing perpendicular to the long axis of the cathode.

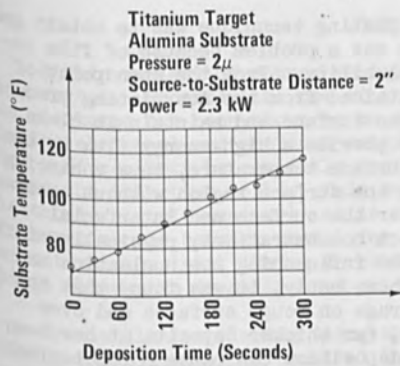


FIGURE 11
Substrate temperature as a function of time.

ION PLATING - REVIEW AND UPDATE*

D. M. Mattox
Sandia Laboratories, Albuquerque, New Mexico 87115

The fundamental concepts of ion plating are reviewed. New applications are presented along with a discussion of several new deposition sources applicable to ion plating. The effect of ion bombardment during deposition on film properties is surveyed and it is shown that ion bombardment may modify film morphology, crystal structure, density, stress, and gas content.

INTRODUCTION

Ion plating is a generic term applied to atomistic film deposition processes in which the substrate surface is subjected to a flux of high-energy ions sufficient to cause appreciable sputtering before and during film formation. By subjecting the substrate surface to ion bombardment prior to deposition, the surface is sputter cleaned. By beginning the deposition while maintaining the ion bombardment, the film is formed without surface recontamination. Thus, surface cleaning is an integral part of the deposition process and not a separate step as is usually the case in other deposition techniques. The fundamental concepts of ion plating and related physics have been discussed in Refs. 1 through 4.

The original goal of the ion plating technique was to obtain good adhesion in systems where adhesion was a problem because of film nucleation, barrier layers, and insolubility. From the standpoint of adhesion the principal benefits obtained from the ion plating process are ability to (1) sputter clean the surface and maintain it clean until the film begins to form; (2) provide a high-energy flux to the substrate surface, giving a high surface temperature, thus enhancing diffusion and chemical reaction in the surface region without necessitating bulk heating; and (3) alter the surface and interfacial structure by introducing high defect concentrations, physically mixing the film and substrate material, and influencing the nucleation and growth of the depositing film. Subsequently, it was found that the process gave improved surface coverage on rough surfaces and over nonplanar geometries. In addition, for thicker deposits it has been found that ion bombardment during deposition can cause morphological changes which may affect the physical properties of the thick deposits.^{5,6}

*Supported by the U.S. Atomic Energy Commission.

Figure 1 shows a typical ion plating system using a thermal vaporization source and a dc diode gas discharge to provide ion bombardment of the substrate. In a typical operation the precleaned substrate is placed in the vacuum system, the system evacuated to an ultimate pressure of $< 10^{-6}$ Torr, the evaporant is premelted and cooled with the shutter closed. The system is then backfilled with argon to a pressure of 0.1-1 ("bleed-back pressure") mTorr. The vacuum pump is then throttled to give a discharge pressure of 1-20 mTorr and a dc gas discharge is established at 2-5 kV dc and ~ 0.5 mA/cm² substrate current density. The surface is then sputter cleaned for a period of time which depends on the material, surface condition, and level of background contamination. At the end of the sputter cleaning portion of the process, the evaporator filament temperature is raised until the film material begins to evaporate. A shutter between the source and substrate is then opened, allowing the material to deposit on the substrate. The important step is to form the surface-coating interface without interrupting the ion bombardment. Of course, for a film to form, the deposition rate must exceed the sputtering rate.

Some attempts have been made to compare the advantages and disadvantages of the ion plating technique to other physical vapor deposition techniques^{7,8} (sputter deposition and vacuum evaporation). The most comprehensive of these is given in Ref. 7.

A number of variations of the basic ion plating system have been described. The fundamental premises of ion plating are concerned with ion bombardment of the substrate before and during film deposition; therefore, the main variations which have been reported deal with the origin of the depositing material (sources), the deposition environment, and source of bombarding ions.

SOURCES

A wide variety of source geometries have been described in Refs. 1 through 4. Recently the use of an inductively heated crucible in a gas discharge has been shown to be a very versatile technique for ion plating elemental and compound materials for a variety of purposes.^{9,10} Such a source must be carefully designed to prevent arcs from puncturing the induction coils. This can be accomplished by the proper electronic circuit design,¹¹ as is done in the "i-gun."[†] This type of source should be very useful for depositing large amounts of non-refractory materials. Using a reactive gas atmosphere in the discharge allows the deposition of oxides, nitrides, and carbides.

Previously ion plating using the disassociation of gaseous species was described and called Chemical Ion Plating.² Such a system is shown in Fig. 2. Recently there have been several descriptions of deposition systems using the decomposition of a gas in a gas discharge. In one

[†]Marketed by Endurex Corp., Box 11154, Dallas, Texas 75223.

such source, boron was deposited from BF_3 gas.¹² In another application an rf-induced plasma is used for gas decomposition and the deposition of a wide variety of oxides.¹³ This is the basis for the design of the "Sputarc" deposition system.[‡]

The ionization and deposition of "atom clusters" onto a negatively charged substrate have been described.¹⁴ This type of deposition system has been used for very high-rate deposition from a heated crucible by evaporating through a filament-supported gas discharge.

DEPOSIT MORPHOLOGY

It has been shown that ion bombardment of depositing material causes changes in the growth morphology of the resulting deposit. This is true whether the ions are of the same material as the deposit or if they are inert gas ions.^{5,6} The columnar morphology of thick deposits may develop due to geometrical shadowing if a rough surface develops because of substrate surface irregularities⁶ or may develop because of differences in nucleation and diffusion on different crystallographic planes.¹⁵⁻¹⁷ The problem of geometrical shadowing has been treated in the studies of step coverage and it is shown that a shadowed region will develop a "pipe" type of void through the film.^{18,19}

In ion plating using rf and dc sputtering targets as sources, it is interesting to note that the deposit morphology and the ability of ion bombardment to modify the deposit morphology differs greatly between the two techniques.⁶ Figure 3 shows the variation in density of chromium deposited from rf and dc sputtering targets as a function of substrate potential. Also shown is the variation of density obtained by e-beam ion plating and vacuum deposition with a substrate potential.⁴ In chromium the columnar structure which develops in thick deposits has a preferred orientation. This preferred orientation may be destroyed by ion bombardment during deposition and may even be changed from one preferred orientation to another. For instance, in the case of rf-sputtered chromium with a dc substrate potential, the preferred orientation changes from (211) at a floating potential (+50 volts) to no preferred orientation at -300 volts to a (200) orientation at -500 volts.²⁰ Ion bombardment during deposition may change the composition of alloy and ceramic deposits.²¹

GAS CONTENT

Ion bombardment before deposition may incorporate gas into the substrate surface that may be subsequently released, causing loss of adhesion.^{22,23} Ion bombardment during deposition may cause an increase or decrease in gas content of the film, depending on the film material, deposition source, deposition environment, and ion bombardment.²⁴

[‡]Marketed by Alcatel Vacuum Products, 7 Pond Street, Hanover, MA, 02339.

Ion bombardment during deposition has been used to deliberately incorporate insoluble inert gases in metals. For helium in gold, up to 40 atomic percent helium has been incorporated²⁵ and under some conditions, the incorporated gas appears to be finely and possibly atomically dispersed in the metal lattice.²⁶

Figure 4 shows the gas content in chromium films using both dc and rf sputtering target sources as a function of substrate potential. For dc sputtering with a dc substrate potential it is found that the oxygen content decreases dramatically with a small negative potential. This is the foundation of the "bias sputtering" technique, where it was found that a small negative substrate potential increases the purity of dc sputter-deposited films.²⁷ Note that the effect is not pronounced in rf sputter-deposited films.

In the chromium depositions, very little argon was incorporated at low substrate potentials but the amount increased with negative potential. The maximum amount of 5 weight percent occurred in rf sputter-deposited films at -400 volts substrate potential. At higher biases it is generally found that the argon gas content decreases, probably due to heating.

Film stress has also been shown to be a sensitive function of the deposition parameters.^{3,6,21,24} Not only can the magnitude of the stress be changed by ion bombardment during deposition but also the sign of the stress may be reversed.²⁰

APPLICATIONS

Numerous applications of ion plating have been cited in the reference. Several new applications have recently appeared. These include new work on the application of ion-plated film tribology²⁸ and the deposition of hard and wear-resistant coatings on tools.¹⁰ The ability of the ion plating process to cover steps, surface discontinuities, and to plate through holes is making the process attractive in some microelectronics applications. The non-line-of-sight deposition of ion plating makes the process attractive for depositing on thermally sensitive substrates where it is desirable to optically shield the substrate from the vapor source.

REFERENCES

1. D. M. Mattox, Sandia Laboratories Report, SC-DR-281-63 (1963); *ibid.*, *Electrochem. Technol.* 2, 295 (1964); *ibid.*, U. S. Patent 3,329,601 (1967).
2. D. M. Mattox, *J. Vac. Sci. Technol.* 10, 47 (1973).
3. D. M. Mattox, Sputter Deposition and Ion Plating Technology, Monograph of the Thin Film Division of the AVS (American Vacuum Society, 335 East 45th Street, New York, NY, 10017, 1973).
4. D. M. Mattox, "Recent Advances in Ion Plating," Proceedings of the 6th International Vacuum Congress, Kyoto, Japan, March 25-29, 1974, to be published in Japan. *J. Appl. Phys.* (supplement).
5. D. M. Mattox and G. J. Kominiak, *J. Vac. Sci. Technol.* 9, 528 (1972).
6. R. D. Bland, G. J. Kominiak, and D. M. Mattox, "Effect of Ion Bombardment on Thick Metal and Ceramic Deposits," Proceedings of the Conference on Structure-Property Relationships in Thick Film and Bulk Coatings, Vacuum Metallurgy Division of the AVS, January 28-30, 1974, San Francisco, CA, to be published in *J. Vac. Sci. Technol.* (July-August, 1974).
7. J. E. Varga and W. A. Bailey, *Solid State Technol.* p. 79 (December, 1973).
8. Vance Hoffman, *Solid State Technol.* p. 93 (December, 1973).
9. Gerald W. White, Proceedings of the Society of Automotive Engineers Meeting, May 14-18, 1973, Detroit, MI, Paper No. 730546; *ibid.*, *R&D Mag.* p. 43 (July, 1973).
10. Bernard Feinberg, *Manuf. Eng. Management*, p. 27 (January, 1974).
11. Gerald W. White, Endurex Corp., private communication.
12. J. P. Flemming, *J. Vac. Sci. Technol.* 10, 932 (1973).
13. M. Hecq and J. Van Cakenberghe, *Thin Solid Films* 11, 283 (1972); also 12, 453 (1972).
14. Toshinori Takagi, Isao Yamada, Kouichi Yanagawa, Masatoshi Kunori, and Shigenitso Kobiyama, "Vaporized-Metal Cluster Ion Source for Ion Plating," Proceedings of the 6th International Vacuum Congress, Kyoto, Japan, March 25-29, 1974, to be published in Japan. *J. Appl. Phys.* (supplement).

REFERENCES (cont.)

15. A. Van der Drift, *Philips Res. Repts.* 22, 267 (1967).
16. B. A. Movchan and A. V. Demshishin, *Fiz. Metal. Metalloved* 28, 653 (1969).
17. John A. Thornton, "Influence of Apparatus, Geometry, and Deposition Conditions on the Structure and Topography of Thick Sputtered Coatings," Proceedings of the Conference on Structure-Property Relationships in Thick Film and Bulk Coatings, Vacuum Metallurgy Division of the American Vacuum Society, January 28-30, 1974, San Francisco, CA, to be published in *J. Vac. Sci. Technol.* (July-August, 1974).
18. I. A. Blech, *Thin Solid Films* 6, 113 (1970).
19. J. L. Vossen, G. L. Schnable, and W. Kern, "Processes for Multi-level Metallization," Proceedings of the 20th National Symposium of the American Vacuum Society, October 9-12, 1973, New York, *J. Vac. Sci. Technol.* 11, 60 (1974).
20. R. D. Bland, J. K. Maurin, and S. F. Duliere, to be published.
21. D. M. Mattox and G. J. Kominiak, *J. Electrochem. Soc.* 120, 1535 (1973).
22. F. B. Kock, R. L. Meek, and D. V. McCaughan, Extended Abstracts of the 142nd National Meeting of the Electrochemical Society (October, 1972), Vol. 72-2, Abs. 250.
23. D. M. Mattox, *Thin Solid Films* 18, 173 (1973).
24. R.S. Nowicki, W. D. Buckley, W. D. Mackintosh, and I. V. Mitchele, "Effects of Deposition Parameters on Properties of RF Sputtered Molybdenum Films," Proceedings of the Conference on Structure-Property Relationships in Thick Film and Bulk Coatings, Vacuum Metallurgy Division of the AVS, January 28-30, 1974, San Francisco, CA, to be published in *J. Vac. Sci. Technol.* (July-August, 1974).
25. D. M. Mattox and G. J. Kominiak, *J. Vac. Sci. Technol.* 8, 194 (1971).
26. R. S. Berg, G. J. Kominiak, and D. M. Mattox, "Incorporation and Behavior of Helium in Co-Deposited Films," Proceedings of the 20th National Symposium of the American Vacuum Society, October 9-12, 1973, New York, *J. Vac. Sci. Technol.* 11, 52 (1974).
27. I. I. Maisel and P. M. Schaible, *J. Appl. Phys.* 35, 237 (1965).

28. Nobuo Ohmae, Tetsuo Nakai, and Tadasu Tsukizoe, "On the Application of Ion Plating Techniques to Tribology," Proceedings of the 6th International Vacuum Congress, Kyoto, Japan, March 25-29, 1974, to be published in Japan. J. Appl. Phys. (supplement).

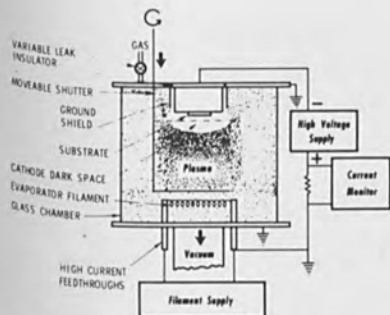


Fig. 1. Typical ion plating apparatus using a dc diode discharge and a resistively heated vaporization source.

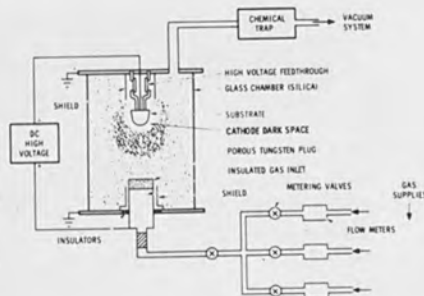


Fig. 2. Chemical ion plating setup for depositing films by decomposition of a gas. Another arrangement would be to establish an rf-supported discharge above the gas diffuser to aid in decomposition and ionization (similar to the "i-gun" or "Sputarc" source).

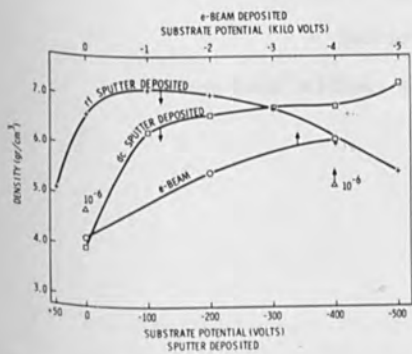


Fig. 3. Density of rf and dc sputter-deposited chromium films. Deposits labeled e-beam were made at 25μ argon pressure. Points labeled 10^{-6} were at 10^{-6} Torr.

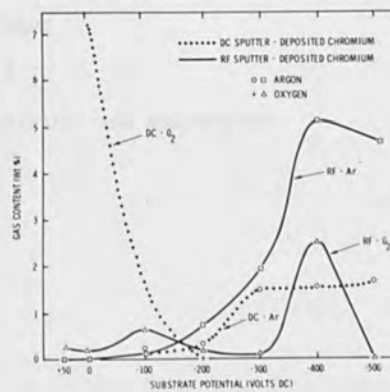


Fig. 4. Oxygen and argon content of ion-plated films using rf and dc chromium sputtering sources and a dc substrate potential.

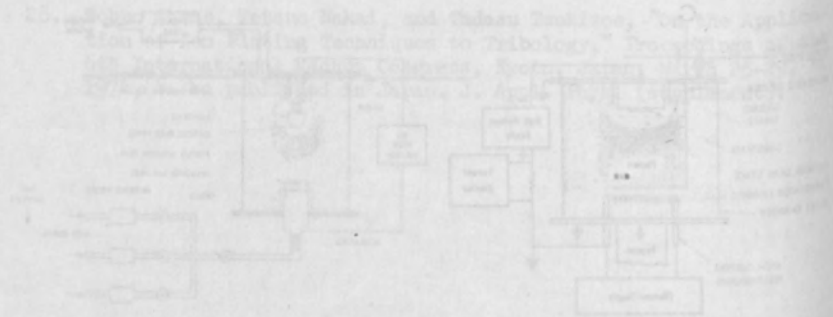


Fig. 2. Schematic for testing edge for separating film of decoupling of a gas. Another arrangement would be to establish an air-coupled discharge above the gas film to aid in determining position and location (relative to the "x-axis" or "y-axis" curves).

Fig. 1. Typical for testing edge using a double film - a charge and a reactively heated vaporization source.

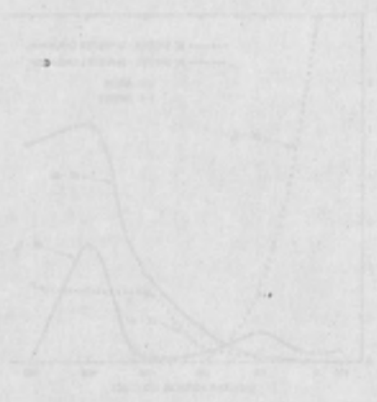


Fig. 3. Oxygen and nitrogen curves of low-pressure films used to determine edge - control surface and a 10-100000 potential.

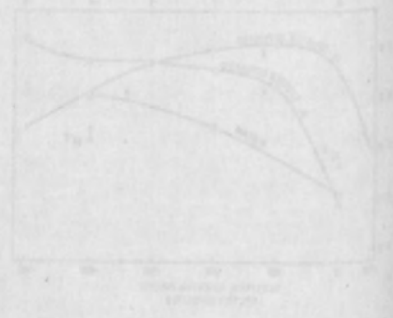


Fig. 4. Density of γ and δ separation - controlled chemical films. Potential labeled 10-100000 was at 25 μ vacuum pressure. Labels labeled 10⁵ were at 10⁻⁵ Torr.

... of the electron beam welding process...
... of the electron beam welding process...
... of the electron beam welding process...

PART II

HIGH POWER BEAMS

Section 1

Electron Beam Welding, Machining, and Evaporation

... of the electron beam welding process...
... of the electron beam welding process...
... of the electron beam welding process...
... of the electron beam welding process...
... of the electron beam welding process...
... of the electron beam welding process...
... of the electron beam welding process...
... of the electron beam welding process...
... of the electron beam welding process...
... of the electron beam welding process...

HIGH VOLUME PRODUCTION OF AUTOMOTIVE
COMPONENTS BY ELECTRON BEAM WELDING

H. A. James

SCIACKY BROS., Inc.
Chicago, Illinois

ABSTRACT

The electron beam welding of a wide variety of automotive components from elements of automatic transmissions, to catalytic reactor canisters, to distributor cam-shaft assemblies is now being accomplished at production rates of 500 to 1500 parts per hour, as a result of soft vacuum welding equipment and technology that has recently been developed.

This paper looks at the production capabilities of sequential versus concurrent performance of the steps of the welding process, and describes the essential role of rotary table workpiece feeding, special "sliding" vacuum seals, electrostatic detection and scanning of the weld path and electromagnetic beam steering, and "dedicated" mini-computers as process controllers, in attaining these new high volume levels of automotive component production.

I. INTRODUCTION

Electron beam weldings characteristic advantages of high weld quality, low joint shrinkage and distortion, minimal edge preparation, and a high level of process precision, have made it a unique and highly valued metal-joining process, as its rapid acceptance and widespread usage in the nuclear and aerospace industries for manufacture of critical components has demonstrated. ^{1/} However, acceptance of the electron beam welding process by the automotive industry, and by other industries which also view high-production capability as a paramount requisite for process acceptance,

has come about only after introduction of electron beam equipment of the type wherein the welding is performed in a soft vacuum. This capability to electron beam weld in a soft vacuum environment - as opposed to the hard vacuum environment in which the process was previously carried (and in which the electron beam itself always must be generated) - has made possible new ways of processing materials thru the welding machine and have multiplied the process productivity capability by a factor of ten to one-hundred over that which could be obtained when welding in hard vacuum. Of course, welding in a hard vacuum - i.e., at a pressure of 0.0001 Torr or less - is still a widely used form of electron beam welding; in fact, it is the preferred form whenever it is required that the electron beam must be as small as possible in diameter or must traverse long distances. But these beam characteristics are seldom required in automotive production electron beam welding applications, and therefore such welding can be done quite satisfactorily in a soft vacuum - i.e., at a pressure of 0.010 to 0.100 Torr - with the very important attendant advantage, due to the lesser time required to evacuate the welding chamber to these higher levels of pressure, that significantly higher rates of production are obtainable.

II. BASIC MACHINE OF THE SOFT VACUUM TYPE

Conceptually, the soft vacuum electron beam welding machine consists (see Fig. 1) of a gun chamber which is kept at a hard vacuum (less than 0.1 milliTorr) and a work chamber which is pumped to a soft vacuum (10 to 100 milliTorr) for welding. The two chambers are joined by a cylindrical passage of a diameter just sufficient to permit passage of the electron beam during welding.

A typical machine of this type is shown in Figure 2. It is a general purpose machine and is particularly well-suited to prototype welding development studies and low volume production runs. Access for loading and unloading of pieceparts is thru a side-hinged door (Fig. 3) and since the work chamber then returns to atmosphere, the passageway between the gun and work chamber is first sealed off by a valve to maintain the hard vacuum environment in the gun chamber. Production rates of 50 to 100 pieces per hour can be obtained in a machine of this sort depending on the various factors.

III. SMALL CHAMBER - BOTTOM DELIVERY - DIAL FEED

Of course, the exact production rate obtained in any soft vacuum welding application depends on the values of the following parameters:

- the volume of the work chamber employed to contain the workpiece and its tooling;
- the volumetric speed of the work chamber vacuum pump;
- the level of pressure at which welding is commenced;
- the length of the weld path;
- the speed of the beam along the path.

The soft vacuum welding machines seen in Figures 4 and 5 illustrate two important forward steps in improving production efficiency:

- the chamber size is reduced to the minimum necessary to contain the work and its tooling;
- a 2-station dial-feed table permits concurrent unload-load and evacuate-weld operations.

Typically, the evacuate-weld time is longer than the unload-load time. If, for example, the evacuate-weld time is 20 seconds and the unload-load time is 10 seconds, the production rate obtained when these operations are performed concurrently is 180 parts per hour, whereas if these operations had been done sequentially, the production rate would be only 120 parts per hour. Thus, in this example concurrent performance of certain of the steps of the welding process permitted a 50% improvement in productivity.

The two machines in Figures 4 and 5 also illustrate the versatility that can be effected thru good machine design to provide in a single machine-type the means for welding in both the horizontal (Fig. 4) and the downhand (Fig. 5)

welding positions. As a result of that broad application capability, this type of soft vacuum electron beam welder has been extensively employed in the automotive industry to assemble 3-speed and 4-speed automatic transmission components (see Figure 6). ^{2/}

IV. SMALL CHAMBER - SLIDING SEAL - DIAL FEED

A. Vacuum Considerations

The example of the previous section makes it quite apparent that any further increases in process productivity have to come thru reduction of the pumpdown time. One approach to this objective is "batch" loading of parts - in effect, thereby making the pumpdown time per part to be $1/N$, where N is the number of parts in the batch. However, this ideal result is seldom realized because of the proportionate increase in chamber volume, and consequently in pumpdown time, that is required to accomodate each additional part. A better approach is to design the machine so that the pumpdown is accomplished in several stages and these stages are performed concurrently. Then significant increases in rates of production are possible.

Thus, if one assumes that the evacuate-weld time of the previous example consists of 15 seconds pumpdown time and 5 seconds weld time, but now assumes further that the pumping is done in 2 stages such that the initial 10 seconds are done in Machine Station #1, and the final seconds of pumping followed by the 5 seconds of welding are done in Machine Station #2, then these being done concurrently, the production rate is 360 parts per hour. Of course, some finite time is required for indexing the parts from one station to the next. If one assumes that the index time is 1 second, then, where the weld time is 5 seconds, the maximum possible rate of production is 600 parts per hour; in this case the 15 seconds of pumpdown time could be provided by means of 3 pumping stations located ahead of the welding station, used in sequence at 5 seconds each.

The equipment concept described above has been very successfully applied to the production welding of a considerable variety of automotive components - from elements of automatic transmissions, to catalytic reactor canisters, to distributor cam-shaft assemblies - with production rates ranging

from 500-1500 parts per hour being realized.

Essential to the successful implementation of this concept have been

- the use of rotary table feeding of the workpieces through the machine stations,
- the development of practical means of vacuum sealing the moving surface of the rotary table containing the work-holding cavities, to the stationary surface of the plate which contains the pumping and welding stations,
- the use of electrostatic seam scanning and electromagnetic beam steering techniques to locate the beam on the joint seam and then drive it along the path,
- and, in conjunction with the preceding point, and also as a means for providing the necessary control of the machine sequence, the use of "dedicated" mini-computers programmed to instantly and continuously assess the operational readiness of the welding machine and the correctness of its operating parameter values.

Thus, in this way it has been possible to achieve new levels of electron beam welding production rates that are not only acceptable, but, in fact, most attractive for high volume production of automotive components, while providing at the same time a welded product of superior quality.

B. Rotary Table Vacuum Sealing

The patented ^{3/} sliding seal concept is a primary feature of the machine (Fig. 7) and well-proven in production use. These vacuum seals are contained within a stationary sealing plate (Fig. 8) that covers a portion of the rotary indexing table and is equipped with roller assemblies to allow rotation of the dial feed table beneath it. The electron beam gun mounts on top of the seal plate and com-

municates directly with the piecepart nest in the table below it through an opening in the seal plate.

The unique sliding seals create two distinct vacuum areas: the inter seal area where the pressure is reduced to 100 to 500 milliTorr and the welding chamber area where the pressure is reduced to 10 to 50 milliTorr. As a workpiece nest slides beneath the outer seal, it enters into the inter seal area. During the dwell time of the dial-feed table, the nest is pumped to a vacuum level relatively close to that at which the workpiece will be welded. During the next index, the nest moves beneath the inner seal and into the welding area where the final reduction of pressure is made and the part welded. This sequence of events is illustrated in Figure 9.

C. Seam Scanning & Beam Steering Considerations

An automatic electron beam scanner system based upon the operation of the SCIAKY Reflectron Scanner ⁴, determines the presence and the exact position of the weld joint.

As the piecepart is indexed into the weld position, the electron beam gun is turned on and a special control circuit causes the beam to oscillate across the weld joint at approximately 60 Hertz at low power. A pulser circuit momentarily interrupts the scanning circuit, allowing the beam to be projected directly to the workpiece. An antenna mounted on the base of the electron beam gun receives reflected electrons from the weld joint.

The weld joint itself reflects differently than the areas on either side of the joint. This difference in reflections is discerned by a special electronic circuit in the sequence logic controller. The controller remembers where the weld joint is located and once scanning has been completed, the controller automatically welds the joint by deflecting the electron beam along the joint path at weld power. Every weld joint is automatically scanned before it is electron beam welded. Like the other functions of the Automatic Monitoring System, tolerance bands can be preset on the scanner. That is, should the weld joint be found by the scanner to exceed the preset amount to either side of the nominal position of the weld joint, the welder

will shut off and not weld that part.

The beam can be programmed to follow a prescribed welding path, thus eliminating work manipulating devices. The beam axis normally passes through the center of the electron gun and the magnetic focus coil. To deflect the beam from this axis, an assembly of two or four magnetic coils is placed below the focus coil; the deflection coils axes are radial to the normal beam path (Fig. 10). A controlled current is then applied to the coils in a manner that produces longitudinal or transverse beam deflection. Time-variable patterns can be generated by the use of appropriate signal voltages. The signal frequency establishes the beam's path speed and the magnitude sets the size of the pattern. The weldment is fixed, while the beam traces the path. The deflection current is scaled to the square root of the accelerating voltage so that the deflection is automatically corrected to allow programming of the accelerating voltage during the weld process.

D. Computer Control & Monitoring System

In keeping with the latest developments in control technology, a DNC computerized system controls part positioning, monitoring, and weld setting functions, including beam deflection. Communication between the computer and the essentially analog welding hardware is carried out by using a specifically designed electronic interface digital to analog converters and digital logic circuits. The operational communications medium for programming input is by pre-punched tape or through an on-line teletypewriter (Fig. 11). A Go/No-Go monitoring system automatically and continuously monitors the critical functions of the welder, providing a 100% reliability check on the electron beam welding operation (Fig. 12). The monitoring system automatically monitors the following:

- Beam power as function of accelerating voltage and beam current.
- Vacuum level of the gun chamber.
- Focusing current.

A high and low limit tolerance band for any of these functions can be selected and preset in the monitoring system. Should one or more of the functions vary more than the preset tolerance, an indicator light shows which function is in variance and whether this variation is high or low. At the end of the weld sequence, the welder "locks out" and cannot be recycled until the malfunction is corrected and the system reset.

E. Automotive Applications

1. Shown in Figure 13 are two of several identical, six-station, soft vacuum, sliding seal, dial feed type electron beam welding machines for production of automotive components; the simulated transmission part pictured in Figure 14 is illustrative of one of the many kinds of automotive applications that are so very effectively carried out in this kind of machine. The production rate of 500 to 800 parts per hour is facilitated by a twelve-station auxiliary loading table (Fig. 15) which is synchronized to feed parts via a part translator to the main dial feed table.

All operations are performed automatically after manual placement of the pieceparts on the load table; the sequence (referring to Fig. 16) is:

- in the weld table loading station, the loading translator moves the piecepart assembly from the load table to the weld table and places it in the table nest that is waiting to receive it.
- in the probe station, a mechanical device, which is actuated by the forward motion of the loading translator, pushes the piecepart assembly into the proper down position for welding; the device incorporates means which stop the machine if a part is missing or misplaced in the nest.
- in the outer seal station, the nest is evacuated to a pressure of 100 to 500 milliTorr.

- in the inner seal and welding station, the nest is evacuated to a pressure of 10 to 50 milliTorr; the nest tooling is actuated to bring the piecepart assembly into fixed dimensional reference; the electron beam gun turns on at low power and scans the joint to be welded; the gun turns on at welding power and its beam is electromagnetically moved along the scanning-confirmed path of the weld joint; the nest tooling is de-actuated.
- in the idle station, no action occurs.
- in the unload station, each welded assembly is lifted out of the table nest by an unloading translator which moves it onto a set of guide rails; the next cycling of the unloader moves this welded assembly into an unloading chute; if it does not exit the chute, the machine stops.

2. Two examples of eight-station dial-feed type machines for larger components are seen in Figures 17 and 19. In both instances, the pieceparts are manually loaded using one or two operators but are automatically unloaded. Production rates of 600 to 900 parts per hour are attained. The sequence of operation of these machines is essentially the same as that described above. Figure 18 gives a close-up view of the weldment unloading mechanism of the first machine; Figure 20 is a view of the probe station of the second machine. The latter machine is particularly interesting because it has two electron guns which are operated simultaneously, each gun making one-half of the piecepart perimeter weld. Both machines employ dedicated computers and solid-state logic to define the irregular weld path and deflect the electron beam there along.

3. The final example to be presented of high production, soft vacuum electron beam welding is the mass production of distributor cams at the General Parts Division of the Ford Motor Company, Ypsilanti, Michigan.

The distributor cams are used for 4, 6, and 8 cylinder engines. It is composed of two parts - a plate and a camshaft (see Figure 21). The plate is of low carbon, mild steel which has been heat treated in a nitriding atmosphere, while the camshaft is 1144 steel which has been heat treated on the cam portion only.

A deep narrow annular weld joins the plate to the end of the camshaft. The weld penetration is 100% and the weld does not project above the top surface of the plate. There are two beam passes per weld, utilizing a circular beam deflection system. During the last three-quarters of the second pass, a taper-out control is used. In effect, this feature diminishes beam intensity to provide a smoother surface to the weld. The welded part requires no finishing. The production rate of the machine is 1200 to 1500 parts per hour. In the first nine months of its operation, this machine produced over 3 million distributor cams.

The sequence of operation of this twelve-station dial-feed machine is noteworthy since it is completely automatic, the assembly components being fed from vibratory hoppers.

- The sequence of operation begins at Station 1 of the dial feed table (see Figure 22). If all the probes are clear (in the "up" position) and the previously ejected piecepart has been counted, a cam is automatically loaded into a tooling nest from the cam load hopper.
- At Station 2 the cam is oriented and set onto fixed locators in the nest. If a cam has not been loaded, a probe sensor at 3 will cause this omission to be retained in the memory circuitry. This will prevent loading of a plate at 4 and indicate NO WELD when the nest reaches the welding station.
- The plate is loaded onto the cam from the plate hopper at 4, and at 5, a probe senses whether the plate is in the nest. If not, the circuitry will insure that no weld occurs when the nest enters the weld chamber,

or it can be programmed to stop the machine sequence. Number 6 is an idle station.

- At Station 7 and 8, the nest enters, first the outer chamber for pre-pumping, then the inner chamber. A circular beam deflection system is used to weld this particular assembly, allowing the assembly to remain stationary.
- Upon index, the welded assembly passes from the inner (weld) chamber to the outer vacuum chamber, which is Station 9. The next index is through the outer chamber sliding seal to 10, another idle station, and on to 11 - also idle.
- At Station 12 (machine's complete cycle), a pneumatic ejection mechanism lifts the assembly from the nest by grasping the plate. As the ejection arm moves toward the unloading chute, a feeder type limit switch determines whether the cam-to-plate has been welded. If not, the ejection arm will complete its motion and the machine will stop. The unwelded parts can be removed manually and the sequence restarted. When the arm moves over the chute with a welded assembly, it is released. As the part drops into the chute it breaks a photocell beam which counts the completed assembly. If the beam is not broken (indicating that nothing was unloaded), the arm will complete its return cycle and the machine will not index.

Since all operations are effected concurrently (load, unload, orientation, pre-pumping, weld, etc.), the production rate of the machine is paced by the sum of the index and weld times. These total about 2.4 seconds and thus the production rate is approximately 1500 parts per hour.

V. CONCLUSION

This paper has reviewed the basic considerations that define the production capabilities of electron beam welding machines of the soft vacuum type and found that they are generally better suited for high production welding than are machines of the hard vacuum type. Study of the several means whereby pieceparts can be processed thru the vacuum welding environment has been found to show that the use of rotary table feeding, employing a sliding seal concept, provides a highly efficient and practical way of maximizing process production capability.

The use of "dedicated" mini-computers and solid-state logic for process control, together with electrostatic seam scanning and electromagnetic beam steering techniques have also combined to maximize operational readiness and process efficiency.

In summary then, the several high production automotive applications that have been presented, simply illustrate that the sliding seal, dial-feed, soft vacuum concept provides metalworking users, for the first time, with a truly high production automated electron beam welding capability.

References:

- 1/ H.A. James, "Electron Beam Welding Equipment: Process Parameters, Limitations and Controls", 1st ELECTRON BEAM METALLURGICAL PROCESSING SEMINAR, Oakland, Calif., Feb., 1971
- 2/ Automotive Industries, Sept. 15, 1972, pp. 29-33
- 3/ U.S. Patent No. 3,742,365
- 4/ U.S. Patent No. 3,609,288

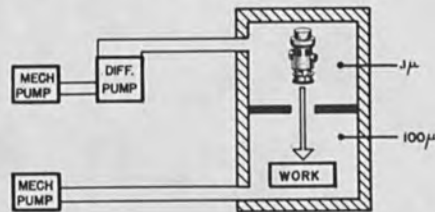


Fig. 1 Soft Vacuum Electron Beam Welding Machine Concept.

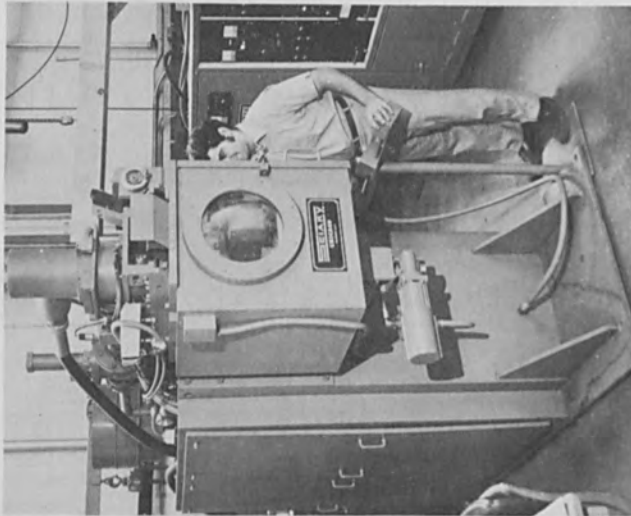


Fig. 2 General Purpose, Soft Vacuum
Electron Beam Welding Machine.

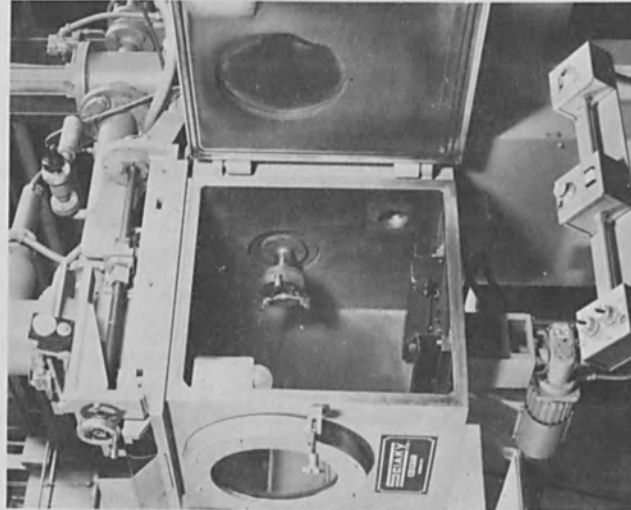


Fig. 3 Interior View of 4 cu. ft.
Vacuum Welding Chamber.

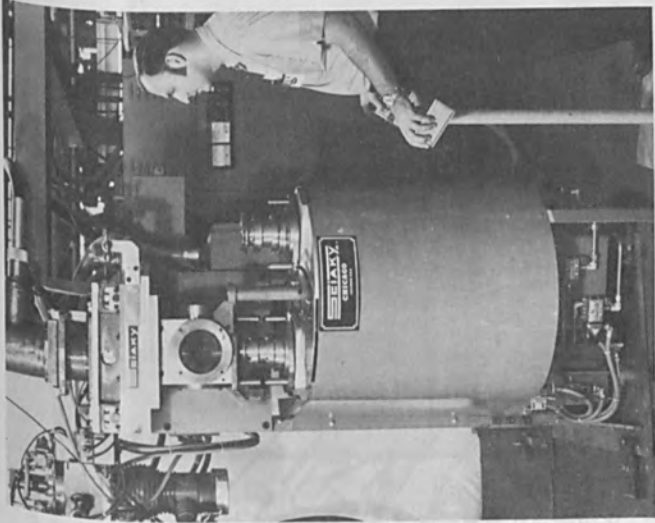


Fig. 5 Small Chamber, Bottom Delivery, Dial-Feed, EBW, Welding in DOWNHAND Position.

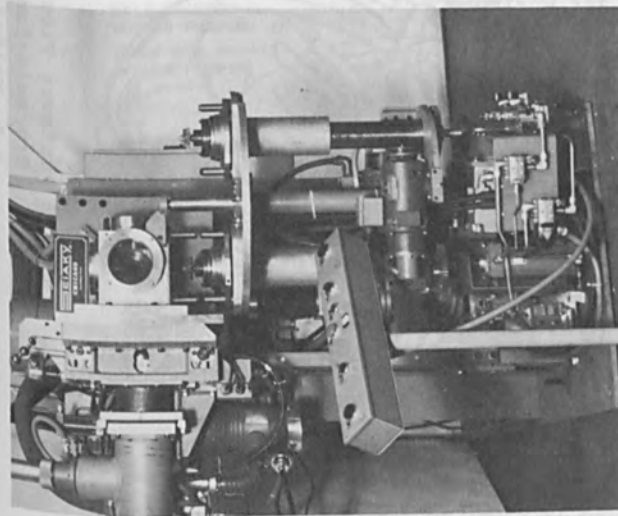


Fig. 4 Small Chamber, Bottom Delivery, Dial Feed, EBW, Welding in HORIZONTAL Position.

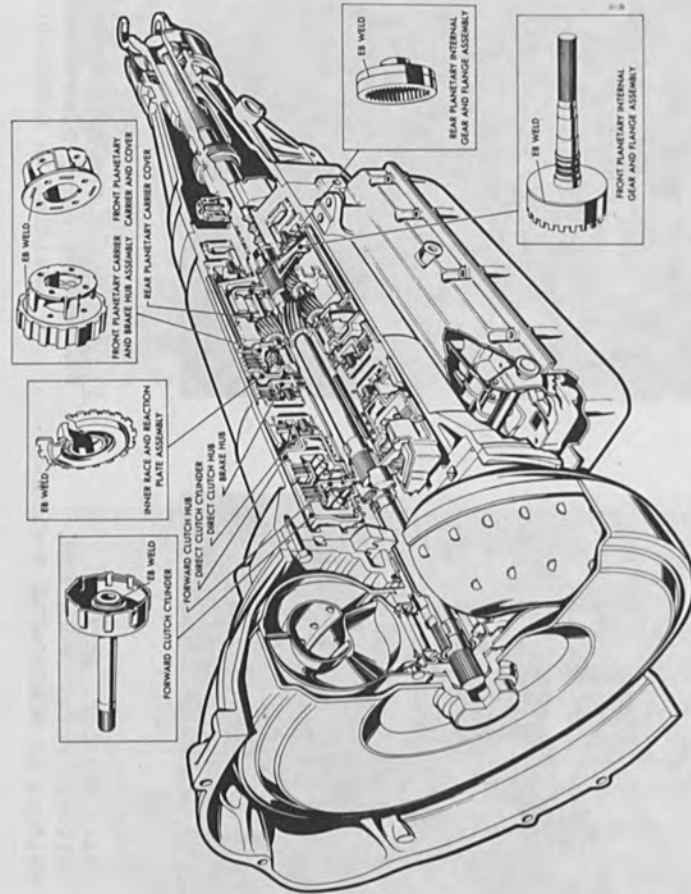


Fig. 6 Cutaway View of Three-Speed Automatic Transmission Showing Location of 5 E.B. Welded Components.

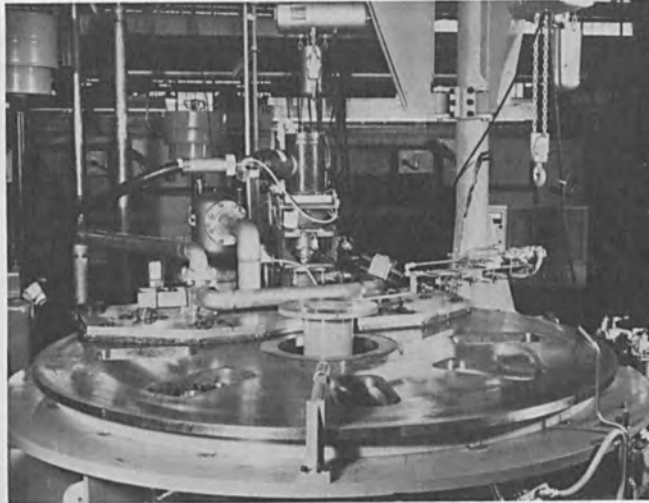


Fig. 7 View of Soft Vacuum Electron Beam Welder Rotary Table & Sliding-Seal Plate.

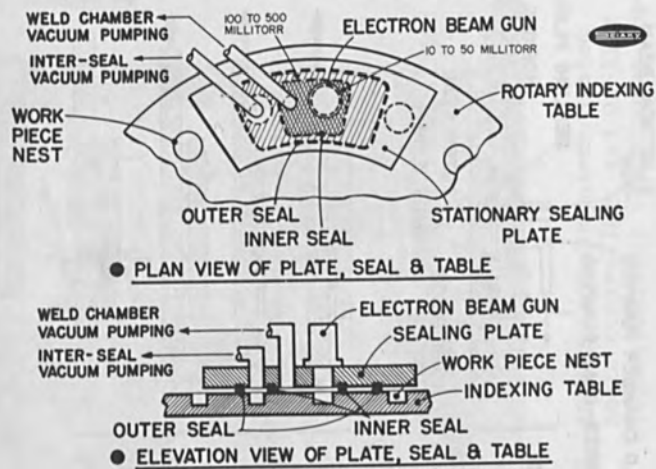


Fig. 8 Schematic View of Mechanical Arrangement of Seal Plate, Sliding Seal, & Rotary Table.

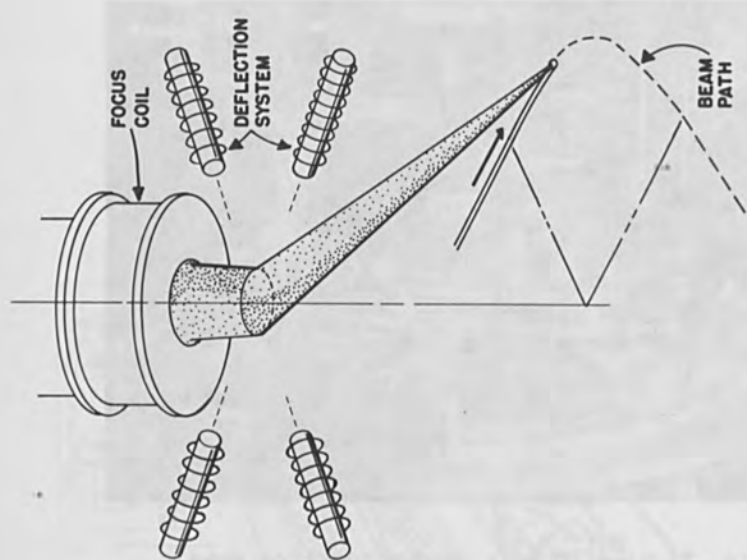


Fig. 10 Electromagnetic Deflection of Electron Beam to follow Complex Weld Joint Path.

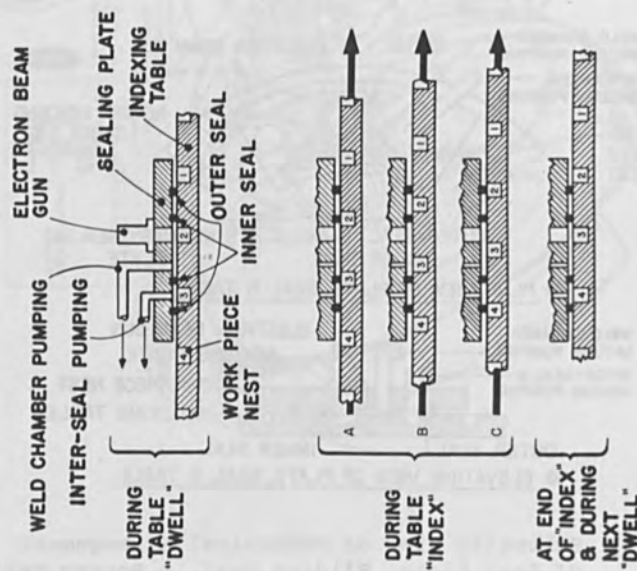


Fig. 9 Mechanical Relationship of Plate, Seal & Table during "INDEX"

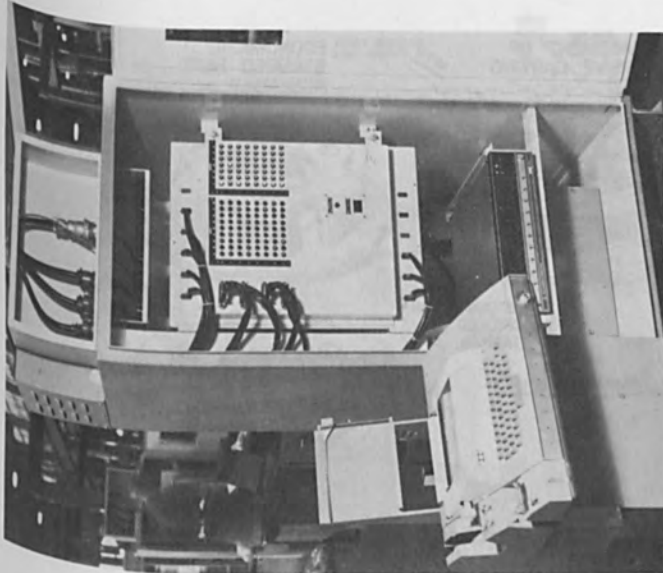


Fig.11 "Dedicated" Computer; System Logic Controller; and On-line Teletypewriter for Program Input.

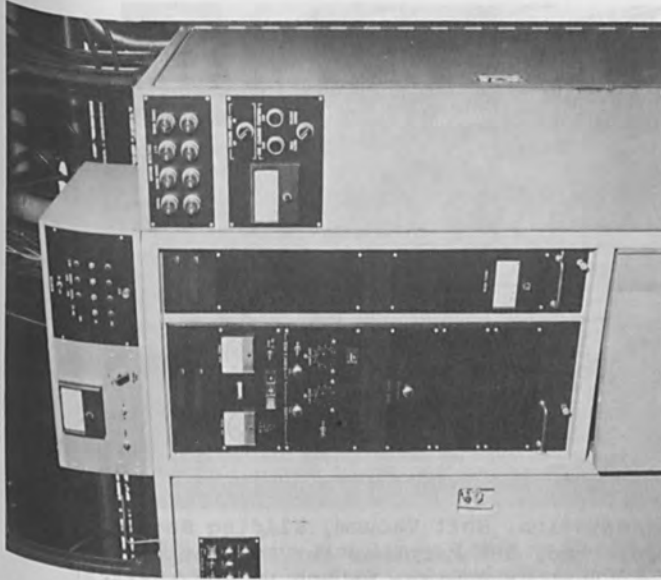


Fig.12 Sequence Control Cabinets with Top-Mounted Function Monitor and Seam Scanner.

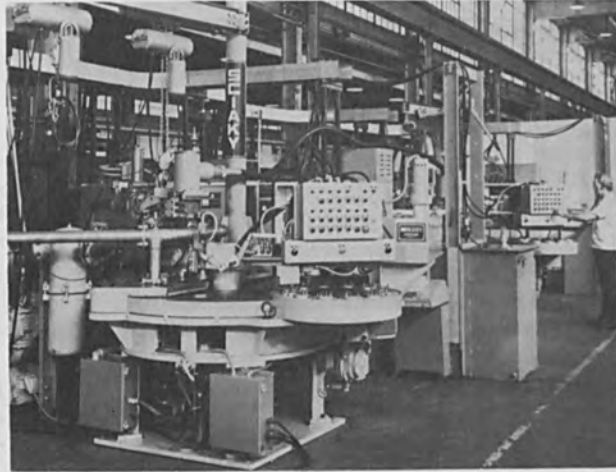


Fig.13 Six-station, Soft Vacuum, Sliding Seal Dial-Feed, EBW Machines for Automotive Component Production at 500 to 800 parts/hr.

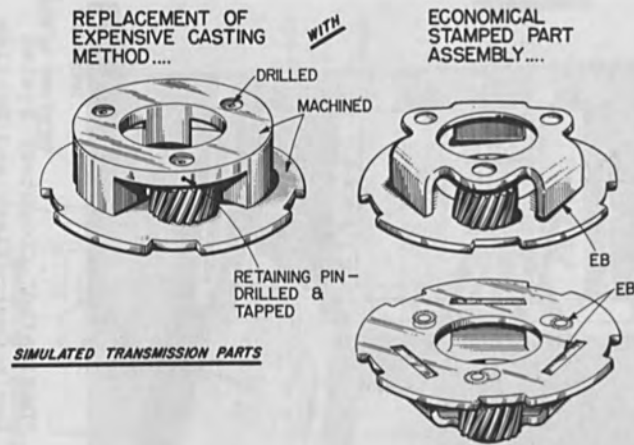


Fig.14 Typical Automotive Application - Mechanical Casting is Replaced by Stamped, Formed and E.B. Welded Sheet or Plate.

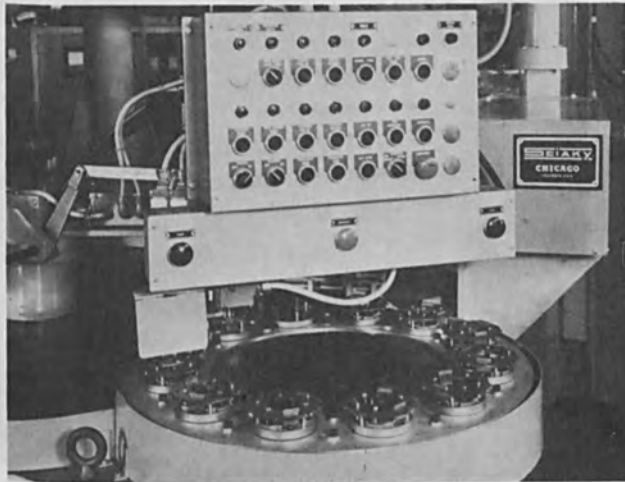


Fig.15 12-Station Auxiliary Loading Table to Serve (6-Station) Main Welding Table.

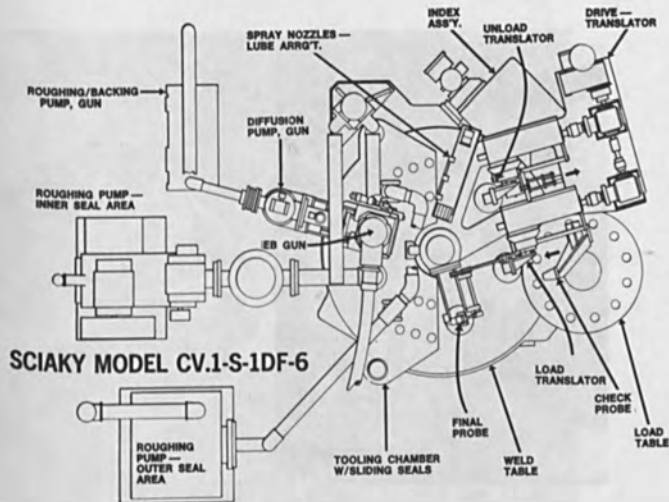


Fig.16 Schematic Layout: 6-Station, Sliding Seal, Dial-Feed, Fully Automated E.B. Facility.

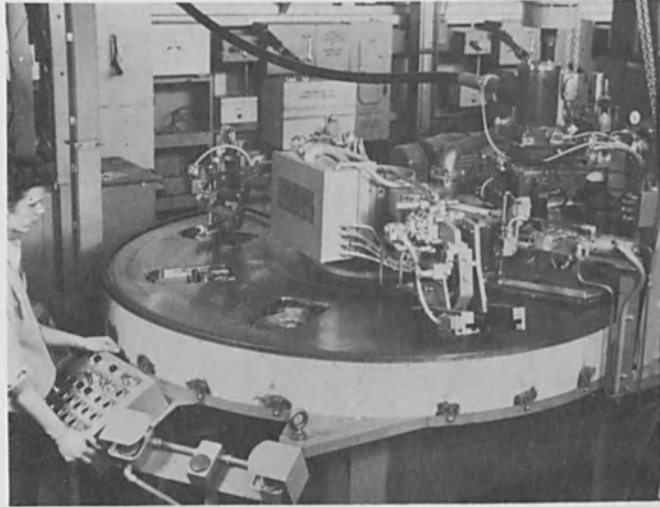


Fig.17 8-Station, Dial-Feed, EBW Machine for Automotive Component Production.

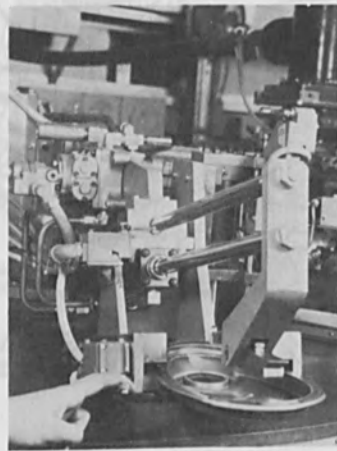


Fig.18 Close-Up View of Weldment Unloading Mechanism and Station.

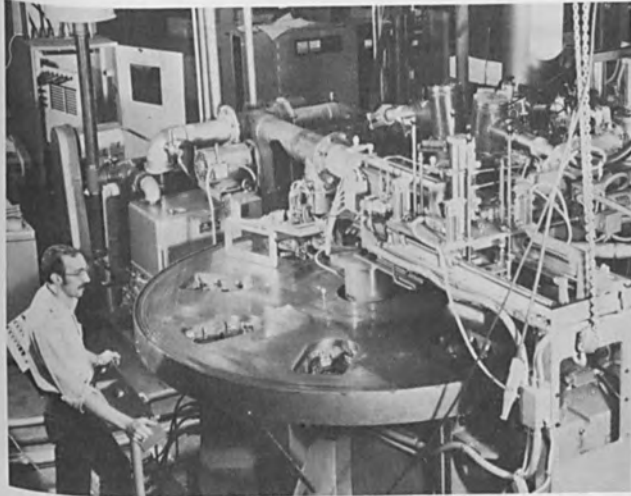


Fig.19 Two-Gun, 8-Station, EBW Machine
for Automotive Component Production.

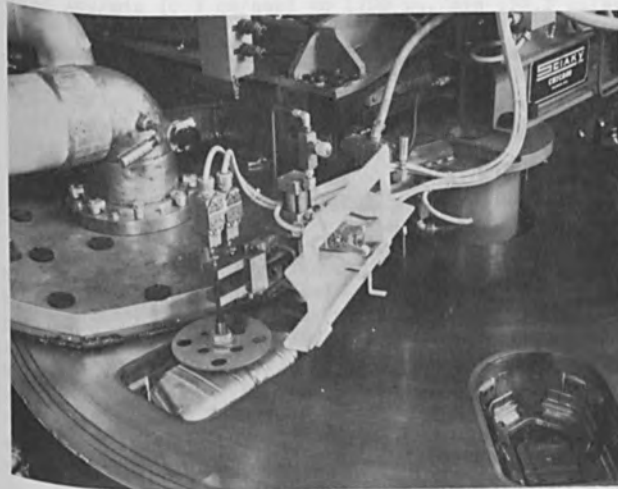


Fig.20 View of Probe Mechanism & Station.

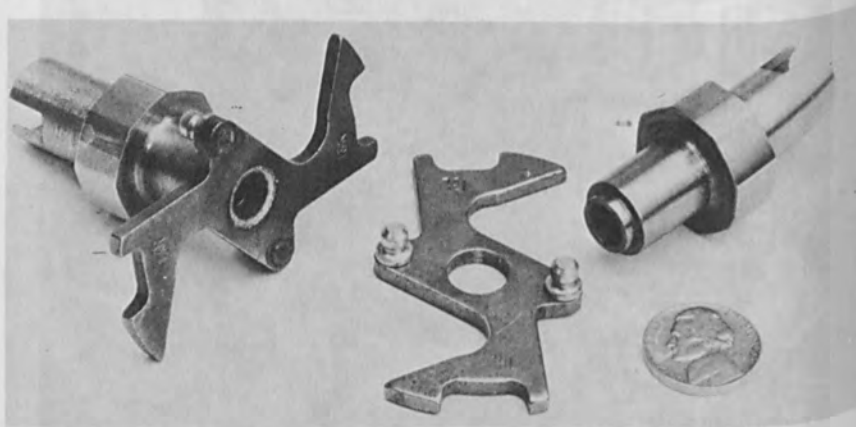


Fig.21 Distributor Cam Assembly for 4, 6, & 8 Cylinder FORD Automobiles: (l.) Welded Assembly; (r.) Assembly Detail Parts.

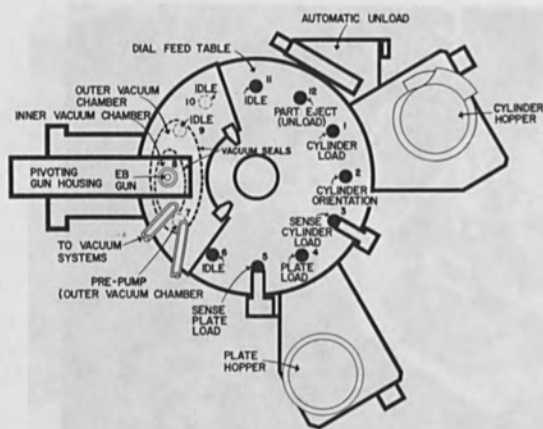


Fig.22 Schematic Layout: 12-Station, Sliding Seal, Dial-Feed, Fully Automated E.B. Facility That Welds the Distributor Cam at 1200 to 1500 parts/hr.

CONSIDERATIONS OF NONVACUUM ELECTRON BEAM WELDING
CAPABILITIES AND APPLICATIONS

Joseph M. Wells

Westinghouse Electric Corporation
Research Laboratories
Pittsburgh, Pennsylvania 15235

ABSTRACT

Nonvacuum Electron Beam Welding (NVEBW) is a relatively recent advanced metals joining technique which has generated considerable interest as a fully automatic, high productivity fusion welding process. Two aspects of NVEBW, namely (1) high speed welding at greater than 100 in./min (4.24 cm/sec) and (2) heavy section - single pass weldments of 1 in. (2.54 cm) or greater are exploitable. A discussion of process parameter effects on penetration depth, cross sectional profile, bead topography and weldment quality is presented for 1010 carbon steel, 5083 aluminum, 304 stainless steel and OFHC copper. General process parameters of interest include power levels to 36 kW, stand-off distances from 1/4 in. (0.62 cm) to 1 in. (2.5 cm), welding speeds of 12 in./min (0.5 cm/sec) to 1200 in./min (50.8 cm/sec) and helium or air gas effluent. Ancillary NVEB Welding Techniques of auxiliary inert gas shielding and wire feed are also discussed. Problem area of weld bead topography degradation is described. Finally, some specific examples of industrial applications are briefly reviewed.

1.0 INTRODUCTION

The chronology and development of Electron Beam (EB) Welding has been well documented (Refs. 1-3). Essentially there are three basic modes of electron beam welding, namely; high (hard) vacuum, partial (soft) vacuum, and nonvacuum (atmospheric or out-of-vacuum). All EB welding modes employ a well defined beam of high speed electrons which transfer their kinetic energy to the workpiece upon impact. By concentrating the total kinetic energy of the impacting electrons into a small area on the workpiece surface, the resulting high power density ($\sim 10^6$ watts/cm²) produces a more efficient fusion penetration mechanism which is not dominated by thermal conduction as is the case in more conventional fusion arc welding processes. Consequently, EB welding results in higher weld penetration depth to width ratios as

well as appreciably greater single pass weld penetration depths than with other fusion welding processes. In addition, a lower total heat (or energy) input is transferred to the workpiece which leads to less distortion or warpage and a significantly smaller heat-affected-zone (metallurgically altered base metal structure). Furthermore, process welding speeds achieved with EB are substantially higher than with more conventional types of fusion welding. These recognized process attributes of EB welding, offer unique technological and manufacturing productivity advantages which are the basis for the wide and growing interest in the field of electron beam welding.

The major impediment to an even wider utilization of EB welding by the general industrial welding community has been the physical size restriction and the unacceptably long delay time associated with either full or partial evacuation of the special vacuum chamber in which the workpiece was located. For this reason, most early applications were identified and developed in the aerospace industry where the relatively low volume and exceptionally high quality requirements are more tolerant of the chamber evacuation delay. More recently (Refs. 4-7), the development of nonvacuum electron beam welding (NVEBW) has eliminated the vacuum work-chamber pumping requirement and thus brought EB welding to the more numerous, although perhaps less exotic, broad industrial high productivity welding application areas.

2.0 NVEB WELDING PROCESS CONSIDERATIONS

The prime objective of any industrial metals joining process or technique is to achieve an acceptable quality joint in the most expeditious and economically favorable manner. To accomplish this objective, a welding or manufacturing engineer must consider many important aspects of the total joining operation which affect both the selection and the qualification of a particular process. Several considerations relating to the effective utilization of the NVEBW process are discussed below.

2.1 Definition and Perspective

NVEBW may be defined as a non-contact fusion welding process employing a high power density beam of electrons which impinge upon a workpiece located at atmospheric pressure completely external to the small vacuum chamber in which the electron beam is generated. Depending upon one's welding experience, NVEB Welding may be considered as either: (1) an evolution of EB welding from high vacuum, through partial vacuum up to atmospheric pressure, or (2) as an extension of more traditional fusion welding processes from gas tungsten arc (GTA) to plasma arc (PA) to NVEBW with the respectively increasing higher power density of an independently controlled heat source being employed.

Contrary to the general impression unfortunately made too often in describing many new joining processes, NVEBW is realistically not the "ultimate" metals joining technique which will resolve all joining problems. There is not now, nor will there be, such a single ultimate or universal metals joining process to best suit any and all applications. Like all welding processes, NVEBW has its own discrete characteristic process advantages and liabilities (See Tables 1 and 2). Moreover, the invariant principles of metallurgy and physics, of course, remain applicable. One must not ignore or forget such principles in attempting to employ the NVEBW process, but rather learn to exploit them in a logical and intelligent manner.

2.2 Beam Power

Beam power levels (i.e. the product of the accelerating voltage and the beam current) of 12, 24 and 36 kilowatts are available with commercial Westinghouse NVEBW Systems. The effect of beam power on weld penetration depth is shown to be almost linear up to 36 kW (see Figs. 1 and 2). The level of penetration per incremental kW of beam power increases appreciably as the welding speed decreases. Penetration depths are greater in 5083 aluminum than in 1010 carbon steel for the same welding conditions. The change in the weld cross-sectional profile of 5083 aluminum as a function of increasing beam power is shown in Fig. 3. The increased depth to width ratio as well as the increased penetration depth with increasing NVEB power level is clearly indicated.

A further indication of the effects of beam power level on penetration depth is shown in Figs. 4 to 6. Here, power levels from 3 up to 36 kW are shown parametrically with depth of weld penetration and welding speed as the dependent and independent variables, respectively. High penetration depths of 1.5 in. (3.8 cm) and more are attainable in carbon steel with 36 kW at a welding speed of 24 ipm (1.0 cm/sec) or less. While the same penetration depth is attainable in aluminum at 50 ipm (2.1 cm/sec) under otherwise identification conditions. The depth of penetration (DOP) at a given power level decreases quite rapidly with increasing welding speed at lower speeds and then more slowly as welding speeds increase beyond 120 ipm (5.1 cm/sec). The DOP attainable at speeds of 360 ipm (15.3 cm/sec) is still quite appreciable.

2.3 Standoff Distance

Another consideration with NVEBW is the standoff distance which is defined as the separation between the outer beam exit chamber surface and the forward surface of the workpiece being welded. Because the power density of the electron beam is gradually dissipated by collisions with air molecules (or auxiliary shielding gas if used), the

effective working or standoff distance is kept relatively small, approximately 2 in. (5 cm) maximum with the present 36 kW systems. Such relatively close working distances, while significantly less than those typical for high or partial vacuum EB welding, are, nevertheless, appreciably larger than standoff distances associated with other more conventional arc fusion welding techniques such as SMA, GMA, or GTA. Figure 7 demonstrates NVEB weld penetration depth as a function of standoff distance with both helium and air gas effluent. The penetration depths attained with the lower atomic number helium gas effluent is approximately twice that achieved with the more dense air effluent. While penetration depth decreases appreciably as the standoff distance increases, significant penetration is still attained at distances of 1 in (2.5 cm) and greater.

2.4 Energy Input

A further significant point demonstrated in Fig. 7 is the difference in penetration especially at the lower standoffs for identical energy input conditions. For example, with 5083 aluminum welded at 3/8 in. (\approx 1 cm) standoff and with air effluent, the penetration depth with 24 kW and 240 ipm (10.2 cm/sec) is approximately 25% greater than with 12 kW and 120 ipm (5.1 cm/sec) even though the energy input per unit length of weld (E/L) is constant at 6 kilojoules/in. (2.4 KJ/cm). An additional demonstration of the invalidity of assuming (as is often done) identical welding results for constant energy input/unit length of weld is shown in Fig. 8 for AISI 1010 carbon steel. Here we see that the weld penetration depth at constant E/L becomes appreciably greater for the higher power level curves as the E/L ratio becomes larger. This differential in weld penetration at the higher power levels cannot be due explicitly to the higher power level per se because the total energy input for a given E/L ratio is the same. This differential can be explained, however, on the basis of a higher power density occurring with the higher power levels since the relative beam "spot" areas are comparable at a constant standoff regardless of the power level.

2.5 Weld Width and Depth/Width Ratio

Additional weld profile parameters of interest are the width (W) and the depth to width ratio (DOP/W). Because NVEB weld cross sections can vary from a deep almost uniformly narrow profile to a wide top face with a narrow root depending upon the specific welding conditions (see Fig. 9), the widest portion of the weld is used herein as a worst case and is designated W_F . For 1010 carbon steel, the variation in W_F is shown in Fig. 10a as a function of standoff for a power level of 24 kW, speed of 120 ipm (5.1 cm/sec) and with helium effluent. The W_F with air effluent would be somewhat greater for the identical welding conditions. The corresponding DOP/ W_F ratios as a function of

standoff is shown in this same figure. In general, the W_f decreases and the DOP/W_f increases as the power level increases, as the standoff distance decreases and with helium versus air effluent gas. Increasing speed also decreases the W_f and the DOP/W_f ratio as shown in Fig. 10b.

2.6 Ancillary NVEBW Techniques

Generally, NVEB weldments are autogenous, i.e. joints are made between two or more adjacent pieces of the base metal without the addition of a supplemental filler metal. However, such filler metal can be added for those applications where either weld appearance, joint fit-up or particular metallurgical constraints require an increased metal volume or an alteration in the chemical composition of the weld metal. Dissimilar metals which are not metallurgically incompatible can be welded with NVEBW and filler metal, properly selected, is often quite beneficial.

Although often not required, with carbon or stainless steel, a protective auxiliary inert shielding gas (not to be confused with the previously mentioned gun column effluent gas) can be effectively utilized to facilitate the welding and improve the quality of certain more reactive metals such as aluminum and titanium alloys. For example, Fig. 11 demonstrates the considerable weld quality improvements achieved when using argon auxiliary gas shielding when NVEB welding a common Ti-6Al-4V titanium alloy. The somewhat wider but more uniform weld profile with the argon gas shielded weld is due to the reduced power density caused by the greater molecular weight or argon versus air shielding gas.

2.7 Weld Topography

A final process consideration to be mentioned herein is the weld surface appearance or topography. A smooth, bright and uniformly convex weld bead is generally desired to provide both good weld integrity and appearance. However, under certain process welding conditions, a condition of weld topography degradation can be induced with all fusion welding processes. One example of weld topography degradation with NVEBW is shown in Fig. 12 where a very high speed weld bead in low carbon rimmed steel sheet has formed as an unstable rope-like column (roping) with periodic swelling and considerable undercutting. This condition was alleviated, as shown in the same figure, by applying an aluminum paint to the metal surface before welding and changing to an air rather than helium effluent gas while otherwise maintaining the same welding condition including the welding speed of 432 ipm (18.3 cm/sec). Another effective technique in alleviating this weld topography degradation state is to either reduce the welding speed or to increase the standoff distance, either individually or in combination.

It should be made explicitly clear that such a degraded topography condition is not unique to NVEBW, and occurs as well with other arc fusion welding processes, but at significantly lower process welding speeds. Such topography degradation conditions are also not limited to carbon steels but have also been induced by the author in alloy steels, stainless steels, aluminum alloys, titanium alloys and OFHC copper. Therefore, one must be cautious of blindly extrapolating or extending welding process conditions beyond the range of documented experience.

One should not, however, assume from the above that a discrete physical limitation has been reached as a maximum welding speed of less than 432 ipm with NVEB welding. To the contrary, thin wall 0.020 in. tubing has been successfully NVEB welded by the author at welding speeds of 1200 ipm as shown in Fig. 13. This 5/16 in. diameter Incoloy 800 alloy tubing shown was hydrostatically tested in the as-welded condition with an average resulting burst rupture strength of 11,000 \pm 200 psi. Although the ductile-lipped ruptures did occur in the weld seam, the calculated stress level at rupture was 86,000 psi, considerably above the annealed yield strength (60,000 psi) for this material.

3.0 SPECIFIC NVEB WELDING APPLICATIONS

NVEB Welding is no longer to be considered as a laboratory curiosity but rather has evolved into a practical industrial high speed automatic fusion welding process. Among the practical industrial applications demonstrated either as an on-line production item or as an effective working prototype are the following examples:

3.1 Collapsible Automotive Steering Column Jacket (Ref. 8)

A longitudinal seam butt weld in .070 in. thick AISI 1017 modified carbon steel is being welded by a major automotive manufacturer by NVEB Welding. In this application, three NVEB Welding machines are being used for two shifts per day with a production yield of 20,000 units/day. Parts 2-3/8 in. O.D. and 20 in. long are successfully welded at 7.9 kW, 0.20 in. standoff, 250 ipm with air effluent and no auxiliary shielding gas.

3.2 Drive Shaft Tube and Coupling Yoke (Ref. 9)

A 3 in. O.D. circumferential butt weld (self-backing) is being made in production between a .083 in. thick AISI 1020 carbon steel tube and a resulfurized AISI 1140 steel yoke. NVEB Welding parameters for this application include a 6.1 kW power level, 1-1/4 in. standoff, 94 ipm with helium shielding gas and the use of a preplaced

Hastelloy W filler wire to prevent cracking induced by the high sulfur content 1140 steel.

3.3 Automotive Emissions Control Device (Fig. 14)

A peripheral edge seam weldment between four sheets of .050 in. thick 409 stainless steel is being produced in the automotive industry with automatic NVEB Welding systems. Several NVEB welders are producing leak tight joints at 36 kW, 1-1/8 in. standoff, welding speeds up to 300 ipm with air effluent and no auxiliary gas shielding or supplemental filler wire.

3.4 Automotive Body Cross Frame Members (Fig. 15)

Several thousand cross frame members have been welded on an advanced NVEB welding prototype system. These frame members contain a longitudinal seam butt weld along the two opposite sides joining two AISI 1008 rimmed steel U-shaped channels of .106 in. and .130 in. in thickness and approximately 3 ft in length. Automatic NVEB welds in these contoured parts prepainted with aluminum are accomplished at 36 kW, 1/2 in. standoff, 280 ipm welding speed with air effluent and with no auxiliary gas shielding or supplemental filler wire.

3.5 Other Applications Under Consideration

Several other NVEB welding applications, predominantly automotive in nature have been receiving active consideration and evaluation testing. Among those recently reported (Ref. 10) but with little detail available publicly are: stamped steel components for automotive transmission housings, front planetary carriers, brake hub assemblies, rear planetary carrier cones, forward clutch cylinder and hub, inner race and reaction plant assembly, and the joining of ring gears to flywheels.

One promising non-automotive application area which has been demonstrated as technically feasible but has not to date been used in production is the high speed NVEB longitudinal seam welding of tubing and pipe.

4.0 SUMMARY

In summary, Nonvacuum Electron Beam Welding is a versatile, high speed, high productivity, automatic fusion welding process which offers discrete and practical advantages in both high speed and thick section welding over both other forms of EB welding and conventional arc fusion welding processes. The relatively recent and accelerating

interest, as well as the proven successful industrial applications with this advanced metals joining process clearly demonstrates that NVEB welding has earned a position of respect due in the overall hierarchy of production welding processes.

ACKNOWLEDGMENTS

The author wishes to acknowledge the following of both the Westinghouse Research Laboratories and the Westinghouse Industrial Equipment Division for their support, cooperation and contributions in the conduct and review of this work: R. J. Lanyi, B. W. Schumacher, G. G. Lessmann, R. A. Miller, R. L. Berrier and M. J. Larkin.

REFERENCES

1. R. Bakish and S. S. White, Handbook of Electron Beam Welding, J. Wiley & Sons, Inc., NY (1964).
2. A. H. Meleka, Ed., Electron Beam Welding: Principles and Practice, McGraw-Hill, NY (1971).
3. R. Ward et. al., "Electron Beam Welding", ASM Metals Handbook, 8th Edition, Vol. 6, p. 519, (1971).
4. M. M. Schwartz, "Nonvacuum (NVW) Electron Beam Welding", Modern Metal Joining Techniques, Wiley-Interscience, NY, p. 121, (1969).
5. D. B. Dallas, "Nonvacuum Electron Beam Welding-The Big Break-through", The Tool and Manufacturing Engineer, p. 65, January 1965.
6. R. F. DuHamel, "Nonvacuum Electron Beam Welding Technique Development and Progress", Welding Journal, V. 44, p. 465, June 1965.
7. R. J. Lanyi, B. W. Schumacher and J. M. Wells, "Nonvacuum Electron Beam Welding (NVEBW)", article to be published in forthcoming issue of Westinghouse Engineer.
8. R. Ward et. al., "Electron Beam Welding", ASM Metals Handbook, 8th Edition, Vol. 6, 1971, p. 529.
9. Ibid, p. 530.
10. Annon., "New Auto Applications for EB Welding", American Metal Market/Metalworking News Edition, January 14, 1974, p. 1.

TABLE 1 - COMPARISON OF NVEBW WITH OTHER EB WELDING PROCESSES

<u>Advantages</u>	<u>Liabilities</u>
Faster Cycle Time - no pump-down delay	Lower penetration depth/width ratios
Adaptable to continuous process welding	Relatively close standoff required
No chamber size limitations	Larger energy/unit weld length input
No weld vapor degradation of vacuum levels or sliding seals	Fewer facilities available for prototype testing
Process insensitive to normal focus variations	Less well-known welding process
Tooling and fixtures need not be vacuum qualified	Larger radiation enclosure normally required

TABLE 2 - COMPARISON OF NVEBW WITH CONVENTIONAL ARC WELDING PROCESSES

<u>Advantages</u>	<u>Liabilities</u>
Greater weld depth/width ratios	Greater system complexity
Higher welding speed and productivity capability	Higher capital equipment cost
Lower energy/unit weld length	Non-portable for field use
Less distortion and warpage	Not suited for low volume items
Smaller heat-affected-zone (HAZ)	Remote controlled-more difficult for direct operator observation
Less (if any) filler wire required	

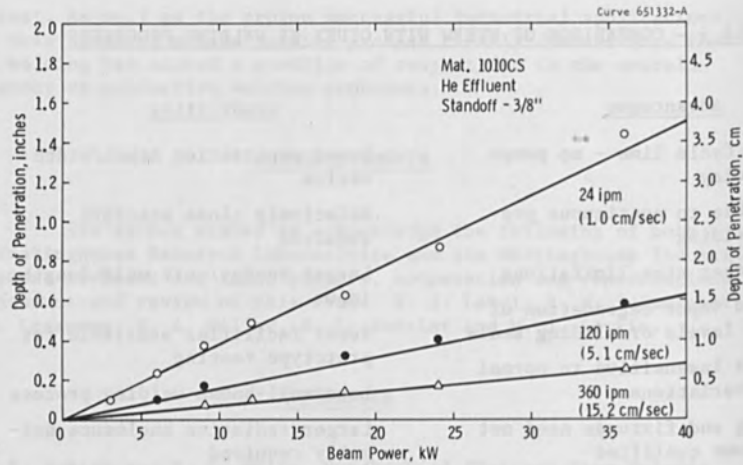


FIGURE 1 -- NVEBW DEPTH OF PENETRATION VS. BEAM POWER AT SELECTED WELDING SPEEDS. MATERIAL 1010 CARBON STEEL, 3/8" STAND-OFF, HELIUM GAS EFFLUENT.

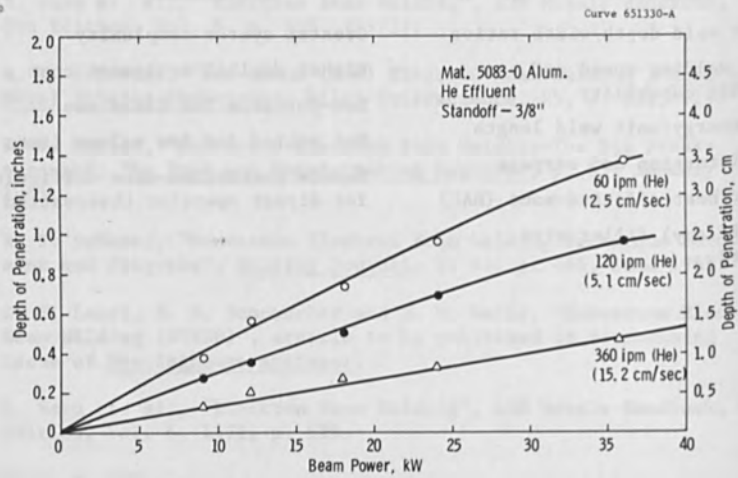


FIGURE 2 -- NVEBW DEPTH OF PENETRATION VS. BEAM POWER AT SELECTED WELDING SPEEDS. MATERIAL 5083 ALUMINUM ALLOY, 3/8" STAND-OFF, HELIUM GAS EFFLUENT.

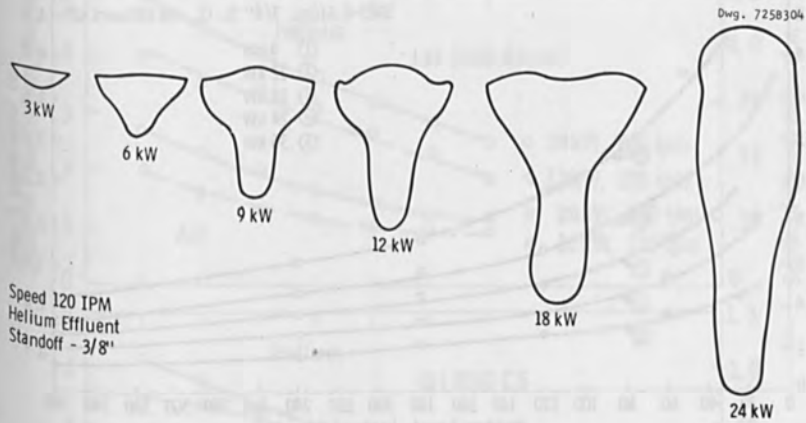


FIGURE 3 -- NONVACUUM ELECTRON BEAM WELD PROFILES SHOWN VS. BEAM POWER LEVEL. MATERIAL 5083 ALUMINUM ALLOY. (X 3.25)

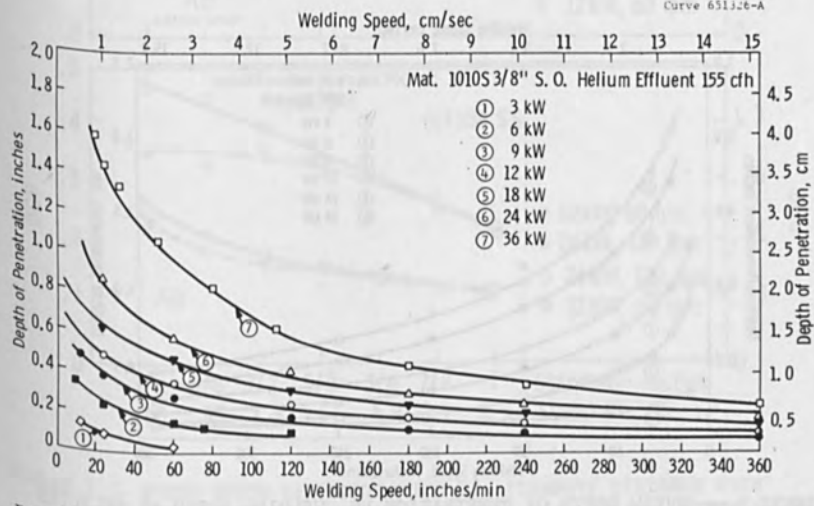


FIGURE 4 -- NVEBW DEPTH OF PENETRATION VS. WELDING SPEED AT SELECTED POWER LEVELS. MATERIAL 1010 CARBON STEEL, 3/8" STANDOFF, HELIUM GAS EFFLUENT.

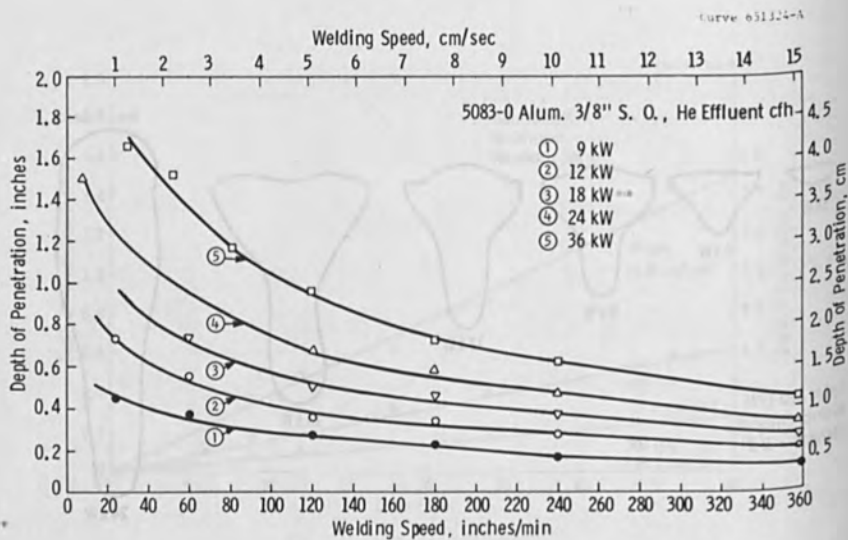


FIGURE 5 -- NVEBW DEPTH OF PENETRATION VS. WELDING SPEED AT SELECTED POWER LEVELS. MATERIAL 5083 ALUMINUM ALLOY, 3/8" STAND-OFF, HELIUM GAS EFFLUENT.

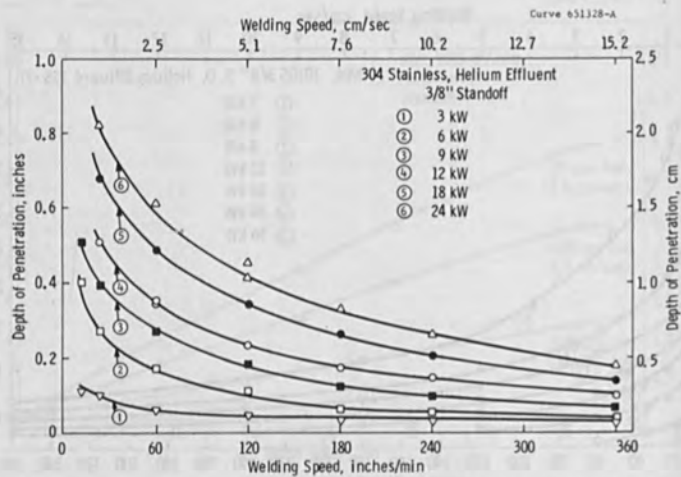


FIGURE 6 -- NVEBW DEPTH OF PENETRATION VS. WELDING SPEED AT SELECTED POWER LEVELS. MATERIAL 304 STAINLESS STEEL, 3/8" STAND-OFF, HELIUM GAS EFFLUENT.

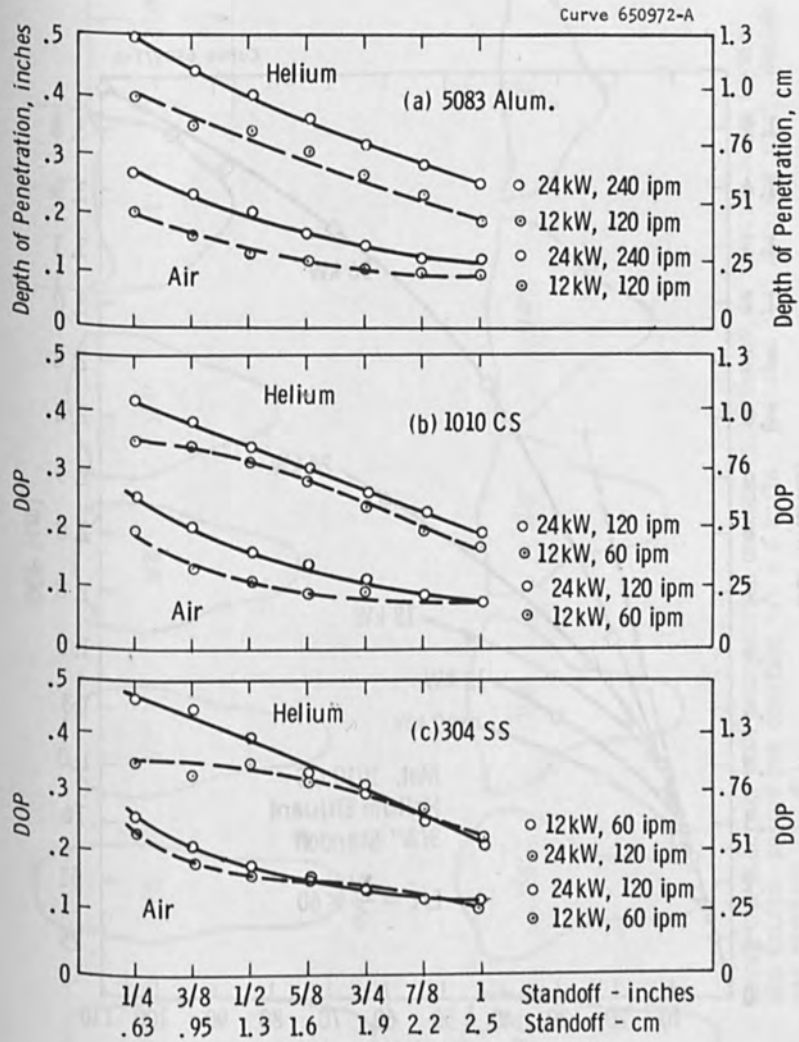


FIGURE 7 -- NVEBW DEPTH OF PENETRATION VS. STANDOFF DISTANCE WITH HELIUM AND AIR GAS EFFLUENT FOR: (a) 5083 ALUMINUM ALLOY, (b) 1010 CARBON STEEL, (c) 304 STAINLESS STEEL.

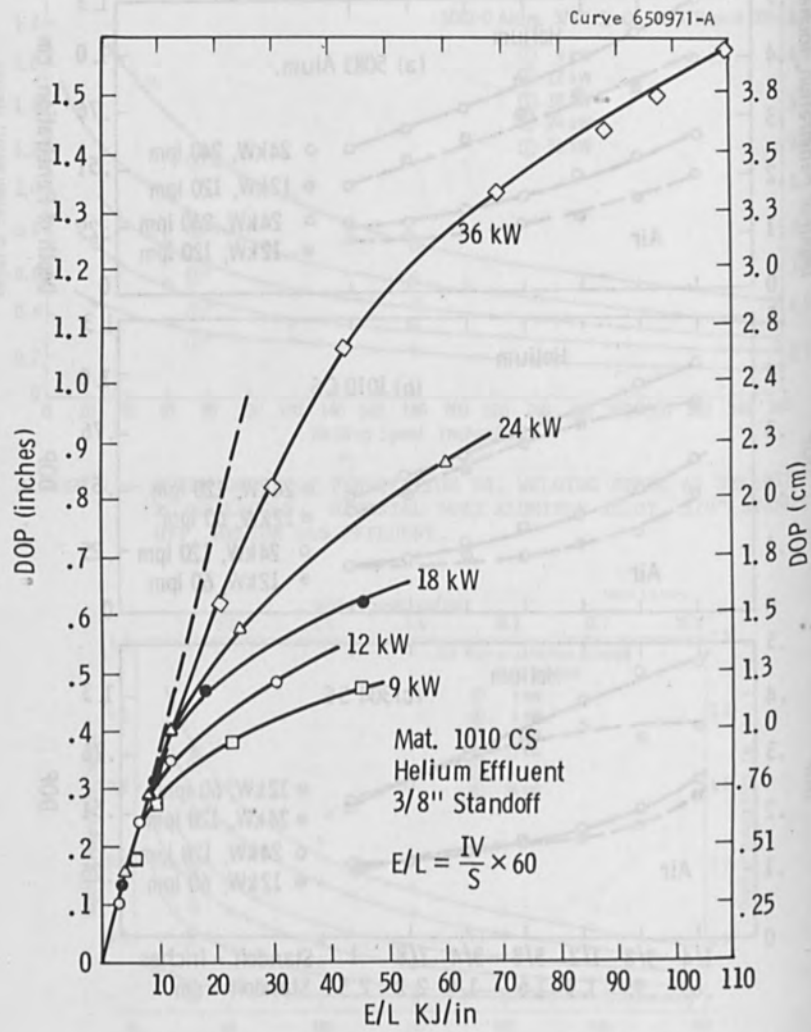


FIGURE 8 -- NVEBW DEPTH OF PENETRATION VS. BEAM ENERGY INPUT/UNIT LENGTH OF WELD. MATERIAL 1010 CARBON STEEL, 3/8" STAND-OFF, HELIUM GAS EFFLUENT.

Dwg. 7258305

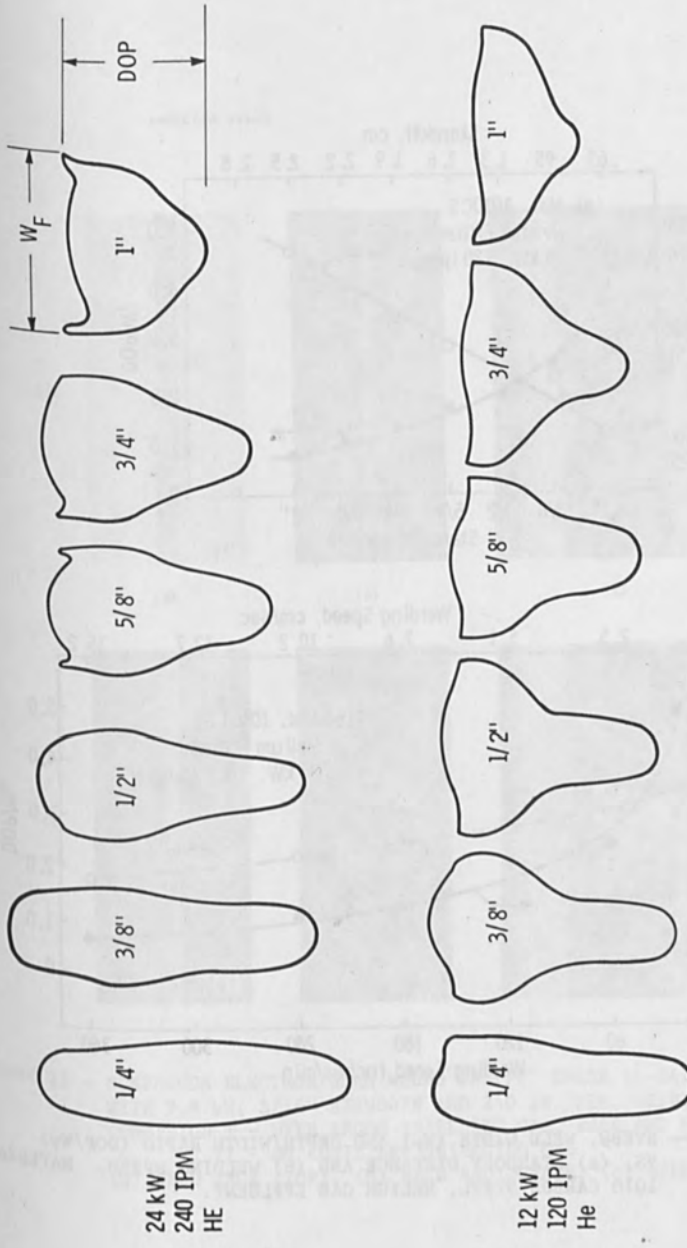


FIGURE 9 -- NONVACUUM ELECTRON BEAM WELD PROFILE CHANGES VS. STANDOFF AT SELECTED POWER LEVELS AND WELDING SPEEDS FOR CONSTANT E/L = 6 KJ/IN. MATERIAL 5083 ALUMINUM ALLOY, HELIUM GAS EFFLUENT (X 2.85).

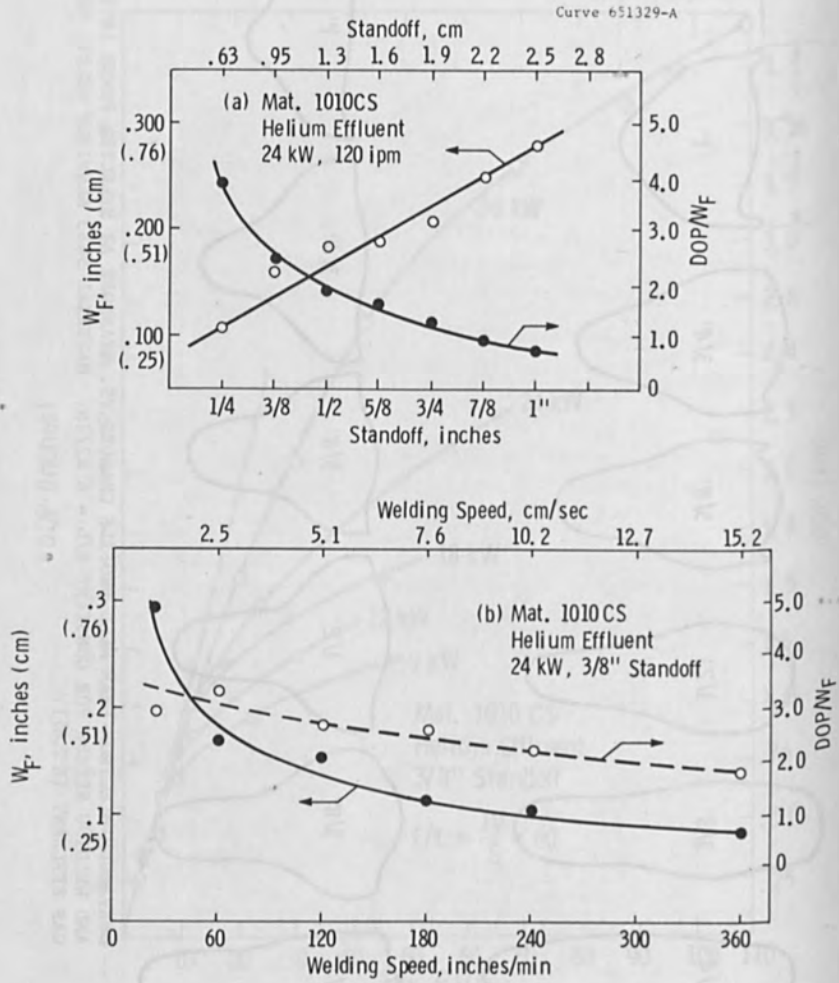


FIGURE 10 -- NVEBW, WELD WIDTH (w_F) AND DEPTH/WIDTH RATIO (DOP/ w_F) VS. (a) STANDOFF DISTANCE AND (b) WELDING SPEED. MATERIAL 1010 CARBON STEEL, HELIUM GAS EFFLUENT.

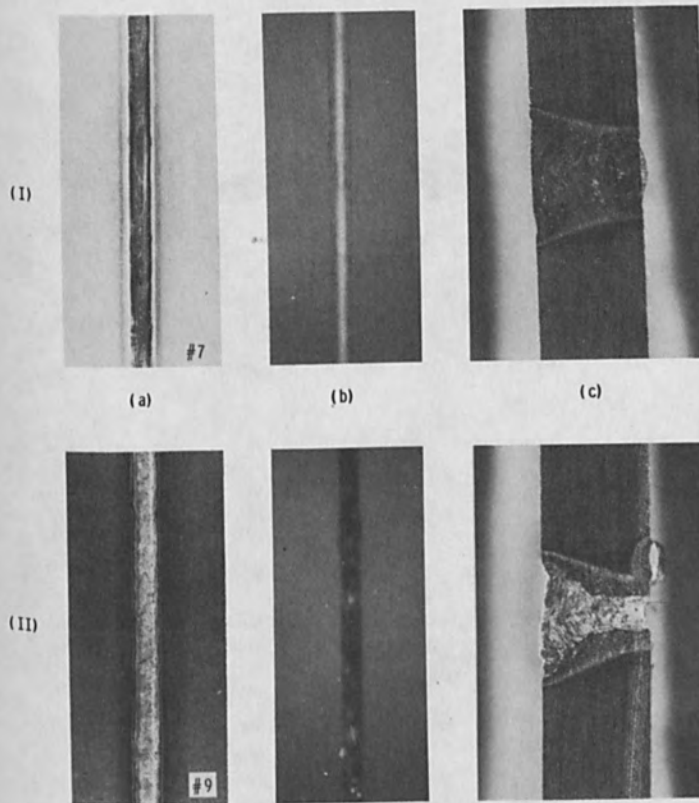
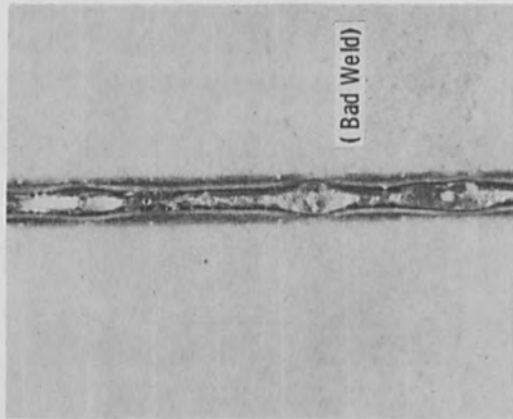
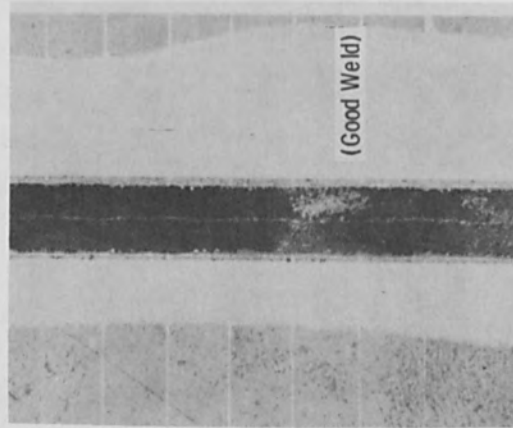


FIGURE 11 - NONVACUUM ELECTRON BEAM WELDS IN 1/8" THICK Ti-6Al-4V ALLOY WITH 7.8 kW, 5/16" STANDOFF AND 240 IN./MIN. WELDING SPEED.
 CONDITION I - WITH ARGON SHIELDING GAS, FACE AND ROOT
 II - NO AUXILIARY SHIELDING GAS
 (a) WELD FACE (TOP), (b) WELD RADIOGRAPH, (c) WELD PROFILE



I



II

FIGURE 12 -- EXAMPLES OF WELD TOPOGRAPHY WITH HIGH SPEED NVEB WELDING AT 24 kW, 5/8" (1.6 cm) STAND-OFF AND 432 IN./MIN (18 cm/SEC) WELDING SPEED IN AISI 1008 RIMMED STEEL SHEET (X)
CONDITION I - DEGRADED WELD TOPOGRAPHY WITH CONSIDERABLE ROPING, SWELLING, AND UNDER-CUTTING - HELIUM EFFLUENT.
CONDITION II - GOOD WELD TOPOGRAPHY WITH ALUMINUM PAINT AND AIR EFFLUENT.



FIGURE 13 - NONVACUUM ELECTRON BEAM WELDMENTS IN 0.020" (0.5 cm) THIN WALL INCOLOY 800 TUBING WELDED AT 7.8 kW, 3/8" STANDOFF (~ 1 cm), 1200 IN./MIN. (51 cm/SEC) WITH AIR EFFLUENT. DUCTILE RUPTURE OCCURRED IN WELD SEAM AT INTERNAL PRESSURE OF 11,000 PSI.

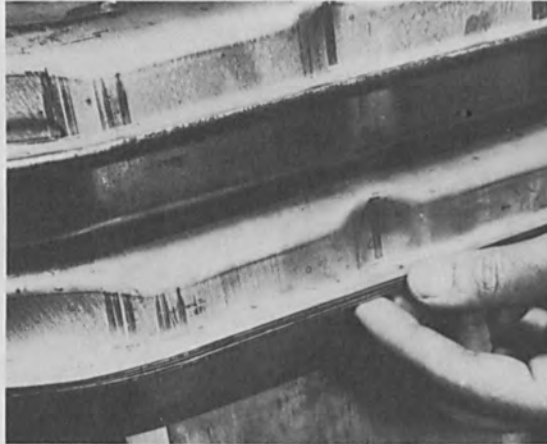


FIGURE 14 - AUTOMOTIVE EMISSION CONTROL DEVICE - WELDED BY NVEBW.
MATERIAL 409 STAINLESS STEEL, 36 kW POWER LEVEL, 1-1/8"
(2.9 cm) STANDOFF, WELDING SPEED OF 300 IN./MIN. (12.7 cm/
SEC).

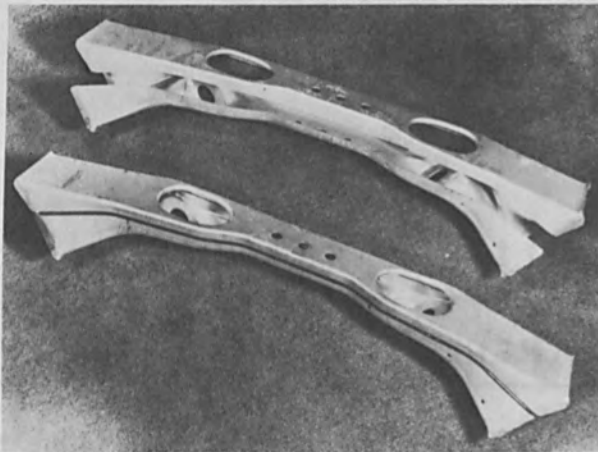


FIGURE 15 - AUTOMOTIVE BODY CROSS-FRAME MEMBER - WELDED BY NVEBW.
MATERIAL 1008 RIMMED STEEL, 36 kW POWER LEVEL, 1/2" (1.3 cm)
STANDOFF, WELDING SPEED OF 280 IN./MIN. (11.9 cm/SEC).

APPLICATION OF ELECTRON BEAM WELDING
TO THE HEAVY CONSTRUCTIONS

R. ROUDIER

CLOVER Company Villejuif (France)

ABSTRACT

To avoid having to put large workpieces completely in a vacuum chamber, portable electron beam welding machines with local vacuum have been produced. As a result of several years development, these machines are relatively light weight and can be easily transported. Here a distinction may be made between the «machine» part, adapted for welding, and the supplies and vacuum part, which may be used in other applications.

1. - INTRODUCTION

More than ten different types of portable apparatus for electron beam welding have been studied and put on work these last years.

The use of specialized portative apparatus is the key which opens a large application field to the process. The real benefit of this technique is not to replace a welding process by another one but to completely change the whole cycle of the manufacturing and the assembling to avoid the high cost of post-weld machinings.

The absence of distortion, the high welding speeds and the deep penetration in a single pass, the facilities of non-destructive measures, are economical and

technical components able to deeply modify the conceptions and the present methods in work-shop. The using of CLOVER welders with local vacuum chamber brings to real lower costs than the use of classical massive vacuum chambers.

2. - AUTOMATIC ELECTRON BEAM WELDING MACHINE FOR TUBE-TO-TUBESHEET ASSEMBLING («Pistolet » type 939.02)

Our first description of portable apparatus concerns handiness-tool designated by E.B. «pistolet».

From the aspect point of view, its presentation looks like portable tools commonly used on site.

In the fabrication of heat-exchanger and boiler, it happens often with TIG or manual process, some delay due to the weld defects.

It's known that the reliability in service gives some problems and that one of the main causes of the stopping of the units where these heat-exchangers are operating, is the leakage of the tube-to-tubesheets welds.

The E.B. process can overcome this major difficulty. Otherwise, the utilization of portable E.B. «pistolets» offers some important advantages :

- . Welds with deep penetration, with high joint integrity, especially with the newer, more sophisticated, materials which benefit from the contamination-free environment provided by the vacuum.
- . Perfect tightness of the assembly in service in spite of thermal shocks.
- . Fully automated welding operation is in accordance with the stringent demands for quality welds in the nuclear industry. Moreover, human factor defects are eliminated and E.B. process increases results productivity.
- . Deep penetration welding is possible with the front face of the tubesheet in the vertical position.

The E.B. «pistolet» is described in Fig. 1.

The contact of the «pistolet» with the plate to weld, through special seal, forms the welding chamber under primary vacuum. The electron gun rotates around the axis of the pistol materialized by the centering mandrel.

- The front part of the gun is set inside the welding chamber so long as the «emission» part is placed under high vacuum inside back chamber of pistol. This back chamber can be «opened» so as to be quickly in order to make at regular intervals the change of gun cathode.
- The back part of pistol is provided for to be fixed on automatic positionner which can be used to hold the axis of the pistol in position strictly parallel with the axis of tubes to weld.

In the same manner, this pistol can be attached instead of tool-holder on numerical control drilling machine (see Fig. 2) ; the same programm like that used in checking the moving on drilling of the plate can be used for all displacements.

The machine is capable of:

- Welding diameter range : 14 to 30 mm
- Minimum distance between the axis of the peripheric holes and the shell that projects beyond the plate : 55 mm
- Maximum penetration in a single pass (steels) : 3 to 8 mm (according to the thickness of tubes)
- Minimum distance between 2 tubes : 7 mm
- Power : 3 kW
- Time for a complete welding cycle : from 40 sec. to 2 mn (according to the tubes diameters.)

3. PORTABLE AND VERSATILE MACHINE FOR CIRCULAR E.B. WELDING

These machines have been designed to allow the installation of different adaptations on a same basic holder, according to the welding to make. This basic system includes all control and moving parts. It owns a rotating high voltage feed-through allowing the complete immobility of the high voltage cable.

Three kinds of welding are possible with this type of apparatus :

3.1. Circular Welding of Tubes-to-Tubes Plates

In this version, the machine is fitted with a gun of 8/10 kW set in a parallel direction with this machine axis and rotating concentrically with this axis. The front part is fitted with an expandable mandrel, which going to set inside the tube to weld, insures the centering of circular courses of the electron beam.

This machine is capable of:

- . Weld diameter : 30 to 70 mm
- . Maximum penetration in a single pass (steels) 30 mm
- . Maximum power : 10 kW
- . Time for a complete welding cycle (including pumping time) 5 to 6 mn

3.2. Bore Welding of Tubes 100 to 300 mm I.D. (see Fig. 3)

We can replace the gun parallel to the axis of the machine by another gun specially designed for bore welding with a radially directed electron beam. This allows another use for the standard model machine.

A special junction part allows the clamping on the part to be welded. This junction box goes to make up the welding chamber.

Inside this chamber, the electron gun completely shielded, is fixed on the rotating part of the basic equipment. This gun has been designed to provide a convergent electron beam with a small gun-to-work distance.

The different components of the electronic optical system of the gun don't exceed 40 mm for maximal size.

Thus fitted this machine is capable of:

- . Weld diameter (I.D. tubes) : 100 to 300 mm
- . Maximum penetration in a single pass (steels) 20 mm
- . Maximum power : 5 kW
- . Time for a complete welding cycle : 5 to 10 mn

This version has been designed and used for thick tubes to tube plates assembling (see Fig. 4). This kind of assembling is specially interesting from a no-deformation point of view. The shrinkage, that is of low amplitude (0,1 to 0,3 mm), happens only perpendicularly at the plate and in a axial manner with regard to tubes. Thus, after welding, there is not any variation on the pitch between tubes, any modification of inside diameter tubes and finally, any deformation of the tube-plate. In this way, one avoids very important after weld-machining on large machine-tools and this enables one to save up money.

3.3. Bore Welding inside tubes 250 to 1 500 mm I.D.

Based on the same principle, this machine fits a gun set perpendicularly with regard to the axis of the tubes to weld. The clamp-on-chamber is made with a plate going entirely to close the pipe in which we want to make the weld. The basic system of the machine is set on this plate.

	10 kW Type	30 kW Type
Weld diameters range (I.D. of tubes)	250 to 1000 mm	350 to 1500 mm
Maximum penetration in single pass	30 mm (steels) 50 mm (light alloys)	70 mm (steels) 120 mm (light alloys)
Time for a complete cycle	1 to 10 mins	5 to 20 mins

4. - PORTABLE MACHINE FOR LARGE CIRCULAR WELDING

This machine is an extrapolation of the machine described in 3.1.

It's a portable machine which can be set either on a positioner on heavy welded structure or on an automatic handling apparatus with the object of production identical welds in series (see Fig. 4).

Mainly, it's made with a cylindrical housing under primary vacuum, forming the welding chamber. This cylindrical housing takes its bearing on the part to weld through the special seal of the clamp-on-system. The necessary vacuum-tightness is got easily even on no bright parts and rough surfaces

In the cylindrical housing a rotating mechanical component supports the electron gun and allows its inclination to operate conical welding.

The gun is pumped separately and it is continuously maintained under a vacuum of 1.10^{-5} TORR.

On the new models of this kind of machine, the gun is supplied by a rotating feed-through that avoids rotary motion and twisting of high-voltage cable.

This machine is capable of:

. Welding diameter range :	. cylindrical welds	70 to 280 mm
	. conical welds	0 to 20°
. Maximum penetration in a single pass (steels)		60 mm
. Nominal power		30 kW
. Maximum power		45 kW

The time to execute a weld (complete cycle including pumping) ranges from 10 to 15 minutes.

It's interesting to compare this time with the welding time of 100 to 300 mm diameter nozzles on heavy wall vessels, where multipass welding process requires to weld over extended periods of time without interruption , intermediate inspections, complicated procedure and wasting of energy.

5. LOCAL VACUUM LINEAR E.B.W. MACHINE

The type 010.01 linear welding machine comprises the following parts, viz. «evacuable enclosure» or plate, gun tractor with its drive and alignment system, electron gun with its separate pumping system, supplies for the electron beam and, the pumping system (see Fig. 5).

5.1. Mechanical parts

The vacuum necessary for the beam is established in an elongated, flat box which covers the joint to be welded. This box or plate also serves as the track for the gun tractor. The monobloc structure gives the great transverse rigidity necessary for the linear accuracy which the guide rails for the tractor must provide.

On the face of the plate adjacent to the weld are the vacuum seals which are applied to the piece to be welded. This seal is maintained by shims.

The plate also carries eyelets or niches for holding jacks or adjusting screws. (these adjustments are made once and for all for a given component at the time of setting up the machine).

This structure also carries lateral support faces or bosses, for controlling the alignment of the beam on the joint to be welded.

The bosses, carefully machined parallel to the carriage movement, allow alignment by simple pressure on a reference face prepared in advance.

A further positioning mechanism (fixed to the lower face of the structure) is used for welding with run-on and run-off tabs, but may be otherwise omitted. On the upper face (tractor side) of the plate, there is a longitudinal opening which allows the electron beam to enter the cavity under primary vacuum and to move along during welding. This opening is surrounded by a surface of a compliant resin cast into a seating. The strip or ribbon of high strength steel then closes the longitudinal slot and forms a seal by pressing on the surface, or rectangular frame, of the compliant resin. This strip is fixed with respect to the slot and is attached to the extremities of the plate. The ribbon is carried by a series of small supports mounted on hinges and raised by cams.

Finally, two steel roller tracks, on either side of the central slot, support the carriage wheels, with the primary vacuum tube held via a mobile clamp.

The gun carriage draws the strip from one side to the other of the welding aperture by synchronised rolling and unrolling to give a linear movement over a distance of 2 or 3 m, while maintaining the primary vacuum between the box enclosure and the electron gun during motion. It also allows precise positioning of the electron gun, and carries the separate gun pumping system. It is composed of a chassis, which holds the driving mechanisms and the rolls which apply the strip to the resin surface seal, with their height adjustment systems.

Also it contains a sliding seal to the multiple chamber, auxiliary pumping conduits, the two sliding seals (which allow the winding and unwinding of the ribbon from reels placed outside the vacuum) and the guidance system consisting of lateral needle rollers and guide blocks. The system permits control of the degree of compression of the sliding joint on the plate and an adjustment for any lateral play.

5.2. Performances (see Fig. 6)

The type 033 electron gun used is the «triode», type with cathode, control (or Wehnelt) electrode, anode and focus coil. An automatic valve allows the part under secondary vacuum to be isolated while work is carried out on the machine. A cooling circuit ensures constant temperature for continuous operation.

The type 033 gun readily permits changing the directly heated cathode without subsequent adjustment. The principal characteristics are accelerating voltage - 50 kV (max.), beam current 0 - 900 mA as required perveance 8×10^{-8} A.V. $^{3/2}$, and working distance 200 mm (fixed). Also magnetic beam deflection is available.

The principal characteristics of the type 010 machine are maximum weld length - 3 metres, setting up time 1 - 5 mins. (according to equipment used) primary pumping to $5 \cdot 10^{-3}$ TORR, 6 - 8 mins. and location or adjustment time - 3 mins. The welding speed varies from 0.1 to 1 m/min. (according to thickness of material).

The machine is fully mechanised and all operations occur following initiating the «start cycle» button, from first closing the air-inlet valve on the welding chamber, to starting welding with a preprogrammed slope up to the working current. During welding, different sections are identified by precise measurement of length by means of photo cell impulse meters. At the finish the current is sloped out and the equipment shut down with finally air let into the welding chamber.

6. - DEVELOPMENTS

- 6.1. Following production of the first serie of linear machines, it is envisaged that a machine for weld lengths of up to 12 m will be developped in the near future. Here the seam tracking system would ensure precise gun guidance whatever the distortion in the backing bar.
- 6.2. Under development is a similar system for welding rings or rotors in a horizontal vertical position (see Fig. 7).
The high penetration obtained in one pass, together with the negligible distortion, should meet the economic requirements of the heavy fabrication industry.
- 6.3. Also under development is sliding machine with two concentric chambers which move alternatively and give, every time, static leaktight (see Fig. 8). We try, at the present, to use this sliding machine on large machine-tools, immediately after machining of large structure.

7. - CONCLUSION

1. Local vacuum E.B. welders can be used for different applications. With these machines, the size of the pieces to be weld has not upper limit.
2. CLOVER machines allow interesting types of assembling, from a no-deformation point of view. Deep penetration in a single pass can save money in many cases.
3. According to the work sequences, several welding heads can be used alternatively with only one basic set of power source, unit control, pumping groups, and so on. This point shows the versatility of the process.

Finally, CLOVER portable machines can be removed easily from place to place along the working sequences, in several work-shops or on the final assembling site.

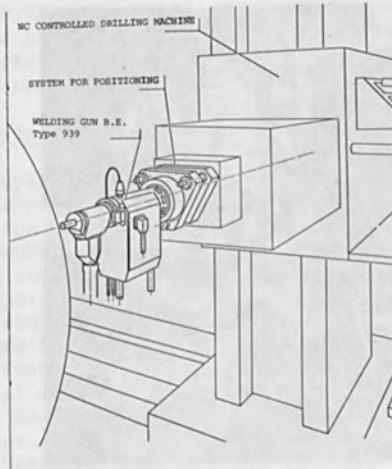
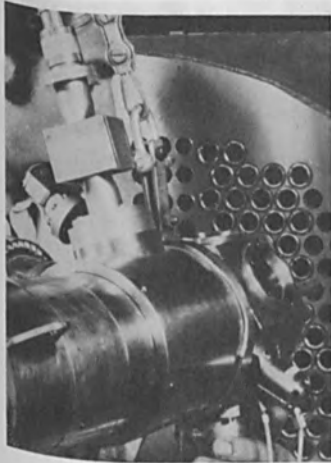


Fig. 1 : E.B. «Pistolet» for tube-to-tubesheet Welding. Fig. 2 : «Pistolet» use on drilling machine

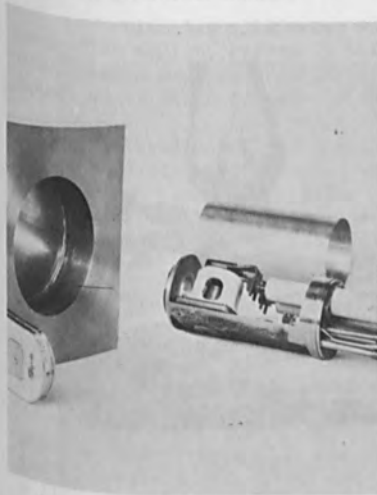


Fig. 3 : Electron gun for bore welding and test-piece. Fig. 4 : Portable E.B. welding machine for nozzles.

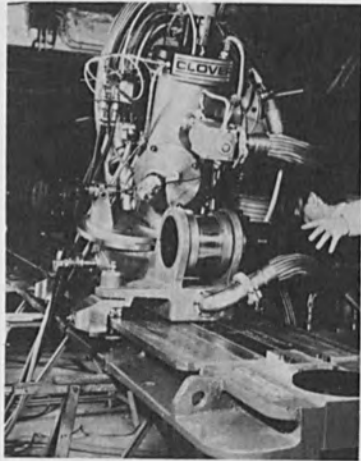


Fig. 5 : Local vacuum linear E.B. welding machine type 010.01



Fig. 6 : 6 m diameters shells E.B. welded by portable machine (doc.Neyrpic).

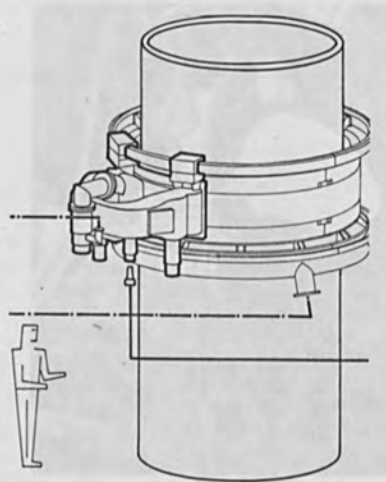


Fig. 7 : «Orbital» local vacuum E.B. welder

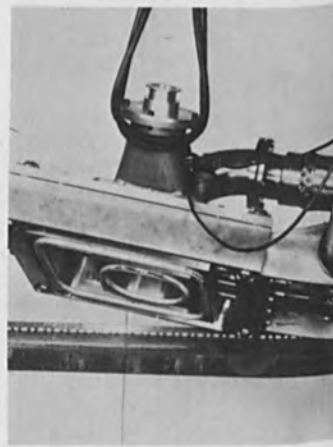


Fig. 8 : CLOVER sliding machine with movable chambers.

ELECTRON BEAM WELDING OF MM WAVEGUIDE FLANGES

B. T. Barcelo and E. J. Canning

Western Electric Company

P. O. Box 900, Princeton, N. J. 08540

Abstract

In an effort to minimize coupling losses in the millimeter waveguide system, investigations were undertaken to optimize the flange-to-tube fusion joining process. Results from these investigations emphasize the importance of using electron beam welding and materials which are compatible with this welding operation. Experimental results from electron beam welding studies form the body of this report and serve as the basis for these conclusions. The major emphasis of the experimental work has been in investigating four topics: material weldability, weld strength, waveguide I.D. temperature, and waveguide distortion. These areas are considered the most critical to welding flanges to millimeter waveguides. Detailed investigations in these areas revealed key information for the design of a facility to perform the desired welds on a production schedule.

Introduction

Circular millimeter waveguide is a new high capacity communication medium, currently being developed by the Bell Telephone Laboratories and Western Electric Company, with unique coupling requirements which led to the use of electron beam welding.

Physically, the installed waveguide portion of the system is shown in figure 1. The waveguide is contained within a protective steel sheath buried 4 to 8 feet underground. The waveguide itself consists of a steel tube with a conducting inner liner of copper. Flanges are attached to the ends of each section of waveguide by electron beam welding and the waveguide sections are joined in the field by GTA (Gas Tungsten Arc) welding the flanges together. The waveguide is supported within the sheath on discrete metallic spring supports. The roller supports allow the waveguide to roll inside the sheath during initial placement and act as the supporting structure for the waveguide within the sheath.

Two distinct waveguide assemblies will be used in the waveguide medium (figure 2). The first type, known as a dielectric waveguide, consists of a 60 mm inside diameter low carbon steel tube with a lining of 180 microns of polyethylene bonded to 13 microns of electro-plated copper. The second type of waveguide, known as helix waveguide, consists of a 64 mm inside diameter low carbon steel tube with a lining of 37 gauge helically wrapped copper wire plus

several layers of glass fiber dielectric material epoxy bonded inside the tube. Helix waveguide acts as an electrical filter for unwanted transmission modes while the dielectric waveguide serves as a low loss transmission medium. The majority of the installed systems will be dielectric waveguide.

The attractiveness of millimeter waveguide stems from the discovery [1] that the attenuation of a specific configuration of a propagating electromagnetic field, the TE_{01} mode, in a right circular cylindrical conductor decreases (monotonically) with frequency. This behavior is in sharp contrast to the behavior of other transmission systems which have losses that increase with frequency. Since the information carrying capacity of a transmission system increases with frequency the circular waveguide appears to be the ideal transmission media with decreasing losses for increasing capacity.

In practice such ideal behavior cannot be realized. The actual total loss for the TE_{01} mode is the sum of two independent losses. Ohmic heating losses occur at the lower frequencies while geometry dependent mode conversion losses are dominant at higher frequencies causing the total loss to show a minimum in the transmission range of 40 to 110 gigahertz (figure 3).

The success of millimeter waveguide as a communication medium is dependent on minimization of periodic geometric distortions which cause intermodal energy transfer and hence introduce transmission losses [2]. These distortions are generally associated with both tube geometry and medium coupling. Because of their inherent periodic nature, the distortions caused by the waveguide splicing operation are frequently very serious.

The objective of the coupling operation is to accurately join the various waveguide sections to form a continuous right circular cylinder. This requires precision alignment of the waveguide tubes with minimal radial and axial deviations, known as tilt and off-set, respectively (figure 4). The coupling and the waveguide sections must have a common flexibility such that the axial curvature in a route bend is smooth and continuous. Additional joining considerations include: adequate strength, a gas tight seal, protection of the dielectric liner, long term stability and an economical joining process.

The present flange coupling design is shown in figure 5. A flange is attached to a waveguide tube with two electron beam welds. One weld is into the face of the flange (a circular square butt weld) and the second is into the back of the flange (a circumferential fillet weld). A GTA weld is used to splice the two flanges together to complete the joint. This report will only be concerned with the initial flange-to-tube attachment process and

references will be made to 51 mm waveguide and 60 mm waveguide. This designation refers to the inside diameter of the waveguide tubes.

In an effort to minimize coupling losses in the millimeter waveguide system, investigations were undertaken to optimize the flange-to-tube attachment process. Although initial waveguide experience was with threaded, bonded, or bolted assemblies, the major emphasis of the recent investigations was on fusion joining methods which had the potential advantages of greater reliability and more rapid production rates. These investigations included inertia welding, laser welding, conventional arc welding (GMA and GTA) and electron beam welding. Of the four fusion techniques evaluated electron beam welding was the most outstanding.

The experimental program concentrated on investigating four areas which are considered the most critical to welding flanges to millimeter waveguides: material weldability, weld strength, waveguide I.D. temperature, and waveguide distortion. Although the areas are interrelated, for the purpose of discussion and evaluation, it is convenient to treat each independently.

Weldability

Weldability in the waveguide flanging application relates to making high quality - high strength welds with a completely reliable welding technique. To achieve the flange attachment requirements previously mentioned, the welds must exhibit sufficient strength and ductility while maintaining a leak rate of less than 5×10^{-5} atm cc/sec. Initial experiments were devoted to the weldability of various potential waveguide materials. Welds were performed on 1010 rim steel, 1010 aluminum killed steel, and 1020 aluminum killed steel to evaluate the electron beam welding process. These three steels were selected as potential waveguide materials because of their sufficient strength, easy formability, surface finish characteristics, long term stability and economics.

To simplify the welding program, short sections of waveguide tubes were spliced together with circular square butt welds. Two sets of partial penetration welds were performed on the various materials. Typical welded samples were tensile tested while other joints were metallographically sectioned with a subsequent examination of the weld microstructure. Weld hardness measurements were recorded for each material and typical fracture surfaces were examined using a scanning electron microscope.

The weldability study showed electron beam welds in 1010 rimmed steel to have excessive porosity in the fusion zone.

Figure 6 shows typical weld root porosity while additional porosity was apparent on the top bead surface not shown in this figure. Excessive porosity in this application is unsatisfactory because it lowers the weld strength and endangers the leak rate integrity. The porosity observed in the rim steel weld is caused by gases (CO and CO₂) generated in the weld puddle being trapped in the fusion zone as the weld metal solidifies. The porosity observed in the rimmed steels has been linked to the carbon boiling mechanism of molten steel by Bibby, et.al.[3].

The lower micrograph in figure 6 exemplifies the solution to the porosity, that is, to use a deoxidized or killed steel. An attempt was made to deoxidize the 1010 rim welds by placing an aluminum foil in the butted joint before performing the weld. The foil* successfully deoxidized the fusion zone of the weld while maintaining the weld strength. Porosity in these locally deoxidized welds was minimal.

Although the rimmed steel could be deoxidized during welding, a killed steel was selected as the waveguide material to simplify and to increase the reliability of the electron beam welding process.

The second aspect of weldability concerned itself with the weld microstructure and material carbon level. The very rapid cooling rates associated with electron beam welding cause the martensite** to be formed within the fusion zones. Typical micrographs are shown in figure 7 for welds in 1010 and 1020 aluminum killed steels. Each micrograph has Vickers hardness readings superimposed on the microstructure. The primary difference is that the martensites in the fusion zones of the welds are equivalent to the carbon level in the respective alloys. In the heat-affected zones, the heating and cooling rates are so rapid that one finds the pearlite colonies have transformed to martensite. A second effect of base metal carbon content is that the higher carbon welds will have a larger volume fraction of martensite in the heat-affected zones.

The consequence of the higher carbon martensite in the weld zone is dramatically displayed by the fracture properties of these welds (figure 8). The 1010 welds showed a ductile fracture behavior with the fracture path being initiated at the stress concentration at the weld root and propagating outside the heat-affected zone. The 1020 welds showed a predominantly brittle fracture, again initiating at the weld root but propagating directly through the weld centerline.

* Other experiments also proved successful in deoxidizing the weld by using high purity aluminum powder instead of a foil.

** The microstructure of the welds fusion zone can be predicted from the theoretical calculations of Goldak, et.al.[4,5] and from the iron-carbon: TTT diagram.

Scanning electron micrographs of the fracture surfaces, seen in figure 9, document the typical ductile and brittle nature of the two welded materials. It is recognized that the brittle behavior may be relieved by instituting a pre or post heat treatment for the welds, or by possibly controlling the microstructure through the welding parameters as suggested by Goldak, et.al.[4]. However, such approaches reduce the welding time, add cost to the manufacture, and, in the case of modifying the welding parameters, result in greater distortions to the waveguide tube.

The selection of a suitable waveguide material and welding process were dependent upon weldability. The selection of electron beam welding process restricted the carbon level in the waveguide material. The final designation of a material for millimeter waveguide tubing was dependent upon the interrelated aspects of formability, surface finish, carbon level, basic strength, stability and costs. Further investigation of these areas led to the ultimate selection of a 1010 aluminum killed steel for the millimeter waveguide tubes.

Weld Strengths

The tube-to-flange joint as currently proposed must withstand a 45,000 lbs. load without failure. The strength criterion was formulated in considering the stresses the connection must withstand during the flange-to-flange welding operation, field placement and various service conditions. Part of each experiment was directed toward evaluating weld strength and weld quality. It was found necessary to examine a number of different welds and flange weld configurations to prove general process feasibility. Simple butt welds were used in some of the early studies while later investigations concentrated on the current flange design.

Tensile tests were performed on the electron beam butt welds by testing the entire welded tube. The variation of yield and ultimate loads with average butt weld penetration is shown in figure 10. The tests were conducted by stressing the butt welds in tension and recording the load versus extension curves. The first deviation from the straight loading line is taken as the "yield" load.

The 1020 Al/K welds have the lowest strength. The low strength is attributable to the brittle fracture nature of the welds and the stress concentration at the root of the weld. High strength welds were recorded with the 1010 rim material which was deoxidized with aluminum during the welding operation. Electron beam welds performed on 1010 rimmed tubes and 1010 Al/K tubes had approximately the same strengths, even though the 1010 rimmed welds displayed considerably more porosity.

A second welding study investigated three partial penetration welds on 60 mm tubes of 1010 material. The welds were of superior quality. The top bead was smooth and the cross-sectional profile had a desirable geometry. Tensile tests on the butt welded joints displayed excellent strengths, which are graphically displayed in figure 11. By careful control of the joint preparation and welding parameters, high strength, partial penetration welds can be performed in waveguide tubing (1010 Al/K). Tensile tests indicate that a 0.060 inch penetration weld has an average yield load of 42,700 lbs., while a 0.075 inch penetration weld has an average yield load of 48,500 lbs.

The tube-to-flange weld configuration was investigated using an electron beam welder with a 50 kv accelerating voltage and the ability to align the joint and the electron beam prior to welding. The welds fused 51 mm waveguide tubing, 1010 Al/K and 1010 rim steel (deoxidized with aluminum), to a low carbon (1015-1020) fully killed steel flange. The welding parameters were varied so as to indicate variations in strength, temperature, and distortion with changes in the face weld penetrations. The attempted penetrations ranged from 0.040 to 0.125 inches while the individual penetrations achieved depended upon the tube-to-flange fit as well as the welding parameters. The actual penetrations were from 0.030 to 0.120 inches, and penetrations varied about the mean value from ± 3 mils to ± 15 mils. The strength of the welded joint varied with the face weld penetration as well as the back weld configuration.

The weld shape of the back fillet has three important dimensions as schematically shown in figure 12. The first is the radial penetration into the tube which is responsible for most of the local distortion on the tube interior diameter. The second measurement is the length of the weld leg along the tube and flange interface, while the last and most important dimension from a strength consideration is the fracture path length. The circumferential back weld is a fillet weld and as such fractures along an angle approximately 45° to the tube axis. The optimum geometry of a "back" weld would have sufficient penetration (approximately 30 to 50 mils) into the tube and along the tube-flange interface while completely filling the corner between the tube surface and flange end. A large uniform fillet weld maximized the amount of material positioned to resist the shearing action of a fillet weld and exhibits the greatest strength. The beam was directed into the joints from an angle of 12° off the vertical for the back fillet weld and 10° above the horizontal for the face weld.

Mechanical tests were conducted on the welded samples to determine the weld strength by recording the load needed to drive the tube from the flange. The flange was rigidly supported while the tube was loaded so that the flange-tube interface was in shear and applied a "tensile" load through the back weld. The method of

loading was chosen to simulate field loading conditions.

Yield and ultimate loads are recorded for the various face weld penetrations in figure 13; back weld strength are displayed in figure 14. The strength of the circular face welds are generally lower than the butt welds due to the differences in loading, that is, the circular face weld is loaded in shear while the butt welds are loaded in tension. Results from mechanically testing the flanged coupling predicted that the design criteria can easily be achieved with a 0.075 inch face weld penetration and a suitable back fillet weld.

Waveguide I.D. Temperature

Temperature requirements for waveguide flange welding fall into two categories. The first is a concern for the deterioration of the dielectric liner due to high weld temperatures and the second is a concern for distortion of the steel caused by stress changes resulting from welding. Although, maximum temperature limits have been imposed on the waveguide internal diameter, the true limit is based on the degradation of the dielectric liner which is affected by both the welding atmosphere and the time-temperature cycle. The specification temperature limit is 250°F but the extremely short heating times of electron beam welding has permitted higher temperatures without degrading the liner. In addition, the safe limit established in a stress relief experiment conducted by Bell Telephone Laboratories revealed no significant geometric changes in the waveguide after one week of annealing at 500°F.

To obtain the internal surface temperature profiles as a function of penetration, circumferential bead-on-plate welds were made on 6 inch long, copper-plated, unlined 51 mm waveguide samples. Welds were made in a hard vacuum environment (10^{-4} torr) with the high voltage and welding speed held constant at 50kV and 100 ipm and varying the beam current. Tempilaq, a temperature sensitive lacquer, was used for all temperature measurements. Results are plotted in figure 15 as temperature profiles for various energy inputs. The nominal penetrations are presented for reference since variations in penetration were quite common. Distances from the weld centerline were obtained from measurements of the melted Tempilaq region on the sample's internal surface.

Results from identical welds on dielectric lined waveguide are shown in figure 16. The lined waveguide in this experiment refers to a 7 1/2 mil thick polyethylene coating (liner) bonded to the copper surface of a 51 mm waveguide tube with approximately 1/2 mil of hydropol adhesive. A bubbling condition

clearly exists for all welds with penetrations greater than 0.075 inches. In fact, examination of the samples gives evidence of the initiation of bubbling near the 0.062 inch penetration weld. Referencing this weld to temperature profiles on unlined 51 mm waveguide established a 375° - 400°F temperature limit for protection of the dielectric liner. Bubbling appears to result from vaporization of the hydropol adhesive and/or expansion of air entrapped under the liner during bonding. Expansion and vaporization are a consequence of localized pressure and temperature gradients produced by welding in a vacuum environment.

Welding of the flange to the waveguide tube required two welds as shown in figure 5 and explained previously. Correlation between the circumferential bead-on-plate weld and back flange fillet weld is expected to be better than the correlation with the face weld because of similarity in welding angles. More important, temperature comparisons reveal lower temperatures with the face weld since the fusion zone is further away from the the tube I.D.

Results of Tempilaq measurements on 6-inch, 51 mm unlined waveguide samples are plotted in figure 17. Additional complications are imposed by the flange (e.g. flange-to-tube clearance, weld runoff, beam alignment, etc.) and hence the temperature measurements are somewhat less reliable. However, the qualitative result of lower temperatures for a given face weld penetration (as compared to bead-on-plate welds) is obvious from figures 15 and 17.

In conclusion, a flange can be welded to 51 mm waveguide tubes with peak internal diameter temperatures less than 400°F with a 0.075 inch face weld penetration and a 0.040 inch back weld penetration. Penetrations greater than 0.065 inches (or equivalent temperatures of 375° - 400°F) on circumferential bead-on-plate welds caused bubbling of the dielectric liner when the samples were welded in a vacuum.

Distortion Studies

Dimensional accuracy is the one aspect which distinguishes waveguide tubing from ordinary tubing. Any changes in the tube geometry from a right circular cylinder results in the conversion of energy from the primary transmitting mode (TE_{01}) into other spurious modes [2]. Such a conversion has the dual effect of decreasing the signal amplitude and causing phase distortions. These phenomena are particularly harmful if the variations occur periodically. Since waveguides are manufactured in finite lengths the potential for a periodic distortion occurring at each joint is high. Minimization these losses, occurring at each coupling, can be accomplished by randomizing the tube lengths and controlling the weld distortions.

Dimensional specifications were established to ensure such a quality control. These requirements restrict the allowed diameter change after welding to ± 0.002 inches from the nominal tube dimensions.

For the majority of the distortion measurements an average diameter air gauge was used. The output of the air gauge is displayed on an X-Y recorder to obtain the average internal diameter of the sample and the probe position. A typical diameter profile of such an output is shown on figure 18. Since two welds are required to attach the flange to the waveguide tube, it is convenient to separate the distortion realized from each weld and to examine them independently.

Based on results of experiments conducted with circumferential bead-on-plate welds, a radial penetration between 0.030 and 0.050 inches was required to meet the waveguide strength and distortion specifications. Figure 18 illustrates the distortion realized from a back weld with a 0.040 inch penetration. On 21 samples, the measured distortions associated with such a back weld revealed an average diameter decrease of 0.36 mils. Variations in the distortion measurements can be attributed to the quality of the weld and the position or alignment of the electron beam and the joint. A beam positioned too high, i.e., favoring the flange, would result in low distortions with the weld fusion zone being more in the flange and less into the waveguide tube. Similarly, a beam positioned too low, i.e., favoring the tube, would result in high distortions with the weld fusion zone being deeper into the tube.

Immediately evident in figure 18 is the opposite direction of the distortion from the face and back welds. The contraction of the molten metal during solidification and cooling introduces additional stresses (circumferential, axial, and rotational [6]) in the base metal which result in the observed distortions. The back welding angle (120° from vertical) and weld geometry are similar to that of a circumferential bead-on-plate weld and as such the welds display similar distortions. Hence, large tensile hoop stresses are expected near the weld centerline which constrict the waveguide and produce a diameter decrease [7]. On the other hand, the face weld solidification is more complex. Residual stresses in the waveguide [8], combined with axial shrinkage and constrictions which cause a rotation about the weld, result in a diameter increase.

As expected the magnitude of these distortions increased with penetration (figure 19). However, in experiments conducted with both the thin flange and the standard flange shown in figure 20, the face weld distortion was reduced by almost one mil with the thin flange design. Figure 21, illustrates the change in the distortion pattern.

Weld solidification can explain the differences in the distortion profile between the standard flange and the thin flange. The additional variable in this case is one of restraint. The flange base metal adjacent to the weld is more restrained by the standard flange than the thin flange as seen in figure 20. Therefore, more distortion is realized in the tube with relatively little deformation in the standard flange. The thin flange, being flexible, reflects a larger portion of the total displacement and results in a lower distortion of the tube I.D.

In conclusion, the distortion created by welding a flange to the waveguide tube is different for the face and back welds. The circumferential fillet (back) weld which had a radial penetration of 0.040 inches results in an average diameter decrease of approximately 0.4 mils whereas the circular square butt (face) weld with a penetration of 0.075 inches resulted in an average diameter increase of 1.1 mils. In addition, the distortion realized from the face weld can be reduced by almost 1 mil by a specially designed flange.

Electron Beam Welding Facility

The design of the electron beam welding system for use in fabrication of millimeter waveguides was centered around two major ideas. The first was the desire for minimizing alterations to a standard electron beam welder so that the system would be useful for experimentation other than waveguide flanging while the second factor was a concern for the output requirements of the millimeter waveguide field evaluation test. Since the best electron beam welds are made with a vacuum chamber, the most difficult design problem centered around welding flanges to 9 meter long waveguides in a vacuum (10^{-4} torr) environment. Utilizing the experience gained while welding samples in the development studies, Western Electric Co. (Engineering Research Center) personnel and engineers from Sciaky Brothers, Inc. collaborated to solve this and other design problems in order to make the welder compatible with waveguide requirements.

The electron beam welding system as shown in figure 22 consists of a high vacuum chamber 62 inches long x 30 inches wide x 42 inches high (inside dimension) with associated pumping equipment. A 600 c.f.m. capacity roughing pump together with a 16 inch oil diffusion pump can evacuate the chamber from atmosphere to 10^{-4} torr in approximately three minutes. The electron beam guns, powered by a 7 1/2 KW D.C. supply, operate with a directly heated filament and an electromagnetic focusing system. Operation of the welder is fully automatic with adjustable cam control of the sequence. Once the sequence has been initiated a closed loop

servo controlled feedback system maintains the desired parameter settings until the welding has been completed.

Alterations made to a standard high vacuum electron beam welder by Sciaky Brothers, Inc., were associated primarily with the need to weld 9 meter long waveguides inside a vacuum chamber. Hence a vertical lift door and special split seals (figure 23) were added which allowed the simultaneous loading of four waveguide tubes into the chamber. One end of each waveguide is plugged internally, and the double split seal in the vertical lift door seals the tube externally. Differential pumping between the seals insures the 10^{-4} torr vacuum. This unique sealing system requires only 2 1/2 feet of the waveguides to be enclosed in the vacuum.

To facilitate handling and to simplify the set-up operation a special tooling fixture locates the flange and tube in position under the welding heads (figure 24). Welding is performed with a dual gun system with one gun making the face weld while the second makes the back weld. A single power supply necessitates switching between each gun to complete the welding operation. A dual set of controls allows each gun to operate independently with individual adjustments for beam current, focus and welding speed but with common high voltage and slope controls. The two welding guns are indexed from one tube to the next until all four have been welded. Since the electron beam is held stationary, welding is accomplished by simultaneous rotation of the four tubes with hard rubber drive rollers located outside the vacuum chamber. The speed range is variable between 0.32 and 32 rpm.

Once the problems associated with welding flanges to the end of waveguide tubes had been solved, attention centered on meeting the requirements for the fabrication of waveguides for the field evaluation test. The schedule dictated welding four flanges with each set-up and thus distributing the pump down time associated with the welding cycle over four tubes. The above operation is capable of welding flanges to four waveguides (both ends) per hour, with most of this time in tube handling since each weld requires approximately 10 seconds.

Summary

The success of millimeter waveguide as a communication medium is dependent on minimization of periodic geometric distortions. However, use of electron beam welding has been shown to minimize the diameter changes (less than 0.001 inch) associated with the flanging operation. In addition, the joint strength of 45,000 lbs. was easily attainable with minimum heat input causing the peak internal tube temperatures to be below 500°F. Welds were

deeper, narrower, and had better quality than any of the other processes evaluated. Reproducibility of the welds was also excellent and resulted from superior control over penetration and other weld dimensions. Finally, the flexibility of electron beam welding with regard to future waveguide and other manufacturing needs may provide improvements to the overall system.

Acknowledgements

The authors wish to acknowledge the helpful waveguide flanging discussions with P. L. Key, A. B. Watrous, and C. Willis of Bell Telephone Laboratories. Special thanks go to T. J. Kelly for his able assistance in sample preparation, testing, and constant help throughout the entire program.

References

1. G. C. Southworth, Eng. Notes, Vol. XI, April 1932.
2. Rowe, H. E. and Warters, W. D., Bell System Technical Journal 41, 1033 (1962).
3. Bibby, M. J., Burbidge, G. and Goldak, J. A., Welding Journal 51, 844 (1972).
4. Goldak, J. A., Burbidge, G. and Bibby, M. J., Canadian Metallurgical Quarterly 9 (3), 459.
5. Goldak, J. A., Burbidge, G. and Bibby, M. J., Canadian Metallurgical Quarterly 9 (3) 467.
6. Masubuchi, K., "Control of Distortion and Shrinkage in Welding", WRC Bulletin 149, (1970).
7. Vaidyanathan, S., Todaro, A. F., and Finnie, I., Journal of Engineering Materials and Technology 95, 233 (1973).
8. Marschall, C. W., "Investigation of Residual Stresses and Dimensional Stability of Steel Waveguide Tubes", Battelle Columbus Laboratories Research Report to Bell Telephone Laboratories, February 28, 1973.

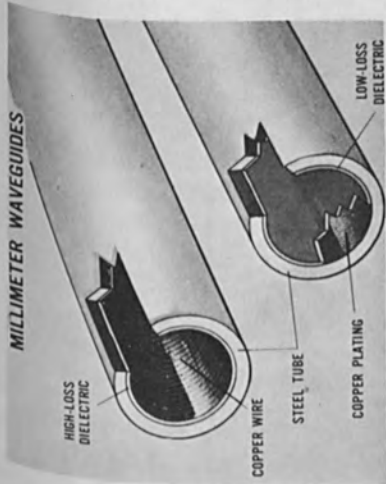


Fig. 2. Helix (top) and dielectric waveguide.

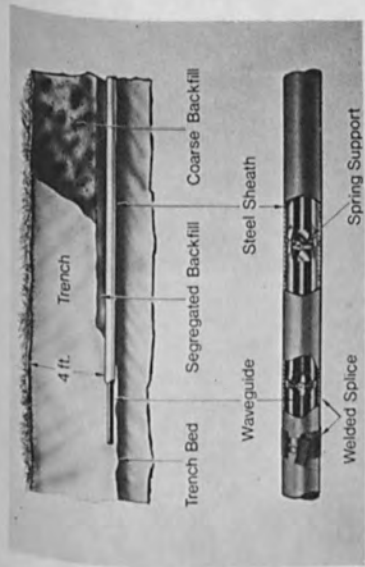


Fig. 1. Photograph of installed waveguide.

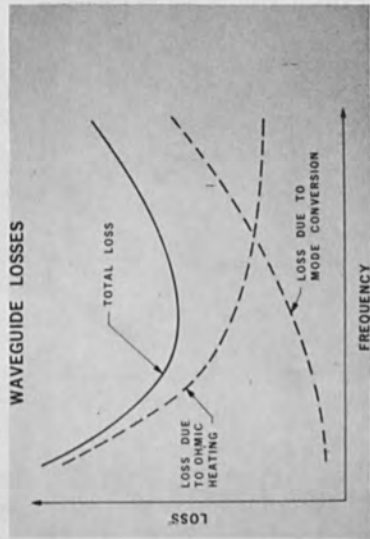


Fig. 3. Loss vs. frequency curve.

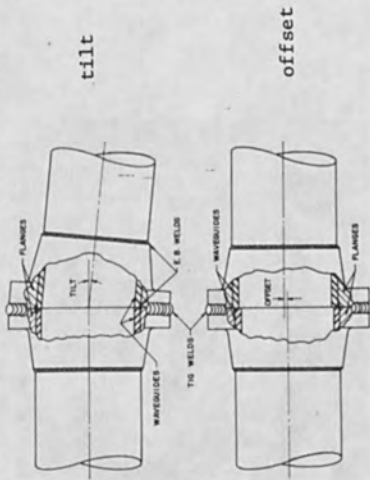


Fig. 4. Waveguide tube alignment.

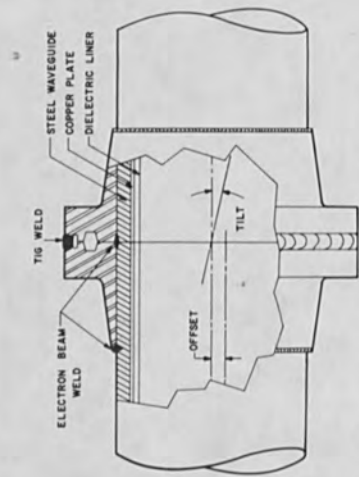


Fig.5. Schematic of 60mm flange coupling.

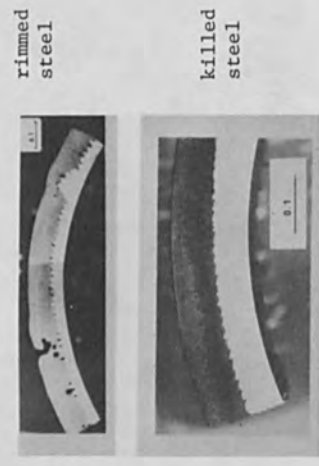


Fig.6. Photograph of weld porosity.

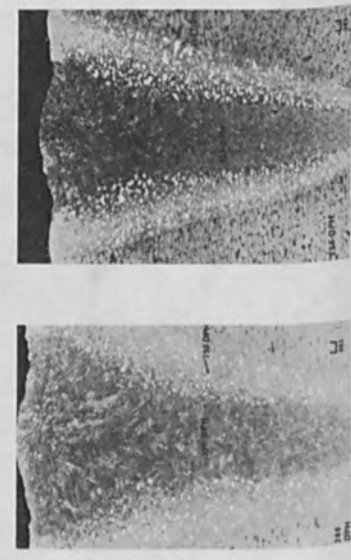


Fig.7. Yield hardness measurements.

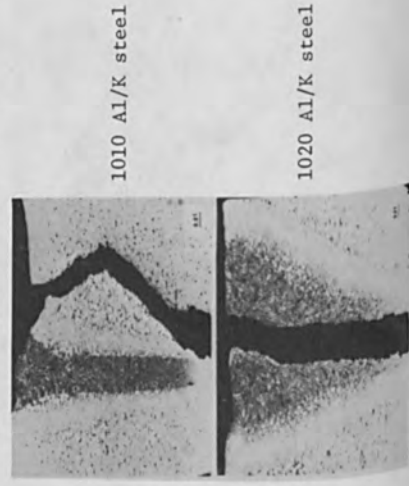


Fig.8. Weld fracture paths.

Fig.8. Weld fracture paths.



Fig.9. SEM of weld fracture surfaces.

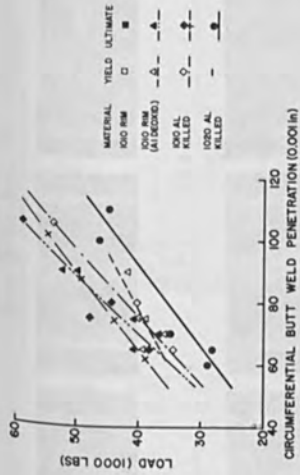


Fig.10. Full butt weld tensile tests (51mm).

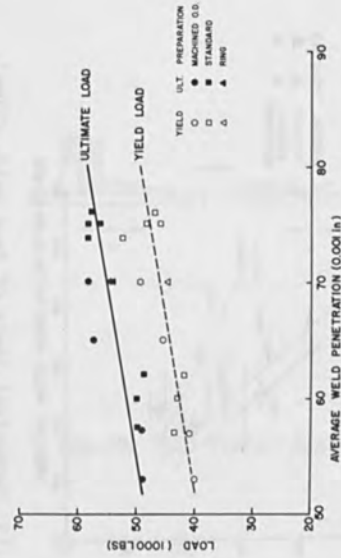


Fig.11. Full butt weld tensile tests (60mm).

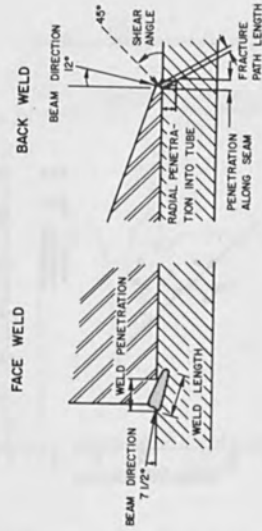


Fig.12. Schematic of weld penetration.

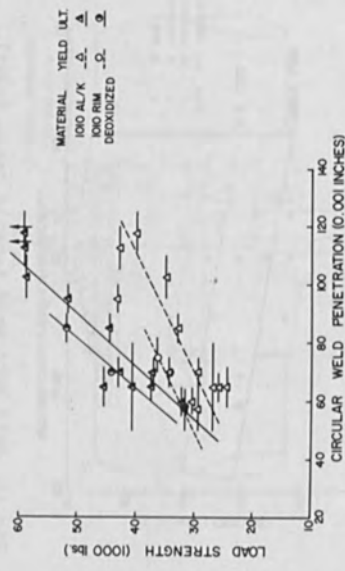


Fig. 13. Mechanical tests of face welds (51mm).

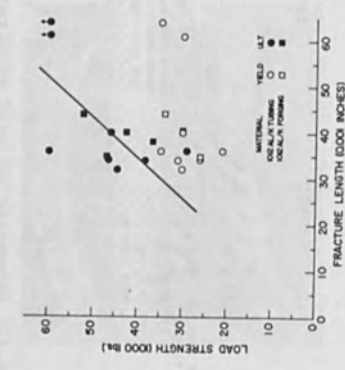


Fig. 14. Mechanical tests of fillet welds (60mm).

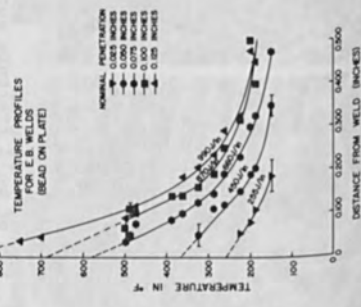


Fig. 15. Temperature profiles for B.O.P. welds.

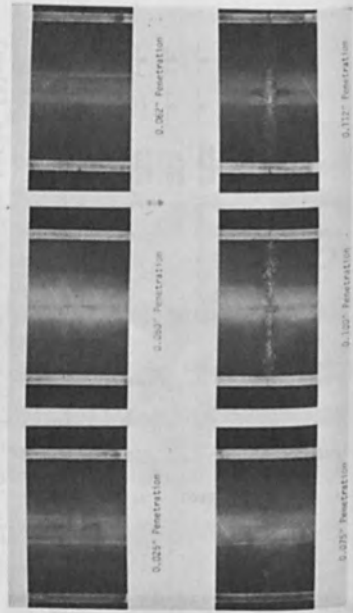


Fig. 16. E.B. welding effects on dielectric liner (B.O.P. welds).

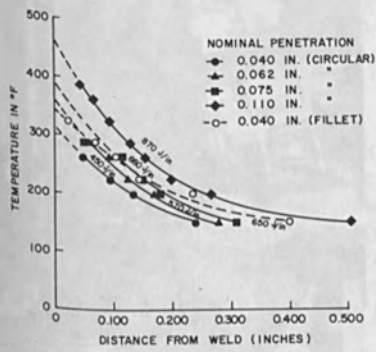


Fig. 17. Temperature profiles of 51mm flange welds.

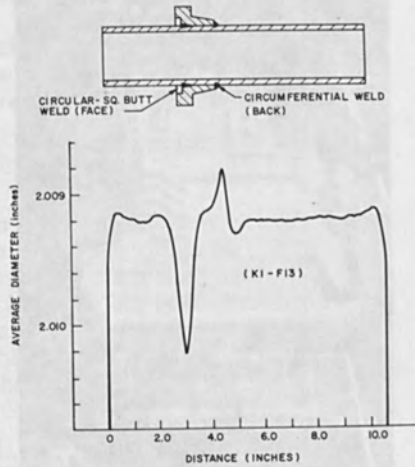


Fig. 18. E.B. weld distortion profiles (51mm).

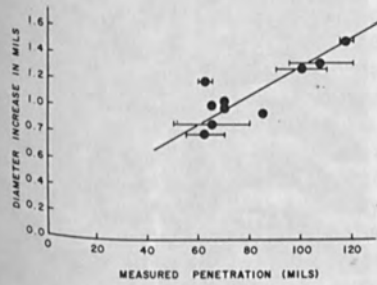


Fig. 19. E.B. face weld distortion (51mm).

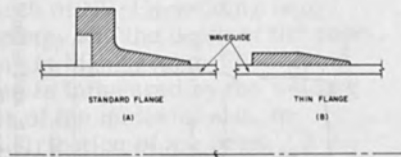


Fig. 20. 51mm flange designs.



Fig. 21. Comparison of thin and standard flange weld distortions.

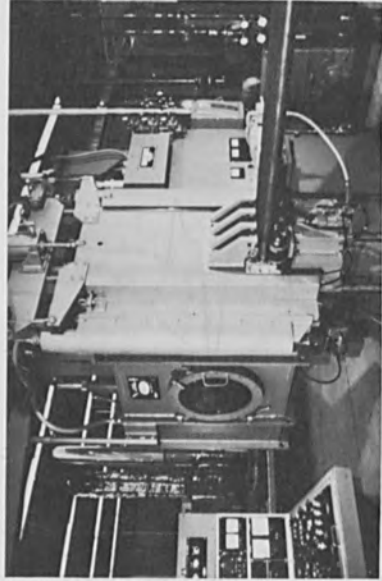


Fig. 22. Overall photograph of E.B. welder.

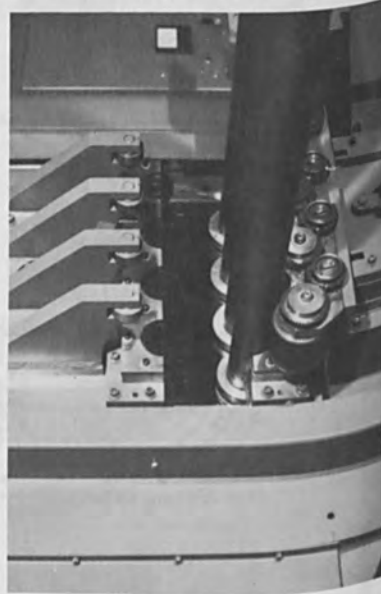


Fig. 23. Photograph of vertical lift door.



Fig. 24. Photograph of chamber interior.

SOME INVESTIGATIONS IN NON-VACUUM EB-WELDING

V. Bödecker,
W. Jüptner,
H.-D. Steffens

IFAM, 2820 Bremen 77, Lesumer Heerstraße 36

Experiments on bead formation in electron beam welding have been carried out at pressures in the range of 1-760 Torr. The experimental results were compared with mathematical equations taking into account beam broadening by electron scattering. Increasing the working distance leads deep penetration to the formation of semi-circular seam geometry, solely due to heat conduction.

1. Introduction

Electron beam welding is characterized by deep penetrations into solid materials. Therefore steel plates of more than 50 mm thickness can be joined by single pass welding. This property is of economical interest especially when dealing with large work pieces. However, there is a significant disadvantage to standard EB-welding: normally it is necessary to weld in a vacuum environment. To avoid the difficulties connected with the construction of large vacuum chambers and pumping systems, current research seeks to weld with an electron beam in atmosphere up to 760 Torr [1]. One point of special interest in the research of NV-EB-welding is to determine the dependence of the geometry and the depth of the seam, on welding parameters. Investigations in high vacuum EB-welding yield that the geometry of welded zone is influenced by the welding speed, the thermophysical properties of the material and, in particular, by the spatial intensity distribution of the beam [2]. This leads to the presumption, that for NV-EB-welding the power density distribution of the electron beam, influences strongly the geometry of the molten zone. In order to calculate the seam geometry as a function of the spatial intensity distribution and other welding parameters, the scattering of the electron beam caused by the working gas is considered. The relation between the shape of the fusion zone and parameters mentioned before will be discussed.

2. Equipment

With the exception of the pressure staging system the equipment is constructed with the same elements as for a high vacuum EB system: an electron beam generator with high voltage part, chamber and pumping system. The generator operates in high vacuum of 10^{-4} Torr. However, in NV-EB-welding the working chamber is necessary only for X-ray-protection.

Additional to these main parts of the machine, there is the need for a pressure staging system to reduce the pressure in the working chamber to that in the generator. This pressure stage must be permeable to the beam. In this research work a system consisting of two separate pressure stages was used, fig. 1.

Each stage is bounded by a nozzle with a diameter of 1 - 1,5 mm. The pressure in the upper stage amounts to 10^{-1} Torr.

3. Spatial Intensity Distribution

The intensity distribution of the electron beam, in a plane perpendicular to the beam axis, is well approximated by a Gaussian profile:

$$L = \frac{N}{2\pi\sigma^2} \exp\left(-\frac{x^2+y^2}{2\sigma^2}\right) \quad (1)$$

L = power density

N = beam Power

σ = standard deviation

x, y, z = Cartesian coordinates, defining the beam axis

The standard deviation σ , is a function of the coordinate z, in the beam direction. The standard deviation σ_u of a non-scattered electron beam is given by:

$$\sigma_u^2 = \sigma_0^2 + \alpha^2 \cdot z^2 \quad (2)$$

σ_0 = Standard deviation in the focal plane

α = beam angle related to the standard deviation

The electron beam is broadened when it passes through a scattering gas, fig. 2.

It is necessary to add a scattering term σ_s , to the standard deviation of the undisturbed beam, such that

$$\sigma^2 = \sigma_u^2 + \sigma_s^2 \quad (3)$$

Corresponding to the theory of scattering σ_s can be calculated by:

$$\sigma_s^2 = \frac{a}{6} \cdot \frac{z^3}{A\lambda} \quad (4)$$

In this formula $A\lambda$ represents the mean free path of electrons and a is a constant related to the scattering cross section of the working gas. This constant, a , depends on the Lenard thickness A_m (A_m is tabulated for the common working gases) in the following manner:

$$a = \frac{3 \cdot \tan^2 10^\circ}{\ln 2} \cdot \frac{A\lambda}{A_m} \quad (5)$$

With this equation, the standard deviation σ_s is given by

$$\sigma_s^2 = 2,24 \cdot 10^{-2} \cdot A_m^{-1} \cdot z^3 \quad (6)$$

In a calculation of σ_s , the scattering of the beam along the whole path, as affected by the pressure distribution must be considered. However, EB-welding experiments in low vacuum yielded the following results: When working with NV-EB-welding the broadening of the beam, due to scattering, essentially occurs along the path between the exit nozzle of the lower pressure stage, and the workpiece. Therefore, the scattering of the beam in the pressure stage system will be neglected in the following considerations.

The real standard deviation of a scattered beam can be expressed as

$$\sigma^2 = \sigma_o^2 + \sigma_z^2 + 2,24 \cdot 10^{-2} A_m^{-1} (z-d)^3 \quad (7)$$

d = distance between exit nozzle and workpiece.

The spatial intensity distributions of electron beams were measured for pressures of 10^{-4} Torr and 760 Torr. The values of the standard deviation σ are shown in fig. 3 as a function of the beam path z .

Taking into account the beam propagation, measured in high-vacuum, the experiments prove the dependance of σ_s to $z^{1.5}$ according to the theory (Eqn 4). The value of the Lenard thickness A_m determined by experiments is 60 mm. However, the tabulated value of A_m is 8 mm. This discrepancy can be attributed to the heating of the working gas by the high power beam. The determination of the dependance of the Lenard thickness on power and power density of the electron beam is one of the aims of future research.

Using the experimentally found value of the Lenard thickness A_m , the spatial intensity distribution of the scattered beam can be computed by equation 7. This formula is valid for all working distances significant for NV-EB-welding.

4. Formation of the Vapor Channel

With the aid of the spatial intensity distribution the width of the vapor channel as a function of the depth z can be calculated by the following equation [2]:

$$x = 2 \cdot \sigma(z) \left[-2 \cdot \ln \left(\frac{\sqrt{2\pi} \cdot \sigma(z) K_m}{N} \right) + \frac{\sqrt{2\pi} \cdot Q_v \cdot v}{N \cdot \sigma(z)} \cdot \int \sigma^2(z) dz \right]^{1/2} \quad (8)$$

- x = width of vapor channel
- K_m = minimum power density for evaporation, integrated over the welding path,
- Q_v = energy per volume for evaporation,
- v = welding velocity

The standard deviation σ at the workpiece surface, must be calculated using equation (7). The beam propagation within the vapor channel is unknown. Therefore, two models were investigated:

For the first model it was suggested that the beam is scattered inside the vapor channel in the same manner as in the working gas. In the other case it was assumed that no scattering occurs in the channel. In both cases the dependence of the weld depth on the electron beam power was evaluated and supported by NV-EB-welding experiments, fig. 4. For comparison, the results of high vacuum EB-welding are shown, too.

Comparing the theoretical curves with the experimental values, there is no information about the scattering effect within the vapor channel. The calculations of the weld depths lead to nearly the same values, independent upon the additional scattering in the capillary. However, these results indicate the good description of EB-welding by the equation (7) and (8), both for high-vacuum and non-vacuum processes. As an example, fig. 5 shows the cross-section of a welding seam and the corresponding theoretical curves for the vapor channel and the molten zone.

The evaluated melting zone well agrees with the experimentally found melting geometry, and a small deviation in the lower part of the seam-cup had to be stated.

Compared to weldments in high-vacuum, the geometry of NV-EB-welded seams are essentially affected by the scattering above the workpiece. To increase the weld depth, it is necessary to decrease the scattering effect in the working gas. This can be done in the following manner:

1. An increase of the accelerating voltage will increase the Lenard thickness A_m , fig. 6.

The broadening of the scattered beam will be reduced, since the standard deviation σ_s is inversely proportional to the square root of A_m .

2. Using Helium as working gas should result in an increase of the weld depth, due to a smaller scattering cross section. However, experiments showed that the passing of helium through the channel in the lower nozzle, blowing against the molten pool, increases the pressure above the workpiece and within the pressure staging system. Therefore, the expected result was not observed [1]. The flooding of the working chamber with helium should prove more successful, but is very expensive.

3. Reducing the working distance is an obvious solution, but leads to the practical problem of nozzle protection [1]. A minimum working distance of 6 mm has been used to this stage. Further experiments are presently being conducted to reduce the working distance.

5. Conclusion

The propagation of electron beams in non-vacuum environment has been investigated. The Lenard thickness, A_m , has been shown to be a suitable quantity for the calculation of spatial intensity distribution under normal operating conditions. With a mathematical model describing the electron beam, it is possible to calculate the weld seam geometry.

The depth and width of fusion zones as predicted by this model, are in good agreement with the results of experimental investigations.

Acknowledgements

The authors wish to thank the Deutsche Forschungsgemeinschaft for their financial support of this research.

References

- [1] Jüptner, W. Non-Vacuum Electron Beam Welding
G. Sepold und 3rd Electron Beam Processing
H. -D. Steffens: Seminar, Stratford-upon-Avon, 1974
- [2] Jüptner, W. Influence of Spatial Intensity
V. Bödecker und Distribution on Deep Welding Geometry
G. Sepold: 6th Int. Conf. on Electron and Ion
Beam Science and Technology,
San Francisco, 1974
- [3] Lenard, P. Quantitative über Katodenstrahlen
aller Geschwindigkeiten
Verl. K. Winter, 1925

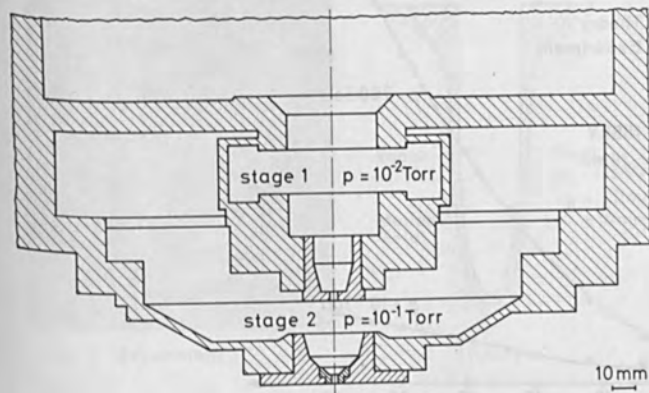


Fig. 1: Pressure staging system of ESW 12/700

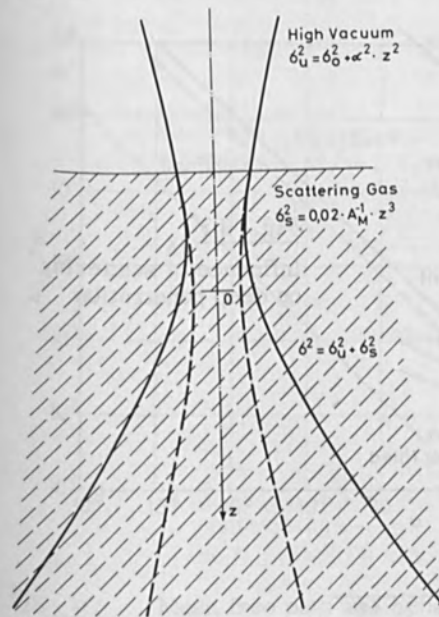


Fig. 2:
Schematic illustration
of scattered electron
beam

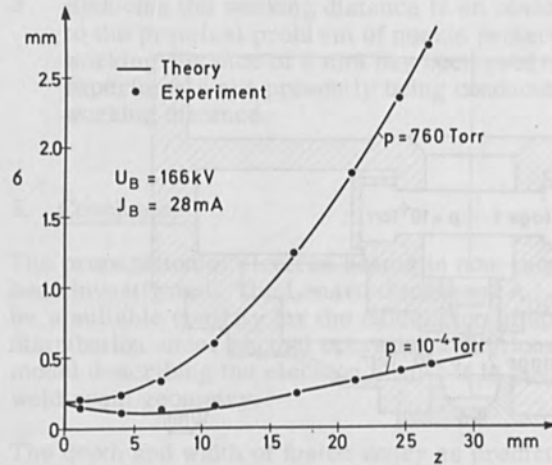


Fig. 3: Spatial intensity distribution of electron beam

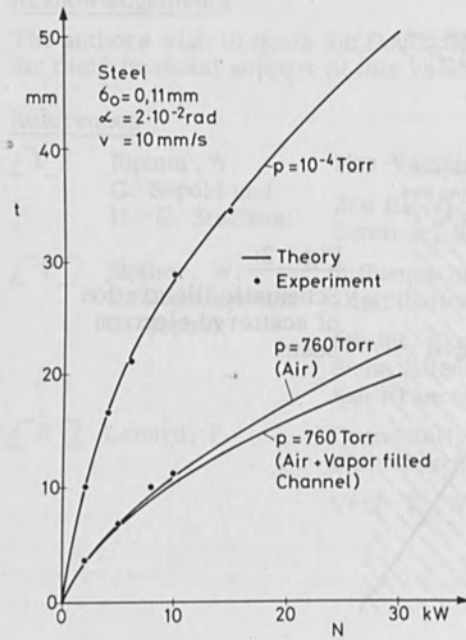


Fig. 4 :
Influence of scattering
on deep penetration

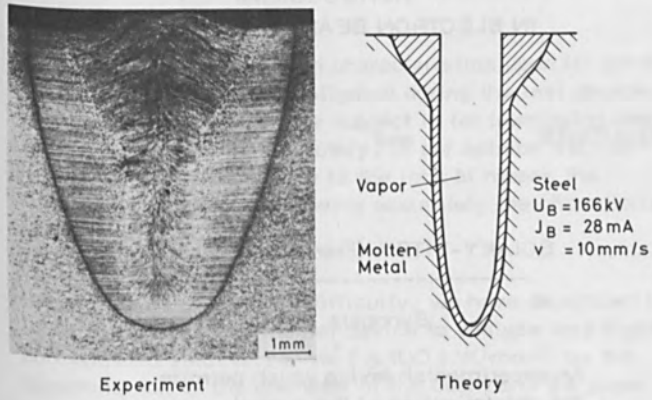


Fig. 5 : Cross section of NV-EB-weldment

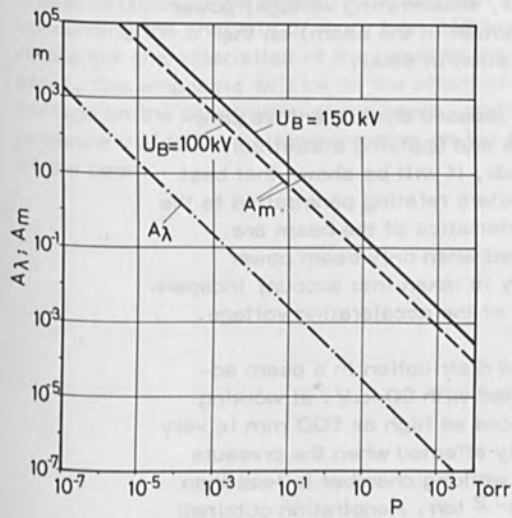


Fig. 6 : Mean free path and Lenard thickness of electrons in air

EFFECT OF WELDING PARAMETERS ON THE PENETRATION
IN ELECTRON BEAM WELDING

P. DUMONTE

and

G. SAYEGH

SCIAKY-VITRY (France)

Synopsis

An experimental device which permits the determination of the current distribution in high power electron beam shall be described.

This device was used to investigate the effect of the beam parameters (power, accelerating voltage, power distribution in the beam) on the penetration in steel.

Using reduced dimensionless parameters and applying statistical methods, it will be shown that best parameters relating penetration to the characteristics of the beam are obtained when only beam power density is taken into account independently of the accelerating voltage.

Current distribution in a beam accelerated with 60 k.V. at working distances as high as 500 mm is very slightly affected when the pressure in the working chamber is less than 3×10^{-2} torr. Penetration obtained at 5×10^{-3} torr is almost identical to that obtained in hard vacuum.

INTRODUCTION

The effect of electron beam characteristics upon its penetration has been extensively investigated during the last decade. Published literature on this subject is far from being unanimous and is sometimes contradictory. In our opinion the main reason for this discrepancy is the lack of means the investigators possess to define accurately the characteristics of the beam.

In order to eliminate this difficulty, we have developed in our laboratories an experimental device to analyse very highly concentrated electron beams ($> 100 \text{ KW/mm}^2$) by the determination of the diameter of the beam and the power distribution at different cross-sections.

First, we shall describe the experimental method and present the way to determine, from the experimental results, the characteristics of the beam. Next we shall discuss results concerning the analysis of more than 140 beams and try to relate the characteristics of the beam to the penetration in steel. The emphasis will be on the effect of accelerating voltage on the penetration of the beam, and on the effect of the pressure inside the working chamber on the power distribution of the beam.

I. EXPERIMENTAL METHOD

1.1. Principle of the experimental method

The principle of the experimental method is to displace the electron beam across a FARADAY cage covered by a tungsten sheet equipped with two narrow slits ($50\ \mu$) and to record the current received in the cage at the different positions of the beam.

When the beam is displaced across the cage, (see figure 1), there is no current until the beam enters the slit; then the current increases to a maximum when the slit is at the center of the beam, and decreases to zero when the beam leaves the slit. The signal in the cage is introduced on a memory oscilloscope and is photographed. Measurements made on the picture are introduced in a computer programme to determine the power distribution in the cross section and to calculate the diameter containing a given part of the beam power.

1.2. Description of the experimental method

The displacement of the beam across the slit is effected by maintaining the FARADAY cage fixed and deflecting periodically the beam with an appropriate magnetic field (see figure 2a).

At rest the deflecting coil 1 is supplied with a current $-I$, so the beam is deflected from the axis of the gun onto a block of copper 2 where the power is dissipated. Then the current in the magnetic coil is changed rapidly to $+I$, and the beam is deflected in the opposite direction onto a second block of copper. While crossing from one block across to another, the beam sweeps very rapidly (150 m/sec) across the FARADAY cage. The high sweeping speed allows to analyse very high power beams (30 KW in less than 0.5 mm diameter was reached).

The signal in the FARADAY cage is composed of two curves which correspond to the passage of the beam over the two slits (figure 2b). These curves will permit to calibrate the diameter of the beam; as a matter of fact, the horizontal distance between the two maxima corresponds to the distance between the axis of the two slits. One of the curves is then isolated, photographed and analysed to determine the power distribution.

It can be noted that the focus point on the surface of the slit can be defined with a very high accuracy; 0.5% variation of the magnetic coil supply, produces a big difference on the signal (figure 2c).

1.3. Determination of the power distribution in the beam

Figure 3a shows the magnified picture which serves to estimate the power distribution. Because of the halo of electrons which surround the beam it is quite difficult to determine the diameter of the envelope of the beam. We have chosen arbitrarily the diameter at 0.9 I max. On the other hand we have defined the diameter of the cylinder which contains 50% of the total beam power.

Current density at a point located on a circle of radius r , will be given by (1) :

$$J(r) = \frac{1}{\ell \pi r} \frac{d}{dr} \left\{ \int_r^R \frac{i(x) x dx}{(x^2 - r^2)^{3/2}} \right\} \quad (1)$$

where : ℓ is the width of the slit

$i(x)$ is the equation of the curve of figure 3a.

Numerical integration of equation 1 needs, in order to be accurate, a very high precision on the measurement both of $i(x)$ and $\frac{d i(x)}{dx}$. We have preferred using a direct method of matrix inversion.

Intensity $I(j)$ at abscissa j , (see figure 1), is the sum of $J(i) \times S_{i,j}$ where :

$J(i)$ is the current density at abscissa i

Numbers between brackets refer to bibliography at the end of the text.

$S_{i,j}$ is the surface comprised between the crown i and the slit.

In matrix notation, this gives :

$$\begin{bmatrix} S_{i,j} \end{bmatrix} \begin{bmatrix} J_i \end{bmatrix} = \begin{bmatrix} I_j \end{bmatrix} \quad (2)$$

All elements of the triangular matrix $S_{i,j}$ can be calculated easily.

Elements of the column matrix $\begin{bmatrix} I_j \end{bmatrix}$ are measured on the figure 3.

The researched matrix $\begin{bmatrix} J_i \end{bmatrix}$ which will present the current density at any point of the beam, will be given by :

$$\begin{bmatrix} J_i \end{bmatrix} = \begin{bmatrix} S_{i,j} \end{bmatrix}^{-1} \begin{bmatrix} I_j \end{bmatrix} \quad (3)$$

A computer programme will calculate all elements of the matrix $\begin{bmatrix} J_i \end{bmatrix}$.

1.4. Comparison to theory

It is interesting to point out that the experimental results were used to test the theoretical methods employed in our laboratories to optimize the components of an electron gun (2), (3). These theoretical methods resolve the different equations which define the physical behavior of the beam in the electron gun: potential distribution, electron trajectories, power in the beam and its distribution in the different cross-sections.

Figure 4 shows the comparison between experimental and theoretical results giving the power distribution in the beam. It can be seen that these results are in quite good agreement.

2. EFFECT OF THE WELDING PARAMETERS ON THE PENETRATION

Even though all authors admit that penetration depends directly on the power of the beam, viewpoints concerning the effect of accelerating voltage on the penetration are very contradictory.

Some authors claim that penetration depends on the accelerating voltage; but the nature of this dependence is variable from one author to another: Arata et al. (4) think, in addition to its dependence on the beam power, that penetration is a function $\sqrt{0.3}$; whereas, AKOP'YANTS (5) thinks that it is function of $\sqrt{0.5}$.

Other authors claim that penetration of the beam is independent of the accelerating voltage, that it is only a function of the specific power in the beam which depends only on the power of the beam and its diameter on the target (6), (7).

This contradiction is due, in our opinion to the fact that from one author to another there is big ambiguity in the definition of beam characteristics. The use of the experimental method described in 1 will help to eliminate this ambiguity by providing the actual characteristics of the beam.

2.1. Domain covered by the experimental method

This experimental method was used to analyse more than 100 beams, for which diameter and power distribution on the surface of the workpiece were determined. Then melt runs were executed on a 15CDV6 steel and penetration of every beam was measured on a macrography.

Ranges of parameters covered are :

beam power	: 1.5 K.W. - 20 K.W.
accelerating voltage	: 30 K.V. to 60 K.V.
welding speed	: 15 cm/mi - 100 cm/mi

The composition of this steel is :

C	O.15%	Mn	O.9%	Si	O.20%
Cr	1.35%	Mo	O.9%	Va	O.25%
S	O.035%	P	O.035%		

penetration : 2.2 mm - 38 mm
diameter of the beam
containing 50% of the power : 0.15 - 0.35 mm
working distance : 525 mm

It is interesting to present photo N°5 which shows a penetration of 100 mm thick obtained with the electron gun analysed in this paper. The welding conditions were: 30 K.W.; 60 K.V.; 20 cm/mi; working distance 450 mm.

These results were added recently to studies, executed on the high voltage, high power gun of the Welding Institute (U.K.), as follows :

beam power : 3 - 12 K.W.
accelerating voltage : 75 - 150 K.V.
welding speed : 50 - 100 cm/mi
penetration : 3 - 25 mm
beam diameter at $\frac{I_{max}}{2}$: 0.32 mm - 1.28 mm
working distance : 400 mm

It is necessary to make the following remarks concerning the results obtained between 75 K.V. and 150 K.V.:

- The high voltage gun, which has been used to cover the experimental points between 75 K.V. - 150 K.V., is designed for working at high powers 75 K.W. - 150 K.V. Consequently penetrations obtained at relatively low powers (3 - 12 K.W.) cannot give an exact idea of its real performances.
- Nevertheless, the purpose of the investigation is to estimate the effect of the accelerating voltage on the penetration of the beam only, taking into account the power density distribution on the workpiece, the thermal characteristics of the workpiece and the welding speed.
- The analysis of the beam at 75 K.V. - 150 K.V. was made at the welding Institute (U.K.) by employing the flying wire method (12). Because of the high ripple on the accelerating voltage and the nature of the experimental method, the recorded curves are not very accurate (figure 3b).

2.2. Discussion of the results

It is very interesting to present the experimental results by using dimensionless variables, as first introduced by LUBIN (8). These variables will be slightly modified in order to take into account the effect of back scattered electrons (9).

Writing the thermal equilibrium between the heat entering the metal and different thermal losses, and admitting some simplified hypothesis, one obtains the following equation :

$$\bar{\delta} = \frac{2n \text{Ln} \frac{1.12}{U}}{\pi \left[n + \bar{U} \text{Ln} \frac{1.12}{U} \right]} \quad (4)$$

$$\bar{\delta} = \frac{4 k T_f \delta}{(1-\beta) VI} \quad \text{is the reduced dimensionless penetration.}$$

k is the thermal conductivity

δ is the actual penetration of the beam

T_f is the temperature of the capillary

β is back scattered coefficient, function of the nature of the metal and of the ratio between the width to the height of the weld

I is the current in the beam

V is the accelerating voltage

n is constant for practically all metals

$\bar{U} = \frac{Ud}{4\alpha}$ is the reduced dimensionless speed

U is the actual welding speed

d is the beam diameter, taken equal to the diameter containing 50% of the total power (9).

α is the thermal diffusivity of the metal

For the experimental results between 75 K.V. and 150 K.V. d was taken = width of the curve at $\frac{I_{\max}}{2}$.

Before presenting the experimental results, it is necessary to make the following remarks :

For the experiments conducted on the 30 - 60 K.V. electron gun, the recorded curves allow to compute accurately the power distribution in the beam and especially the diameter of the cylinder which contains 50% of the whole beam power. This is the diameter "d" used when plotting $\bar{\delta} - \bar{U}$.

The problem is different for the experiments done on the 75 - 150 K.V. electron gun. As a matter of fact, the experimental curves which are obtained by recording the current which falls on a wire passing across the electron beam at a given speed, are not very accurate because of the high ripple on V and the back-scattered electrons. So the power distribution in the beam and the diameter of the cylinder which contains 50% of the beam power could not be computed accurately. Nevertheless and in order to discuss the results, we have chosen as diameter of the beam which was used in plotting the experimental results, the mean value of the width of different recorded curves, measured at $\frac{I_{max}}{2}$. Furthermore, the penetration of the beam was taken equal to the mean value of three penetrations taken at different cross sections of the weld.

Because of the different methods used in defining the diameter of the beam, it is necessary, when using statistical methods for discussing the experimental results, to consider separately the 30 - 60 KV.results and the 75 - 150 KV.results.

Figure 6(a and b) shows on a log-log plot, the variation of $\bar{\delta}$ as a function of \bar{U} for the two types of experimental results : 30 - 60 K.V. and 75 - 150 K.V. One can remark that even though the range of variation of the different parameters used in penetration is wide, all experimental results can be represented by a single curve independently of the beam power, of the accelerating voltage, of the welding speed or of the beam diameter. Dispersion of the experimental points is about $\pm 20\%$, which can be acceptable if we have in mind the simplified hypothesis (8) used in obtaining equation 4.

If now we put together all the experimental points obtained between 30 and 150 K.V., we obtain figure 7. This figure shows that even though the values of the diameters of the beams were defined by different considerations, the experimental points could be consi-

dered as scattered around a single curve for the whole range of the accelerating voltage between 30 K.V. and 150 K.V.

2.3. Effect of the accelerating voltage

Let us suppose now that the penetration is a function of the accelerating voltage as given by:

$$\delta = f_1(w, d, U) \left(\frac{V}{V_0} \right)^\xi \quad (5)$$

f_1 is a function of the beam power W , welding speed U and beam diameter d .

V_0 is an arbitrary constant reference accelerating voltage.

ξ is a constant exponent.

Then a new reduced dimensionless penetration which depends on the accelerating voltage can be defined :

$$\delta^* = \bar{\delta} \left(\frac{V_0}{V} \right)^\xi \quad (6)$$

Our experimental results were analysed by plotting δ^* as a function of \bar{U} , for different values of the exponent ξ .

It is to be noted that the variation of the constant V_0 does not affect the dispersion of the experimental points. As a matter of fact, if V_1 is taken instead of V_0 for a given ξ , then all experimental points will shift the same distance $\left(\frac{V_0}{V_1} \right)^\xi$ on the δ^* axis. For this reason, only the influence of ξ was investigated between 0 and 1.5.

Figure 8a shows the plot of the experimental points obtained at V between 30-60 K.V. for $\xi=0.5$. Figure 8b shows the plot of the experimental points obtained for $V = 75$ K.V., 150 K.V. and for $\xi = 0.5$.

On figure 9, we have plotted for all the experimental points ($V = 30$ K.V. to 150 K.V.) the variation of δ^* as a function of \bar{U} . It is easy to see by examining figure 6 and 7 on one side, and figure 8 and 9 on the other side, that the dispersion of the plotted experimental points is higher for $\xi = 0.5$ than for $\xi = 0$. This means that the actual distribution of δ^* against \bar{U} which minimizes the standard deviation of the experimental results is obtained for $\xi = 0$; that is, when the penetration does not depend upon the accelerating voltage.

In order to generalize the investigation, we have first assimilated the curve $\delta^* - \bar{U}$ in the range of variation to a straight line; then, for each value of the exponent ξ , the standard deviation of the experimental points was estimated.

ξ was taken equal to 0; 0.05; 0.10; 0.25; 0.5; 1; 1.5.

Figure 10 shows the variation of σ , the standard deviation of the experimental points, as a function of ξ . It is clear that the minimum value of the standard deviation is obtained for $\xi = 0$; that is when the accelerating voltage does not affect the penetration. In other words, best representation of the experimental results is obtained when only the beam power and the diameter of the beam are taken into consideration independently of the accelerating voltage.

3. EFFECT OF THE PRESSURE IN THE WORKING CHAMBER

Soft vacuum electron beam welding has been extensively introduced since several years in the automotive industry. The feasibility of the welding process for different values of the pressure in the working chamber has been investigated by several authors (10), (11). The conclusions concerned more particularly the variation of the penetration of the electron beam as a function of the pressure.

As it has already been said, in our opinion the most important parameter which affects electron beam penetration is the specific power (power per unity of surface) and its distribution on the workpiece. So our investigation consisted to analyse the variation of the specific power distribution in the beam as a function of the pressure in the working chamber. This was done for two values of the accelerating voltage (60 K.V. and 30 K.V.) and for pressures ranging from 10^{-5} torr to 11×10^{-2} torr.

The photographs of figure 11 shows the analysed curves obtained at 10^{-5} , 3×10^{-2} , 5×10^{-2} , and 11×10^{-2} torr for a 60 K.V. - 90 m.A. beam at a working distance of 525 mm.

In order to compare these results, the analysed curves were plotted with the same magnification factor on figure 11a. It can be seen that the electron beam is almost the same for a pressure as high as 3×10^{-2} torr. When the pressure attains 5×10^{-2} torr, then the maximum of the curve is decreased by about 20%. For this pressure the penetration of the beam was almost the same as that at 3×10^{-2} torr; this is due to the fact that even though the maximum of the curve is decreased by 20%, the diameter of the beam that contains 50% of the beam power is only increased by 5%.

When the pressure in the working chamber becomes greater than 11×10^{-2} torr, then the maximum of the curve is decreased by about 75% and welding at distances as high as 525 mm becomes delicate.

Figure 12 shows the same results for an electron beam accelerated by 30 K.V. It can be seen that the maximum of the curve is reduced by about 13% for a pressure of 10^{-2} torr. This reduction attains 40% when the pressure is 2×10^{-2} torr, but penetration obtained at this pressure is only 15% less than that done at 10^{-4} torr. The use of 30 K.V. accelerating voltage should be limited only to machines using primary vacuum which does not exceed 10^{-2} torr.

It is to be noted that in the soft vacuum technique, the welding is executed at pressure around 3×10^{-2} torr. For this pressure and for an accelerating voltage near 60 K.V., the electron beam's characteristics are still very similar to those obtained in hard vacuum. Furthermore, excellent metallurgical qualities of the weld are obtained at pressures as high as 5×10^{-2} torr. When the working distance is shorter than 525 mm, the effect of pressure on the beam characteristics is still less critical. It has been found experimentally, by other investigators, that welds obtained between 10^{-5} and 5×10^{-2} torr are almost identical.

CONCLUSIONS :

The need for a device capable of analysing the characteristics of focussed electron beam was emphasized in order to understand the relationship between beam characteristics and weld qualities. An experimental method which allows the analysis of very high specific power beams (100 K.W./mm^2) was described, and results concerning more than 140 beams were presented.

The experimental results served first to test the theoretical method used in our company to optimize the components of an electron gun by using a computer. Then the experimental results were used to investigate the effect of two important welding parameters on the penetration of the electron beam :
accelerating voltage and pressure in the working chamber .

Using reduced dimensionless variables and statistical analysis it was shown that the best representation of the experimental results is obtained when only the specific power of the beam is taken into account. This shows that, when beam characteristics are determined accurately, the electron beam penetration is independent of the accelerating voltage.

With 60 K.V. accelerating voltage, electron beam power distribution is very slightly affected for pressures as high as 5×10^{-2} torr and for working distances exceeding 50 cm. This confirms what was known since several years about the capability of 60 K.V. beam to operate in soft vacuum.

BIBLIOGRAPHY

- 1 H.J. HARKER J.A.P. Vol. 28, n° 11, 1957 p. 1354 - 57.
- 2 SAYEGH, ALAIS, SAGOT
4th int. con. on electron and ion science and technology, 1970.
- 3 SAYEGH, DUMONTE
3rd electron beam processing seminar, Stratford U.K., march 1974.
- 4 ARATA & AL Trans. of J.W.R.I. Vol. 2 n° 1, 1973 (p. 7)
- 5 AKOP'YANTS Automatic Welding Vol. 25, n° 11, nov. 72 p. 11
- 6 WEISNER ZIS - Mitteilungen 1/72 p. 36
- 7 SANDSTROM 5th conference Electron and ion beam science and technology (1972)
- 8 LUBIN Welding Journal, March 1968 p. 140s.
9. DUMONTE, SAYEGH 3rd int. conf. on adv. in weld. processes Harrogate U.K., May 7-9 1974
- 10 HASHIMOTO & AL Trans. of N.R.I.M. Vol. 11 n° 2, 1969
- 11 SOLOMON & JAMES
2nd int. conf; on electron and ion beam processes sciences, April 66
- 12 SANDERSON British Welding Journal. Oct. 68, vol. 15 n° 10.

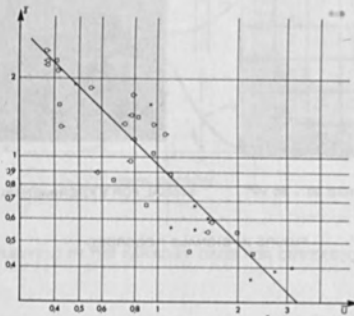


Fig. 6a. Experimental points $\bar{\delta} - \bar{U}$ for 75 kV - 150 kV

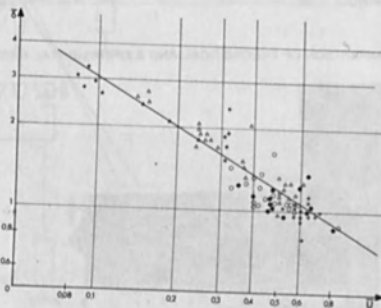


Fig. 6b. Experimental points $\bar{\delta} - \bar{U}$ for 30 - 60 kV

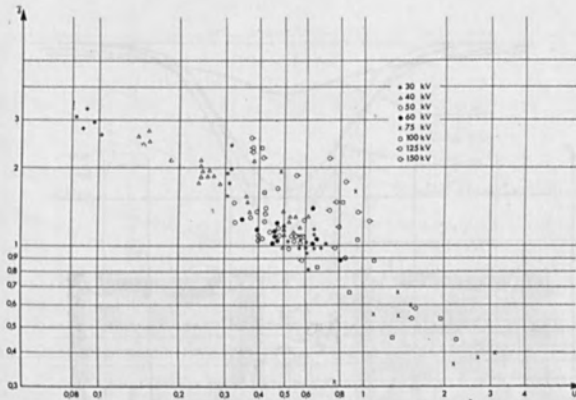


Fig. 7. Experimental points $\bar{\delta} - \bar{U}$ 30 kV - 150 kV

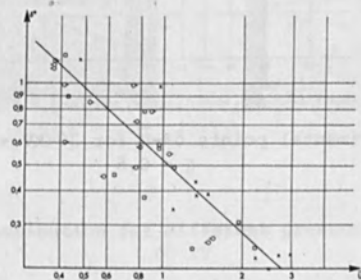


Fig. 8a. Experimental points $\delta^* - \bar{U}$ for 75 kV - 150 kV
 $\zeta = 0.5$

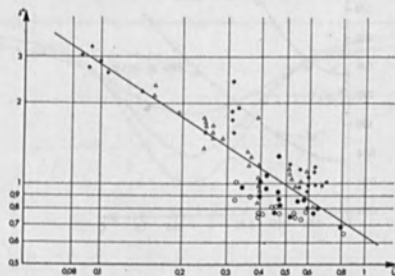


Fig. 8b. Experimental points $\delta^* - \bar{U}$ for 30 kV - 60 kV
 $\zeta = 0.5$

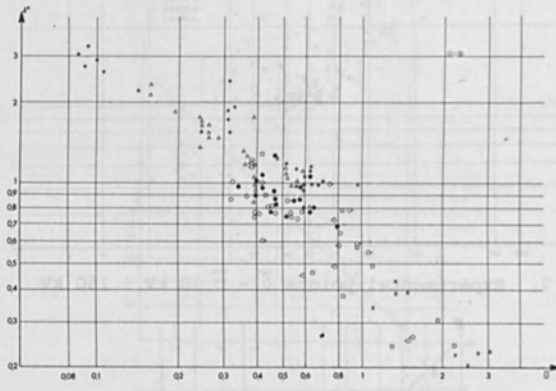


FIGURE 9 : EXPERIMENTAL POINTS $\delta^* - \bar{U}$ for 30 kV - 150 kV $\zeta = 0.5$

Fig. 9. Experimental points $\delta^* - \bar{U}$ for 30 kV - 150 kV
 $\zeta = 0.5$

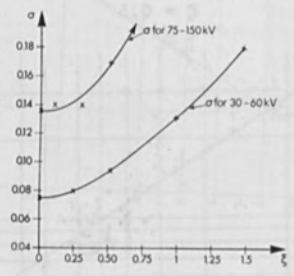


Fig. 10. Variation of standard deviation σ against ζ for 30-60 kV and 75-150 kV

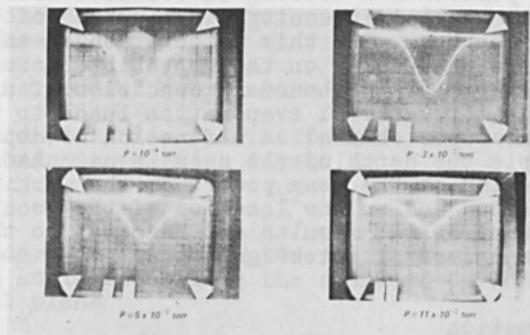
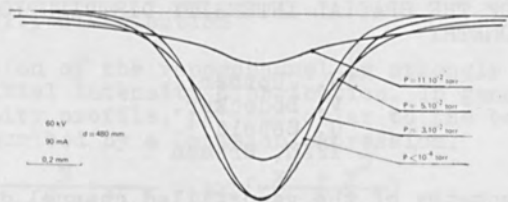


Fig. 11. Power distribution for different pressures in working chamber, 60 kV

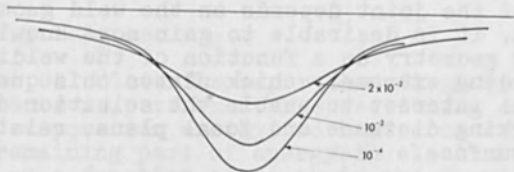


Fig. 12. Power distribution for different pressures at 30 kV

INFLUENCE OF THE SPATIAL INTENSITY DISTRIBUTION ON DEEP WELDING GEOMETRY

W. Jüptner,
V. Bödecker,
G. Sepold
IFAM, Bremen

The geometry of the vaporfilled channel during deep penetration welding is evaluated with respect to the spatial intensity distribution of the electron beam. For this calculation an energy balance, depending on the depth in the workpiece, is performed. The boundary condition of a minimum energy for material evaporation leads to the width of the vapor channel as a function of depth. For example the depth of the seam is calculated depending on the beam power, on the working distance, and on the location of the focal plane. The theoretical results are compared to those of experimental investigations.

1. Introduction

Electron beam welding was developed approximately twenty years ago and since 1958 the process has been investigated more intensively [1,2].

However, there is a need to clarify the influence of beam parameters on the formation of the welded joint. Of particular interest is the variation in geometry of the fusion zone, which will resemble either a Gaussian, a bulged or a parallel profile, since the mechanical behaviour of the joint depends on the weld geometry. For this reason, it is desirable to gain more knowledge about the welding geometry as a function of the welding parameters. Welding extremely thick plates this question is of practical interest to enable the selection of the optimal working distance and focal plane, relative to the workpiece surface.

Since the seam geometry strongly depends on the formation of a vapor filled channel [3], in this paper, the influence of the spatial intensity distribution on the channel geometry will be evaluated. The validity of the theoretically established relation will be proved by experimental investigations.

2. Vapor channel geometry

2.1 Intensity distribution

The formation of the vapor channel is strongly influenced by the spatial intensity distribution. In general the power density profile, perpendicular to the beam axis, can be described by a Gaussian expression.

$$L = \frac{N}{2\pi\delta^2(z)} \cdot \exp\left(-\frac{x^2 + y^2}{2\delta^2(z)}\right) \quad (1)$$

where L = intensity
 N = beam power
 δ = standard deviation
 x, y, z = Cartesian coordinates

The standard deviation δ is a function of the coordinate z , in the beam propagation direction:

$$\delta^2(z) = \delta_0^2 + \alpha^2(z - z_0)^2 \quad (2)$$

δ_0 = standard deviation in the focal plane
 α = beam angle related to the standard deviation
 z_0 = focal plane

The intensity distribution in the neighbourhood to the focal plane is shown in fig. 1. Normally the beam geometry is described by its caustic which is related to the beam width, fig. 1a. However, the curves of equal intensity are more relevant to the problem of deep penetration, since for melting or evaporating the material, particular intensities can be selected.

2.2 Evaluation of the channel geometry

2.2.1 Energy balance

In order to calculate the vapor channel geometry an energy balance is performed. The sectioning of the input energy to evaporation energy, to heat conduction losses and to a remaining part of energy in electron beam, is evaluated as a function of depth in the workpiece. In this way the electron beam energy which reaches the elementary area $(\Delta x, \Delta y)$ in a defined depth z of the channel is determined. The energy E_0 of the beam, without interaction with work material, on this elementary area is given by

$$E_0(z; \Delta x, \Delta y) = \int_{x_1}^{x_1 + \Delta x} \int_{y_1}^{y_1 + \Delta y} \int_{-\infty}^{+\infty} L_0(x, y, z) dx dy dt \quad (3)$$

L_0 = intensity of the original beam

When the beam impinges upon an intermediate workpiece the material will be evaporated to a depth z . The volume of evaporated material is determined from the beam propagation curves, fig. 2. The energy for evaporation E_V is given by

$$E_V(z; \Delta x, \Delta y) = \int_{x_1}^{x_1 + \Delta x} \int_{y_1}^{y_1 + \Delta y} \int_0^z Q_V dx dy dz \quad (4)$$

where Q_V is the total energy required to pre-heat and evaporate a unit volume.

The remaining electrical energy E_m is given by

$$E_m(z; \Delta x, \Delta y) = \int_{x_1}^{x_1 + \Delta x} \int_{y_1}^{y_1 + \Delta y} \int_{-\infty}^{+\infty} L_m(z) dx dy dt \quad (5)$$

Using $L_m(z)$, the apparent intensity in the depth z , the real energy flux through the elementary area can be calculated.

Taking into consideration additional energy losses E_L , such as heat conduction, the energy balance becomes

$$E_0 = E_V(z) + E_m(z) + E_L(z) \quad (6)$$

2.2.2 Solution of the energy equation

In order to solve equation (6), several terms must be integrated along the propagation curves of the considered part of the beam, fig. 2. However, before executing the integration, a coordinate transformation is introduced, which ensures that, for the undisturbed beam, the energy flux through the elementary area remains constant at all depths. This transformation is given by

$$b(z_1) \cdot x_2 = b(z_2) \cdot x_1 \quad (7)$$

Additionally, the size of the elementary area is selected, such that the values of L_0 and L_m are approximately constant over the area. Taking into account the validity of $v \cdot dt = dy$, the equations (3-7) combine to give

$$\int_{-\infty}^{+\infty} L_0(x, y, z) dy = \int_{-\infty}^{+\infty} L_m(x, y, z) + \frac{Q_V \cdot v}{b^2} \int_0^z b^2(z) dz + E_L \cdot \frac{v}{b^2} \frac{1}{\Delta x \cdot \Delta y} \quad (8)$$

This relation is valid for any given intensity distribution of an electron beam, where b is a quantity defined for

a particular width of the beam cross-section. If the power density distribution L is known, the related integral can be solved to a function of x and z . For simplification, K_m is defined as

$$K_m = \int_{-\infty}^{+\infty} L_m(x, y, z) dy$$

Therefore, for a given value of K_m , all points x , characterized by the same energy density K_m/v , can be calculated as a function of depth z . This is valid for any point in the vapor channel. Since a specific energy is required to evaporate the material, the vapor channel can be calculated as the curve $x(z)$. The boundary condition is that K_m/v equals the above mentioned specific energy density at the channel walls. The smallest energy density, needed for evaporation, can be estimated from the theory of heat conduction. The energy E_w conducted from a surface element ($\Delta x, \Delta y$), is given by

$$E_w = \Delta x \cdot \Delta y \cdot \lambda \frac{\partial T}{\partial R} \cdot \tau \quad (10)$$

λ = heat conductivity

$$\text{if } \frac{K_m}{v} = \frac{E_w}{\Delta x \cdot \Delta y} \quad (11)$$

then K_m defines the boundary surface in which the total impinging energy is lost to conduction. In this way the boundary of the vapor channel can be found.

The equation of heat conduction yields [4]:

$$\tau \cdot \frac{\partial T}{\partial R} = T_v \cdot \frac{1}{v} \cdot \left(1 + \frac{v \cdot x}{a}\right) \quad (12)$$

T_v = boiling temperature
 $\frac{1}{a}$ = thermal diffusivity

From the equations 10, 11, 12 there results

$$K_m = T_v \cdot \lambda \cdot \left(1 + \frac{v \cdot x}{a}\right) \quad (13)$$

The losses E_L , due to heat conduction in the welding direction, can be neglected, if the welding velocity exceeds a critical velocity, v_c [5]. This velocity v_c depends on the thermophysical properties of the material. For steel v_c equals 8 mm/s. This implies

$$E_L \ll E_o \quad (14)$$

Taking into consideration the Gaussian intensity distribution of the electron beam, equation (8) becomes

$$x = b \left[-2 \ln \left(\frac{\sqrt{2\pi} \cdot b \cdot KM}{N} + \frac{\sqrt{2\pi} \cdot Q_v \cdot v}{N \cdot b} \right) \cdot \int_0^z b^2(z) dz \right]^{1/2} \quad (15)$$

This formula describes the geometry of the vapor channel, as a function of the spatial beam distribution, the thermophysical properties of the material, and the welding velocity.

3. Conclusions from the theoretical considerations

Typical welding geometries as a result of the theory are shown in fig. 3. With increasing b_0 and decreasing α , the bulged seam becomes parallel and finally a Gaussian shaped fusion zone results. The optimum values corresponding to the deepest penetration can be evaluated. In this regard, the parallel welding geometry prevails.

For small angles

$$\alpha \cdot z_{\max} \ll b_0$$

an equation for the dependence of the welding depth on the welding parameters has been derived:

$$z_{\max} = \frac{N}{b_0 \cdot v} \cdot \frac{1}{\sqrt{2\pi} \cdot Q_v} \quad (16)$$

The validity of this approximation permits the following statements to be made:

1. The welding depth is not proportional to the intensity, as is often assumed, but it is proportional to the energy incident on the workpiece, divided by the length of the joint and the beam width, fig. 4.

2. Equation 16 can be written in the form:

$$z_{\max} = \sqrt{\frac{N}{b_0^2}} \cdot \sqrt{N} \cdot \frac{1}{\sqrt{2\pi} \cdot v \cdot Q_v} \quad (17)$$

The welding depth is proportional to the square root of the beam intensity, if the beam power and the welding velocity are constant, fig. 5.

Furthermore, the welding depth, as a function of the working distance, can be evaluated from equation 15, assuming a constant brilliance. The brilliance R_L is defined as the power density divided by the solid angle. With this assumption, the value of b increases and α decreases, with increasing working distance, but, the product $\alpha \cdot b_0$

remains constant.

The theoretical and the experimental weld depth are shown in fig. 6. These weldments indicate that the diminishing of the working distance may reduce the penetration depth, if the working distance is below an optimum value. This occurs even though the beam diameter decreases with shorter working distances. The optimum distance is related to an optimum beam angle, which depends on the brilliance R_D in the following manner:

$$\alpha \sim R_D^{-1/3} \quad (18)$$

The angle, α , of the electron beam leads to another consequence: To achieve the deepest penetration, for a given set of parameters, it is necessary to locate the focal plane of the electron beam in the workpiece.

The dependance of weld depth on the distance between the focal plane and the workpiece surface is shown in fig. 7.

4. Conclusions

The geometry of the vapor channel was calculated by considering the spatial intensity distribution. For this calculation an energy balance, depending on the depth, was performed. In this way, the width of the channel was evaluated as a function of the depth. Without further assumptions, this model permits the determination of the dependence of the weld depth on the welding parameters. Even the influence of the working distance and the location of the focal plane can be calculated. By the knowledge of the vapor channel geometry, the spatial-temporal temperature distribution can be computed. Further investigations are aimed at the determination of the relationship between the seam geometry and the metallurgical and mechanical properties of the joint.

5. Acknowledgements

The authors wish to thank the Deutsche Forschungsgemeinschaft and the AIF for their financial support of this research work.

Literature

- [1] Steigerwald, K.H.: Materialbearbeitung mit Elektronenstrahlen, Phys. Verh. 4 (1953), S. 123
- [2] Bas, E.B., G. Cremonik: Schweißen im Hochvakuum mit Elektronenstrahlen, Vakuu-Techn. 8 (1959) 7, S. 181-188
- [3] Tong, H., W.H. Giedth: A Dynamic Interpretation of Electron Beam Welding, Weld.J. 49 (1970), p 259s-266s
- [4] Hashimoto, T., F. Matsuda: Effect of Welding Variables and Materials upon Bead Shape in Electron-Beam Welding, Trans. of N.R.J.M 7 (1965) 3, p. 27/40
- [5] Sepold, G., W. Jüptner: Der Einfluß von Temperatur und Zeit beim Schweißen von Baustählen mit Strahlen hoher Intensität, Zeitschrift.f. Werkstofftechnik 2 (1971) 7, S. 356-361

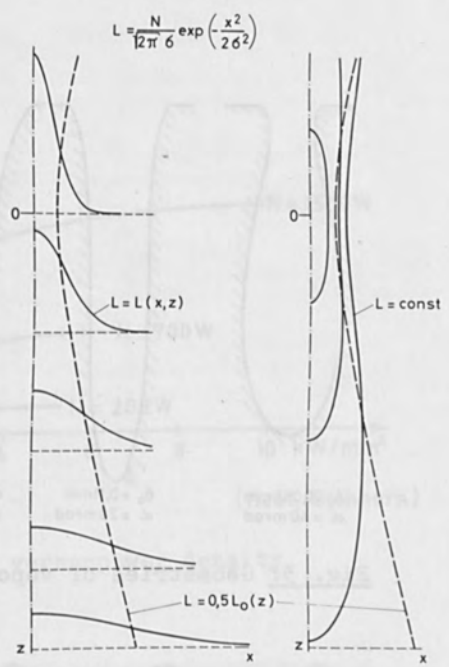


Fig. 1: Geometry of electron beam

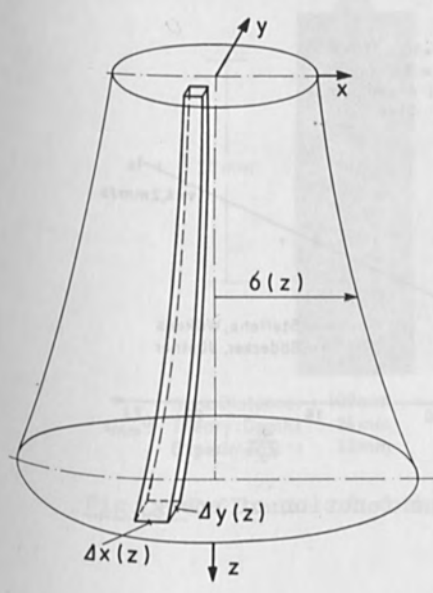


Fig. 2: Schematic illustration of volume element

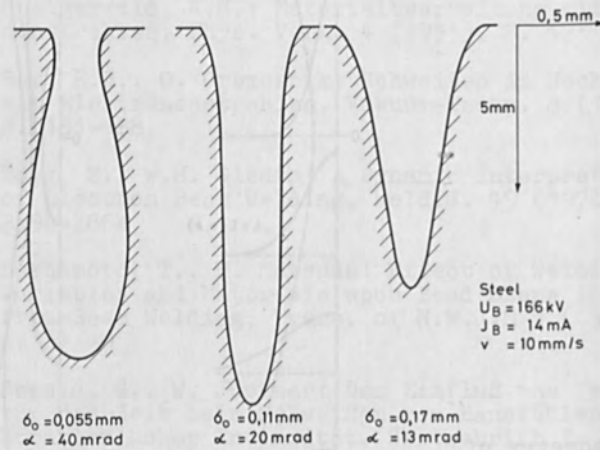


Fig. 3: Geometries of vapor channel

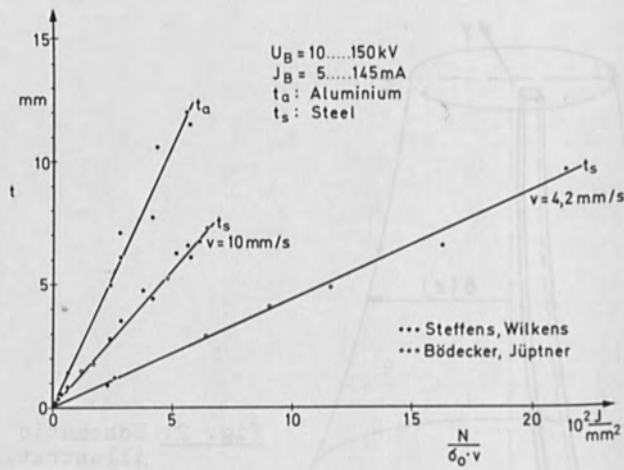


Fig. 4: Weld depth as function of energy density

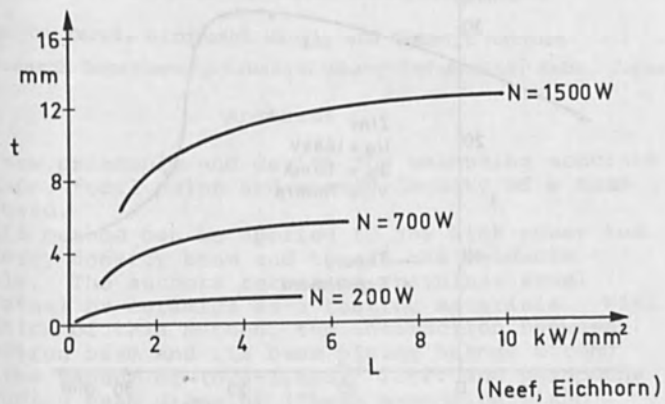
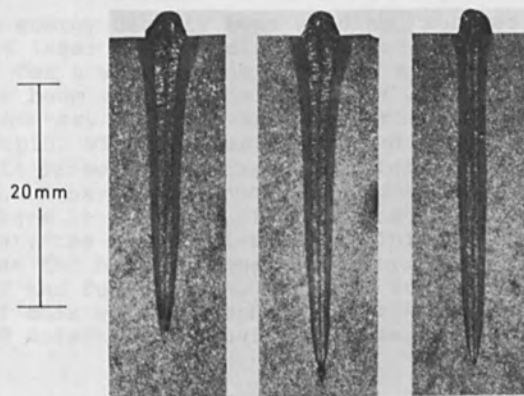


Fig. 5: Weld depth versus power density



Work.Distance:	100mm	200mm	300mm
Theory:Deptht	24mm	31mm	30mm
Experiment:t	23mm	31mm	29mm

Fig. 6: Influence of working distance on weld depth

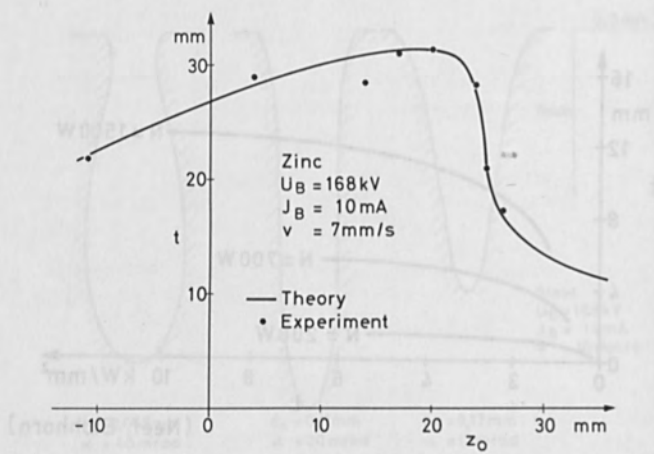


Fig. 7: Weld depth t versus position of focus z_0

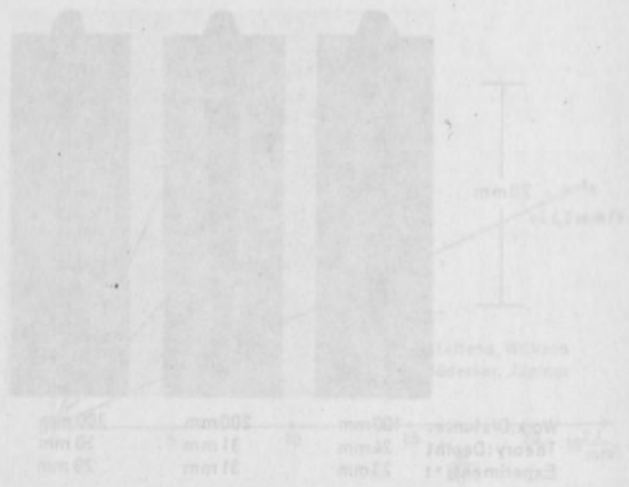


Fig. 8: Comparison of theoretical and experimental values of weld depth

SHAPE DECISION OF HIGH ENERGY DENSITY BEAM

Yoshiaki Arata and Michio Tomie
Faculty of Engineering, Osaka University, Japan

Kiyoshi Terai, Hiroyoshi Nagai, and Tetsuji Hattori
Welding Research Department, Kawasaki Heavy Industries, Kobe, Japan

Abstract

A new principle and device for measuring accurate beam shape, focal point and energy density of a beam is proposed.

This method can be applied to any high power and high energy density beam and to all the weldable materials. The authors recommend stainless steel, killed steel or ceramics as a testing materials. With application of this method, the interaction between the electron beam and its beam plasma become strong around the vacuum of $(0.3-1) \times 10^{-1}$ Torr. and phenomena of expanding beam diameter ("beam expansion") and marked decrease of the energy density of the beam were observed.

1. Introduction

In the high energy density beam welding, such as electron beam and laser beam welding, the location of the beam focal point for a workpiece appears as a fundamental parameter besides beam voltage, beam current and welding speed. This parameter, A_p , acts as an important factor on penetration depth, width of bead, shape of bead and appearance of weld defects, and the definition and characteristics of which have been reported in detail by Arata and co-workers 1) 5). Fig. 1 shows the vicinity of the focal point, the beam active zone. This is the location which has the highest energy density. It gives both the shape of the fusion zone, the most remarkable characteristic of this welding method, and also can lead to such weld defects as porosity, spikes and cold shuts.

In order to clarify the mechanism of beam penetration one should know accurately the beam shape, i.e. beam diameter variation in relation to the distance from the focusing coil and its energy density at the focal point.

Though diverse methods have been tried, no satisfactory method has as yet been established due to the extreme difficulty in measuring the shape of a beam having high power and high energy density comparable to those used in welding process. Furthermore, no experiment has so far been designed making it possible to determine the shape of beam and focal point during the process of welding.

A method is here proposed to accomplish this.

2. Preliminary Research

The measuring methods for the shape of beam can be classified depending on the presence or absence of molten metal at the irradiation point. For the former, use of sheet material, the burn through phenomenon and use of easily vaporized material are considered necessary. However, there has been lack of reproducibility and reliability in the conventional testing methods. For the latter, measurements have been made by the linear or circular movement of the colling plate or bar⁶). Since application of this method is limited to low beam power in which the cooling plate is not melted, it is not a suitable method to measure the shape of high power and high energy density beams used in welding.

In this paper, the authors describe methods for measuring of the effective beam diameter for the practical electron beam. Its suitability is studied through various experiments.

Initially, effects of various plate thickness on the burn through phenomenon at the weld zone were examined by using the step type workpiece having its thickness from 2mm to 20mm (40(W) x 240(L), 40mm length for each thickness) as shown in Fig. 2. In this test, effects of welding speed were also examined with the speed varied in four steps as the only parameter. Austenitic stainless steel AISI 304 was used as a test piece, and the bead was produced by an electron beam machine rated at 150KV-40mA (6KW). The resulting kerf or "beam groove", moving zone of beam hole where molten metal is not filled up, on both side and its width are shown in Photo. 1 and Table 1.

The following appear as reasonable conclusions based on this test.

- 1) Marked variation of kerf or beam groove by plate thickness change despite a constant parameter.

- 2) Key hole action as seen in plasma arc welding appears as the plate thickness becomes smaller, molten metal residue without burn through, which resulted in appearance of "secondary melting phenomenon" giving varied kerf or beam groove.

- 3) This method is considered not practical because a large number of test pieces are required to observe continuous change of the shape of the beam along its axis.

Subsequently the "slope welding" method was applied as shown in Fig. 3 by using the test piece with much smaller plate thickness for the purpose of clarifying correlation between kerf width and beam diameter when beam cutting was performed, and continuous change of the shape of beam. In this test, stainless steel (AISI 304) with 1mm plate thickness, nickel with 0.4mm and monel metal with 0.2mm were used.

The results are as shown in Photo 2. Secondary melting effect of the molten metal decreases as welding speed increases, and the kerf width which makes it possible to estimate continuous change of beam diameter can be obtained. Adhesion phenomenon of molten metal to the kerf wall by surface tension is promoted. This phenomenon appears, as shown in Photo. 3, even when different materials with much smaller plate thickness are used. This cannot be avoided. It has been proved, however, that the slopewelding method used here was extremely effective in observation of the shape of beam at a glance.

From the above findings, it has been concluded that slope welding is the most suitable testing method for the shape of beam (simply called "beam test method" or "beam test"). It permits observing the shape of a beam in a wide range. For effective tests it should be necessary to have sufficiently thick specimen for effective removal of molten metal.

The authors have found that such function of the test piece can be given by the application of "edge effect" of a thick plate. Properties of a sharp edge of the thick test piece with suitable angle may be easily estimated as follows.

- 1) The tip will be vaporized or melted by the low beam energy.
- 2) Excess beam energy given around the tip is absorbed rapidly in the base zone, cool and large heat absorber expanding under the tip in the form of heat energy. This action is so powerful that condensation of molten metal by the surface tension will not be allowed to occur, as shown in Photos. 2 and 3.
- 3) In the case of a powerful beam having so much excess power that even melts the heat absorber as in welding, most of the energy is absorbed in melting the heat

absorber. And at the same time, such melted heat absorber will be removed from the edge zone rapidly enough not to permit secondary melting. The authors refer to this behavior as "edge effect". The test piece with such "edge effect" therefore is used for the beam test performed. In order to obtain a practical test piece as well as to meet their objectives, the authors examined edge effects with various shapes and sizes as shown in Fig. 4. As a result, test piece with edge shapes as shown in Fig. 5 were selected from more than 10 types of test pieces for use in the beam test methods types A and B.

Type A as formerly described, is so called "slope welding" using a test piece having slope angle $\theta_s \approx 0 \sim 90^\circ$ which makes one-dimensional movement in horizontal axial direction. Type B is a method called "glide-welding" by the authors using a test piece having $\theta_s = 0^\circ$ which makes oblique movement (two-dimensional movement) along the gradient with glide angle θ .

Fig. 6 is the basic drawing of the test device. The slope angle is determined by the length of beam zone to be measured (length of test piece required for the purpose) and the conditions of the liquid metal from the molten pool. When the beam power becomes large or speed is slow, it is necessary to have small $\theta_s = \pm(15 \sim 45^\circ)$ is most frequently used. In this test $\theta_s = \pm 30^\circ$ was used.

The symbol, +, shows upslope-welding which gives a welding bead going toward upside along a slope with θ_s , and symbol, -, shows downslope-welding which gives a welding bead going toward downside along the same sloping surface. As shown in Fig. 7, when $\theta_s = +30^\circ$ the molten metal is rather widened in the vicinity of the most narrowly focussed beam active zone (focal point) compared to that in case of $\theta_s = -30^\circ$. This is because, in case of upslope-welding, liquid metal in the molten pool tends to flow only downward and to gather in the beam groove near the surface. Such tendency becomes more and more conspicuous with larger θ_s and slower welding speed at the narrower beam groove, i.e., near the focal point to occur secondary melting.

Accordingly, $\theta_s = -30^\circ$ was used for any A type with edge shape of a test piece as shown in Fig. 5. It is natural that, for B type, no such action needs to be considered because $\theta_s = 0^\circ$.

3. Shape Decision of High Energy Density Beam

3-1. Materials used and test device

Table 2 shows materials and their chemical composition used for the test. The test piece has the edge

shape shown in Fig. 5 from the results of preliminary research with the size 40(W) x 350(L). The welding device is 150 KV-40 mA Hamilton type 6 KW EB welder which has variable gas pressure in vacuum chamber from 10^{-1} Torr to more than 5×10^{-4} Torr.

3-2. Test methods

The test adopts the shape of test piece and beam test methods based on the results of Preliminary Research. For test procedures, firstly austenitic stainless steel AISI 316L was selected as a representative test piece, which was fixed with a jig at slope angle 30° based on Fig. 5 A type test method, and downslope welding was performed to examine effects of various factors (beam voltage: V_b , beam current: I_b , welding speed: v_b , a_p value and gas pressure in vacuum chamber: P_{ch} on the shape of beam). The same method was applied on test piece of titanium, copper and its alloy, aluminium alloy to examine effects of materials on the shape of beam.

In order to examine effects of vaporization on the measurement of the shape of beam, A type beam test method was applied by using 7075 Al alloy, in which easily vaporized element (zinc, etc.) is contained, and quartz to measure the shape of beam. Quartz test piece used here was a thin plate having 2mm (t) x 40(w) x 200(L).

A similar test to A type was further performed on AISI 316L steel and titanium based on B type beam test method as shown in Fig. 5 using a device as shown in Fig. 6 to compare with the results of A type test method. Prior to welding, grease was removed from all the test pieces with methyl-ethyl ketone. For the determination of the value of beam diameter, average of three points, i.e., the measured point, a point before it and behind it, was calculated.

3-3. Test results

3-3-1. Effects of welding factors on the shape of beam
AISI 316L stainless steel was used to examine effects of various welding factors on the shape of beam. Figs. 8-12 show the results. When burn through region of each edge for the test piece, i.e., its kerf width or beam groove represents the beam diameter, these figures show the changes of such beam diameter by the distance from the focusing lens.

Fig. 8 shows how the beam diameter becomes larger as beam voltage decrease, Fig. 9 shows how the beam diameter becomes larger as beam current increases. These tendencies can easily be predicted when one considers velocity of electrons and space charge effects.

Fig. 10 shows effects of welding speed, indicating that change of speed within the range does not effect the shape of beam for AISI 316L stainless steel.

Fig. 11 shows effects of visual focal point on the beam diameter. The visual focal point is defined as the target position where the beam spot is the smallest and its brightness the highest. It is observed visually when a beam of small current (1.2mA) is irradiated on a target of movable tungsten. The results of Fig. 11 show that the true focal point of the practical welding beam is located considerably above each visual focal point. For example, true focal points for Hamilton type 6KW electron beam welding machine are located approximately 3cm, 5cm, 7.5cm above from each visual focal point 18.5cm, 22.5cm, 30.0cm. Since these facts play extremely important roles, true focal point of the welding beam at a given beam power must be measured prior to actual welding.

The minimum beam diameter tends to be widened slightly as visual focal point becomes longer.

Fig. 13 shows relation between visual focal point $D^*_{F'}$, penetration depth h_p and object distance D_o (distance from focusing coil to test piece). Such relation is more clearly expressed by visual beam active parameter $a^*_b (=D_o/D^*_{F'})$ as shown in Fig. 14. The object distance corresponding to each maximum penetration depth as shown in Fig. 13, is located near the real focal distance obtained from Fig. 11. Using the same visual focal distance mentioned above the observation can be explained by consideration of the beam energy density η . It can then be said that penetration depth reaches the maximum when the focal point is immediately below the test piece surface as shown in Fig. 15.

Fig. 12 shows effects of gas pressure in the vacuum work chamber, P_{ch} , on the beam diameter. It seems that the beam diameter measured in the vacuum chamber having gas pressure from high vacuum condition to 3×10^{-2} Torr is so slightly effected by P_{ch} that it can be disregarded. The appearance of the beam diameter slightly smaller around 10^{-2} Torr than at high vacuum may be due to the action of plasma lens force. When the degree of vacuum lowers to 1×10^{-1} Torr, it is observed that the beam diameter suddenly widens largely. This suggests that interaction between the electron beam and its beam plasma becomes abruptly strong in the vacuum range of $(0.3-1) \times 10^{-1}$ Torr, and a change in the mechanism of collision prevails. Such vacuum range is called "beam expansion vacuum". This new fact was obviously discovered for the first time by A type beam test device, which indicates abrupt decrease of the beam energy density in this vacuum range. It is considered that the above fact will make extremely important contribution to understanding and application of welding phenomenon. For example, well known relation between gas pressure in vacuum chamber and penetration depth as shown in Fig. 16 is remarkably well explained η .

3-3-2. Effects of variation in material on the shape of beam

The same method as that for AISI 316L stainless steel was applied to titanium, copper, phosphor bronze and 4083 Al alloy to examine effects of materials on the shape of beam. The results are shown in Fig. 17 21. These results show similar tendency to AISI 316L stainless steel for the effect of each welding parameter on the shape of beam. As shown in Fig. 19, however, welding speed has a marked effect on the shape of beam for copper and 5083 Al alloy. Particularly, when welding speed becomes slow, secondary melting effect appears as shown in Photo. 4 so that actual beam diameter is not indicated around the focal point. Also, the result in Fig. 18 shows widened beam diameter in small current range, which may give rise to the beam acting as surface heat source producing slightly melted surface, concerning both effects of large heat conductivity of the material and lower beam power, and molten metal remained at the edge without burn through as shown in Photo. 5.

However, if special conditions are used in these materials (copper and 5083 Al alloy, etc.), as for example, exceedingly fast welding speed with large beam power similar results to those for other materials can be obtained. It has been shown, therefore, that measurement of the shape of beam by this method can be applied to any material.

3-3-3. Effects of vaporization on the shape of beam

In order to examine effects of vaporization on the shape of beam, slope welding was performed using 7075 Al alloy in which easily vaporized elements (Mg and Zn, etc.) were contained. Effect of gas pressure in vacuum work chamber was examined under the fixed welding conditions ($V_b = 150\text{KV}$, $I_b = 40\text{mA}$, $V_d = 1500\text{mm/min}$, $D^*_F = 300\text{mm}$). The results shown in Fig. 22 indicate the similar shape of the beam to the other materials described above. When gas pressure in the vacuum work chamber is decreased and vaporization becomes vigorous, they make it impossible to obtain the correct shape of beam. It is natural that such disorders should appear, and determination of gas pressure in the vacuum work chamber in relation of vapor pressure for easily vaporized elements contained in the material and beam expansion vacuum is required for a material with high vapor pressure. As shown in Fig. 23, when quartz (2mm (T) x 40mm (W) x 300mm (L)) which brings extremely vigorous vaporization was used as a test piece, similar beam shape to that of an ordinary metal material was obtained though narrow. It is considered that this result is caused by the effect of space charge which is charged up on the test piece.

To prevent such space charge effect, authors used parallel-arranged ceramic strips fixed by a steel jig, as shown in Fig. 24 to make the space charge escape to the fixed steel jig through plasma generated around the ceramic specimen. Here beam shape is approximately similar to the one in the specimen of AISI 316L stainless steel as shown in Fig. 25.

3-3-4. Tests on reliability of A type testing method

The problems of A type testing method in which downslope welding was used, i.e., effects of flow of molten metal with the test piece placed obliquely on the measured value of beam diameter were examined by using B type testing method ($\theta_s = 0^\circ$) in which glide welding was used as shown in Fig. 5.

AISI 316L stainless steel and titanium were adopted as test pieces and relatively smooth beam shape was obtained in the A type testing method. The results are shown in Figs. 26-29.

3-3-5. Summary

The above results are summarized in Fig. 30 and trends and minimum beam diameter for each material agree well except for Cu and quartz. It is therefore felt that this measuring method can be applied to any type of material. In the case of Cu, it is believed that equivalent results can be obtained if the welding is performed with a larger beam power at much faster welding speed. The most suitable test piece materials are stainless steel followed by killed steel. The shape of the beam, its focal point and energy density often vary with the use of filament and or replacement, suggesting that these be measured before welding.

4. Conclusion

- 1) The new beam test method has been achieved by using 2 types of welding methods ("slope welding", particularly "downslope welding" and "glide welding") and a test piece having function of edge effect.
- 2) Since the test can be performed under conditions prevailing in practical welding, test pieces of the material being welded can be used to measure effective beam diameter and energy density.

The only difference between this testing method and actual welding is that the test piece has function of edge effect.

- 3) This method allows to observe effective profile at a glance: focal point of beam and its effective energy density under any welding condition can thus be measured correctly.

- 4) It was shown that, in the vacuum range $(0.3 - 1) \times 10^{-1}$ Torr. interaction between the electron beam and its

beam plasma became vigorous, and the energy density abruptly decreased due to abrupt expansion of beam diameter ("beam expansion"). The above also indicates that the so-called "beam expansion vacuum" exists for powerful electron beams and the relation between gas pressure in the work chamber and penetration depth, which was already measured but remained unexplained, could be properly explained.

5) This testing method can be applied to all the weldable materials. Stainless steel is best as a test piece followed by killed steel.

6) Welding conditions for the test piece to obtain effective beam diameter for materials such as stainless steel and steel having inferior heat conductivity and good fluidity are readily developed. By contrast conditions for those materials having good heat conductivity as Cu and Al or a high vapor pressure element with high vapor pressure are not.

7) Remarkable secondary melting phenomenon may appear on some materials under certain welding conditions and the burn through effect disappears. In such a case, true beam diameter does not show. This phenomenon should help to study properties of the material at high temperatures.

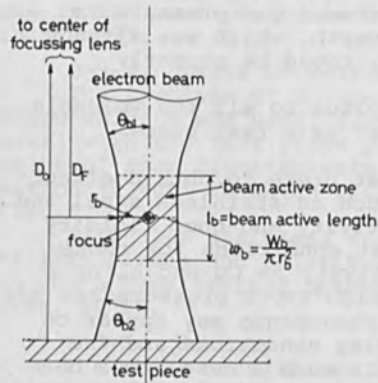
8) In an insulating material, beam shape approximately resembles that of AISI 316L stainless steel obtained by use of parallel-arranged ceramic specimen fixed by a steel jig.

References

- 1) Y. Arata: "Characteristics of Electron Beam Heat Source and View of Development on Electron Beam Welding Technology", J. Japan Welding Society, Vol. 4., No. 11 (1972).
- 2) Y. Arata, M. Tomie and Y. Katoh: "Some Properties of 30-KW class Electron Beam for Welding", Vol. 2, No. 1 (1973).
- 3) Y. Arata, K. Terai and S. Matsuda: "Study on Characteristics of Weld Defect and Its Prevention in Electron Beam Welding (Report 1)", Vol. 2, No. 1 (1973).
- 4) Y. Arata, M. Tomie, K. Terai, H. Nagai and T. Hattori: "Shape Decision of High Energy Density Beam (Report 1)", Document of Committee of Electron Beam Welding, JWS, No. EBW-69-72 (1972).
- 5) Y. Arata, M. Tomie, K. Terai, H. Nagai and T. Hattori: "Shape Decision of High Energy Density Beam (Report 2)", Document of Committee of Electron Beam Welding, JWS, No. EBW-76-73 (1973).
- 6) H. Suzuki, T. Hashimoto and F. Matsuda: "Characteristics of Electron-Beam for welding", J. Japan Welding Society, Vol. 32, No. 5 (1963).
- 7) K. Terai, T. Toyooka and H. Nagai "Effects of Process Parameter on the Penetration Depth in High Voltage Electron Beam Welding", Transaction of Japan Welding Society, Vol. 3, No. 1 (1972).

Table 1. Bead width for various test piece thickness.
($V_b = 150$ K V, $I_b = 40$ mA, $v_b = 200$ mm/min).

thickness (mm)	20	16	12	8	4	2
bead width (mm)	0.81	1.05	0.88	0.95	1.50	1.70



a_b : beam active parameter
 $a_b = \frac{D_b}{D_f}$
 D_b : object distance
 D_f : focal length

Fig. 1. Schematic diagram illustrated both shape of electron beam and beam parameters.

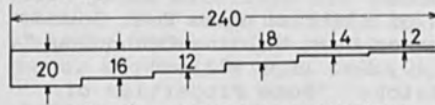


Fig. 2. Step type test piece

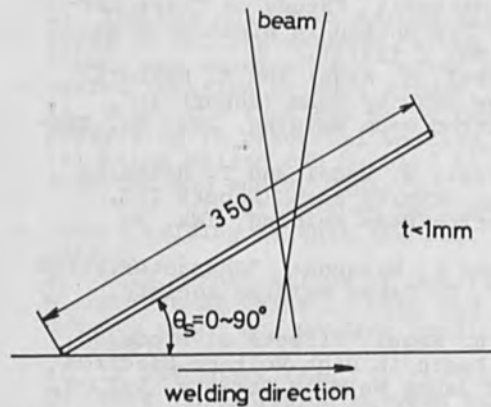


Fig. 3. Schematic drawing of slope welding with thin plate.

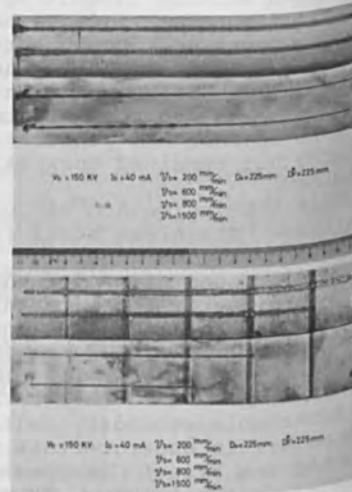


Photo 1. Surface and reverse bead profile for various welding speeds.



Photo 2. Secondary melting effect of condensation of molten metal by surface tension for various welding speeds (stainless thin plate).

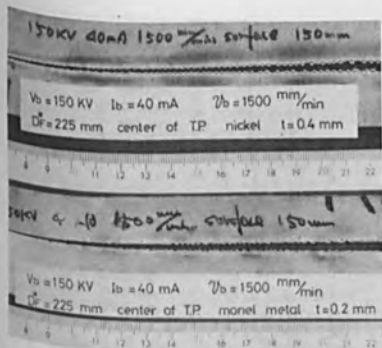


Photo 3. Condensation of molten metal by surface tension in case of changing plate thickness.

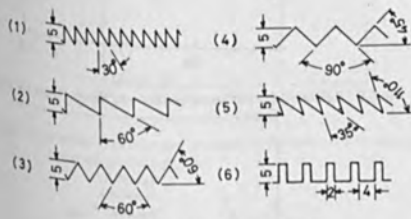


Fig. 4. The kinds of edge shapes.

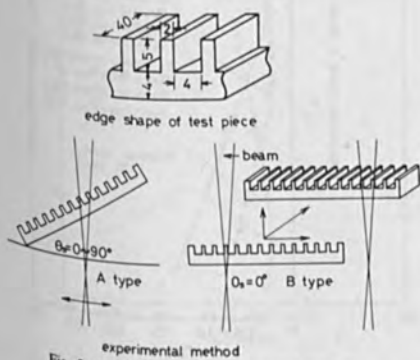


Fig. 5. Schematic drawing of beam test methods.

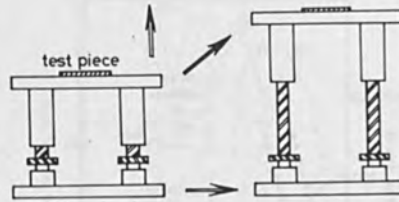


Fig. 6. Schematic drawing of glide beam test method device.

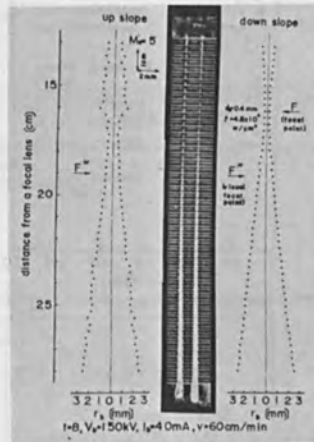


Fig. 7. Difference of measured beam shape between up slope welding and down slope welding.

Table 2. Chemical composition of test piece.

material	mark	chemical composition									
stainless steel	AISI 316L	C	Si	Mn	P	S	Ni	Cr	Mo	Fe	
		0.08	1.00	2.00	0.04	0.03	12.00	16.00	2.00		Bal
phosphor bronze	PBC-1	Sn	P	Pb+Zn+Fe			Cu				
		10.0	0.05	<1.5			Bal				
copper	DCuP2-1/2	P					Cu				
		0.004					0.040		Bal		
titanium	KS-40	C+Fe+N		O		H		Ti			
		-0.60		-0.300		-0.010		Bal			
aluminum alloy	5083	Cu	Si	Fe	Mn	Mg	Zn	Ti	Cr	Al	
		0.1	0.4	0.4	0.3	3.8	0.1	0.2	0.5	Bal	
aluminum alloy	7075	Cu	Si	Fe	Mn	Mg	Zn	Ti	Cr	Al	
		12	0.4	0.5	0.3	2.1	5.1	0.2	0.18	Bal	

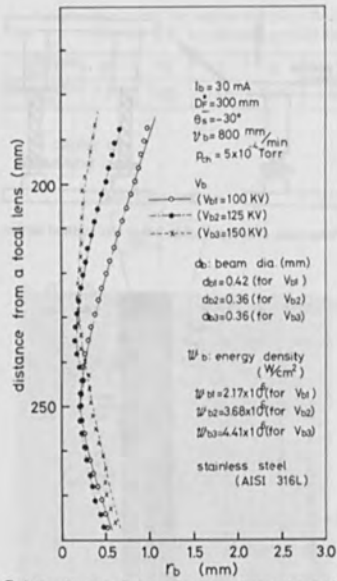


Fig. 8.

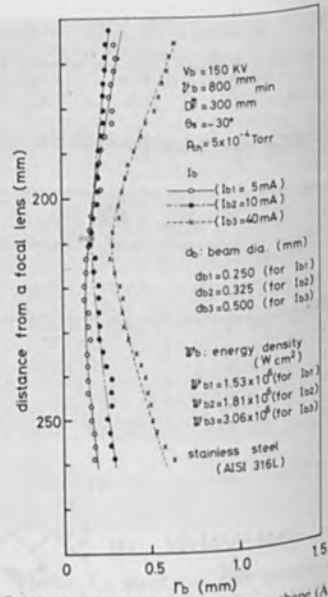


Fig. 9.

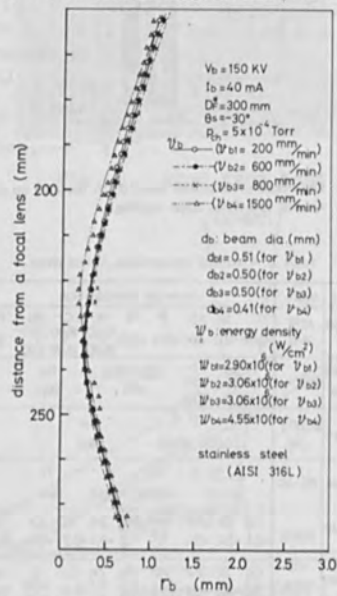


Fig. 10.

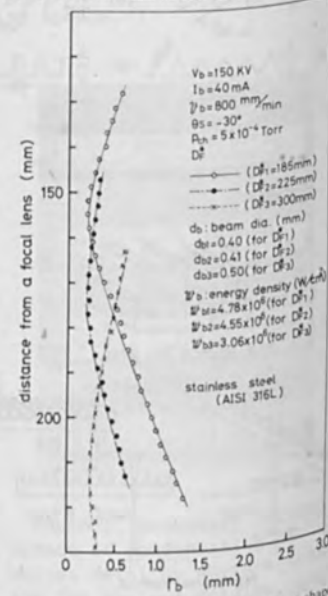


Fig. 11.

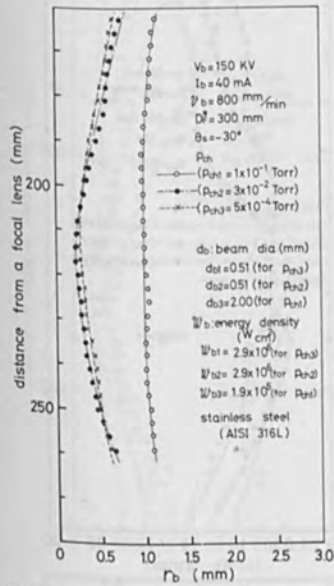


Fig. 12. Relation between gas pressure in vacuum work chamber and beam shape (A type test).

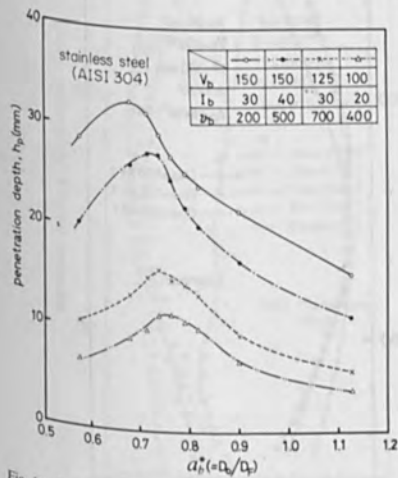


Fig. 14. Relation between penetration depth and visual active parameter: a_p^* .

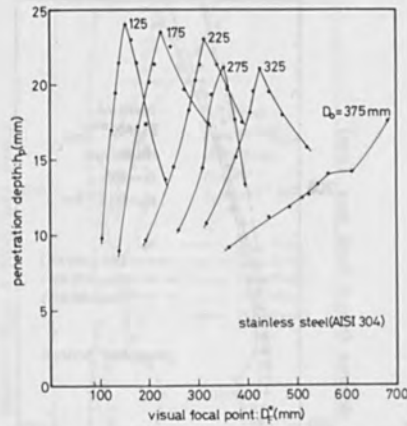


Fig. 13. Relation between penetration depth and visual focal point for various object distance, ($V_b = 150$ KV, $I_b = 30$ mA, $v_s = 500$ mm/min).

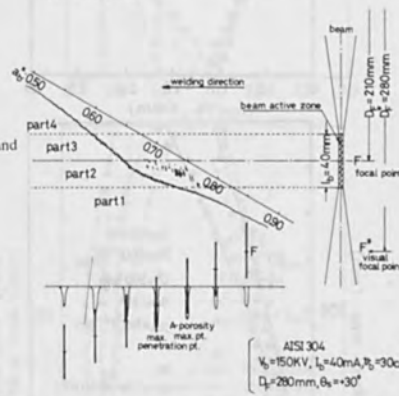


Fig. 15. Schematic explanation of mutual relation on situation between occurring range of porosity, and beam.

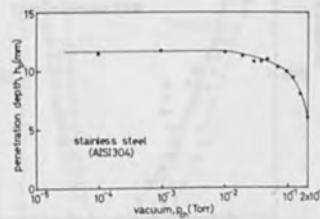


Fig. 16. Relation between penetration depth and gas pressure in vacuum work chamber.

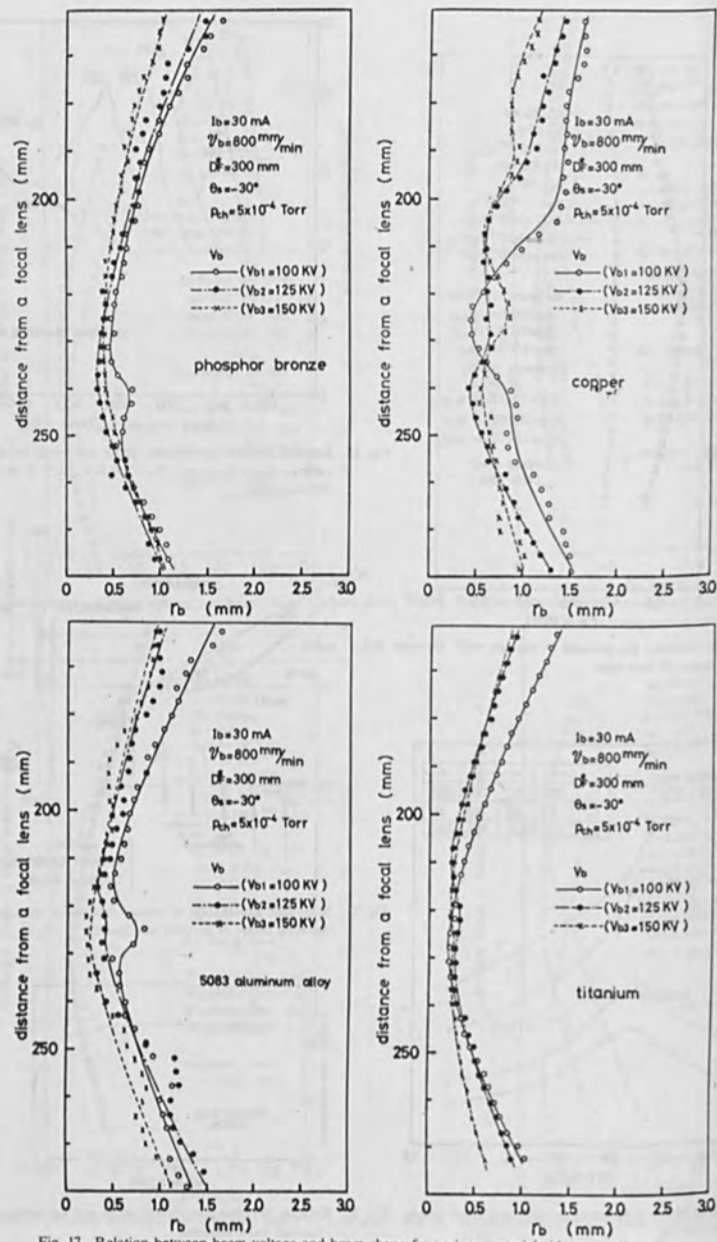


Fig. 17. Relation between beam voltage and beam shape for various materials (A type test).

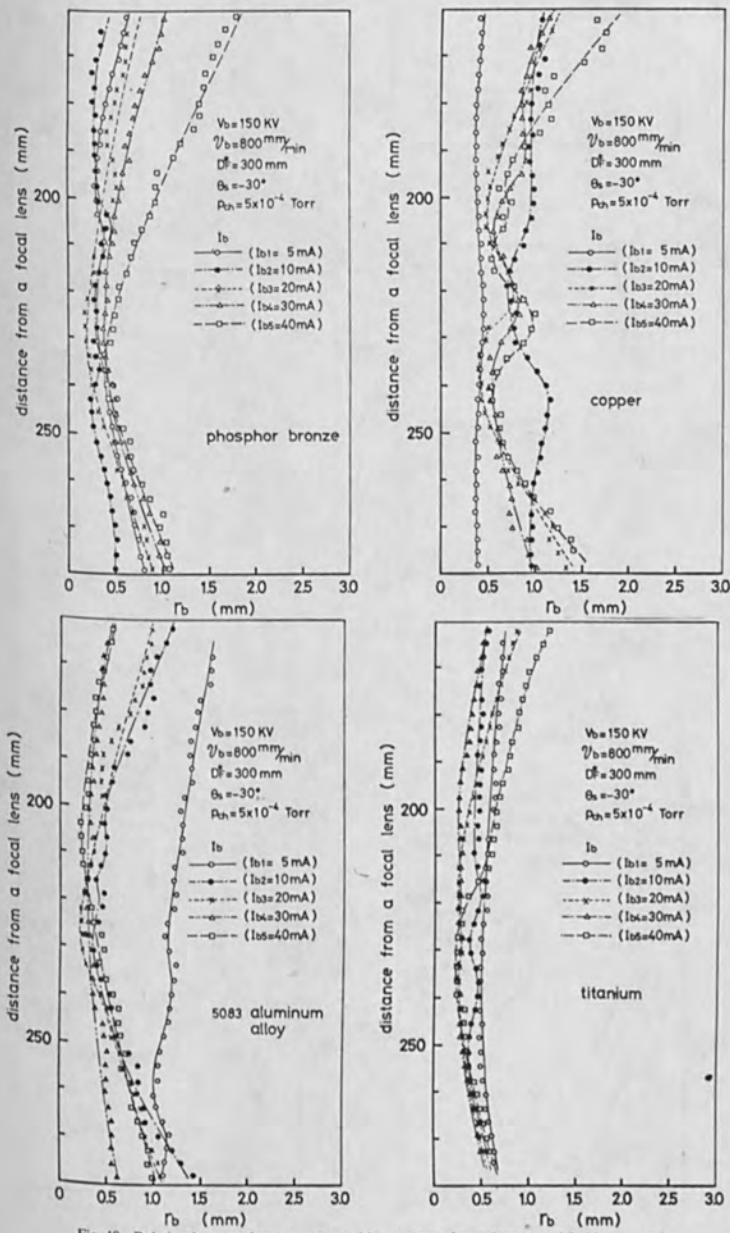


Fig. 18. Relation between beam current and beam shape for various materials (A type test).

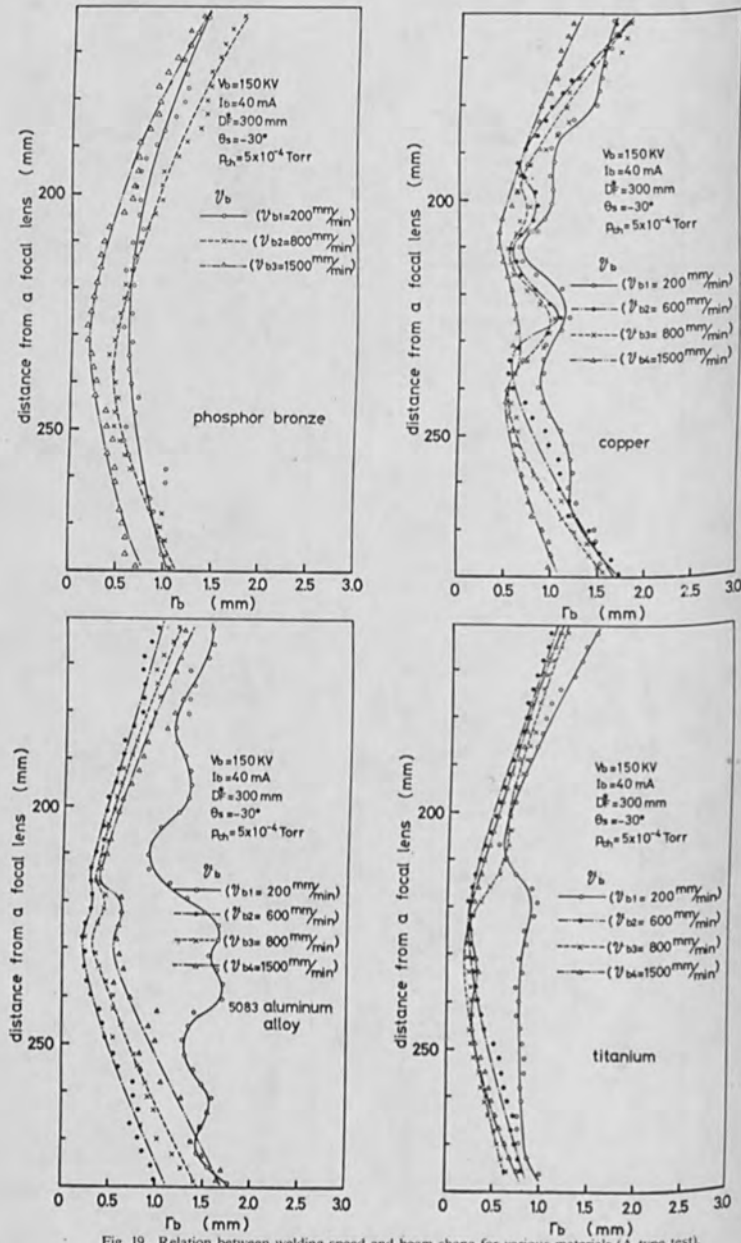


Fig. 19. Relation between welding speed and beam shape for various materials (A type test).

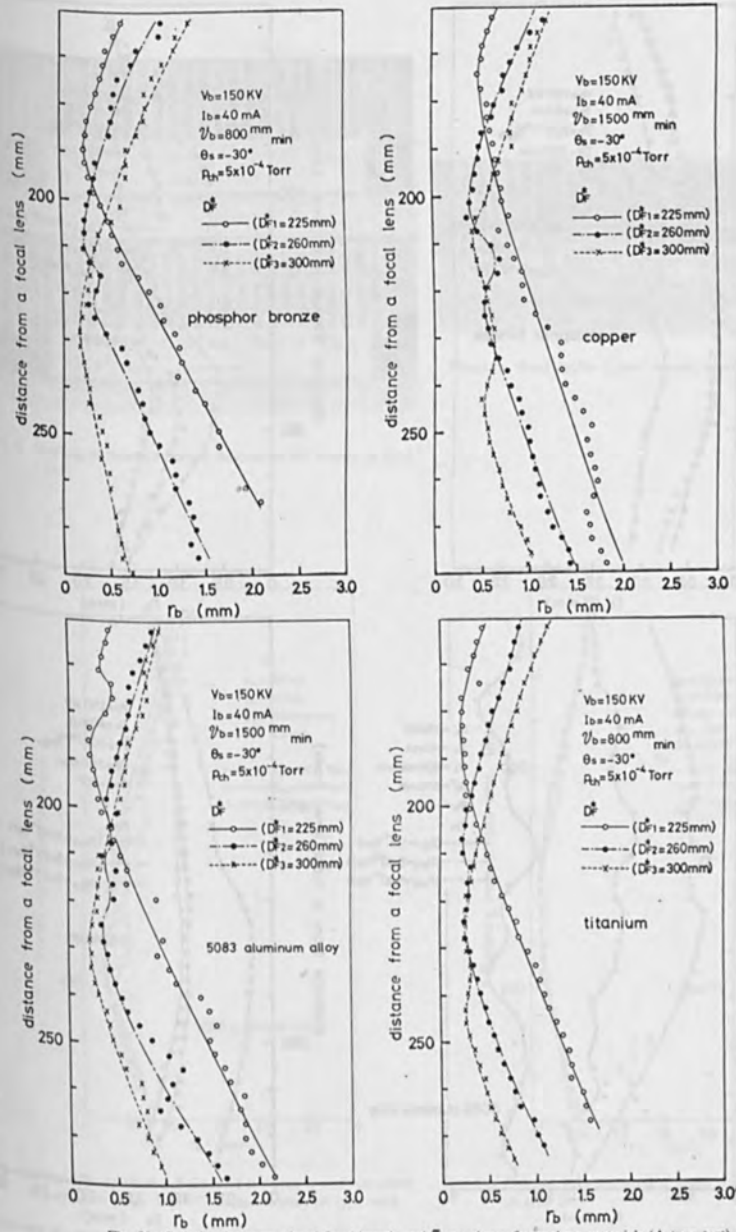


Fig. 20. Relation between visual focal length and beam shape for various materials (A type test).

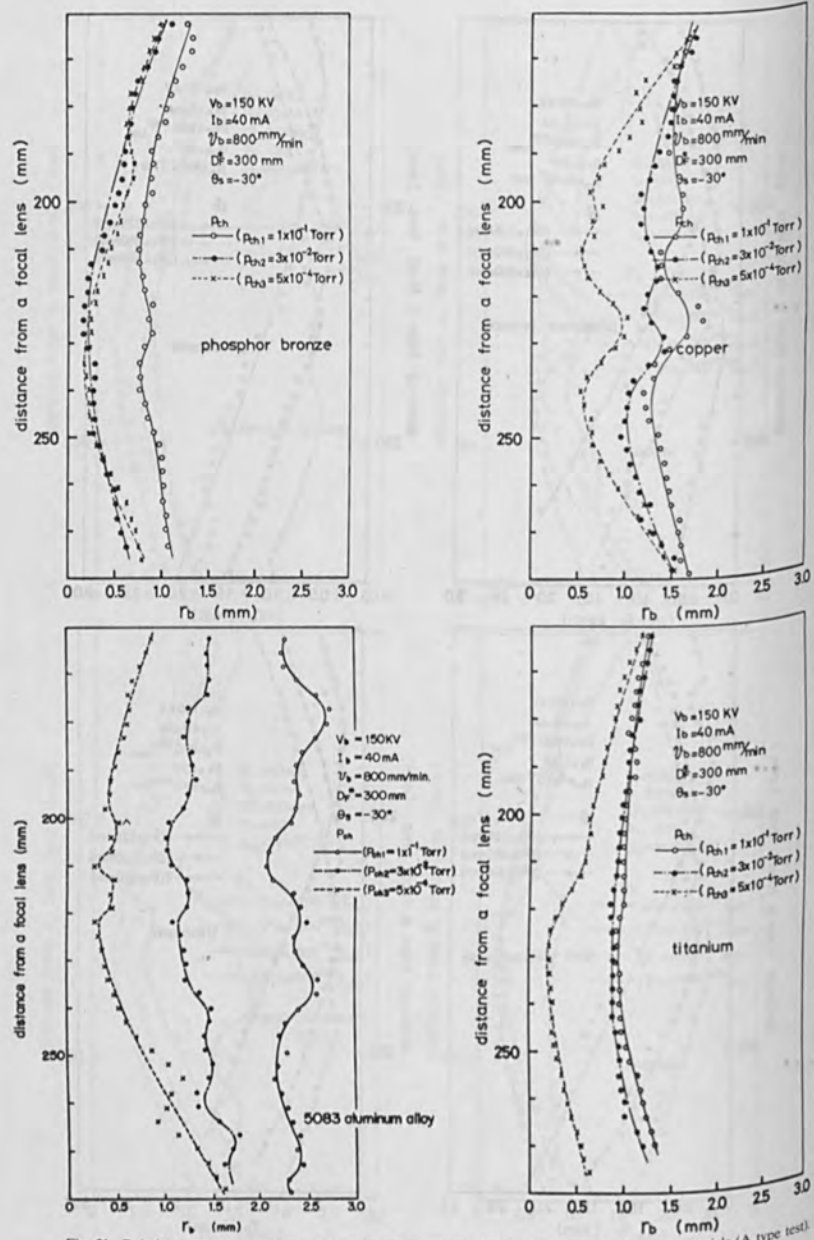


Fig. 21. Relation between gas pressure in vacuum work chamber and beam shape for various materials (A type test).

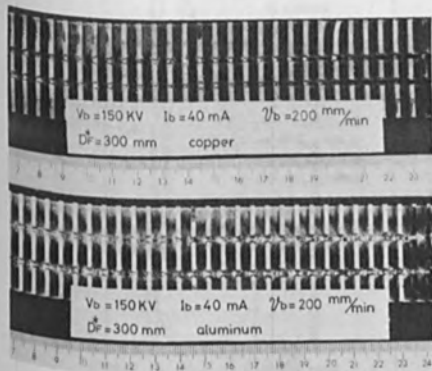


Photo 4. Swelling of measured beam diameter in the vicinity of focal point.

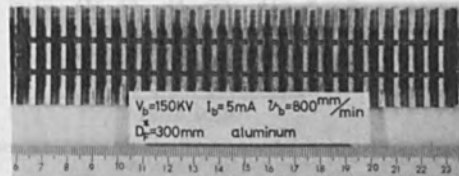


Photo 5. Bead profile in case of using small beam current.

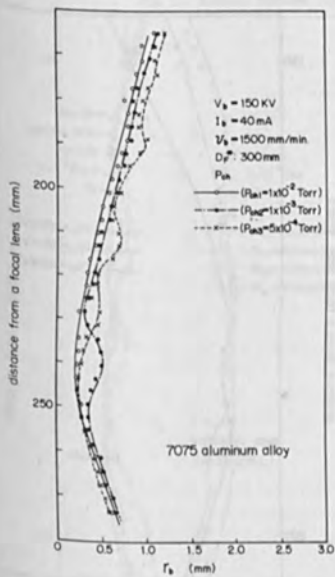


Fig. 22. Relation between gas pressure in vacuum work chamber and beam shape for 7075 aluminum alloy (A type test).

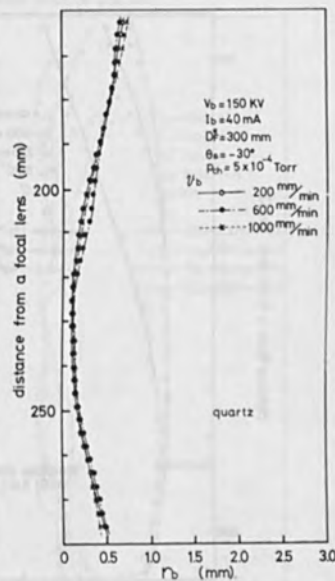


Fig. 23. Relation between welding speed and beam shape for (A type test).

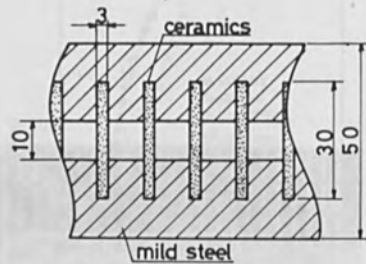


Fig. 24. Schematic drawing of test piece with parallel-arranged ceramic strip fired by jig of steel.

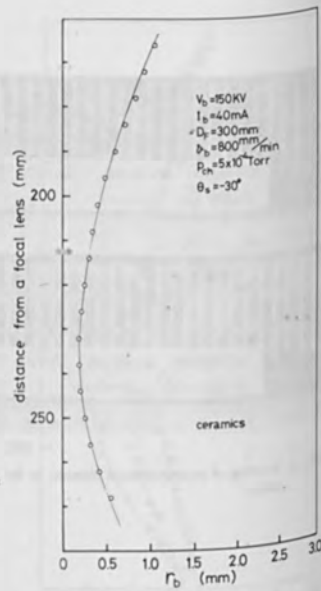


Fig. 25. Beam shape in test piece with parallel-arranged ceramic strip fixed by jig of steel.

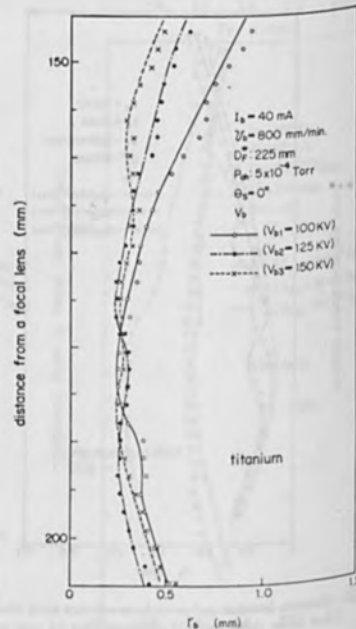
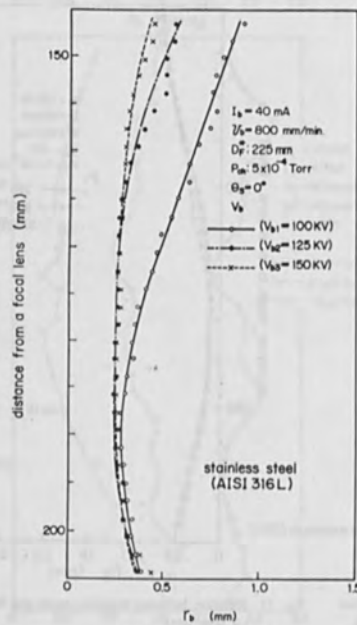


Fig. 26. Relation between beam voltage and beam shape (B type test).

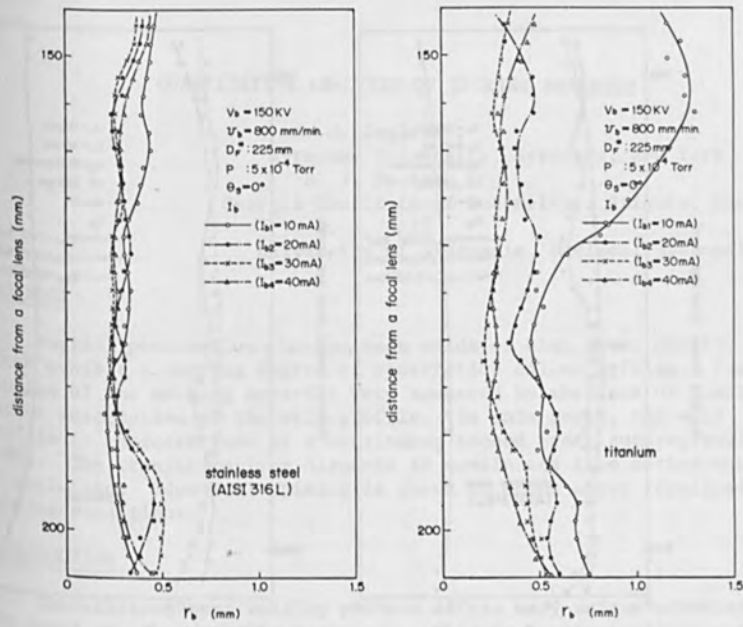


Fig. 27. Relation between beam current and beam shape (B type test).

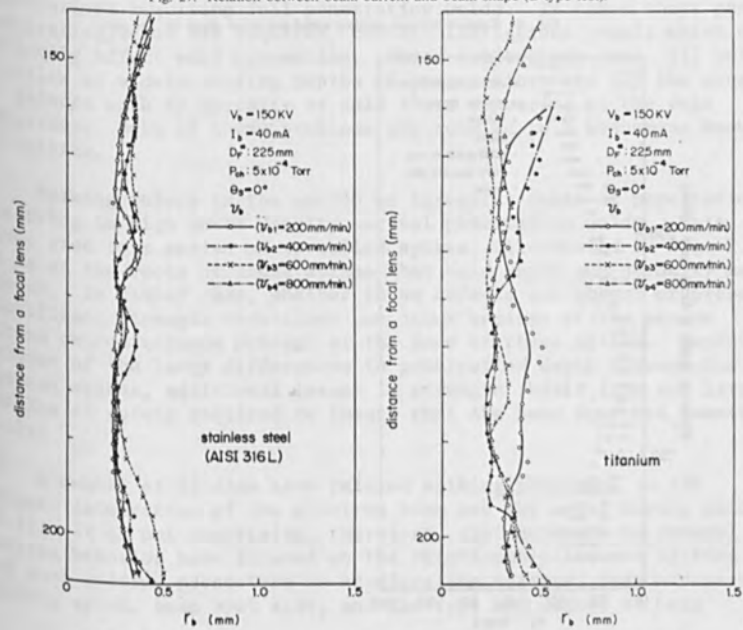


Fig. 28. Relation between gas pressure in vacuum work chamber and beam shape (B type test).

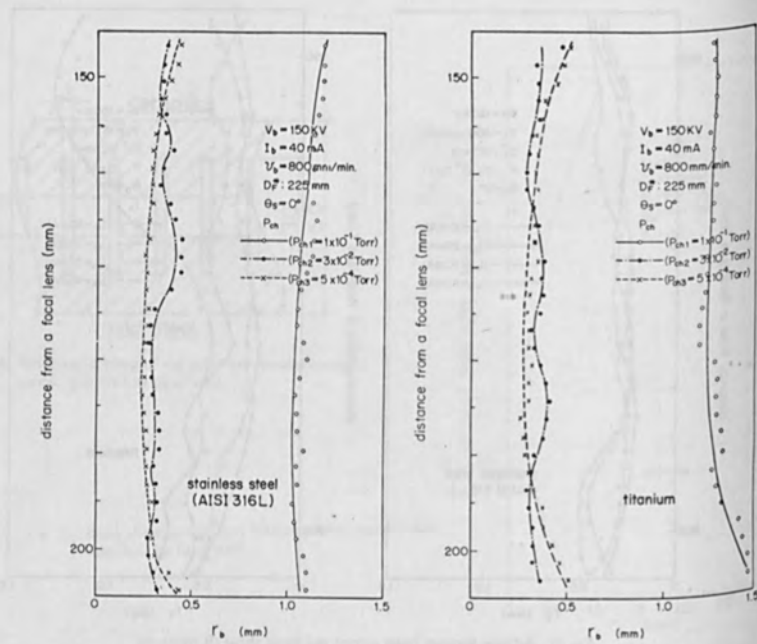


Fig. 29. Relation between welding speed and beam shape (B type test).

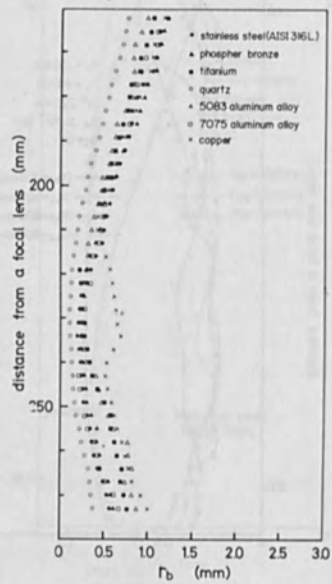


Fig. 30. Summarization of proper beam shape for each type of materials.

QUANTITATIVE ANALYSIS OF SPIKING BEHAVIOR

A. M. Joglekar,
Syracuse University, Syracuse, New York
S. J. Deutsch,
Georgia Institute of Technology, Atlanta, Georgia
R. A. Moll
University of Wisconsin, Madison, Wisconsin

ABSTRACT

Partial penetration electron beam welds of high power density often exhibit a varying degree of penetration called spiking. Past studies of the spiking behavior were hampered by the lack of quantitative description of the weld profile. In this paper, the weld profile is characterized by a continuous second order autoregressive model. The transition from discrete to continuous time series models is explained. Identical spiking is shown to occur under identical welding conditions.

INTRODUCTION

The electron beam welding process offers many unique advantages not found in other welding processes. This is particularly true for applications requiring full penetration welds. In cases where partial penetration welds are required, certain limitations result which can seriously affect weld properties. These limitations are: (1) weld profiles of widely varying depths of penetration, and (2) the presence of defects such as porosity or cold shuts appearing at the weld interface. Both of these problems are related to a phenomena known as spiking.

Spiking refers to the uneven or irregular depth of penetration occurring in high power density partial penetration welds. This gives rise to a series of so-called spikes, illustrated in Fig. 1. It is at the roots of these spikes that cold shuts and porosity may appear. In either case, whether these defects are absent or present, significant strength reductions can occur because of the severe stress concentrations present at the base of these spikes. Moreover, because of the large differences in penetration depth between the various spikes, additional losses in strength result from the large margins of safety required to insure that the beam does not penetrate fully.

A number of studies have related spiking phenomena to the dynamic interaction of the electron beam and the metal during welding [1-5]. It is not surprising, therefore, that attempts to control spiking behavior have focused on the relationship between spiking and such welding parameters as accelerating voltage, beam amperage and welding speed, beam spot size, and the type and degree of beam

oscillation [6,7,8]. In addition, impurity content [9,10] gas content, [11] surface condition and fit up [12], and the use of multi-pass weld techniques [6,13], have also been found to effect spiking and its associated defects. All of the attempts to control and relate spiking to these variables, have been limited by the ability to describe the spiking phenomena. Descriptive approaches have been visual [7,8]. These visual analyses have indicated the occurrence of spiking behavior in different parts of a continuous weld made under the same welding conditions.

In this paper, a statistical model building procedure is utilized to quantitatively describe the spiking phenomena. The experimental procedures used in obtaining cross-sectional configurations of the non uniform penetration imparted in E. B. welding is first described. From a digitized record of these continuous tracings, empirical-stochastic models are then developed. These discrete "time" models are then reparameterized to continuous time representations eliminating any undue approximation in the continuous data caused by the selection of a given sample interval. The parameters of these continuous time models are then analyzed to establish consistency in the descriptive ability of the resulting models developed from weld samples obtained under identical process conditions.

EXPERIMENTAL PROCEDURES

Photographs of a long, continuous electron beam weld were obtained from the Lawrence Radiation Laboratory. The weld joined two four inch thick rings of depleted uranium which were cut into small sections and broken along the weld seam revealing the spiking profile. Because the photographs were obtained from a single continuous weld, variations in voltage, amperage, travel speed and focus point inherent in any electron beam welder and which could effect any portion of the weld profile, were assumed to have influenced any section equally throughout the weld profile.

Data measurements of the weld profile, were obtained in the following manner. First, the spikes and a reference line were traced on a clear sheet of plastic from a photograph of the weld cross-section. The reference line chosen for measurement of the penetration distance of the spikes, was the bottom surface of the specimen. Along this reference line at an interval of 1/32 of an inch, measurements of the penetration depths were sequentially recorded. Sections of two different welded rings were sampled in this fashion, to obtain two discrete series of 200 sequential observations. Figure 2 contains a plot of these data sets.

CHARACTERIZATION BY DISCRETE TIME SERIES MODELS

In this section the two profiles are characterized by discrete time series models following the iterative procedure of model

identification - parameter estimation - diagnostic checking of residuals suggested by Box and Jenkins (14). Let X_t denote the deviation of the profile height from the mean profile height μ .

Fig. 3 exhibits the estimated sample autocorrelation function $(\hat{\rho}_k, k=1,2,3\dots)$ and sample partial autocorrelation function $(\hat{\rho}'_k, k=1,2,3\dots)$ obtained from the discrete profile 1. The simultaneous occurrence of sinusoidal decay of $\hat{\rho}_k$ and the cutting off of $\hat{\rho}'_k$ after lag $k=2$ suggests x_t to follow a discrete autoregressive process of order 2 (AR(2) process) given by,

$$x_t - \phi_1 x_{t-1} - \phi_2 x_{t-2} = a_t, \quad (1)$$

where ϕ_1 and ϕ_2 are the autoregressive parameters and $a_t, t=1,2,3\dots$ which are assumed to follow a discrete white noise process,

$a_t \sim \text{NID}(0, \sigma_a^2)$.

The maximum likelihood estimates of the four independent parameters ϕ_1, ϕ_2, μ and σ_a^2 which completely characterize an AR(2) process and their individual 95% confidence intervals are given in Table 1(a). The fitted model for observation set 1 is thus,

$$\begin{aligned} x_t &= 1.3965 x_{t-1} - 0.5381 x_{t-2} + a_t \\ \hat{\mu} &= 0.2315 \quad \text{and} \quad \hat{\sigma}_a^2 = 0.00108 \end{aligned} \quad (2)$$

Figure 4 shows the estimated residual autocorrelation function and the histogram of the estimated residuals a_t . These diagnostic checks indicate no reason to suspect departure from the assumptions, that $a_t \sim \text{NID}(0, \sigma_a^2)$. Therefore, the model as described in equation 2 is adopted as an adequate representation of the discretized profile 1.

Similar procedures were followed for the second discrete profile representation. The following model was found to adequately represent profile 2.

$$\begin{aligned} x_t &= 1.3339 x_{t-1} - 0.4446 x_{t-2} + a_t \\ \hat{\mu} &= 0.1876 \quad \text{and} \quad \hat{\sigma}_a^2 = 0.00124 \end{aligned} \quad (3)$$

The individual 95% confidence intervals for ϕ_1, ϕ_2 and μ are also given in Table 1(a). The joint confidence regions for $\hat{\phi}_1, \hat{\phi}_2$ for profiles 1 and 2 are shown in figure 5.

It is to be noted, that the given sets of parameters estimated are conditional upon the choice of the sample interval Δ . For example, figure 6 exhibits the sample autocorrelation and partial correlation functions for profile 1 based upon a sample interval $\Delta = 1/16$ inch. This discrete data set was generated by taking alternate observations from the previous data set. The estimated autocorrelations in figure 6 are identical to those obtained by taking alternate autocorrelation values from figure 3.

CHARACTERIZATION BY CONTINUOUS TIME SERIES MODELS

In this section the discrete time models developed are reparameterized to continuous time series representations in order to eliminate the effect of the sample interval. This characterization depends upon the following result proved in [15]. Let $x(t)$ be a stationary continuous ARMA(2,1) process given by

$$\frac{d^2x(t)}{dt^2} + a_1 \frac{dx(t)}{dt} + a_0 x(t) = z(t) + b_1 \frac{dz(t)}{dt}, \quad (4)$$

with continuous autoregressive parameters $a_0, a_1 > 0$ and continuous moving average parameter b_1 , $-\infty < b_1 < \infty$ and where $z(t)$ is a continuous white noise process with variance σ_z^2 . If $x(t)$ is sampled at a uniform sampling interval Δ , then the sampled process is discrete ARMA(2,1) represented by

$$x_t - \phi_1 x_{t-1} - \phi_2 x_{t-2} = a_t - \theta a_{t-1}, \quad (5)$$

where θ is the discrete moving average parameter (μ has been assumed to be zero without loss of generality). The relationships between the parameters of the continuous ARMA (2,1) process and the discrete ARMA(2,1) process which provide a means of estimating the parameters of the continuous time series model are given in the Appendix.

Discrete ARMA (2,1) models were fitted to profiles 1 and 2 with $\Delta = 1/32$ inch. The results are given in Table 1(b). For both profiles, θ is effectively zero, hence the previous AR(2) fit is adequate. However $\hat{\theta}$ was retained while obtaining the estimates of the continuous ARMA(2,1) model parameters to permit unconstrained estimation. The estimated parameter values and the 95% individual confidence intervals are given in Table 1(c). Since the confidence interval on b_1 includes zero, the appropriate model to consider is the continuous AR(2) model given by

$$\frac{d^2x(t)}{dt^2} + a_1 \frac{dx(t)}{dt} + a_0 x(t) = z(t) \quad (6)$$

The parameters a_1 , a_0 , μ , σ_z^2 were estimated by the constrained estimation technique given in the Appendix. Table 1(d) contains the parameter estimates and the 95% confidence intervals for the four combinations of the two profiles and the two sample intervals.

It is observed from Table 1(d) that a change in the sample interval does not have a significant effect on the estimated parameter values. Therefore, characterization of the weld profile by a continuous AR(2) model is invariant under changes in the sample interval. Additionally, the four characteristic parameters are not significantly different for the two profiles.

The nature of the spiking characteristics can be interpreted and quantified directly from the model parameters. Equation (7) can be written as,

$$\frac{d^2x(t)}{dt^2} + 2\xi\omega_n \frac{dx(t)}{dt} + \omega_n^2 x(t) = z(t), \quad (7)$$

where the natural frequency, $\omega_n = \sqrt{a_0}$ and the dampening factor, $\xi = a_1/2\sqrt{a_0}$. The weld profile $x(t)$ represented by Equation (8) can be interpreted as a damped second order random vibration with white noise forcing function $z(t)$. In this form, $x(t)$ is completely characterized by μ , ω_n , ξ , and the profile variance, $\gamma_0 = \sigma_z^2/4\xi\omega_n^3$. These parameters have the following physical interpretation; μ is the mean depth of penetration, ω_n is the natural frequency of oscillation of the weld profile, ξ is the damping factor and determines the extent to which a disturbance in the natural oscillation is damped and γ_0 represents the variability of the profile from its mean level.

CONCLUSIONS

- (a) The EB weld profile can be completely characterized by a continuous AR(2) model given by

$$\frac{d^2x(t)}{dt^2} + a_1 \frac{dx(t)}{dt} + a_0 x(t) = z(t).$$

- (b) Under the same welding conditions, identical spiking behavior occurs and is characterized by this AR(2) model with statistically identical parameter values.

ACKNOWLEDGEMENTS

The authors wish to acknowledge the help of Mr. Robert Armstrong and Mr. Gary Fenner.

REFERENCES

1. Weber, C. M., Funk, E. R. and McMaster, R. C., "Penetration Mechanism of Partial Penetration Electron Beam Welding", Welding Journal, p. 905-945, February 1972.
2. Tong, H. and Giedt, W. H., "A Dynamic Interpretation of Electron Beam Welding", Welding Journal, 49 [6], p. 2595-2665, June, 1970.
3. Tong, H. and Giedt, W. H., "Interpretation of the Observed Oscillation of an Electron Beam Welding Cavity", 4th International Conference on Electron and Ion Beam Science Technology, pp. 148-164, 1970.
4. Weber, C. M., "Direct Observation of the Penetration Mechanism of Partial Penetration Electron Beam Welding", 5th International Conference on Electron and Ion Beam Science and Technology, pp. 307-320, 1972.
5. Hicken, G. K. and Booco, W. G., "Penetration Variations in Electron Beam Welding", 3rd International Conference on Electron and Ion Beam Science and Technology, pp. 398-411, 1968.
6. Sandstrom, D. J., "The Relationship of Beam Parameters to Weld Geometry in Electron Beam Welds", 4th International Conference on Electron and Ion Beam Science and Technology, pp. 165-178, 1970.
7. Armstrong, R. E., "Spiking in Partial Penetration, Electron Beam Welds". 4th International Conference on Electron and Ion Beam Science and Technology, pp. 179-194, 1970.
8. Armstrong, R. E., "Control of Spiking in Partial Penetration Electron Beam Welds", Welding Journal, pp. 3825-3885, August, 1970.
9. Moll, R. A., "The Effect of Carbon on the Spiking Characteristics of Uranium and Related Observations", A.E.C. Document SC-DR-69-487. Steering Group meeting on Electron Beam Welding Research, April 1969.
10. Hashimoto, T., Matsuda, F., and Suzuke, H., "Some Experiment on Electron-Beam Welds", Transactions of National Research Institute for Metals, Vol. 7 No. 4, pp. 35-43, 1965.
11. Huber, R. A. and Turner, P. W., "Electron-Beam Welding at the Oak Ridge Y-12 Plant", Welding Journal, pp. 787-799, October 1969.
12. Sayer, L. N., "Quality in Electron Beam Welding", British Welding Journal, pp. 163-169, April 1967.

13. Bradburn, E. H., Huber, R. A., and Turner, P. W., "Multipass Electron Beam Welding for Controlled Penetration", Welding Journal, pp. 190s-193s, April 1971.
14. Box, G.E.P. and Jenkins, G. M., Time Series Analysis Forecasting and Control, Holden-Day, San Francisco, Calif, 1970.
15. Phadke, M. S. and Wu, S. M. "Modeling of Continuous Stochastic Processes From Discrete Observations with Applications to Sunspots Data" Journal of American Statistical Association, Vol. 69, No. 346, 1974.

APPENDIX

ESTIMATION OF CONTINUOUS ARMA(2,1) MODEL PARAMETERS

Estimation of continuous ARMA(2,1) model parameters is based upon the relationship between the parameters of the continuous stationary stochastic process given by

$$\frac{d^2 x(t)}{dt^2} + a_1 \frac{dx(t)}{dt} + a_0 x(t) = z(t) + b_1 \frac{dz(t)}{dt}$$

and the corresponding sampled discrete ARMA(2,1) process

$$x_t - \phi_1 x_{t-1} - \phi_2 x_{t-2} = a_t - \theta a_{t-1}$$

The relationship between ϕ_1 , ϕ_2 , θ and a_1 , a_0 , b_1 depends upon the following three cases. In each case, a_1 , a_0 can be directly computed from ϕ_1 and ϕ_2 but b_1 has to be recursively obtained by solving the equation

$$\theta^2 - A\theta + 1 = 0 \quad , \quad |\theta| < 1$$

where

$$A = 1 + \frac{\phi_1 - \phi_1 \rho_1 - \phi_2 \rho_2}{\phi_1 + (\phi_2 - 1) \rho_1} \quad ,$$

ρ_1 and ρ_2 are functions of b_1 , a_0 and a_1 . b_1 is computed such that the solution of the above equation yields θ equal to the estimated θ . The expressions for a_1 , a_0 , ρ_1 , ρ_2 are given below.

Case 1: $\phi_1^2 + 4\phi_2 < 0$

$$a_1 = -\ln(-\phi_2)/\Delta$$

$$a_0 = 0.25 \{a_1^2 - [(2/\Delta) \cosh^{-1} (\phi_1/2\sqrt{\phi_2})]^2\}$$

$$\rho_1 = e^{-\frac{a_1 \Delta}{2}} \left\{ \cos\left(\frac{\sqrt{4a_0 - a_1^2}}{2} \Delta\right) + \frac{1 - b_1^2 a_0}{1 + b_1^2 a_0} \cdot \frac{a_1}{\sqrt{4a_0 - a_1^2}} \cdot \sin\left(\frac{\sqrt{4a_0 - a_1^2}}{2} \Delta\right) \right\}$$

$$\rho_2 = e^{-a_1 \Delta} \left\{ \cos\left(\sqrt{4a_0 - a_1^2} \Delta\right) + \frac{1 - b_1^2 a_0}{1 + b_1^2 a_0} \cdot \frac{a_1}{\sqrt{4a_0 - a_1^2}} \cdot \sin\left(\sqrt{4a_0 - a_1^2} \Delta\right) \right\}$$

Case 2: $\phi_1^2 + 4\phi_2 = 0$

$$a_1 = -\ln(-\phi_2)/\Delta$$

$$a_0 = a_1/2$$

$$\rho_1 = e^{-\sqrt{a_0} \Delta} \left(1 + \frac{1 - b_1^2 a_0}{1 + b_1^2 a_0} \sqrt{a_0} \Delta \right)$$

$$\rho_2 = e^{-2\sqrt{a_0} \Delta} \left(1 + \frac{1 - b_1^2 a_0}{1 + b_1^2 a_0} 2\sqrt{a_0} \Delta \right)$$

Case 3: $\phi_1^2 + 4\phi_2 > 0$

$$a_1 = -\ln(-\phi_2)/\Delta$$

$$a_0 = 0.25 \{ a_1^2 + [(2/\Delta) \cos^{-1}(\phi_1/2\sqrt{\phi_2})]^2 \}$$

$$\rho_1 = -\frac{a_0}{(1+b_1^2 a_0) \sqrt{a_1^2 - 4a_0}} \left\{ \frac{1-b_1^2 \alpha_1^2}{\alpha_1} e^{\alpha_1 \Delta} - \frac{1-b_1^2 \alpha_2^2}{\alpha_2} e^{\alpha_2 \Delta} \right\}$$

$$\rho_2 = -\frac{a_0}{(1+b_1^2 a_0) \sqrt{a_1^2 - 4a_0}} \left\{ \frac{1-b_1^2 \alpha_1^2}{\alpha_1} e^{2\alpha_1 \Delta} - \frac{1-b_1^2 \alpha_2^2}{\alpha_2} e^{2\alpha_2 \Delta} \right\}$$

where $\alpha_{1,2} = 0.5 (-a_1 \pm \sqrt{a_1^2 - 4a_0})$

To obtain the parameters of a continuous AR(2) process, b_1 is constrained to be zero. In each case, σ_z^2 is given by

$$\sigma_z^2 = \frac{2 a_1 \theta \sigma_a^2}{[\phi_1 + (\phi_2 - 1)\rho_1] [b_1^2 + \frac{1}{a_0}]}$$

TABLE I

SUMMARY OF FITTED TIME SERIES MODELS

(a) AR(2) DISCRETE		$\hat{\phi}_1$	$\hat{\phi}_2$	$\hat{\mu}$	$\hat{\sigma}_a^2$
PROFILE	Δ				
1	1/32	1.3965+0.12	-0.5381+0.12	0.2315+0.033	0.00108
2	1/32	1.3339+0.13	-0.4446+0.13	0.1876+0.045	0.00124
1	1/16	0.9608+0.19	-0.3163+0.19	0.2308+0.035	0.00366
2	1/16	1.0113+0.20	-0.2601+0.20	0.1848+0.048	0.00347

(b) ARMA(2,1) DISCRETE		$\hat{\phi}_1$	$\hat{\phi}_2$	$\hat{\theta}$	$\hat{\mu}$	$\hat{\sigma}_a^2$
PROFILE	Δ					
1	1/32	1.2746+0.23	-0.4277+0.22	-0.1740+0.26	0.2318+0.036	0.00108
2	1/32	1.2124+0.30	-0.3324+0.28	-0.1539+0.31	0.1875+0.048	0.00124

(c) ARMA(2,1) CONTINUOUS		\hat{a}_0	\hat{a}_1	\hat{b}_1	$\hat{\mu}$	$\hat{\sigma}_z^2$
PROFILE	Δ					
1	1/32	0.8491+0.52	0.2317+0.11	0.1954+0.34	0.2318+0.036	0.1024
2	1/32	1.1017+0.84	0.2015+0.13	0.2089+0.41	0.1875+0.048	0.1307

(d) AR(2) CONTINUOUS		\hat{a}_0	\hat{a}_1	$\hat{\mu}$	$\hat{\sigma}_z^2$
PROFILE	Δ				
1	1/32	1.0158+0.34	0.2565+0.10	0.2315+0.033	0.1363
2	1/32	1.3818+0.49	0.2345+0.12	0.1876+0.045	0.1917
1	1/16	0.9268+0.53	0.2458+0.11	0.2308+0.035	0.0650
2	1/16	1.1355+0.72	0.1966+0.11	0.1848+0.048	0.0781

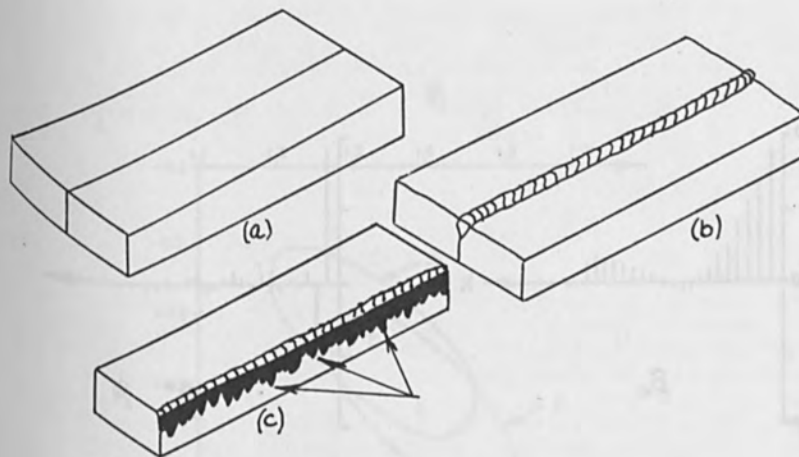


Figure 1 - Illustration of spiking behavior in partial penetration electron beam welds. (a) workpieces before welding, (b) after welding, (c) bars broken apart exposing spiking behavior. Arrows point to typical spikes.

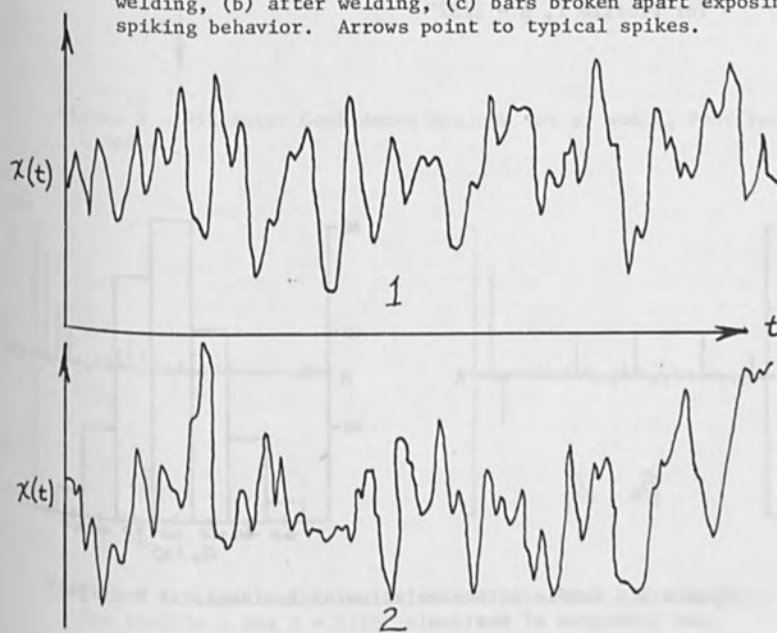


Figure 2 - Profile Plots

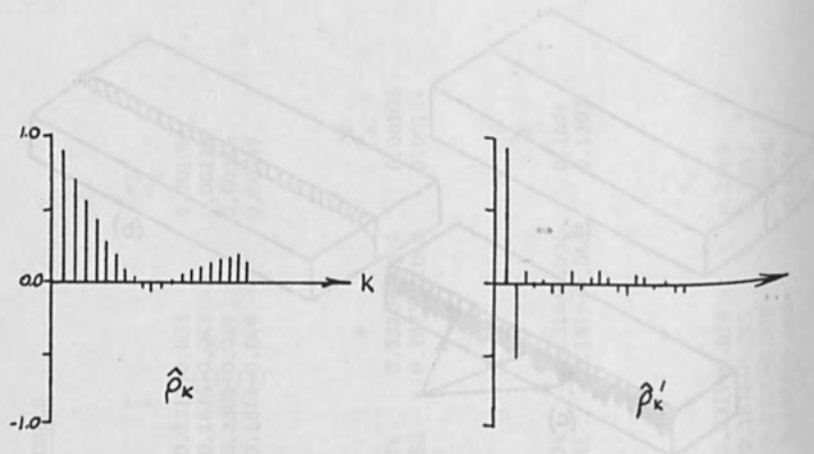


Figure 3 - Sample Autocorrelation and Partial Autocorrelation for Profile 1, $\Delta = 1/32''$

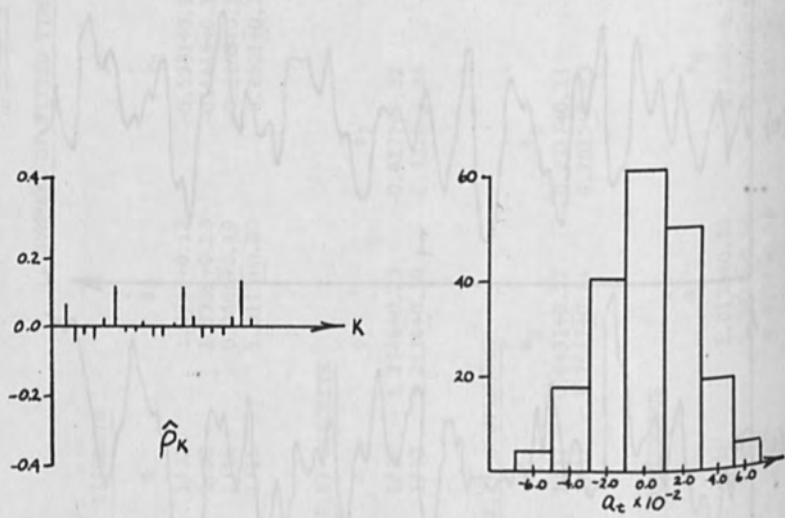


Figure 4 - Sample Autocorrelation of Residuals of Profile 1 and Histogram of Residuals

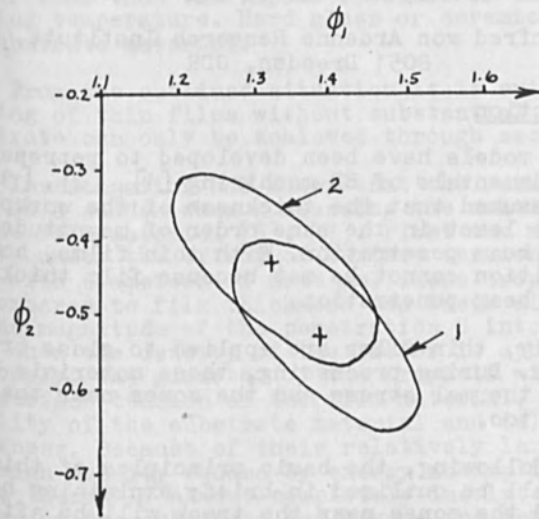


Figure 5 - 95% Joint Confidence Regions for ϕ_1 and ϕ_2 Profiles 1 and 2

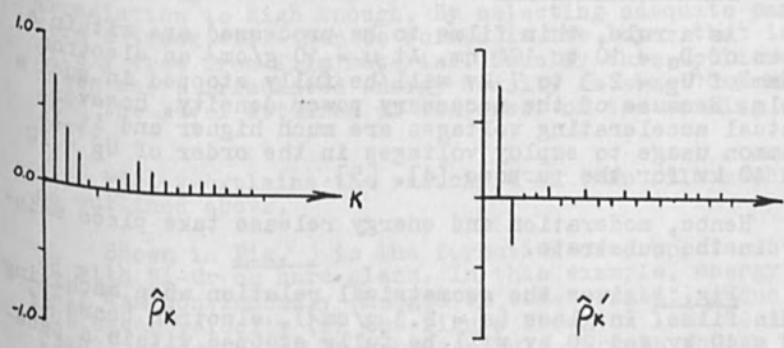


Figure 6 - Sample Autocorrelation and Partial Autocorrelation for Profile 1 for $\Delta = 1/16''$

THE PHYSICAL FUNDAMENTALS OF THIN FILM MACHINING

S. Schiller, S. Panzer, and U. Heisig

Manfred von Ardenne Research Institute,
8051 Dresden, GDR

1. Introduction

Various models have been developed to represent the physical fundamentals of EB machining [1], [2], [3]. Usually it is assumed that the thickness of the workpiece is greater or at least in the same order of magnitude than the depth of beam penetration. With thin films, however, this precondition cannot be met because film thickness is smaller than beam penetration.

Generally, thin films are applied to glass or ceramic substrates. During processing, these materials are subject to high thermal stress and the zones near the track will suffer, too.

In the following, the basic principles of thin film machining shall be outlined in brief; explaining how glass substrate and the zones near the track will be affected by such a procedure.

2. Machining Process

As a rule, thin films to be processed are within a span of $D_S = 10$ to 100 nm. At $\mu = 10$ g/cm³ an electron beam of $U_B = 2.3$ to 7 kv will be fully stopped in such a film. Because of the necessary power density, however, actual accelerating voltages are much higher and it is common usage to employ voltages in the order of $U_B = 20$ to 40 kv for the purpose [4], [5].

Hence, moderation and energy release take place mainly in the substrate.

Fig. 1 gives the geometrical relation when machining thin films. In glass ($\mu = 2.3$ g/cm³), electron beams of $U_B = 40$ kv and 20 kv will be fully stopped within a penetration depth of $S = 15$ μ m and 4 μ m, respectively. The beam diameter ranges from $d_p = 10$ to 30 μ m and therefore is in the same order of magnitude as the depth of penetration S .

But electron beam machining aims at the removal of the layer without noticeable substrate erosion. So it must

be taken into account that the vapour pressure of the usual film materials (e.g., Ni-Cr or Fe-Ni) should be equal to or less than the vapour pressure of the substrate at working temperature. Hard glass or ceramics are often used as substrate material.

From the outlined situation it is evident that machining of thin films without substantial injury to the substrate can only be achieved through secondary actions.

Investigation has shown that the working effect occurs on a sudden when surpassing the melting temperature of the film material [6], [7]. First the molten layer contracts under the effect of surface tension, forming droplets with diameters of some μm . These droplets are large as compared to film thickness and their diameter approaches the magnitude of the penetration S into the film material when the density of the latter is approx. 10 g/cm^3 . Obviously, the diameter of the droplets will depend (a) on the surface tension of the film material, (b) on the wettability of the substrate material and (c) on the film thickness. Because of their relatively large diameter, and the high density caused by energy absorption from the beam, these thermally almost completely insulated droplets are heated on the substrate far beyond the temperature of the substrate material; thus causing increased evaporation. From various studies it can be seen that - probably due to Leidenfrost's phenomena - these droplets migrate toward the edges of the processed track provided the energy irradiation is high enough. By selecting adequate parameters a track will then be formed in the layer that is entirely free from film material. Usually this applies to cases where irradiated energy density is some 10 % higher than the level attained at the onset of the working effect.

Fig. 2 explains the principle of thin film machining as outlined above.

Shown in Fig. 3 is the formation of droplets obtained with Ni-Cr on hard glass. In this example, energy density was continuously changed by some percent; reducing the sweep velocity (in the figure from the left to the right) accordingly. By approaching a certain energy threshold the film surface becomes disrupted and droplets are formed when the energy density increases still further. The fate of the droplets - that migrate towards the edges - then depends on both beam parameters and properties of the film.

Fig. 4 shows the behaviour of films with various thickness, using Ni-Cr layers as example. With the thinnest layer (Fig. 4a) some droplets did not migrate toward the edge of the track. With rising film thickness the droplets at the margin will unite to form larger ones (Fig. 4b) which may finally form a continuous bulb should the film thickness be increased beyond this level (Fig. 4c). Verified by experiments, it can be shown that Eb milling without substantial substrate evaporation becomes possible in a wide range of beam and film parameters.

For reasons of good reproducibility, however, adiabatic heating of the working site becomes a must; selecting pulsed mode operation when compact bodies have to be processed. In case of thin film machining, adiabatic heating may also be obtained with continuous energy irradiation if the sweep velocity of the beam is high enough.

Fig. 5 clearly reveals that adiabatic heating actually occurs as soon as a critical sweep velocity is exceeded.

With lower sweep velocities the irradiated energy required per metre of track length is velocity-dependent. This means, however, that heat dissipation during beam action cannot be neglected. But with a sufficiently high velocity - in this example a value well above 1 m/s - the effect of heat dissipation during beam action will be immaterial and need not be considered.

3. Changes in the Substrate

As mentioned in the previous chapters, glass and ceramics predominate as substrate material. Most of all thin films to be processed consist of materials having a melting temperature that is higher than 1,000 °C and the substrate also fuses at working plane. The high temperature gradient in the immediate vicinity of the track - which amounts to approximately 10^6 °C/cm - and the thus resulting high cooling rate cause the substrate to be permanently stressed along the track. This impairs the mechanical strength of the substrate and gives rise to local crack formation when films of a higher melting point have to be processed. Such side effects should be duly considered when selecting the substrate material. Although quartz glass would be of special advantage, economical reasons often dictate the use of hard glass and comprehensive results of pertinent studies on this material are now at hand.

Some examples of crack formation in glass are shown in Figs. 6 through 8. These cracks propagate perpendicular to working direction and penetrate into the film. It is also evident that under thermal and mechanical stress all existing cracks become more extended in the course of time which, at least in part, may seriously impair the properties of thin film components.

Fig. 7 reveals the communication of two cracks that - caused by thermal stress - originate in two adjacent tracks so that the film is completely disrupted.

It is mainly due to local variations in glass properties, that any quantitative proposition on crack formation has to be based on statistic evaluation. Here it is the density D_R and the length of a crack that are of decisive importance for the working result.

Fig. 9 gives the relationship of crack density D_R (with D_R being the number of cracks per cm track length) versus sheet resistivity ρ of the film; with the latter being a measure of film thickness. From this the statistical nature of crack formation becomes evident at a glance. With a sufficiently low film thickness - and thus a sheet resistivity equal to or greater than $130 \Omega \square^{-1}$ - crack formation is entirely avoided.

Fig. 10 shows the crack density versus working speed v . Again, crack formation ceases if v is greater than 1 m/s.

The effect of beam current is illustrated in Fig. 11. With the cited parameters the beam current should be equal to or less than $30 \mu A$ to keep the track width well below $20 \mu m$.

But there are still other relations with respect to crack formation that can be approximated as follows: -

$$D_R \sim \frac{1}{U_B} \quad (1)$$

$$L_R \sim U_B^2 \approx S \quad (2)$$

Here D_R is the crack density and L_R the extension of the cracks perpendicular to the track.

The change in ultimate strength of the glass in the vicinity of the track follows similar relationships as found with crack formation.

For crack-free processing it is therefore necessary to optimize various beam parameters in combination with the features of the film-substrate system.

4. Changes in the Film Adjacent to the Track

Owing to the Gaussian distribution of beam power density, thermal conductivity in film and substrate, and the mechanism discussed in this paper, changes are likely to occur also in the immediate vicinity of the track.

Shown in Figs. 12 through 14 are some examples of characteristic edge effects. Structural changes in an indium layer close to the machined track are depicted in Fig. 12. In thick films or layers of poor adhesion there is a risk of warping (Fig. 13).

With the thermal conductivity as pronounced influencing factor it can further be shown that - prevalently with low-melting films - the track is much wider than the beam diameter. Such a case has been illustrated in Fig. 14. This figure also reveals the formation of rather large droplets along the track edges. The shape of the molten boundaries as well as the location of the droplets depend on the direction of beam deflection.

Ranges of parameters have been set up for a series of film-substrate combinations where machining becomes possible without detrimental edge effects or injury to the substrate.

From Fig. 15 it is evident that proper EB milling without troublesome edge effects can be achieved even with tantalum layers. Fig. 16 shows a Ni-Cr film on hard glass just to cite another example [8].

In practice, thin film machining is mainly used for structurizing Ni-Cr resistive layers. Apart from the resistance value itself it is the temperature coefficient that must be considered as a decisive quantity. Among other things, it depends on the structure of the film. From the statements about edge effects in the layer it is to be expected that screening the film with high line density - i.e., small distances between the lines - may change the temperature coefficient. Fig. 17 proves that - with line spacings in the same magnitude as the track width - there actually is an increase of the temperature coefficient. Wherever line spacings are great as compared to track width, however, such an alteration in the temperature coefficient can be neglected.

5. Summary and Conclusions

With respect to the physical process, electron beam machining of thin film substantially differs from the processing of compact bodies. Based on various model assumptions, the mechanism of thin film machining is explained and supported by experiment. But even minor effects on substrate and film in the vicinity of the track may be of importance with reference to processing quality. In assessing the workability of thin films it is therefore necessary to consider not only the physical properties of the film but also the features of the substrate. To achieve particular working results, it shall be pointed out once more that beam parameters and properties of the film-substrate system have to be properly matched.

References

- [1] Steigerwald, K.H.:
Materialbearbeitung mit Elektronenstrahlen.
4. Int. Kongreß Elektronenmikroskopie,
Berlin 1958, 1, Springer Verl. Berlin 1960, p.276-278
- [2] Kuper, G.:
Werkstoffabtrag nichtmetallischer Werkstoffe mit Elektronenstrahlen unter besonderer Berücksichtigung der Leistungsdichteverteilung und der Werkstoffbeeinflussung.
Dissertation 1969, TU Braunschweig
- [3] Schleich, F.:
Electron Beam Machining.
Paper submitted to the 2nd Electron Beam Processing Seminar, June 1972, Frankfurt/M., published by Universal Technology Corporation, 1388 Research Park Drive Dayton, Ohio 45432, p. 3f1-3f85
- [4] Hawkes, P.L.; Bowen, G.; Mather-Lees, S.:
The preparation of microcircuit stencils and patterns by photomechanics and electron beam machining.
Microelectronics and Reliability 4 (1965), No. 1, p. 65-79
- [5] Millard, P.A.:
Experiments on the low-voltage machining of thin films.
Microelectronics and Reliability 4 (1965), No. 1, p. 25-29

- [6] Panzer, S.:
Zur Elektronenstrahlbearbeitung dünner Ni-Cr-Schichten auf Hartglassubstrat und zur Anwendung des Verfahrens für die Strukturierung und den Abgleich von Dünnschichtwiderständen.
Dissertation 1968, TH Karl-Marx-Stadt
- [7] Schiller, S.; Panzer, S.; Heisig, U.:
Electron Beam Machining of Thin Films.
3rd electron beam processing seminar
Stratford-upon-Avon, March 1974,
published by Universal Technology Corporation
1656 Margon Drive, Dayton, Ohio 45432/USA
- [8] v.Ardenne, M.; Heisig, U.; Panzer, S.; Thieme, O.; Henneberger, J.:
Automatisiertes Elektronenstrahlabgleichen von Dünnschichtwiderständen mit kontinuierlichem Durchlauf der Bauelemente durch die Bearbeitungskammer.
In Berghammer, J. (Ed.): Microminiaturization.
JFAC/JFJP
Symposium Munich, Oct. 1965, Oldenbourg Verl. 1966,
p. 531-546

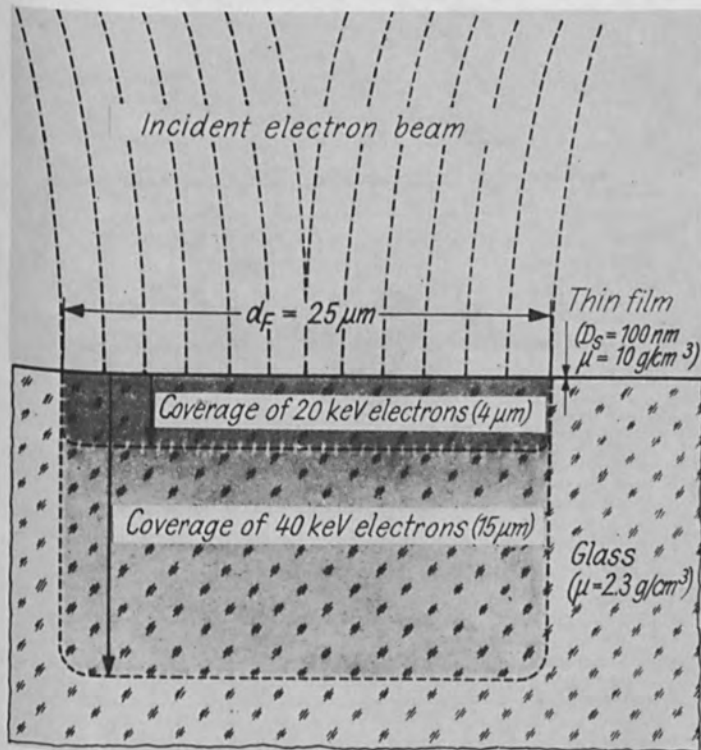


Fig. 1 Schematic representation concerning the geometrical relations of focal spot diameter d_F , film thickness D_S and electron coverage as obtained with thin-film machining.

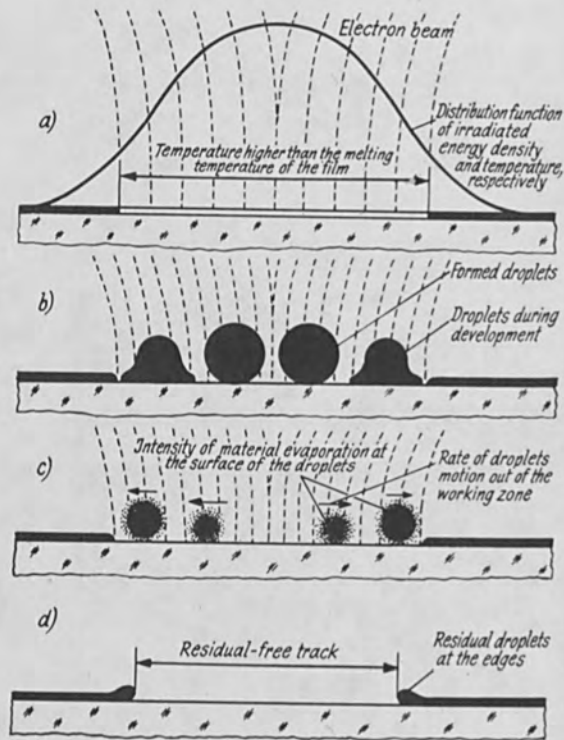


Fig. 2 Phenomenological explanation of thin-film machining.

Phase 1: Heating the film to melting temperature.

Phase 2: Formation of droplets from the molten layer.

Phase 3: Evaporation and simultaneous drift of droplets out of the track.

Phase 4: Produced bare track and bulbous deposition of residual droplets at the edges.

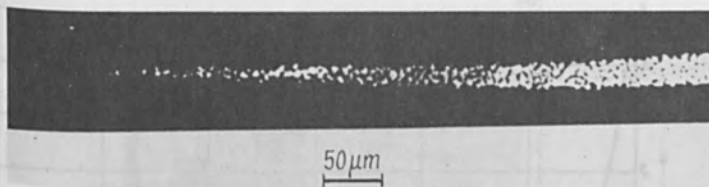


Fig. 3 Onset of working effect and formation of droplets with increasing energy density from the left to the right. (Ni-Cr film on hard glass substrate, $U_B = 20$ kv, transmitted-light exposure).

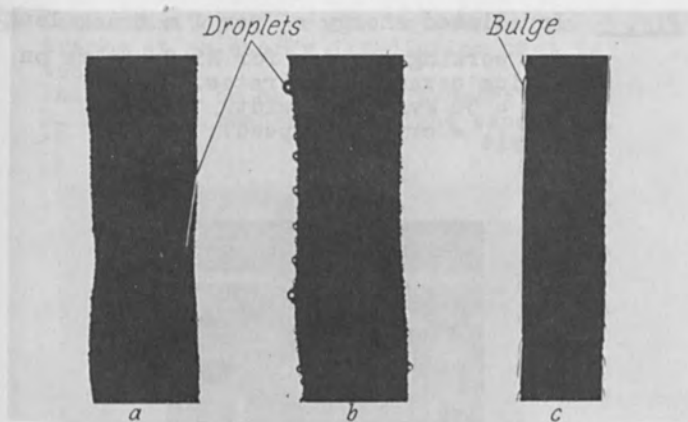


Fig. 4 Deposition of residual layers on and at the edge of the track obtained through electron beam machining Ni-Cr films of different thickness D_S . (a: $D_S \approx 10$ nm, b: $D_S \approx 30$ nm, c: $D_S \approx 100$ nm; $U_B = 20$ kv, $v = 1$ m/s, incident light exposure).

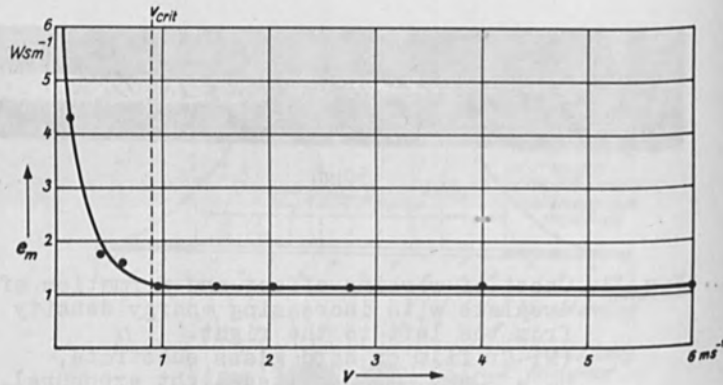


Fig. 5 Irradiated energy e_m per 1 m track length vs. working speed v for Ni-Cr films on silica ceramic substrates. ($U_B = 50$ kv, track width $17 \mu m$, v_{crit} = critical speed).

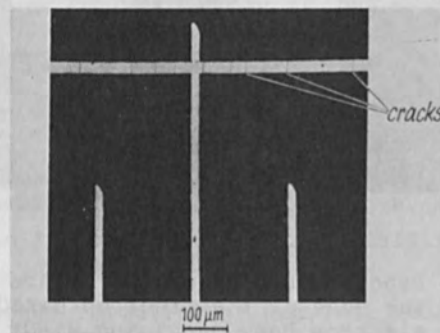


Fig. 6 Crack formation in the track when machining a Ni-Cr-film on hard glass substrates. ($U_B = 20$ kv, transmitted-light exposure).

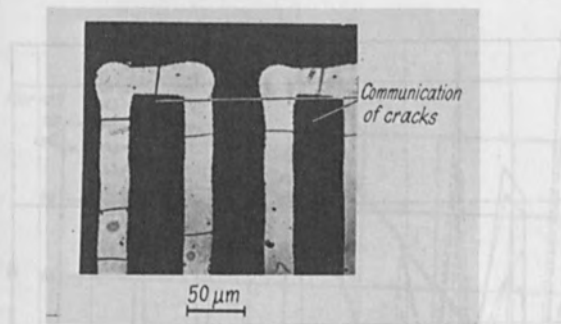


Fig. 7 Communication of cracks between adjacent tracks at an energy irradiation that is too high. (Ni-Cr film on hard glass substrate, $U_B = 20$ kv, transmitted-light exposure).



Fig. 8 Communication of a crack between adjacent tracks after thermal shock load. (Ni-Cr film on hard glass substrate, transmitted-light exposure).

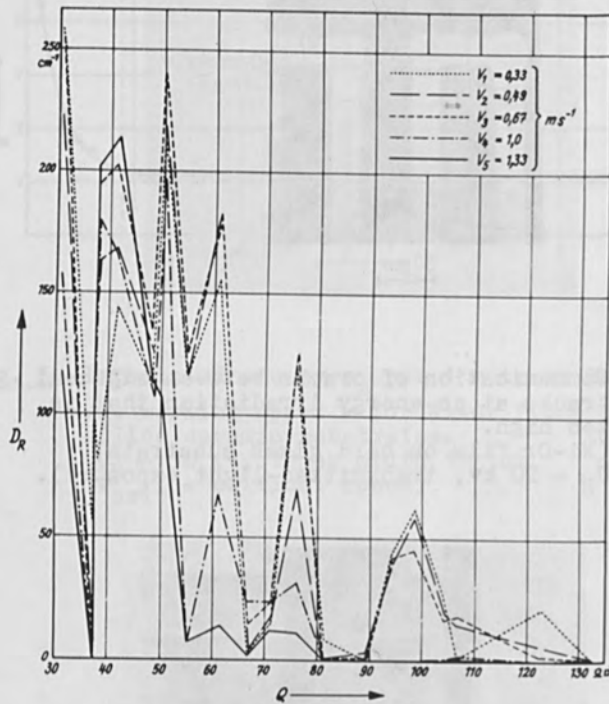


Fig. 9 Crack density D_R vs. Sheet resistivity ρ of Ni-Cr films on hard glass substrates for various working speeds v . ($U_D = 20$ kv, track width $25 \mu m$, Rasotherm glass).

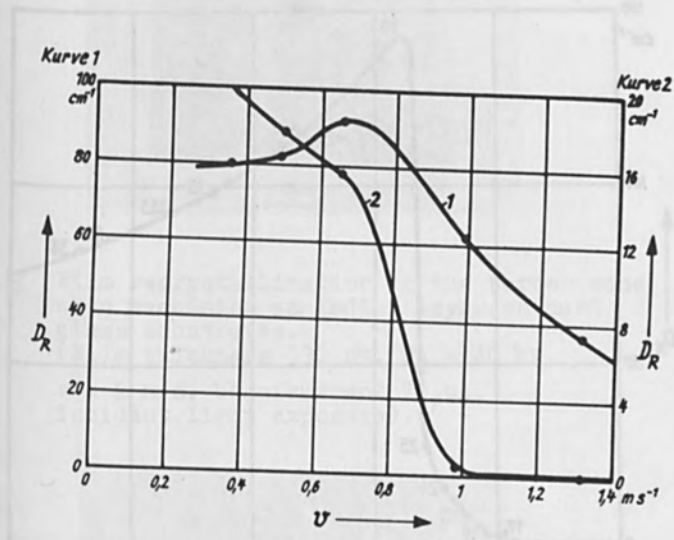


Fig. 10 Crack density D_R vs. working speed v when machining Ni-Cr films on hard glass substrates.

(Curve 1: Mean value with a sheet resistivity of 30 to 130 $\Omega \square^{-1}$;

Curve 2: Mean value with a sheet resistivity of 80 to 130 $\Omega \square^{-1}$;

$U_B = 20$ kv, track width 25 μ m).

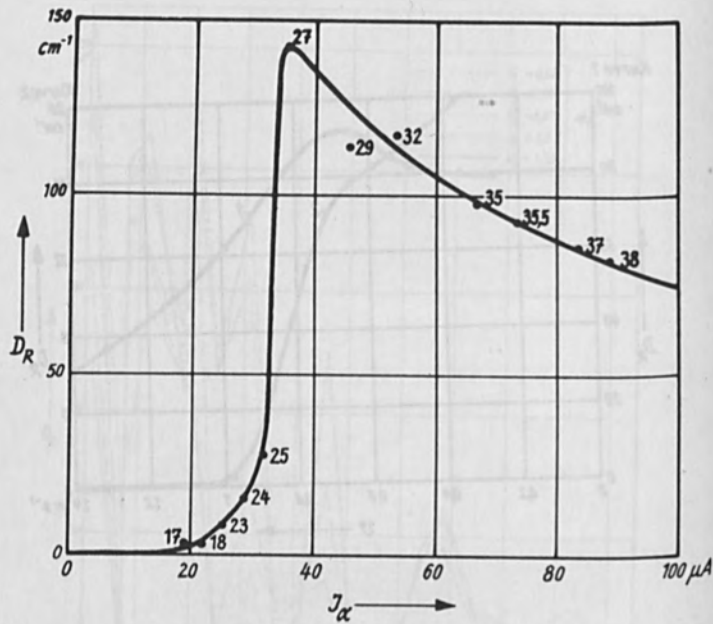


Fig. 11 Crack density D_R vs. beam current I_α when machining $60 \Omega \square^{-1}$ Ni-Cr films on hard glass substrates. ($U_B = 20$ kv, working speed $v = 0.35$ m/s; numerical values at the curve: track width in μm).

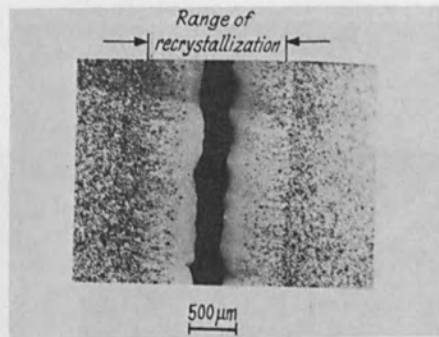


Fig. 12 Film recrystallization in the border zone when machining an indium layer on hard glass substrates.
 (Film thickness 530 nm, $U_B = 40$ kv, $v = 2$ m/s, beam current $70 \mu\text{A}$, incident light exposure).

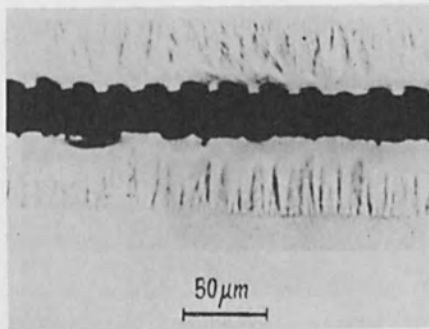


Fig. 13 Warping of the film at the edge when machining a thick indium layer on hard glass substrates.
 (Film thickness $1 \mu\text{m}$, $U_B = 40$ kv, $v = 2$ m/s, beam current $150 \mu\text{A}$, incident light exposure).

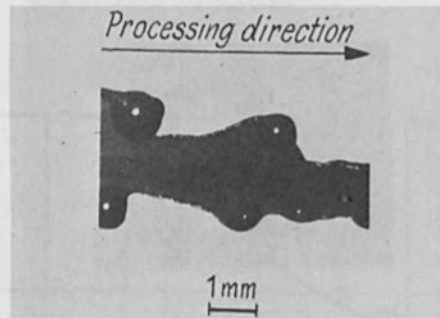


Fig. 14 Track widening combined with the formation of larger droplets along the track edges during thick-film machining. (Film thickness $2.3\mu\text{m}$, $U_B = 40\text{ kv}$, $v = 2\text{ m/s}$, beam current $150\mu\text{A}$, incident light exposure).

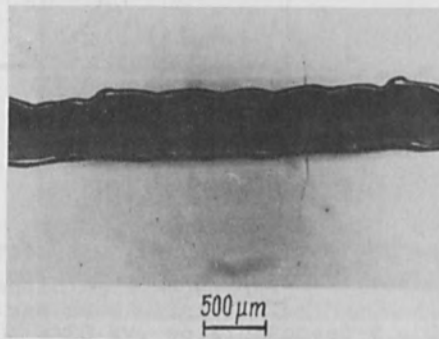


Fig. 15 Satisfactory track in a tantalum layer on hard glass substrates. ($U_B = 40\text{ kv}$, beam current $150\mu\text{A}$, $v = 2\text{ m/s}$, film thickness 210 nm , incident light exposure).

ELECTRON BEAM MACHINING -
THE PROCESS AND ITS APPLICATIONS

Dietrich v. Dolanek
Alfred Arellis

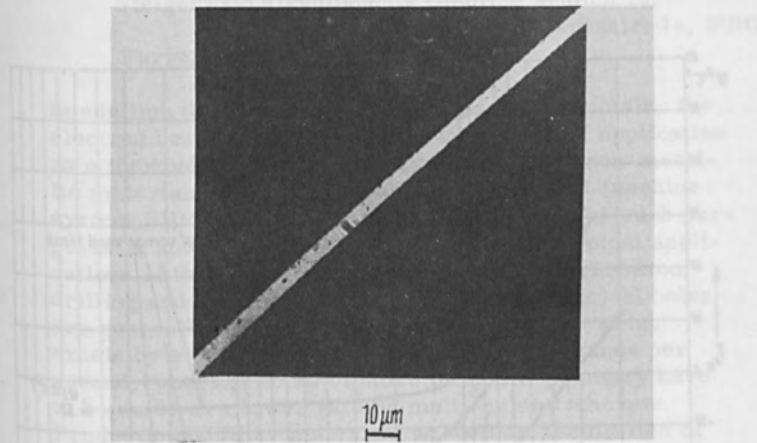


Fig. 16 Narrow track in a Ni-Cr film on hard glass substrate without interfering edge effects. ($U_B = 20$ kv, beam current $20 \mu A$, $v = 1.5$ m/s, film thickness approx. 20 nm, transmitted-light exposure).

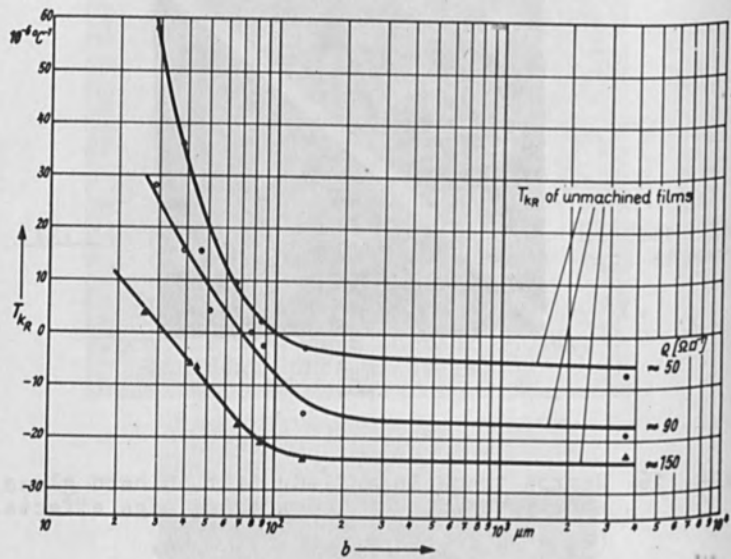


Fig. 17 Temperature coefficient TC of a resistive track vs. track width b after electron beam machining (track width $25 \mu\text{m}$).

ELECTRON BEAM MACHINING -
THE PROCESS AND ITS APPLICATIONS

Dietrich v. Dobeneck
Alfred Parrella
Steigerwald Strahltechnik GmbH, 8 Munich 70,
Haderunstr. 1a, FRG
Farrel Company, Ansonia, Conn.

In addition to its use for melting and welding metals, the electron beam has conquered further fields of application as a thermal tool for machining metallic and non-metallic materials. The numerically controlled EB-machine system EBM 10/4 which has been developed for such purposes is shortly described. Principles and typical applications of the various processes, such as perforation, drilling and engraving, are explained. Cylindrical holes are generally made by single-pulse technique which excels by a perforation rate up to some thousands per second, whereas holes of more intricate geometry have to be made at a lower rate by multi-pulse technique. Production of filter materials as well as perforation of jet engine parts for cooling purposes are typical examples. On the field of non-metallic materials, the production of "breathing" plastics for shoes and upholstery is of growing interest. Other EB processes which are still under development are dealt with in brief. Development and process engineers will take advantage from this progress for economically and technically improving their products.

The electron beam is a versatile thermal tool, although up to now only electron beam welding found its way into industrial applications. It is estimated that about 1000 electron beam welding machines are installed in the United States. But for other applications than welding there was only equipment with limited capabilities for the study of processes by electron bombardment. However, the results hardly found its way to production.

Let us have a short review of the various fields of electron beam processes. They may schematically be presented by figure 1. By using low power densities, irradiation of monomeric paint systems induces chemical processes such as polymerization within fractions

of a second. Besides beam curing the electro-resist-technique for producing integrated circuits with high resolution may be mentioned.

By focussing the beam to a small spot and increasing power density it is possible to perforate plastic materials as used as foils for filter purposes. One of the most important applications is the perforation of synthetic leather in order to make it permeable for transpiration.

Based on electron bombardment a steel hardening technique has been developed which results in excellent hardness within defined areas. With power densities in the range of $10^5 - 10^6$ Watt/cm² practically all metals can be melted. From this fact vacuum melting of metals and alloys, fusion treatment of work pieces and the wide field of electron beam welding derive.

If the energy input within a small volume is high enough to evaporate the material it is possible to perforate, drill, and engrave even the hardest materials at high speed. Maximum power densities (10^9 Watt/cm²) are required by sublimation processes.

The basic design of an electron beam drilling machine

For dealing with the different electron beam machining processes and their applications I should like to give a short description of the basic design of an electron beam drilling machine, as incorporated in the systems produced by Steigerwald Strahltechnik.

Similar to electron beam welding machines the beam is generated by a triode; a heated cathode emits electrons thus forming a space-charge cloud. By means of a voltage between 100 and 150 kV between cathode and anode high velocity is imparted to the electrons. The bias electrode, negatively charged relative to the cathode, allows the beam current to be switched on and off thus forming the pulses required for all drilling operations. Also the intensity of the beam is controlled by the bias electrode.

An electro-magnetic lens focusses the divergent electron beam to a power density at least two orders of magnitude higher than used for welding applications. By means of magnetic coils the beam can be deflected in any desired direction.

In order to avoid dispersion of the beam by collision of the electrons with gas molecules, the whole system of beam generator and working

chamber is evacuated, the acceleration space to a pressure better than 10^{-4} mm Hg and the working chamber to about 10^{-2} mm Hg.

This general principle has been adapted by Steigerwald Strahltechnik for an electron beam equipment, especially developed for machining processes. The machine type EBM 10/4 was designed as a versatile equipment for experimental work with the possibility of a small batch production (figure 2). Using the experience gained with this equipment, special production machines were built for sheet metal perforation and for the perforation of massive bodies.

The distinguishing properties of this machine system are the high stability of the electrical parameters as well as their controllability by a computer. The average beam power is 1 kW, stabilized to 10^{-4} , however, an overload up to 15 kW within a single pulse can be obtained, still being stabilized to 2×10^{-3} . This is necessary as the focal length depends on the speed of the electrons. The pulse width can be varied continuously between 10 μ sec and 20 msec. The pulse frequency is up to 10 kHz.

The machine can be controlled manually as well as by a digital computer. As machining operations with an electron beam are extremely fast, a special computer control was incorporated in the equipment.

Numeric control

The specific behaviour of an electron beam, which is a beam of charged particles with very low mass but very high velocity, offers ideal conditions for the application of numeric control. The low-inertia beam can simply be controlled by electro-magnetic fields, thus giving the possibility to economically adapt this extremely fast process to intricate machining geometries. A simultaneous control of the beam and of the work piece movement is required.

The on-line computer control is applied to the work piece movement, to the beam deflection and to the beam focus. This combination allows three-dimensional movement of the focal point in combination with a defined operating speed on the work piece. Furthermore, the computer controls the beam current as a function of work piece position and of time and also triggers the energy pulses. The advantage of this system is that the actual physical positions and electron beam parameters are continuously recorded in the computer and compared with the required positions and parameters which have previously been stored in the computer memory.

The error signal is then used to correct any deviations. To make this principal more obvious, its application to high speed perforation shall be explained.

The work piece is moved continuously under the beam, the position being recorded to the computer. If the position of a hole is reached, the computer will trigger the electron beam pulse. During the pulse width the beam follows the motion of the work piece in order to impact on the same spot.

So far, the main properties of an electron beam drilling machine have been described.

The electron beam as a thermal tool

And now, please, allow me some words on the mutual reaction of electron beam and material:

If electrons collide with solid material at a certain speed, their kinetic energy will be immediately translated into thermal energy. What happens within the workpiece after this initial effect, depends on the one hand on the electron beam parameters, such as total power, power density, duration of impact etc. and on the other hand on the thermal properties of the target, such as heat capacity, level of melting and vaporizing points, heat conductivity, heat of fusion and vaporization etc. The material can be heated, melted or vaporized.

For removing material by electron-beam machining, there are two different mechanisms. Either the material is evaporated or it is only melted and the liquid phase is taken away by additional forces such as centrifugal forces. In general, a combination of fusion and evaporation is used in such a way that the vapor pressure is used as additional force to eject the liquid material. Similarly to electron beam welding, there is also a capillary and a cylindrical fusion zone, using a pulsed beam. Because of the high power density in such a beam, the vapor pressure in the capillary increases so much that the material is ejected in a sudden burst. To save energy and thus optimise the economy of the process, the minimum evaporation rate is aimed at. Roughly 75 per cent of the energy of impulse is necessary to melt the volume to be removed. The remaining 25 per cent of the energy are used to evaporate about 5 per cent of the volume. The pulse interval and thus the time of impact of the beam on the workpiece is between 10 μ sec and 10 msec. The main task of the process control is to chose suitable beam parameters which

allow the shape of the molten volume to be controlled as well as the position and maximum temperature and thereby the vapor source so that the liquid material is ejected completely and rapidly. This is necessary with respect to the thickness of the heat-influenced zone forming the wall of the bore hole. The main control parameters for shaping the hole are the pulse width for the depth of the hole, the beam current for the diameter of the hole and the power distribution within the beam as well as the position of the focus with respect to the workpiece. These parameters can be combined in many ways and each can be varied with respect to time. The resulting range of possible hole shapes is wide.

If it is not possible to achieve the desired size and shape of the hole with a single pulse (figure 3), a multi-pulse drilling technique is applied (figure 4). With pulse frequencies between 50 and 1000 cycles per second, the beam is deflected or the focus varied according to the intended operation. To obtain the required machined shape, sequences of some hundred to some thousand of pulses are necessary. Reproducibility of the machining operations is ensured by a suitable computer control.

Sublimation is based on a quite different mechanism of material removal. By increasing the power density, a direct transition of the solid into the gaseous phase is achieved. In order to avoid formation of a molten pool due to the effect of heat conductivity, extremely short impact times are advantageous. This can be achieved by high-frequency pulsing of the beam or by a fast relative movement between workpiece and beam.

If the efficiencies of the single-pulse-drilling (perforation), multi-pulse drilling and sublimation are compared it becomes obvious that the removal rate of volume per unit of time has the ratio of 1000 : 10 : 1. This result, however, has its reason partly in the physics of the removing process and partly in the equipment.

The present state of the art of electron beam machining (EBM) allows removal rates of up to $40 \text{ mm}^3/\text{sec}$ with the single-pulse technique. It is evident that this process is some orders of magnitude faster than electro-discharge machining (EDM), electro-chemical machining (ECM) or laser beam machining (LBM). The reproducibility of a result and the achievable tolerances are within $\pm 5\%$ of the nominal value and the surface roughness is about $5 \mu\text{m}$, i.e. the quality is similar to EDM and ECM and much better than LBM. These values represent today's performance; further impro-

vements can be expected.

Some industrial applications

Owing to different specific capabilities electron beam machining made several approaches to industrial application.

1. High speed perforation
2. Perforation of any kinds of materials
3. Perforation of small diameter holes in thick material
4. Perforation of tapered holes
5. Perforation of inclined holes
6. Drilling of non-circular holes
7. Engraving of metal
8. Engraving of ceramic
9. Engraving of vapor-deposited layers

Practical applications generally require more than one of the above mentioned techniques.

1. High speed perforation

The actual capability of electron beam perforation is shown in figure 5. The range of possible holes in common materials is between 25 μm diameter in a 20 μm thick material and up to 1 mm hole diameter in a 5 mm thick material. This means that the electron beam operates in a field which is difficult for mechanical drilling or punching, but which is specific for electrochemical and spark-erosion machining.

Figure 6 shows the perforation rate depending on material thickness and hole diameter. However, this high perforation rate can only be realised if it is possible to move the workpiece under the beam with sufficiently high speed, or if the distance between one hole and the other is sufficiently small. The drilling operation itself is fast enough that it is not necessary to stop the piece during the time of impulse. If the full perforation speed is used the correct position of each hole on the piece can only be achieved with the necessary precision by using an adequate computer control. The hole pattern has to be programmed either according to a homogeneous grid or according to any required pattern.

A typical hole produced with an electron beam is round (figure 7) with a trumpet shaped entrance (figure 3); holes with an elliptical

or longitudinal cross section can also be produced (figure 8).

Typical examples for a varying hole density are cooling bores on jet engine skirts or cover bands or on suction screens in order to remove boundary layers on aircraft wings. The hole density is adapted to the continuously changing requirements. As millions of holes for each of these applications are needed, sometimes also with changing diameters, only a high speed perforation allows the economical introduction of these techniques.

2. Perforation of any kinds of materials

As already mentioned above, the electron beam perforation is independent of materials behaviour, such as mechanical hardness or electrical conductivity. Two extremely different materials may be used as example: the perforation of heat resistant super-alloys and the perforation of plastic material. Figure 9 shows a spinning head used for the production of glass fibres which is up to now drilled by electro-discharge machining. Today this can be done about hundred times faster with the electron beam. The hole diameters may vary from line to line. There are only electrical parameters which determine the diameter of the drilling tool "electron beam". According to a computer program this diameter can be changed as required.

Modern shoes are made out of plastic material applied on a textile substrate (figure 10). This artificial leather is not permeable for moisture and air and the wear comfort is poor. A breathing skin can be produced by fine perforation of the plastic surface (figure 11). Thus treated, the material can be used for shoes, for clothing and upholstery. To make this process economically interesting for production, a machine with the capacity for drilling 50000 holes per second was built.

3. Perforation of small diameter holes in thick material

The specific property of all electric machining operations is the possibility of drilling deep holes having relatively small diameters. Let us speak of a diameter to depth ratio of 1 : 10.

The trailing edge of turbine blades needs for cooling purposes a line of such deep holes (figure 12).

Screens and filters as used for example in centrifuges, very often undergo an important abrasive wear. By increasing the

material thickness - keeping hole diameter and transparency at the same value - the life of such filters can be improved (figure 13). The cost saving results mainly from the fact that in order to change a worn-out filter for a new one means stopping the complete production line which fact costs much more than the filter screen itself.

4. Perforation of tapered holes

There is the additional possibility of drilling holes with a certain taper in order to reduce the danger of filters and screens getting blocked by the sludge (figures 13 and 14). By increasing the number of holes per unit area, which means by increasing the transparency of the filter, more material can be put through the screens, thus improving the efficiency of the centrifuge. EB perforated filters made of corrosion resistant materials such as stainless steel, titanium or even molybdenum were used in the chemical industry.

5. Perforation of inclined holes

The angle, under which an electron beam hits the target can be anything between 20° and 90° against the surface. The application of electron-beam perforation to turbine blades (figure 15), combustion chamber rings (figure 16) mixer plates (figure 17) and other parts of gas turbines which are exposed to high temperature, is based on this capability. Cold air is pressed through the fine bores thus forming a lamellar gas film on the surface of the metallic parts which protects these parts against the high temperature of the combustion gases.

A more recent development for blade cooling is the so-called transpiration cooling which needs up to 30000 holes per blade. Such a development and its economic realization in production is only possible with a high-speed drilling tool such as the electron beam.

6. Drilling of non-circular holes

If it is not possible to perform the required shape or size of a hole with a single pulse, then a multi-pulse technique is applied. According to a suitable computer program the electron beam is deflected along the predetermined contours. The electron beam being pulsed at a high frequency (figure 18). This multi-pulse technique includes cutting and milling. Only vertical walls can

be performed.

7. Engraving of metal

The high precision and speed by which an electron beam can be controlled using only electric parameters open a new field of development which was up to now reserved for chemical etching and mechanical engraving, namely roto-gravure (figure 19). Small grooves on the surface of the roto-gravure cylinder are filled with ink. The volume of these grooves being varied in diameter and depth according to the picture to be printed. Small volume means light colour, big volume means dark colour. Besides several advantages in the printing area, this extremely fast engraving method incorporates the future possibility of remote control of production over long distances by transmitting specific instructions in digitally encoded form. Very high quality and virtually instantaneous information transfer is possible. An exciting idea if you think on the poor quality of today's newspaper pictures.

The roto-gravure is still under development but it shows that the rapid reproduction of a picture by means of an electron beam is not only restricted to the television tube. Three-dimensional control of the machining operation with extremely smooth surfaces and very narrow tolerances is a precondition for this application.

8. Engraving of ceramic

The electronic industry, and especially the computer technique, is moving towards ever increasing frequencies. More compact methods of construction and manufacturing techniques which permit finer structures are required. Engraving and drilling of green ceramic material with an electron beam created as a new product the multi-layer ceramic module (figure 20). Several of such thin engraved plates are put together, the fine channels being filled with metal paste and then the module is heated. The result is a three-dimensional system of conductors.

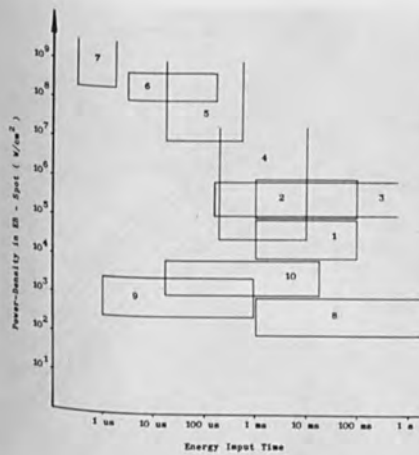
9. Engraving of vapor-deposited layers

Similar to the above example, the electron beam is also controlled according to a computer program so that the desired geometries were achieved when engraving hybrid circuits (figure 21). Resistors were cut out of a vapor-deposited metal layer, e.g. tantalum on a glass substrate. During the machining operation

the resistors can be measured and calibrated. The high engraving speed of more than 5 metres/sec results in an economic manufacturing technique for large quantities. The design of the circuits can easily be changed by using another computer program. This is of interest for the production of single pieces or small batches in the field of research and development.

To summarize, it may be stated that electron-beam machining found its way to industrial application in cases where, due to the high operating speed or to the better properties of the piece, economical advantages could be achieved. By using the capabilities of electron beam machining, new processes and new products emerged which could - at least economically - not be realized by conventional methods of machining.

Electron beam machining is still in the stage of extensive expansion. It is now the important task of development and process engineers to use the extraordinary capabilities of electron beam machining for designing and manufacturing their products.



- | Metals | Plastics |
|-------------------------|-----------------------|
| 1 Hardening | 8 Polymerization |
| 2 Fusion-Transformation | 9 Electro-Resist |
| 3 Joining | 10 Plasma-Perforation |
| 4 Perforation | |
| 5 Drilling/Milling | |
| 6 Engraving | |
| 7 Sublimation | |

Fig. 1.



Fig. 3



Fig. 4



Fig. 2

Fig. 1 Application range of electron beams: power density and time of impact are typical for the various techniques.

Fig. 2 The electron beam equipment EBM 10/4 produced by Steigerwald Strahltechnik is suitable for the study of all machining processes.

Fig. 3 Typical trumpet shaped hole as performed with a single pulse in 0,4 mm thick Nimonic 90. As the pulse width is only about 50 μ sec there is nearly no heat influence on the matrix.

Fig. 4 Cross section showing a cylindrical hole as drilled with multipulse technique. Inconel 600, 1,5 mm thick, drilling time 20 sec. A recast layer can be observed.

EB METAL PERFORATION

Diagram 1

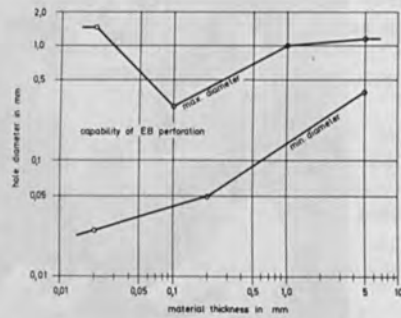


Fig. 5

EB METAL PERFORATION

Diagram 2

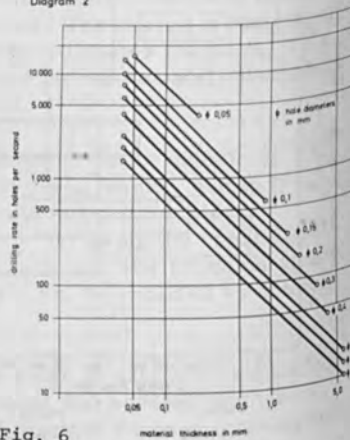


Fig. 6

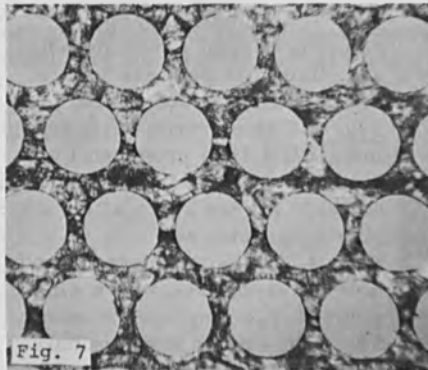


Fig. 7

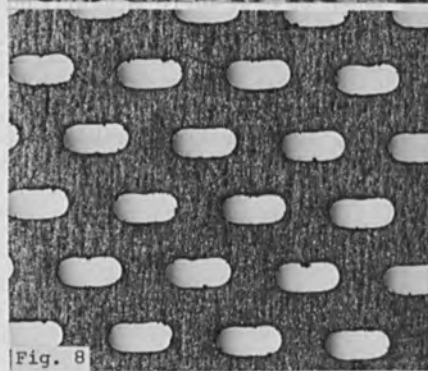


Fig. 8

Fig. 5 The capability range of EB perforation valid for steel and nickel alloys.
 Fig. 6 EB-Perforation rate of steel and nickel alloys.
 Fig. 7 Electron beam perforated screen: stainless steel, 0,1 mm thick, hole dia 0,2 mm, drilling speed 3000 holes per second. Such screens may be used for filter purposes or for screen printing.
 Fig. 8 Longitudinal holes drilled in stainless steel 0,5 mm thick, length of slot 0,6 mm. This screen is used as a basket within a nuclear reactor holding small uranium balls.

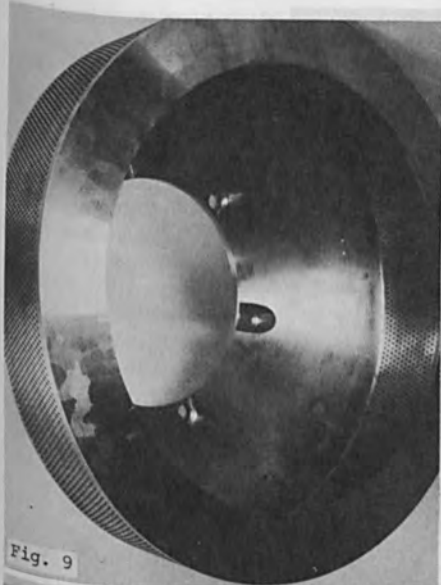


Fig. 9



Fig. 10

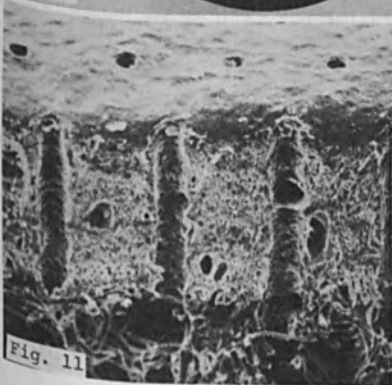


Fig. 11

Fig. 9 Spinning head for the production of glass fibres. Dia 200 mm, 3 mm thick, 6000 holes of 0,8 mm dia drilling speed 20 holes/sec.

Fig. 10 Shoe upper: textile substrate with PVC lining, hf-moulded.

Fig. 11 Cross section through a shoe upper showing the perforation which allows the material to breathe. Dia of capillaries 120 μ m.

Fig. 12 Cooling holes in the trailing edge of a turbine blade. Hole depth 5 mm, dia 0,4 mm.



Fig. 12



Fig. 13



Fig. 14

Fig. 13 Cross section through a tapered hole as used in filter screens for salt centrifuges. Stainless steel 1 mm thick, 130 μ m hole diameter, 400 holes/sec.

Fig. 14 Cross section through a tapered hole as used for separating cellulose fibres for paper production. Stainless steel 3 mm thick, 1 mm hole diameter, 20 holes/sec.



Fig. 15



Fig. 16

Fig. 15 Cooling holes in the leading edge of a turbine blade, drilled at various angles.

Fig. 16 Cross section through a ring which forms part of a combustion chamber. Cooling holes 2,5 mm deep, 0,4 mm dia, 50 holes/sec.

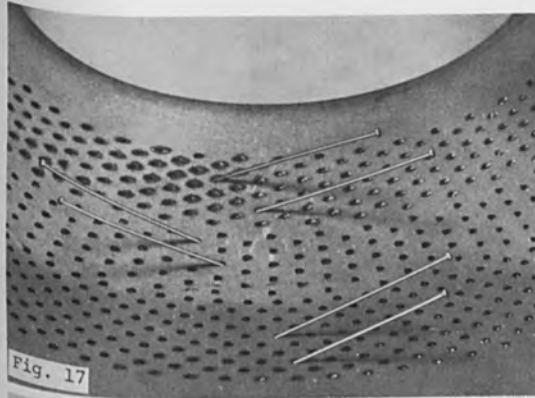


Fig. 17



Fig. 18

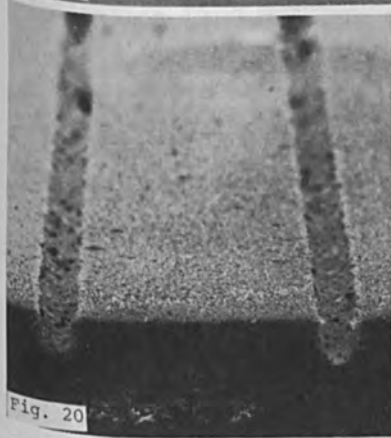


Fig. 20

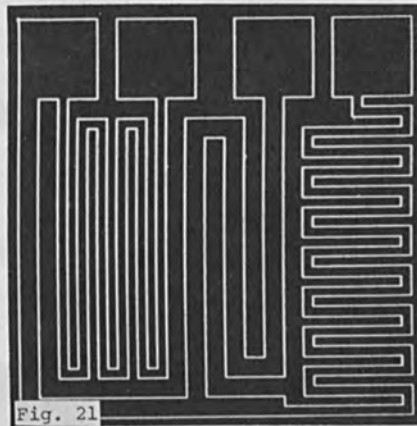


Fig. 21

Figure 17 Mixer plate of a small engine drilled at 2 opposite angles.

Figure 18 Multi-pulse drilling of non-circular holes

Figure 20 Green ceramic plate with engraved channels.
Width 100 μm , speed up to 10 m/sec.

Figure 21 Hybrid circuit engraved with 40 μm wide traces. Speed more than 5 m/sec.

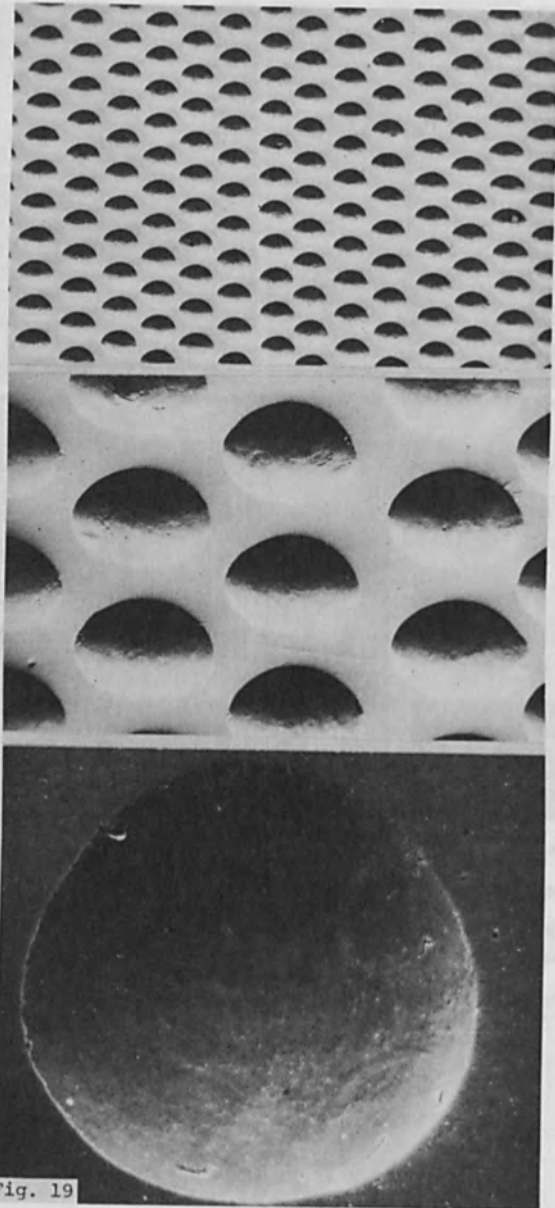


Figure 19
Roto-gravure: the surface of a copper cylinder is engraved with grooves of 70 - 120 μm dia and 5 - 40 μm depth depending on the colour tones. Note the smooth surface.

Fig. 19

ON THE ELECTRON-METAL VAPOUR INTERACTION IN HIGH-POWER EVAPORATORS

S. Schiller, and G. Jäsch

Manfred von Ardenne Research Institute
8051 Dresden, GDR

1. Introduction

The possibility to achieve very high evaporation rates is one of the main reasons for the ever increasing utilization of EB evaporation. Design and function of high-power electron guns were described by us on occasion of the 5th Conference [1]. EB evaporation coating of strip steel with aluminium showed to be one of the most essential fields of application [2, 3, 4]. But with the very high evaporation rates required for this purpose, collisions between vapour particles on their way from the crucible to the strip steel surface cannot be neglected any more. In addition, there are interactions between developing vapour cloud and beam. The thus obtained power losses have to be taken into consideration already during evaporator system dimensioning and beam parameter selection.

2. Test Set-up

An axial gun of up to 250 kw serves for electron beam generation and guidance [5]. Injection into the evaporation chamber is horizontally and magnetic deflecting and beam turning systems are used for directing the beam onto the evaporant. Fig. 1 gives a schematic of the electron beam evaporator assembly. For surface admission of the evaporant the beam is dynamically deflected in two coordinates. The corresponding magnetic deflecting system is directly attached to the electron gun. In this way the layers deposited on the system can be kept small so that dynamic deflection is not impaired by eddy currents. Aluminium serves as evaporant and the internal crucible dimensions are about 500 mm x 500 mm.

Here a power of 250 kw is sufficient to evaporate approximately 50 kg aluminium per hour. The strip steel to be coated is passed over the vapour-emitting surface of the evaporant at a distance of some 100 millimetres, and at a speed of 1 to 3 metres per second.

3. Vapour Particle Interaction and its Effect on Vapour Stream Propagation

Without considering the interaction of vapour particles, film thickness distribution on the substrate can be predicted from the geometric configuration and productivity of the vapour source alone. Fig. 2 gives the film thickness distribution on a plane substrate when evaporation takes place from a point-like vapour source having a Lambertian characteristic; i.e., with a deposition rate α at the target point on the plane substrate that can be equated by $\alpha = \alpha_0 \cos^3 \varphi$. Here φ is the angle between the straight line from target point to vapour source and the crucible normal whilst α_0 denotes the deposition rate for $\varphi = 0$. From this, it can be seen that the film thickness at the edge of a strip steel with 400 mm width has dropped to 55% of maximum film thickness. In general, however, it is especially the unevenness of the vapour-emitting surface which excludes a true Lambertian characteristic so that the actual drop in film thickness will still be greater. For comparison, Fig. 2 further contains the film thickness distribution at $\alpha = \alpha_0 \cos^4 \varphi$.

Neglecting vapour particle interaction, a rather uniform film thickness distribution may theoretically be obtained over a great strip width by using several evaporators with matched productivity. The result of such a computation is shown in Fig. 3.

To achieve high evaporation rates, the evaporant must have a surface temperature of 1,600 °K to 1,700 °K. This corresponds to a saturated vapour pressure of 0.2 to 0.8 torr above the evaporant. In practice, however, such a state of equilibrium cannot be attained because the whole environment of the vapour-emitting surface has to be considered as vapour sink. The actual density of the vapour cloud may then be determined by measuring the evaporation rates at various spatial points. Fig. 4 gives an assessment of such a vapour cloud density distribution obtained with an electron beam irradiation that has been kept constant with respect to time and location. The beam power of 250 kw was distributed over a surface of 120 cm².

The free path of particles in gases depends on the pressure and can be expressed by the known relation: -

$$\lambda = \frac{c}{p} \quad (1)$$

with c being a constant depending on the type of gas; i.e., $5 \cdot 10^{-2}$ torr·mm for air. When equating the mean free

path between vapour particle collisions - or between particles of vapour and residual gas - it is necessary to consider (a) evaporator-substrate preferred direction, (b) initial velocity and (c) atomic radius of the vapour atoms. As per Eq. (1) a coarse assessment of the interesting mean free path between vapour particles should be based on a value of $c \approx 5 \cdot 10^{-2}$.

Because of the high deposition rates of 10 to 30 $\mu\text{m/s}$, a vapour pressure in the order of 10^{-1} torr is required in the vicinity of the strip to be coated [4]. With a pressure of 10^{-1} torr, the mean free path at the strip surface then amounts to $\lambda \approx 0.5$ mm. So the strip steel is in a dense vapour cloud; i.e., evaporation takes place in the so-called virtual source [3, 4]. Customary considerations of evaporation technique - where the mean free path of vapour particles in the vicinity of the substrate is at least comparable with the distance between substrate and evaporator - must therefore be abandoned here and film thickness distribution is determined by the site-dependent productivity distribution of the vapour-emitting surface only indirectly. This is why prediction of film thickness distribution from vapour source distribution and productivity is not possible any more.

To investigate the effect of the vapour cloud on film thickness distribution, dynamic sinusoidal deflection is used for sweeping the beam over a distance of 200 mm in strip transfer direction. With reference to film thickness distribution across the strip width, this mode simulates a point-like source. Fig. 5 gives the result of these measurements and clearly indicates that the film thickness at the edge has dropped to about 65 % of its maximum value. Furthermore, Fig. 5 contains the film thickness pattern obtained through an analogous sinusoidal deflection of the beam perpendicular to strip transfer direction. At a first glance it seems that there is no pronounced difference of film thickness distribution at such widely differing electron beam deflections. As per Figs. 2 and 3 (without interaction), on the other hand, noticeable differences should be expected. Owing to vapour particle interaction, however, film thickness distribution remains practically unaffected by source distribution and productivity. In addition, it can be shown that beam deflection perpendicular to strip transfer direction does not result in such a uniform film thickness distribution as should be expected theoretically when assuming a Lambertian characteristic without interaction.

4. The Vapour Cloud and its Effect on Electron Beam Propagation

From the foregoing it is evident that, on its way to the evaporant, the beam has to pass through ranges of high vapour pressure. Even at a high accelerating voltage of $U_B = 30$ kv, the energy losses caused by collisions in the vapour cloud cannot be neglected any more. Theoretically it is known that energy losses at otherwise constant conditions are proportional to $1/U_B^2$. Thus, high accelerating voltages will be of advantage to keep the losses on a low level. Fig. 6 gives the results of energy loss measurements obtained with various accelerating voltages U_B versus pressure p . For accelerating voltages of $U_B \geq 50$ kv, these losses have to be taken into account only with pressure levels higher than 1 torr. At 30 kv, however, noticeable losses will occur even in a range of 10^{-1} to 1 torr. These measurements resulted in the following relationship: -

$$\frac{\Delta E}{E} \sim \frac{1}{U_B^n} \quad \text{with } 1 \leq n \leq 2 \quad (2)$$

Therefore, it was not possible to verify the known relationship $\Delta E/E \sim 1/U_B^2$ between energy loss and accelerating voltage.

But higher accelerating voltages, used to reduce the energy losses in the vapour cloud, are practically limited by the increasing expenses for high-voltage generation and the required degree of X-ray shielding. With accelerating voltages up to 35 kv, the walls of vacuum chambers made of sheet steel up to 15 mm are still sufficient for adequate X-ray shielding [6].

Apart from pressure and accelerating voltage it is the path within the vapour source which substantially affects the scattering loss. In close approximation this yields: -

$$\frac{\Delta E}{E} = f\left(\int \psi(p) ds\right) \quad (3)$$

where

p = pressure of vapour or residual gas
 s = beam path

Fig. 7 gives the energy losses of electrons with $U_B = 100$ kv at various path lengths versus pressure. Theoretically energy loss depends in a simple matter from the product pressure and path length. A comparison with Fig. 6 and 7 yields however this ordinary relationship is not valid.

In accordance with Eq. (3), electron beam injection into the vapour cloud has to be optimized when dimensioning the evaporator system.

Especially at very high power levels there are interactions not only between vapour atoms but also with the beam-generated plasma. It is known that ionization probability reduces with increasing accelerating voltage. Thus, rather high accelerating voltages will be favourable also for this reason. With a power of 250 kw, current densities of less than 1 A/cm^2 , and accelerating voltages of 30kv it has been found that, due to narrow beam formation, the plasma generated in the vapour cloud still has a focussing action on beam guidance. Obstructions of dynamic beam deflection caused by the plasma have not been observed. But it is to be assumed that the plasma and its oscillations - that may still be enhanced by the beam - substantially contribute to the scattering losses as a whole.

With given geometry of the evaporator system it is the accelerating voltage which determines the maximum permissible vapour pressure and thus the maximum admissible deposition rate. When using accelerating voltages of approximately 10 kv, it has been found that the specific energy expended - i.e., electron beam energy required for evaporating one mass unit - noticeably increases with rising power [7]. In this way a considerable portion of energy is wasted by scattering events in both vapour cloud and plasma. Fig. 8 gives the specific energy consumption measured at $U_B = 30 \text{ kv}$ versus irradiated beam power. The drop in specific energy consumption obtained with increasing power can first be explained by the fact that the contribution of heat radiation to the portion of evaporating power still decreases. It is estimated that, at a power of 250 kw, the scattering losses in the vapour source are in the order of 10 to 20 % of irradiated power. On its way to the evaporant, the beam must pass through vapour cloud pressure ranges of up to 1 torr. According to Fig. 8 it can be expected that, with the presented evaporation system, specific energy consumption will continue to drop up to a power of 300 kw.

5. Conclusions

It has been explained to what degree film thickness distribution can be affected by collisions between vapour atoms when evaporation takes place in a range of 10^{-1} to 1 torr. By selecting a suitable accelerating voltage of approximately 30 kv the scattering losses may be kept

small even at an overall power of 250 kw; permitting profitable industrial application of guns with high electron beam power and rather high power densities.

References

- [1] S. Schiller, H. Förster, P. Lenk, G. Jäsch: High-Power Electron Guns for Evaporation (Axial Systems) Edited by Robert Bakish, Bakish Materials Corporation, Englewood, New Jersey
5th International Conference of Electron and Ion Beam Science and Technology 1972
- [2] W. Reichelt, W. Dietrich, A. Hauff: Das großtechnische Aufbringen von Schutzschichten auf Stahlbänder durch Bedampfen im Vakuum. *Metalloberfläche* 20 (1966) p. 474
- [3] H. R. Smith: Principles of Electron Beam Technology. Paper submitted to the 2nd Electron Beam Processing Seminar, June 1972, Frankfurt/M., published by Universal Technology Corporation, 1388 Research Park Drive Dayton, Ohio 45432
- [4] S. Schiller, P. Lenk, H. Förster, G. Jäsch, G. Kühn: Industrial Electron Beam Evaporation Coating of Strip Steel. Paper submitted to the 3rd Electron Beam Processing Seminar, March 1974, Stratford upon Avon
- [5] S. Schiller, U. Heisig, P. Lenk: Theory and Development of Electron Heat Sources. Paper submitted to the 2nd Electron Beam Processing Seminar, published as under [3]
- [6] S. Schiller, H. Förster, G. Jäsch: Zum Stand der Entwicklung der Elektronenstrahltechnologie in der DDR. *Elektrothermia*, Moscow 1974 (in print)
- [7] Catalogue of Messrs. Airco Temescal Corporation, p. 198

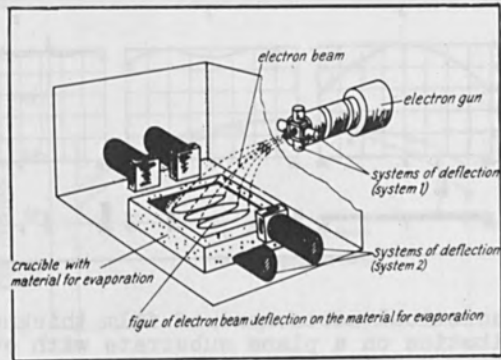


Fig. 1 Schematic design of evaporator system.

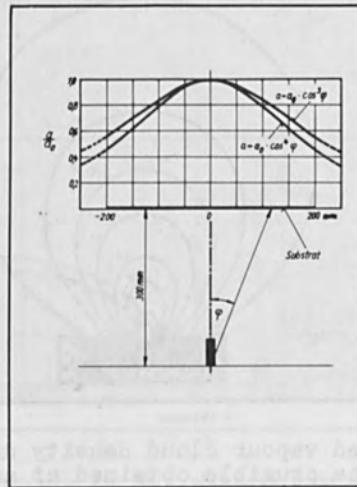


Fig. 2 Theoretical assessment of film thickness distribution on a plane substrate with evaporation from a point-like source having a Lambertian characteristic.

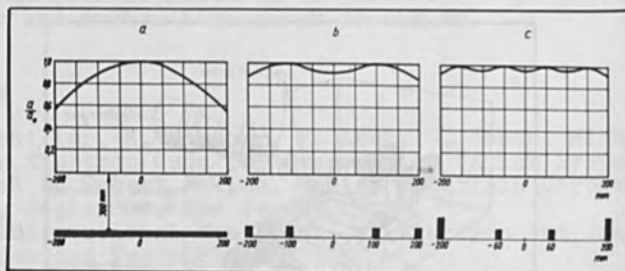


Fig. 3 Theoretical assessment of film thickness distribution on a plane substrate with evaporation from several point-like sources of various strength ($a = a_0 \cos^3 \varphi$).

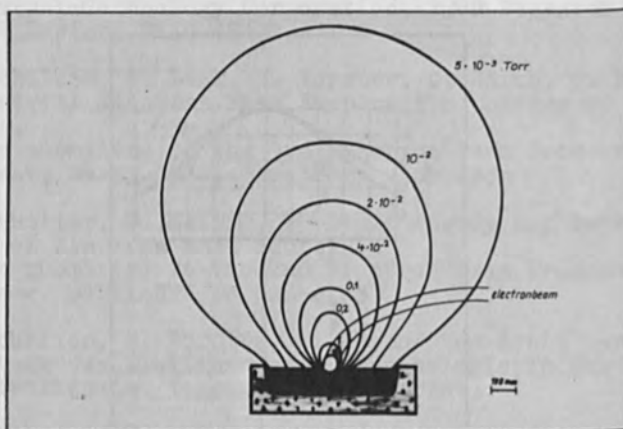


Fig. 4 Estimated vapour cloud density distribution above the crucible obtained at an irradiated power of 250 kw and a power density of 2 kw/cm^2 .

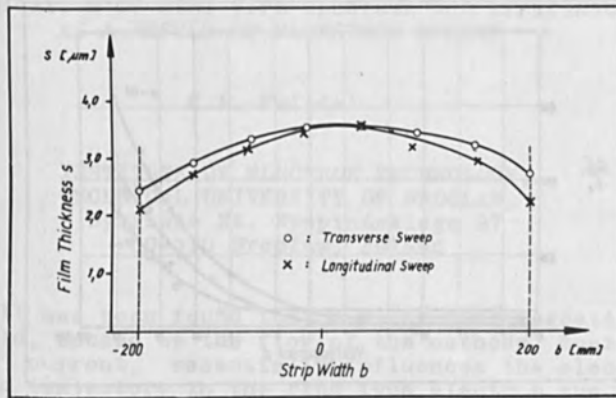


Fig. 5 Effect of vapour cloud on film thickness distribution over the strip width with the dynamic deflection turned off in one direction.

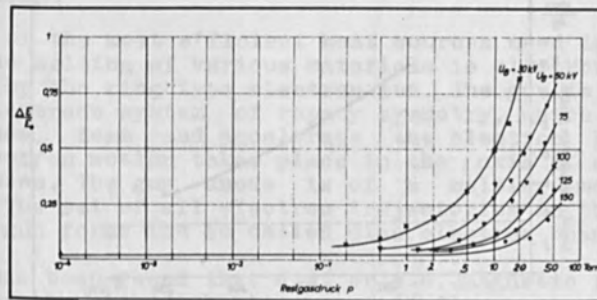


Fig. 6 Energy losses of the beam $\Delta E/E_0$ versus pressure p at various accelerating voltages U_B .
EB path length in residual gas: 10 mm.

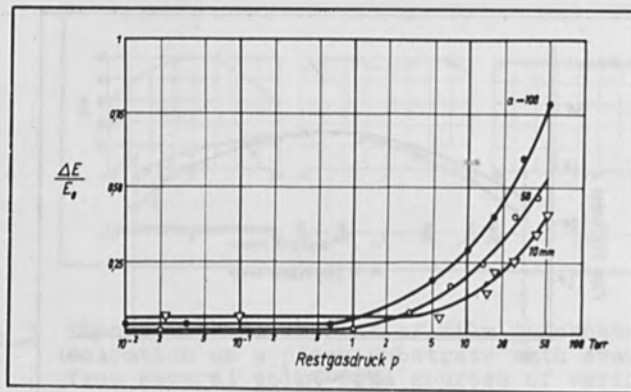


Fig. 7 Energy losses of the electron beam $\Delta E/E_0$ versus pressure p at various path lengths of the beam in residual gas ($U_B = 100$ kv).

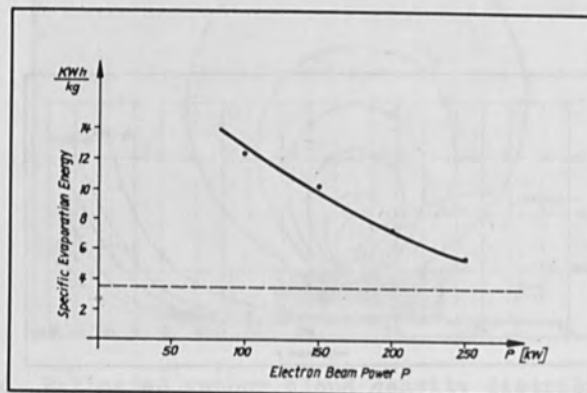


Fig. 8 Specific energy expended for evaporating one mass unit of aluminium versus irradiated beam power.

LIMITATION OF RING TYPE ELECTRON GUN EFFICIENCY
AS A RESULT OF MAGNETRON EFFECT

K.P. Friedel

INSTITUTE OF ELECTRON TECHNOLOGY,
TECHNICAL UNIVERSITY OF WROCLAW,
Wybrzeże St. Wyspiańskiego 27
50-370 Wrocław, Poland

It has been found that a.c. or d.c. magnetic field, caused by the flow of the cathode heating current, essentially influences the electron trajectory in the ring type electron gun.

The conditions under which the electron trajectories pass by the anode are determined, and limitation of the electron gun efficiency by the phenomenon called the magnetron effect is indicated. The compensation methods of this effect is shown and some recommendations for design are formulated.

INTRODUCTION

One of the most efficient heat sources used in floating zone melting of various materials is electron beam produced by the ring type electron gun. The gun is formed by an electrode system of rotary symmetry, which allows to produce, form and accelerate the electron beam in which electron motion takes place in the axis of symmetry direction. The gun anode is of a melting material /Fig.1/. The set of all electron trajectories in the ring electron gun forms the so called disc electron beam.

It has been found that d.c. or a.c. magnetic field, caused by the cathode heating current flow, essentially influences the electron trajectories in such a beam /magnetron effect/ causing the limitation of the ring electron gun efficiency [1].

ELECTRIC AND MAGNETIC FIELD IN THE RING TYPE ELECTRON GUN

Electric field is symmetrical as well towards the system axis $/z/$ as towards the plane $/z=0/$, in which the

cathode is situated. Near the symmetry plane, potential may be expressed in the form of a series developed after z:

$$\Phi(z, r) = \varphi_0(r) + \varphi_2(r) z^2 + \varphi_4(r) z^4 + \dots \quad /1/$$

In this formula φ_0 denotes potential distribution in the symmetry plane.

Magnetic induction distribution in the plane $z=0$ for $r < r_f$ is:

$$B_0(r) = \frac{\mu_0 i_h}{\pi r_f (1 - \rho^2)} E(\rho^2) \quad /2/$$

In this formula: r_f - cathode filament radius,

$$\rho = \frac{r}{r_f},$$

i_h - actual value of heating current,
 $E(\rho^2)$ - complete elliptic integral of the second kind.

ELECTRON TRAJECTORY EQUATIONS IN THE RING ELECTRON GUN

Disc electron beams are so complex objects that a mathematical description of their properties is impossible unless assume some simplifying presuppositions. So it has been found that:

- electric and magnetic fields are stationary or quasi-stationary,
- electrons are emitted by the equipotential cathode with zero initial velocities,
- electron trajectories are situated near the symmetry plane of the ring type electron gun,
- disc electron beam is treated as a beam of low permeance.

Electron motion in the ring type electron gun region is expressed by the following equations:

$$\left. \begin{aligned} \ddot{r} &= \frac{\partial Q}{\partial r} \\ \ddot{z} &= \frac{\partial Q}{\partial z} \\ \dot{\Theta} &= \frac{1}{r} \left(\frac{\eta}{2\pi} \Psi + c \right) \end{aligned} \right\} \quad /3/$$

where Ψ - magnetic induction flux through the radius r circle surface,

$$Q = \eta \Phi - \frac{1}{2r^2} \left(\frac{\eta}{2\pi} \Psi + c \right)^2,$$

C - integration constant.

For boundary conditions $r=r_f, \Psi=\Psi_f, \dot{\Theta}_f=0$:

$$c = - \frac{\eta}{2\pi} \Psi_f \quad /4/$$

In order to eliminate the time, the energetic equation is used:

$$\dot{r}^2 + \dot{z}^2 + r^2 \dot{\Theta}^2 = 2\eta \Phi \quad /5/$$

and we obtain

$$z'' + \frac{1}{2Q} \frac{\partial Q}{\partial r} z' - \frac{1}{2Q} \frac{\partial Q}{\partial z} = 0 \quad /6/$$

Because Q potential near the $z=0$ plane may be presented in the form of a series:

$$Q = Q_0 + Q_2 z^2 + Q_4 z^4 + \dots \quad /7/$$

then

$$\begin{aligned} \frac{\partial Q}{\partial r} &\approx Q'_0; \quad \frac{\partial Q}{\partial z} \approx 2zQ_2; \\ z'' + \frac{Q'_0}{2Q_0} z' - \frac{Q_2}{Q_0} z &= 0 \end{aligned} \quad /8/$$

This is the equation of electron trajectory projection onto the meridional plane. Commas denote differentiation after r. The equation of the electron trajectory projection onto the plane $z=0$ may be derived similarly, obtaining:

$$r' - \sqrt{\frac{Q}{\eta\Phi - Q}} \quad r = 0 \quad /9/$$

In this case comma denotes differentiation after Θ . For electrons moving in the $z=0$ plane this equation will assume the form of:

$$r' - \sqrt{\frac{Q_0}{\eta\psi_0 - Q_0}} \quad r = 0 \quad /10/$$

Depending on the conditions of the ring electron gun supply, the electron trajectory may be finished on the anode or on the cathode, the focusing electrode or the additional anode /Fig.2/. Values of the anode potential and of

the magnetic induction, at which the electron trajectories are tangent to the anode, are called critical values. Interdependence of these values, in the form of the so called critical parabola, is derived from the equation /10/, assuming that $r=0$ at $r=r_a$:

$$\varphi_{oc} = \frac{\eta}{8r_a^2 \pi^2} (\Psi_{oc} - \Psi_f)^2 \quad /11/$$

where φ_{oc}, Ψ_{oc} - critical values of anode potential and magnetic induction flux respectively,

$$\Psi_{oc} = 2\pi \int_0^{r_a} B_{oc} r dr,$$

$$\Psi_f = 2\pi \int_0^{r_f} B_{oc} r dr.$$

Taking into account the equation /2/ we finally obtain:

$$\varphi_{oc} = \frac{\mu_0^2 \eta^2 i_{hc}^2}{2\pi^2 \rho_a^2} K^2(\rho_a) \quad /12/$$

where i_{hc} - actual value of the heating current generating the magnetic field of B_{oc} induction,

$$\rho_a = \frac{a}{r_f},$$

$$K(\rho_a) = \int_{\rho_a}^1 \rho \frac{E(\rho^2)}{(1 - \rho^2)} d\rho. \quad /13/$$

The family of critical parabolas is shown in Fig.3.

In real ring type electron guns width of the disc electron beam /measured along z axis/ is not large as compared to the cathode radius, then the above considerations concern, in substance, all electron trajectories of the beam.

RING TYPE ELECTRON GUN EFFICIENCY

In the case of supplying the gun cathode with alternating current of amplitude \bar{I}_h , in moments when actual value of this current

$$i_h = \bar{I}_h \sin \omega t \quad /14/$$

is higher than critical value of i_{hc} , the electron trajec-

tory pass by the anode and in the circuit of the anode the current doesn't flow /Fig.4/.

The efficiency coefficient of the ring type electron gun related to this effect is equal to the ratio of the rms current flowing in the anode circuit to the value of direct current equal to peak current flowing in the anode circuit at the moment when $i_h=0$:

$$s = \frac{I_a}{I_{\max}} \quad /15/$$

In spite of periodical changes of the heating current the cathode temperature is stable and hence also emissive current and I_{\max} don't change. As follows from Fig.4:

$$I_a = \sqrt{\frac{2\omega_c t}{\pi}} I_{\max} \quad /16/$$

where, on the ground of equations /12/ and /14/:

$$\omega_c t = \arcsin \sqrt{\frac{2\pi^2 \rho_a^2 \varphi_a}{\mu_0^2 \eta \bar{I}_h^2 K^2(\rho_a)}} \quad /17/$$

So the efficiency coefficient:

$$s = \sqrt{\frac{2}{\pi}} \arcsin \sqrt{\frac{2\pi^2 \rho_a^2 \varphi_a}{\mu_0^2 \eta \bar{I}_h^2 K^2(\rho_a)}} \quad /18/$$

This dependence is valid only in the range:

$$0 \leq \frac{2\pi^2 \rho_a^2 \varphi_a}{\mu_0^2 \eta \bar{I}_h^2 K^2(\rho_a)} \leq 1 \quad /19/$$

When the above fraction is higher than 1, in the anode circuit flows direct current equal to I_{\max} and $s=1$. In this case magnetron effect influences advantageously homogeneity of current density on the anode surface. In Fig.5 the efficiency coefficient s dependence on the values of ρ_a and φ_a/\bar{I}_h^2 parameters is shown. As proceeds from these diagrams, limitation of the gun efficiency due to the magnetron effect occurs especially distinctly at small anode diameters and low accelerating voltages. The above considerations are confirmed by the measurements of the ring type electron gun efficiency.

It must be added here that the current flowing in the

anode circuit is, as a matter of fact, a difference of two currents, namely the primary electron current reaching the anode, and the current of reflected electrons.

MAGNETRON EFFECT COMPENSATION

The magnetron effect compensation allows to obtain the equally high efficiency of the ring type electron gun with in wide range of anode diameters. Such a compensation is attained as a result of compensating current flow in the additional ring type electrode, situated near the cathode /Fig.6/. The critical parabola, as a result of superposition of magnetic fields produced by the cathode heating current and the compensating current, will under such conditions be determined by the formula:

$$\varphi_{oc} = \frac{\mu_0^2 \eta_{hc}^2}{2\pi^2 \rho_a^2} K_k^2(\rho_a) \quad /20/$$

where

$$K_k(\rho_a) = \int_{\rho_a}^1 \rho \frac{E(\rho^2)}{(1-\rho^2)} d\rho + \gamma_c \rho_k \int_{\rho_a}^1 \rho \frac{E(\rho^2 \rho_k^2)}{(1-\rho^2 \rho_k^2)} d\rho \quad /21/$$

$$\rho_k = \frac{r_f}{r_{fa}},$$

r_{fa} - radius of ring type electrode in which the compensating current i_k flows,

$$\gamma_c = \frac{i_k}{i_{hc}}.$$

Full compensation of the magnetron effect is possible only when $K_k(\rho_a)=0$, so when

$$\gamma_c = - \frac{\int_{\rho_a}^1 \rho \frac{E(\rho^2)}{(1-\rho^2)} d\rho}{\rho_k \int_{\rho_a}^1 \rho \frac{E(\rho^2 \rho_k^2)}{(1-\rho^2 \rho_k^2)} d\rho} \quad /22/$$

Compensation at $\rho_k=1$ and $\gamma_c=-1$ requires putting the compensation electrode in the same place as cathode. From the viewpoint of technical reasons such a compensation is

not possible. Most convenient for compensation is to use the multiplied heating current $\gamma_c = -2, -3 \dots$. In this case the compensating electrode must consist of an appropriate number of coils placed very nearly each other. In Fig. 7 $K_k(\rho_a)$ dependencies for various values of ρ_k and γ_c is presented. At $\gamma_c = -2$, in the range of small values ρ_a effective compensation is possible for $\rho_k = 0,91 \dots 0,93$.

The efficiency coefficient of the ring electron gun at compensated magnetic field is expressed by the formula:

$$s = \sqrt{\frac{2}{\pi} \arcsin \sqrt{\frac{2\pi^2 \rho_a^2 \varphi_a}{\eta \mu_0^2 I^2 K_k^2(\rho_a)}}} \quad /23/$$

This equation being valid only for:

$$0 \leq \frac{2\pi^2 \rho_a^2 \varphi_a}{\eta \mu_0^2 I^2 K_k^2(\rho_a)} \leq 1 \quad /24/$$

The efficiency coefficient of the ring electron gun with compensated magnetic field, as a function of φ_a/I^2 and ρ_k is presented in Fig.8.

Introduction of the compensating electrode results in a change of electric field distribution near the cathode. With respect to fairly significant length of the cathode, the drop of the heating voltage along the cathode causes that a part of the cathode may have in some moments lower potential than the compensation electrode; due to this, the current emitted by this portion of the cathode for the most part reaches the compensating electrode. However, it is not advisable, with respect to total gun efficiency. Therefore, the compensating electrode must be screened from the cathode /Fig.9/.

CONCLUSIONS

The magnetic field, caused by the cathode heating current flow, influences considerably electron trajectories in the ring type electron gun. In the case of using the small diameter anodes this effect unadvantageously limits the ring electron gun efficiency, but at large anode diameters advantageously influences the homogeneity of anode heating.

So, designing the ring electron gun intended for materials floating zone melting in the form of rods of con-

siderably differentiated diameters, the use of compensating electrode is advisable. This electrode should be so designed as to enable three variants of the gun operation:

- without compensation /the compensating electrode not connected/,
- with compensation / the compensating current flows in the opposite direction than the cathode heating current/,
- with amplified magnetron effect / compensating current flows in the same direction as the cathode heating current/.

In the last case the electron trajectories are more strongly deviated in time with the heating currents changes, which is a contribution to the above mentioned increase in the anode heating homogeneity.

REFERENCE

1. K.P. Friedel - Conf. on Vac. Techn. and Appl. in Ind. and Sci. Res. - Świeradów Zdrój, 1973.

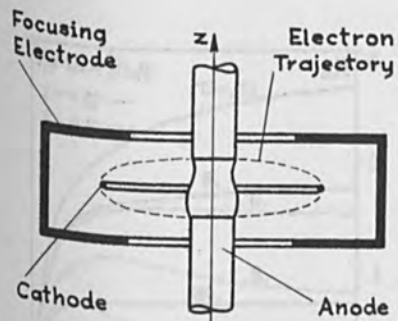


Fig.1. Ring type electron gun.

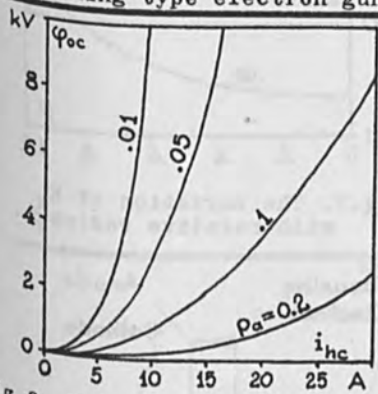


Fig.3. Critical parabolas.

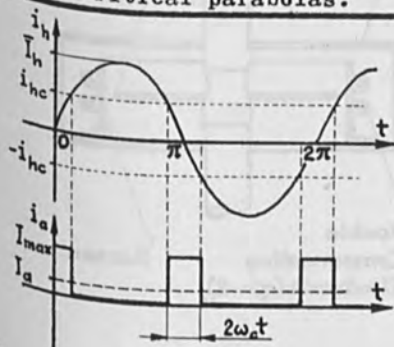


Fig.4. The heating current and the anode current in ring electron gun.

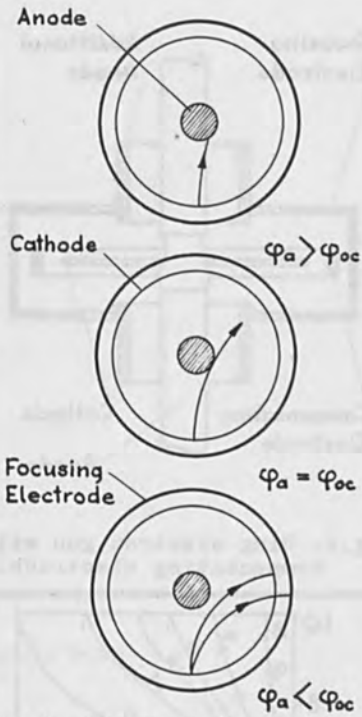


Fig.2. Electron trajectories at various values of anode potential

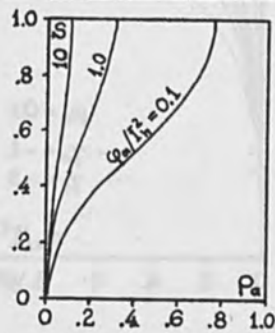


Fig.5. Ring electron gun efficiency vs ρ_a .

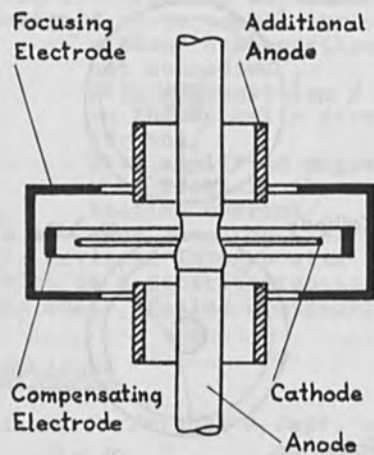


Fig.6. Ring electron gun with compensating electrode.

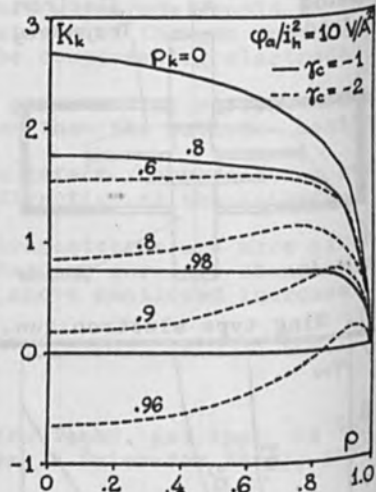


Fig.7. The variation of K_k with relative radius ρ .

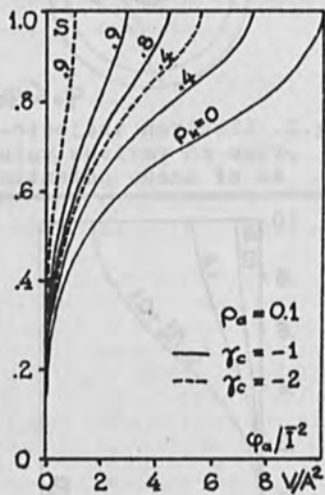


Fig.8. Efficiency s vs parameter ϕ_a/I^2 at compensated magnetic field.

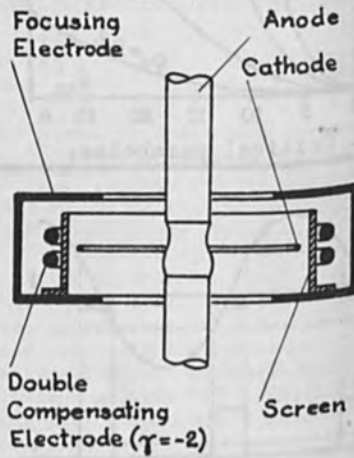


Fig.9. Ring gun with double compensating electrode screened from cathode.

THE NEPTUNE-C PULSED ELECTRON BEAM

Robert E. Wentzel

Ion Physics Corporation
Burlington, Massachusetts 01803

ABSTRACT

The Ion Physics Corporation Neptune-C Low Impedance Pulsed Electron Beam Generator, capable of operating at peak electron currents with mean energies from 100 to 500 keV at a power level of approximately 70 megawatts, is described. Beam energies as high as 5 MeV are possible in the Neptune-C and Neptune-D at the end of a 200 cm drift tube in a drift chamber are possible. The pulse generator provides the 100 to 500 keV electron beam generator.

PART II

Section 2

Relativistic Electron Beams

INTRODUCTION

The Ion Physics Corporation Neptune-C Pulsed Generator is a low impedance electron beam generator. The generator is capable of operating at peak electron currents of 100 to 500 kA at a power level of approximately 70 megawatts. The generator is capable of operating at peak electron energies from 100 to 500 keV and mean energies as high as 5 MeV are possible. The generator is capable of operating at peak electron energies from 100 to 500 keV and mean energies as high as 5 MeV are possible. The generator is capable of operating at peak electron energies from 100 to 500 keV and mean energies as high as 5 MeV are possible.



Fig. 6. Ring electron gun with compensating electrode.



Fig. 7. The variation of η with relative radius r .



Fig. 8. Efficiency η vs parameter q_0/T^2 at compensated magnetic field.



Fig. 9. Ring gun with double compensating electrode increased from cathode.

THE NEPTUNE-C PULSED ELECTRON BEAM

Robert S. Wenstrup
Ion Physics Corporation
Burlington, Massachusetts 01803

ABSTRACT

The Ion Physics Corporation Neptune-C Low Impedance Pulsed Electron Beam Generator, capable of several hundred kiloampere currents with mean energies from 100 to 500 keV in a power pulsewidth of approximately 70 nanoseconds, is described. Beam energies as high as 5 kilojoules in the anode plane and 2.3 kilojoules at the end of a solid guide cone in a drift chamber are possible. The pulse generator and diode characteristics for electron beam generation are discussed. Beam uniformity over 5 and 18 cm² target areas were measured with a high resolution graphite calorimeter; measurements show the beam fluence is uniform over the central 0.8 inches of a 1.0 inch diameter beam. Maximum fluences delivered to a target at the end of a solid guide cone are 30 cal/cm² over 18 cm², 90 cal/cm² over 5 cm², and 150 cal/cm² over 2.85 cm². Shot-to-shot reproducibility at beam fluences from 26 to 68 cal/cm² is better than ± 7 percent. The energy deposition in a graphite target has been measured in a transmitted fluence experiment; the measured depth-dose profile agrees well with the calculated profile.

INTRODUCTION

The Ion Physics Corporation Neptune-C Pulse Generator shown in Figure 1 is the latest model in the Neptune series of low impedance electron pulse generators. The pulser is capable of generating intense reproducible bursts of electrons with peak powers in the tens of gigawatts in a power pulsewidth (FWHM) of approximately 70 ns. Mean accelerating voltages from 100 to 500 kV and diode beam currents as high as 300 kA are possible. Neptune-C has been operated extensively in the electron beam mode, where an electron beam of uniform spatial dimensions over a target surface is desired;

for this purpose the electron beam is transported from the diode through a drift chamber containing a neutral gas at typically 2.5 torr pressure and is focused by a guide cone on the target. Diode impedance for these electron beam experiments are typically 2 to 3 ohms; energies deposited in the sample can be as high as 2.3 kJ.

The Neptune-C generator has three stages: the energy storage section, the water-dielectric coaxial pulse-forming line, and the field emission diode with associated beam-handling equipment. Neptune-C was specifically designed as a high-energy pulse forming generator with beam pulses reproducible to ± 5 percent RMS. Since all switches are command triggered, gas-insulated switches, Neptune-C features very low timing jitter (± 5 ns RMS), mechanical stability, and exceptionally reproducible beam energy and spatial resolution. The gas insulated switches isolate the diode from the pre-pulse inductive to water-insulated overvolted switches, and the design facilitates cleanup of the diode region between shots; a turn-around time between shots of 15 minutes, involving cleanup of the diode, replacement of the anode window and positioning of the target at the guide cone exit, is representative of the speed at which experimental data can be obtained.

THE PULSE GENERATOR

Electron beam pulses are formed and discharged as indicated in the Neptune-C block diagram in Figure 2. Energy is stored in a set of twenty $0.43 \mu\text{F}$ capacitors rated at 80 kV charging voltage by DC charging through a set of opposite polarity power supplies. The energy store capacitor bank consists of five modules of four capacitors connected so that the net voltage across each charged module is zero. A command trigger pulse initiates a Marx generator trigger pulse which fires a distorted-field midplane switch on each capacitor bank module, discharging the energy stored in one pair of capacitors through an inductor into the other set of capacitors in the module; the voltage across this LC circuit rises sinusoidally, peaking $5 \mu\text{s}$ after the command pulse. At peak voltage a second Marx generator triggers a high-pressure gas "trigatron" switch, discharging the energy stored in the LC circuit in a 1.5 ohm water-dielectric coaxial pulse-forming line. Voltage in the water line rises sinusoidally reaching a peak value approximately 380 ns after start of the pulse; at this instant a third Marx generator simultaneously triggers eight channels of a large high-pressure gas-insulated trigatron switch, sending the pulse energy into a water-insulated transformer section which reduces the voltage and increases the current in the

pulse. In the transformer section the pulse shape is approximately trapezoidal and has a pulse length equal to the double transit time in the line (120 ns); the water line impedance at the diode-water line interface is 1 ohm.

The diode and drift tube regions appear in Figure 3. The field-emission graphite cathode is mounted on a 16 cm long shank which projects through the anode door. To record the diode accelerating voltage the cathode shank is surrounded by a capacitive voltage monitor placed 5 cm behind the cathode and isolated from the cathode by a 3.0 nH inductance. The capacitive divider directly monitors the diode accelerating voltage, eliminating deduction of the diode voltage from pulse monitors located in the coaxial water line.

THE ELECTRON BEAM

Hollow graphite cathodes with a 1.0-inch inner diameter and outer diameters from 1.8 to 3.5 inches have been used for electron beam experiments. A 0.00025-inch aluminized Mylar foil forms the anode window for the diode. During the beam pulse electrons easily vaporize the Mylar and enter a drift chamber maintained at typically 2.5 torr of nitrogen gas to provide a positive ion current, thus avoiding the self-pinching effect of the magnetic field generated by an intense net negative current. The electron beam pulse is compressed to a smaller diameter at the target plane by a solid graphite or apertured wire guide cone, then impinges upon the target.

The mean accelerating voltage and beam energy can be chosen by varying several parameters in the generator and diode areas:

- (1) the energy stored in the LC circuit, which is determined by the peak charging voltage of the DC supplies used to energize the capacitor bank. The stored energy increases with the square of the charging voltage.
- (2) the time at which the sinusoidally rising pulse in the water line is discharged into the transformer section; the switching time determines the energy transferred to the diode. Since the switch transferring energy from the water line to the transformer section (and then the diode) is a command triggered trigatron switch--as contrasted to the usual overvolted switch whose firing is somewhat random--this discharge

TABLE 2
REPRODUCIBILITY DATA FOR NEPTUNE-C

Mean Fluence, cal/cm ²	Range, percent	Standard Error, percent	Number of Shots
25.9	+ 6, - 5	± 4	9
40.2	+ 8, - 5	± 4	17
54.7	+ 9, -16	± 7	14
67.9	+ 9, -12	± 6	22

Energy deposition within the target, a function of the target density, charge number, and energy of the electron beam is an important parameter in thermomechanical response studies. The energy deposited by the Neptune-C electron beam as electrons are slowed and stopped by ionizing and radiative collisions in the target has been calculated from voltage and current monitor traces and has been measured in a transmitted fluence measurement using thin graphite foils. The depth-dose profile in graphite, deduced from results of the transmitted fluence experiment, has been compared to the profile calculated using ELTRAN, a Monte Carlo electron deposition code. In the experimental measurement an electron beam of approximately 230 kV mean accelerating voltage and diode spectrum shown in Figure 9 was incident on sets of graphite foils placed in front of a total stopping graphite calorimeter. Thin foils of 0.003 and 0.005-inch thick pressed graphite sheet were used to form successively thicker filters for the transmission measurement. The foils were mounted so that they broke and fell away from the calorimeter face after beam transmission; this mounting technique avoided spurious heat transfer from the foils to the calorimeter that can occur when foils remain in close proximity to the calorimeter face after beam heating. The filter thickness was increased until the transmitted energy became negligibly small; several measurements were made for each foil thickness and the free field fluence was measured between transmission measurements. A total of 25 calorimeter measurements was made during the experiment.

Energy transmitted through the foils to the calorimeter as a function of filter thickness is shown by the data points in Figure 13. The average free field fluence for this experiment, $43.5 \pm 5\%$ cal/cm², was corrected for front surface backscatter, as predicted by an ELTRAN calculation based on the diode spectrum shown in Figure 9 and an assumed beam incident angle of 15 degrees. The ELTRAN calculated transmission curve, representing the energy transmitted to the calorimeter as a function of filter thickness, is plotted as the smooth curve in Figure 13.

The depth-dose profile for a given electron beam energy spectrum and target material is defined as the rate of energy loss with penetration in the target material, that is:

$$\frac{dE}{dm} = \lim_{\Delta m \rightarrow 0} \frac{\Delta \phi}{\Delta m}$$

where $\Delta \phi$ is the decrease in fluence in passing through an absorber of thickness Δm . The fluence transmitted through an absorber of thickness x can be related to the free field fluence, ϕ_0 , by

$$\phi(x) = \phi_0 T(x),$$

where $\phi(x)$ is the fluence at a depth x in the material and $T(x)$ is the fractional energy transmitted through the absorber thickness x . The depth-dose profile can then be expressed as

$$\frac{dE}{dm} = \phi_0 \lim_{\Delta x \rightarrow 0} \frac{dT}{dx}$$

The experimental depth-dose profile derived in this manner is shown by the dashed curve in Figure 14, along with the solid curve, representing the ELTRAN profile calculated using voltage and current monitor traces.

CONCLUSION

In summary, the Neptune-C generator produces intense electron pulses with mean accelerating voltages from 100 to 500 kV, peak power of tens of gigawatts and peak current pulses of the order of 70 to 300 kA. The nominal power pulsewidth is approximately

70 ns FWHM with beam energies as high as 2500 joules at the end of a beam focusing guide cone. Electron beams varying from 0.5 inch to 1.8 inch have been carefully diagnosed. In addition to the small area, intense beam pulses, large surface area, low density beam pulses of comparable power pulsewidth are also possible for applications using a large surface, low density (of the order of 10 A/cm^2) electron bursts.

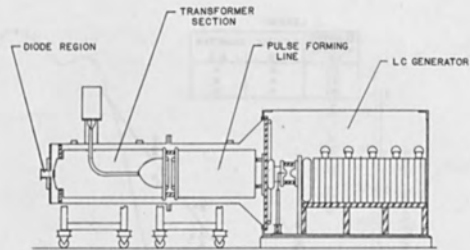


Fig. 1. Outline of the IPC Neptune-C electron pulse generator.

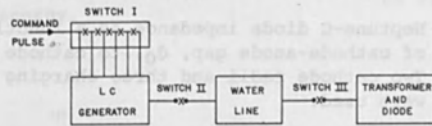


Fig. 2. Block diagram of Neptune-C system

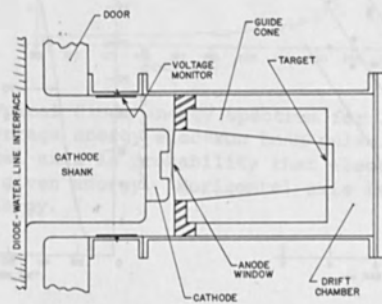


Fig. 3. Neptune-C diode and drift tube region

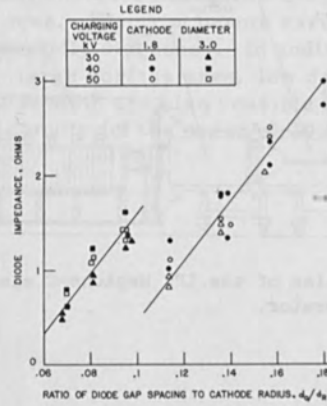


Fig. 4. Neptune-C diode impedance as a function of ratio of cathode-anode gap, d_0 , to cathode radius, d_R . Two cathode radii and three charging voltages were used.

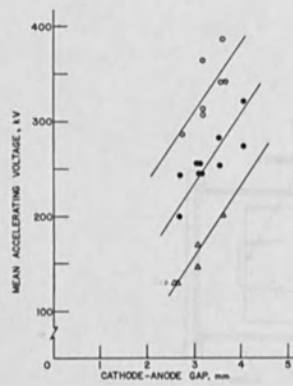


Fig. 5. Neptune-C mean accelerating voltage as a function of diode gap. Δ - 30kV LC generator charging voltage; ● - 40kV; ○ - 50 kV.

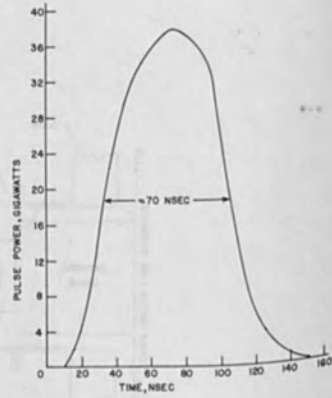


Fig. 6. Calculated Neptune-C diode power during pulse discharge. Assuming a Gaussian power distribution, the FWHM is approximately 70 nsec.

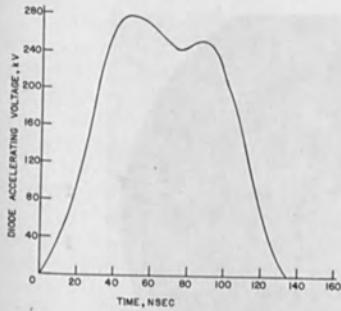


Fig. 7. Typical Neptune-C diode accelerating voltage for electron beam of 228 keV mean energy.

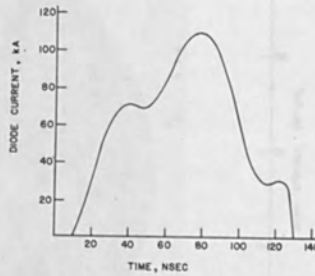


Fig. 8. Typical Neptune-C diode current for electron beam of 228 keV mean energy.

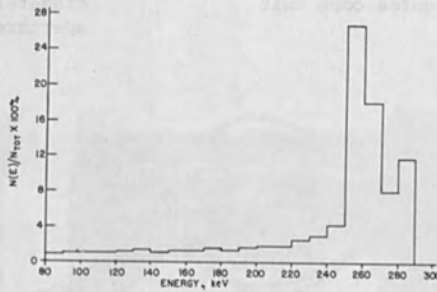


Fig. 9. Typical diode energy spectrum for 228 keV average energy electron beam pulse. Vertical axis is probability that electron has a given energy. Horizontal axis is electron energy.

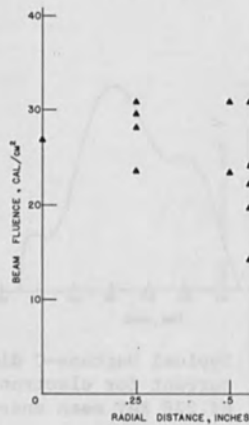


Fig. 11. High resolution calorimeter measurement of Neptune-C beam uniformity with 1.8 in. diameter guide cone exit aperture.



Fig. 12. High resolution calorimeter measurement of Neptune-C beam uniformity with 1.0 in. diameter guide cone exit aperture. Shot 1071.

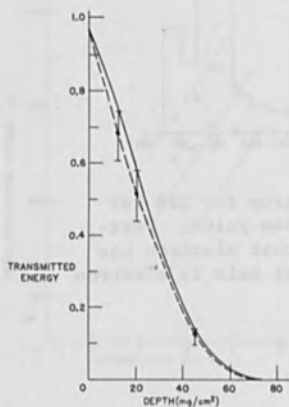


Fig. 13. Measured transmitted dose (corrected for front surface backscatter) and ELTRAN calculated transmission curve for a 226 keV beam incident on a carbon target.

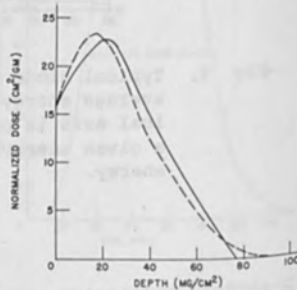
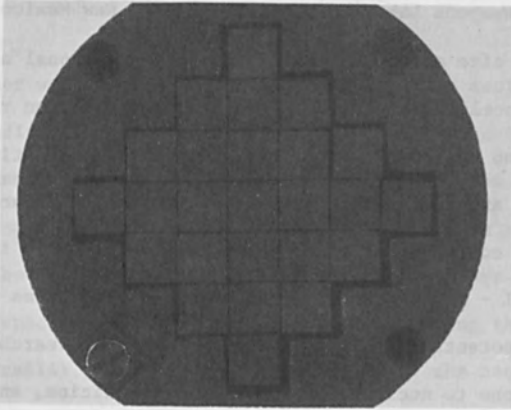
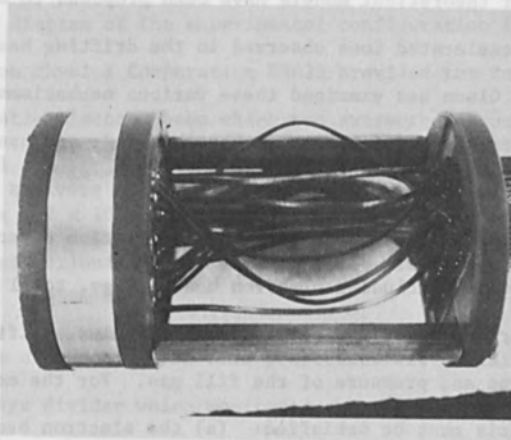


Fig. 14. Measured depth-dose profile (dashed curve) and ELTRAN calculated profile (solid curve) for a 226 keV beam incident on carbon target.



(a)



(b)

Fig. 10. High resolution total stopping carbon calorimeter. a, Front view showing 25 element array with diameter 1.75 in. b, Side view showing wiring connections.

CHARGED PARTICLE ACCELERATION WITH INTENSE RELATIVISTIC ELECTRON BEAMS
David C. Straw* and R. B. Miller

Air Force Weapons Laboratory, Kirtland AFB, New Mexico 87117

INTRODUCTION

In view of size and cost limitations in conventional accelerator design novel acceleration concepts, such as the electron ring accelerator (ERA) and collective acceleration by intense relativistic electron beams are receiving increasing attention. If successful, these concepts could possibly achieve accelerating field increments as great as 0.1 - 1.0 GeV/meter.¹ Interest in such beams results not only from the potential for unique plasma physics research, but also from applications to nuclear physics, nuclear medicine, and cancer radiation therapy.

A number of theoretical models have been proposed to explain the collectively accelerated ions observed in the drifting beam geometry.²⁻⁷ Recently C. L. Olson has examined these various mechanisms in depth, pointing out serious difficulties with each model, and has suggested a new model which appears to correlate well with previous experimental results.⁸ In the new model, ion acceleration depends on several parameters, including electron beam energy, total beam current, voltage and current risetimes, electron beam radius, drift tube radius, and type and pressure of the fill gas. For the mechanism to work two criteria must be satisfied: (a) the electron beam diode must supply a beam current in excess of the space charge limiting current so that an initial, deep stationary potential well may be formed; and (b) the electron beam risetime to the limiting current value must be less than the gas ionization time, otherwise the background ion density will neutralize the beam charge density too

rapidly, and the electron beam front will propagate before the initial well is formed.

In this paper we report the results of experiments designed to assess the validity of the Olson model and to enhance the ion acceleration mechanism. Since such parameters as electron beam energy, total beam current, and voltage and current risetimes are essentially determined by the available electron beam machine, we have concentrated on varying the space charge limiting current (by varying the beam and drift tube radii), and the type and pressure of the background neutral gas.

EXPERIMENTAL PROCEDURES

A schematic diagram of the experimental configuration is shown in Figure 1. An Ion Physics Corporation FX-25 provided the intense pulsed relativistic electron beam which was extracted through a 0.025 mm Al foil anode. A vacuum window of 0.127 mm mylar separated the low pressure ($\sim 2 \times 10^{-5}$ Torr) diode from the drift chamber which was maintained at various gas pressures from 50 mTorr to about 600 mTorr.

Measurements of the electron beam properties were obtained from a capacitive voltage divider which monitored the anode-cathode voltage, and a 5 m Ω current shunt for return currents passing through the diode wall. Further characterization of the electron beam was obtained by placing a Faraday cup over the diode exit aperture. The net electron beam current in the drift tube was monitored with integrated dB/dt probes. All measurements were recorded with fast risetime oscilloscopes (Tektronix 519's and 7903's).

Comparison of the three oscilloscope traces in Figure 2 reveal similar behavior for all the current measurements. The peak current as seen in Figure 2(a) is 19.3 kA for the anode-cathode arrangement giving the largest ion production. The Faraday cup and the first of eight dB/dt probes, placed 15 cm from the anode, register smaller values of 15.5 kA and 7.6 kA, respectively. The decrease is due to beam degradation in the aluminum and mylar foils, ionization of the background gas, radial blow-up of the beam and possibly the mechanism which accounts for ion acceleration.

Figure 3(a) displays a typical voltage signal for the same configuration. Both current and voltage quickly rise to their peak values with risetimes of 6 nsec for the current and 10 nsec for the voltage. A computer generated plot, Figure 3(b), shows that the most energetic electrons are also the most numerous.

In order to explore the facets of the Olson model pertaining to limiting current and its dependence on the ratio of guide tube radius to electron beam radius, several experimental configurations involving various diode geometries and drift tube radii were used. The combinations of experimental arrangements are listed in Table 1. In the diode, three cathode tips of 2.5 cm, 1.27 cm and 3 mm provided three electron beam radii. The ends of each cathode were flat, i.e., each cathode was a right circular cylinder with the flat side parallel to the anode. For the 2.5 cm and the 1.27 cm aluminum cathode tips, the anode-cathode gap (A-K gap) was set at 3.18 cm and 2.54 cm, respectively. The 3 mm brass tip was set at an A-K gap of 1.43 cm. This

gap represented a compromise. With smaller spacings gross physical damage occurred in the mylar window, and with larger gaps the beam would blow up radially. Seven sets of experiments were performed but two configurations of diode and drift tube resulted in the same R/r_b ratio. Hence, only six different values of R/r_b were involved with the two coincident values providing a consistency test. The three drift tubes had identical lengths, 63 cm.

In varying the diode parameters it was desired to maintain the output current and voltage at comparable levels from one configuration to another. Unavoidable impedance and current changes did occur but variations were less than 5% due in part to the fact that the cathode changes occurred only in the last 15 cm.

Nuclear activation methods were used to detect and analyze the accelerated ions by using appropriate target materials, a NaI crystal, and a multichannel pulse-height analyser. For the deuterium fill gas experiments, carbon target blocks, 3.8 cm x 3.8 cm squares, demonstrated the existence of high energy deuterons through the $C^{12}(d,n)N^{13}$ reaction which has a threshold energy of 0.3 MeV. The induced radioactivity was observed through measurement of the annihilation radiation following positron emission. By using aluminum absorber foils over the blocks, range-energy relations and total cross-sections as a function of energy, it was possible to obtain accelerated ion yields and energies. A similar arrangement was used for the hydrogen fill gas experiments, but the target was a 10 mil beryllium foil. A Los Alamos type silver activation neutron detector was used to record

the neutron yield from the $\text{Be}^9(p,n)\text{B}^9$ reaction which has a threshold of 2.0 MeV.

In order to study the origin and behavior of the accelerating region, additional activation experiments were carried out in the 12.5 cm radius drift tube with two diode configurations and D_2 as the fill gas. The activation of small, 2.5 cm x 2.5 cm carbon blocks suspended at various radii and distances from the anode was investigated as a measure of the degree of collimation of the accelerated deuterons and to determine the minimum anode separation at which energetic ($E > 0.3$ MeV) deuterons first appear. The separation, z , was increased to follow the production and acceleration of deuterons down the tube.

RESULTS AND DISCUSSION

The Olson model of collective acceleration may be qualitatively explained as follows. As an intense electron beam with current exceeding the space charge limit enters the drift tube containing neutral gas at low pressure, the electrostatic field near the anode will degrade the beam kinetic energy causing the beam to blow up radially, provided the beam risetime is less than the gas neutralization time. This deep, stationary well accelerates ions from the region of the neutralization front to form an initial, broad ion energy spectrum. As the background gas becomes sufficiently ionized by accelerated ions, beam electrons, and radiation, the electron beam front propagates, moving at a velocity determined by the background ion density. The potential well follows the beam front and decreases in amplitude, imparting net energy to the ions. Since accelerated ions with

where I_L is the limiting current, β is the usual ratio of electron speed to that of light in a vacuum, $(\gamma-1)$ is the ratio of the electron kinetic energy to rest mass energy, m is the electron rest mass, e is its charge, and f_e is the fractional electrostatic neutralization. f_e was assumed to be zero in these calculations, representing the condition when the beam initially enters the neutral gas. The time for space charge neutralization, as given by Putnam,¹¹ was determined to be ~ 30 nsec, a time much larger than the electron beam risetime.

Our data demonstrates that ion acceleration does not occur until the ratio of beam current to space charge limiting current (I/I_L) exceeds approximately unity. For the R/r_b ratio of 4 no target activation was observed. The first evidence of accelerated ions ($E > 0.33$ MeV) occurs for R/r_b equal to 8 resulting in a limiting current of 13.2 kA and a current ratio, I/I_L , of 1.2.

The results cited above indicate substantial changes in the ion beam as the ratio R/r_b is varied and suggest that the accelerating fields must also change. The data from the suspended carbon target experiments, presented in Figures 7 and 8, serve to illustrate such dependence. For $R/r_b = 10$, no N^{13} activity was observed when the targets were placed less than approximately 17.5 cm from the anode plane. For distances 17.5 cm to 25 cm behind the anode, higher activities were noted on the targets farthest from the center axis of the drift tube, while for still larger distances from the anode, the highest activation occurred on axis. Radially accelerated ions were also observed with carbon blocks situated along the bottom of

velocities substantially different from the well velocity will eventually fall out of the well, the output ion energy spectrum also depends on the background neutral gas pressure.

In order to compare our activation data with various facets of the Olson model, range-energy⁹ and cross section¹⁰ tabulations were used to reduce the raw data. Figure 4 indicates the total deuteron beam energy incident on the C12 target as a function of pressure for two values of the parameter R/r_b . Reducing the beam diameter from 2.5 cm to 3 mm increases the total ion beam energy on target by two orders of magnitude. The peak of the curve is also shifted to higher pressures. Figure 5 indicates a similar behavior for hydrogen.

A summary of the significant results of the deuterium experiments is presented in Table 2. The average ion energy at the pressure for which peak beam energy occurs was obtained from the peaks in the curves like those of Figure 4. The average ion energy was plotted against the natural logarithm of the R/r_b ratio and is shown in Figure 6. The straight line was added as an aid in determining the appropriateness of a linear fit.

Olson's model does not address the dependence of the ion energy on the R/r_b parameter, however, the lack of ion-induced activity for $R/r_b \leq 4$ may be interpreted in terms of Olson's criteria for ion acceleration. A minimum current must be established in a time short with respect to the time required for space charge neutralization of the beam. The electron beam current must exceed a value given by

$$I_L = \beta(\gamma - 1) (mc^3/e) (1 + 2 \ln R/r_b)^{-1} (1 - f_e)^{-1} \quad (1)$$

the drift tube at various distances from the anode plane. These results indicate that the accelerating fields for this geometry initially have radial and axial components approximately equal in magnitude.

For the case of $R/r_b = 84$, however, substantial activation occurred 10 cm behind the anode plane and increased dramatically to a distance of 25 cm from the anode. In all trials maximum activity was observed to occur on axis, indicating that the accelerating fields are predominantly axial. Beyond 25 cm no further increase in activation was observed indicating that the accelerating region was limited to 25 cm behind the anode plane. These results are consistent with the concept of a deep initial well which creates a broad accelerated ion energy spectrum, and a shallow, moving secondary well which provides little or no additional acceleration.

SUMMARY

We have investigated collective ion acceleration in the drifting beam-neutral gas geometry as a function of pressure for a variety of electron beam and drift tube radii. We conclude that variations in the ratio of the radii have a most important effect on the resulting ion beam. For values of $R/r_b \leq 4$ no ion acceleration is observed. By increasing this parameter over the range from 8 to 84 we have increased the ion beam energy on target by over three orders of magnitude, due primarily to an increase in the number of energetic collectively accelerated ions.

REFERENCES

* A National Research Council Postdoctoral Research Associate.

1. G. Yonas, Particle Accelerators 5, 81 (1973).
2. N. Rostoker, Bull. Am. Phys. Soc. 14, 1047 (1969).
3. J.R. Uglum, S.E. Graybill, and W.H. McNeill, Bull. Am. Phys. Soc. 14, 1047 (1969).
4. S.E. Rosinskii, A.A. Rukhadze, and V.G. Rukhlin, JETP Lett. 14, 34 (1971).
5. J.W. Poukey and N. Rostoker, Plasma Physics 13, 897 (1971).
6. S. Putnam, Bull. Am. Phys. Soc. 14, 1048 (1969).
7. J.M. Wachtel and B.J. Eastlund, Bull. Am. Phys. Soc. 18, 1356 (1969).
8. C.L. Olson, Bull. Am. Phys. Soc. 18, 1356 (1973).
9. M. Rich and R. Madey, Lawrence Berkeley Laboratory Report No. UCRL-2301, (1954) (unpublished).
10. Von K. Wohleben and E. Schuster, Radiochim. Acta 8, 78 (1967).
11. S. Putnam, Physics International Co. Report PIFR-72-105, (1972) (unpublished).

TABLE 1. ION ACCELERATION EXPERIMENTAL CONFIGURATIONS

Diode	Drift Tube Radius	Ratio of Drift Tube Radius, R, to e ⁻ Beam Radius, r _b	Gas
	R (cm)	R/r _b	
1" diameter Al cathode A-K gap: 1"	2.5	2	D ₂
	5.0	4	D ₂
	12.7	10	D ₂
1/2" diameter Al cathode A-K gap: 1"	2.5	4	D ₂
	5.0	8	D ₂
	12.7	20	D ₂
3mm diameter brass cathode A-K gap: 9/16"	12.7	84	D ₂
			H ₂

TABLE 2. SUMMARY OF EXPERIMENTAL RESULTS

Ratio of Drift Tube and e ⁻ Beam Radii R/r _b	Ratio of Injected Current to Limiting Current I/I _L	Maximum Ion Beam Energy on Target (joules)	Average Ion Energy at Maximum Beam Energy (Mev)	D ₂ Pressure at Maximum Beam Energy (mTorr)
2	0.54	---	<0.5	---
4	0.86	---	<0.5	---
8	1.2	~2x10 ⁻³	~ 1	60
10	1.3	3x10 ⁻²	1.6	100
20	1.6	~ 0.2	~2.3	200
84	2.2	2.9	3.1	250

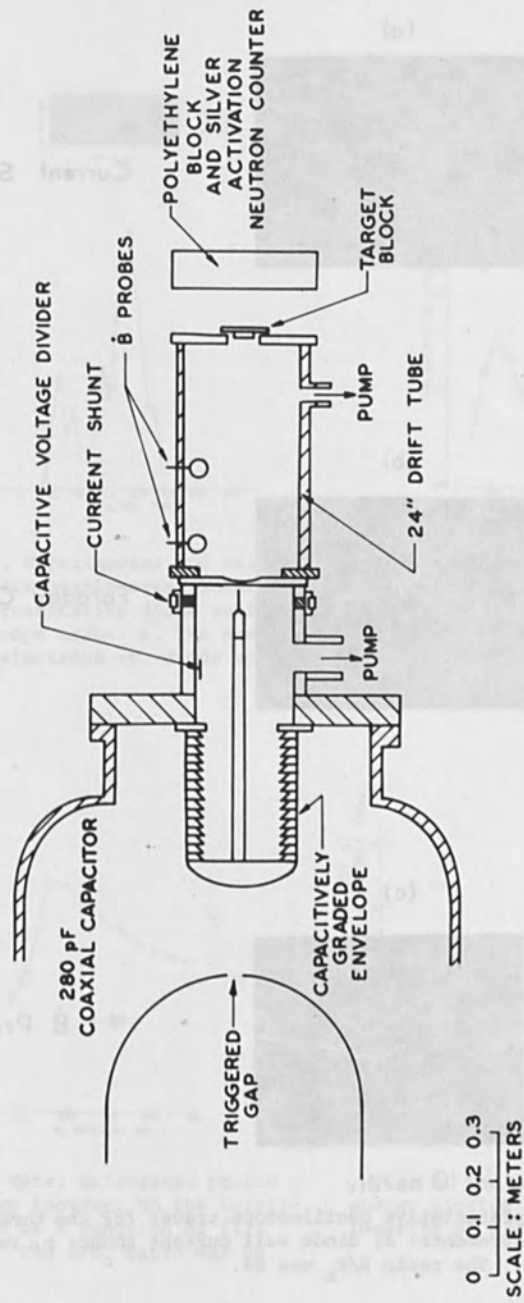


Fig. 1. Schematic diagram of the experimental arrangement.

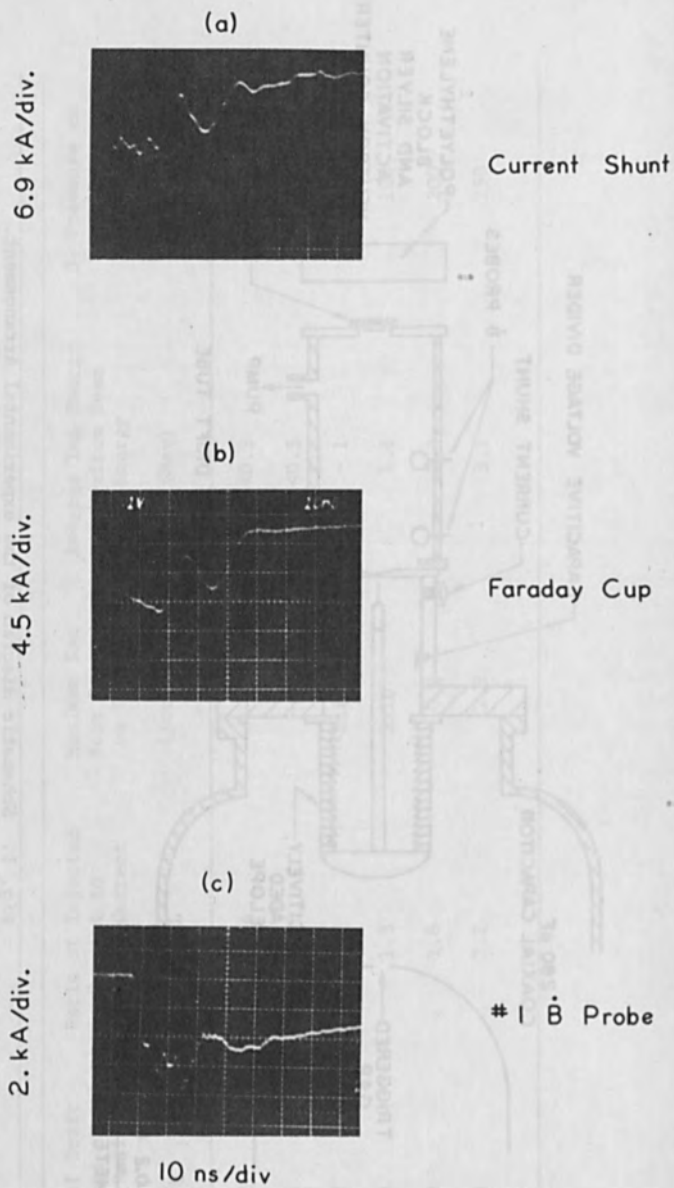


Fig. 2. Representative oscilloscope traces for the three current diagnostic measurements: a, diode wall current shunt; b, Faraday cup; c, dB/dt probe. The ratio R/r_b was 84.

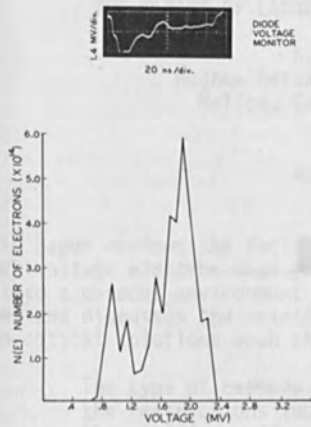


Fig. 3. Experimental and calculational diagnostic measurements. a, A representative diode voltage oscilloscope trace. b, The number of beam electrons vs. diode voltage.

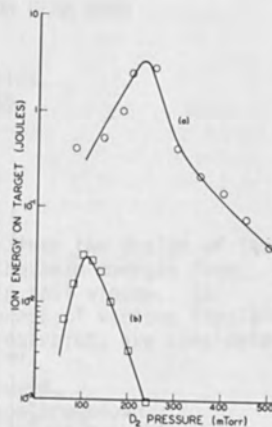


Fig. 4. Total calculated deuteron beam energy incident on the carbon block as a function of fill pressure. a, For the radii ratio R/r_b of 84; b, for R/r_b of 10.

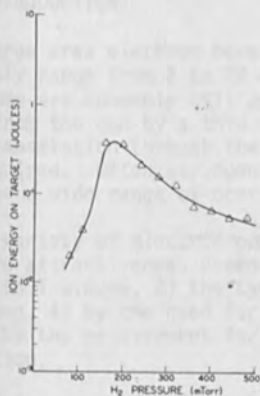


Fig. 5. Total calculated proton beam energy incident on the beryllium target as a function of fill pressure. The R/r_b ratio was 84.

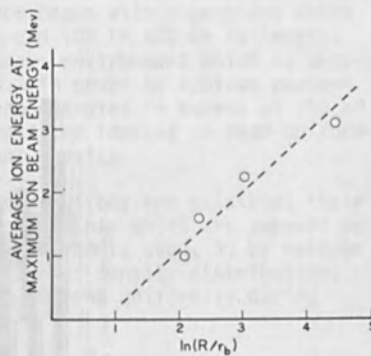


Fig. 6. The average deuteron energy plotted vs. the natural logarithm of R/r_b .

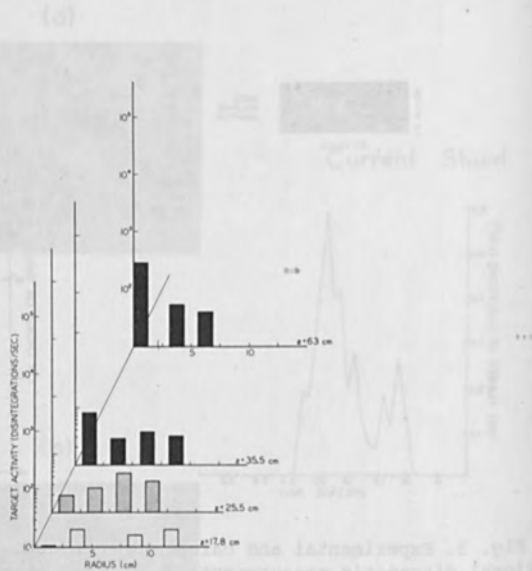


Fig. 7. Carbon block activation for various radial and axial positions (anode separation, z) in the drift tube. The ratio R/r_D was 10.

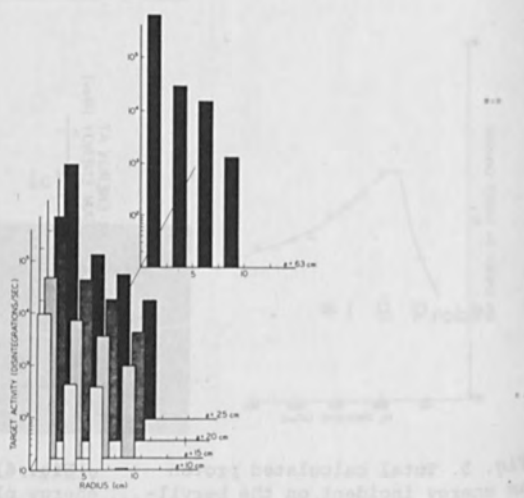


Fig. 8. Carbon block activation for various radial and axial positions in the drift tube. The ratio R/r_D was 84.

THE DESIGN OF LARGE AREA ELECTRON BEAM GUNS

K. Amboss
Hughes Research Laboratories
Malibu, California 90265

ABSTRACT

This paper reviews the factors which enter into the design of large area high voltage electron beam guns in which the beam emerges from vacuum into a gaseous environment through a thin foil window. It describes and discusses the relative attractiveness of various feasible electron optical solutions when the following restraints are considered.

The type of cathode which can be used,
the restrictions imposed by voltage breakdown,
the need for uniform current density distribution,
the maintainance of uniformity during modulation, and
the restrictions imposed by the foil window

The design of a 5-cm wide by 125-cm long gun for cw operation is described.

I. INTRODUCTION

Large area electron beam guns produce beams with dimensions which presently range from 2 to 20 cm in width and 100 to 400 cm in length. The beams are commonly utilized in a gaseous environment which is separated from the gun by a thin foil window. In order to achieve reasonable transmission through the window, beam energies in excess of 150 kV are required. Often stringent requirements are imposed on beam uniformity over a wide range of operating current density.

A variety of electron optical design solutions are possible; their relative attractiveness depends on the constraints which are imposed by 1) the foil window, 2) the type of cathode which is used, 3) by voltage breakdown, 4) by the need for a uniform current density distribution, and 5) by the requirement for maintaining current uniformity during modulation.

In this paper we examine each of these requirements in turn and show how the restraints imposed determine the electron optical design. Using the criteria developed we describe the design of a 5 cm by 125 cm cw electron beam gun and present measurements taken on such a gun.

II. THE EFFECT OF CONSTRAINTS

A. The Foil Window

Energy losses in the foil window set an upper limit to the current density which the gun has to produce. Figure 1 shows the energy and current transmission for two typical window materials, 0.001 inch thick aluminum and titanium foil. The aluminum foil is sometimes preferred in cw operation for its superior thermal conductivity, whereas the titanium foil finds application in high current pulsed operation since it can withstand a considerably higher temperature rise.

The advantages of operating at high beam voltage are readily apparent from Fig. 1. It can also be seen that the energy transmission rises only slowly above about 250 kV; power supply and x-ray shielding costs rise drastically with increasing voltage and 300 kV is therefore a practical upper limit of operation for electron beam guns; this is particularly so in industrial applications.

Support of the thin foil is necessary for it to withstand the pressure differential. The support structure can be designed to incorporate cooling in order to conduct away the heat generated in the foil; however, since the support bars have a finite shadow fraction there is an upper limit to the amount of heat which can be carried away and to the width of the foil. A practical limit to the foil width appears to be about 20 cm and for the maximum cw energy dissipation about 10 W/cm^2 in aluminum foil. From Fig. 1, which shows a 5% energy loss at 250 kV, one therefore calculates that a maximum cw current density of about 0.8 mA/cm^2 is achievable after the foil.

No similar upper limit can be projected so simply for pulsed operation. However, requirements¹ for the pumping of electron beam controlled and pumped lasers call for current densities of up to 20 A/cm^2 .

A further restraint is on the angle of arrival of the electrons at the foil since the increased path length associated with oblique incidence leads to increased energy and current loss. Figure 2 shows the variation of transmission with arrival angle for 0.001" thick aluminum foil at 250 kV. It can be seen that in order to keep this additional energy loss well below the unavoidable loss at normal incidence, it is necessary to restrict the angle of arrival to about 20° .

B. The Cathode

The requirements on the cathode are as follows: a) it must give ample emission, b) it must have an adequate lifetime under possibly adverse vacuum conditions, including catastrophic vacuum failures, c) it must operate with a minimum of heater power input, d) it must exhibit structural rigidity at the operating temperature, and e) if the gun is used in a production environment, it must be economically viable.

Electrons are obtainable by numerous means, by field emission, by secondary emission processes, by extraction from a plasma and by thermionic emission. Tolerance to poor vacuum rules out thermionic cathodes with low work function emitting surfaces, since these are most easily poisoned, i.e. have their work function increased by adsorbed materials. Tolerance to adverse vacuum conditions is thus only obtained by using higher work function cathodes and is therefore bought at the expense of heater power input. Figure 3 puts this into perspective by displaying emission density as a function of cathode temperature and work function. All of the cathodes, with the exception of perhaps the oxide coated cathode, operate in a temperature regime where radiation losses predominate and since these losses increase with the 4th power of the temperature, there is a strong incentive to operate with the lowest temperature cathode capable of withstanding the environment.

Figure 4, from a paper by Gallagher² shows the oxygen poisoning characteristics of several of these cathodes. The figure also shows the effect of air on the emission of the impregnated tungsten (Ba-W) cathode. It is seen that LaB₆ has the best poisoning characteristics of the thermionic cathodes. However, Loeffler³ has shown that LaB₆ is subject to rapid chemical erosion in poor vacuum. In spite of this drawback LaB₆ is of considerable interest and methods of constructing such cathodes have appeared in the recent literature.⁴

Heater requirements can be calculated⁵ by assuming that radiative losses from the emitting area of the cathode are a fraction η_H of the input power P. Thus

$$P = 5.73 \times 10^{-12} \epsilon_T T^4 A / \eta_H \quad \text{Watts} \quad (1)$$

where T is the emitter temperature and ϵ_T the emissivity and A the area of the cathode. Using representative values of

$$\epsilon_T = .40, \quad \eta_H = .56 \quad (2)$$

obtained from designs of ionizers for high efficiency ion engines for space propulsion, Table 1 lists the heater requirements for several cathode types and emitting areas. It is readily seen that the more poison resistant cathodes impose severe thermal design problems. Although the oxide coated cathode is unfortunately unacceptable because it poisons too readily, the Ba-W cathode offers a suitable compromise for the design of guns which call for moderate foil (and therefore, also cathode) loading. Guns operating under cw conditions fall into this category and designs using matrix cathodes have been described in the literature.⁶ The gun described below uses such a cathode.

Very large area cold cathodes and field emission cathodes do not exist although smaller cathodes have been described. Basov⁷ has described an electron beam pumped laser in which a 13 cm by 1.6 cm Mylar foil is irradiated with 700 kV electrons in 10 nsec pulses of

current density of 10 to 20 A/cm² obtained from three transversely mounted cold tungsten cathodes.

TABLE 1
HEATER POWER REQUIREMENTS FOR VARIOUS
CATHODES EMITTING AT 1.0 A/cm².

Cathode Type	Temp. °K	Power, kW		
		Area of Emitter		
		1 cm ²	100 cm ²	1000 cm ²
Oxide	950	.0033	.33	3.3
Dispenser Ba-W	1250	.0099	.99	9.99
Thoria-Coated Ir	1550	.0236	2.36	23.62
LaB ₆	1625	.0285	2.85	28.54
Thoriated Carburized W	1850	.0479	4.79	47.93
Pure W	2600	.187	18.70	187.04

Field emission is usually obtained from a single etched tungsten needle to which a high electric field is applied. Small bundles of such needles are being used in commercial instruments⁸ to produce nano-second high current pulses. In the 2.3 MeV electron beam generator produced by Hewlett Packard a .100" dia. cathode consisting of concentric rings of needles produces a current of 6000 A for a period of 30 nsec. Spindt⁹ has described low voltage field emitting cathodes which, while not capable of ultra-high emission, can however be operated cw at emission densities of up to 2 A/cm². The cathodes are in the form of a two-dimensional array of cones, about 1 micron high facing a similar size aperture which is used for current control and which is located a small distance above the tip of the cone. Because the voltage on this gating electrode is on the order of 200 V, the emitters are not as rapidly degraded by ion bombardment as the normal field emitting cathodes and can therefore be operated cw with a life expectancy of hours. To date only small 10 by 10 arrays on 25 micron centers have been manufactured, however.

Loda et al¹⁰ have studied a cold cathode consisting of a parallel array of 10 cm long tantalum blades approximately 10 micron wide which are separated from each other by spacers 1.5 mm wide to form a 10 cm by 10 cm area emitter. A movable planar anode in front of this arrangement completed the plane parallel diode. Electron emission of up to 50 A/cm²

has been reported from this cathode with the emission density remaining stable for several microseconds at a value which can be calculated from the Child-Langmuir equation for space-charge-limited emission

$$j = 2.33 \times 10^{-6} \frac{V^{3/2}}{d^2} \quad (3)$$

The applied voltage is V and the diode spacing d . However, the diode current increases rapidly from the above calculated value after a time lapse of several microseconds for reasons which are not understood. The current uniformity is within 20% and repeatability is also of that order. Although the 100 cm^2 cathode has not been scaled to larger values, there appear to be no obvious reasons which prevent this. The cathode appears to be able to withstand the rigor of a relatively poor vacuum.

The feasibility of a large area electron gun in which the electrons are extracted from a plasma has been demonstrated by Bayless, Knechtli and Mercer.¹¹ Pulsed current densities of up to 1 A/cm^2 with a pulse width of up to $100 \mu\text{sec}$ and cw current densities of $.7 \text{ mA/cm}^2$ have been obtained from a gun producing a $10 \times 3 \text{ cm}^2$ beam. The device which has been operated up to 140 kV is shown schematically in Fig. 5. The source of the electrons is the plasma which is produced within the hollow cathode discharge struck between the hollow cathode surface and the anode grid G1. The discharge operates at a voltage which is typically between 500 to 800 V and is initiated by pulsing the igniter electrode up to 800 V for about $1 \mu\text{sec}$. The working gas is helium at pressures between 10 to 50 m Torr and is chosen for its desirable high voltage breakdown characteristics and low sputtering efficiency. The neutral helium gas is free to diffuse into the accelerating region where Paschen breakdown will occur unless the restraints on gas pressure, accelerating voltage and electrode spacing are met.

The limitation on the gas pressure is set by the need to maintain a stable discharge, this sets the lower limit, and by the need to prevent ionizing collisions in the accelerating region from producing an unacceptably large energy spread which, according to Fig. 1, would greatly increase foil losses. This sets the upper limit.

With the gas pressure thus bracketed and the voltage determined by user considerations, only the accelerating region spacing d remains to be determined. This, however, is subject to the constraint of Paschen breakdown as discussed in Section II-C.

Although the plasma cathode is a "cold" cathode, energy is required to produce and maintain the plasma neutrality. The current drawn through the anode grid ultimately also flows through the plasma sheath

in the form of an ion current to the cathode wall. To extract a beam with current density j A/cm² requires a power of

$$W = j(V_{G1} - V_c) \text{ W/cm}^2 \quad (4)$$

where, according to Ref. 11, $(V_{G1} - V_c) \approx 650$ V. To obtain maximum cw current density of .8 mA/cm² which the foil can withstand, requires a power input of .52 W/cm². To obtain the same emission density from the Ba-W cathode, which would be operated at 1000°K, would require according to Eqs. 1 and 2, a heater power input of $P = 4.1$ W/cm². On the other hand, the extraction of a current density of 1 A/cm² from the plasma cathode would require an input power of $P = 650$ W/cm², whereas Table I gives 9.9 W/cm² for the impregnated cathode.

This comparison is, however, not entirely justified since the large emission density would probably only be used in pulsed operation. Because the thermionic cathode must be heated continuously to stabilize it whereas the plasma cathode only takes power during beam extraction, the real power loss is very dependent on the actual mode of operation. The economics of construction, and poisoning considerations favor some form of cold cathode or plasma cathode.

C. Voltage Breakdown

Vacuum breakdown determines the minimum spacing between electrodes in the case of a thermionic emitter. A useful formula for the initiation of voltage breakdown has been derived by Cranberg¹² who shows that the product of (the field E at the negative electrode) \times (voltage between electrodes) must not exceed 10^{10} V²/cm. Figure 6 plots the vacuum breakdown voltage V as a function of the accelerating region width d according to this rule.

As the gas pressure is increased the probability of gas or Paschen breakdown is increased. As is well known, the Paschen breakdown voltage depends only on the product pd , where p is the gas pressure and d the electrode spacing. Bayless has shown that the presence of an electron beam does not materially affect this formula. Also plotted in Fig. 6 is the Paschen breakdown voltage as a function of d with p kept constant at pressures of 25 and 50 m Torr. It is seen from Fig. 6 that a region exists between the two breakdown characteristics where high voltage operation without breakdown is possible. A wide scatter exists in the data for vacuum breakdown as well as for Paschen breakdown in helium. For this reason Fig. 2 presents also a vacuum breakdown curve assembled by Bayless from data in the literature.

III. ELECTRON OPTICAL DESIGNS

Most of the applications for large-area guns to date have called for beams with a high degree of uniformity. Typical requirements are for a uniformity of $\pm 5\%$ and a current density range which changes by about two orders of magnitude. In such guns it is to be presumed that a beam which is produced by a uniformly emitting cathode may, by judicious electron optical design, maintain this distribution all the way to the foil, but that a beam which is originally nonuniform cannot hope to produce a uniform distribution at the foil.

In the case of an electron gun utilizing a plasma cathode, uniform emission is associated with a uniform arrival rate of the electrons at the anode grid (see Fig. 5). In turn, this implies a hollow cathode which has a surface area which is large compared to the area of the extraction anode. The constraint of voltage breakdown then determines the spacing d between the outside of the hollow cathode which is at high potential and the foil and its support and the vacuum wall at ground level. Since the spacing d can be varied only slightly at high voltage, only designs which approximate to planar flows are feasible. A design based on these considerations is shown in Fig. 7.

In the case of thermionic emitters repeatable results can only be guaranteed when the cathode is operated in the space-charge-limited regime and hence the extraction optics are limited to designs in which a closely spaced control grid faces the cathode or to Pierce-type electron optics which can be designed to produce an exceedingly uniform emission.¹³

In order to make informed decisions about the type of geometry to adopt we consider first several related problems which exist in all designs but which are most easily discussed in terms of a planar geometry. These problems relate to the need for employing a control grid, to the electron optical effects such a grid produces, and to the effects of the finite velocity distributions of the electrons from the hot cathode.

A. The Need For a Control Grid

Voltage breakdown considerations set a minimum distance for the high voltage electrodes. With the assumption that the Cranberg criterion

$$\frac{V^2}{d} < 10^{10} \text{ V}^2/\text{cm} \quad (5)$$

holds we can calculate from Eq. 3 the maximum current density j_{\max} which a diode can produce without running into breakdown problems disregarding the fact that Eq. 3 implies zero field at the cathode when a current is flowing. We find that

$$j_{\max} = 2.33 \times 10^{14} V^{-5/2} \text{ A/cm}^2 \quad (6)$$

Figure 8 plots j_{\max} as a function of the accelerating voltage V . It is seen that over the range of interest, from 100 to 300 kV, the current density is considerably higher than most applications call for. The curve given by Bayless would lead to even higher values. Figure 9 compares the required spacings for various space-charge-limited emission densities including j_{\max} over this voltage range. It is readily seen that the lower current densities require unrealistically large spacings if space-charge-limited flow is to be obtained throughout the whole diode region. Almost invariably one is forced to adopt a triode configuration with a control grid close to the cathode. Unfortunately, this grid produces deleterious electron optical effects.

B. The Dispersion Produced by a Control Grid

When a control grid separates two regions in which the electric field E is different, a lens action takes place which is calculated from the well-known Davisson-Calbick¹⁴ equation. The focal length f for the thin lens at the grid is

$$\frac{1}{f} = \frac{E_1 - E_2}{4 V_g} \quad (7a)$$

for grids with round apertures and

$$\frac{1}{f} = \frac{E_1 - E_2}{2 V_g} \quad (7b)$$

for grids with slit apertures. In these equations V_g is the voltage of the grid and E_1 the field prior to the grid and E_2 the field the electron encounters after passage through the lens.

In the present context the field between the cathode and the grid is small in comparison with the field between the grid and the foil and can be neglected. Hence Eq.(7a) becomes

$$\frac{1}{f} = \frac{1}{4d} \left[\frac{V_f}{V_g} - 1 \right] \quad (8a)$$

where d is as before the length of the acceleration region and V_f the potential of the foil.

Inspection of Eq.(8a) shows that for

$$\frac{V_f}{V_g} - 1 = 4$$

that the focus coincides with foil. In practice, this would require operating the grid at 1/5th of the full potential. Although this would minimize the dispersion of the beam to the point where only aberrations and thermal velocities produce a beam spread, this would lead to unacceptably high grid heating. Hence V_g/V_f must be considerably smaller and the focus occurs close to the grid.

In the simple aberration-free model we employ here, each aperture of radius a (or half width a) focuses a bundle of initially parallel electrons to a point focus as shown in Fig. 10. The maximum deflection ϕ is experienced by an electron which grazes the aperture and is given by

$$\phi = \tan^{-1}\left(\frac{a}{f}\right) \quad (9)$$

The motion of this electron beyond the focus in the uniform field can be shown¹⁵ to be given by the equation

$$x = 2 \left[\frac{V_g}{V-V_g} \right] d \sin\phi \cos\phi \left[\sqrt{1 + \frac{4(z-f)}{d} \frac{V-V_g}{V_g} \frac{1}{\cos^2\phi} - 1} \right] \quad (10)$$

where V is the potential at a distance z from the grid. This equation is considerably simplified when it is evaluated at the foil where $z \approx d$ for $V = V_f \gg V_g$. The position x_{\max} of the edge electron at the foil is then

$$x_{\max} = 2 \left[\frac{V_f}{V_f - V_g} \right]^{1/2} d \tan\phi \quad (11)$$

Substitution for $\tan\phi$ from Eq. 9 then leads to

$$x_{\max} = \frac{a}{2} \left[\frac{V_f}{V_g} - 1 \right]^{1/2} \quad (12)$$

Comparison of this equation with computer calculations, as in Fig. 10, shows Eq. 12 to give results which are consistently higher. For value of $a/d > .02$ this error was about a factor of two. The cause of inaccuracy is in the calculation of ϕ which is considerably reduced by the accelerating field.

It is clear from Eq. 12 that the dispersion is more severe at the lower current levels. We illustrate the extent of this dispersion by presenting in Fig. 11 x_{\max}/a calculated from Eq. 12 as a function of V_g with V_f as a parameter but reduce by a factor of 3 in accordance with the computer results. It can be seen that low grid voltages produce a considerable dispersion.

For instance, for a grid operating at 250 V, with a voltage of 300 kV on the foil, using circular holes 1 mm in diameter this leads to

a dispersion $2 x_{\max}$ of approximately 0.6 cm for each beamlet as it passes through the grid hole.

The effect of this dispersion summed for all of the separate beamlets is illustrated in Fig. 12. The overlapping beams produced by adjacent lenslets give rise to a linear current density build up as shown in Fig. 12c. For beams of width $W \gg 2 x_{\max}$, this dispersion does not pose a problem, but for narrow beams this can lead to a serious nonuniformity.

There are two options open to the designer. One may reduce the mesh size of the grid at the expense of grid transmission or one may choose to throw the dispersion into the long direction of the gun by the use of a bar grid. As Eq. 7b shows, the price paid for elimination of the dispersion in the width of the beam is a doubling of the dispersion in the long direction. However, if the gun is sufficiently long or if current uniformity across the width is crucial, this may be the preferred option.

When a high degree of beam uniformity is required, the fact that the dispersion $2 x_{\max}$ varies with current density eliminates designs in which a series of gun modules mounted transverse to the long direction of the gun make up the beam. Although the module spacing can probably be so arranged at one current level that the overlapping density distributions add up to a uniform beam, this condition does not hold at other current settings since x_{\max} is a function of V_g .

C. The Effect of the Thermal Velocity of the Electrons

The dispersion of sheet electron beams by thermal velocities has been discussed by Crumly¹⁵ and follows closely the theory developed by Cutler and Hines¹⁶ for axially symmetric beams. In these first-order theories which assume a Maxwellian emission the dispersion is calculated from a knowledge of only two electron trajectories. One, having a path designated $Y_e(z)$ leaves the edge of the cathode with zero transverse velocity as shown in Fig. 13. It defines the beam edge in absence of thermal velocities. The other trajectory $\sigma(z)$ leaves from the axis of the cathode with transverse velocity $\sqrt{kT/M}$, where T is the temperature of the emitter and follows the path indicated in Fig. 13. The ratio of the displacements Y_e/σ has associated with it a computed dispersion of the beam edge, which is shown in Fig. 14 for values of Y_e/σ up to 9.

For the planar beam of width W the trajectory Y_e is simply

$$Y_e = W/2 \quad (13)$$

The σ trajectory, in the field of the space-charge-limited diode portion of the gun up to the cathode grid has a trajectory

$$\sigma = 3d_{cg}^{2/3} z^{1/3} \sqrt{\frac{kT}{eV_g}} \quad (14)$$

Here d_{cg} is the diode spacing, T the temperature of the cathode, and V_g the potential on the grid. k and e are as usual the Boltzman constant and the charge on the electron.

At the grid the σ electron has a slope

$$\sigma_g = \sqrt{\frac{kT}{eV_g}} \quad (15)$$

which it is assumed it retains on passing through the grid. This assumption is true for an electron which passes through the center of a grid aperture. Beyond the grid the flow is in the uniform field and is given by Eq. 10 or Eq. 11 with d_{GA} replacing d and σ replacing $\tan\phi$. At the foil

$$\sigma_f = \sqrt{\frac{kT}{eV_g}} \left[3d_{cg} + 2d_{ga} \sqrt{\frac{V_g}{V_f}} \right] \quad (16)$$

The contribution to σ_f from the part containing d_{ga} is small for d_{ga} equal to the breakdown spacing calculated from Eq. 5 and is neglected in Fig. 15, which shows σ_f as a function of grid voltage with d_{cg} calculated from Eq. 3 for various emission densities. It can be seen that σ_f is small for large emission densities and only becomes significant at current levels below 1 mA/cm² where the gun would be operated cw. Unfortunately for economy in heater power and cost, such guns use relatively narrow cathodes,⁶ approximately 1 cm wide and hence V_e/σ can be as low 3. As Fig. 14 shows, such a beam has a very non-uniform current density distribution.

D. Gun Geometries

The planar triode, Fig. 16a, is conceptually the simplest geometry. When used with a thermionic emitter the size of the gun is patently limited by the power dissipation of the cathode. Other less obvious effects arise which are nevertheless important. With increasing width it becomes more difficult to keep a closely spaced low voltage control grid aligned parallel to the emitter to ensure that the emission remains constant. Although a close grid ideally maintains a uniform emission to the edge of the beam, the lens action produced by low voltage operation produces a considerable dispersion of the beam edge as Fig. 12 and the graph of Fig. 11 show. This dispersion can be shared between the length and width of the gun by the use of a grid consisting of round apertures. On the other hand, it can be directed into either direction by the use of a bar grid.

The use of a higher voltage and more distant grid reduces the lens action, however, at the expense of power dissipation on the grid and by

a thermal dispersion of the beam edge due to the increased low voltage path length. Moreover it becomes necessary to terminate the emitting area by Pierce-type focus electrodes to ensure uniform emission.¹⁷

Another solution to the production of large-area beams consists of using divergent flow geometries. Two variations are shown in Figs. 16b and c. Figure 16b shows a cylindrical low voltage beam forming region terminated by a curved grid at potential V_g which faces a planar foil. This geometry has the disadvantage that the trajectory of the electrons in the high field region is a function of V_g and hence the beam width W at the foil varies with current density. On the other hand, although the angle of divergence θ may be large in the beam-forming region, it is reduced considerably at the foil.

Figure 16c shows a divergent flow geometry produced between concentric cylinders of radius R_f and R_g in which the electron flow is entirely radial. Because of this the flow is independent of V_g and hence the same for all current settings. The dispersion produced by the grid lenses can however be greater than in the planar case since the electric field can be higher at the inner electrode. The field at the inner electrode is given by

$$E = \frac{V_f - V_g}{R_g} \frac{1}{\log(R_f/R_g)} \quad (17)$$

and depends very strongly on the radius R_g of the inner cylinder. The field may be minimized by preserving the ratio of $R_f/R_g = e = 2.71828$ between the two cylinders. Since the nominal beam width at the foil is related to R_f by

$$W = 2 R_f \theta_g \quad (18)$$

this choice may not always be available. The thermal velocity dispersion is reduced by Y_e , given by

$$Y_e = R\theta \quad (19)$$

grows with distance from the grid, whereas σ stays sensibly constant.

E. Pierce Electrodes

The design of the Pierce electrodes to ensure uniform emissions is not entirely straightforward since the anode beam forming electrode which carries the grid (see Fig. 17a) has a curvature outside the beam which conflicts with the form of the field in the acceleration region. The theoretical electrodes^{18,19} can, however, be modified as shown in Fig. 17b by the standard electrolytic tank technique¹⁸ to permit the Pierce anode electrode to conform to the desired equipotentials. It should be noted that the thin anode electrode can aggravate the grid heat dissipation problem.

IV. THE 5 cm x 125 cm ELECTRON BEAM GUN

The criteria discussed above were applied to the design of a cw electron beam gun operating at a voltage of 200 kV and delivering a uniform 125 cm long by 5 cm wide beam with a current density at the foil which could be varied from .1 mA/cm² to 1 mA/cm². A current uniformity of $\pm 5\%$ was required.

A divergent flow geometry similar to that shown in Fig. 16c was chosen with a minor modification to the beam generating portion. Figure 18 shows the geometry. The beam is obtained from a segmented planar tungsten matrix cathode .75 cm wide and 10% longer than the length of the foil. It is formed into a parallel flow by precisely machined Pierce electrodes. The anode slit is ungridded and adjoins a short field-free region in which some of the thermal electrons are trimmed off. This region is terminated by a cylindrical bar grid which effectively decouples the drift region from the radial accelerating region. The radial field is established by the wall of the vacuum vessel and the foil support structure on the one hand and the cylindrical bar grid and its support on the other hand.

The anode slit acts as a divergent cylindrical lens with a focal length given by Eq. 7b. Conditions are so arranged that the virtual line focus of this lens coincided with the common axis of the field forming cylinders. The beam therefore enters the radial accelerating field along field lines and produces a radial flow which is independent of the voltage on the control grid. The bar grid produces an axial dispersion which is a function of grid voltage; it leaves the distribution across the width of the beam unaltered. An allowance is made for the variable axial dispersion by making the beam generating region longer than the foil and by intercepting the nonuniform excess.

The cathode is conservatively loaded; with allowances for grid and foil interception the maximum loading is below 10 mA/cm². In practice the cathode has survived numerous catastrophic environmental changes and has reactivated to full emission each time.

Figure 19 is a photograph of the gun with the end cover of the vacuum chamber and the foil window removed. The gun is set up to deliver a horizontal beam.

Measurements of the current density distribution were made on a separate 20 cm long module of the gun on which the current density distribution at the end of the gun, in the interior, and at the joint of two cathode segments could be investigated. To avoid x-ray hazards these tests were conducted at low voltage by replacing the 30 kV equipotential with a rotatable cylindrical electrode. This electrode contained three small holes behind which Faraday cups were mounted.

Figure 20 shows the current density profiles measured at the above locations taken with the voltage on the gridded electrode constant at 400 V. The voltage on the rotating cylinders was varied from 400 volts to 20 kV volts. Higher voltage profiles were taken which were essentially the same as the 20 kV series.

The effect of thermal velocities is to be noted on these profiles and also the fall off in current density at the edge of the gun. The beam exhibits an asymmetry which is directly attributable to a .010" tilt in the cathode which occurred on heating to the operating temperature of 1200°K. The peaks which develop at the beam edge are due to the fringing field at the location where the grid bars are joined to the tunnel wall. The straight sides of the profiles also indicate that a small percentage of the thermal electrons are intercepted on the tunnel wall.

Figure 21 is a comparison of the measured 20 kV, "interior" current density profile of Fig. 20 with the profile computed by considering thermal velocities. Agreement between theory and experiment is good, showing that large area electron guns may be designed with a high degree of confidence.

ACKNOWLEDGEMENTS

The author wishes to thank Dr. G. R. Brewer, Dr. J. Bayless and Dr. J. E. Etter for many helpful discussions. The construction of the 125 cm long gun was under Dr. Etter's supervision.

REFERENCES

1. O. R. Wood, II., Proc. IEEE 62, 355 (1974).
2. H. Gallagher, J. Appl. Phys. 40, 44 (1969).
3. K. H. Loeffler, R. M. Schneider, J. R. Werning, "Development of a High Resolution Electron Gun for Airborne Electron Beam on Film Recorders", IBM Report #1 under Air Force Contract No. F33615-68-C-1045, Project # 6263 (1969).
4. M. Nasini, G. Redaelli, Rev. Sci. Instr. 42, 1765 (1971).
5. G. R. Brewer, "Ion Propulsion" (Gordon and Breach, New York, 1970) p. 123, Eqs.4-9.
6. W. A. Frutiger, J. R. Uglum, B. S. Quintal and S. V. Nablo, J. Vac. Sci. Technol. 10, 955 (1973).
7. N. G. Basov, Laser Focus 8, 45 (1972).
8. Field Emission Corporation, McMinnville, Oregon. Febetron E. Beam Generator.
9. C. A. Spindt, IEEE Conf. Record of 1973 Conference on Electron Device Techniques, p. 61.
10. G. Loda, T. DeHart, "Investigation of Pulsed Cold Cathode Electron Guns for use as a Laser Discharge Sustainer", Physics International Report PIRF-326 prepared for Defense Nuclear Agency as Report DNA 2777F (1972).

11. J. R. Bayless, R. C. Knechtli, G. N. Mercer, IEE QE-10, 213 (1974).
12. L. Cranberg, J. Appl. Phys. 23, 518 (1952).
13. K. Amboss, IEEE ED-11, 479 (1964).
14. C. J. Davisson, C. J. Calbick, Phys. Rev. 38, 585 (1931).
15. C. B. Crumly, "Thermal Velocity Effects in Two-Dimensional Electron Beams", Technical Report 457-2, Stanford Electronics Laboratory, Stanford University (1958).
16. C. C. Cutler, M. E. Hines, Proc. I.R.E. 43, 307 (1955).
17. R. J. Lomax, J. Electron Control 6, 39 (1959).
18. J. R. Pierce, "Theory and Design of Electron Beams (Van Nostrand, Princeton, New Jersey, 1954), 2nd Ed, Chapter 10.
19. D. E. Radley, J. Electron Control 4, 125 (1958).

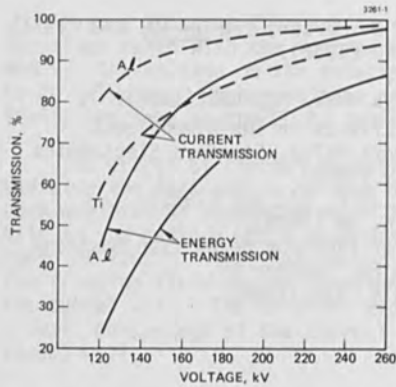


Fig. 1. Electron transmission through 0.001 in. thick aluminum and titanium foil as a function of beam energy.

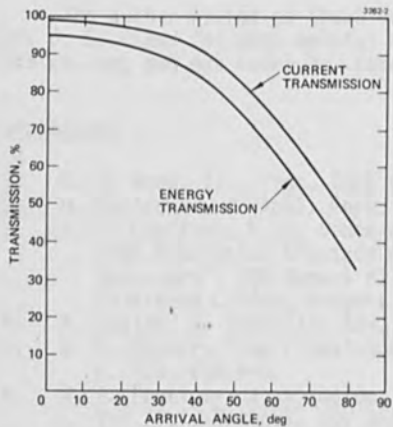


Fig. 2. Electron transmission through 0.001 in. thick aluminum foil at 250 kV as a function of angle of arrival at the foil.

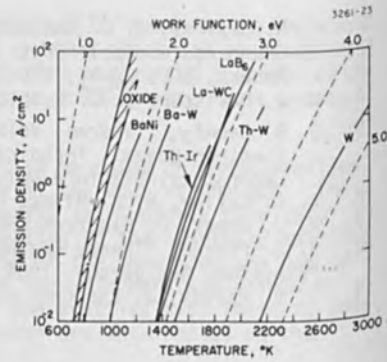


Fig. 3. Saturated emission current density versus temperature for several types of cathodes (solid lines). The Ba-W line is representative of the impregnated tungsten cathode. The dashed lines are drawn for constant values of work function.

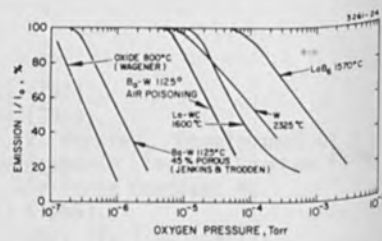


Fig. 4. Reduction in emission of various cathodes as a function of oxygen pressure. Also shown is the air poisoning characteristic of a Ba-W cathode at 1125°K.

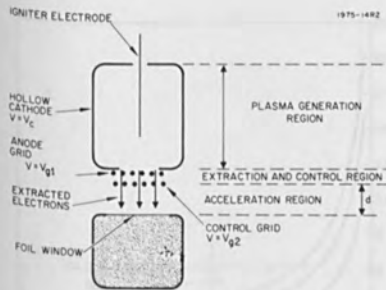


Fig. 5. Schematic of a plasma cathode electron gun.

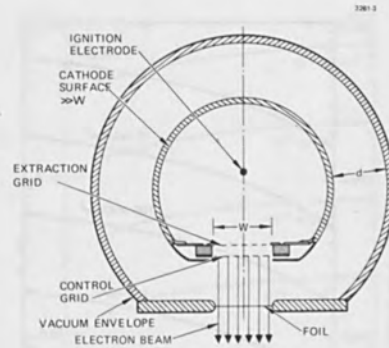


Fig. 7. Schematic cross-section of a cylindrical high voltage plasma gun design.

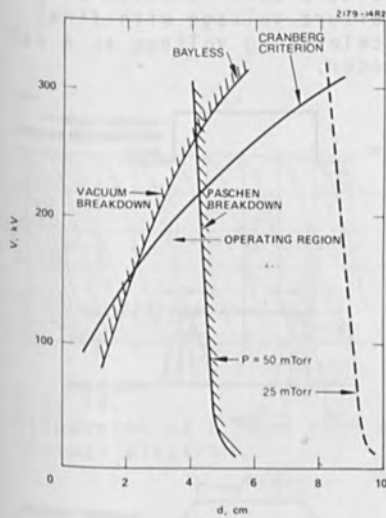


Fig. 6. Low pressure breakdown characteristics for $p = 25$ and 50 mTorr.

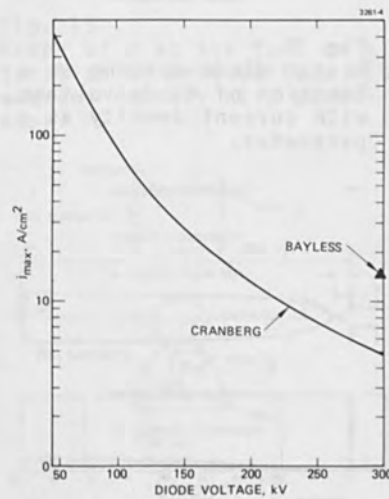


Fig. 8. Maximum space-charge limited planar diode current as a function of the breakdown threshold voltage.

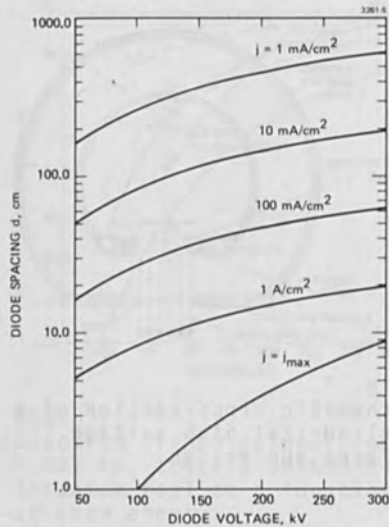


Fig. 9. Planar diode spacing as a function of diode voltage, with current density as a parameter.

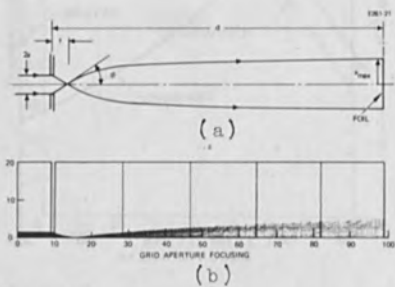


Fig. 10. Focusing produced by the lens effect of an aperture. (a) Divison Calbick model. (b) Results obtained by computer.

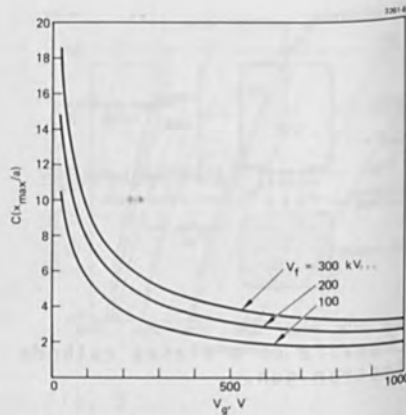


Fig. 11. Beam dispersion for a circular aperture as a function of grid aperture voltage with final accelerating voltage as a parameter.

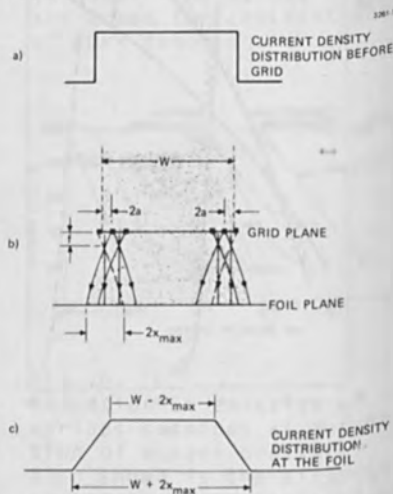


Fig. 12. The effect of the dispersion produced by the grid aperture on the current density distribution.

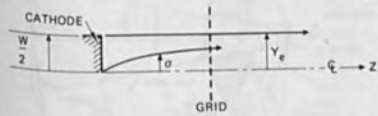


Fig. 13.
The paths of the trajectories $y_e(z)$ and $\sigma(z)$ in the vicinity of the cathode.

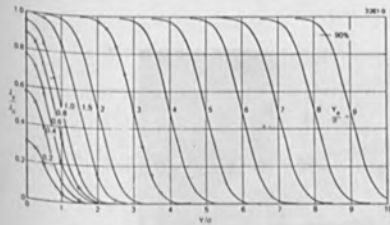


Fig. 14.
Dispersion of a beam edge by thermal electrons.

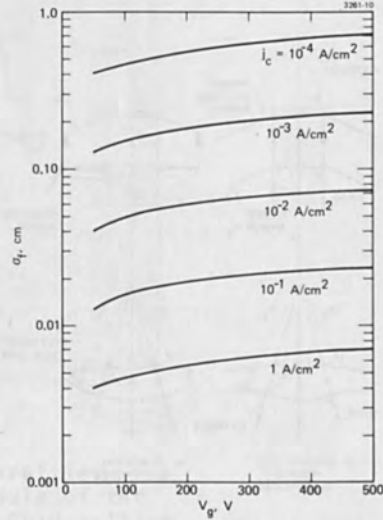


Fig. 15.
Graph of σ at the foil as a function of grid voltage with current density as a parameter.

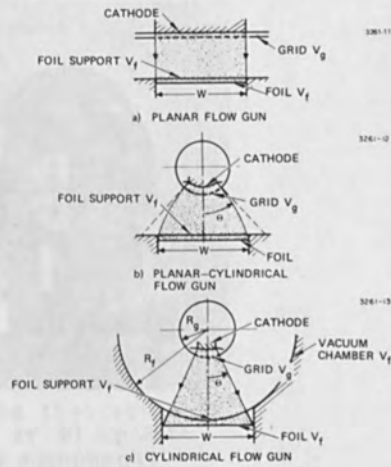


Fig. 16.
Electron optical schemes for producing large area flows.

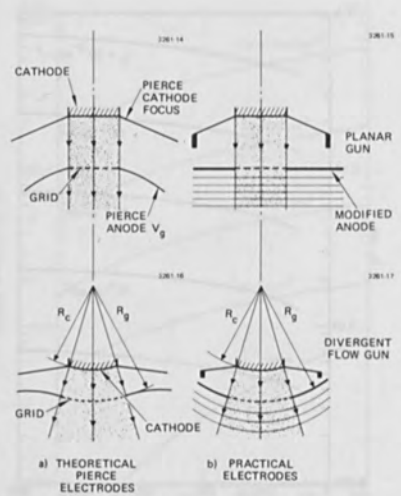


Fig. 17. Theoretical Pierce electrodes for planar and practical divergent cylindrical flows.

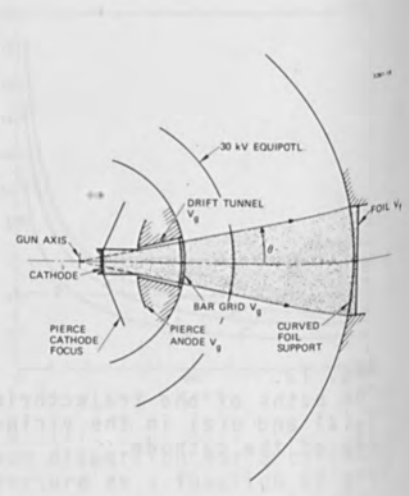


Fig. 18. Schematic of the geometry of the electron gun built to produce a $5 \times 125 \text{ cm}^2$ beam.

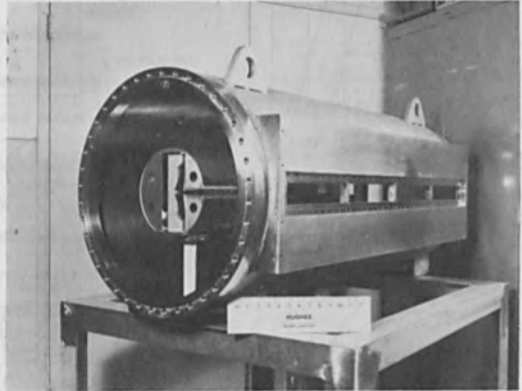


Fig. 19. Photograph of the partially assembled $5 \times 125 \text{ cm}^2$ electron beam gun.

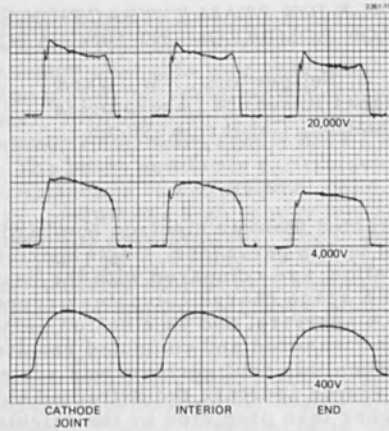


Fig. 20.
Current density profiles
measured on a module of the
 $5 \times 125 \text{ cm}^2$ gun. Grid voltage
 $V_g = 400$ volts.

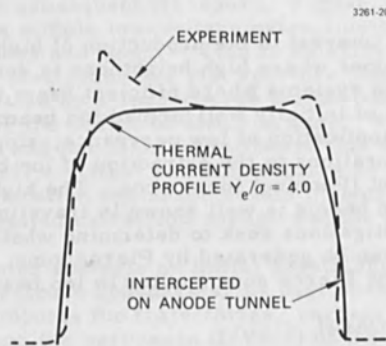


Fig. 21.
Comparison of the theoretical
current density at 20 kV with
that measured at interior
location.

LOW PERVEANCE ION BEAM EXTRACTION FROM AN ELECTRON BOMBARDMENT DISCHARGE

R. L. Seliger and J. W. Ward
Hughes Research Laboratories
Malibu, California 90265

ABSTRACT

Ion beams extracted from an electron bombardment (Penning) discharge by low perveance, single aperture Pierce electrode configuration, are compared with the beam properties predicted by a space charge computer program. For a 1 mm diam source aperture, and an electron perveance of $1 \times 10^{-8} \text{ AV}^{-3/2}$, the measured and computed results are in good agreement. When this configuration was scaled up to have a 4 mm diam source aperture the extracted current was as much as 40% higher than predicted by the calculated electron perveance of $1 \times 10^{-8} \text{ AV}^{-3/2}$. In the case of an electrode configuration with a calculated electron perveance of $3.5 \times 10^{-8} \text{ A/V}^{-3/2}$, that was also scaled to a 4 mm diameter source aperture, the extracted current was also 40% higher than predicted. In the latter case at 70 kV a maximum beam current of 4.3 mA (or argon) could be extracted with 0.8 A of discharge current. Plasma sheath instabilities occurred at currents above ~ 2 times the calculated perveance.

INTRODUCTION

There is a growing interest in the production of high quality ion beams. In ion microscopes where high brightness is desired and in complex ion implantation systems where efficient beam transport is required, the generation of initially well formed ion beams is essential. This paper studies the application of low perveance, single aperture Pierce electrode configurations to the extraction of ion beams from an electron bombardment (Penning) ion source. The high quality of Pierce guns for electron beams is well known in traveling wave tube applications. Our investigations seek to determine whether similarly high quality ion beams can be generated by Pierce guns, and just how well the design theory for Pierce guns applies to ion beam extraction.

CONVENTIONAL APPROACH

Before considering the low perveance electrode configurations, it is useful to review one conventional approach to high energy ion beam formation. Figure 1 presents the top view of a 150 kV ion implantation

system. To meet the requirement of good beam collimation at the target, such a system is typically three to four meters long. For efficient beam transport over this long path which includes the mass analyzer, deflection plates for beam rastering and drift regions, the initial stages of beam formation must be of very high quality. That is, at exit of the accelerator the beam should have a narrow angle and low aberrations. The beam emittance (or trajectories) should also be matched to the acceptance of the subsequent column. The implantation system of Fig. 1 forms the high energy ion beam in three stages - extraction, focusing, and acceleration. The beam is not of very high quality and some current is lost along the way to the target. Beam transmission is particularly poor at high beam currents and/or low beam voltages, indicating that space charge effects are not accounted for systematically.

An analysis of the 10 kV/in. linear accelerator¹ showed that it was not well suited for accelerating ion beams with currents in excess of 1.25 mA of protons. The focusing forces in this linear accelerator were strong at the entrance, but could not counterbalance the divergent spacecharge forces in the linear region. The analysis also predicted that a considerably higher and nonlinear axial voltage gradient would be required to accelerate ion beams in order to maintain their narrow angles.

A consideration of the initial low voltage beam extraction employed in the system in Fig. 1 shows that while it is easy to fabricate electrodes that will extract several milliamperes of ion current from a discharge ion source, the quality of the extracted beam will probably be inadequate for subsequent transport. Figure 2 presents the ion trajectories for a simple low-voltage extraction system that was analyzed by Amboss and Nudd.² This is an axisymmetric configuration in which the electrodes are just aperture plates. The ion trajectories are calculated by a spacecharge digital computer program that was developed for the design of electron guns. A principal difference between electron and ion beam formation is that when ions are extracted from a plasma only a virtual emitting surface or plasma sheath exists. In operation the location and shape of this plasma sheath varies as a function of the applied extraction voltage and the plasma density.

In the computer analysis an initial sheath shape was assumed, along with the electrode boundaries, as part of the input data. The program then computes the trajectories, current density profile, equipotentials, and the perveance ($I/V^{3/2}$) of the extracted beam in a self-consistent manner assuming space-charge-limited flow at the emitting surface. The electrode configuration of Fig. 2 is a so-called high perveance extraction. For electrons, the perveance is about $3 \times 10^{-6} \text{ IV}^{-3/2}$; for argon ions this corresponds to about 3.8 mA at 5 kV, which is a reasonable current for the first stage of beam formation in Fig. 1. The characteristic that makes this configuration have high perveance is the close spacing of the electrodes, relative to the

diameter of the emitting surface. But this close spacing causes significant difficulties in determining an electrode configuration that produces a high quality narrow-angle beam. One complication is that the overall beam quality is strongly affected by the assumed shape of emitting plasma surface (or sheath) and by the strong anode lens effect of the extraction aperture. For the case shown in Fig. 2, the sheath shape was varied until the current density of the extracted beam agreed with the substantially uniform ion arrival rate expected from the plasma. The beam shape is highly sensitive to the discharge conditions as is observed in practice.

The electrode configuration of Fig. 2 was intended for electric thrusters in which beam transport after acceleration is not required. This extracted beam would not be well suited for subsequent acceleration and transport in an ion implantation system. The aberrations are high as is evidenced by the trajectory crossovers. Also, this extraction system produces a beam which strongly diverges a short distance downstream of the extraction electrode, typical of high perveance configurations. Thus, even if the aberrations could be reduced, say by employing more elaborate electrode shapes, the difficult problems of refocusing and accelerating the beam would remain.

LOW PERVEANCE EXTRACTION

The approach of high voltage, low perveance ion extraction studied in this paper is intended to eliminate the problems associated with high perveance, low voltage extraction systems. Figure 3 shows an example of a low perveance electrode configuration ($p_{e-} = 1 \times 10^{-8} \text{ AV}^{-3/2}$).³ This configuration was taken from an electron gun designed by Amboss.³ In this low perveance configuration, the spacing between the electrodes along the axis is about eight times the diameter of the emitting area. The focus and extraction electrodes are specially shaped to achieve, along the beam edge, a potential distribution which closely matches the theoretical Langmuir potential for a spherical diode.

For the geometry shown in Fig. 3, the computed variation in current density was less than 5% across the planar emitting surface. The ion trajectories for this low perveance electrode configuration are of the high quality that is desired for beam transport systems. The beam is quite laminar (i.e., has very few trajectories crossing over each other) and has a narrow angle.

Once an electrode configuration such as that shown in Fig. 3 is determined, all dimensions can be scaled by the same factor without changing the perveance. The two dimensions that are most critical in these applications are the diameter of the extraction aperture which controls the ion source current density for a given extraction voltage, and the minimum interelectrode spacing which determines the maximum extraction voltage.

ELECTRODE CONFIGURATIONS STUDIED

The electrode configuration of Fig. 3 was fabricated in two sizes which correspond to cases A and B in Fig. 4. For case A the extraction aperture diameter d_A is 1 mm, and the minimum electrode spacing is ~ 1.1 mm. At the maximum operating voltage of 20 kV, the predicted argon current is 0.1 mA, and the ion source current density is 12.3 mA/cm^2 . Case B corresponds to a version scaled four times that of case A. The source current density is significantly reduced. The maximum extraction voltage is increased to 100 kV, at which time the argon current is 1.2 mA, and the source current density is 9.2 mA/cm^2 .

In an effort to increase the beam current, a third electrode configuration (C) was fabricated. It employs the same 4 mm diam extraction aperture as in case B, but with an increased perveance of $3.5 \times 10^{-8} \text{ AV}^{-3/2}$. For this case the maximum argon beam current is predicted to be 4.5 mA at a source current density of 37 mA/cm^2 .

All three electrode configurations were set up to extract argon ion beams from a hot filament electron bombardment discharge. The ion source is shown schematically in Fig. 5. The anode voltage was 80 V in all cases. The magnetic field was ~ 200 G.

The insulator length was ~ 2 in. for case A and 12 in. for cases B and C. In these latter cases the ion source and focus electrode were supported on the end of a re-entrant tube inside of the insulating cylinder. The ion source power supplies and gas feed valve were isolated for 100 kV operation. Each electrode configuration was found to operate at stable, reproducible points. After initial high voltage conditioning, each could operate at its maximum rated voltage without arcing.

EXPERIMENTAL RESULTS

Data was taken on the three electrode configurations to determine their perveances experimentally. This was accomplished by measuring the extracted beam current and intercepted ion current as a function of the total extraction voltage at a constant ion arrival rate. These measurements are then repeated at other ion arrival rates obtained by varying the discharge current while maintaining a constant discharge voltage. The beam current was measured on a downstream collector which was biased positively to suppress all secondary electrons. The results of these experiments are shown in Figs. 6, 7, and 8 for configurations A, B and C, respectively. The straight lines in each of these figures are the computer calculated perveances for the electrode geometries in which a planar plasma sheath boundary was assumed. For both geometries the Pierce focus electrode made the usual $67\text{-}1/2^\circ$ angle with the beam edge. It is seen that all the curves exhibit the expected saturation regime when the extracted voltage is high enough to extract

and focus the fixed ion arrival rate. In all cases the plasma surface is changing its position and shape, so that the applied electric field is just sufficient to carry away the number of ions which arrive from the plasma. It was expected that the plasma sheath would have its design position and shape when the intercepted current was a minimum. Reference to Fig. 6 shows this to be the case for configuration A. The fact that the current follows the perveance line for voltages below the design value was somewhat surprising, since it would be expected that the plasma sheath would advance and create a higher perveance geometry than that calculated. It appears that the small aperture diameter (1 mm) for this configuration has anchored the plasma boundary at the design position, and has created a situation analogous to that described in Ref. 4 in which a grid was used to shape and anchor the plasma boundary.

This behavior was not observed for the larger aperture (4 mm) configurations B and C. In these geometries for voltages below the saturation regime, there is an extremely rapid rise in the intercepted current. A plasma instability occurs which shorts out the high voltage power supply. It is also seen that configurations B and C have experimental perveance values that are approximately 40% higher than the design values. The experimental perveance is defined by points of minimum extraction electrode interception current.

There are several explanations for why the measured perveance values exceed the calculated values. The effects of initial ion velocities, the precise shape, and the actual location of the plasma sheath are examples of possible causes of increased perveance. Further analysis of these effects, together with experimental measurements of ion beam current density profiles are hoped to resolve the differences. Although such additional investigations will be required before an accurate design theory is established for ion guns, it is felt that the results presented have demonstrated the advantages of using low perveance extraction for applications where high quality narrow angle ion beams are required.

REFERENCES

1. R. L. Seliger, "Acceleration of Ion Beams with Spacecharge," Presented at the 11th Symposium on Electron, Ion and Laser Beam Technology, May 1972.
2. R. L. Seliger, G. R. Nudd, G. R. Brewer, and K. Amboss, "Analysis of Expected Thrust Misalignment of Kaufman Thrusters," *J. of Spacecraft and Rockets*, 7, No. 4, April 1970, pp. 422-428.
3. K. Amboss, Hughes Research Laboratories, private communication.
4. O. Reifenschweiler, K. Fröhner, "A New Principle of Ion Extraction from a Gas Discharge Plasma," *Nucl. Instr. Methods*, 30, 298 (1964).

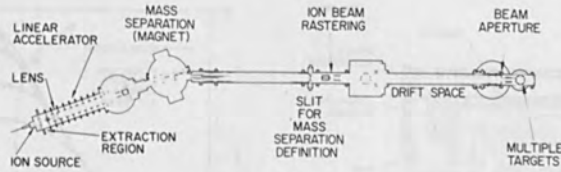


Fig. 1. 150 kV ion implantation system.

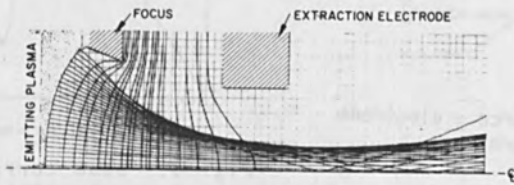


Fig. 2. High perveance plasma extraction
 $p_e \sim 3 \times 10^{-6} AV^{-3/2}$.

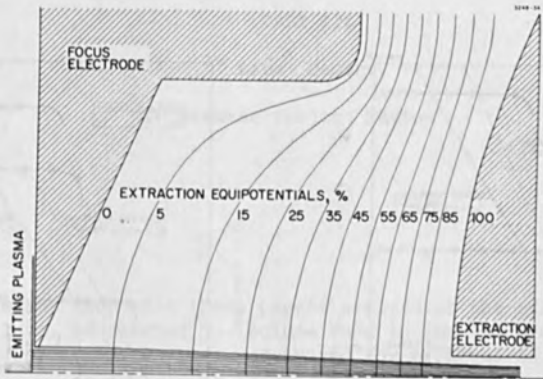


Fig. 3. Low perveance plasma extraction ($p_e = 1 \times 10^{-8} AV^{-3/2}$).

3248-29

CONFIGURATION	D_A (mm)	P_e ($A/V^{3/2}$)	V_{MAX} (kV)	I_{MAX} (mA) ARGON	J_{MAX} (mA/cm^2) ARGON
A	1.0	1×10^{-8}	20	0.1	12.3
B	4.0	1×10^{-8}	100	1.2	9.2
C	4.0	3.5×10^{-8}	100	4.5	37.0

Fig. 4. Calculated performance of three low perveance electrode configurations.

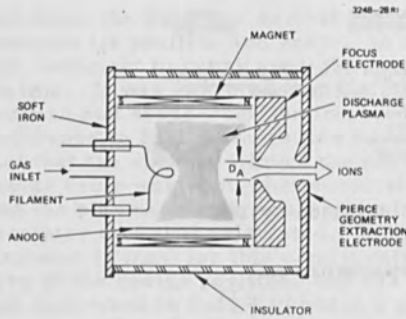


Fig. 5. Ion source - electrode configuration.

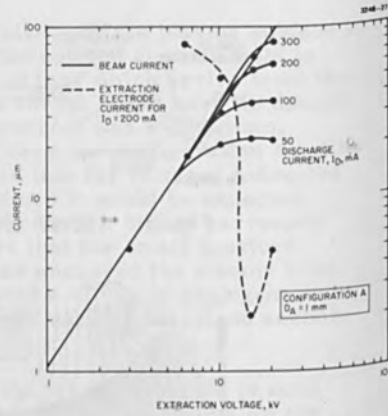


Fig. 6. Beam current versus extraction voltage for case A: $D_A = 1 \text{ mm}$, $p_{e-} = 1 \times 10^{-8} \text{ AV}^{-3/2}$.

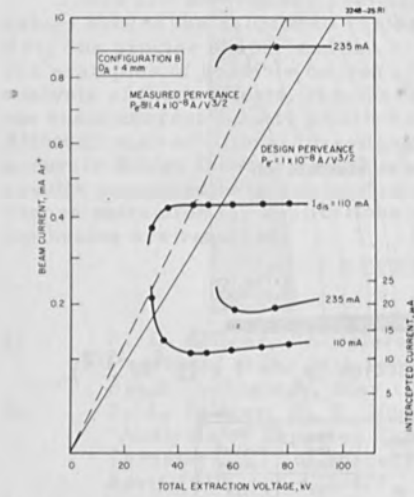


Fig. 7. Beam current versus extraction voltage for case B: $D_A = 4 \text{ mm}$, $p_{e-} = 3.5 \times 10^{-8} \text{ AV}^{-3/2}$.

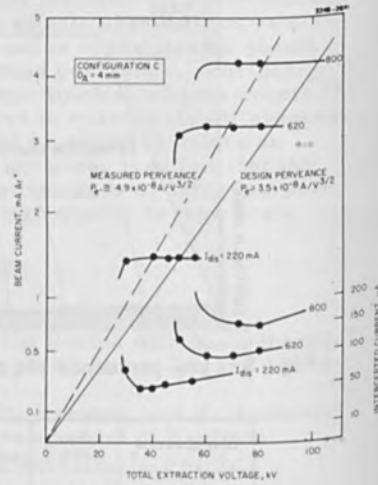


Fig. 8. Beam current versus extraction voltage for case C: $D_A = 4 \text{ mm}$, $p_{e-} = 3.5 \times 10^{-8} \text{ AV}^{-3/2}$.

ALIGNMENT BY X-RAY METHOD OF AN ELECTRON PROJECTION SYSTEM

Bernard PAT

THOMSON-CSF, Laboratoire "Recherches de Technologie"
Boulevard de Courcouronnes, 91406 - ORSAY (France)

ABSTRACT

The X-ray alignment method of an electron projection system is described in detail. Results show that registration accuracy better than 0.1 micron can be readily obtained. Fabrication of low-impedance light-effect transistors demonstrate the compatibility of permanent alignment marks of tantalum oxide with the high-temperature processing of low-impedance devices.

PART III

Late Papers

Diverse Subject Matter

Despite the fact that these papers arrived at the Editor's desk much too late, he elected to include them in the Proceedings. The papers, however, are neither referenced nor arranged in any specific order.

- Alignment is achieved by sequential displacement of the mask with respect to the wafer through the use of piezo electric transducers acting in their direction to provide X, Y and Z corrections.
- The alignment signal is an X-ray signal generated from permanent alignment marks made of tantalum oxide deposited on the wafer.



Fig. 2. Schematic diagram of the investigated structure.

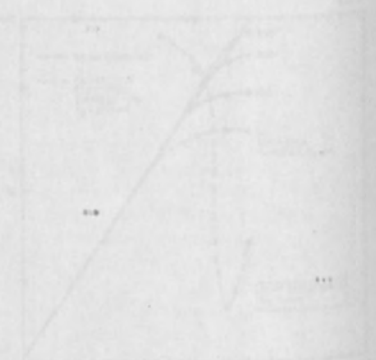


Fig. 3. Dependence of the investigated parameter on the independent variable.

PART III

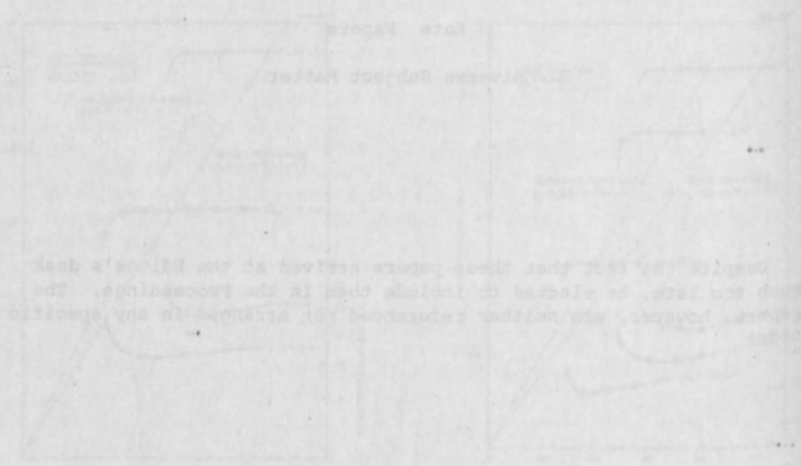


Fig. 4. Detailed technical drawing or graph showing multiple curves and parameters.

MASK ALIGNMENT BY X-RAY METHOD IN AN ELECTRON PROJECTION SYSTEM

Bernard FAY

THOMSON-CSF, Laboratoire Central de Recherches
Domaine de Corbeville, 91401 - ORSAY (France)

ABSTRACT

The X-ray alignment method in an electron projection system is described in detail. Results show that registration accuracy better than 0.2 micron can be readily obtained. Fabrication of ion-implanted field-effect transistors demonstrate the compatibility of permanent alignment marks of Tantalum oxide with the low temperature processing of ion-implanted devices.

INTRODUCTION

The need for a fast, parallel exposure system for imaging high resolution mask patterns with submicron features onto resist coated Silicon wafers is becoming of utmost importance now that electron-beam pattern generators are commercially available. At Thomson-CSF, we have been developing an electron projection system with the goal of overcoming the through-put limitation of most electron beam pattern generators (1). The emphasis being on submicron resolution our system differs from other existing systems (2), (3), (4), by the following.

- 1 - The focusing magnetic field is constant and uniform, with a homogeneity of better than 10^{-4} over a 2" diameter. A static magnetic field is preferable from the standpoint of best image resolution and minimum image distortion.
- 2 - Alignment is achieved by mechanical displacement of the master mask relative to the wafer through the use of piezoelectric transducers acting in three directions to provide X, Y and θ corrections.
- 3 - The alignment signal is an X-ray signal produced from permanent alignment marks made of Tantalum oxide deposited on the wafer.

This paper presents the latest results obtained with our prototype system, with special emphasis on the X-ray alignment method.

SYSTEM DESCRIPTION

Figure 1 is a view of the experimental projection system. Figure 2 shows the mask positioning system. The master mask is attached to a movable platform which is actuated by means of three stacks of piezoelectric transducers, each one providing ± 10 microns of displacement with a sensitivity of better than 0.1 micron. Two alignment marks are located roughly at the intersection of the three axes of displacement.

The wafers, 2" in diameter, are inserted into the system on a loading bar holding 4 samples. They are prepositioned on the loading bar to better than ± 10 microns with the help of an optical prealigner.

The X-ray alignment method is based on the property that a small fraction of the electron energy absorbed by any target is converted to X rays. The intensity of X-ray emission (Bremsstrahlung) is proportional to the atomic weight of the target. A good contrast is thus obtained with a Tantalum ($Z = 73$) mark over silicon ($Z = 12$). For better stability Tantalum pentoxide marks are preferred.

Figure 3 is a schematic of the X-ray alignment system.

A single UV lamp is used for alignment and for exposure. At the present time, alignment is done manually with an average duration of 5 minutes. Thus a removable attenuator is necessary to prevent excessive exposure during the alignment phase. The X ray signal is detected through the wafer of thickness 200 to 250 microns with a gas flow proportional counter. A standard nuclear instrumentation chain provides a digital and analog display of the detector signal.

In the manual alignment mode, the operator adjusts the voltage applied to each transducer sequentially in order to maximize the alignment signal. Alignment accuracy of 0.2 μm can be obtained in 5 minutes typically. Figure 4 shows an experimental alignment curve obtained from an X-Y recorder, with an attenuation ratio of 40 : 1. The Y signal is the integrated X ray signal. The X signal (the voltage applied to the piezoelectric transducer) represents the displacement of the master mask. The displacement scale is non-linear due to hysteresis effects. The alignment mask geometry is a coded pattern with a 3 micron minimum linewidth resulting in a 6 micron base width for the correlation peak displayed.

In the automatic alignment mode (in preparation), alignment will be done digitally, also in a sequential mode. The expected alignment time is 1 minute for 0.1 μm accuracy.

FABRICATION OF THE ALIGNMENT MARKS

The fabrication of the alignment marks does not require any additional masking step. It requires only two operations to be performed after the first masking (thick oxide window).

- a) - Lift-off deposition by sputtering of 1500 \AA of Tantalum after oxide etching and before removal of resist.
- b) - Oxidation of Tantalum to Tantalum oxide during thin oxide regrowth, if required by the process. Otherwise the oxidation can be performed at low temperature (600°C) for several hours.

A software program has been developed for generating superposable master masks with the electron beam pattern generator (1). This program generates identical alignment marks for each mask. A special sample holder allows accurate placement within one micron of the alignment marks on successive master masks. This small error is just added to the prepositioning error and can therefore be neglected.

ALIGNMENT TEST RESULTS

Alignment of successive masks depends critically upon the absence of non reproducible image distortion.

An important source of image distortion in our system is found in the circular rim of the wafer holder, which has a thickness of 0.5 mm ; the interelectrode spacing is 6.5 mm.

Image displacement is significant in the vicinity of the rim and decreases exponentially with the distance from the rim.

The distortion is non reproducible because the wafer position, with respect to the rim, is only reproducible to within ± 10 microns. This theoretically limits the usable area on the 2" wafer to a circle of diameter 35 mm for 0.1 μm distortion.

The result of a superposition test carried out with a single mask (to eliminate mask-to-mask errors) is shown in Figure 5. The alignment error vectors measure the relative position of two successive images of a test pattern.

The first image, defined by lift-off, is a pattern of sputtered Tantalum 1500 Å thick including the two alignment marks.

The wafer is then coated with a new resist layer and a second image is formed in the resist after alignment using the Tantalum marks.

It can be seen that the alignment accuracy over a circle of diameter 32 mm is better than 0.2 μm which is the confidence level of the optical measuring technique. Figure 6 is an SEM photograph showing the superposition of two images of a set of 1 micron lines spaced 2 microns apart for which an alignment error of 0.15 micron can be measured.

TRANSISTOR FABRICATION RESULTS

The successful fabrication with the projection system of Schottky gate ion-implanted FET's requiring 4 masking levels has demonstrated the possibilities of the X ray alignment method. The permanent Ta₂O₅ alignment marks were not affected by the fabrication process and they did not affect the characteristics of the transistors made. The highest temperature to which the wafer with its alignment marks was raised was 1000°C.

The stability of the Ta₂O₅ marks was checked independently for higher temperature processes such as wet oxidation at 1100°C and Boron diffusion at 1150°C (for 2 hours in each case).

Each dice contained two transistors as shown in figure 7 for a completed cell. The smallest transistor is a 2-1-2 micron structure and the larger one is a 3-1-3 micron structure. Only one wafer has been completed so far, three are awaiting final processing. Because of uneven quality of the particular set of master masks used and process difficulties the yield obtained was very low. Out of 70 usable cells only 2 smaller and 33 larger transistors had measurable characteristics. Figure 8 shows the transistor characteristic curves measured on a typical transistor of the larger geometry.

CONCLUSION

The fabrication of working transistors with an electron projection system has demonstrated the potential of this method and in particular of the X ray alignment scheme. More work is required to demonstrate the ability of the system to produce submicron devices. Automation of the alignment sequence should be achieved shortly.

REFERENCES

- 1 - J. TROTEL , this issue
- 2 - T.W. O'KEEFE
IEEE Trans. Electron Devices. ED-17 (6), 465-469, (1970)
- 3 - W.R. LIVESAY
J. Vac. Sci. Technol. Vol.10, n°6, 1028-1032, (1973)
- 4 - J. SCOTT, this issue



Figure 1

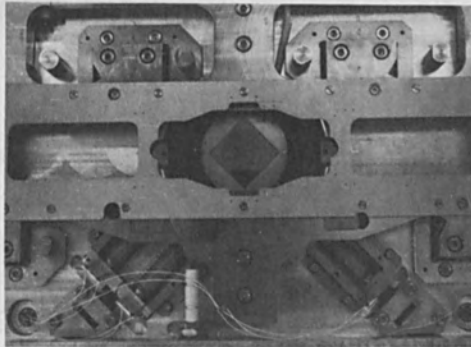


Figure 2

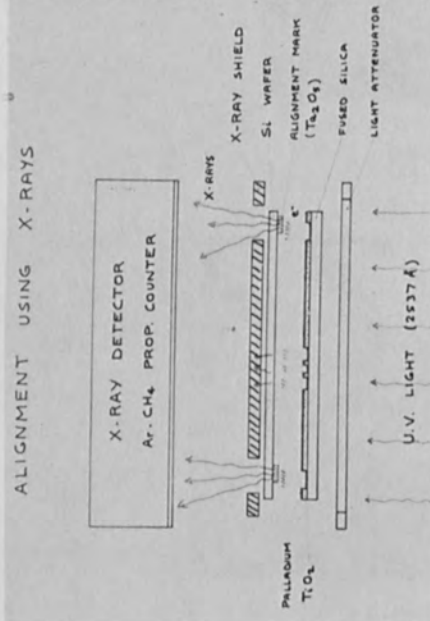


Figure 3

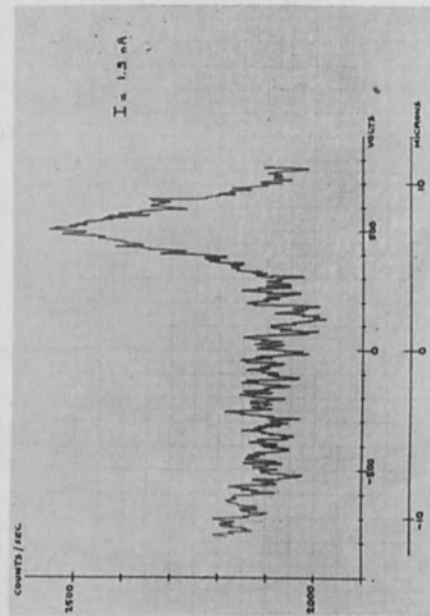


Figure 4

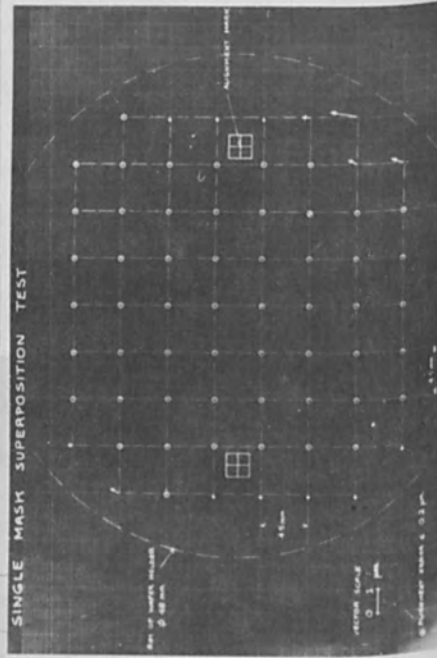


Figure 5

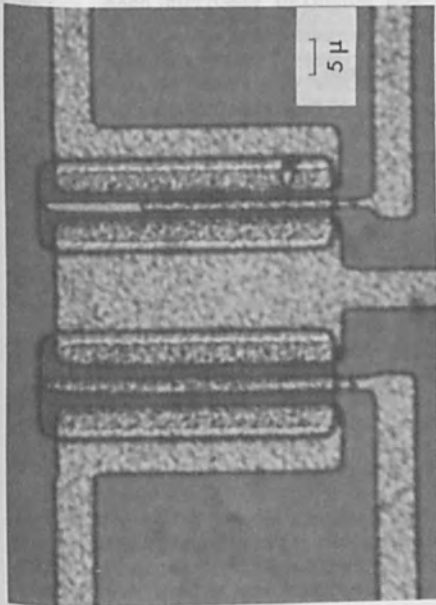


Figure 7

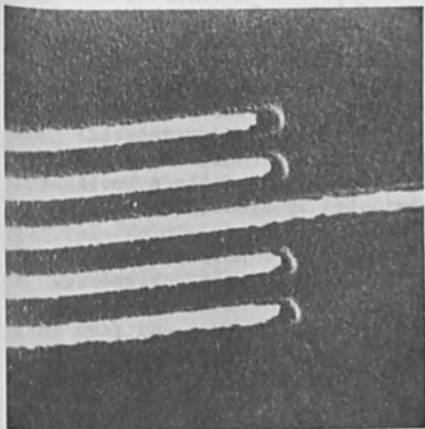


Figure 6

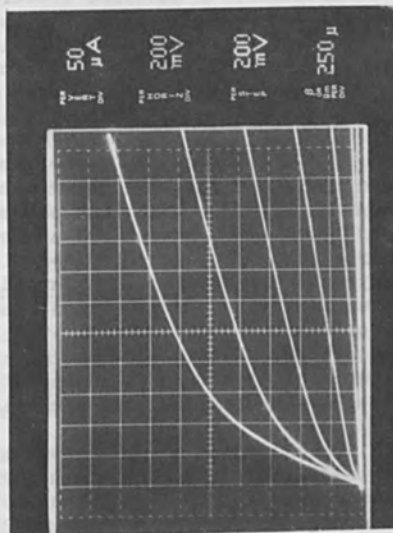


Figure 8

A LARGE FIELD DEFLECTION SYSTEM FOR SCANNING ELECTRON BEAM
TECHNOLOGY

G. Owen and W.C. Nixon

Cambridge University Engineering Department
Trumpington Street
Cambridge
CB2 1PZ

A low aberration post-lens single-deflection system for use in scanning electron beam microfabrication instruments is described. The design philosophy adopted has been to choose a coil geometry which gives extremely small values of the uncorrectable aberrations. It is then only necessary to dynamically correct for field curvature. A combined electrical and mechanical method has been used to align the deflection coils. The measured performance comes up to predicted expectations, being 30 times better than that of conventional pre-lens double-deflection systems, in terms of spot size.

Introduction

Low aberration probe forming systems, working over image fields of 1 mm x 1 mm or more are required for use in scanning electron beam microfabrication instruments. In a previous paper (Owen and Nixon, 1973) a conventional probe forming system, incorporating pre-lens double-deflection has been theoretically analysed. Two conclusions emerged from this analysis. Firstly, it was found that the dominant aberrations were produced by the deflection coils, rather than the lenses. Secondly, it was found that spherical aberration was not a limiting factor, so there was no reason why post-lens single-deflection should not be used in deflection systems working over fields of 1 mm x 1 mm or more.

A design was proposed for a low aberration post-lens single-deflection system which would produce a spot size 30 times smaller than those produced by conventional instruments. The design philosophy adopted was to minimise the uncorrectable aberrations (anisotropic astigmatism and coma) by a suitable choice of coil geometry, without regard to the magnitude of the correctable aberrations. The latter would be eliminated by dynamic correction.

Such a deflection system has now been constructed, and this paper describes the problems involved and the performance obtained.

The deflection coils

A schematic diagram of the coil geometry adopted, called the 'improved' geometry is shown in Fig.1 - this geometry gives rise to extremely small values of the uncorrectable aberration coefficients. (Anisotropic astigmatism and coma.) Note that only one pair of coils has been shown in the diagram. Of the correctable aberrations, isotropic astigmatism was negligible so dynamic correction of this aberration was not necessary. However, field curvature was significant, and so this aberration was eliminated dynamically. The non-linearities resulting from the distortions amounted to 1.6% - no correction was made for these.

Physical realisation of the 'improved' geometry necessitated interleaving the windings, as is shown in Fig.2. The mean dimensions of the windings correspond to those shown in Fig.1.

An important problem was the alignment of the coils. For small deflections, alignment is not important, but for deflections of 0.5 mm or more, it is essential. Ideally, alignment would be carried out by moving each pair of coils independently. However, the construction of the 'improved' coils ruled this possibility out. Instead, a combined electrical and mechanical alignment procedure was adopted.

The combined electrical and mechanical alignment procedure

Fig.3 shows the principle of the procedure. Fig.3a shows the unaligned coils of the X deflection system. The coils were moved a distance d in the X direction to produce the situation depicted in Fig.3b. The coils were then electrically unbalanced by a ratio to give the aligned arrangement shown in Fig.3c.

The progress of the alignment procedure was monitored using the method shown in Fig.4. Fig.4a shows the system under consideration with the coils unexcited. Fig.4b shows what happens when the coils are excited in opposition. The coils then act as a combination of a stigmator and a lens, and produce two line foci instead of the original point focus. If the excitations of both coils are reversed, the line foci reverse, as is shown in Fig.4c. To monitor the progress of the alignment procedure, the coils were connected in opposition and excited with a 100 Hz square wave. The lens was excited so that the upper line foci appeared on a screen at the bottom of the column. The two upper line foci then appeared to be displayed simultaneously. They only intersected symmetrically when the coils were aligned, as is shown in Fig.5.

Both pairs of coils were aligned in this way - the effectiveness of the alignment procedure will be discussed later.

The dynamic correction for field curvature

The correction was applied by altering the excitation of the final lens of the system. When the spot was deflected to the point (X_s, Y_s) , the lens excitation was decreased by an amount:

$$\Delta I = \frac{q_3 I}{2Cc} \{X_s^2 + Y_s^2\}$$

where q_3 (metres)⁻¹ was the field curvature coefficient of the deflection system

Cc (metres) was the coefficient of chromatic aberration of the final lens

I was the lens current, with the lens focused to an on-axis point in the image plane

A function proportional to $(X_s^2 + Y_s^2)$ was produced from the scan generator outputs using an analogue multiplier and an adding circuit.

The performance of the 'improved' deflection system

The criterion of performance was the 'spot plot'. The spot plot of a spot at (X_s, Y_s) is a polar plot of the increase in diameter of the spot caused by deflecting it from $(0, 0)$ to (X_s, Y_s) .

The spot at $(0, 0)$ was round, being limited only by Gaussian spot size and the spherical aberration of the final lens - corrugation and ellipticity astigmatism were eliminated using a stigmator, and misalignment coma was negligible.

Spot size was determined from edge scan measurements, the spot diameter being taken as the 1% to 99% rise distance. Under the experimental conditions used, the spherical aberration of the final lens, and vertical movement of the scanned edge (in practice a large aperture) combined to give a total experimental error of ± 0.2 micron in measured spot plot diameter.

Fig. 6a shows spot plots for the 'improved' coils without defocusing at the perimeter of a 3 mm x 3 mm square at an angular aperture of 0.008 radian.

Constructional

inaccuracies in the coils prevented symmetrical spots from being produced at symmetrical points in the image plane. The alignment of the coils was, however sufficient to ensure that the spots produced at symmetrical points were of approximately the same maximum diameter.

Fig.6b shows spot plots at the perimeters of 2 mm x 2 mm and 3 mm x 3 mm squares when dynamic correction for field curvature was applied. The maximum diameter of the largest spot at the perimeter of the 3 mm x 3 mm square was reduced from 6.5 microns to 1.2 microns by the application of dynamic correction for field curvature.

Conclusions

A low aberration deflection system has been described. The design philosophy adopted has resulted in an extremely simple system which performs considerably better than conventional deflection systems. With the dynamically corrected 'improved' deflection system a 1.2 micron diameter spot is obtained at the corner of a 3 mm x 3 mm square at an angular aperture of 0.008 radian, an improvement of about 30 times over conventional pre-lens double-deflection systems.

Reference

G. Owen and W.C. Nixon, J. Vac. Sci. Technol., Vol. 10, No. 6, Nov./Dec. 1973.

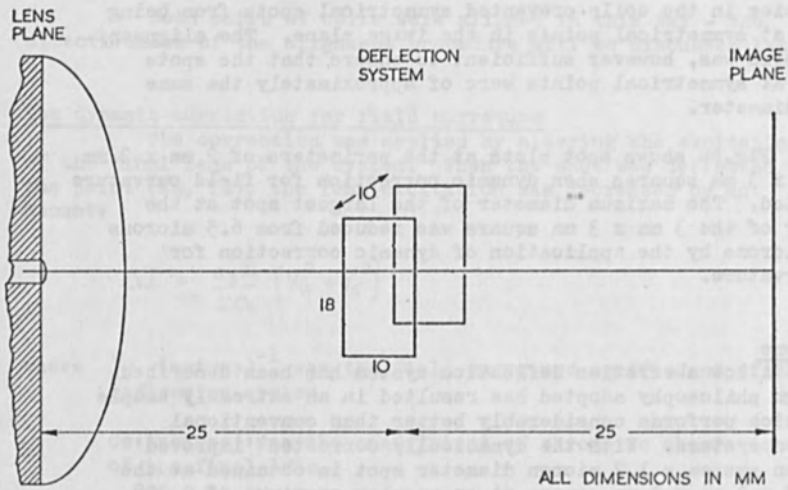


Fig.1 A schematic diagram of the 'improved' geometry

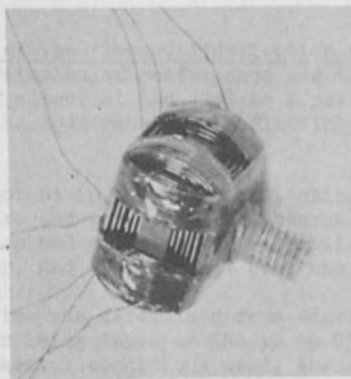
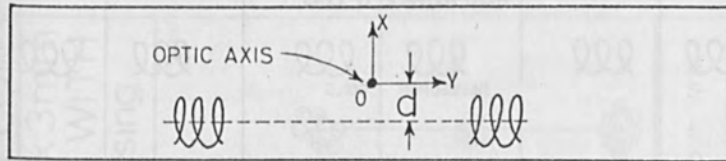
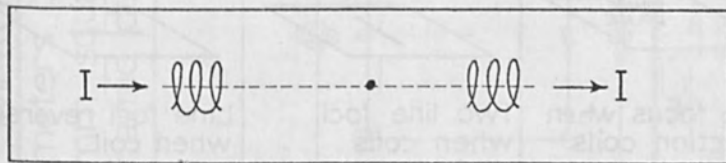


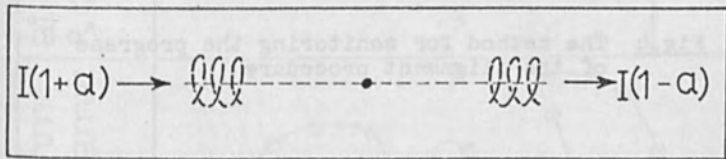
Fig.2 A photograph of the 'improved' coils



(a)



(b)



(c)

Fig. 3 The principle of the combined electrical and mechanical alignment procedure

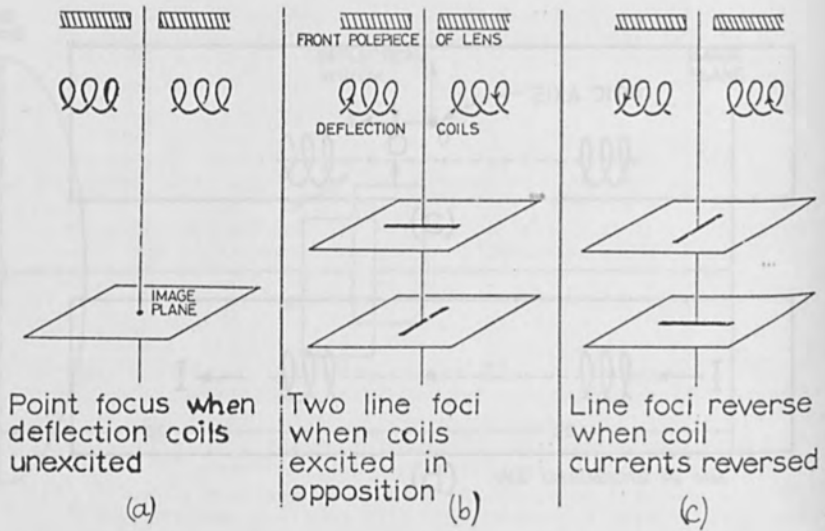


Fig.4. The method for monitoring the progress of the alignment procedure

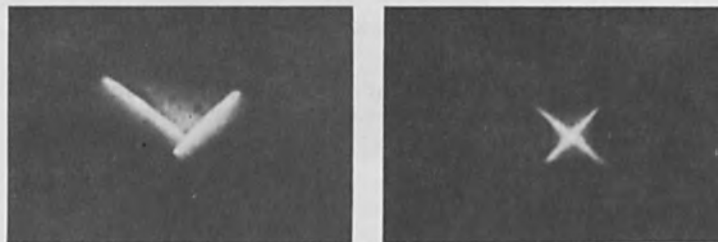


Fig.5 Line foci for unaligned and aligned deflection coils

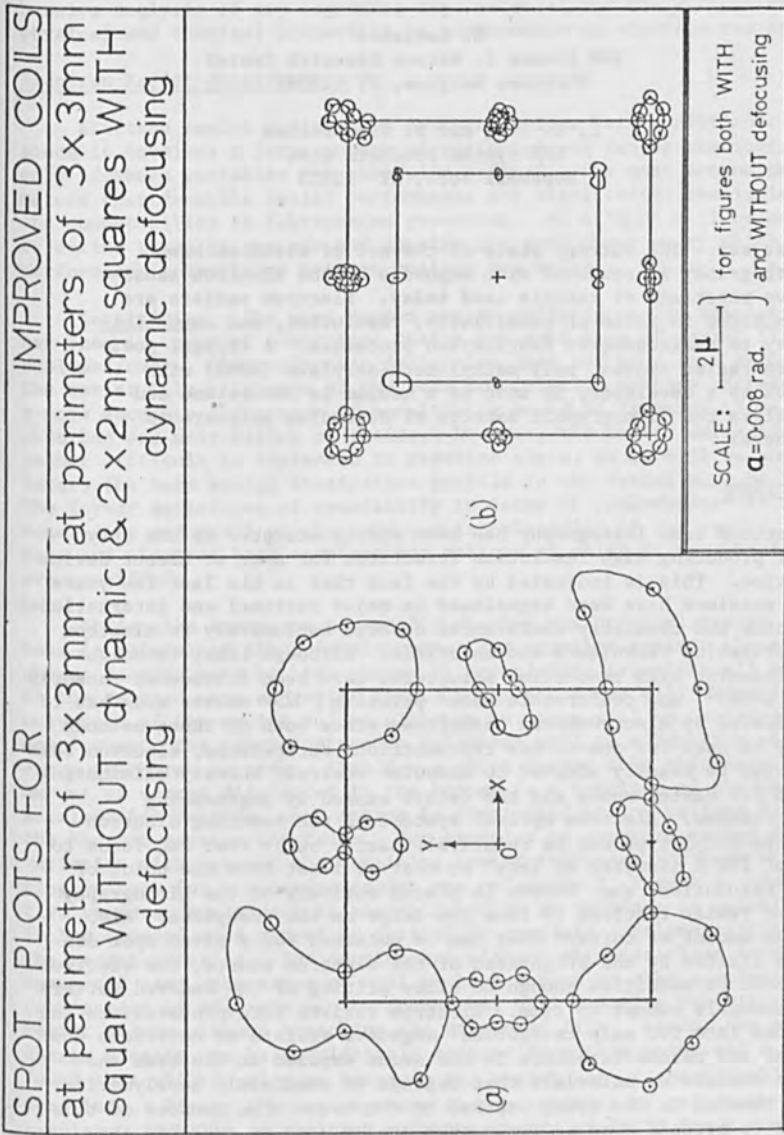


Fig.6 The performance of the 'improved' coils

FUNDAMENTAL ASPECTS OF ELECTRON BEAM
EXPOSURE OF POLYMERIC RESIST SYSTEM

M. Hatzakis
IBM Thomas J. Watson Research Center
Yorktown Heights, NY 10598

C. H. Ting and N. Viswanathan
IBM System Products Div.
Hopewell Jct., NY 12533

Abstract - The current state-of-the-art of electron beam lithography is reviewed with emphasis on the electron sensitive materials or resists used today. Electron resists are evaluated in terms of sensitivity, resolution, and compatibility to semiconductor fabrication processes. A typical positive resist system, poly-methyl-meth-acrylate (PMMA) with MIBK as a developer, is used as a medium to understand and analyze the lithographic aspects of degrading polymers in general.

Introduction

Electron beam lithography has been widely accepted as the only means of producing high resolution structures for mask or direct device fabrication. This is indicated by the fact that in the last few years special sessions have been organized in major national and international electronics and chemistry conferences devoted exclusively to electron beam fabrication techniques and materials. Although other techniques for reproducing high resolution structures have been introduced recently such as x-ray¹ and conformable mask² printing, the master mask has to be fabricated by electron-beam techniques since both of these methods can only be used for one-to-one reproduction. Furthermore, electron beam systems can be readily adapted to computer control³ thereby eliminating the need for master masks and the delays caused by engineering circuit changes. Electron optical systems of the scanning electron microscope (SEM) type can be relatively easily built that can focus to a spot of 100 Å diameter or less⁴ so that at least from the point of view of resolution, the burden is placed entirely on the lithography medium or resist required to form the image on the workpiece. Also since the amount of current that can be obtained for a given spot diameter is limited by the brightness of the electron source, the electron resist must be sensitive enough to allow writing of the desired pattern in a reasonable amount of time. Electron resists like photoresists can be divided into two main categories: negative resists or materials that crosslink and become insoluble in the areas exposed to the beam and positive resists or materials that degrade or completely depolymerize and are removed in the areas exposed to the beam. The purpose of this paper is to present some criteria that can be used to evaluate the

performance of any electron resist material. Also poly(methyl-methacrylate), a positive resist, is used as the medium for a comprehensive analysis of any degrading type material and the effects of its physical and chemical properties on performance as electron resist.

Electron Resist Requirements

Electron resist performance evaluation is a rather difficult task since it involves a large number of variables and can be meaningful only if these variables are carefully defined. The most common parameters that describe resist performance are sensitivity, resolution and compatibility to fabrication processes. An attempt will be made to define these parameters and specify the conditions under which performance comparisons between resists are valid.

Sensitivity - The most common way of defining resist sensitivity has been in terms of electrical charge per unit area of resist film (in coulombs/cm²). Obviously this definition does not take into account the resist film thickness or the beam accelerating voltage therefore a more accurate definition of sensitivity would be in terms of energy absorbed per unit volume of resist. However, the latter definition is rather difficult to implement in practice since, as it will be shown later, the beam energy dissipation profile in the resist must be known. The former definition of sensitivity in terms of coulombs/cm² is very convenient and still widely used but is only valid if the resist thickness and electron beam accelerating voltage at which it was obtained are specified.

It is also important to specify whether the original resist thickness is maintained after development. For negative resists the exposure charge density must be high enough to completely crosslink all molecules in the exposed area of resist film. Lower exposures will crosslink only part of the resist volume although an image will be obtained after development, the remaining resist thickness will be a function of the exposure charge density. Also for a given resist film thickness the amount of energy dissipated in the resist is a function of the beam accelerating voltage, more energy is dissipated at low voltage due to the shorter penetration range. For examples of exposure charge density variation with respect to the remaining resist thickness and beam accelerating voltage for a negative resist see reference 5, figure 1. In positive resists development is accomplished by an increase in solubility in the exposed area caused by partial or complete depolymerization of the resist material. For development without thickness loss in the unexposed area, the exposure must be high enough so that a solvent or combination of solvents can be found that will dissolve the exposed resist volume without attacking the unexposed film. Again, the exposure charge density can be considerably reduced from this point and a solvent found that will develop an image in the resist but at considerable thickness loss. Figure 1 shows exposure characteristics of poly(methyl-methacrylate) (PMMA)^{1,2}, a positive resist prebaked at 160°C for 1 hour and

developed in methyl-isobutyl-ketone. Note that while the original resist thickness in the unexposed area is preserved only for exposures of close to 10^{-4} coul/cm², an image can still be obtained at exposures two orders of magnitude lower or at 10^{-6} coul/cm² although the resist thickness is reduced to less than 20% of the original value. Figure 2 shows the dependence of charge density on beam accelerating voltage for an 8000 Å thick layer of PMMA resist on silicon substrate. The left hand inflection points represent minimum charge density required for each voltage to produce complete development without thickness loss in the unexposed regions. Note that this minimum charge density varies by a factor of two from 6 to 25kV.

In summary, sensitivity data for both negative and positive resists must include resist thickness before and after development, beam accelerating voltage, developed image resolution, which will be defined later, developer solution and development time.

Resolution - Resolution is usually indicated by the minimum line width that can be developed in a given resist layer. This will depend on the resist layer thickness as well as the line to line spacing. Resolution is also a function of the beam acceleration voltage which determines the amount of incident electron beam spreading in the resist layer. An example of linewidth dependence on beam voltage is shown in Figure 3 which is a scanning electron micrograph of lines exposed and developed in a thick PMMA resist layer at 10, 15 and 25 kV and identical exposure charge densities. It is apparent from this photo that for thick resist layers higher resolution can be obtained at 25kV than 10kV, since for maximum line density the walls of lines developed in any resist should be vertical. In addition, for any beam accelerating voltage vertical walls can be obtained by adjusting the exposure charge density. This is illustrated in figure 4 which is a composite SEM photo of three resist profiles exposed at 25 kV and various charge densities. Note that vertical walls can be obtained at an exposure charge density of slightly less than 2×10^{-4} coul/cm² while for lower or higher exposures the edge slope becomes positive or negative respectively.

A slightly negative slope can be desirable if the lift-off metallization process^{1,2} is to be employed with a positive resist. A good criterion for resolution would be to obtain line patterns exposed with a spacing equal to the linewidth in a resist layer of thickness equal to the linewidth. An example of resolution with PMMA resist is shown in figure 5 which is SEM photo of a zone plate fabricated with the lift-off technique by evaporating 1000 Å thick gold through a pattern exposed and developed in a 2000 Å thick PMMA resist layer. Minimum linewidth and spacing at the edge of the pattern is 1000 Å.

The dependence of resolution on exposure charge density for negative electron resists is illustrated in Figure 6 which shows crosssection of lines exposed on one micron thick layer of Kodak "Microneg" photoresist. Note that in this case the highest resolution is obtained at 10^{-5}

coul/cm², 25kV. This is the lowest exposure at which no thickness loss was observed after resist development. Higher exposures result in an increase in linewidth.

In summary, resolution of any electron resist system should be specified in terms of minimum linewidth and line spacing and should include resist thickness, beam accelerating voltage, and exposure charge density required for optimum resolution.

Compatibility to Fabrication Processes - Electron beam exposure and development of resist layers is only the first step in the fabrication process and further processing of the sample is in general required. The nature of the process depends on the type of device or circuit under consideration and it is therefore impractical to attempt to describe all applications of electron beam microfabrication. There are, however, several processes common to most applications and these will be listed here:

- a) Resistance to etching: an electron resist material should be able to withstand most acidic and basic etching solution employed in the silicon semiconductor industry. These include buffered hydrofluoric acid for etching SiO₂, sodium hydroxide or phosphoric and nitric acid solutions for aluminum etching and other solutions designed to etch chromium, gold, polysilicon, silicon nitride etc.
- b) Adhesion to the substrate: one of the most important requirements of any resist system is adhesion to the variety of substrates encountered in microfabrication. Poor resist adhesion will be detrimental to all wet chemical etching processes and metallization processes that involve plating through a resist mask. For specific adhesion tests, see reference 17.
- c) Resistance to heating: This is particularly important in additive metallization processes such as the lift-off evaporation or sputter deposition process during which substrate surface temperature can exceed 100°C. Any resist flow at this temperature will cause image distortion and will prevent completion of the lift-off process.
- d) Resistance to sputter etching or ion milling: this requires relatively low sputtering rates of the resist material in comparison to the material being etched and also resistance to heating in this case at even higher temperatures than those encountered during metal deposition.

A list of some resist materials proposed for electron beam fabrication is presented in Table I with resolution, sensitivity and compatibility to fabrication processes as reported by the respective authors. Note

that PMMA resist has received significant attention mainly because of its superior resolution although lacking in sensitivity. Of the recently reported materials the poly-sulfones seem very promising and combine high sensitivity with good resolution. These materials however are still under study. For this reason PMMA has been chosen as the vehicle for a detailed study of physical and chemical properties that determine the behavior of any positive polymeric resist system.

Factors Affecting PMMA Resist Sensitivity

Effect of Development Process - The sensitivity of the PMMA/MIBK system has been studied extensively in the past¹⁹. It has been shown that the sensitivity of this resist system does not have a unique value, different sensitivity can be obtained by for example changing the developing condition, beam acceleration voltage, resist thickness, molecular weight of the polymer, etc. After one fixes all the variables, one still can obtain high quality patterns in resist films over a very wide range of exposure density if some loss in resist thickness in the unexposed area can be tolerated. The loss of resist thickness in the unexposed area for several different exposure conditions is illustrated in Fig. 7. It is shown in Fig. 7 that the required developing time increases with decreasing exposure density. Since the loss of resist in the unexposed area increases linearly with developing time, the thickness loss is significant at lower exposure densities. In practice, significant loss in resist thickness will reduce the reliability of resist films in subsequent process due to increased pin-hole density and poor accuracy in the developed patterns. The amount of resist remaining after developing is determined by the difference in solubility between the exposed and unexposed resist in a particular developing solution, therefore, a useful figure of merit for the resist system is the ratio of solubility rates (SR) of the exposed and unexposed resist i.e.

$$SR = \frac{S}{S_0} = (1 + S'/S_0) \quad (1)$$

where S is the solubility rate of the exposed resist S_0 is the solubility rate of the unexposed resist $S' = S - S_0$ or the increase in solubility rate of the resist due to electron beam exposure.

The increase in solubility rate, S' , for a particular PMMA resist material has been determined as a function of exposure dosage. This is illustrated in Fig. 8. With the aid of Fig. 7 and Fig. 8 one can choose the necessary exposure density for different applications.

Effect of Electron Acceleration Voltage - It has been shown previously that the sensitivity of electron beam resists is a function of the accelerating voltage and also a function of resist thickness. This is because the energy dissipated in the resist film is not constant.

The energy dissipation per unit volume decreases with the increase of acceleration voltage. Furthermore, the energy dissipation is not uniform with the depth of penetration, it first increases with depth reaching a maximum at approximately 0.4 of the penetration range. This depth-dose relationship has been studied quite extensively in the past. A convenient expression of this depth-dose function was given by Everhart²⁷ and is illustrated in Fig. 9a.

In Fig. 9a the normalized depth z/R is used where z is the distance normal to the surface and R is the penetration range of the impinging electrons. Using the empirical formula given in Fig. 9a and the published data on electron range²⁸ the energy absorbed by a given resist layer can be readily obtained for various beam acceleration voltages. The calculated results for some typical resist thickness and acceleration voltages are summarized in Fig. 9b. When the penetration range of the electrons is less than the resist film thickness, kinetic energy of the electrons will be completely dissipated in the resist film. This is represented by a straight line with unity slope in Fig. 9b. As the incident energy increases the absorbed energy for a given resist film decreases. In all practical cases the energy absorbed by the resist film is only a small fraction of the incident energy. It should be pointed out here that in calculating the absorbed energy given in Fig. 9b, the contributions of backscattered electrons were ignored for simplicity. This approximation is good only for low density substrate materials with low atomic number such as silicon, silicon dioxide etc. As will be shown later, the radiation chemical efficiency of the resist does not change with the energy of the electron beam for the limited range of interest in electron beam microfabrication, therefore, the difference in sensitivity of the resist film at various beam acceleration voltages is due to the difference in the amount of energy dissipated in the resist.

Therefore, when the sensitivity for a specific resist film thickness and beam acceleration voltage is known, the resist sensitivity at any other beam acceleration voltage or film thickness can be obtained from the above simple calculations.

Experimental verifications of these calculations were carried out by measuring the developing rate of the exposed resist film for 15 kV beam and 25 kV beam at several exposure densities. The results are shown in Fig. 10. Also shown in Fig. 10 are the calculated values for 15 kV, 25 kV and 30 kV beams by fitting only one experimental point at 25 kV. The results between the calculated and measured values are in good agreement.

The Effect of Molecular Weight - One of the most important parameters of a polymer resist is the average molecular weight of the polymer. The effect of molecular weight on resist sensitivity has been investigated by Ku and Scala.¹⁴ They concluded that for positive electron resist the sensitivity is independent of molecular weight. This

conclusion was based on a simplifying assumption valid only at very high exposure dosage. It will be shown here that at lower exposure dosage the average molecular weight of the resist material has a very significant effect on the resist sensitivity, therefore, should be optimized for maximum sensitivity.

It has been shown that the decrease in the number average molecular weight due to radiation induced scission is given by¹⁴

$$M'_n = \frac{M_n}{1 + P M_n} \quad (2)$$

Where M_n is the original number average molecular weight M'_n is the new molecular weight after radiation, p is the probability of scission.

The probability of scission, p , depends on the material properties as well as the radiation dosage, it can be expressed as

$$P = \frac{Q E G M_o}{q \rho t N_a 100} \quad (3)$$

Where: Q is the exposure dose in coul/cm²
 E is the absorbed energy in eV
 G is the radiation chemical efficiency or number of chemical events per 100 eV absorbed
 M_o is the molecular weight of the monomer and is 100 for PMMA
 q is the electronic charge
 ρ is the density of the material
 t is the thickness of the material
 N_A is the Avogadro's number

By combining equations (2) and (3) the decreased molecular weight can be expressed as

$$M'_n = \frac{M_n}{1 + \frac{e g M_o}{q \rho t N_a 100} Q M_n} = \frac{M_n}{1 + K Q M_n} \quad (4)$$

Where K is a constant for a fixed beam acceleration voltage and resist film thickness and assuming that the G value is not a function of acceleration voltage and molecular weight.

Assuming the G value to be 1.65 as reported in the literature¹⁴ the molecular weight of the exposed resist was calculated as a function of the molecular weight of the original resist polymer for a 5000 Å

resist film and beam acceleration voltage of 15 kV. The results are presented graphically in Fig. 11. It is clearly demonstrated that the molecular weight of the exposed resist decreases with increasing exposure density. For a given exposure density the molecular weight of the exposed resist reaches a constant value, and is therefore independent on the initial molecular weight as long as the initial molecular weight exceeds a certain value.

Even though the molecular weight of the exposed resist approaches a constant value at moderate dosages it does not follow that the selection of initial material has no effect on the resist sensitivity. It has been pointed out before that for moderate exposures the important parameter is the difference in solubility and therefore the difference in molecular weight between the exposed and unexposed resists. For example, if two samples of PMMA resist one with $M_n = 10^4$ and the other with $M_n = 10^5$ initially, were exposed with charge density of $100 \mu\text{C}/\text{cm}^2$ at 15kV, the molecular weight of the exposed region for both samples were approximately 2×10^3 from Fig. 11. However, the decrease from their original value was a factor of 5 for the first polymer as indicated by Δ_1 in Fig. 11 and the decrease for the second polymer was a factor of 1/50 as indicated by Δ_2 in Fig. 11.

The solubility of the polymer in a solvent is, in general, a function of molecular weight and it can be described by some power law relationship such as³¹

$$S = B M_n^{-A} \quad (5)$$

Where A and B are constants, therefore the solubility ratio between the exposed and unexposed resists can now be expressed in terms of their molecular weights i.e.

$$SR = \frac{S}{S_0} = \frac{M_n}{M_n}^A = (1 + K Q M_n)^A \quad (6)$$

It can be seen clearly from equation (6) that for a given resist and exposure condition (i.e. K and Q are constants) higher values of solubility ratio can be achieved by increasing the initial molecular weight of the resist material. The effect is illustrated graphically in Fig. 12 by plotting the ratio of the exposed and unexposed resist as a function of the number average molecular weight of the initial polymer for several exposure charge densities. The advantages of the high molecular weight material is now obvious.

Determination of Radiation Chemical Efficiency - The radiation chemical efficiency or "G" value, defined as the number of chemical events for every 100 eV absorbed energy, has not been determined under experimental conditions similar to that of electron beam exposure of resist films. Several "G" values for PMMA were reported in the

conclusion was based on a simplifying assumption valid only at very high exposure dosage. It will be shown here that at lower exposure dosage the average molecular weight of the resist material has a very significant effect on the resist sensitivity, therefore, should be optimized for maximum sensitivity.

It has been shown that the decrease in the number average molecular weight due to radiation induced scission is given by¹⁴

$$M'_n = \frac{M_n}{1 + P M_n} \quad (2)$$

Where M_n is the original number average molecular weight M'_n is the new molecular weight after radiation, p is the probability of scission.

The probability of scission, p , depends on the material properties as well as the radiation dosage, it can be expressed as

$$P = \frac{Q E G M_o}{q \rho t N_a 100} \quad (3)$$

Where: Q is the exposure dose in coul/cm²
 E is the absorbed energy in eV
 G is the radiation chemical efficiency or number of chemical events per 100 eV absorbed
 M_o is the molecular weight of the monomer and is 100 for PMMA
 q is the electronic charge
 ρ is the density of the material
 t is the thickness of the material
 N_A is the Avogadro's number

By combining equations (2) and (3) the decreased molecular weight can be expressed as

$$M'_n = \frac{M_n}{1 + \frac{e g M_o}{q \rho t N_a 100} Q M_n} = \frac{M_n}{1 + K Q M_n} \quad (4)$$

Where K is a constant for a fixed beam acceleration voltage and resist film thickness and assuming that the G value is not a function of acceleration voltage and molecular weight.

Assuming the G value to be 1.65 as reported in the literature¹⁴ the molecular weight of the exposed resist was calculated as a function of the molecular weight of the original resist polymer for a 5000 Å

resist film and beam acceleration voltage of 15 kV. The results are presented graphically in Fig. 11. It is clearly demonstrated that the molecular weight of the exposed resist decreases with increasing exposure density. For a given exposure density the molecular weight of the exposed resist reaches a constant value, and is therefore independent on the initial molecular weight as long as the initial molecular weight exceeds a certain value.

Even though the molecular weight of the exposed resist approaches a constant value at moderate dosages it does not follow that the selection of initial material has no effect on the resist sensitivity. It has been pointed out before that for moderate exposures the important parameter is the difference in solubility and therefore the difference in molecular weight between the exposed and unexposed resists. For example, if two samples of PMMA resist one with $M_n = 10^4$ and the other with $M_n = 10^5$ initially, were exposed with charge density of $100 \mu\text{C}/\text{cm}^2$ at 15kV, the molecular weight of the exposed region for both samples were approximately 2×10^3 from Fig. 11. However, the decrease from their original value was a factor of 5 for the first polymer as indicated by Δ_1 in Fig. 11 and the decrease for the second polymer was a factor of 150 as indicated by Δ_2 in Fig. 11.

The solubility of the polymer in a solvent is, in general, a function of molecular weight and it can be described by some power law relationship such as³¹

$$S = B M_N^{-A} \quad (5)$$

Where A and B are constants, therefore the solubility ratio between the exposed and unexposed resists can now be expressed in terms of their molecular weights i.e.

$$SR = \frac{S}{S_0} = \frac{M_n}{M_n^0} = (1 + K Q M_n)^A \quad (6)$$

It can be seen clearly from equation (6) that for a given resist and exposure condition (i.e. K and Q are constants) higher values of solubility ratio can be achieved by increasing the initial molecular weight of the resist material. The effect is illustrated graphically in Fig. 12 by plotting the ratio of the exposed and unexposed resist as a function of the number average molecular weight of the initial polymer for several exposure charge densities. The advantages of the high molecular weight material is now obvious.

Determination of Radiation Chemical Efficiency - The radiation chemical efficiency or "G" value, defined as the number of chemical events for every 100 eV absorbed energy, has not been determined under experimental conditions similar to that of electron beam exposure of resist films. Several "G" values for PMMA were reported in the

literature. These values were obtained with either gamma ray or MeV electron irradiations on bulk samples. It is, therefore, necessary to determine the "G" value for PMMA resist films under typical electron beam microfabrication conditions.

The "G" value for PMMA resist can be obtained from eq. (4) if one experimentally determines the initial and final molecular weight of the resist film under a known exposure condition. For simplicity eq. (4) can be rearranged to give the following

$$\frac{1}{M_n'} = \frac{1}{M_n} + K'GQ \quad (7)$$

Therefore, a straight line relationship should be obtained when $\frac{1}{M_n'}$ is measured as a function of exposure density Q. The slope of this straight line should be K'G. Since K' is a known constant, the "G" value can be obtained from the slope of the straight line.

Experimentally, resist coated wafers were exposed in a scanning electron beam system over the entire wafer surface. The resist films from these exposed wafers were then stripped with a solvent and Gel Permeation Chromatography (GPC) were performed with these samples to determine the average molecular weight of the exposed resist. The details of GPC measurements have been treated quite extensively in polymer chemistry literature and, therefore, will not be described in any detail here. For illustration purpose, Fig. 13a gives the schematic of our GPC apparatus and Fig. 13b the typical results obtained. Experimental results for three different PMMA resist samples exposed with 25 kV scanning beam are summarized in Table II. A typical $1/M_n$ vs exposure plot is given in Fig. 14. The experimental results give a "good" straight line as expected from eq. (7).

The "G" values determined from the experimental results for three different PMMA polymers are summarized in Table III. Also given in Table III is the "G" value of polymer #1 obtained from a separate experiment using a 15 kV scanning beam. The "G" value obtained with 15 kV beam is essentially the same as that obtained with 25 kV exposures. Three significant, even though somewhat tentative, conclusions can be obtained from the experimental results given in Table III, i.e.

- 1) The "G" values obtained by scanning thin resist films with kev electrons differ significantly from that obtained by Mev electrons and gamma rays on bulk samples.
- 2) The "G" value is independent of the electron acceleration voltage for the limited range used in the study (15-25 kV).
- 3) The "G" value is not a function of the initial molecular weight of the resist for the limited range used in this study (20 K to 110 K).

Experimental Verification of the Resist Sensitivity Model - Using the "G" value determined from experimental measurements, eq. (4) can now be used to calculate quantitatively the changes in molecular weight as a function of initial molecular weight and exposure densities. This was carried out for a 25 kV beam and 1.0 μ m thick PMMA film. The calculated results are summarized in Fig. 15. Also shown in Fig. 15 are the experimental values determined by GPC measurements for three different PMMA polymers with widely different initial molecular weights. The agreement between the calculated and measured values is quite good.

We have also measured the dissolution rate of the exposed resist (polymer #1) in MIBK developer for several exposure densities. The dissolution rate is plotted in Fig. 16 as a function of the number average molecular weight obtained from GPC measurements. A straight line gives good approximations to the experimental data. This straight line relationship satisfies the behavior predicted by eq. (5). Furthermore, this straight line relationship gives a value of 1.4 on the experimental dependence of dissolution rate on molecular weight changes. Since the molecular weight change is directly proportional to exposure density for moderate dosage, this exponential dependence agrees rather well with the value of 1.3 obtained from Fig. 8 under entirely different experimental conditions.

A further agreement between this sensitivity model and early experimental results¹⁹ is illustrated in Fig. 17. Here, the experimental points represent the remaining resist thickness determined for a wide range of exposure dosages. The curved line was obtained from the sensitivity model established above and was plotted by matching one experimental point to the solubility relationship. Again, agreement over the wide range of exposure is very good.

Simulation of Developed Resist Profiles

In electron beam microfabrication, it is important to know the developed resist profiles for different exposure and developing conditions. As it was shown previously, it is the edge of the developed resist that determines the accuracies and tolerances of the exposed patterns. In particular, proper resist profiles are necessary in using the lift-off technique to fabricate small metal lines. Extensive experimental as well as theoretical studies have been carried out in the past on the scattering and energy dissipation of finely focused electron beam in resist films.^{16,23} However, all previous studies have neglected the effect of development process and assumed the developed resist profile to be the same as the contours of equal absorbed energy in resist films. While this assumption is reasonably good approximation for very high exposure density, i.e. when S/S_0 approaches infinity, it is not good in the case of relatively low exposure density used in high speed electron beam microfabrication.

In this work we attempted to provide a more complete approach to this problem by combining the effects of scattering and energy dissipation of electrons in solids with the resist solubility change and development process.

A Simple Model for Computer Simulation - To obtain the developed resist profile one must first know the electron intensity distribution in the resist film. When an energetic electron enters a solid, the electron will suffer many small-angle scatterings due to interactions with the atoms of the solid material. The cumulative effect of those small-angle scattering events will determine the spatial distribution of electrons inside the resist film. By assuming those scattering events to be elastic and small-angle the spatial probability distribution of scattered electrons can be expressed as²³

$$H(r,z) = \frac{3\lambda}{4\pi z^3} \cdot \exp\left(-\frac{3\lambda r^2}{4z^3}\right) \quad (8)$$

Where r is the radial distance from axis of the incoming electron and z is the vertical distance along axis of electron penetration. The constant, λ , is the transport mean free path and is determined by the properties of the target material and the energy of the impinging electrons.

The above equation shows that the spatial distribution of electrons is Gaussian at any depth for an impulse input function. When the impinging electrons have an arbitrary distribution X , then the resulting density distribution inside the solid will be given by the convolution integral of the input function X and the response function H . Specifically, for electrons inside the surface is given by²³

$$D(r,z) = \frac{N_0 \cdot 3\lambda}{4\pi z^3} \int_0^{2\pi} \int_0^{\infty} \exp\left(-\frac{3\lambda}{4z^3} r^2\right) \exp(-aR^2) R dR d\phi \quad (7)$$

In addition to the above small-angle scattering, large-angle scattering due to interactions with atomic nuclei also takes place. These are called backscattered electrons. The amount of backscattered electrons, or reflection coefficient, is a function of the atomic number of the target material.²⁴ For resist films coated on low atomic number substrate the contribution due to backscattered electrons can be several orders of magnitude lower than the incoming electron density for a point source.²⁵ For simplicity reason, the contribution due to backscattered electrons will be neglected in the following analysis.

As electrons penetrate the resist film, part of the kinetic energy of the electrons will be transferred to the resist due to numerous

collisions. To obtain spatial distribution of energy dissipation elaborate Monte Carlo calculations have been carried out by several investigators.²⁶ The Monte Carlo approach involve a great deal of computer time and the results are difficult to adopt for various different experimental conditions. The energy distribution function can also be obtained from analytical considerations.²⁵ However, the mathematics is rather complicated even with some simplifying assumptions. Another way of obtaining the energy dissipation function is the empirical approach by measuring the amount of ionization as a function of beam penetration.²⁷ The depth-dose functions obtained by experimental measurements have been expressed as universal energy loss functions in terms of the normalized depth z/R where R is the penetration range of electrons in the target material. An example of the depth-dose function is given in Fig. 9a. The penetration range, R , can be obtained from published literature for various materials and energy range of interest.²⁸ For simplicity reasons, we shall assume the energy loss of incoming electrons in resist film is given by the empirical formula given in Fig. 9a. This assumption, although adopted by several investigators, is an over simplification and is good only for relatively broad beam in thin resist films.

It has been shown earlier that the resist development depends on the difference in the dissolution rate of the exposed and unexposed resist in the developer. The change in molecular weight due to electron beam exposure can now be obtained from the amount of energy dissipated in the resist, since the radiation chemical efficiency, or G value, has already been determined. This molecular weight change can then be expressed in terms of the change in solubility according to eq. (5). As an example the solubility rate of polymer #2 is expressed in terms of the absorbed energy density in Fig. 18.

The developed resist profile due to an axially symmetric beam can now be obtained by numerical calculation using a digital computer to manipulate a large two dimensional solubility matrix. A computer program to test the presence or absence of resist material in a two dimensional matrix has been developed by F. Dill.²⁹ Fig. 19 gives the schematic diagram of the entire procedure in calculating the resist profiles. Resist profiles at different developing time can now readily be obtained for a wide range of exposure parameters such as dosage and acceleration voltages.

Single Gaussian Spot - Starting with a Gaussian spot at the resist surface, the electron intensity distribution inside the resist can be obtained from Eq. (7) by numerical integration.²³ This was carried out for a 15 kV, 0.5 μ m spot in a 2 μ PMMA resist film. The results are illustrated in Fig. 20a by plotting the equal intensity contour lines inside the resist surface. As expected, the contour lines spreads out with increasing depth of penetration from resist surface. The results for a similar beam of 25 kV are given in Fig. 20b. At any given depth the spread in the contour lines for the 25 kV beam is considerably less than the 15 kV beam.

The contour lines for equal absorbed energy in the resist film is simply the product of the electron intensity distribution and the energy dissipation function. This was calculated for 15 kV and 25 kV beams and the results are illustrated in Fig. 21a and 21b respectively. Because the energy dissipation function increases with the depth of penetration for thin films, the maximum energy dissipation is not at the surface but below the surface as illustrated by the closed contour lines in Fig. 21a and b.

From the values of energy absorbed by the resist, a solubility matrix can be obtained by using the solubility model given in Fig. 18. A computer program can now be used to test the presence or absence of resist material in a large two dimensional matrix after various developing times. A plotting routine was used to obtain the developed resist contours for any desired exposure conditions and developing times.

Fig. 22a gives the developed resist contours at several developing times for a 15 kV Gaussian Spot with rather low exposure dosage of $10 \mu\text{C}/\text{cm}^2$. The exposure dosage given is the value at the center of the Gaussian spot on the resist surface. It is clearly demonstrated that the loss of resist in the unexposed area is very significant. This represents the extreme case when the solubility difference between the exposed and unexposed resist is very small at this low exposure density.

The developed resist contours for heavier exposure dosage are shown in Fig. 22b. The loss of resist thickness in the unexposed area is relatively small in this case. The developed resist contours have some resemblance to the energy contours given in Fig. 21, indicating that in this case the resist contour is no longer completely dominated by the developing process. However, even at this large dosage the developed resist profile deviates considerably from the original beam profile.

Multiple Gaussian Spots - It has been demonstrated that for single Gaussian spot the developed resist deviates considerably from the original electron beam spot size, therefore, single Gaussian spot exposures are seldom used where accurate dimensional control has to be maintained. In order to achieve accurate dimensional control, an electron beam spot much smaller than the desired minimum dimension is generally used. For example, the beam spot size in the neighborhood of 2000 \AA is used in fabricating $1 \mu\text{m}$ lines.³⁰ This is illustrated in Fig. 23, where 5 Gaussian spots are joined together to give the minimum desired linewidth. The Gaussian spots are joined at 50% intensity level so that a more or less uniform electron intensity distribution is obtained within the desired geometry.

The electron intensity distribution inside the resist surface, for the case illustrated in Fig. 23, can be obtained by adding the contribution from the individual spots. The results obtained are given in Fig. 24a for 15 kV beam and in Fig. 24b for 25kV beam. The energy distribution inside the resist is illustrated in Fig. 25a and Fig. 25b respectively for 15 and 25 kV beam.

The developed resist profiles can now be obtained the same way as in the single spot case. The results are illustrated in Fig. 26 for the case of 15 kV beam, Fig. 26a is for a moderate exposure dosage of $50 \mu\text{C}/\text{cm}^2$, Fig. 26 b is for a higher dosage of $100 \mu\text{C}/\text{cm}^2$ and Fig. 26c is for the rather high dosage of $200 \mu\text{C}/\text{cm}^2$. The developed resist profiles illustrated in Fig. 26, differ considerably from the single spot case given by Fig. 22 in that the developed resist now has relatively flat bottom and steep side walls. The lateral dimension no longer changes drastically with small variation in developing time, particularly for the higher exposure dosages. These features make accurate dimensional control possible. Another important feature is that the developed resist gives a slight "undercut" for long developing times. This "undercut" is more pronounced for heavier exposure dosages thus, agrees qualitatively with the experimental results shown in Fig. 3. For comparison, the developed resist contours for 25kV beam are illustrated in Fig. 27a and b for exposure dosages of $100 \mu\text{C}/\text{cm}^2$ and $200 \mu\text{C}/\text{cm}^2$ respectively.

Some Experimental Observations - By using a rather simple model, we have demonstrated that the developed resist profile depends not only on the scattering of the highly focused electrons in the solid material but also on the exposure dosage and developing time. For low exposure dosages with single Gaussian spot, the resist profiles are completely dominated by the relative dissolution properties of the exposed and unexposed resist. Under this condition, the developed resist exhibit significant thickness loss and shallow side wall angle. For high exposure dosages with multiple Gaussian spots, the developed resist profiles are dominated by the scattering of electrons inside the resist. The developed resist profiles under this condition exhibit rather small thickness loss and steep or undercut side walls. These features can be observed by taking photomicrographs of the cross section of the developed resist for various exposure conditions.

This was carried out using a 25 kV beam with a Gaussian spot diameter of approximately 2000 \AA , the resist used is $1.6 \mu\text{m}$ thick PMMA films (Polymer #1) on silicon wafers. Fig. 28a gives the results for a $1.0 \mu\text{m}$ wide line and Fig. 28b for a $2.0 \mu\text{m}$ line obtained under a wide range of exposure dosages. The photographs in Fig. 28 clearly demonstrate that at low exposure densities the resist thickness loss is severe and the developed resist profiles have rather shallow side walls. For higher exposure densities the thickness loss decreases and the side wall angle increases. For very high exposure densities, i.e. 100 to $200 \mu\text{C}/\text{cm}^2$, the developed resist starts to show the "undercut" feature.

By comparing the profiles in Fig. 28a and b, one can see that the undercut is more pronounced for the wider line ($2 \mu\text{m}$) than the narrower line ($1 \mu\text{m}$) at a given exposure density (i.e. $100 \mu\text{C}/\text{cm}^2$).

All these features agree qualitatively with the results obtained from computer simulations. This gives some confidence in the validity of the simple model used to carry out the calculations.

Conclusion

Advances in electron beam resist processing techniques are essential in realizing the advantages of the electron beam lithography for micro-fabrication. The performance of some more common resist materials is reviewed. The important features of the resist materials such as sensitivity and resolution are discussed in some detail in terms of experimental parameters readily measurable in practice. A typical positive resist system, PMMA resist with MIBK developer, is singled out for detailed experimental as well as theoretical studies. The concept of using differential solubility is explained in detail. The effects of beam induced molecular weight change are quantitatively examined. The chain scission efficiencies of PMMA has been experimentally measured. This radiation chemical efficiency, or G value, remains constant for various beam parameters as well as different molecular weights of PMMA used in this study. A simple phenomenological model is used to calculate the developed resist profiles for different beam voltages and exposure dosages. It has been shown that the developed resist profiles are dominated by the developing process at low exposure densities but changes to the shape dominated by electron scattering at high exposure dosages. The calculated profiles agrees qualitatively with our experimental observations.

References

1. H. I. Smith, D. L. Spears and S. E. Bermacki, *J. Vac. Sci. and Tech.* Vol. 10, (1973).
2. H. I. Smith, F. J. Bachner and N. Efremow, *J. Electrochem. Soc.*, 118, (1971).
3. D. F. Spicer, A. C. Rodger and G. L. Varnell, *J. Vac. Sci. and Tech.* 10, (1973).
4. A. N. Broers, *J. Vac. Sci. and Tech.*, 10, (1973).
5. S. Nonogaki, H. Morishita and N. Saitou, *Appl. Polymer Symp.*, 23, pp. 117-123, (1974).
6. R. F. Thornley and T. Sun, *J. Electrochem. Soc.*, 116, 980, (1969).
7. R. K. Matta, *Electrochem. Tech.*, 5, 382 (1967).
8. B. Broyde, *J. Electrochem. Soc.*, 116, 1241 (1969).
9. E. D. Roberts, *Proc. 3rd Internat. Conf. on Electron and Ion Beam Science and Tech.*, p. 571, *Electrochem. Soc.*, New York (1968).
10. Y. Yatsui, T. Nakata, K. Umehara, *J. Electrochem. Soc.*, 116, 94, (1969).
11. T. Hirai, Y. Hatano and S. Nonogaki, *J. Electrochem. Soc.*, 118, 669, (1971).
12. M. Hatzakis, *J. Electrochem. Soc.*, 116 1033, (1969).
13. I. Haller, M. Hatzakis, and R. Srinivasan, *IBM J. of Res. and Dev.* 12, 251, (1968).
14. H. Y. Ku and L. C. Scala, *J. Electrochem. Soc.* 116, 980 (1969).
15. R. Herzog, J. Greeneich, T. Everhart, and T. Van Duzer, *IEEE Trans. on Electron Device*, ED-19, 635 (1972).
16. E. D. Wolf, F. S. Ozdemir, W. E. Perkins, and P. J. Coane, *Record*

- of the 11th Symp. on Electron, Ion, and Laser Beam Tech., 331, San Francisco Press, Inc. (1971).
17. R. A. Harris, J. Electrochem. Soc., 120, 270 (1973).
 18. C. H. Ting, Record of the 11th Symp. on Electron, Ion, and Laser Beam Tech., 345, San Francisco Press, (1971).
 19. M. Hatzakis and A. N. Broers, Record of the 11th Symp. on Electron Ion and Laser Beam Tech., 337, San Francisco Press (1971).
 20. E. D. Roberts, Prepring Div., Organic Coatings Plastics Chem., 165, Nat. ACS Meeting (1973).
 21. M. J. Bowden and L. F. Thompson, Preprint of 165th meeting of ACS, Organic Coatings and Plastics Chemistry (1973).
 22. J. L. Bartelt, Preprint of 165th meeting of ACS, Organic Coatings and Plastics Chemistry (1973).
 23. R. W. Nosker, J. Appl. Phys. 40, p. 1872 (1968).
 24. P. R. Thornton, Scanning Electron Microscopy, London, Chapman and Hall (1968).
 25. J. S. Greeneich, T. Van Duzer, IEEE Trans. ED-21, p. 286, (1974).
 26. R. Shimizu, T. E. Everhart, Optik, 36, 59, (1972).
 27. P. Hoff, T. E. Everhart, Rec. of 10 Symp. on Electron, Ion, and Laser Beam Tech. L. Morton, Ed., San Francisco Press, p. 454, (1969).
 28. M. J. Berger, S. M. Seltzer, Nasa Report SP-3012, (1964).
 29. F. Dill, IBM Research Yorktown, Private Communication.
 30. F. Fang, M. Hatzakis and C. H. Ting, J. Vac. Sci. Technol., 10, p. 1082, (1973).
 31. J. Crank and G. S. Park, Diffusion in Polymers, London, Academic Press (1968).

MATERIAL	TYPE	TYPICAL SENSITIVITY (coul/cm ²)	RESOLUTION (E/B EXPOSURE) MINIMUM LINE WIDTH REPORTED	COMPATIBILITY WITH SEMICONDUCTOR FABRICATION PROCESSES	AUTHORS	REFERENCE
KFR - KMER -KPR (KODAK)	NEGATIVE	5×10^{-6}	1 μ	GOOD	THORNLEY - SUN MATA	6 7
	NEGATIVE	10^{-5}	0.5 μ	FAIR	BROYDE	8
	NEGATIVE	5×10^{-8}	?	FAIR	ROBERTS YATSUI-NAKATA- UMEHARA	9 10
EPOXIDIZED POLYBUTADIENE	POSITIVE	5×10^{-5}	1 μ	GOOD	HIRAI-HATANO- NONOGAKI	11
	POSITIVE	10^{-4}	?	POOR	MATA HATZAKIS	7 12
SHIPLEY AZ - 1350	POSITIVE	5×10^{-5}		GOOD	HALLER-HATZAKIS- SRINIVASAN KU-SCALA	13 14
POLY (G-METHYL STYRENE)	POSITIVE	5×10^{-5} *	< 1000 Å	GOOD	HALLER-HATZAKIS SRINIVASAN HATZAKIS	13 12
POLY (METHYL METHACRYLATE)	POSITIVE	5×10^{-6} **		GOOD	KU-SCALA HERZOG, ET AL WOLF, ET AL HARRIS TING HATZAKIS-BROERS ROBERTS	14 15 16 17 18 19 20
POLY(BUTENE - 1 SULFONE)	POSITIVE	2×10^{-6}	0.5 μ	GOOD	BOWDEN-THOMPSON	21
POLYDIALYLORTHO- PHTHALATE	NEGATIVE	10^{-6} **	2 μ	GOOD	BARTELT	22

NOTE: * NO THICKNESS LOSS AFTER DEVELOPMENT

** SIGNIFICANT THICKNESS LOSS

TABLE I

TABLE II

All exposures at 25 kV

Polymer	Dose Coul/cm ² X10 ⁻⁶	M _n X10 ⁻³	M _w X10 ⁻³	M _w /M _n	
PMMA I	0	114.22	459.0	4.01	
	8	39.42	85.75	2.18	
	8	39.96	84.96	2.13	
	16	21.84	41.93	1.92	
	16	22.45	44.62	1.99	
	20	14.36	41.53	2.89	
	20	17.57	39.77	2.26	
	24	19.04	33.04	1.73	
	32	14.67	26.51	1.81	
	32	11.31	24.80	2.19	
	40.	11.35	22.34	1.97	
	PMMA II	0	49.5	110.3	2.22
8		27.8	52.1	1.87	
12		27.1	51.9	1.92	
12		24.6	49.09	2.0	
16		19.73	36.82	1.87	
20		16.32	32.42	1.99	
24		14.51	29.83	2.05	
32		12.08	22.47	1.86	
36		10.80	28.51	1.99	
40		10.64	21.23	1.99	
PMMA III		0	19.62	56.21	2.86
		0	20.95	67.00	3.20
	8	15.35	37.31	2.43	
	8	17.19	34.25	1.99	
	16	12.45	32.96	2.65	
	16	11.79	29.52	2.50	
	32	9.62	24.91	2.60	
	36	9.43	19.43	2.30	

TABLE III

M _n	M _n		G
	
114,000	0.78
49,500	0.77
19,600	0.73
114,000	0.75

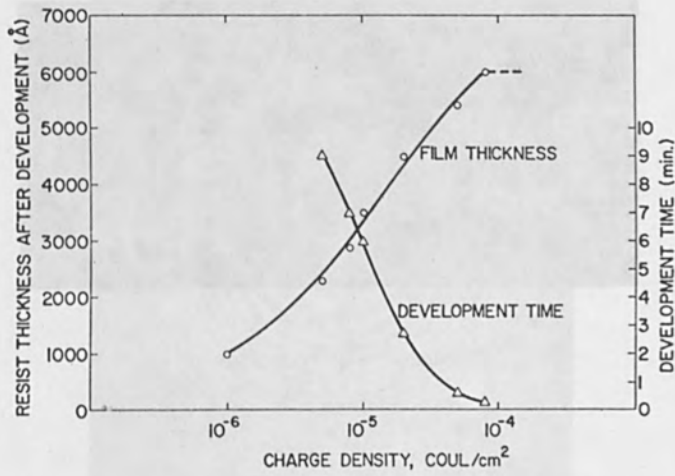


FIGURE 1. REMAINING RESIST THICKNESS AND DEVELOPMENT TIME VERSUS EXPOSURE FOR PMMA RESIST.

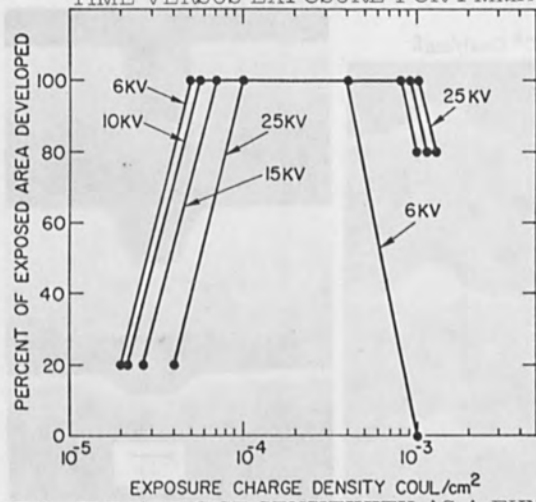


FIGURE 2. PMMA RESIST SENSITIVITY AS A FUNCTION OF BEAM ACCELERATING VOLTAGE.

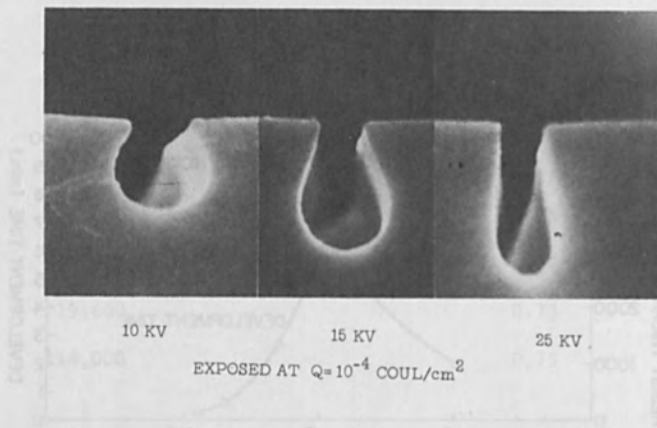
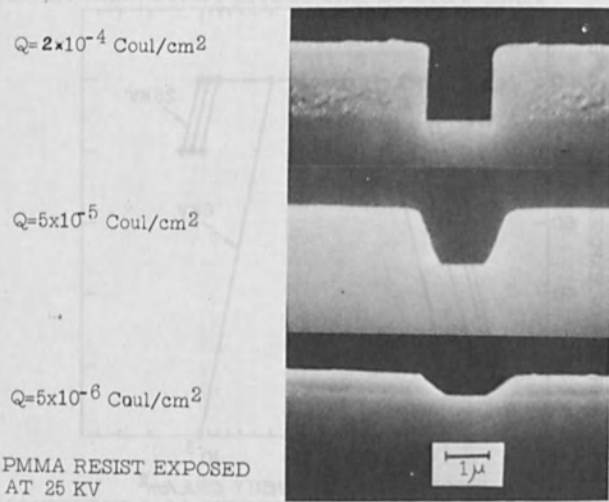


FIGURE 3. PROFILES OF PMMA RESIST EXPOSED AT 10, 15 AND 25KV.



PMMA RESIST EXPOSED AT 25 KV

FIGURE 4. PROFILES OF PMMA RESIST EXPOSED AT VARIOUS CHARGE DENSITIES

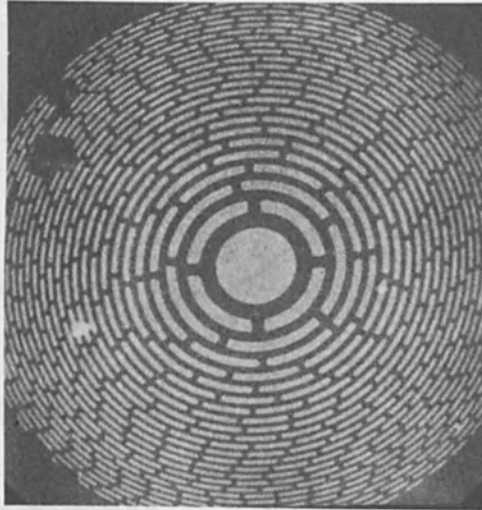


FIGURE 5. HIGH RESOLUTION ZONE PLATE FABRICATED WITH PMMA RESIST

$Q = 10^{-4}$ Coul/cm²

$Q = 5 \times 10^{-5}$ Coul/cm²

$Q = 10^{-5}$ Coul/cm²

KODAK MICRONEG RESIST
EXPOSED AT 25KV

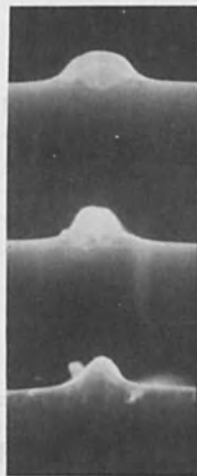


FIGURE 6. KODAK MICRONEG RESIST EXPOSED AT 25KV AND VARYING CHARGE DENSITY.

DEVELOPMENT RATES AT 15KV MIBK DEVELOPER

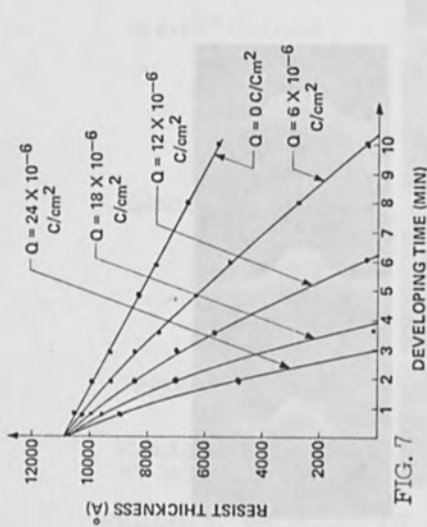


FIG. 7

ENERGY DISSIPATION vs DEPTH

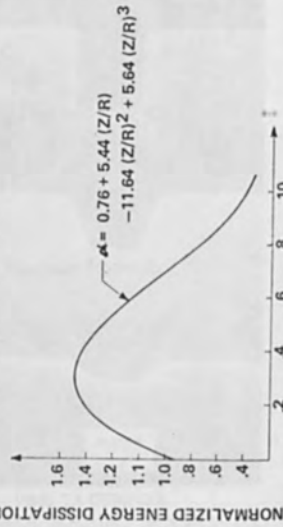


FIG. 9a

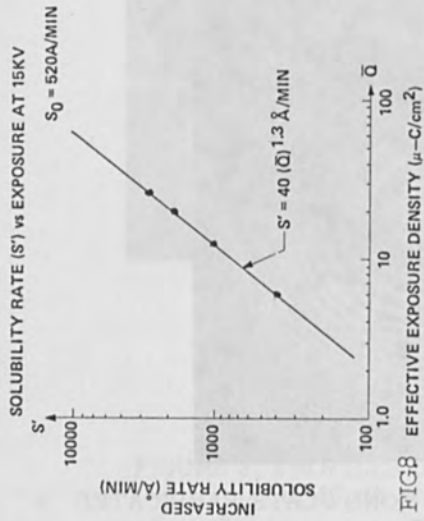


FIG. 8

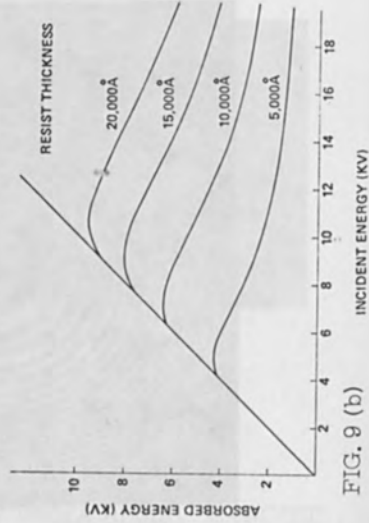


FIG. 9 (b)

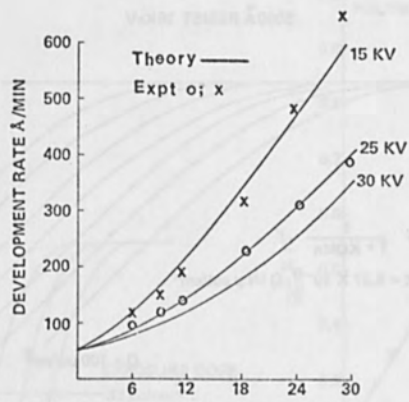


FIGURE 10 DOSE MICRO COULOMBS/cm²

MOLECULAR WEIGHT EFFECT ON EXPOSURE
5000 Å PMMA AT 15KeV

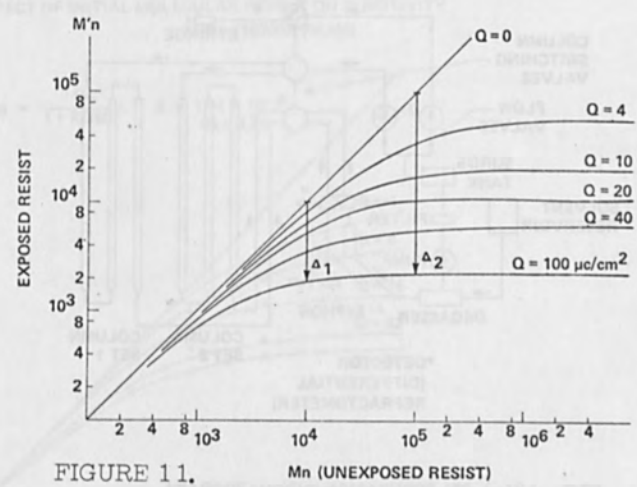


FIGURE 11.

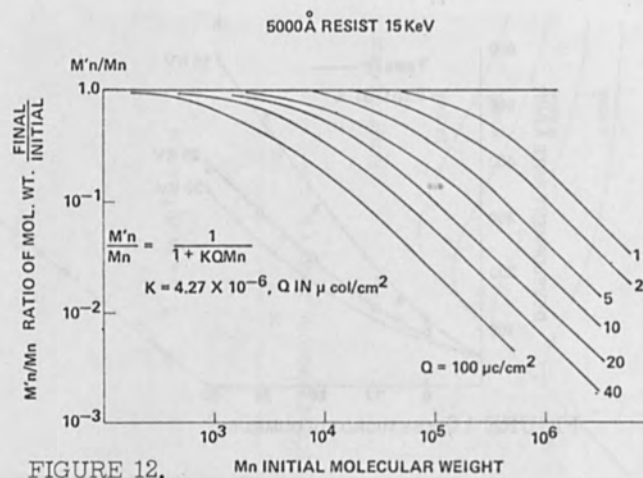


FIGURE 12. Mn INITIAL MOLECULAR WEIGHT

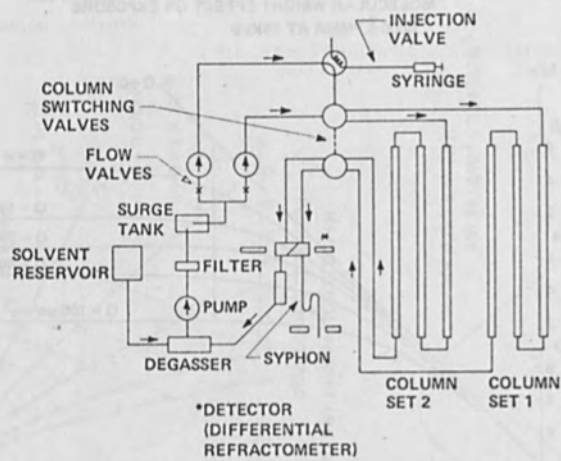
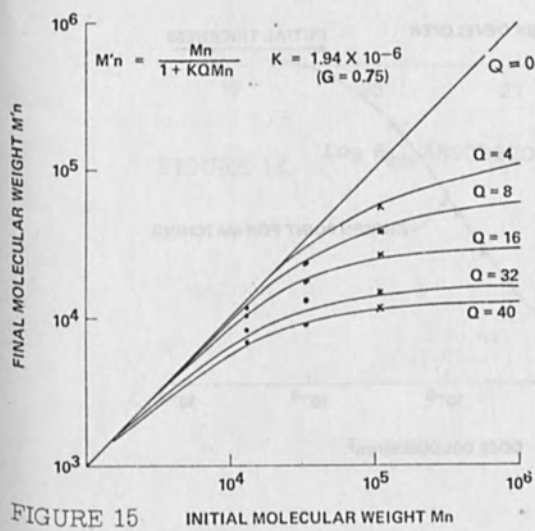
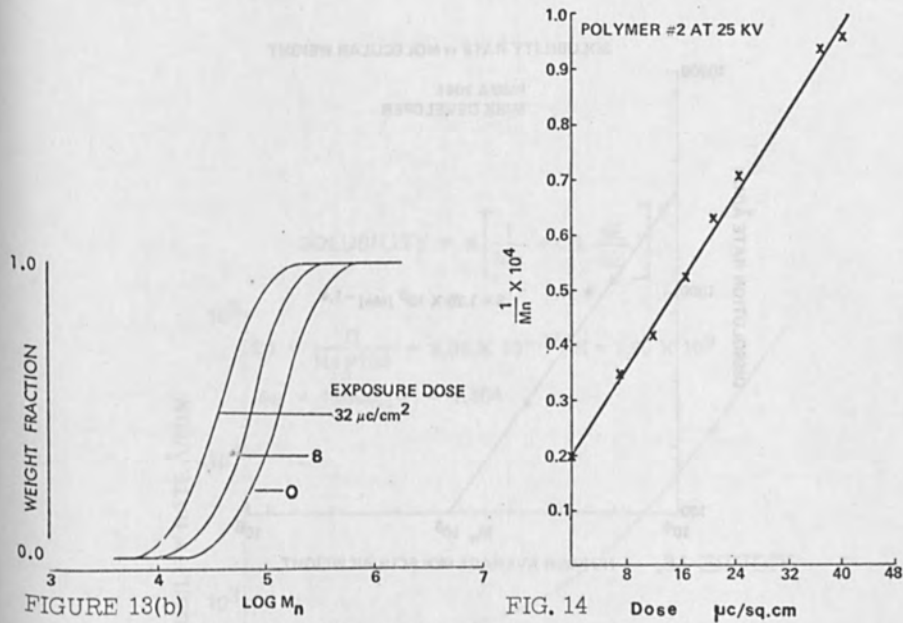


FIG. 13(a) GEL PERMEATION CHROMATOGRAPH



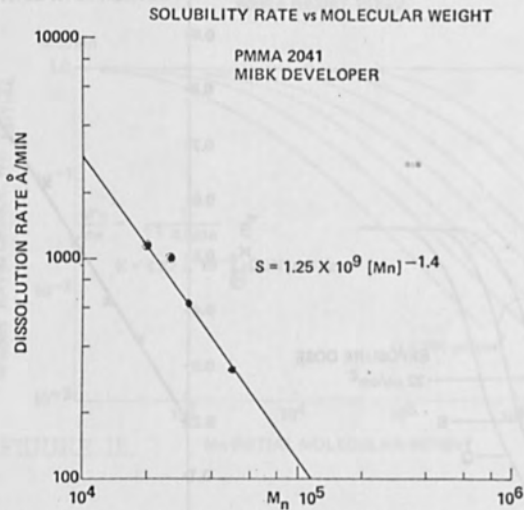


FIGURE 16. NUMBER AVERAGE MOLECULAR WEIGHT

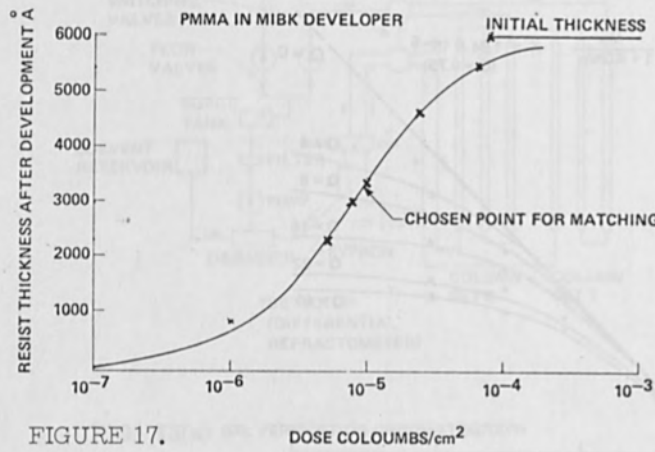


FIGURE 17. DOSE COLOUMBS/ cm^2

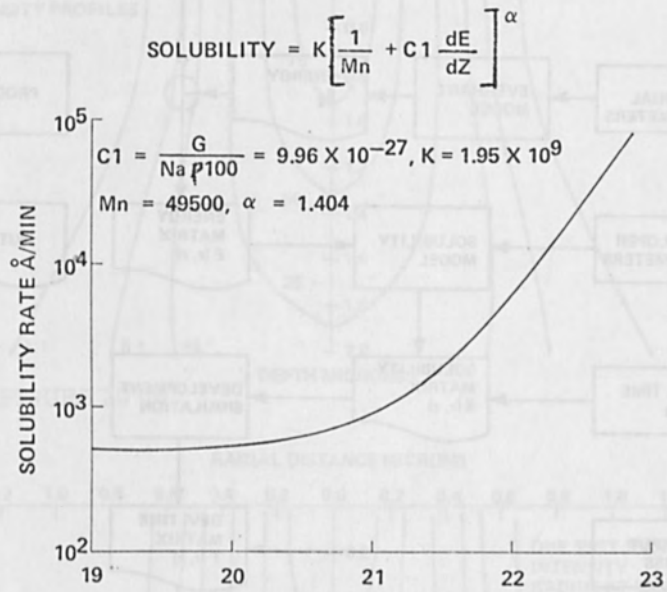


FIGURE 18. $\text{Log } E_{\text{abs}} \text{ ABSORBED DOSE } eV/cm^3$

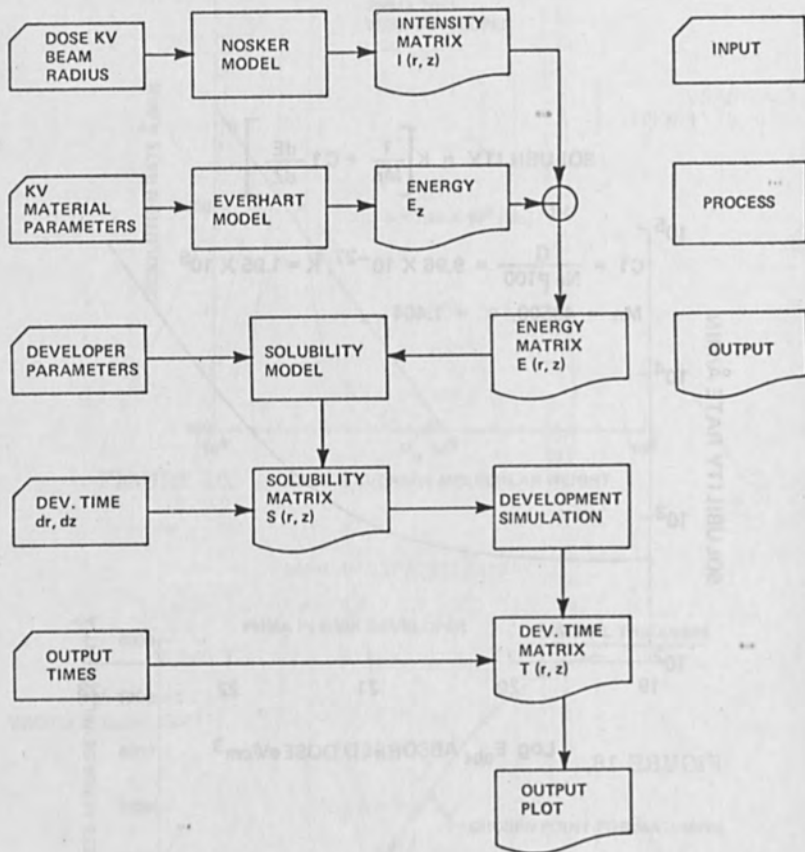


FIGURE 19. FLOW DIAGRAM OF COMPUTER SIMULATION OF DEVELOPED RESIST PROFILES

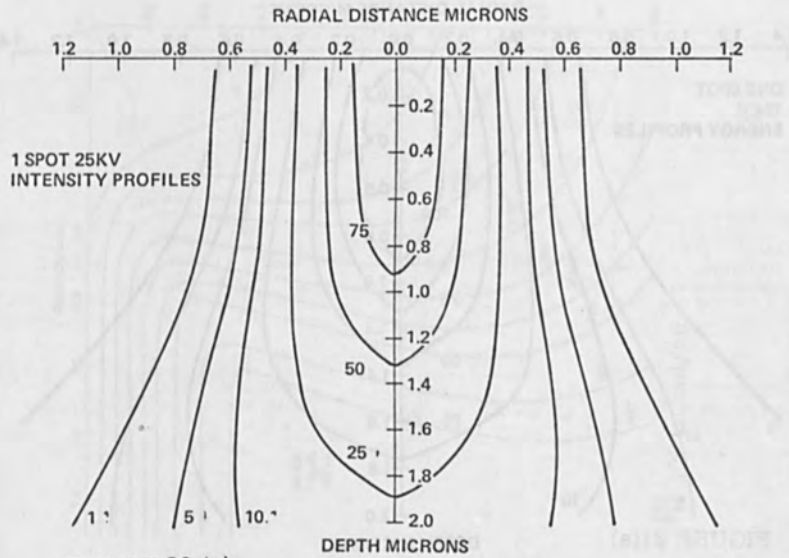


FIGURE 20 (a)

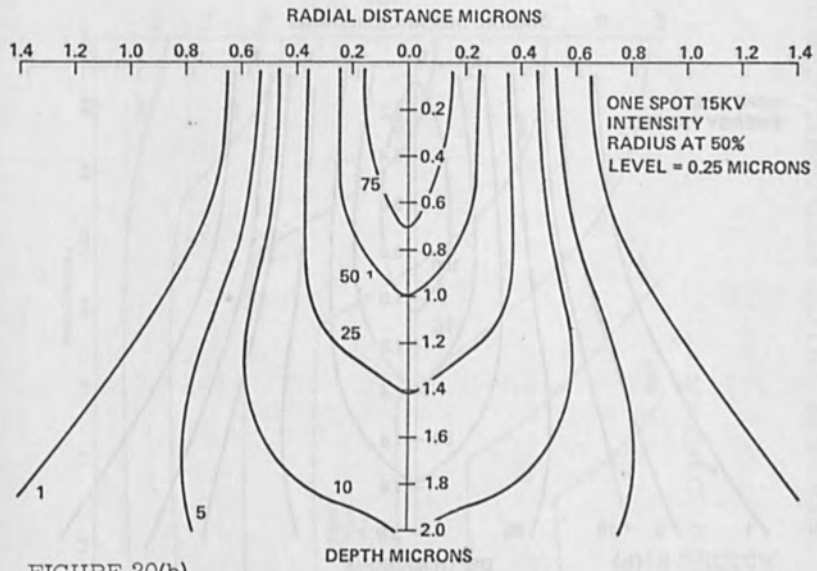


FIGURE 20(b)

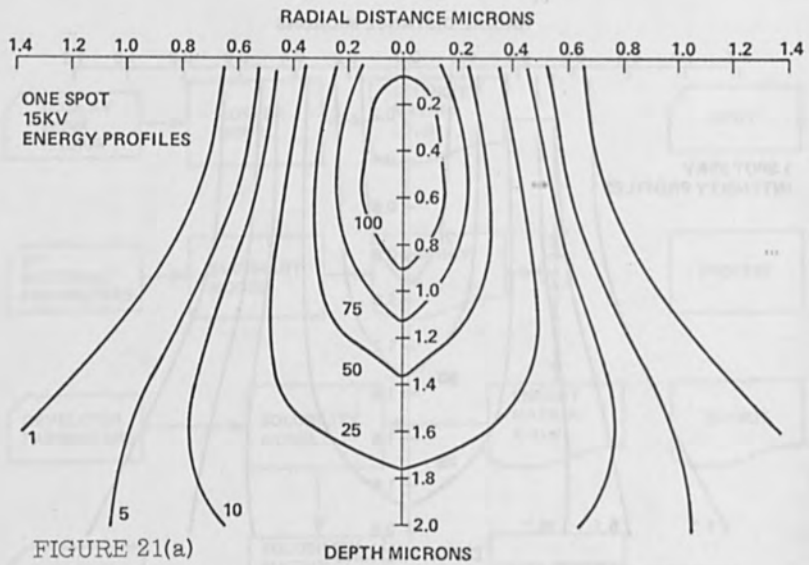


FIGURE 21(a)

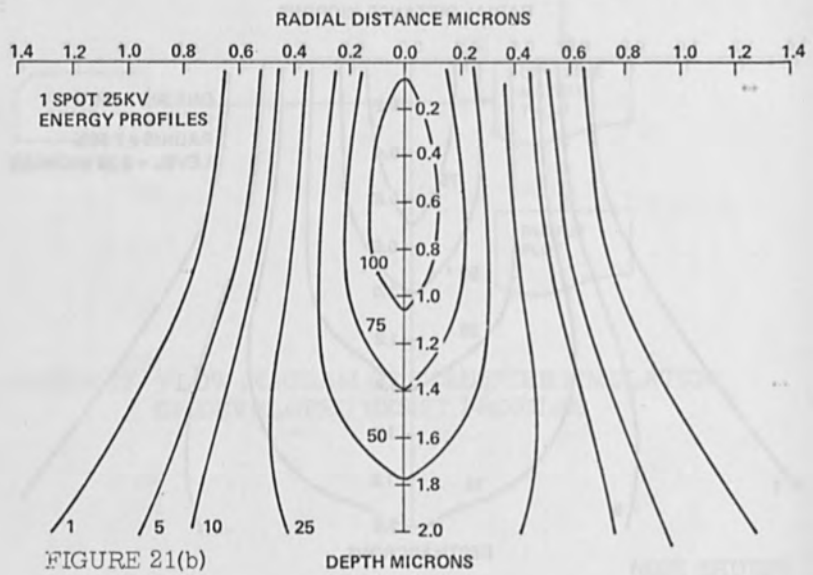


FIGURE 21(b)

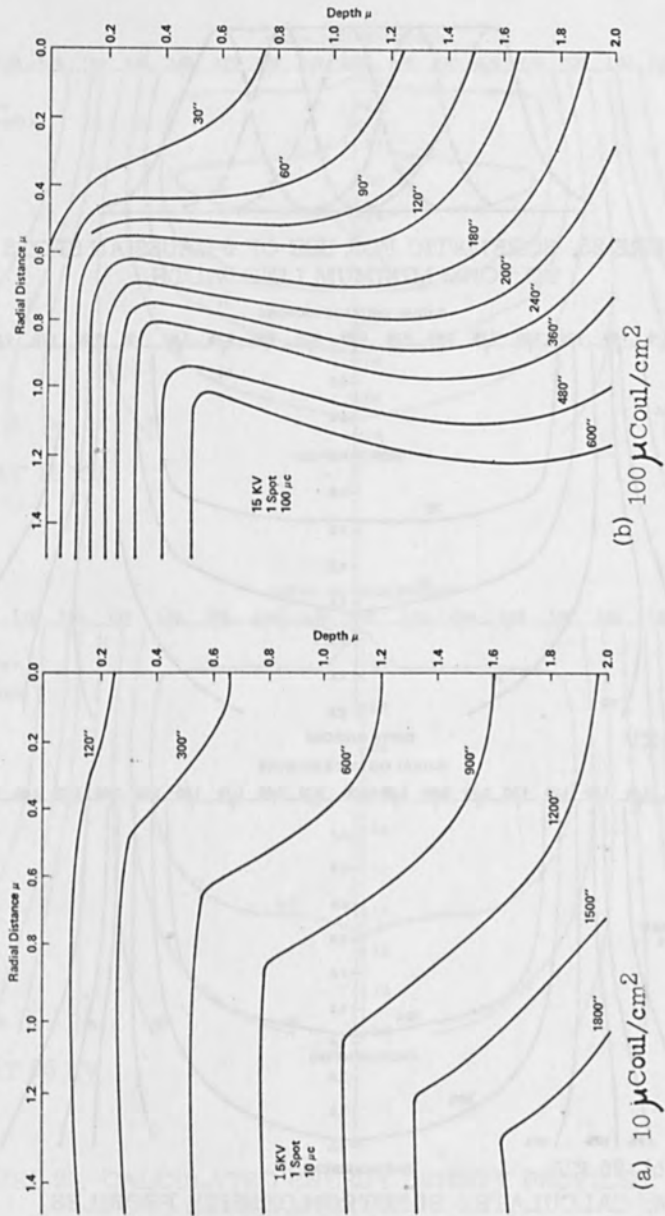


FIGURE 22. CALCULATED DEVELOPED RESIST PROFILES AT 15 KV.

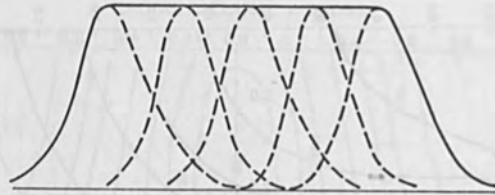


FIGURE 23. SCHEMATIC FOR USE OF 5 GAUSSIAN SPOTS TO FORM MINIMUM LINE WIDTH,

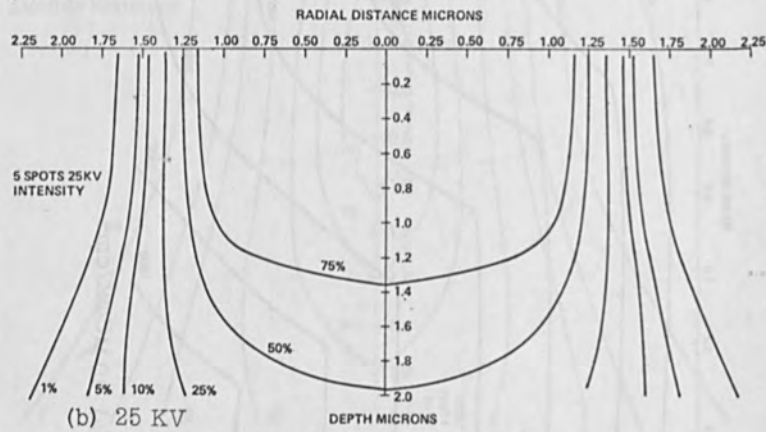
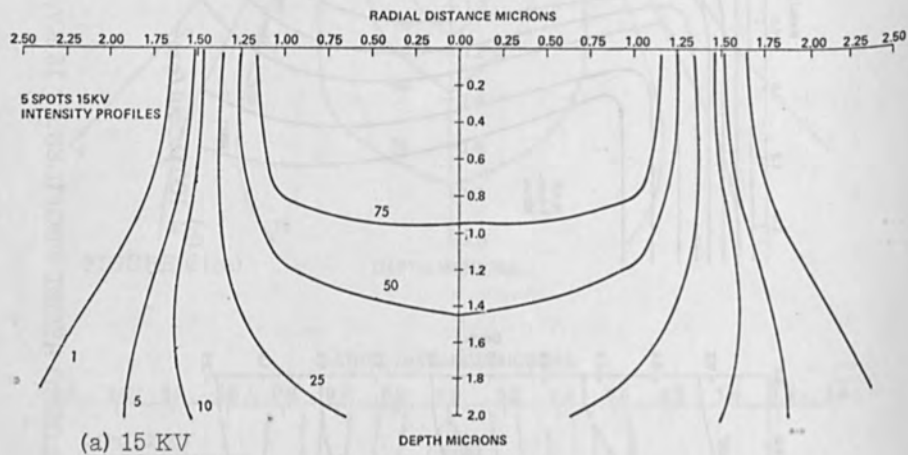
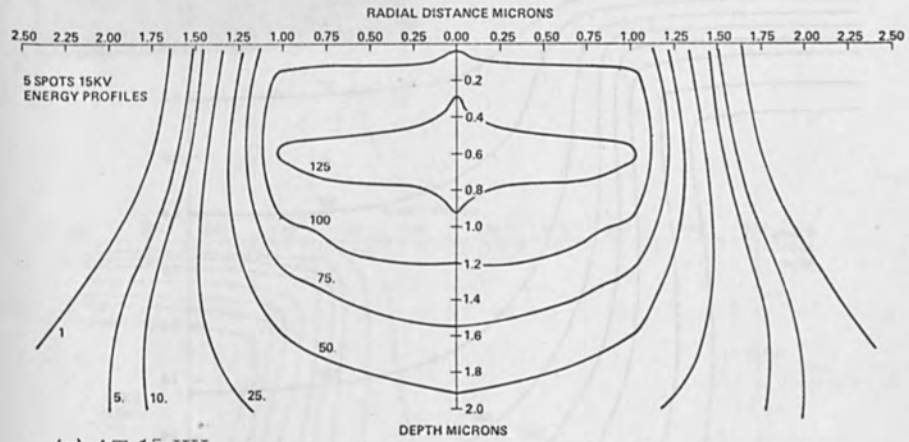
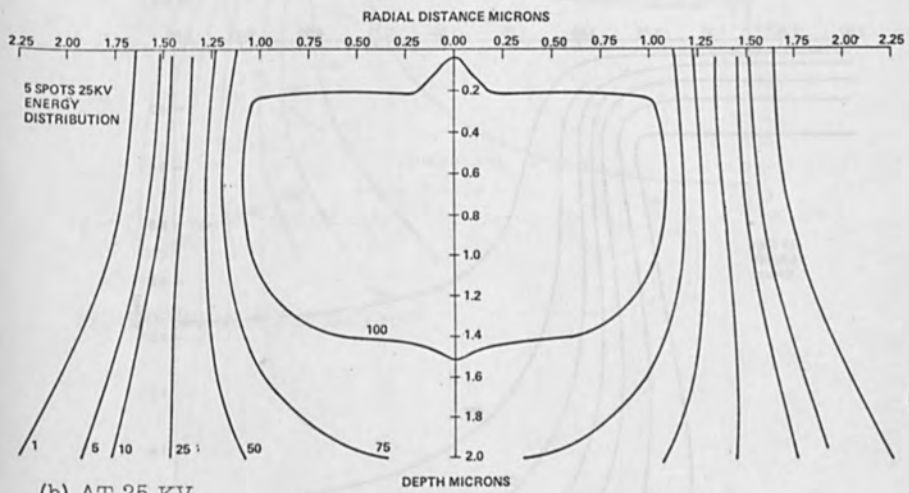


FIGURE 24. CALCULATED ELECTRON DENSITY PROFILES FOR 5 GAUSSIAN SPOTS



(a) AT 15 KV



(b) AT 25 KV

FIGURE 25. CALCULATED ENERGY DENSITY PROFILES FOR 5 GAUSSIAN SPOTS

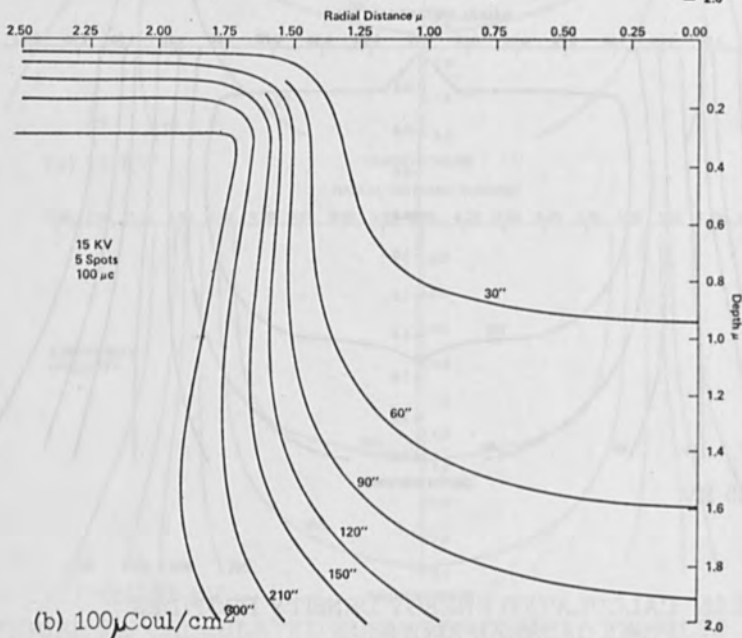
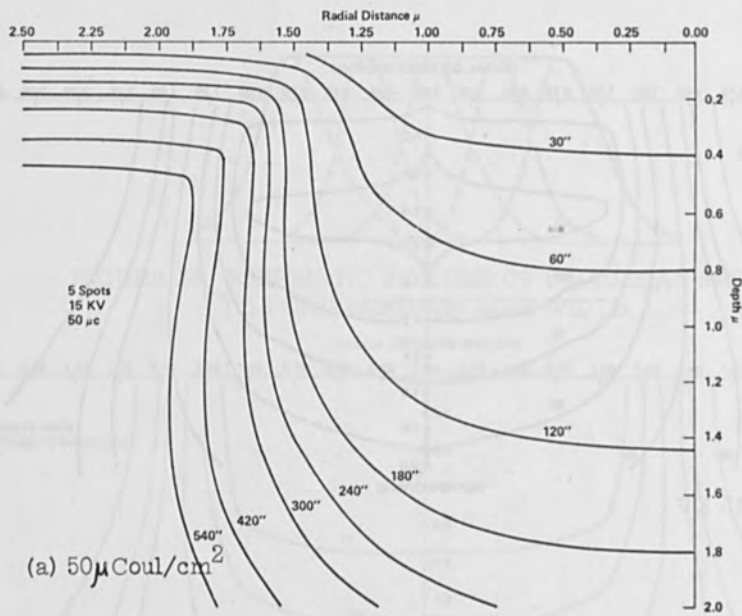


FIGURE 26. CALCULATED DEVELOPED RESIST PROFILES FOR 5 GAUSSIAN SPOTS.

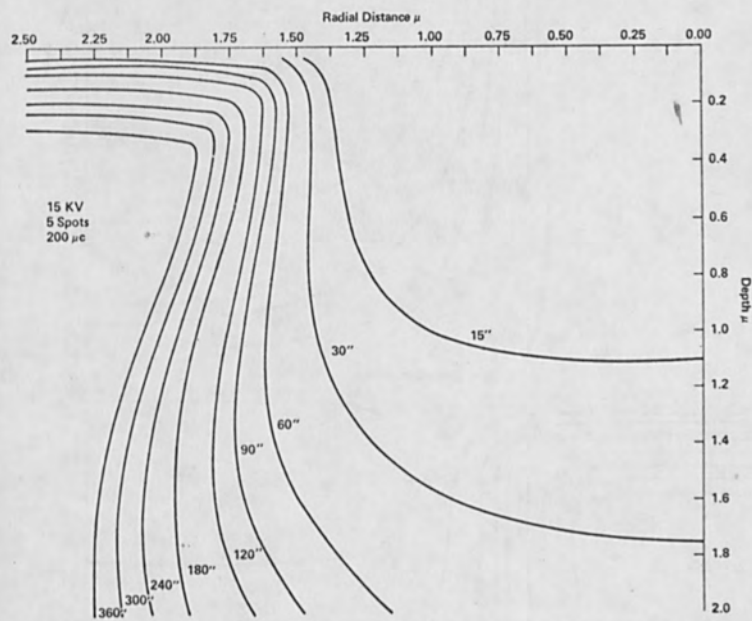


FIGURE 26 (c) $200 \mu\text{Coul/cm}^2$

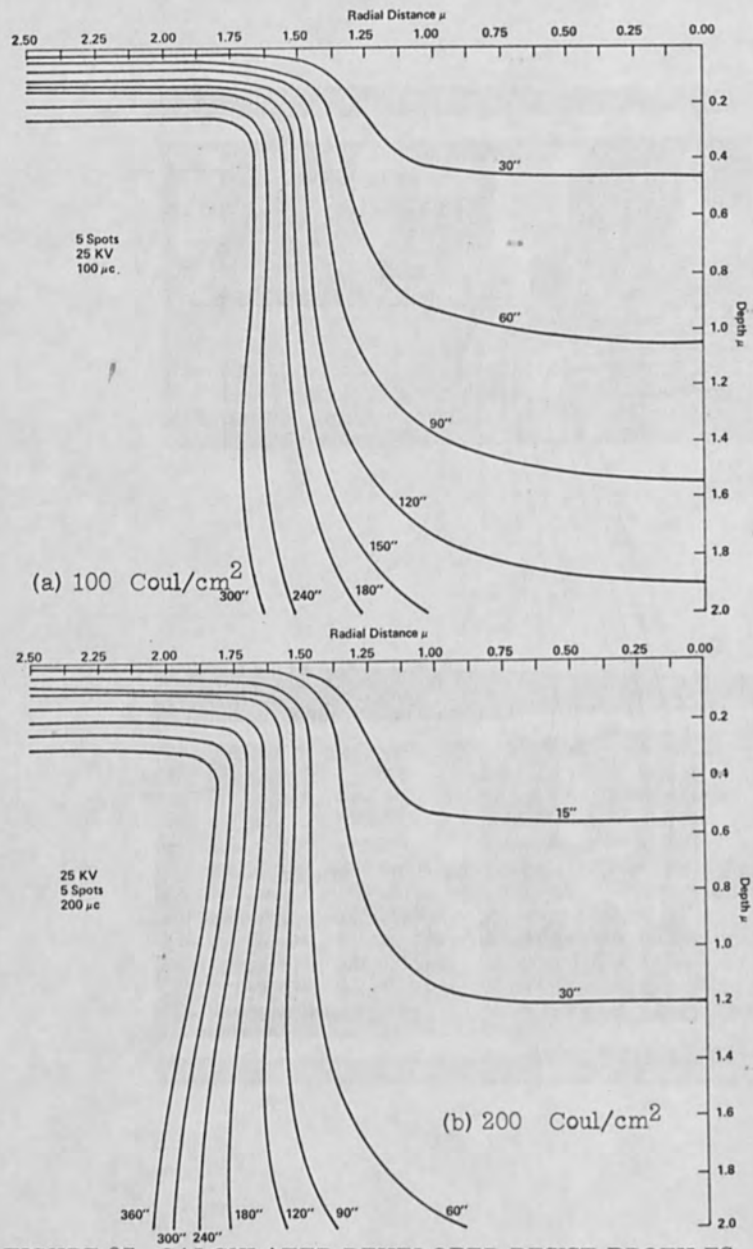
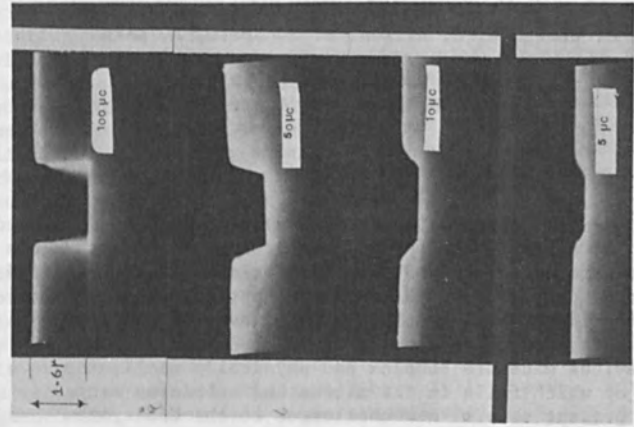
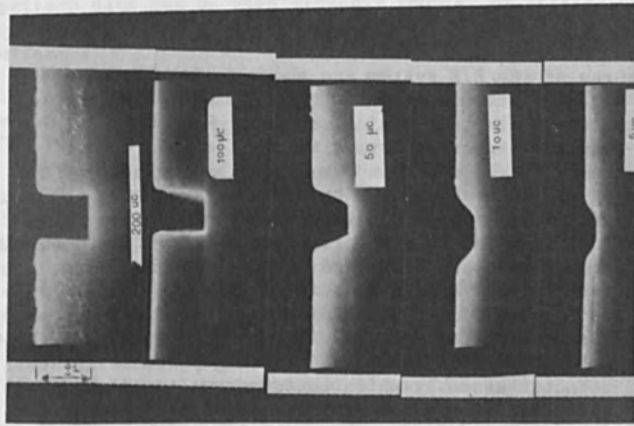


FIGURE 27. CALCULATED DEVELOPED RESIST PROFILES FOR 5 GAUSSIAN SPOTS AT 25 KV



(a) 1 MICRON WIDE LINES



(b) 2 MICRON WIDE LINES

FIGURE 28. ACTUAL DEVELOPED PMMA RESIST PROFILES FOR MULTIPLE SPOT EXPOSURE AT 25KV. INITIAL RESIST THICKNESS 1.6 MICRONS.

ELECTRON BEAM LITHOGRAPHY FOR COMPLEX HIGH DENSITY DEVICES

T. H. P. Chang, A. D. Wilson, A. J. Speth, A. Kern

IBM Thomas J. Watson Research Center
Yorktown Heights, NY 10598

Introduction

A computer controlled electron beam (E/B) system has been developed for the evaluation of electron lithographic technology. The system can be used for direct-wafer exposure and for fabrication of masks required by various contact or projection high resolution optical or x-ray lithography techniques. In E/B lithography applications, the required pattern is produced by using electrons to expose a resist coating. In most cases, the devices made are complex and physically small, the minimum linewidth of which falls in the micron and submicron range. Such requirements present several new challenges to the E/B system which deserve some careful consideration. One of these is the compensation for "proximity effect" and some of the experience in solving this problem will be discussed. The use of an E/B instrument as a new lithography tool has been successfully demonstrated.¹⁻⁵ This technique offers the important advantages of resolution, flexibility, and a high degree of adaptability to automation.

The Instrument

The main features of the E/B system are shown in Fig. 1 and the functional layout of the system is shown in the schematic diagram of Fig. 2. It consists of an electron optical column, which uses a LaB₆ gun,⁶ two electro-magnetic lenses to form a finely focussed beam of electrons. The scanning of the electron beam over the surface of the wafer is performed by a double deflection system using magnetic coils housed inside the final lens. Special attention has been given to the design of the final lens and to the deflection coil system to obtain a good compromise between exposure speed and field coverage. Also, suppression of the eddy current effect associated with the magnetic deflection system has been attained. Beam blanking is achieved by a set of electrostatic plates placed immediately after the gun. Detection of the electron signal for registration and focussing purposes is achieved by a special detector assembly which contains two types of detectors, one for the collection of the secondary-electron and another for backscattered-electrons.⁷ The wafer or the mask plate to be exposed is placed on an x-y workstage which is traversed by stepping motors. The column is generally operated at a beam accelerating potential of 25 kV and the beam diameter can be readily varied to cover the range of 500 Å to several microns.

The system is controlled by a dedicated computer (IBM 1130) with a 32K words memory backed up by several magnetic disc packs each capable of storing 500 K 16 bit words. Data is generally read into the computer via card decks, however, direct linkage of the system computer to a much larger host computer (IBM 91) has also been established. Digital and analog electronic hardware and necessary software have been developed to enable the electron beam system to perform and execute several lithography functions under computer control. The major examples of these automated functions are pattern writing, work stage movement, and registration of overlaid patterns.

The microcircuit pattern to be exposed is composed of an assemblage of basic geometric shapes such as rectangles and parallelograms. Each of these elements can be specified by a few data words. For example, in the case of a rectangle, 4 words are used to specify the x and y coordinates of the diagonally opposite corners. The electron beam is programmed to access each of these basic elements sequentially in a vector manner and expose each by a fill-in scan. For a specified geometrical shape, fill-in is accomplished by a special logic unit, the pattern generator, that generates addresses for the deflection D/A converters according to a predetermined recipe. Vector-scan method of pattern writing is chosen to attain high throughput because in this technique the beam is required to scan only over areas where exposure is required. Furthermore, vector-scan technique has also revealed several additional attributes: 1) the computer storage required for pattern data can be significantly reduced by several compaction techniques, and 2) a convenient solution to the control of the "proximity effect".

The "Proximity Effect"

One of the problems observed when writing complex patterns in a resist coating is that the exposure requirement at different areas of the pattern can be different depending on pattern geometries and packing densities. The main reason for this variation is that the exposure is due to the primary electrons of the incident beam and electrons backscattered from the substrate. The backscattered electrons can emerge over a relatively large region and can therefore affect the exposure of areas some distance away from the point of beam incidence giving rise to the effect generally known as "proximity effect". Because of this effect larger pattern geometries usually require less exposure dosage than the smaller ones and small patterns in closely packed areas would also require less exposure than those in the isolated locations.

Fig. 3 is an experimental result showing the variation of exposure dosage over a range of linewidth and packing density. The ordinate of Fig. 3 represents the normalized exposure dosage (i.e. charge per unit area) with the exposure dosage required for half micron lines at infinitely large gap spacing taken as unity. The abscissa represents the

packing density which is measured as the gap width ie the clear spacing between the lines. Four families of curves are given, representing from top to bottom a series of $1/2 \mu$, 1μ , 2μ and 10μ lines. This result is obtained with a beam accelerating potential of 25kV and a 6000 \AA thick PMMA resist⁸ on silicon substrate. It can be seen that for isolated lines (i.e. large gap value), the exposure dosage variation between a half micron line and a ten micron line can be as high as 50%. Also the variation of exposure dosage for half micron lines in an isolated location (gap spacing $> 3\mu$) to those in a closely packed area (gap spacing = $1/2\mu$) can be as much as 25 to 30%. Such variations become less significant as the linewidth and gap spacing are increased. It should also be pointed out that because "proximity effect" is created by backscattered electrons, the variation of exposure is thus dependent on beam accelerating potential, resist material and thickness, and substrate material. It can be seen from Fig. 3 that in the case of a simple pattern with relatively large geometries (above one micron) the variation of required exposure can usually be taken care of by the latitude in resist exposure tolerance. However, for more complex patterns with micron and submicron geometries, such required exposure variation is often larger than the acceptable latitude of the resist exposure and some means of providing an adjustment to the exposure dosage is therefore required.

Compensation Technique for "Proximity Effect"

It has been found that an effective way of solving this problem is to selectively vary the scanning speed of the beam according to the exposure requirement. During vector-scan write, a convenient way to adjust for the exposure dosage is to vary the speed of the fill-in scan of each of the basic pattern elements. The basic principle of this approach is as shown in Fig. 4. In order to achieve selective exposure dosage automatically, a digital clock controlling the scanning speed of the electron beam is placed under the control of the computer. The information needed to instruct the computer to apply such adjustment is incorporated into the data which defines the pattern elements. This additional instruction can be introduced into the data file during preparation of the pattern data. By this means, the computer automatically varies the exposure speed as the pattern is being written. This approach has been successfully put into operation and it has demonstrated a higher flexibility than several other potential solutions to this problem such as applying adjustment to beam current or special tailoring of pattern geometries etc.

Fig. 5 shows a test pattern consisting of a family of lines ranging in line width from 0.5μ to 10μ at a range of packing density of 0.5μ gap to 10μ gap. The pattern also contain some 1μ and 2μ squares at different packing densities. Successful exposure of this data cannot be made without the adjustment of scanning speed to compensate for the "proximity effect". However, by the application of scanning speed

adjustment, good exposure results have been achieved for all elements as shown in Fig. 5, 5A and 5B.

This compensation technique has also been successfully applied to the exposure of complex device patterns. Fig. 6 shows an 8K bit bubble device fabricated by electron beam exposure with the aid of this compensation technique. All major functions of this device have been tested and were found to operate satisfactorily.⁹ The minimum linewidth of the permalloy bars in this device is 1μ with a critical spacing of 0.75μ as required for the generation of 2μ bubbles. A considerable variation of packing density of pattern lines is required in this kind of device. For example the Y-bars in the center of the field are much more loosely packed than the chevrons at the outskirts of the field as shown in Fig. 6A and 6B which are scanning electron micrographs of the elements in these two areas respectively fabricated with the compensation technique applied. Several other critical areas in these devices are also severely affected by the "proximity effect" and these include the transfer gate area and the bubble generator area etc. It has been found that without applying the compensation technique, correct exposure of such device pattern is extremely difficult whereas with the compensation applied satisfactory exposure is achieved routinely. Successful exposures have also been achieved for the same pattern with $1/2\mu$ lines using this compensation technique.

Summary

An operating computer controlled vector-scan E/B microcircuit/mask fabrication system has been briefly described. High performance capability of the system is evident by an example of an 8K bit bubble memory test chip.

A new and relatively simple technique for the compensation of "proximity effect" in the exposure of electron resist coating is introduced. The basic principle of this technique is to adjust the scanning speed of the electron beam at each pattern element according to need via the computer. Such a solution can be easily incorporated in a vector-scan system.

Acknowledgment

The authors gratefully acknowledge the technical contribution of W. W. Blair, W. L. Keller, H. Luhn and helpful discussions with A. N. Broers and M. Hatzakis. The fabrication of the bubble device was carried out in conjunction with the magnetic bubble group under H. Chang at IBM Thomas J. Watson Research Center. The scanning electron micrographs were taken by H. Luhn.

References

1. Hatzakis, M. and Broers, A. N., Record of 10th Symp. on Electron, Ion and Laser beam Tech., L. Morton, Ed., San Francisco Press, San Francisco, (1969) p. 107.

2. Chang, T. H. P., and Wallman, B. A., IEEE Trans. on Electron Devices, ED-19, p. 629, 1972.
3. Wolf, E. D., 1973 Ultrasonics Symp. Proceedings, J. de Klerk, Ed., IEEE, New York, (1973), p. 510-516.
4. Varnell, G. L., Spicer, D. F. and Rodger, A. C., J. Vac. Sci. and Tech., 10, (1973) p. 1048
5. Pease, R. F. W., Henderson, R. L. and Dalton, J. V., J. Vac. Sci. and Tech., 10, (1973) p. 1078.
6. Broers, A. N., J. Sci. Instr., Ser. 2, 2, (1969).
7. Chang, T. H. P., 8th Internat. Congress on Electron Microscopy, Canberra, Australia, August 1974.
8. Haller, I., Hatzakis, M., and Srinivasan, R., IBM J. Res. and Devel., 12, (1968) p. 251.
9. Kryder, M. H., Ahn, K. Y., Almasi, G. S., Keefe, G. E., and Powers, J. V., Proc. Internat. Mag. Conference, May 1974, Toronto, Canada.

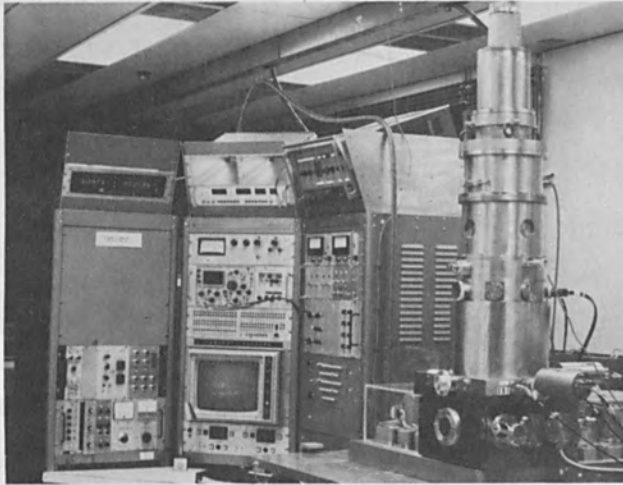


Fig. 1
The Electron Beam Column and the Control Console

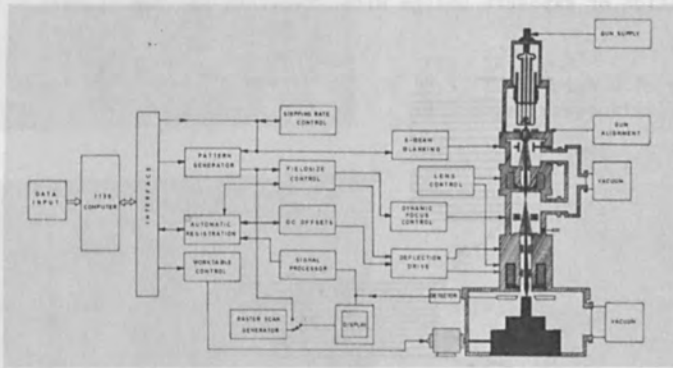
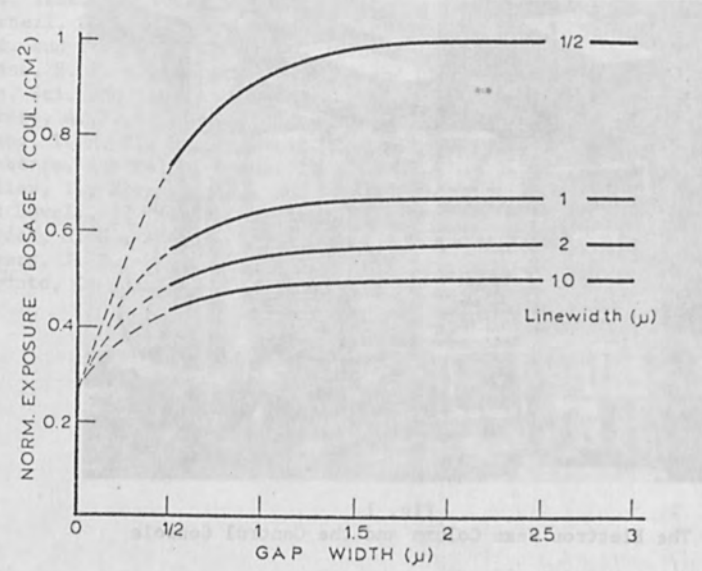


Fig. 2
Computer Controlled Electron Beam System

Cheng, T. H. P., and Villanar, S. A., 1982 Trans. of Electron Microscop. 21-15, p. 374, 1977.
 Villanar, S. A., 1979 Ultramicroscopy 3, p. 107, 1979.

FIG. 3



Variation of Exposure Dosage with Linewidth and Gap Spacing.

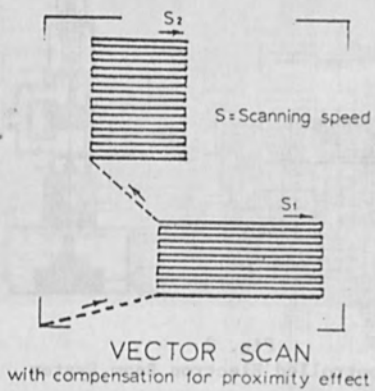


FIG. 4

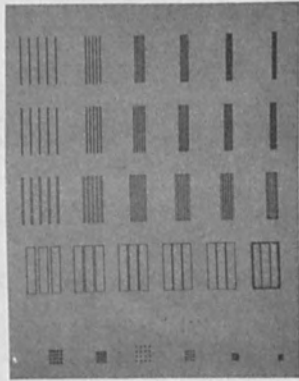


Fig. 5
"Proximity Effect" Test Pattern

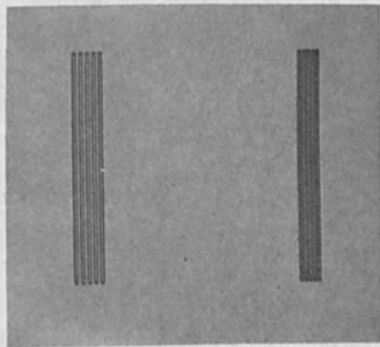


Fig. 5A
0.5μ lines with 0.5μ gaps and
0.75μ gap respectively

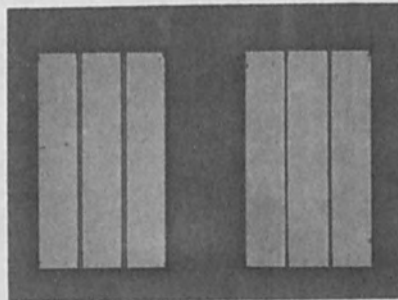


Fig. 5B
10μ lines with 0.5μ gap and
0.75μ gap respectively

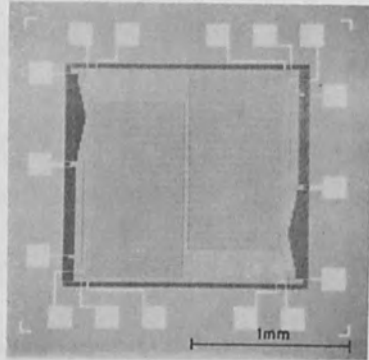


Fig.6
An 8k bit bubble memory chip

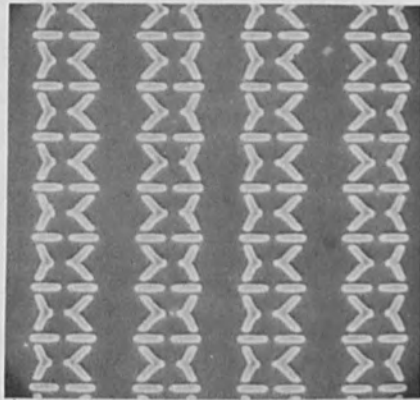


Fig.6A
Details of Y-bar region
showing 1μ linewidth
structures

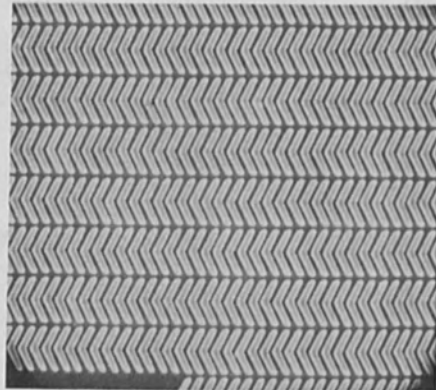


Fig.6B
Details of chevron region
showing high packing den-
sity of 1μ lines

INDEX

A

Accel-decel system, 165
 Acoustic impedance, 201
 -surface wave, 3
 Active silicon devices, 139
 Adiabatic heating, 414
 AES, 139, 140, 141, 142
 Air cored magnet, 123, 124
 -guage, 334
 AISI 316L, 388
 Al 5083, 381
 -7075, 383
 Amorphous layer, 230
 Annealing, 231
 Annular aperture, 191
 Anode, 248
 Arc welding (GMA, GTA), 321
 Area exposure, 55
 Argon primary ions, 140
 As-vacancy, 229, 231, 232
 Attenuation constant, 28
 Automotive, 264, 271
 Average backscatter energy, 214

B

Backscattered electrons, 211
 Backscattering, 52, 53
 -correction, 147
 Backscatter yield, 214
 Bead-on-plate welds, 325
 Beam converting mask, 158
 -plasma, 377
 -test method, 379
 Bethe energy loss, 207
 -electron range, 89
 Bias sputtering, 257
 Blaze angles, 25
 Blazed diffraction gratings, 23,
 27, 29
 Boron diffusion, 10
 -glass, 10
 Bremstrahlung x-rays, 37
 Brittle, 322
 Bubble memory, 111
 Butadiene polymers, 77
 Butt welds, 323

C

Caesium photocathode, 126
 Carbon phenolic, 194
 Carriage, 314
 Cartesian coordinates, 339
 Catalytic reactor, 264
 Cathode, 248, 498, 500
 Ceiling temperature, 85
 Changes in
 -film, 416
 -substrate, 413
 Channeling effect measurement, 227
 Chemical effects, 141
 Chemical ion plating, 255
 Child Langmuir equation, 501
 Clamp on system, 312
 Circular welding, 310
 CMOS, 242
 Cold cathode, 501
 Collapsible steering, 292
 Communication, 319
 Compensating electrode, 464
 Computer
 -control, 270
 -pattern generation, 113
 -trajectories, 525
 Contactless text method, 153
 Continuous time series mode, 402
 Control grid, 503
 Controlled secondary electron
 emission, 154
 Crack formation, 415
 Craneberg criterion, 503
 Crosslinking yields, 79

D

Deep welding geometry, 366, 369
 Defects, 229
 Deflection
 -aberrations, 188
 -coils, 99
 -width measurement, 181
 Depolymerization, 83
 Deposition morphology, 256
 Depropagation, 84
 Depth

- doze profile, 474
- resolution, 141, 145
- Depth/width ratio, 290
- Deuterium, 488
- Deuteron, 486
- Dial feed, 266, 267
- DIDA, 165, 172
- Dielectric liner, 325
 - waveguide, 319
- Diode, 471, 472
 - energy, 472
 - fabrication, 38
 - gaps, 472
 - graph, 45
 - impedance, 472
- Disc electron beams, 457
- Discharge pressures, 255
- Discrete time model, 400
- Dislocation densities, 14
- Distortion, 307, 326
- Distribution, 250
- Drift
 - chamber, 472, 483
 - tube, 483, 484, 486
- Drifting beam geometry, 482
- Drilling by electron beam, 432
- Drive shaft, 292
- Ductile, 322
- Dynamic
 - beam deflection, 451
 - focus, 189
 - focussing, 97
 - range, 172

E

- EBIC, 178, 179
- Effect of
 - accelerating voltage, 355
 - vaporization, 383
 - workchamber pressure, 356
- Efficiency coefficient, 457
- Electrode configuration, 521
- ECM, 435
- Electron
 - bombardment discharge, 518
 - chemical, 177
 - demagnified image, 3
 - gun, 166
 - image projector, 121
 - irajectories, 506
 - metal vapor interaction, 447, 448
 - projection lithography, 3
 - rest mass, 487
 - scattering, 86, 204
 - sensitivities, 76
 - trajecting equation, 458, 463
- Electron beam, 111, 115
 - conversion, 157
 - current, 482
 - current density, 139
 - diameter, 382
 - diode, 482, 483
 - energy, 379, 482
 - evaporation, 3
 - generator, 499
 - gun, 432
 - lithography, 113, 214
 - machining (EBM), 435
 - non vacuum, 337
 - pattern generator, 97, 104
 - power, 297
 - power density, 432
 - propagation, 450
 - pumped laser, 498
 - scanning, 3
 - voltage, 214
 - welding, 264, 319, 368
 - writing, 96
- Electrostatic, 489
- ELTRAN, 474, 475
- Emission control, 301
- Emitter-base junction, 146
- Energy
 - deposition, 214
 - dissipation, 497
 - distribution, 473
 - equation, 368
 - filter, 165
 - input, 288
 - loss, 206
- Engraving by
 - ceramics, 439
 - electron beam, 439
 - roto-gravure, 439
 - vapor-deposited layers, 439
- Equi-energy, 207
- Equipment welding, 338
- Ethylene diamine procatechol etch, 10
- Evaporation systems, 457

Exposure
 -contours, 49
 -patterns, 49
 -results, 36
 Exposures at edges, 53

F

Faraday
 -cage, 348, 349
 -cup, 483
 Feed-through, 310
 FET, 3, 242
 Field emission, 499
 Flange, 320, 322
 Floating zone melting, 457
 Fluence, 469
 Flying spot scanner, 112
 Fracture, 322
 -path length, 324

G

GaAs, 226
 Gas content, 256
 Gaussian distribution, 369, 472
 Geometric distortion, 4
 Glide welding, 380, 383
 Gigawatts, 474
 GPC, 72
 Graphite calorimeter, 474, 475
 Grueneisen parameter, 194
 Gun
 -efficiency, 457
 -geometry, 507

H

Hardness, 322
 Hard vacuum, 357
 Heat
 -affected zone, 322
 -exchanges, 308
 -shield, 8, 14
 -treatment, 232
 Helix waveguide, 319
 He-Ne laser, 101
 High energy density beam, 380

High power evaporators, 447
 High ripple, 354
 High speed electron beam pattern
 generation, 95
 High speed electron resist, 71
 Hollow cathode, 501
 Holographic grating technique, 23
 Hoop stresses, 327
 Hydrogen, 482

I

IGFET, 3
 Igniter electrode, 501
 Impedance, 470
 Implantation system, 519
 Implanted
 -arsenic, 146
 -boron, 146
 -phosphorus, 144
 In-depth analyzer, 163
 Inertia welding, 321
 Integrated optics, 3
 Intensity distribution, 366
 Interferometer, 102
 Ion
 -beam extraction, 518
 -bombardment, 254
 -energy, 486, 487
 -implantation, 254
 -implanted diode, 180
 -microscopy, 518
 -milling, 238
 -plating, 254
 -source, 519
 -trajectories, 519
 -yield, 168
 Irradiated polyvinylacetate, 80
 Irradiation system, 72

J

Junction measurement, 177

K

Killed steel, 321, 385
 Kodak microresist, 8, 12

- L
- La B₆, 499, 500
 Lambertian characteristics, 448
 Langmuir potential, 520
 Large area electron beam, 497, 509
 Laser, 243
 -welding, 321
 Laser pumped dense plasma, 8
 LBM, 435
 LC circuit, 471
 Legendre polynomials, 124
 Lenard thickness, 341, 342
 Lift-off, 10
 Lift-off technique, 52
 Linear, 313
 Line source, 207
 Line width, 55, 212, 213
 Low perveance
 -extraction, 520
 -ion beam, 518
- M
- Machining
 -by electron beam, principles, 434
 -industrial applications, 436
 -machine system, 432
 -numerical control, 433
 -process, 412
 -removal rates, 435
 Magnetic
 -bubble device, 242
 -confinement, 248
 -domain, 242
 Magnetron effect compensation, 468
 Mandrel, 309
 Martensite, 322
 Marx generator, 470
 Mask
 -fabrication, 35
 -generation, 114
 -transmission, 26
 Mass filter, 168
 -resolution, 170
 Maxwellian emission, 503
 Mean free path, 216
 Metal acrylate resist, 7, 11
- Michelson mode, 196
 Microfabrication, 111, 115, 188
 Micro ion milling, 241, 243
 Micromovement stage, 15
 Microstructure, 322
 MIE Grueneisen form, 196
 Millimeter waveguide, 319
 Minicomputer, 264
 Monte Carlo
 -calculation, 88, 89
 -code, 474
 -models, 87
 MOS, 242
- N
- Negative resist, 74
 Neptune-C pulsed electron beam, 469, 473
 Neutralization time, 486
 Neutron deflector, 486
 Ni-C, 416
 Non vacuum electron beam welding, 287, 288, 293
 Normarski microscope, 188
 Nozzles, 320
 Nuclear activation, 485
 Nuclear physics, 482
- O
- Off-contact lithography, 7
 Olson model, 483, 484, 488
 Optical grating, 28
 Orientation effects, 141
 Oxygen primary ions, 140
- P
- Packaging components, 153
 Palladium photocathode, 126
 Parallel exposure, 4
 Parallel-line exposure, 52
 Partial penetration, 399
 Paschen breakdown, 501
 Pattern registration, 101, 108
 Pearlite, 322
 Penetration, 324, 337, 346, 351, 352
 Penumbral region, 126
 Penumbral shadowing, 5

Perforation

- applications to various materials, 437
- by electron beam, 436
- hole geometry, 437
- inclined holes, 438

Permalloy, 243

Phase detector, 15

Phase sensitive detection, 128

Photocathode, 125

Photochemical, 177

Photolithography, 95

Photolithography, 3, 38

Photoluminescence, 223

Photomultiplier package, 199

Photoresist, 25, 28

Pierce electrode, 508

Pierce gun, 518

Piezoceramic transducer, 15

Pistolet, 308

Pitch, 311

Planar, 26

Plane source, 210

Plasma

- density, 519
- physics research, 482
- cathode, 501, 503
- sheath, 519

Plate, 309

- thickness, 378

PMMA (polymethylmethacrylate), 7

9, 10, 25, 29, 37, 38, 72, 73, 88, 90, 91, 211

p-n junction, 177

Point source, 210

Polyglycidyl methacrylate-co ethyl acrylate, 8

Polymers, 71

Poly (olefin sulfones), 81

Porosity, 322

Portable, 307

Positional accuracy, 105

Positive resist, 74

Power density distribution, 349

Primary mask generation, 114

Production system, 115

Projection machine, 130

Pulse generator, 469

Pumping speed, 249

Pyrolytically, 11

Q

Quantitative analysis, 399

R

Radial blow up, 484

Radial fluence map, 473

Random scission, 81

Rate, 249, 250

Relativistic electron beams, 481

Residual stresses, 327

Resistance discrimination, 156

Resist contrast, 73

RF

- backspattering, 241
- plasma etching, 241

Rim steel, 321

Ring type electron gun, 457, 460

RMS, 242

Rotary table, 268

Rotors, 315

Rutherford expression, 206

S

Saito equations, 74

Scanning electron microscopy, 188

Scattering, 339

Schottky Barrier, 181

Seam scanning, 269

Secondary ion mass spectrometry, 165

SEM, 113

Semiconductor detectors, 125, 126

Shape decision, 377, 380

Short test method, 153, 158

Silicon (100), 10

- elastic deformation, 13
- fracture, 13
- membrane, 12

SIM, 137, 140

Single lens, 167

SiO₂, 232

Slater's method, 198

Sliding, 315

- seal, 264

S-melting phenomenon, 379

Soft vacuum, 265

- exposure time, 7
- flux, 7

- lithography, 3, 4
- source, 6, 7
- x-ray, 29
- Sources, 255
- Space charge limited, 519
- Spatial profiles, 210
- Spectra physics model, 199
- Spiking behaviour, 399, 403
- Sputter clean, 254
- Sputtering, 248
 - yield, 140
- Stage shift, 103
- Standoff distance, 289
- Step length, 206
- Strip, 313
- Submicron patterns, 3
- Substrate, 213
 - atomic number, 208

T

- Talystep, 140, 141
- Tantalum resistors, 139
- Tellurium, 226, 227, 228
- Temperature, 250, 325
- Tensile strength, 323
- Test methods, 381
- Theoretical considerations, 370
- Thermal equilibrium, 353
 - expansion, 10, 14
 - model, 6
 - velocity, 506
- Thin film, 206
 - machining, 412
- Timing jitter, 470
- Tracking, 315
- Transistor, 179
 - cross section, 45
 - mode, 320
 - picture, 46
- Transmission, 170
- Trigatron switch, 470
- Trigger pulse, 470
- Triode, 314

U

- Ultimate strength, 323
- Undercut resist, 52
- Unexposed gaps, 55

V

- Vacuum, 323
 - breakdown, 501
 - window, 9
- Vapor channel, 340
- Vapor channel geometry, 367
- Vapor cloud, 449, 450, 451
 - development, 81, 84
 - steam propagation, 448
- Vasterlogic, 100
- Vickers hardness, 322
- Voltage breakdown, 497, 502

W

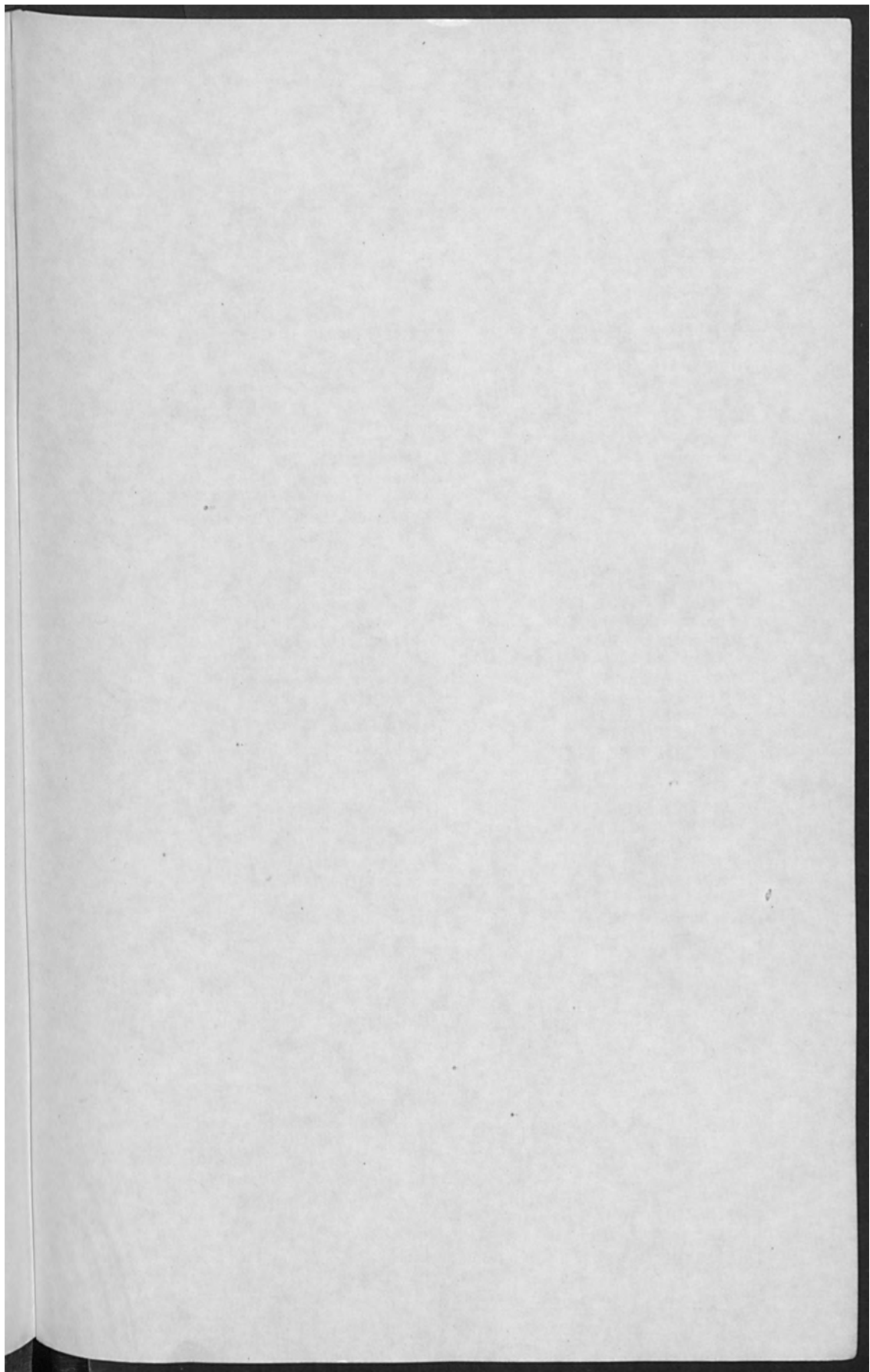
- Waveguide, 319
- Weld
 - topography, 297
 - width, 296
- Weldability, 321
- Welding, 319
 - parameters, 346, 351
 - speed, 337
- Work shops, 316

X

- X-ray
 - alignment, 123
 - energy flux, 37
 - lithography, 23, 38, 39
 - mask figures
 - quanta, 37

Y

- Yield strength, 323



lithography, 3, 4
-sources, 6, 7
-ray, 25
Sources, 215
Space charge limited, 715
Spatial profiles, 210
Spectra physics model, 139
Spiking behavior, 389, 403
Sputter clean, 254
Sputtering, 244
-yield, 240
Step width, 103
Standoff distance, 289
Step length, 104
Strip, 313
Substrate patterns, 1
Substrate, 217
-strain sensor, 208

T
Tape, 140, 141
Tantalum resistors, 125
Tolluam, 225, 227, 228
Temperature, 230, 232
Tensile strength, 223
Test methods, 261
Theoretical considerations, 275
Thermal equilibrium, 252
-expansion, 13, 14
-model, 6
-velocity, 204
Thin film, 224
-mechanics, 412
Timing filter, 434
Tracking, 215
Transistors, 179
-cross section, 47
-mode, 170
-structure, 47
Transmission, 170
Trigger switch, 478
Trigger pulse, 470
Trough, 224

Ultimate strength, 222
Undriven resist, 52
Unexposed paper, 51

V
Vacuum, 24
-breakdown, 201
-clean, 9
Vapor channel, 240
Vapor channel geometry, 247
Vapor cloud, 417, 420, 421
-development, 41, 24
-atom propagation, 422
Vastarlogia, 200
Vickers hardness, 122
Writing breakdown, 197, 202

W
Waveguide, 212
Weld
-typography, 229
-width, 226
Weldability, 221
Welding, 219
-parameters, 240, 251
-speed, 217
Wet angle, 216

X
X-ray
-alignment, 221
-energy line, 11
-lithography, 21, 22, 23
-mask cleaning
-particle

Y
Yield strength, 221

